SEPTEMBER 15, 1990

Analytical CHEMISTRY

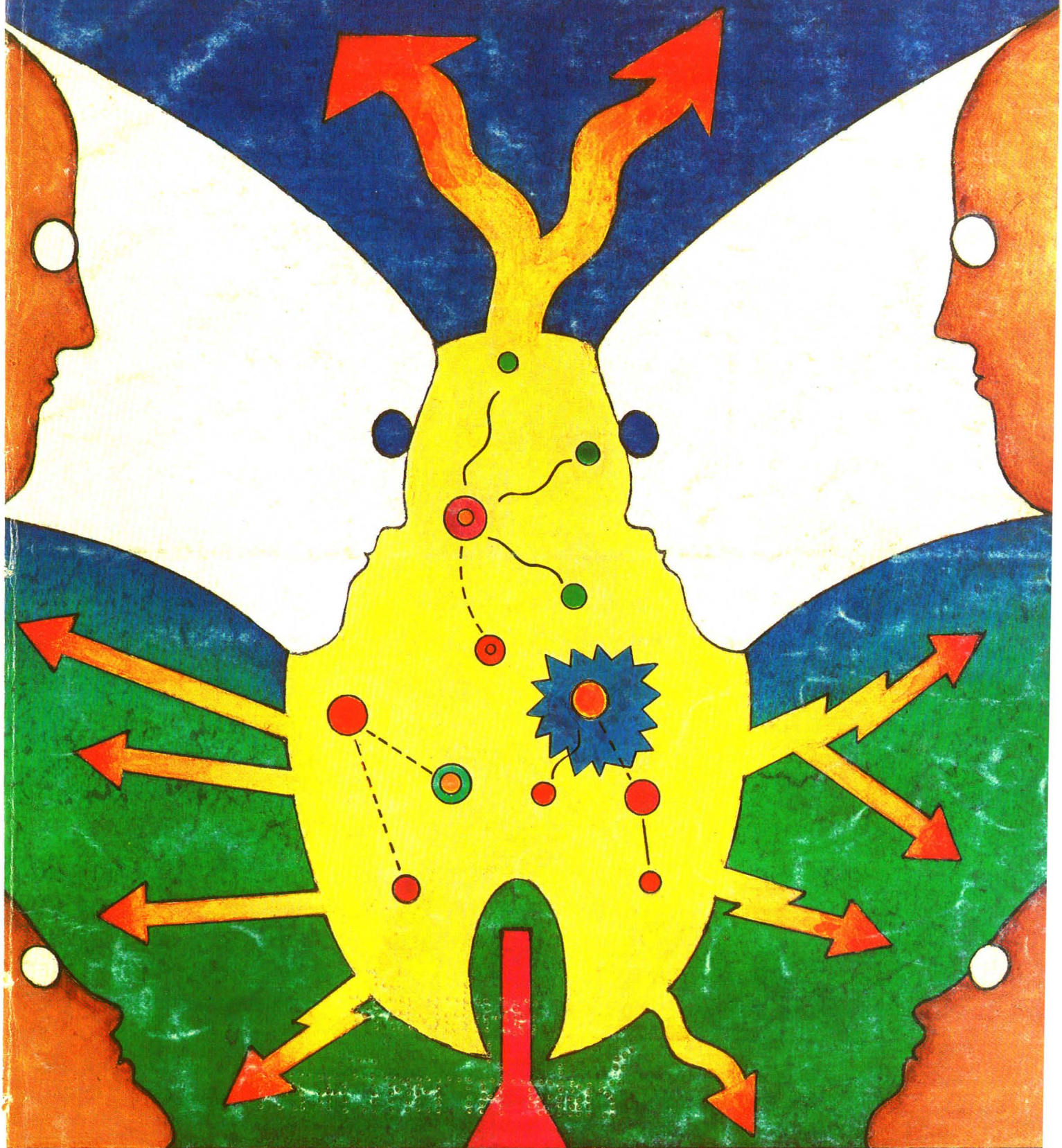

GLOW DISCHARGE TECHNIQUES 943 A

Full Power FTIR Spectroscopy

Integrated sampling solutions with Mattson Instruments' Galaxy™ series of FTIR spectrometers.

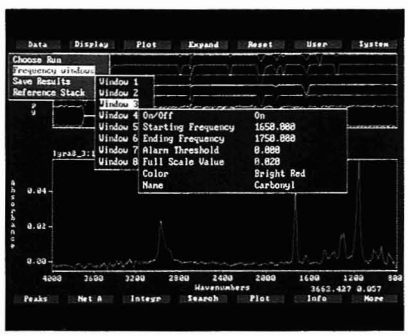

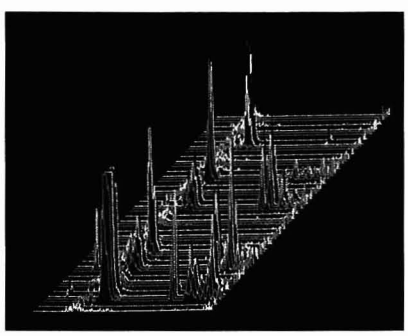

Grob test mixture with the Series 100 GC-FTIR interface; Entropy reconstruction and 3-D spectral display.

Mattson Instruments' Galaxy series of FTIR spectrometers provides the highest value ever available in infrared analysis.

- ☐ Reliable, high performance operation for analysis of your toughest samples.
- ☐ Research grade interferometer control.
- ☐ Enhanced speed of analysis.
- ☐ Small instrument footprint.
- ☐ Compatible with all standard sampling accessories.

Full-featured data analysis software with real-time spectral acquisition.

- ☐ Real-time display of infrared spectrum and reconstructed chromatogram or thermal data.
- ☐ Up to eight functional group specific reconstructions for instant compound recognition.
- ☐ Full access to all spectral acquisition parameters allows operator selection of time based resolution.
- ☐ The substantial FIRST™ Software package that includes PLS Quant, Deconvolution, Curve Fitting, Macro capability and quality graphics.

For Less Than You Would Expect

Compare our specifications, capabilities and price. Call us for a quote!

GC-FTIR
TGA-FTIR
FT-RAMAN
FTIR-Microscopy
Galaxy™ Series FTIR

Mattson Instruments, Inc.
1001 Fourier Drive
Madison, WI 53717
Tel. (608) 831-5515
Fax: (608) 831-2093

CIRCLE 90 ON READER SERVICE CARD

If You're Shopping For A Sequential Plasma Spectrometer, Tear Out This Ad & Take It With You.

(TEAR HERE)

In the words of our chief engineer, our *AtomScan™ 25 Spectrometer* is "everything anyone ever wanted in a sequential ICP instrument."

It's the culmination of more than three decades of developmental work, incorporating the best features—RF generator, monochromator, sample delivery and excitation, data system and software—of all previous generations of Jarrell Ash plasma spectrometers.

And whether you are a research spectroscopist or an occasional user, that simply means you are going to get better accuracy and detection limits on every element in any sample matrix with the AtomScan 25 than with instruments costing twice as much.

Don't take our word for it.

Tear out this ad and take it with you on your trip to see brand X. See if they offer you anywhere near as much for so little.

We think we'll make you a believer.

For literature or a demonstration of the AtomScan 25, call (508) 520-1880. Or write Thermo Jarrell Ash Corp., 8 East Forge Parkway, Franklin, MA 02038-9101.

Thermo Jarrell Ash Corporation

A Division of Thermo Instrument Systems, Inc.

CIRCLE 134 ON READER SERVICE CARD

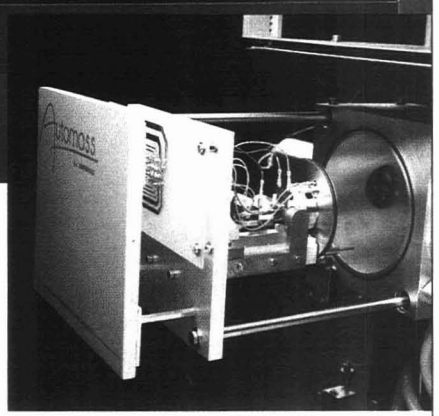

Automass

The Power of Original Thinking

When Nermag set out to develop the premier Automated Benchtop GC/MS Workstation, we were aware there was a need - *your need*, for more analytical power. Power that is simple to use, yet flexible enough to tackle the toughest problems. A true research-grade mass spectrometer was required, not a compromised mass analyzer camouflaged by glitzy game-show software.

Introducing Automass, the benchtop mass spectrometer that only Nermag could build, and the only one of its kind in the world today. The basis of Automass is a state of the art quadrupole with plug-in prefilters and an optimized Ionization Source for EI, CI, and negative ions. Our original Off Axis Ion - Photon Conversion Detector and patented Resolver electronics are enhanced by a differentially pumped vacuum system for real CI spectra.

Automass is controlled by our exclusive LUCY™ software. LUCY does window after window of instrument configuration setting, auto or manual tuning, calibration, mass spectra, chromatographic trace, and data reduction; while simultaneously examining the complete library and quantifying results. You'll Love LUCY.

Automass can flawlessly perform routine analysis all day virtually unattended, or help you tackle the most difficult analytical problem.

Automass advances Mass Spectrometry into the 90's.

Powerfully.

DELSI NERMAG
INSTRUMENTS

France: Delsi-Nermag Instruments, 98terBlvd. Heloise, Argenteuil 9500, Tel: (1) 39.47.66.22, Fax: (1) 39.47.85.66
USA: Delsi Inc., 15701 West Hardy Rd. Houston, TX 77060, Tel: (713) 847-0811, Fax (713) 591-2132
Netherlands: Delsi Instruments BV, Gebouw aetsvelt, van Houten Ind Pk 11, 1381 Weesp, Tel: (0)2940-19611
U.K.: Delsi Instruments Ltd, 38 Thrapston Rd., Brampton, Huntington, Cambs PE 18 8TE, Tel: 0480 431 609
West Germany: Delsi Instruments Gmbh, Otzbachstr 1 D4020 Mettmann, Tel: 02104/25086-87-88
Belgium: Intersmatt, 103, Av. des Volontaires, 1160 Bruxelles, Tel: 2 733.16.32

CIRCLE 28 ON READER SERVICE CARD

SEPTEMBER 15, 1990
VOLUME 62
NUMBER 18

The Audit Bureau

ANCHAM
62(18) 927A–974A/1905–2064 (1990)
ISSN 0003-2700

ANALYTICAL CHEMISTRY (ISSN 0003-2700) is published semimonthly by the American Chemical Society at 1155 16th St., N.W., Washington, DC 20036. Editorial offices are located at the same ACS address (202-872-4570; FAX 202-872-4574; TDD 202-872-8733). Second-class postage paid at Washington, DC, and additional mailing offices. Postmaster: Send address changes to ANALYTICAL CHEMISTRY Member & Subscriber Services, P.O. Box 3337, Columbus, OH 43210.

Claims for missing numbers will not be allowed if loss was due to failure of notice of change of address to be received in the time specified; if claim is dated (a) North America: more than 90 days beyond issue date, (b) all other foreign: more than one year beyond issue date, or if the reason given is "missing from files."

1990 subscription rates include air delivery outside the U.S., Canada, and Mexico

	1 yr	2 yr
Members		
Domestic	$ 29	$ 49
Canada and Mexico	64	119
Europe	96	183
All Other Countries	118	227
Nonmembers		
Domestic	59	100
Canada and Mexico	94	170
Europe	186	336
All Other Countries	208	380

Three-year and other rates contact: Member & Subscriber Services, ACS, P.O. Box 3337, Columbus, OH 43210 (614-447-3776 or 800-333-9511).

Subscription orders by phone may be charged to VISA, MasterCard, or American Express. Call toll free 800-333-9511 in the continental United States; in the Washington, DC, metropolitan area and outside the continental United States, call 202-872-8065. Mail orders for new and renewal subscriptions should be sent with payment to American Chemical Society, Department L-0011, Columbus, OH 43268-0011.

Subscription service inquiries and changes of address (Include both old and new addresses with ZIP code and *recent mailing label*) should be directed to the ACS Columbus address noted above. Please allow six weeks for changes to become effective.

ACS membership information: Lorraine Bowlin (202-872-4567)

Single issues, current year, $8.00 except review issue, $14.00, and LabGuide, $49.00; **back issues and volumes and microform editions** available by single volume or back issue collection. For information or to order, call the number listed for subscription orders by phone; or write the Microform & Back Issues Office at the Washington address.

Nonmembers rates in Japan: Rates above do not apply to nonmember subscribers in Japan, who must enter subscription orders with Maruzen Company Ltd., 3–10 Nihonbashi 2-chome, Chuo-ku, Tokyo 103, Japan. Tel: (03) 272-7211.

Analytical® CHEMISTRY

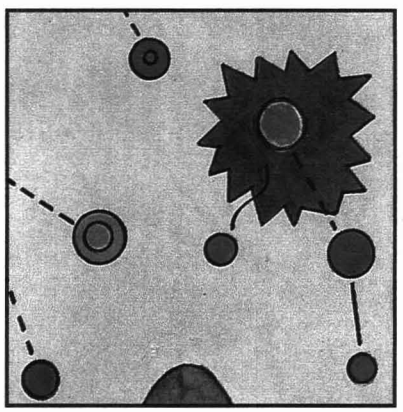

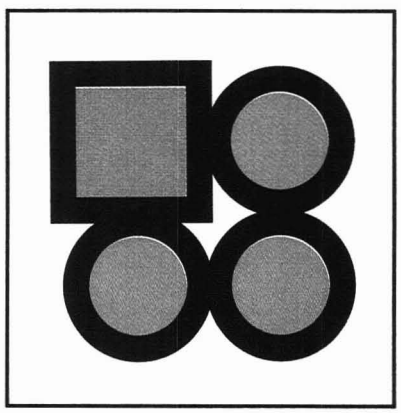

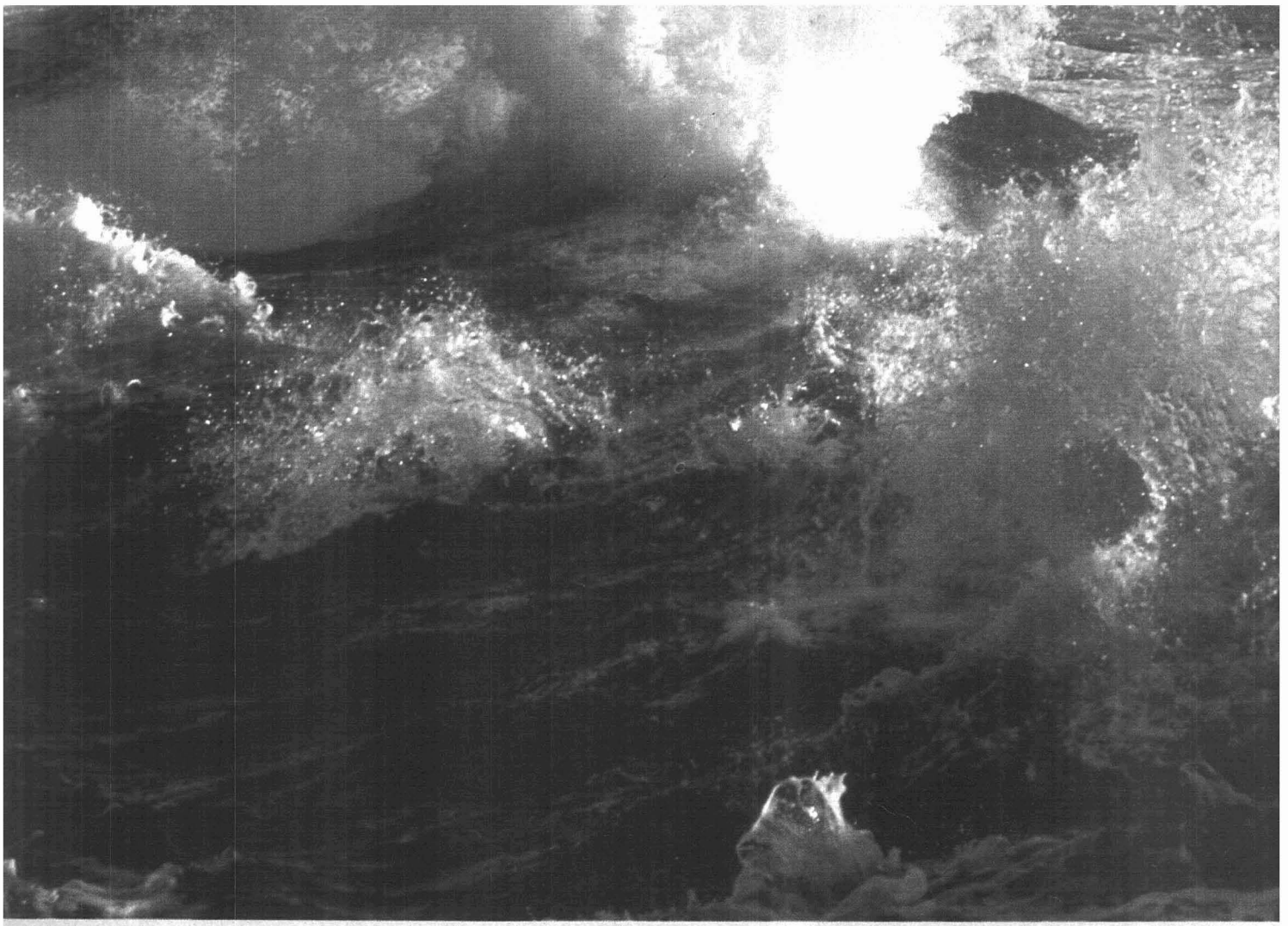

sartorius

0 100 %

+ 00.001 g

R1

T

With 1 mg readability, this is how your balance perceives a liquid sample

Perception is a matter of perspective. To an ordinary balance, a liquid sample with 1 mg readability is as dynamic as a raging sea. In this world made small, slight nudges are earthquakes. A draft from a closing door is a hurricane.

Scientists commonly call these normal laboratory disturbances "ambient conditions." But these common conditions present an uncommon challenge for a high-precision balance, and the display can flicker madly as it tries to stabilize on the correct weight.

Sartorius balances with MC 1 technology are the only balances with a microcomputer—a functioning intelligence *beyond* microprocessors. A microcomputer programmed to filter *out* noise, vibrations, and other disturbances. The result? The display stabilizes in *half the time* of the competition.

With MC 1 technology, your balance will keep its balance, and your results will be true to your world.

For more information on this breakthrough in balance technology, call, write, or circle the number below. Sartorius Instruments, 1430 Waukegan Rd., McGaw Park, IL 60085. Phone: 800•544•3409 FAX: 708•689•2038.

sartorius

Sensitive. Smart. Sartorius.

CIRCLE 125 ON READER SERVICE CARD

BRIEFS

Articles

*Corresponding author

Optical Sensor for Calcium: Performance, Structure, and Reactivity of Calcichrome Immobilized at an Anionic Polymer Film 1964

An optical sensor that exhibits a response time of < 15 s for Ca(II) is developed, based on the immobilization of calcichrome at a porous anion-exchange polymeric film. Structural details related to reactivity of the immobilized reagent are examined. Equations to determine various reactivity constants from diffuse reflectivities are developed.

Lai-Kwan Chau and Marc D. Porter*, Ames Laboratory—USDOE and Department of Chemistry, Iowa State University, Ames, IA 50011

Selective Determination of Histamine by Flow Injection Analysis 1971

Control of reaction timing via flow injection analysis yields a transient, chemical kinetic selectivity enhancement of the reaction of *o*-phthalaldehyde with histamine, eliminating the usual requirement for separation of histamine from potential interferences in biological samples.

James M. Hungerford*, Kevin D. Walker, Marleen M. Wekell, Jack E. LaRose, and Harold R. Throm, Seafood Products Research Center and Science Branch, Food and Drug Administration, Bothell, WA 98041-3012

Noninvasive Method for Monitoring Ethanol in Fermentation Processes Using Fiber-Optic Near-Infrared Spectroscopy 1977

A noninvasive method for the on-line measurement of ethanol production in a yeast fermentation based on short-wave near-IR spectroscopy and multivariate analysis is presented. The method produces a calibration model that can be transferred from one fermentation to another.

Anna G. Cavinato, David M. Mayes, Zhihong Ge, and James B. Callis*, Center for Process Analytical Chemistry, Department of Chemistry, BG-10, University of Washington, Seattle, WA 98195

Continuum-Source Atomic Absorption Spectroscopy with an Echelle Spectrometer Adapted to a Charge Injection Device 1983

Multiwavelength absorption data are acquired in 40-nm spectral ranges with resolution of 0.003 nm in the 300–430-nm range. Typical values of characteristic concentrations (1% absorption) are in the range of 1.6–3.8 ng/mL with detection limits in the range of 3–70 ng/mL.

Chunming Hsiech, Steven C. Petrovic, and Harry L. Pardue*, Department of Chemistry, Purdue University, West Lafayette, IN 47907

Scanned Laser Fluorescence Line Narrowing Spectroscopy of Photosensitive Organic Chromophores 1989

Distortions in fluorescence line-narrowed spectra caused by site depletion are explained by using a convolution model. These effects are overcome by frequency scanning the excitation laser while acquiring the fluorescence spectrum.

Bradford B. Price and John C. Wright*, Department of Chemistry, University of Wisconsin—Madison, Madison, WI 53706

Preconcentration of Copper on Algae and Determination by Slurry Graphite Furnace Atomic Absorption Spectrometry 1994

Unicellular green algae are used to preconcentrate Cu ions from sea water and riverine water samples. The algae pellet is analyzed as slurry by GFAAS. The determined values of Cu are in good agreement with certified values.

Mo Shengjun and James A. Holcombe*, Department of Chemistry and Biochemistry, The University of Texas at Austin, Austin, TX 78712

Correction for Fluorescence Response Shifts in Polyaromatic Hydrocarbon Mixtures with an Innovations-Based Kalman Filter Method 1998

A Kalman filter-based approach for the correction of spectral response shifts in fluorescence spectra of mixtures of PAH compounds in common LC solvent mixtures is described.

Todd L. Cecil and Sarah C. Rutan*, Department of Chemistry, Virginia Commonwealth University, Box 2006, Richmond, VA 23284

Resolution of Multicomponent Fluorescence Emission Using Frequency-Dependent Phase Angle and Modulation Spectra 2005

A frequency-domain fluorometer is used to record phase angle and modulation spectra at multiple light modulation frequencies. Least-squares analysis yields the emission spectra and decay times of the components. Examples shown include the resolution of three overlapping emission spectra, structured emission spectra, and trace components in a mixture.

Joseph R. Lakowicz*, Ranjith Jayaweera, Henryk Szmacinski, and Wieslaw Wiczk, Department of Biological Chemistry, School of Medicine, University of Maryland at Baltimore, 660 West Redwood Street, Baltimore, MD 21201

Thin Film Planar Waveguide Sensor for Liquid Phase Absorbance Measurements 2012

A tantalum pentoxide thin film planar optical waveguide with grating coupling is studied for application as a chemical sensor for liquid-phase absorbance measurements in the visible spectrum.

Michael D. DeGrandpre and Lloyd W. Burgess*, Center for Process Analytical Chemistry, Department of Chemistry, BG-10, University of Washington, Seattle, WA 98195 and **Patricia L. White and Don S. Goldman,** Battelle Pacific Northwest Laboratory, Richland, WA 99352

Effect of Structural Variations within Lipophilic Dibenzocrown Ether Carboxylic Acids on the Selectivity and Efficiency of Competitive Alkali-Metal Cation Solvent Extraction into Chloroform 2018

Structural variations within lipophilic dibenzocrown ether carboxylic acids influence both the selectivity and efficiency of alkali-metal cation extractions into chloroform.

Wladyslaw Walkowiak, Witold A. Charewicz, Sang Ihn Kang, Il-Woo Yang, Michael J. Pugia, and Richard A. Bartsch*, Department of Chemistry and Biochemistry, Texas Tech University, Lubbock, TX 79409-1061

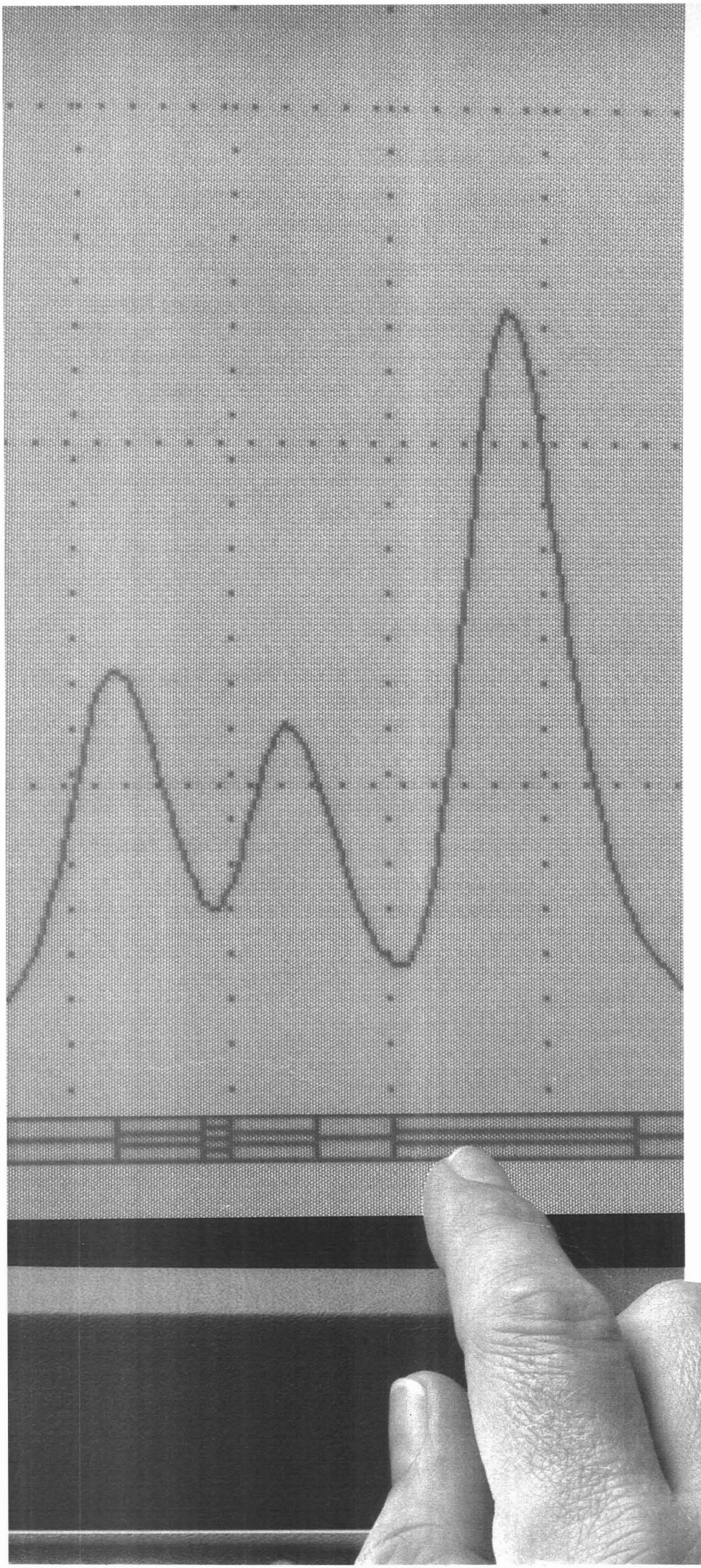

Only Smart Diode Array Detection points out the impurities.

In real time.

Smart Diode Array Detection shows you which peaks are impure. And how many components exist in each. Automatically, and in *real-time*.

Unique Purity Lines below each peak make it obvious. So you don't have to guess like you did with vague, unclear 3-D plots and isograms from older generation detectors. Or wait for time-consuming post-run analyses.

The next generation of diode array detection is here today. It's the System Gold™ 168 Diode Array Detector. It's Smart. And it's only from Beckman.

For a free electronic brochure, circle the reader service number below. Or contact Beckman. Offices in major cities worldwide.

Beckman Instruments, Inc., Bioanalytical Systems Group, 4550 Norris Canyon Road, P.O. Box 5101, San Ramon, CA 94583.

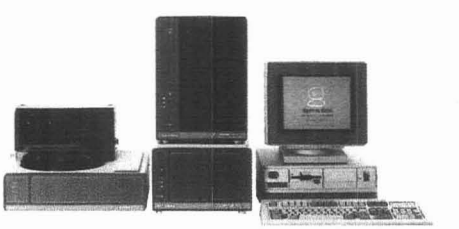

BECKMAN

Australia, Sydney. **Austria,** Vienna. **Canada,** Toronto. **France,** Gagny. **Germany,** Munich. **Hong Kong,** Aberdeen. **Italy,** Milano. **Japan,** Tokyo. **Mexico,** Mexico City. **Netherlands,** Mijdrecht. **Puerto Rico,** Carolina. **Singapore. South Africa,** Johannesburg. **Spain** Madrid. **Sweden,** Bromma. **Switzerland,** Nyon. **Taiwan,** Taipei. **United Kingdom,** High Wycombe.

16 for representative and literature.
17 literature only.

Correspondence

Technical Notes

More For Less.

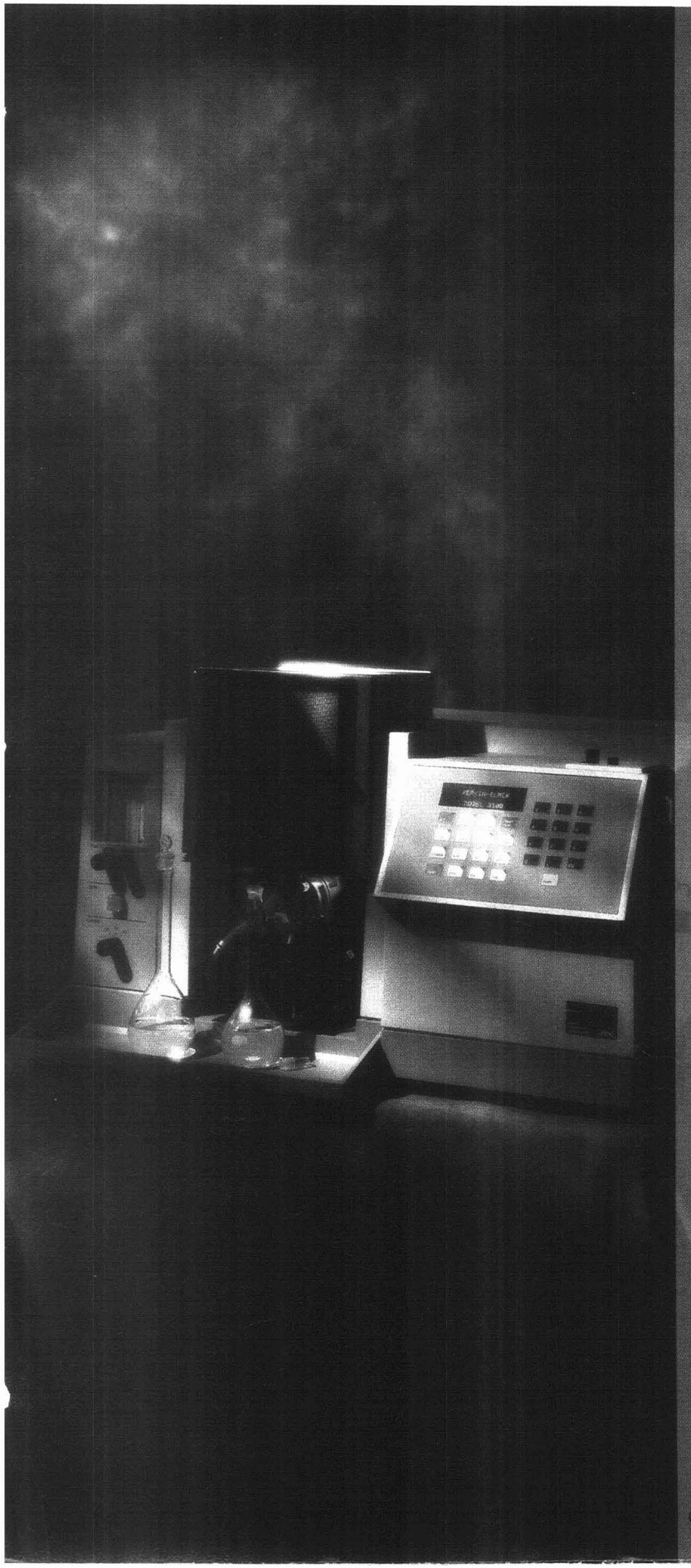

Cost-effective and easy to use, Perkin-Elmer's Model 3100 Atomic Absorption Spectrometer delivers exceptional performance and versatility. And it's affordable.

State-of-the-art design and manufacturing procedures increase reliability and lower cost with no loss of features.

Double-beam optics provide exceptional stability and precision.

A two-line alphanumeric display shows analytical results, helps set up methods and provides troubleshooting information. All in easily understood terms.

And since the 3100 is going to help your lab grow, we designed it so it can grow right along with you.

For literature on the Model 3100 call 1-800-762-4000. Or contact your local office for more information on the 3100 or other AA products from Perkin-Elmer, the acknowledged leader worldwide in atomic absorption.

Add the Enhanced Data System for advanced data handling and accessory control features.

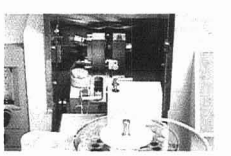

With the Stabilized Temperature Platform Graphite Furnace you get unrivaled detection limits and freedom from interferences.

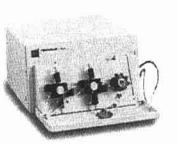

The FIAS-200 flow injection system provides new levels of speed, performance and cost effectiveness for automated sample pretreatment.

Perkin-Elmer combines experience, expertise, and worldwide resources to provide unmatched products, service, and support for analytical laboratories.

PERKIN ELMER

The Perkin-Elmer Corporation
Norwalk, CT 06859-0012

CIRCLE 112 ON READER SERVICE CARD

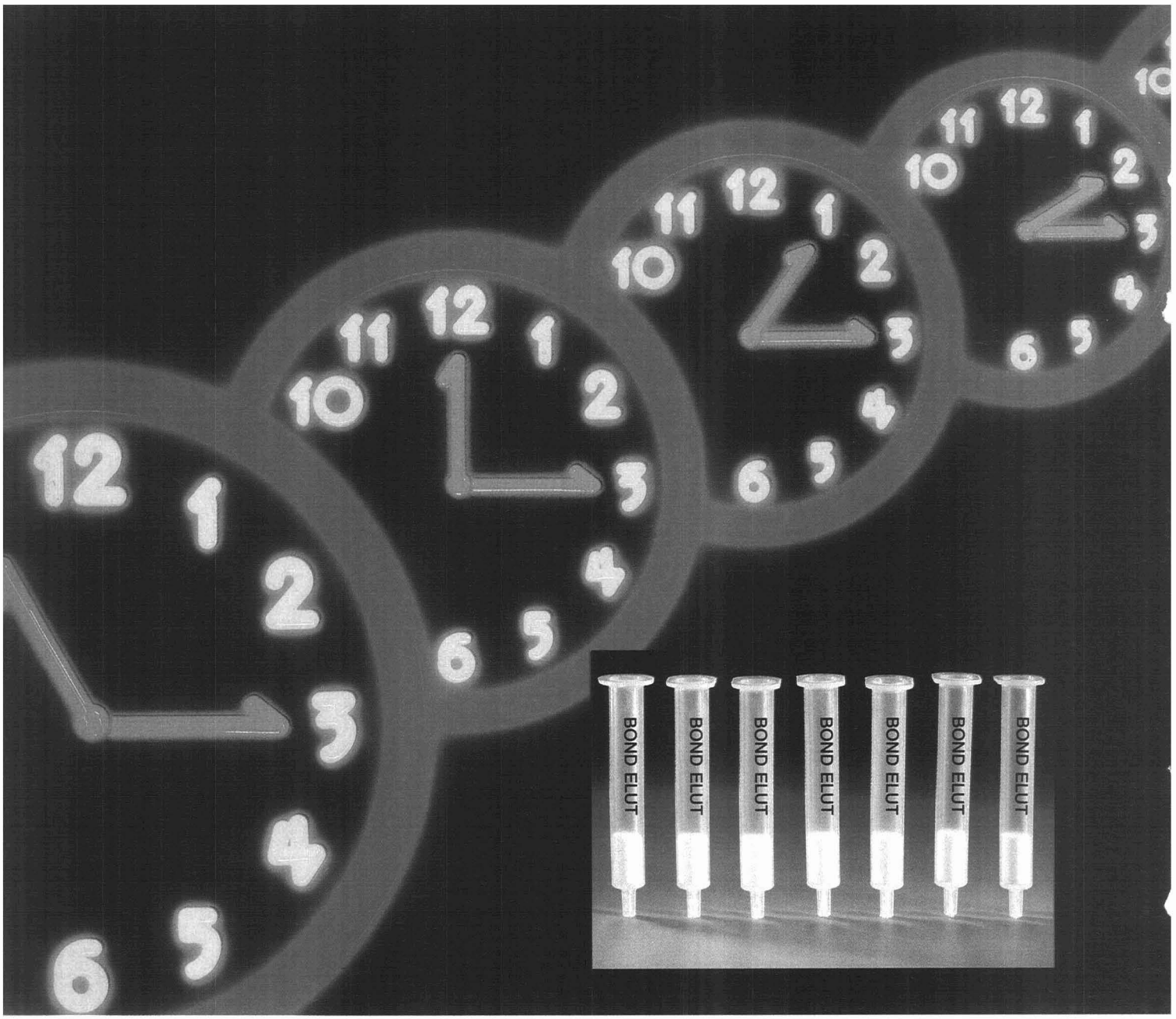

TIME AFTER TIME.

Reproducible results with Bond Elut™.

When all is said and done, results are what really count. Bond Elut will give you results. Reproducible results. From one batch to the next. Every time.

Of course, sample clean up results are only as good as the purity of the system you use. That's why Analytichem requires every lot of Bond Elut to pass rigorous quality control procedures.

This means that we do it right the first time. Every time. Our sole business is solid phase extraction; and it shows. Analytichem tested Bond Elut against the competition. The result? Bond Elut columns provide a more contaminant free extraction than inexpensive look alikes*.

That's because for over a decade, experts at Analytichem have adhered to strict quality assurance standards. No matter how complex the separation, or how many times the procedure is performed, you can always be sure of superior analytical results with Bond Elut.

Don't settle for anything less than the most accurate sample preparation system available. Bond Elut from Analytichem. A reflection of quality.

*For more information and test results contact:

Analytichem International
A Division Of Varian Associates, Inc.
24201 Frampton Avenue, Harbor City, CA 90710
(800) 421-2825
(213) 539-6490

CIRCLE 138 ON READER SERVICE CARD

CHEMISTRY WITH A FUTURE

Analytichem
a division of varian

Yeung Wins Strock Award

Edward S. Yeung, distinguished professor in sciences at Iowa State University and humanities and program director of Environmental Sciences at Ames Laboratory, will receive the 1990 Lester Strock Award. The award, established by the New England Section of the Society for Applied Spectroscopy (SAS), recognizes an outstanding scientific author and consists of $500 and a medal. Yeung will receive the accolade in October at the SAS awards dinner held in conjunction with the Federation of Analytical Chemistry and Spectroscopy Societies (FACSS) Meeting in Cleveland, OH.

Yeung was born in Hong Kong and received an A.B. degree from Cornell University (1968) and a Ph.D. in chemistry from the University of California, Berkeley (1972). His research interests lie in the fields of spectroscopy and chromatography—nonlinear spectroscopy, high-resolution atomic spectroscopy, laser-based detectors for LC, capillary zone electrophoresis, trace gas monitoring methods, photochemistry, and data treatment procedures in chemical measurements.

An Associate Editor in spectroscopy for ANALYTICAL CHEMISTRY, Yeung was awarded an Alfred P. Sloan Fellowship in 1974. He is also the recipient of the 1987 ACS Division of Analytical Chemistry Award in Chemical Instrumentation and a 1989 R&D 100 Award.

Soft Research

Add small-angle scattering to the expanding list of new imaging techniques. Small-angle scattering determines the size and shape of objects 0.01–1.0 μm in size, using low energy or "soft" X-rays that should not harm biological materials. Objects in this size range, such as proteins, are too small to be seen with visible light and too large for conventional X-ray imaging techniques.

To obtain useful data from soft X-rays with wavelengths between 10 and 50 Å, researchers at the Lawrence Berkeley Laboratory (LBL) have developed a multilayered mirror to reflect and focus the radiation. The curved mirror is coated with alternating layers of W and C applied by an ion-sputtering technique.

X-ray light reflected by the mirror at the sample generates interference patterns. Analysis of the resulting patterns yields information on size and shape, size distribution, and solidness or hollowness of the sample. LBL researchers have already shown that small-angle scattering can determine periodic and nonperiodic structures in thin films deposited directly on the mirror as well as fiber size and orientation in polymers and plastics. Using this technique, researchers should also be able to study biological materials in aqueous solution.

For Your Information

The ACS Division of Analytical Chemistry has awarded 365 **undergraduate students** with four-month **subscriptions** (Oct. 1–Jan. 15) to ANALYTICAL CHEMISTRY. The awardees are selected annually by chemistry faculty at U.S. colleges and universities. The awards are designed to recognize outstanding scholastic achievement and to stimulate interest in the field of analytical chemistry. Students will also receive the Division newsletter.

Henry Freiser of the University of Arizona and **Taitiro Fujinaga** of Kyoto University in Japan were chosen as the first international **honorary members of The USSR Scientific Council of Analytical Chemistry.** The two chemists are also the first non-Soviet scientists to receive the Kurnakov Medal, awarded by the N. S. Kurnakov Institute of General and Inorganic Chemistry in Moscow.

In a report to Congress, the Office of Technology Assessment (OTA) has concluded that **"DNA tests to identify individuals are valid and reliable** when properly performed." However, OTA warned that questions about the accuracy of these tests in forensics "underscore the need to set technical and procedural standards for DNA testing now."

Analytical chemist Thomas O'Haver's software package entitled SPECTRUM (Signal Processing for Experimental Chemistry Teaching and Research/University of Maryland) has won the **1990 Best Chemistry Software and Best Design Award** from the National Center for Research to Improve Postsecondary Teaching and Learning. The software, written for the Macintosh, offers an interactive graphics program that students use to extract and enhance information from digitized signals generated by scientific instruments.

The Analytical Chemistry Division at Oak Ridge National Laboratory has established a **Distinguished Research Fellow program** that enables outstanding research professors to work with research groups at the laboratory. The first fellow is Alan Marshall of the Ohio State University, who will work with Michelle Buchanan's research group on trapped ion MS. For more information, contact W. D. Shults, Analytical Chemistry Division, Oak Ridge National Laboratory, P.O. Box 2008, Oak Ridge, TN 37831-6129 (615-574-4881).

NIST has collected the latest information on the data compilations, publications, and computerized databases it offers and has created the ***NIST Standard Reference Data Products 1990 Catalog***. Among the databases listed is the **Chemical Kinetics Database for PCs**, which has recently been upgraded to offer information on more than 5000 reactions, faster searching speed, and simultaneous display of abstracts and graphics. For information, contact the Standard Reference Data Program, A323 Physics Bldg., NIST, Gaithersburg, MD 20899 (301-975-2208).

Introducing the VG TRIO-2000:

dedicated to GC/LC-MS . . .with total flexibility.

Consider the criteria:

- Design a compact quadrupole mass spectrometer to deliver research grade performance - on a routine, day to day basis.
- Ensure that all tasks can be automated to the user's specification and that operation will be simple and efficient - to guarantee maximum productivity.
- Utilize only the highest quality field tested and proven components to provide the utmost reliability.
- Accommodate, without compromise, both the established and the most recent advances in ionization and introduction techniques.

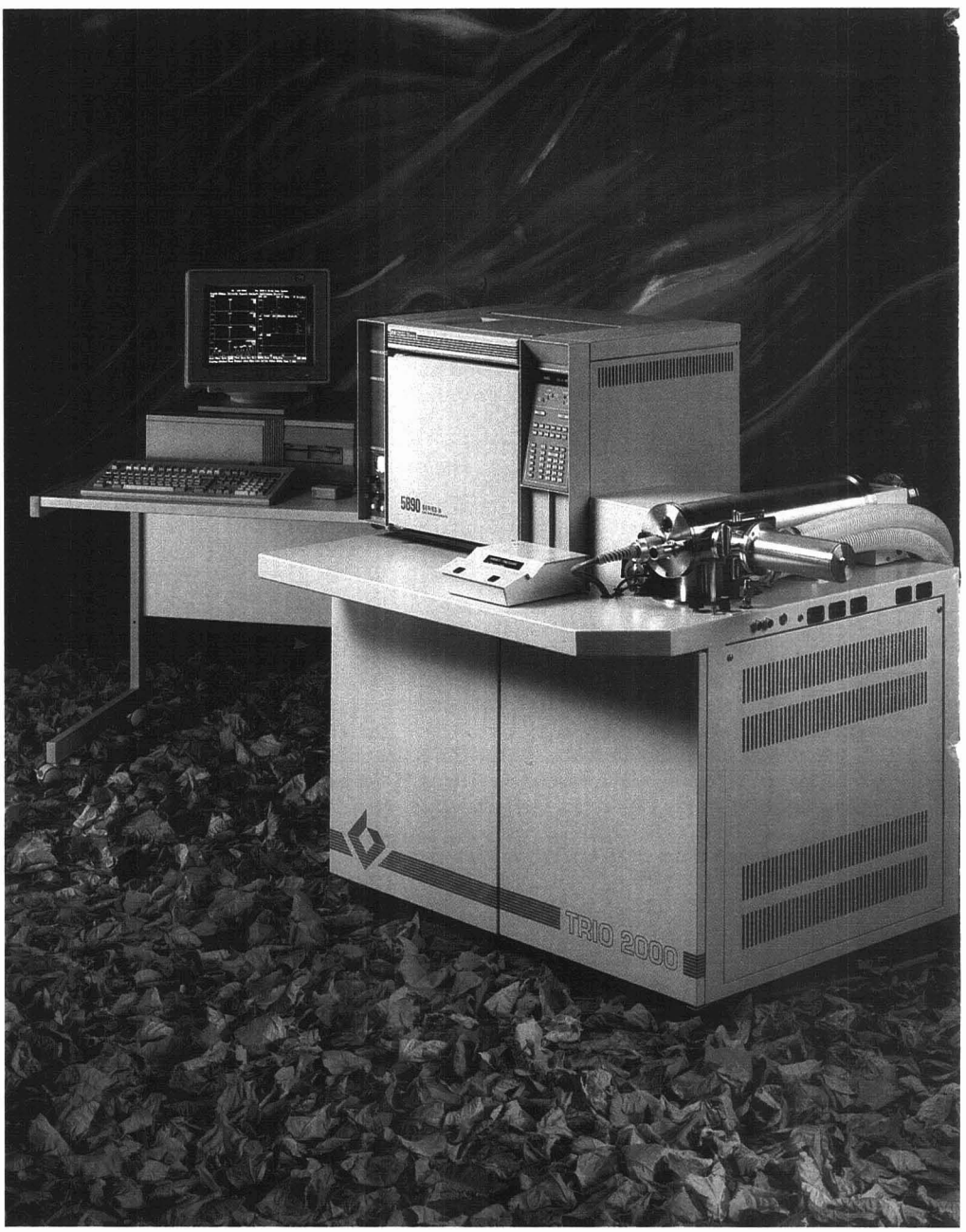

The result?

The VG TRIO-2000.

Encompassing GC-MS and Electrospray, Robot Driven Probes and Thermospray, Particle Beam and Fast Atom Bombardment, the TRIO-2000 combines unrivaled freedom of choice with the most exacting specifications.

To find out more about how the TRIO-2000 delivers performance to put it at the top of its class, contact your local VG representative.

FISONS Instruments

VG INSTRUMENTS

organic mass spectrometry

CIRCLE 140 ON READER SERVICE CARD

UNITED KINGDOM. VG BioTech, Tudor Road, Altrincham. WA14 5RZ. England. Tel: 061-929 9666.
USA. VG Instruments Inc. 32 Commerce Center, Cherry Hill Drive, Danvers, MA 01923. Tel: (508) 777 8034.
CANADA. VG Instruments Canada Inc. 5929 Transcanadienne, St. Laurent, Quebec H4T 1A1. Tel: (514) 744 5519.
WEST GERMANY. VG Instruments GmbH. Postfach 5869, Hasengartenstrasse 14, 6200 Wiesbaden. Tel: (06121) 71090.
FRANCE. VG Instruments. 5 Avenue Gallieni, 94250 Gentilly. Tel: (1) 47406160.
ITALY. VG Instruments. Viale Dell'Assunta 101, 20063 Cernusco Sul Naviglio, Milano. Tel: (2) 924 8808.
THE NETHERLANDS. VG Instruments BV. PO Box 171, 1380 AD. Weesp. Tel: (2940) 80484.
BELGIUM. VG Instruments NV. Excelsiorlaan 1 Box 2, 1930 Zaventem. Tel: 322 725 2410.
SCANDINAVIA. VG Instruments AB. Box 45199, S-104 30 Stockholm. Tel: 08-311035.
CHINA. VG Instruments. Apartment 1008 Beijing Yanshan Hotel, Beijing 100086, Tel: 1 256 4309. Telex: 211203 .
KOREA. VG Instruments Korea. Dong-il Building, 58-6 Nonhyun-dong, Kangnam-Ku, Seoul. Tel: (01) 548 2983. Telex: 28523.
JAPAN. Jasco International Co. Ltd. 2-4-21 Sennin-cho, Hachioji City, Tokyo 193. Tel: 010813 42666 1321. Telex: 2862515.

GLOW DISCHARGE TECHNIQUES IN ANALYTICAL CHEMISTRY

W. W. Harrison, C. M. Barshick, J. A. Klingler, P. H. Ratliff, and Y. Mei
Department of Chemistry
University of Florida
Gainesville, FL 32611-2046

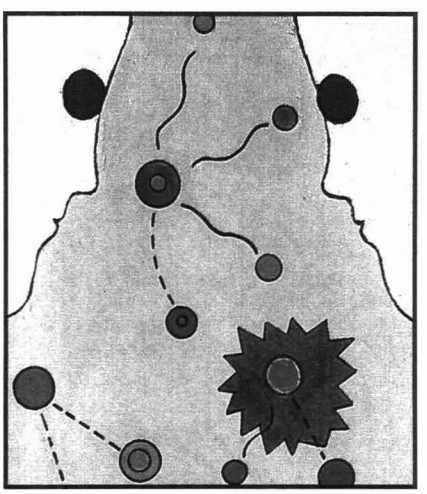

REPORT

The glow discharge (GD) is an old source that is finding many new uses in analytical spectroscopy. Its simplicity of operation, coupled with versatility of application, has led to increasing commercial interest. From an obscure analytical method focusing primarily on metal analysis, the glow discharge has developed into a sophisticated technique suitable for analysis of nonmetals, thin films, semiconductors, insulators, and organic materials. More effort is also being made to understand better the many chemical and physical phenomena that influence the effectiveness of the GD source.

The GD is a low-pressure (0.1–10 Torr) plasma composed of two electrodes immersed in a partially ionized noble gas (*1*). The name arises from the relatively bright central glow originating from excited gas atoms emitting their characteristic optical radiation. A complex combination of atomic and ionic species, from both the discharge gas and the cathode sample, is available for analytical use.

Compared with other plasma sources, such as the inductively coupled plasma, the GD is a compact, small-volume source that operates at low wattage. It is inexpensive to build and maintain, and plasma gases are consumed at quite modest rates (cc/min). The deceptively feeble appearance of the GD may account for analysts failing to take it seriously over the years. In actual practice, the atomic collision processes occurring in the GD are sufficiently robust to break many tenaciously bonded species.

GDs have been used for years with each of the analytical techniques discussed in this REPORT. For the most part, however, such use had been, until more recently, sporadic in nature and centered in academic research laboratories. Growing interest and acceptance have led to the availability of numerous types of GD instrumentation, permitting GD techniques to become more competitive with other established elemental methodologies.

Analytical modes

Figure 1 illustrates the primary analytical techniques that now incorporate a GD in their experimental schemes. Although most GD measurements are designed to use only one of these approaches, simultaneous application of more than one technique is possible.

As the discharge ablates the cathodic (sample) material into the plasma, elemental species are available for a number of different measurements. The large atom population in the discharge makes sensitive atomic absorption (AA) measurements possible; and because a fraction of these atoms is excited, the subsequent decay produces atomic emission (AE). In addition, atoms may be stimulated by external sources for atomic fluorescence (AF). Some atoms may even be sufficiently excited to lose an electron; the resultant ions can be sampled by mass spectrometry (MS).

For two of these techniques, GDAE and GDMS, the GD is self-sufficient (i.e., atomic excitation and ionization result without any external assistance). For GDAA and GDAF, an external stimulation probe is necessary to measure the atomic absorption or to pump sputtered atoms to an energy level suitable for atomic fluorescence.

Although these solid-sample elemental applications make up the bulk of GD work today, the introduction of organic vapors directly into the negative glow for ionization purposes is another important use that promises continued growth.

Sputter atomization

The key to the success of the GD is the ease with which it creates an atom reservoir of the sample material directly from the solid state. This step, known as sputtering (*2*), is depicted in Figure 2. Almost all of the discharge potential is dropped across the cathode fall (dark space), a region very close to the cathode surface. Argon ions are accelerated across this dark space by the cathode fall potential and strike the sample surface, creating a collision cascade with sufficient energy to dislodge one or more surface atoms for each incoming ion. Secondary ions are also released, but the cathode fall potential returns them to the surface. Secondary electrons are accelerated by the same field into the negative glow and help maintain the discharge.

The negative-glow region appears as a luminous cloud surrounding the dark space and extending outward toward

0003-2700/90/0362-943A/$02.50/0

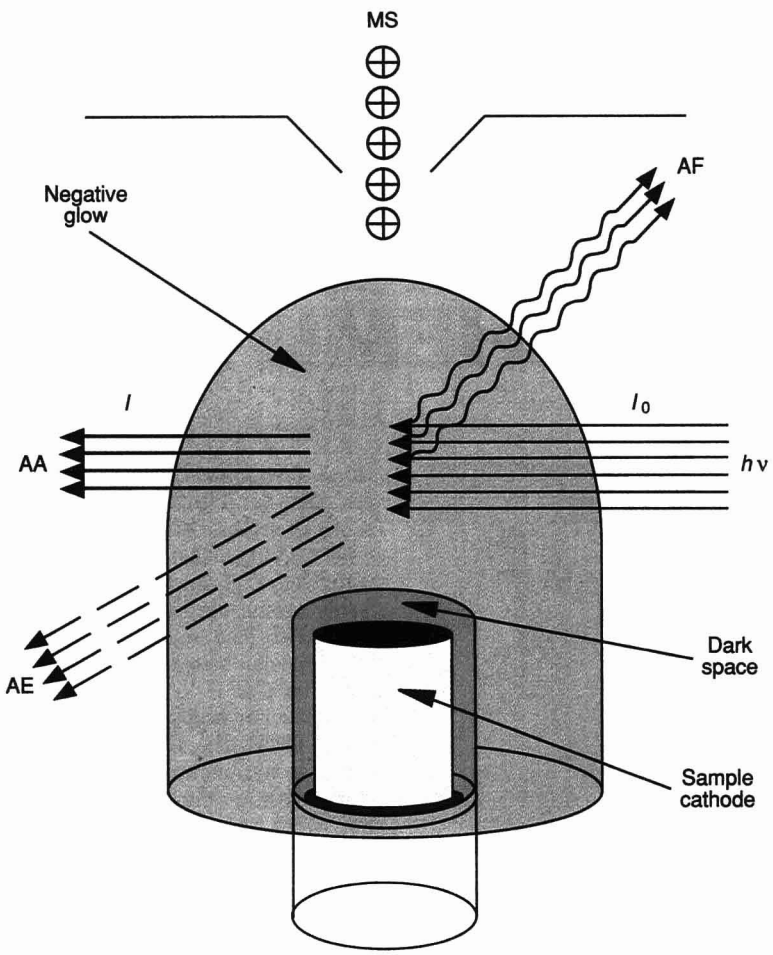

Figure 1. Analytical methods using a GD.
I_0 is the incident radiation; I is the attenuated radiation.

the chamber wall, which normally serves as the anode. The glow results from the discharge gas colliding with electrons moving through the region, causing excitation of the fill-gas atoms, normally argon. Relaxation of these atoms causes emission at a wavelength characteristic of the discharge gas (e.g., blue for argon). Because the electric field is dissipated across the dark space, the negative glow is considered essentially a field-free region. Atoms, ions, and electrons all possess relatively low energy.

At typical GD pressures, a short mean-free path results, so that most accelerated ions undergo numerous charge exchange collisions before reaching the cathode, causing the average ion energy to be much smaller than the discharge voltage. As shown in Figure 2, a fast argon ion, Ar_f^+, can collide with a slow argon atom, Ar_s^0, yielding a fast atom and a slow ion. Some of the fast atoms that result from the charge exchange collisions bombard the cathode and contribute to the net sputter rate. Sputtered atoms tend to diffuse away from the cathode, although two-thirds or more are redeposited on the target cathode by collisions with the dominant argon atoms. Those atoms that escape redeposition diffuse into the negative glow, where they can be excited or ionized by collisions with metastable argon atoms or electrons. Thus, the sputtered sample exists in the discharge as ground state atoms, excited atoms, and ions. Although some polyatomic species also exist in the glow discharge, the sputter–plasma process is primarily atomic in nature.

The reactions shown in Figure 2, however, represent a gross oversimplification of the plasma chemistry involved. Many other species of transient stability are formed and may be observed, particularly by GDMS. The glow discharge chamber is essentially a small chemical reaction cell that can be controlled to the analyst's benefit. A facet of GDs that has yet to be extensively studied for analytical utility is the modification of the plasma chemistry (*3*) to produce unique chemical environments. In addition, pulsed GD operation (*4*) also introduces new opportunities for time-resolved decoupling of plasma reactions and products.

A major strength of the GD is the separation of the sampling step (sputter atomization) from the subsequent analytical steps of excitation and ionization. This process can be thought of as an atom generator delivering a steady-state population of sample atoms to analytical measurement sites separated in space and time from the sample. The atoms have no "memory" of their original chemical environment; thus, sample matrix effects are minimized.

Samples must be electrically conducting for use in dc discharges. Metals, alloys, and even semiconductors work quite well in this mode. Nonconducting samples must be mixed with a conducting matrix, such as pure copper or silver, and pressed into a suitable sample form. Alternatively, a radio frequency (rf) discharge can handle nonconducting samples directly, eliminating the need for matrix modification.

Solution analysis is possible, but requires special handling. Small (μL) volumes are placed on a host electrode and the solvent is removed, leaving a thin-film sample residue that can be sputtered like any other solid. Alternatively, it may be possible to use flow injection methods to introduce directly small volumes of liquid samples. The major use of GDMS, however, is clearly for solids analysis. At a time when many complex procedures are being studied for introduction of solid samples into plasmas that are, by nature, more suited for solution injection, GD sputter sampling represents a simple process for conversion of a solid into an atomic vapor.

GDMS

Much of the early analytical work in GDMS (*5*, *6*) was aimed toward replacement of the spark ion source, a vacuum discharge ionization source that yields broad energy spreads, an erratic ion beam, and generally unreliable quantitative results. The GD ion source has gained popularity in recent years because of its stability, sensitivity, and simplicity of operation. At least three commercial instruments are now available, two from VG Microtrace and one from Extrel.

Elemental analysis by GDMS offers critical advantages over competing techniques in that it responds to metals

and nonmetals, exhibits high sensitivity, suffers from minimal matrix effects, and provides isotopic information (*7*). Thus it is not surprising that GDMS has developed into the most prominent of the GD methods.

Figure 3 shows a cross section of a typical GDMS source, illustrating the cathode–anode relationship. Although a pin-type source is shown, other geometries, such as a disk or pellet, are equally feasible. A key difference in MS compared with the optical methods is that a physical transfer of sample material out of the source must take place. Analyte ions are extracted by electrostatic lenses and transferred through a mass analyzer for eventual detection. Although ions are formed throughout the source cell, only those created very close to the exit orifice are able to survive the high-collision environment and depart in the charged state. Both magnetic-sector and quadrupole-based instruments have been used for GDMS, and commercial versions of each are available. Typical discharge operation conditions for GDMS are 1–5 mA, 800–1500 V, and 0.2–2 Torr.

Sample preparation for metals and alloys usually consists of brief cleaning and/or polishing, although the sputter process itself serves as a self-cleaning mechanism to remove surface impurities. Powder samples are compacted in a special die to form pins or disks. Solutions can be analyzed by evaporation to a residual film on the surface of the host cathode (e.g., glassy carbon or a high-purity metal), followed by sputter ablation of the sample film into the plasma. Reduction of the solution sample into a thin surface residue permits very low detection limits from the transient signal.

GDMS has been widely applied to the analysis of metals, alloys, and high-purity materials, offering perhaps the only method that combines the required sub-part-per-billion detection limits with the breadth of coverage necessary for survey analysis. GD mass spectra are much simpler than line-rich optical spectra, making qualitative analysis rapid and straightforward. Elemental ion ratio intensities are used for quantitation, usually with the matrix element acting as an internal standard. Polyatomic mass spectral interferences resulting from chemical combination of the discharge gas and the sample matrix (e.g., $FeAr^+$) can create problems at low detection limits. Given the capabilities of modern detection systems, however, GDMS ion intensities are linear over a wide range of concentrations, from major components to trace constituents.

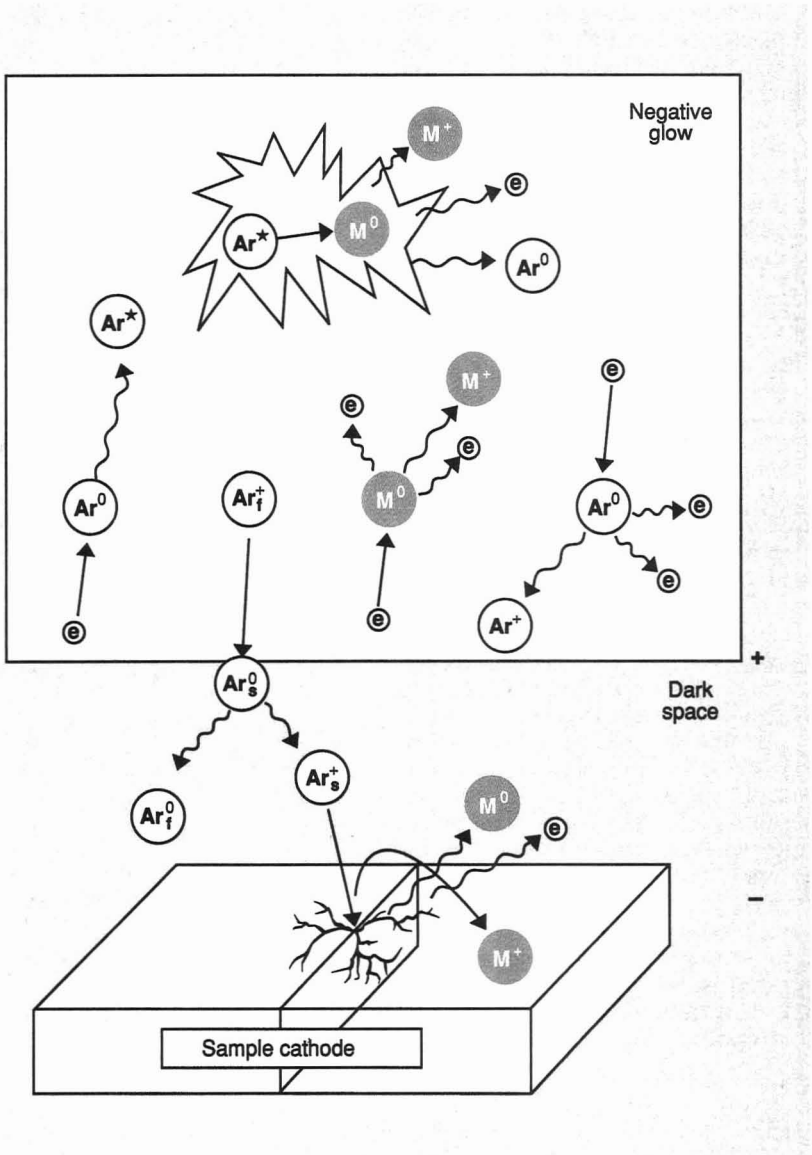

Figure 2. Atomization, excitation, and ionization processes typically occurring in a GD.
M is the sample species.

The advantages of GDMS have resulted in its becoming a routine technique that turns out reliable data on a daily basis in commercial laboratories. Quantitative analysis of such difficult elements as B, C, Si, P, and S in NBS 1164 steel samples yielded good results (*8*). The surface-active nature of glow discharge ablation also permits the analysis of thin films and coatings. Si doped into a GaAs wafer can be resolved from different layers at concentrations of 1, 10, and 20 ppm with resolution of about 100 nm (*9*). Although redeposition phenomena somewhat limit the sharpness of layer resolution, GDMS can be used effectively for such samples. Routine use of GDMS is often not reflected in the literature, leading to an underassessment of its real utility. Several recent reviews describe various applications of GDMS (*10–12*).

GDAE

GD emission techniques (*13*) offer simpler instrumentation and a less expensive approach to solids elemental analysis than does GDMS. Major tradeoffs, however, include poorer detection limits and reduced elemental coverage. Although compact commercial GDAE instruments (Jobin-Yvon, ARL/Fisons, and Spectrumat) have enjoyed popularity in Europe in recent years, their use in the United States has been limited.

Two commonly used versions of GD emission sources are illustrated in Figure 4. The planar cathode, or Grimm source (*14*), shown in Figure 4a, is used

more often. Also adapted for GDMS applications, the Grimm source is an obstructed discharge in which the anode extends into the cathode dark space, defining the area of the sample that is sputtered. The sample is located outside of the source for easy access and interchange. Such a configuration is particularly adaptable to the analysis of metal sheets, disks, or any flat conducting sample that can be brought up to the source opening; powder samples pressed into disks are also suitable. Discharge operation conditions for a Grimm source are 500–1000 V, 25–100 mA, and 1–5 Torr. Detection limits are ~0.1 ppm.

The planar cathode discharge is featured in commercial instruments designed for applications in solids trace elemental analysis. Of special interest is its use for depth profiling of layered metal samples (*15*) and for analysis of geological materials such as granite, basalt, mica, and feldspar without the thermal effects and self-absorption evident in arc–spark operation (*16*).

The other less commonly used source for GDAE is the hollow-cathode discharge (HCD) shown in Figure 4b, which features a cavity cathode rather than the planar cathode of the Grimm source (*17*). The net effect of this difference, for a given discharge voltage, is concentration of the plasma within the constraining cavity, which enhances elemental emission intensities. Typical operating conditions are 200–500 V, 10–100 mA, and 0.1–1.0 Torr.

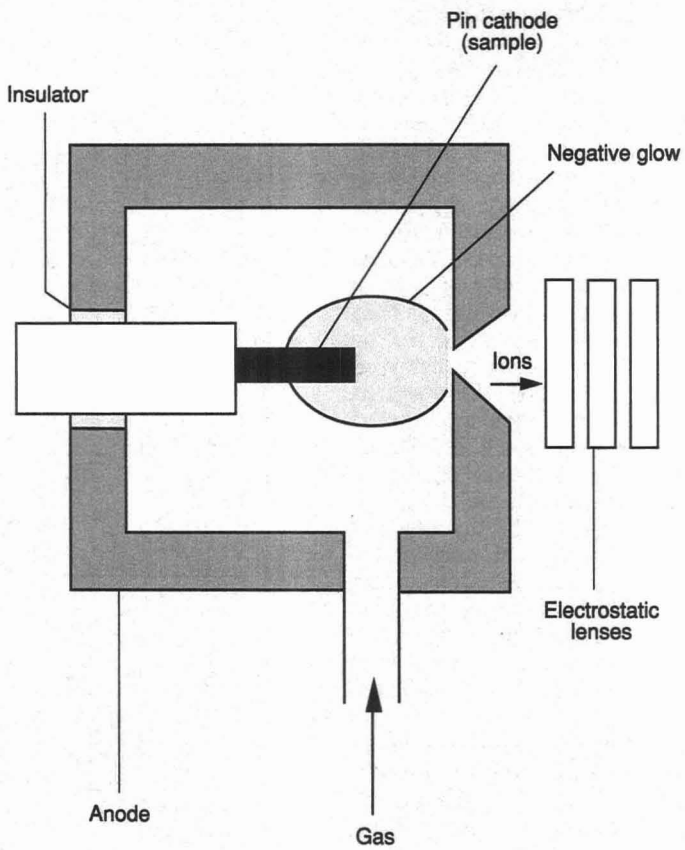

Figure 3. Ion source for GDMS.

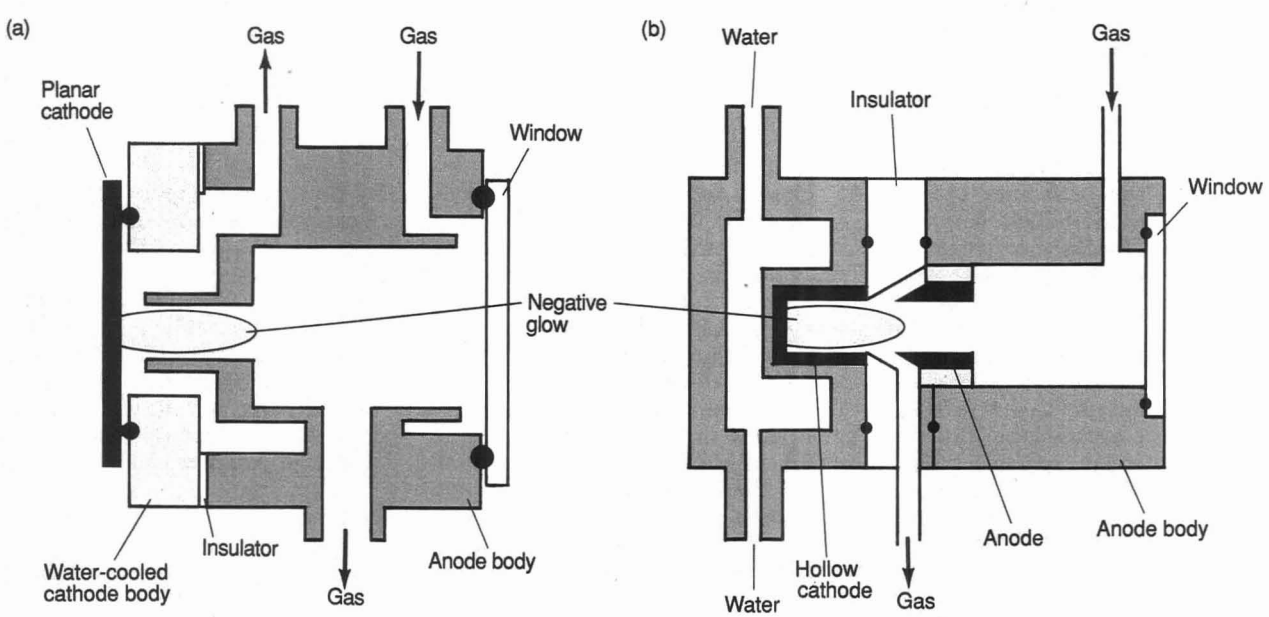

Figure 4. Sources for GDAE. (a) Grimm (planar cathode) source; (b) hollow-cathode discharge.

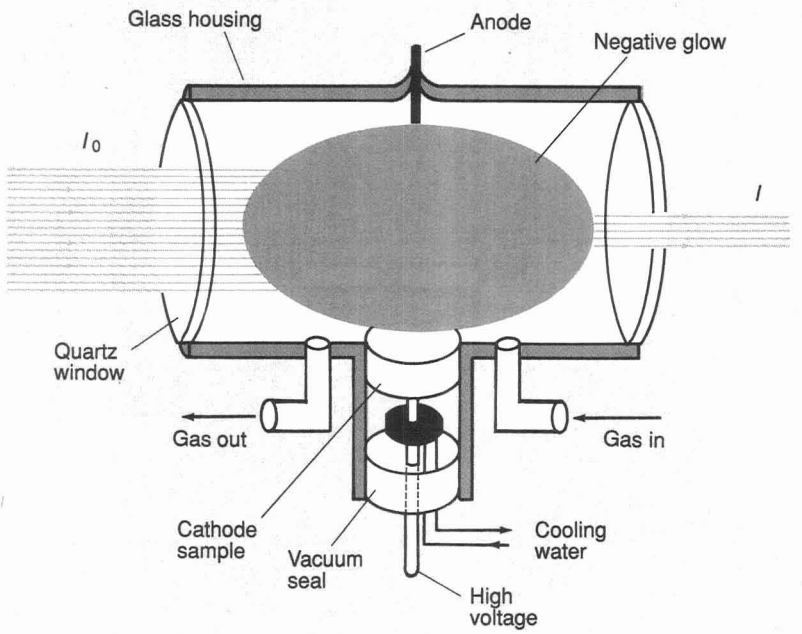

Figure 5. Sputter atomization cell for GDAA.

For analysis of metals and alloys, the hollow cathode is either machined from the bulk metal, or the sample (e.g., chips or powder) is placed in the hollow cavity of a pure material such as graphite. Solutions can be analyzed by evaporating the sample to a residual film in the hollow cathode. Detection limits generally range from 0.1 to 10 ppm. Current research includes coupling of the HCD with microwave sources and development of microcavities to improve sensitivity.

GDAA

The GD is particularly appropriate for AA because the overwhelming majority of the sputtered species is neutral atoms. This ability to produce a steady-state population directly from a solid matrix has obvious advantages that led Russell and Walsh to suggest use of the GD in the early development of AA (*18*). Despite this attractive incentive, little concerted effort took place to capitalize on the idea until the introduction of commercial instrumentation.

Figure 5 shows a sputter atomization cell for AA measurements. Compared with GDMS and GDAE sources, a longer pathlength is necessary to enhance absorbance, which is integrated across a broad volume of the cell. Greatest atom density is near the cathode, with a gradient extending to the cell walls. Like other GD sources, a flow-through gas system is used. Analyte Corporation's commercial instrument features gas jets directed onto the sample surface, which reduces redeposition by sweeping sputtered atoms into the negative glow and results in significant sensitivity enhancements. Typical operating conditions are 4–10 Torr, 60–200 mA, and 300–800 V. Detection limits for solid samples are generally in the low part-per-million range.

Sample preparation is much the same as for other GD techniques. Metal or alloy disks or compacted conducting samples are most often used. Solution samples have been examined by deposition onto graphite, aluminum, or copper cathodes. Quantitative analysis is typically performed with a calibration curve prepared from standard reference materials, a process requiring considerably more time than the preparation of a corresponding solution-based curve. Conversely, time is saved in the direct analysis of solids, and the inert atmosphere of a GD cell reduces the spectral interferences sometimes found in flame atomizers.

Although GDAA is not widely used at this time, the recent availability of commercial instrumentation, coupled with the increasing number of reports from a few laboratories, may stimulate additional interest. Sputter atomization offers special advantages for element analysis in solid samples that present problems for other types of AA measurements. For example, Zr in steel can be determined at 0.005–0.19% levels, and La in high-purity Zn can be determined at concentrations of 0.008–0.07% (*19*).

GDAF

Because the GD creates a cloud of sputtered atoms in a low-pressure, rare-gas environment that is an excellent quenching medium, it is an effective source for atomic fluorescence. In addition, the inert gas diluent provides few chemical interferences and the elemental absorption lines are relatively narrow. Although GDAF has not been

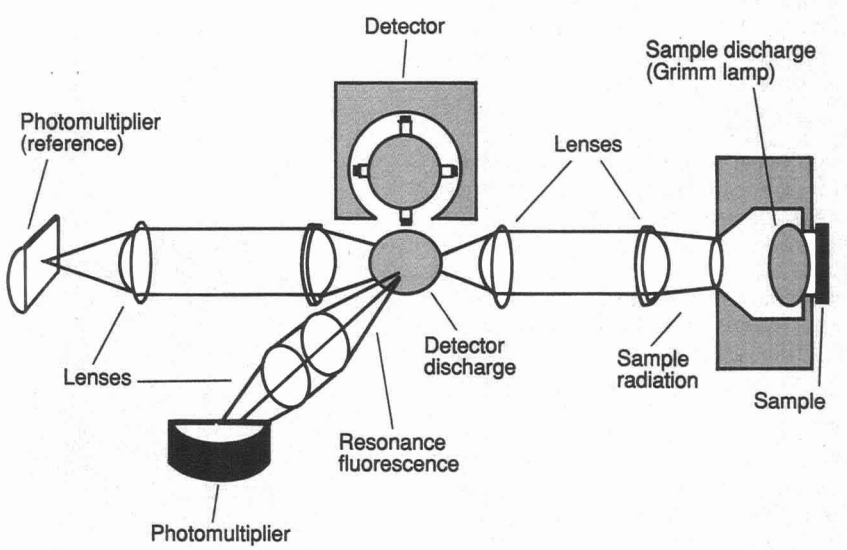

Figure 6. Resonance detection instrument for GDAF.
(Adapted with permission from Reference 22).

used as much as other GD techniques, some interesting applications have been reported (*20*, *21*).

The use of a laser to cause fluorescence from the GD atom reservoir is a natural consideration in the experimental approach to GDAF. The small background noise from the GD leads to projected detection limits at the attogram level. Although there are no "typical" GDAF operation conditions, given the scarcity of reports in this area, GD parameters would normally be set to generate a high atom population, more in line with GDAA than the low currents associated with GDMS. The use of a pulsed laser as an excitation source in GDAF makes a complementary pulsed GD advantageous in terms of efficient sample utilization and background noise reduction.

A less conventional GDAF system (*22*) is shown in Figure 6. In this case, the instrumentation takes advantage of two different GDs serving complementary purposes. The analytical Grimm discharge produces atomic emission from the elements in the sample. This radiation is directed into the second discharge, a resonance detector with a cathode composed of the analyte element. Radiation from the sample strikes the resonance discharge, causing fluorescence of the analyte element only. By rotating successive pure cathodes into the resonance discharge, multielement AF is possible without dispersion optics.

FANES

Conventional uses of GDs take advantage of the sputter atomization characteristics to convert a solid to a vapor. The combination of an alternative atomization source, with the GD used as an excitation or ionization source, has drawn attention to furnace atomization nonthermal excitation spectrometry, or FANES (*23*). Figure 7 shows a typical FANES source in which a graphite cylinder is used both for thermal atomization of solution residues and as the hollow cathode of a GD for excitation of the sample. A high current is applied to the graphite cylinder, producing a pulse of sample atoms and a subsequent emission pulse signal as the atoms interact with the GD. The similarities to electrothermal atomization AA are obvious (*24*).

Small (5–50 μL) samples are pipetted onto the cathode, dried, and ashed at atmospheric pressure while the system is flushed with argon. Typical discharge conditions are 1–5 Torr, 20–30 mA discharge current, and up to 500 A atomization current, producing temperatures near 3000 °C. The transient emission signal persists for 0.3–1.0 s,

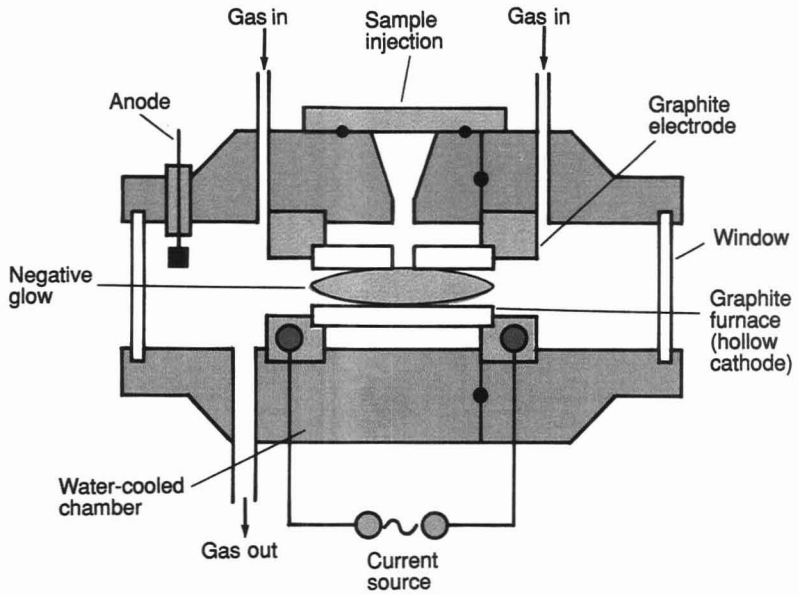

Figure 7. GD cell used as a furnace atomization nonthermal excitation source with electrothermal atomization.

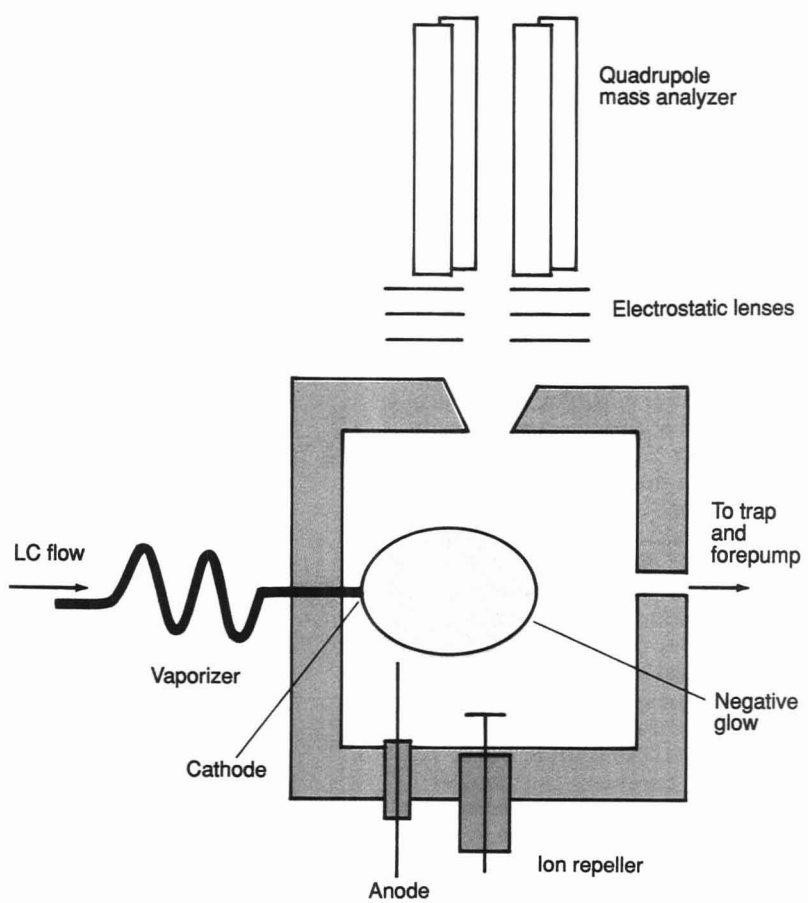

Figure 8. GD used as an ionization cell for the effluent from a liquid chromatograph.

and detection limits range from 0.04 pg for Ag to 800 pg for Se. There is also a complementary technique called FINES (furnace ionization nonthermal excitation spectrometry) in which ionic emission is measured. Direct mass spectrometric measurement of such ions has recently been demonstrated (*25*).

Organic GD applications

Of increasing interest is the use of a GD as an ionization source for organic compounds. Although one might assume that the energetics of the discharge would reduce organic vapors to the elemental state, eliminating any molecular information, this does not appear to be true under certain conditions. For example, direct atmospheric sampling of organic compounds has been developed to detect trace effluents from explosives (*26*). The simple experimental arrangement features a sampled air stream that flows past two parallel plates between which a GD is produced. Ionization of the air is monitored by extraction of the ions into a mass spectrometer. When 2,4,6-trinitrotoluene solutions of known concentrations were used, detection limits of 1–2 pptr were calculated and a linear dynamic range of 6 orders of magnitude was reported.

A commercial application of GD ionization of organic compounds is found in detectors used in a number of thermospray LC/MS instruments. As shown in Figure 8, the effluent from a heated capillary forms a supersonic jet that is injected into a GD for ionization before extraction into a quadrupole mass analyzer and ion detector. Electron filament ionizers can exhibit short lifetimes when oxidizing components are used, but a GD arrangement has a virtually unlimited lifetime, and the ionization is comparable in sensitivity and sample fragmentation to that obtained with an electron gun. Typically, the discharge current is ~1 mA.

Outlook for the future

Although the GD has yet to find acceptance to the degree merited by its analytical potential, this situation may be changing. A perusal of the programs of recent analytical chemistry conferences finds numerous symposia devoted to GD techniques. Leading analytical groups in academia, government, and industry are applying various GD methodologies. Instrument manufacturers are responding to and often contributing to this interest by producing not only instrumentation but also technical reports that detail the striking capabilities of GD methods.

We appear to be reaching a point at which the GD will have a fair test of its real value to the analytical community. The combination of interest from leading research groups, coupled with effective commercial instrumentation, will provide a competitive comparison of these techniques with the stable of other analytical methods. It appears from this vantage point that the GD will be extremely visible in the 1990s.

References

(1) Chapman, B. *Glow Discharge Processes;* John Wiley and Sons: New York, 1980.
(2) Westwood, W. D. *Prog. Surg. Sci.* **1976,** *7*, 71.
(3) Mei, Y.; Harrison, W. W. *Spectrochim. Acta, Part B*, in press.
(4) Klingler, J. A.; Savickas, P. J.; Harrison, W. W. *J. Am. Soc. Mass Spectrom.* **1990,** *1*, 138.
(5) Magee, C. W.; Harrison, W. W. *Anal. Chem.* **1974,** *46*, 461.
(6) Bruhn, C. G.; Bentz, B. L.; Harrison, W. W. *Anal. Chem.* **1978,** *50*, 373.
(7) Harrison, W. W.; Hess, K. R.; Marcus, R. K.; King, F. L. *Anal. Chem.* **1986,** *58*, 341 A.
(8) Jakubowski, N.; Steuwer, D.; Vieth, W. *Fresenius Z. Anal. Chem.* **1988,** *331*, 145.
(9) Hall, D. J.; Sanderson, N. E. *Surf. Interface Anal.* **1988,** *11*, 40.
(10) King, F. L.; Harrison, W. W. *Mass Spec. Rev.* **1990,** *9*, 285.
(11) Harrison, W. W.; Bentz, B. L. *Prog. Analyt. Spectrosc.* **1988,** *11*, 53.
(12) Harrison, W. W. In *Inorganic Mass Spectrometry;* Adams, F.; Gijbels, R.; Van Grieken, R., Eds.; John Wiley & Sons: New York, 1988; Vol. 95, Chapter 3.
(13) Broekaert, J.A.C. *J. Anal. At. Spectrom.* **1987,** *2*, 537.
(14) Grimm, W. *Spectrochim. Acta, Part B* **1968,** *23B*, 443.
(15) Bengtson, A.; Lundholm, M. *J. Anal. At. Spectrom.* **1988,** *3*, 879.
(16) Brenner, I. B.; Laqua, K.; Dvorachek, J. *J. Anal. At. Spectrom.* **1987,** *2*, 623.
(17) *Improved Hollow Cathode Lamps for Atomic Spectroscopy;* Caroli, S., Ed.; Ellis Horwood Limited: Chichester, West Sussex, England, 1985.
(18) Russell, B. J.; Walsh, A. *Spectrochim. Acta* **1959,** *15*, 883.
(19) Ohls, K. *Fresenius Z. Anal. Chem.* **1987,** *327*, 111.
(20) Smith, B. W.; Womack, J. B.; Omenetto, N.; Winefordner, J. D. *Appl. Spectrosc.* **1989,** *43*, 873.
(21) Smith, B. W.; Omenetto, N.; Winefordner, J. D. *Spectrochim. Acta, Part B* **1984,** *39B*, 1389.
(22) Bubert, H. *Spectrochim. Acta, Part B* **1984,** *39B*, 1377.
(23) Falk, H.; Hoffman, E.; Ludke, Ch. *Spectrochim. Acta, Part B* **1981,** *36B*, 767.
(24) Falk, H.; Hoffman, E.; Ludke, Ch. *Spectrochim. Acta, Part B* **1984,** *39B*, 283.
(25) Ratliff, P. H.; Harrison, W. W. *Proceedings of the 38th ASMS Conference on Mass Spectrometry and Allied Topics;* Tucson, AZ, June 3–8, 1990.
(26) McLuckey, S. A.; Glish, G. L.; Asano, K. G.; Grant, B. G. *Anal. Chem.* **1988,** *60*, 2220.

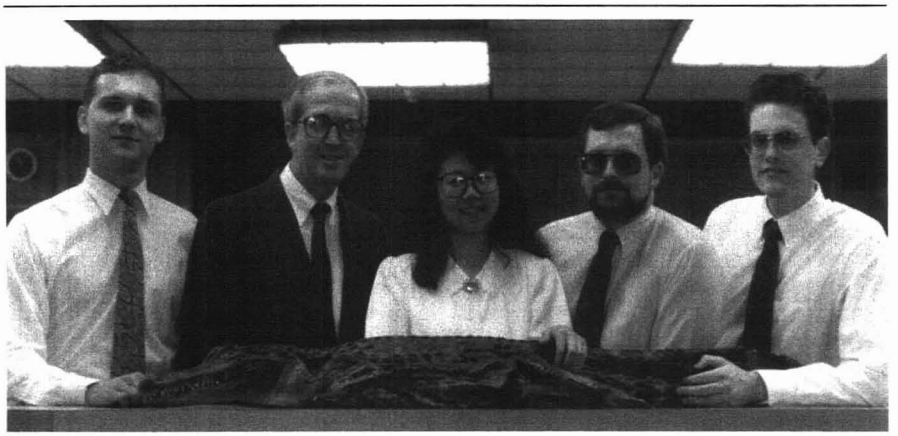

W. W. Harrison (second from left) is professor of chemistry and dean of the College of Liberal Arts and Sciences at the University of Florida. He earned a B.A. degree from Southern Illinois University and a Ph.D. in analytical chemistry from the University of Illinois. His research concerns the use of GDs in MS and atomic spectroscopy.

Chris Barshick (left) received his B.A. degree from Washington and Jefferson College and a Ph.D. in analytical chemistry from the University of Virginia. His research involves the use of analytical probes such as lasers and ion/atom beams to study GD sputter–redeposition processes.

Harrison's remaining co-authors are all Ph.D. candidates at the University of Florida.

Yuan Mei (third from left) earned her B.S. degree in chemistry from Beijing University. Her research centers on manipulating the chemistry of the GD plasma by introducing modifiers such as gettering reagents.

Jeffrey Klingler (second from right) earned his B.A. degree in chemistry from the University of Southern Indiana. His research interests include studies of time-resolved pulsed dc and rf plasmas, both for analytical applications and as tools for investigating fundamental processes in the GD.

Philip Ratliff (right) earned his B.A. degree from East Tennessee State University. His research involves thin-film ablation and the use of electrothermal atomization in GDMS.

Isothermal Titration

Ernesto Freire, Obdulio L. Mayorga[1], and Martin Straume
Biocalorimetry Center
Department of Biology
The Johns Hopkins University
Baltimore, MD 21218

Calorimetric techniques have contributed a great deal to our current understanding of the mechanisms of regulation and control of biological structures and processes at the molecular level. Over the past decade and a half, advances have been made in both the development of highly sensitive microcalorimetric instrumentation and the development of analytical procedures to extract thermodynamic information about biological systems (see References 1–4 for reviews).

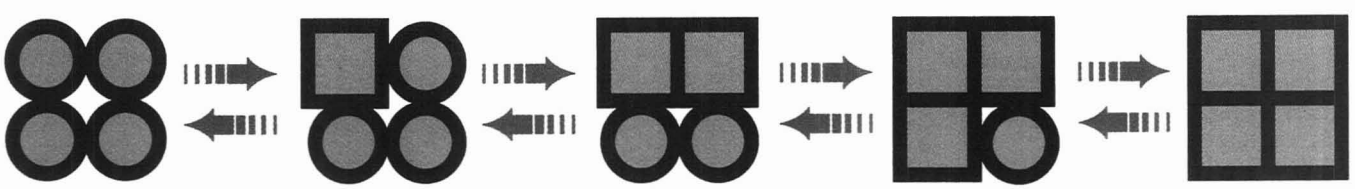

The principal calorimetric techniques that have contributed this information are differential scanning calorimetry (DSC) and isothermal titration calorimetry (ITC). By applying DSC, researchers have learned about the nature and magnitude of the forces that stabilize biological macromolecules (such as proteins and nucleic acids) and macromolecular assemblies (lipid bilayers, protein–lipid complexes, and protein–nucleic acid complexes). Accurate determination of the energy of stabilization of these biological structures by DSC has made possible elucidation of mechanistic details regarding interactions between regions within macromolecules and among components in multimolecular assemblies. DSC experiments involve perturbing the system under study by varying the thermal energy content of the sample (i.e., by scanning temperature as the independent variable under experimental control). The heat capacity of the system is then measured against temperature as the direct thermodynamic observable (recall that the heat capacity is the temperature derivative of enthalpy).

In contrast, ITC measures the energetics of biochemical reactions or molecular interactions (ligand-binding phenomena, enzyme–substrate interactions, and interactions among components of multimolecular complexes) at constant temperature. In this case, reaction is triggered by changing the chemical composition of the sample by titration of a required reactant. The heat associated with the reaction is the direct thermodynamic observable (related to both the enthalpy and extent of reaction). In an ITC experiment, the total concentration of reactant is therefore the independent variable under experimental control.

Because the majority of biological reactions can be induced isothermally, the potential range of applications of ITC far exceeds that of DSC. However, until recently, the use of ITC has been limited because of a lack of sufficient sensitivity. The situation has changed with the recent development of instruments capable of measuring heat effects arising from reactions involving as little as nanomole amounts of reactants (*5–11*). This new generation of titration calorimeters makes possible direct thermodynamic characterization of association processes exhibiting very high affinity binding constants (10^8–10^9 M^{-1}) that are frequently found in biological reactions (*5–11*).

In this article we will present an overview of ITC and recent advances in ITC technology, discuss future directions for further evolution and application of ITC to biomedical research, outline the mathematical treatment of data for some simple binding models, and describe some recent applications of ITC to systems of biological interest.

Binding equilibrium

The association of biological macromolecules with one another as well as their association with small ligand molecules plays a central role in the structural assembly and functional regulation of biological systems and thus has attracted the attention of many investigators in recent decades. Throughout the years, biologists have studied these processes using a variety of experimental techniques and analytical methods to obtain accurate descriptions of their equilibrium behavior.

Several parameters must be included in the description of binding or association equilibria. First is the number of binding sites or stoichiometry of the reaction. Second is the strength of the association, usually expressed in terms of the association constant, K_a, or the Gibbs free energy of association, $\Delta G = -RT \ln K_a$. Third is the characterization of multiple sites and positive or negative cooperative interactions for those cases in which more than one binding site is present. Fourth is the characterization of the enthalpic and entropic contributions to the Gibbs free energy of association ($\Delta G = \Delta H - T\Delta S$). Fifth is the characterization of the dependence of the binding equilibrium on other environmental variables such as pH, ionic strength, and so forth. Most experimental techniques and analytical methods for binding studies are designed to evaluate these different parameters.

Two different approaches are normally used to study the binding equilibrium between two molecules. One approach relies on the direct measurement of the concentrations of free and bound ligand molecules using a technique such as equilibrium dialysis. The other approach takes advantage of the existence of changes in physical observables that are proportional to the extent of binding saturation. The binding of oxygen to hemoglobin, for example, causes changes in the optical absorbance in the Soret region (~420 nm) of hemoglobin (*12–14*). The magnitude of these changes is proportional to the degree of saturation and has been used extensively in the analysis of this binding process (*12–14*).

Calorimetric titration, which belongs to this second type of approach, measures the heat released or absorbed by

[1] Permanent address: Department of Physical Chemistry, University of Granada, Granada, Spain

0003-2700/90/0362-950A/$02.50/0

Calorimetry

Direct Thermodynamic Characterization of Biological Molecular Interactions

INSTRUMENTATION

the stepwise addition of a ligand molecule to a solution containing the macromolecule under study. In general, whatever the approach used to examine binding, the goal is to generate a binding isotherm, a curve that represents the degree of saturation in terms of the ligand concentration. In ITC, the degree of saturation is defined in terms of the heat associated with the reaction.

Throughout the years, different mathematical procedures have been devised to estimate association constants, numbers of binding sites, and cooperative interactions from ligand-binding isotherms. In this respect, the analysis of calorimetrically determined binding isotherms follows the same principles. Among biologists, linearized representations of the data have been widely used in the past. A particularly popular transformation has been the Scatchard plot, in which the ratio of the concentrations of bound and free ligand is plotted against the concentration of bound ligand. These transformations, however, usually introduce statistical biases in the analysis because they obscure the distinction between dependent and independent variables.

In general, a more robust and statistically significant parameter estimation can be achieved by direct nonlinear least-squares analysis of the dependent versus independent variable. With the widespread availability of computers, the trend toward this type of analysis has gained popularity in recent years (*15*, *16*) and this is the type we will discuss here.

The major advantage of titration calorimetry derives from the fact that the binding isotherms are defined in terms of the heats of reaction and as such they allow a direct estimation of enthalpy changes in addition to the association constant. Use of the relation $\Delta G = -RT \ln K = \Delta H - T\Delta S$ allows further calculation of the entropy change. Thus a single calorimetric titration provides a complete characterization of the energetics of binding. In contrast, estimation of enthalpy and entropy changes using noncalorimetric techniques requires several binding experiments at multiple temperatures and subsequent analysis of the temperature dependence of the association constant. Calorimetry is unique because it provides direct measurement of the thermodynamic quantities of interest.

What is ITC?

With ITC, one measures directly the energetics (via heat effects) associated with reactions or processes occurring at constant temperature. Experiments are performed by titration of a reactant into a sample solution containing the other reactant(s) necessary for reaction. After each addition, the heat released or absorbed as a result of the reaction is monitored by the isothermal titration calorimeter. Thermodynamic analysis of the observed heat effects then permits quantitative characterization of the energetic processes associated with the binding reaction.

Applications of ITC in the 1970s were directed toward characterization of the thermodynamics of enzyme-catalyzed reactions (*17–19*), ligand binding to macromolecules (*20–23*), and ligand- or pH-induced macromolecular conformational changes (*24*). However, reliable measurement of heat effects could be performed only at levels of 10^{-3} cal or greater (see References 25–27 for reviews). Because of these limits in sensitivity, only those biological reactions exhibiting relatively strong heat effects could be studied. Entire binding isotherms for ligand-binding reactions could be obtained only for reactions exhibiting ligand association constants of 10^4 M^{-1} or less because sufficiently low reactant concentrations could not be examined to determine higher affinity binding constants. For those binding reactions with $K_a > 10^4$ M^{-1}, only overall binding enthalpies, but not binding constants, could be determined directly from calorimetric titrations (some other method was required to determine K_a).

Over the years, technologies and instrument designs have evolved to produce isothermal titration calorimeters with much improved capabilities for detection of ever smaller heat effects. Such efforts during the 1980s led to the design and construction of titration microcalorimeters capable of measuring heat effects down to levels of 10^{-6} cal (*5–11*). The most significant of these developments have been those related to increasing the specific sensitivity and improving the time response of titration microcalorimeters. Because biomolecular association reactions are frequently characterized by very high binding constants (in the range of 10^8 M^{-1} or greater), experiments must be conducted under conditions of very dilute reactants (10^{-6} M or less) to accurately determine equilibrium constants as well as binding enthalpies. As such, a major goal in calorimetric design is optimization of the specific instrument sensitivity (heat per unit volume) rather than the absolute sensitivity.

Fundamental principles of isothermal titration calorimeter operation

Figure 1 is a schematic showing a differential, power compensation isothermal titration calorimeter (ITC-2) developed at the Biocalorimetry Center at The Johns Hopkins University. Detection of heat effects in this isothermal calorimeter is accomplished by use of semiconductor thermopiles interposed between the titration cells and a heat sink (a large metal mass in thermal equilibrium with a thermostatted water bath). Two titration cells reside in the calorimeter assembly; one acts as the reference and the other as the sample titration cell. When an ITC experiment is being performed, the reference cell contains buffer only and the sample cell contains buffer plus the reactant to which the injected material will be titrated.

Prior to beginning the experiment, the instrument's injection mechanism is filled with titrant, the titration cells are filled with the material to be titrated, and the calorimeter is equilibrated

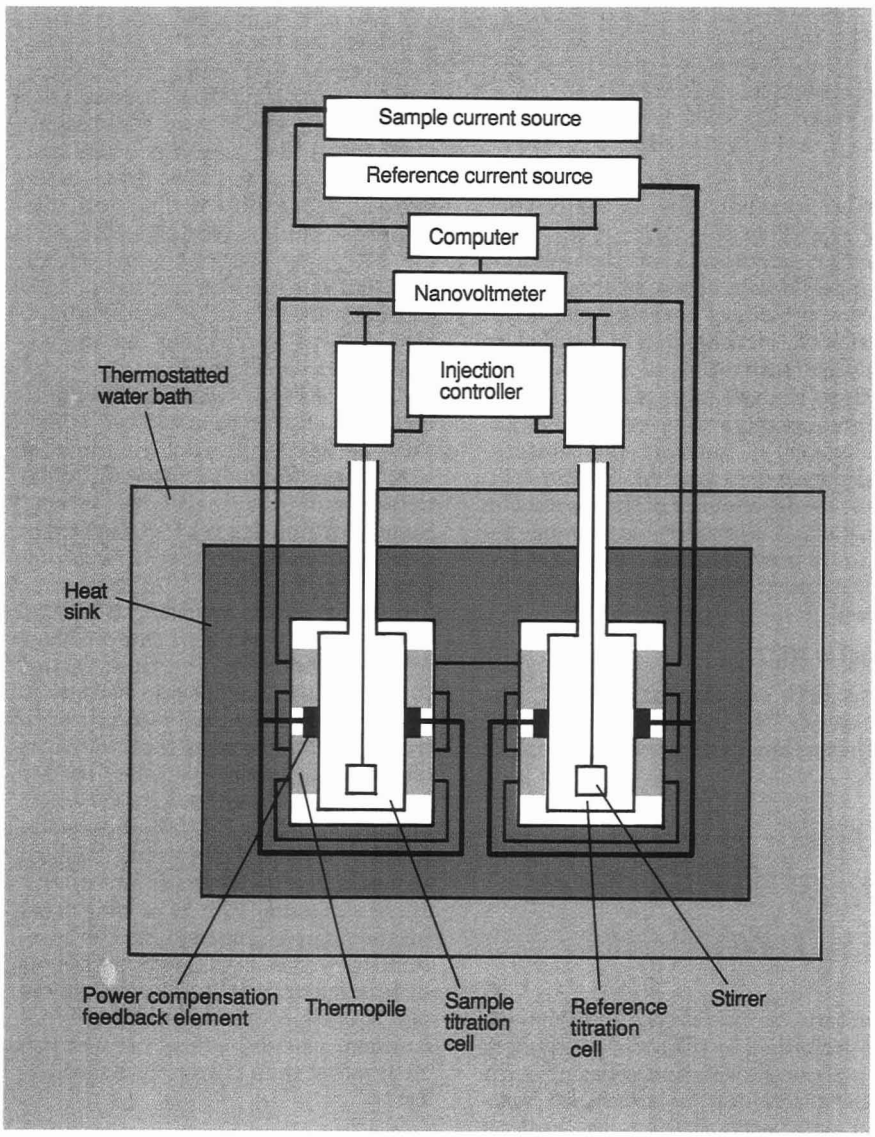

Figure 1. Schematic of the differential, power compensation isothermal titration calorimeter.
See text for operational details.

to the desired temperature such that all components of the instrument (i.e., titration cells, heat sink, and thermostatted water bath) have come to thermal equilibrium relative to each other. Identical injections of reactant are then introduced into both mechanically stirred titration cells by a dual-injection mechanism. The contents of the reference cell exhibit heat effects arising from injection and dilution of the reactant being titrated. The contents of the sample cell exhibit these same heat effects in addition to that associated with the reaction under study. Dual-injection isothermal tiration calorimeters compensate in real time for both the heat effects arising from dilution of the injected reactant into the sample and for any mechanical heat effects arising from injection, yielding the heat of reaction of interest directly.

The titration cell compartments are constructed to permit heat flow between the titration cells and the heat sink only through the thermopile thermal detectors. The output of the thermopiles, an electrical potential (voltage), is directly proportional to the temperature difference across the faces of the thermopiles. This temperature difference, in turn, is proportional to the thermal power (rate of heat transfer [cal s^{-1}]) being exchanged between the titration cells and the heat sink. In the absence of power compensation, the time integral of this rate of heat transfer is the total heat of reaction induced in the respective titration cells as a result of injection.

Because the thermopiles of the sample and reference titration cells are connected in opposition electrically, the experimental quantity actually monitored by this differential isothermal titration calorimeter is the difference in the rates of heat production or absorption between the sample cell and the reference cell. A nanovoltmeter measures the differential voltage output produced by the thermopiles and transmits this information to a computer interfaced for data acquisition and dynamic control of a power compensation mechanism. Power compensation is accomplished by continuously regulating the amount of heat applied to the titration cells so as to drive the temperature difference between the two cells toward the baseline, steady-state value.

The computer monitors the nanovoltmeter output (which is proportional to the temperature difference between the two titration cells) and adjusts the current applied to the cell feedback elements to compensate for the detected change in differential temperature between the cells. The applied thermal power as a function of time required to return the isothermal titration calorimeter to its steady-state temperature differential following an injection then becomes the experimentally determined quantity and is directly proportional to the heat of reaction of interest.

Increased intrinsic sensitivity

Very precise determination of temperature changes is necessary for reliable detection of heat effects on the order of 10^{-6} cal or less. The output of thermopile temperature detectors, as employed in the isothermal titration calorimeter developed in our laboratory and discussed here, is an electrical potential proportional to the temperature difference across the thermopiles. The magnitude of the voltage change per change in temperature is therefore an important consideration in instrument design so as to produce the maximum measurable response. During the past decade, semiconductor bismuth–telluride thermopiles have been introduced possessing 70 thermocouples (the individual temperature-sensing elements of thermopiles) per square centimeter. The use of thermopiles with a high density of thermocouple junctions per unit area provides enhanced voltage per degree response. The ITC-2 is equipped with 1056 of these junctions and is able to detect changes on the order of 10^{-8} cal s^{-1} (i.e., 40–50 nW) in thermal power.

Minimization of baseline noise is another factor important for improving isothermal titration calorimeter sensitivity levels. In the ITC-2 we have housed the titration calorimeter assembly in an ultrastable thermostat-

ted water bath to regulate temperature. Any fluctuations in bath temperature will transmit the temperature change via the heat sink to the titration cells and contribute to baseline noise, compromising instrument performance. The thermal damping effect provided by the mass of the metal heat sink in ITC-2 coupled with a stable thermostat capable of maintaining temperatures to within 10^{-6}–10^{-5} °C over periods of minutes (and within 10^{-4} °C over 8 h) (*28*) has reduced the magnitude of baseline noise to a level on the order of 10^{-8} cal s^{-1} (i.e., tens of nanowatts), thereby facilitating detection of small heat effects.

The ability to perform differential measurements of reference and sample responses in dual-injection instruments facilitates more accurate determination of heats of reaction. Because reaction is initiated in an ITC experiment by injection of a reactant, heat effects resulting from the mechanical disturbance of the injection event itself and dilution of the titrant are present in addition to the heat of reaction, which is the quantity of interest. A differential, dual-injection isothermal titration calorimeter compensates for these heat effects in real time. This eliminates the need for two separate experiments (a reference experiment to yield heats of injection and dilution and a sample experiment to exhibit these effects and that of the reaction of interest) as required in a single-injection ITC (*11*).

Treatment of data obtained from single-injection ITC experiments involves subtracting these two individually observed responses to yield estimates of the heat of reaction of interest (*11*). Because they compensate in real time for any mechanical and dilution heat effects, dual-injection titration microcalorimeters capable of differential measurements do not introduce the additional error arising from consideration of two separate measurements.

Improved time response

The implementation of power compensation mechanisms some years ago has been a major factor in improving the time response of isothermal titration and differential scanning calorimeters and therefore in providing more accurate measurement of small heats of reaction (*7*). Because the total heat associated with a reaction is the time integral of the differential thermal power released or absorbed as a result of the reaction, reducing the time response is a means to more sensitive detection of total heat effects per injection. Heat conduction isothermal titration calorimeters passively transfer heat between the titration cell(s) and heat sink, giving rise to instrument time responses with lifetimes on the order of 100–300 s (*8–10*). The instrument discussed here uses continuous power compensation for active heat transfer and exhibits both considerably reduced instrument response times and improved signal-to-noise (S/N) characteristics. Active power compensation mechanisms, as introduced by McKinnon et al. (*7*), lead to reduced instrument response times and produce greater thermal power amplitude (the experimental observable) for equivalent heat effects. In other words, the S/N is increased as a result of the enhanced thermal power amplitude necessary to generate the same total observed heat signal (area under the thermal power versus time curve) in a shorter period of time before return to baseline.

This effect is demonstrated in Figure 2 in which the response signal of the instrument to identical 25 μcal pulses is recorded for both the case in which power compensation is active and in which it is not (heat conduction mode). In both cases, the areas under the curves are identical but the signal deflection is approximately four times larger when power compensation is active. In the absence of power compensation, the instrument time response is 100 s whereas under power compensation conditions it is only 15 s. The recorded quantity in a power compensation titration calorimeter is the amount

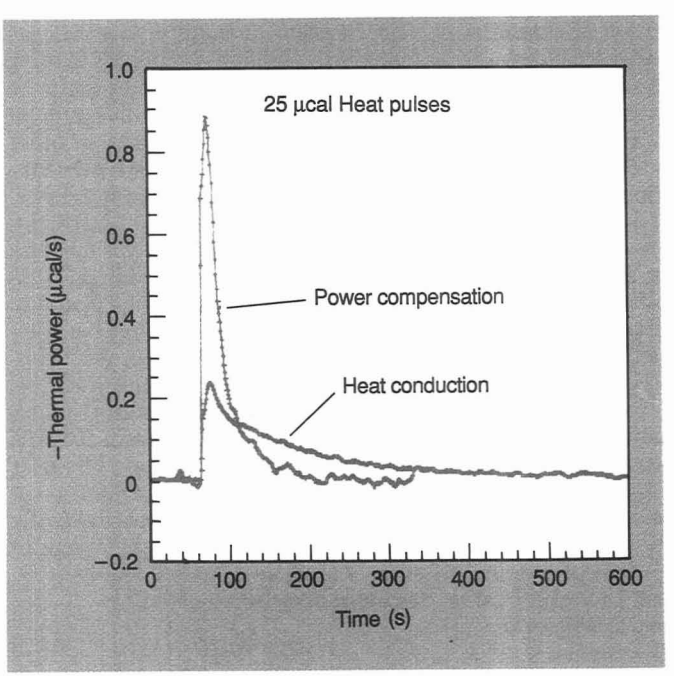

Figure 2. Power compensation vs. heat conduction modes of ITC-2 operation.

The observed differential thermal power vs. time response in the power compensation mode is distributed over a shorter period of time than that measured in the heat conduction mode. The amplitude of the thermal power response in the power compensation mode is greater than that detected in the heat conduction mode because of the more rapid instrument response.

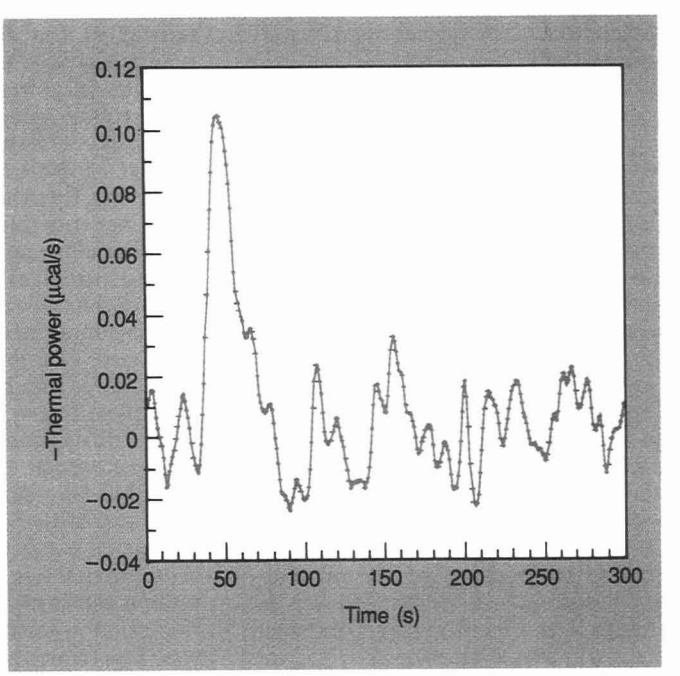

Figure 3. Differential thermal power vs. time response obtained from introduction of a 0.5 μcal mL^{-1} electrical calibration pulse into the sample titration cell of ITC-2 (sample contains 5 mL of water).

The maximum peak amplitude is 105 ncal s^{-1} (21 ncal s^{-1} mL^{-1}) with S/N sufficiently high to permit reliable measurements to considerably less than 1 μcal mL^{-1} $event^{-1}$.

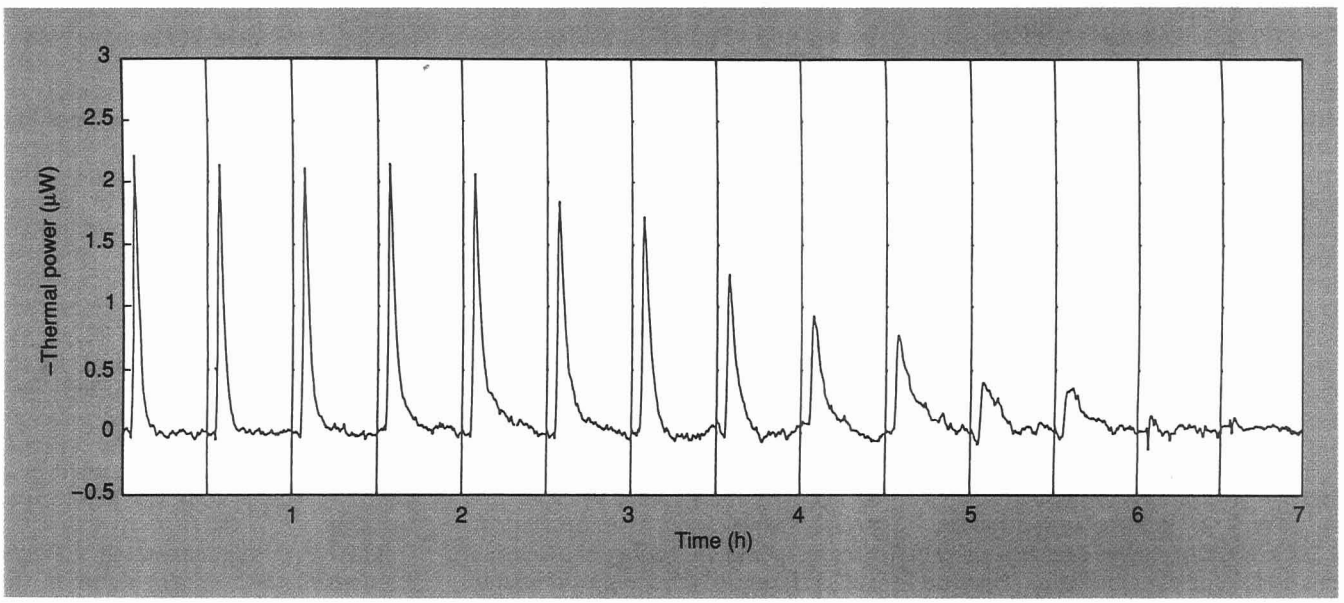

Figure 4. Isothermal calorimetric titration of cholera toxin B-subunit pentamer with oligo-G_{M1}, the oligosaccharide cell surface receptor for cholera toxin.

The differential power output in microwatts (4.184 μW = 1 μcal s^{-1}) is shown as a function of time and was obtained from successive injections of 3 nmol of oligo-G_{M1} (30-μL injections of 0.1 mM oligo-G_{M1}) into a solution of 4.9 nmol of B-subunit pentamer in 1.4 mL. (Reprinted from Reference 10.)

of thermal power that must be applied to compensate for the heat of reaction induced by injection. Because the intrument is both continuously monitoring the temperature differential (thermopile output) and continuously regulating the amount of applied thermal power (through the feedback elements) to actively return the system to the preinjection, steady-state temperature differential, the time required to obtain the total heat associated with the induced reaction is reduced.

In order to have the capability to compensate for exothermic and endothermic effects, a constant amount of thermal power is applied to both titration cells and a steady-state flux of thermal throughput from the cells to the heat sink is established. The amount of steady-state power applied to the cells is sufficiently small (0.5 mA of current through ~230 Ω of resistance, producing 14–15 × 10^{-6} cal s^{-1} of thermal power in 5 mL of cell volume) so that the overall temperature is not perturbed beyond the fluctuation regime of the thermostat. Compensation is accomplished by regulating the power introduced through the feedback elements (by changing the amount of applied current) in proportion to the change in thermopile output (detected change in temperature).

In addition to power compensation, the thin, disk-shaped gold titration cells used in the ITC-2 contribute to optimizing the response time. Positioning the walls of the titration cells in close opposition to each other minimizes the distance heat must travel through the medium prior to encountering the thermopiles (which are in direct contact with the cell faces between the titration cells and heat sink). This design facilitates rapid detection of heat effects induced in the titration cell contents by injection of titrant.

Definitions used for reporting response times and noise levels vary in the literature and commercial documentation. Our definition of response time is the time required for decay of the thermal power amplitude to $1/e$ of its maximum value. Response times are frequently referred to, however, in the context of rise times to half maximal amplitude. By that definition, the ITC-2 has a response time of 3–4 s. In considering baseline noise levels, we report baseline noise as the standard deviation of the noise amplitude in individual baselines, in contrast to the standard error of reproducibility obtained from a large number of multiple, identical injections.

The differential, power compensation isothermal titration calorimeter described here currently has a limit of resolution of 10^{-6} cal of total heat. This represents a substantial improvement of approximately 3 orders of magnitude in sensitivity from the ~10^{-3} cal resolution in earlier reaction calorimeters. The titration cell volume is 5 mL, making the limit of specific sensitivity ~0.2 × 10^{-6} cal mL^{-1}.

An example of the limiting resolution of the instrument is presented in Figure 3, which shows its response to a pulse of 0.5 × 10^{-6} cal mL^{-1} (2.5 × 10^{-6} cal total heat) introduced into the sample titration cell. The baseline noise level is ±4–8 × 10^{-9} cal s^{-1} (standard deviation) or a peak-to-peak noise of 40 × 10^{-9} cal s^{-1} corresponding to a specific noise level of ±0.8–1.6 × 10^{-9} cal s^{-1} mL^{-1} (standard deviation) or a peak-to-peak specific noise of 8 × 10^{-9} cal s^{-1} mL^{-1}.

Analysis of ITC data

The function of many biological systems is modulated by ligand binding (e.g., binding of hormones or toxins to their target receptors, allosteric or feedback control of enzymes or other functional proteins, signal peptide–membrane interactions, and protein–nucleic acid interactions). Characterization of the energetics of such processes may be accomplished by ITC experiments. Upon binding of a ligand to a macromolecule (e.g., protein) or macromolecular assembly (e.g., multisubunit protein or membrane systems), heat will be released or absorbed accompanying the binding event (i.e., the enthalpy of ligand binding). The heat effects associated with each addition of ligand represent the experimentally observed response in an ITC experiment. For each injection, the heat released or absorbed is given by

$$q = V\Delta H\Delta[L_B] \qquad (1)$$

where q is the heat associated with the change in bound ligand concentration, $\Delta[L_B]$ is the change in bound ligand concentration, ΔH is the enthalpy of binding (mol ligand)$^{-1}$, and V is the reaction volume.

Because q is directly proportional to

the increase in ligand bound resulting from each injection, its magnitude decreases as the fractional saturation of the system is titrated stepwise to completion. This is illustated in Figure 4 in which the B-subunit pentamer of cholera toxin is calorimetrically titrated with oligo-G_{M1}, the oligosaccharide binding region of its glycolipid cell surface receptor (see the section "Cholera toxin binding to oligo-G_{M1}" later in this article for more detail). The total cumulative heat released or absorbed is directly proportional to the total amount of bound ligand as

$$Q = V\Delta H \sum \Delta[L_B] = V\Delta H[L_B] \quad (2)$$

where Q is the cumulative heat and $[L_B]$ is the concentration of bound ligand.

Evaluation of calorimetric titration data as either individual or cumulative heat requires consideration of the heat evolved or absorbed as a function of total ligand added, or the total ligand concentration (the independent variable). Therefore, in the analysis of experimental data, the binding equations must be expressed in terms of the individual or cumulative heat released or absorbed as a function of total ligand concentration because these are the quantities experimentally known.

Multiple sets of independent binding sites

The most widely used theoretical framework for the analysis of binding data in biology is the so-called Multiple Sets of Independent Binding Sites model (for a complete review, see References 29 and 30). Within this framework, a macromolecule possesses an arbitrary number of sets of noninteracting binding sites. All of the sites in the same set possess the same intrinsic affinity for the ligand molecule. The great popularity of this model is due in part to its flexibility, which allows characterization of a large number of situations (See References 29 and 30 for some representative examples).

As expressed in Equation 1, the heat associated with the binding reaction is directly proportional to the concentration of bound ligand, $[L_B]$. For a system exhibiting multiple sets of independent binding sites, the concentration of ligand bound to each set is given by

$$[L_{B,i}] = [M]\frac{n_i K_i[L]}{1 + K_i[L]} \quad (3)$$

where $[L_{B,i}]$ is the concentration of ligand bound to binding sites of set i, $[M]$ is the total concentration of macromolecule available for binding ligand, K_i is the intrinsic site association constant for binding sites of set i, n_i is the number of binding sites of set i on each macromolecule M, and $[L]$ is the concentration of free ligand.

The cumulative amount of heat released or absorbed as a result of ligand binding is given by the sum of the heats corresponding to each set as

$$Q = V\sum_i \Delta H_i[L_{B,i}]$$

$$= V[M]\sum_i \frac{n_i\Delta H_i K_i[L]}{1 + K_i[L]} \quad (4)$$

where ΔH_i is the enthalpy of binding (mol ligand)$^{-1}$ to binding sites of set i. This equation can be expressed in terms of the total ligand concentration by way of the mass conservation expression $[L_T] = [L_B] + [L]$ (where $[L_T]$, $[L_B]$, and $[L]$ represent the total, bound, and free ligand concentrations, respectively). Analysis of calorimetric titration data is then performed by estimating the variable model parameters (n_i, K_i, and ΔH_i) by fitting either to the cumulative heat, Q, or to the individual heat, q (where the individual heat associated with the j-th injection event is q_j such that $q_j = Q_j - Q_{j-1}$). Analysis of data directly in terms of individual heats, q, is preferable because it eliminates propagation of the uncertainties associated with each successive injection that are necessarily present in cumulative heat data.

The two simplest cases are for one and two independent sets of ligand-binding sites. These cases allow explicit, closed-form expressions for Q as a function of total ligand concentration as illustrated in Figures 5 and 6.

Figure 5 presents a schematic depiction and the closed-form equations characteristic of ligand binding to a macromolecule possessing one set of independent ligand-binding sites, the simplest special case of the general expression given by Equation 4. In the example depicted in this figure, the ligand-binding macromolecule possesses four independent and equivalent ligand-binding sites. Although $n = 4$ in this example, the expressions presented here are valid for any value of n. The open circles in the figure correspond to binding sites without bound ligand whereas the shaded squares represent binding sites with ligand bound. The binding constant, K, characterizes the affinity of each ligand-binding site for ligand L. The factors of 4, 3/2, 2/3, and 1/4 are the particular statistical factors necessary to define the respective macroscopic equilibria for this case (i.e., $n = 4$) in terms of the site affinity constant, K.

The total cumulative heat, Q, is most conveniently expressed in terms of the free ligand concentration, $[L]$. However, the independent variable in ITC experiments is the total ligand concentration, $[L_T]$ (where $[L_T] = [L_B] + [L]$ and $[L_B]$ is the concentration of bound ligand). By recognizing that $[L_B] = Q/V\Delta H$ (where V is the reaction volume and ΔH is the binding enthalpy per mole of ligand), a closed-form expression is obtained for the cumulative heat, Q, in terms of the total ligand concentration, $[L_T]$. The energetics of a system obeying this model for ligand

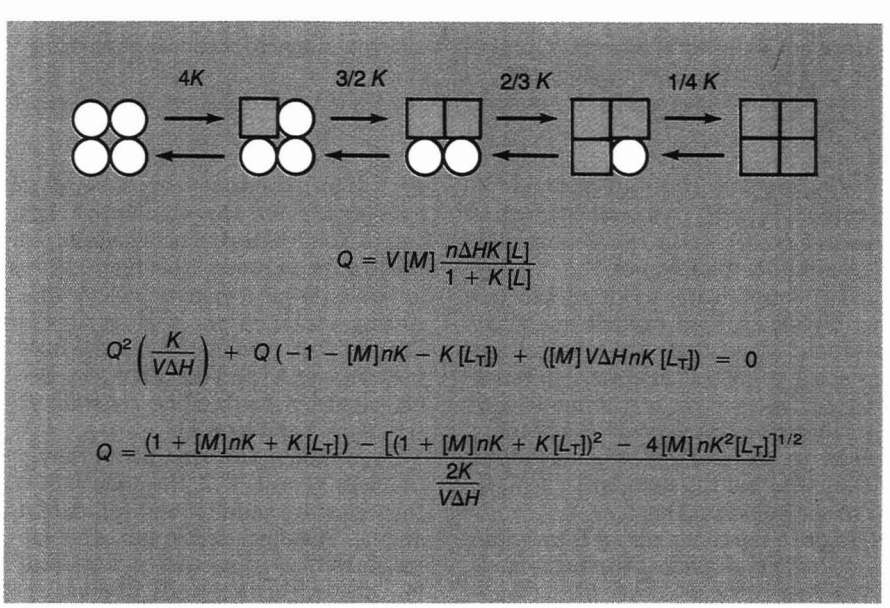

Figure 5. Schematic depiction and closed-form equations characteristic of ligand binding to a macromolecule possessing one set of independent ligand-binding sites. Shaded regions represent subunits to which ligand is bound. See text for a detailed description of relevant concepts.

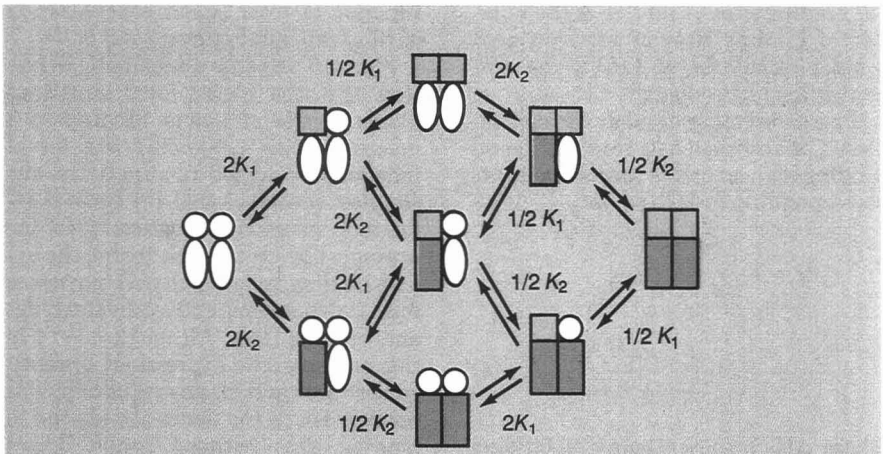

$$Q = Q_1 + Q_2 = (\Delta H_1[L_{B,1}] + \Delta H_2[L_{B,2}])\,V$$

$$Q = V[M]\left(\frac{n_1\Delta H_1K_1[L]}{1 + K_1[L]} + \frac{n_2\Delta H_2K_2[L]}{1 + K_2[L]}\right)$$

$$[L_B] = [M]\left(\frac{n_1K_1[L]}{1 + K_1[L]} + \frac{n_2K_2[L]}{1 + K_2[L]}\right)$$

$$[L] = [L_T] - [M]\left(\frac{n_1K_1[L](1 + K_2[L]) + n_2K_2[L](1 + K_1[L])}{(1 + K_1[L])(1 + K_2[L])}\right)$$

$$[L] = 2(-y)^{1/2}\cos\left(\frac{\phi}{3}\right) - \frac{B}{3A}$$

$$\phi = \arccos\left[\frac{-x}{(-y^3)^{1/2}}\right]$$

$$x = \left(\frac{B}{3A}\right)^3 - \frac{BC}{6A^2} + \frac{D}{2A}$$

$$y = \frac{C}{3A} - \left(\frac{B}{3A}\right)^2$$

$$A = K_1K_2$$

$$B = K_1 + K_2 + K_1K_2[[M](n_1 + n_2) - [L_T]]$$

$$C = 1 + [M](n_1K_1 + n_2K_2) - [L_T](K_1 + K_2)$$

$$D = -[L_T]$$

Figure 6. Closed-form equations for ligand binding to a macromolecule possessing two sets of independent binding sets.

Shaded regions represent subunits to which ligand is bound. See text for a detailed description of relevant concepts.

binding may therefore be considered in terms of $[L_T]$, $[M]$ (the total concentration of ligand-binding macromolecule), n, K, and ΔH for a known V.

This simple case is one of the few permitting such an explicit analytical solution. In general, a numerical approach is needed to express Q in terms of $[L_T]$. Estimation of the model parameters characteristic of this binding model (n, K, and ΔH) then requires fitting to either the cumulative heat, Q, or to the individual heat, q.

Figure 6 shows the closed-form equations for ligand binding to a macromolecule possessing two sets of independent binding sites. This case is an extension of the model presented in Figure 5 according to the general expression of Equation 4 and permits derivation of convenient closed-form expressions for the cumulative heat versus total ligand concentration. For illustrative purposes, this figure shows an example of a macromolecule possessing a total of four binding sites for ligand L, two of which have a site binding constant K_1 and the other two characterized by site binding constant K_2 (i.e., $n_1 = 2$ and $n_2 = 2$).

Even though the example in the figure uses $n_1 = n_2 = 2$, the equations in the figure are valid for any values of n_1 and n_2. The open circles and ovals represent the two respective types of binding sites without ligands whereas the shaded squares and rectangles correspond to the respective types of sites with ligands. The factors 2 and $\frac{1}{2}$ are the statistical factors necessary to define the indicated macroscopic equilibria in this example in terms of the site binding constants, K_1 and K_2 (i.e., for the case where both n_1 and $n_2 = 2$).

The total cumulative heat, Q, will be composed of contributions from binding to each of the two sets of ligand-binding sites on the macromolecule, Q_1 and Q_2. These, in turn, are related to the reaction volume, V, the respective site-binding enthalpies, ΔH_1 and ΔH_2 (per mole of bound ligand), and the concentrations of ligand L bound to the respective types of sites on the macromolecule, $[L_{B,1}]$ and $[L_{B,2}]$. Although the solution for this case is considerably more involved than that for the single-set-of-sites case (see Figure 5), expressions in terms of the total ligand concentration, $[L_T]$ (the independent variable in a titration experiment), may be obtained explicitly.

Cases in which more than two sets of binding sites are present cannot be solved in closed form and iterative numerical procedures must be used to solve Equation 4. In general, other situations like those in which cooperative interactions are present can be approached following the same philosophy, that is, development of the binding equations in terms of the total ligand concentration. For example, this approach has been used for the cooperative binding of cholera toxin to oligo-G_{M1}, the oligosaccharide binding region of its glycolipid cell surface receptor (*10*).

ITC applied to biological systems

We conclude this article by surveying some representative biological systems that have been studied by ITC.

Nucleotide binding to ribonuclease A. The detailed thermodynamic properties of 3′-cytidine monophosphate (3′CMP) binding to ribonuclease A (RNaseA) were studied in a comprehensive calorimetric titration study undertaken by Biltonen and co-workers in the 1970s (*20*, *21*, *31*, *32*). Initial experiments were directed toward characterizing the fundamental thermodynamic binding properties of this system (Gibbs free energy, enthalpy, and entropy of interaction) in addition to binding stoichiometry and how these properties are influenced by salt concentration (*20*). In low-ionic-strength solution (μ = 0.05 in either NaCl or KCl, pH 5.5), a binding stoichiometry of one 3′CMP bound per RNaseA molecule was found exhibiting ΔG = ~−6.2 kcal mol^{-1} (corresponding to an association constant of 3.7×10^4 M^{-1}), ΔH = ~−15.5 kcal mol^{-1}, and ΔS = ~−30 cal K^{-1} mol^{-1} for the binding process.

The thermodynamic binding param-

eters varied in a continuous manner with increasing ionic strength until at $\mu = 3$ (in sodium acetate, pH 5.5), the ΔG for binding became less favorable to ~ -4.5 kcal mol^{-1} (corresponding to an association constant of 2.1×10^3 M^{-1}) as a result of a considerably less favorable ΔH for binding (which became ~ -6 kcal mol^{-1}) and despite a somewhat more favorable ΔS for binding (~ -5 cal K^{-1} mol^{-1}).

Analysis of the enthalpic and entropic contributions to the free energy of protonation of the four histidine residues of RNaseA suggested that binding of 3′CMP is coupled to ionization of three of these residues. It has been suggested that the negative phosphate moiety of 3′CMP interacts electrostatically with two positively charged histidines and that interaction with the third (which shows an anomolously large enthalpy of protonation) involves a conformational rearrangement of the structure of RNaseA (*21*). The dependence on pH of the enthalpic and entropic contributions to the overall free energy of 3′CMP binding, when considered in conjunction with structural information, led to the conclusion that both van der Waals and electrostatic interactions contribute to binding but that the binding process is only weakly coupled to the conformational change associated with protonation of the histidine residues (*31*, *32*).

Ligand binding and conformational transitions in human hemoglobin. The energetics associated with the binding of a variety of ligands to native and mutant human hemoglobins have been examined by application of titration calorimetric methods (*33–36*). By performing calorimetric titrations in buffers differing in their heats of protonation, the enthalpies of protonation of ionizable groups (histidines and/or α-amino groups) in response to oxygen, carbon monoxide, and inositol hexaphosphate (IHP) binding have been determined at different pHs. Enthalpies of carbon monoxide binding have been reported to be ~ -23 kcal (mol CO)$^{-1}$ in the pH range from 6 to 9 (after correction for enthalpies of ionization of protein groups) (*33*).

These results were shown to be consistent with a model in which two ionizable histidines explain the origin of the Bohr proton effect. Interpretation of the relative enthalpic contributions of carbon monoxide binding and protein group ionization in a mutant and native human hemoglobin suggests that the enthalpy of protonation of ionizable protein groups is an important driving force for regulating heme site ligation as well as subunit association and hemoglobin tetramer conformational transitions.

The regulation of hemoglobin's functional properties is related to its ability to bind oxygen cooperatively. Calorimetric information from carbon monoxide-binding results obtained from a mutant hemoglobin (Hb M Iwate) and native hemoglobin, in conjunction with independent determinations of T-to-R transition free energies, suggests that the structural transition responsible for modifying the affinity of human hemoglobin for oxygen (the T-to-R transition, which gives rise to its cooperative oxygen-binding properties) is enthalpically controlled at pH 7.4 (with $\Delta H = 9 \pm 2.5$ kcal mol^{-1}) but entropically controlled at pH 9 (with $\Delta H = -12 \pm 2.5$ kcal mol^{-1}) (*34*).

The interaction of the regulatory ligand inositol hexaphosphate exhibits binding enthalpies of up to ~ -25 kcal mol^{-1} at pH 7.4 (after correction for buffer ionization effects). This binding corresponds to ~ -11 kcal (mol H$^+$ absorbed)$^{-1}$ associated with IHP binding. The binding of this regulatory ligand has therefore been concluded to be driven primarily by the exothermic protonation of histidine and/or α-amino groups as induced by the proximity of the negative phosphate charges on IHP (*35*, *36*).

Signal peptide–lipid association. The interactions of the signal peptide of ornithine transcarbamylase with phospholipid vesicles of varying composition have recently been studied by isothermal titration calorimetry (*9*). It is the signal peptide sequences of newly translated mitochondrial proteins that have been recognized as being responsible for targeting and facilitating transport of these proteins into mitochondria. Because these sequences contain a large proportion of basic amino acids, they are expected to exhibit a strong interaction with the highly negative charged inner mitochondrial membrane. Titration of the signal peptide into phospholipid bilayers of surface charge density similar to that of the inner mitochondrial membrane reveals a strong binding characterized by an association constant on the order of 10^6 M^{-1} and an enthalpy change of -60 kcal mol^{-1}.

The experiments were consistent with a binding stoichiometry of 1 peptide bound per 20 negatively charged phospholipid molecules. The magnitude of the binding constant indicates a strong membrane association, similar to that required for mitochondrial protein import and similar to that obtained from inhibition studies of the precursor protein (pre-ornithine transcarbamylase) by the synthetic signal sequence (*37*).

Cholera toxin binding to oligo-G_{M1}. Cholera toxin is a multisubunit protein consisting of a five-subunit ring, the B-subunit pentamer (M_r = 58 000), which surrounds the dimeric A-subunit (M_r = 27 000). The B-subunit pentamer binds to five ganglioside G_{M1} molecules on the outer surface of the cell membrane, and subsequently the A-dimer penetrates the cell membrane where it activates adenylate cyclase. The association of the B-subunit pentamer with the oligosaccharide region (oligo-G_{M1}) of the ganglioside triggers the sequence of events that leads to the release of the A-subunit from the B-subunit pentameric ring and its insertion into the interior of the membrane.

For many years it was known that the association of oligo-G_{M1} with the toxin exhibited positive cooperativity (*38*) even though the actual energetics and mechanism of this behavior remained difficult to elucidate by conventional techniques. These cooperative effects have their origin at the oligosaccharide–protein interface and result in the modification of the behavior of the pentameric ring (*39*) during membrane association, presumably facilitating the release of the A-subunit into the membrane interior.

Recently, the binding of oligo-G_{M1} was measured by isothermal titration calorimetry (*10*). These experiments also indicated positive cooperativity and allowed a complete mapping of intrinsic as well as cooperative interactions. The data were consistent with a nearest-neighbor model in which the binding of oligo-G_{M1} to one B-subunit enhances the affinity of adjacent B-subunits. The experiments yielded an intrinsic association constant of 1.05×10^6 M^{-1} at 37 °C and a cooperative free energy of -850 cal mol^{-1}. The magnitude of the cooperative free energy indicates a fourfold enhancement in the oligo-G_{M1} binding affinity of a B-subunit adjacent to a subunit to which oligo-G_{M1} is already bound. The intrinsic enthalpy change of binding was -22 kcal (mol oligo-G_{M1})$^{-1}$ and the cooperative interaction enthalpy was -11 kcal mol^{-1}.

The magnitude of the cooperative interaction enthalpy is consistent with a moderate structural "tightening" of the B-pentamer in agreement with spectroscopic data. Within the context of the cholera toxin–cell surface interaction, the cooperative enhancement has a twofold effect: It facilitates a complete (i.e., productive) attachment of the toxin to the membrane surface once the initial contact has occurred and it facilitates the release of the A-subunit into the interior of the mem-

brane through its associated conformational change.

Amino acid interactions with human plasminogen. A thermodynamic characterization by titration calorimetry of the binding of ϵ-amino caproic acid (EACA) to the isolated kringle 4 region (K4) of human plasminogen has recently been reported (*40*). Activation of human plasminogen is effected by the binding of α- and ω-amino acids. The K4 of human plasminogen is one of five highly homologous regions that are believed to be quite independent domains. These domains are believed to be the functionally significant structural components of plasmin(ogen) responsible for mediating interactions with substrates as well as with negative and positive effectors. Calorimetric titrations with EACA were consistent with a single-set-of-binding-sites model and produced model parameters of $n = 0.87$, $K_a = 3.82 \times 10^4$ M^{-1}, $\Delta H = -4.50$ kcal mol^{-1}, and $\Delta S = 6.01$ cal K^{-1} mol^{-1} (*40*). The lack of a significant pH dependence on the thermodynamics of EACA binding (in the range from 5.5 to 8.2) suggested that titratable groups on K4 do not affect this binding interaction.

Further experiments with a series of structural analogues of EACA (3-aminopropionic acid, 4-aminobutyric acid, 5-aminopentanoic acid, 7-aminoheptanoic acid, 8-aminooctanoic acid, *trans*-(4-aminomethyl)cyclohexanecarboxylic acid, and L-lysine) demonstrated that both the length of the hydrophobic region between the amino and ω-carboxyl groups of the ligand and ligand steric structural constraints are important factors in determining the affinity of interaction (*40*).

Calcium and magnesium binding to oncomodulin. The calcium- and magnesium-binding properties of oncomodulin, a calcium-binding protein found in a variety of tumor, transformed, and nonembryonic placental cells, have been thermodynamically characterized by direct binding studies and calorimetric titration experiments (*41*). Oncomodulin possesses two Ca^{2+} and/or Mg^{2+} binding sites. The first site binds either Ca^{2+} or Mg^{2+} ions and exhibits a much higher affinity for Ca^{2+} than Mg^{2+} ($K_a(Ca^{2+}) = 2.2 \times 10^7$ M^{-1}, $K_a(Mg^{2+}) = 4.0 \times 10^3$ M^{-1}). Calcium binding to this site is competitively inhibited by Mg^{2+}. The second site binds Ca^{2+} only, but with a lower intrinsic affinity than the first ($K_a = 1.7 \times 10^6$ M^{-1}). Despite these differences in Ca^{2+} binding affinity, the exothermic Ca^{2+} binding enthalpies were the same for each site ($\Delta H = -4.52$ kcal mol^{-1}) giving rise to different positive Ca^{2+} binding entropy changes for the two sites ($\Delta S = 18.4$ cal K^{-1} mol^{-1} for the high affinity site and $\Delta S = 13.4$ cal K^{-1} mol^{-1} for the low affinity site). Binding of Mg^{2+} is associated with an endothermic enthalpy change and an even more positive entropy change than that seen with Ca^{2+} binding to either site ($\Delta H = 3.1$ kcal mol^{-1} and $\Delta S = 26.5$ cal K^{-1} mol^{-1}).

The thermodynamics of ion binding to the Ca^{2+}–Mg^{2+} site are similar to those observed in parvalbumins, a family of structurally related Ca^{2+} and Mg^{2+} binding proteins that are believed to function simply as intracellular Ca^{2+} and Mg^{2+} buffers. The presence of a Ca^{2+}-specific site on proteins of this class, however, suggests that oncomodulin may function as a signal-transducing Ca^{2+} binding protein (*41*). The presence of such specific Ca^{2+} binding properties has been associated with other proteins of this class that are involved in signal transduction (e.g., calmodulin, troponin C, S100, calpains, squidulin, and Ca^{2+} vector protein) and is believed to provide a mechanism for inducing conformational changes that regulate interactions with target proteins in response to changes in intracellular Ca^{2+} (*41*). Comparison of the thermodynamics of Ca^{2+} binding to oncomodulin at its Ca^{2+}-specific site to that of calmodulin shows some interesting differences. Whereas modulation of the exposure of hydrophobic protein regions is suggested to be involved in the functional regulation of calmodulin by Ca^{2+} binding (because of the strong entropy-driven nature of the binding interaction), Ca^{2+} binding to oncomodulin may be primarily electrostatic in nature (because of the nearly equal favorable enthalpic and entropic contributions of Ca^{2+} binding) (*41*).

Conclusion

The ability to measure small heats of reaction on the order of 10^{-7}–10^{-6} cal (mL of solution^{-1}) has opened the door to a direct thermodynamic characterization of many biological systems. Current sensitivity levels of isothermal titration microcalorimeters allow direct examination of binding processes exhibiting K_as as high as 10^8–10^9 M^{-1}. High sensitivity is also important when considering structurally complex systems like biological membranes, intact cells, or other biological systems that are difficult to concentrate or obtain in relatively large amounts. The recent developments in ITC technology presented here together with parallel advancements in data analysis methods are permitting a direct calorimetric characterization of biological phenomena previously beyond the scope of this experimental technique.

References

(1) Biltonen, R.; Freire, E. *CRC Crit. Rev. Bioc.* **1978,** *5*, 85.
(2) Privalov, P. L. *Adv. Prot. Chem.* **1982,** *35*, 1.
(3) Freire, E. *Comments Mol. Cell. Biophys.* **1989,** *6*, 123.
(4) Privalov, P. L.; Tiktopulo, E. I.; Venyaminov, S., Yu.; Griko, Yu., V.; Makhatadze, G. I.; Khechinashvili, N. N. *J. Mol. Biol.* **1989,** *205*, 737.
(5) Spokane, R. B.; Gill, S. J. *Rev. Sci. Instrum.* **1981,** *52*, 1728.
(6) Donner, J.; Caruthers, M. H.; Gill, S. J. *J. Biol. Chem.* **1982,** *257*, 14826.
(7) McKinnon, I. R.; Fall, L.; Parody, A.; Gill, S. J. *Anal. Biochem.* **1984,** *139*, 134.
(8) Ramsay, G.; Prabhu, R.; Freire, E. *Biochemistry* **1986,** *25*, 2265.
(9) Myers, M.; Mayorga, O. L.; Emtage, J.; Freire, E. *Biochemistry* **1987,** *26*, 4309.
(10) Schon, A.; Freire, E. *Biochemistry* **1989,** *28*, 5019.
(11) Wiseman, T.; Williston, S.; Brandts, J. F.; Lin, L-N. *Anal. Biochem.* **1989,** *179*, 131.
(12) Mills, F. C.; Johnson, M. L.; Ackers, G. K. *Biochemistry* **1976,** *15*, 5350.
(13) Chu, A. H.; Turner, B. W.; Ackers, G. K. *Biochemistry* **1984,** *23*, 604.
(14) Doyle, M. L.; DiCera, E.; Gill, S. J. *Biochemistry* **1988,** *27*, 820.
(15) Straume, M.; Johnson, M. L. *Biochemistry* **1988,** *27*, 1302.
(16) Straume, M.; Johnson, M. L. *Biophys. J.* **1989,** *56*, 15.
(17) Goldberg, R. N. *Biophys. Chem.* **1975,** *3*, 192.
(18) Goldberg, R. N. *Biophys. Chem.* **1976,** *4*, 215.
(19) Johnson, R.; Biltonen, R. *J. Am. Chem. Soc.* **1975,** *97*, 2349.
(20) Bolen, D. W.; Flogel, M.; Biltonen, R. L. *Biochemistry* **1971,** *10*, 4136.
(21) Flogel, M.; Biltonen, R. L. *Biochemistry* **1975,** *14*, 2603.
(22) Atha, D. H.; Ackers, G. K. *Biochemistry* **1974,** *13*, 2376.
(23) Gaud, H. T.; Barisas, B. G.; Gill, S. J. *Biochem. Biophys. Res. Commun.* **1974,** *59*, 1389.
(24) Atha, D. H.; Ackers, G. K. *J. Biol. Chem.* **1971,** *246*, 5845.
(25) Eftink, M.; Biltonen, R. In *Biological Microcalorimetry;* Beezer, A. E., Ed.; Academic Press: New York, 1980; pp. 343–412.
(26) Barisas, B. G.; Gill, S. J. *Ann. Rev. Phys. Chem.* **1978,** *29*, 141.
(27) Langerman, N.; Biltonen, R. *Methods Enzymol.* **1979,** *61*, 261.
(28) Suurkuusk, J.; Wadso, I. *Chemica Scripta* **1982,** *20*, 155.
(29) van Holde, K. E. *Physical Biochemistry,* 2nd ed.; Prentice-Hall: Englewood Cliffs, NJ, 1985; Chapter 3.
(30) Cantor, C. R.; Schimmel, P. R. *Biophysical Chemistry, Part III: The Behavior of Biological Macromolecules;* W. H. Freeman: New York, 1980; Chapter 15.
(31) Flogel, M.; Biltonen, R. L. *Biochemistry* **1975,** *14*, 2610.
(32) Flogel, M.; Albert A.; Biltonen, R. L. *Biochemistry* **1975,** *14*, 2616.
(33) Rudolph, S. A.; Gill, S. J. *Biochemistry* **1974,** *13*, 2451.
(34) Gaud, H. T; Gill, S. J.; Barisas, B. G.; Gersonde, K. *Biochemistry* **1975,** *14*, 4584.
(35) Noll, L. A.; Gaud, H. T.; Gill, S. J.; Gersonde, K.; Barisas, B. G. *Biochem. Biophys. Res. Commun.* **1979,** *88*, 1288.
(36) Gill, S. J.; Gaud, H. T.; Barisas, B. G. *J. Biol. Chem.* **1980,** *255*, 7855.
(37) Gillespie, L. L.; Argan, C.; Taneja,

A. T.; Hodges, R. S.; Freeman, K. S.; Shore, G. C. *J. Biol. Chem.* **1985,** *260,* 16045.
(38) Sattler, J.; Schwartzmann, G.; Knack, I.; Rohm, K. H.; Wiegandt, H. *Hoppe-Seyler's Z. Physiol. Chem.* **1978,** *359,* 719.
(39) Goins, B.; Freire, E. *Biochemistry* **1988,** *27,* 2046.
(40) Sehl, L. C.; Castellino, F. J. *J. Biol. Chem.* **1990,** *265,* 5482.
(41) Cox, J. A.; Milos, M.; MacManus, J. P. *J. Biol. Chem.* **1990,** *265,* 6633.

Ernesto Freire is a professor in the Department of Biology and director of the Biocalorimetry Center at The Johns Hopkins University. He received B.S. and M.S. degrees in biochemistry from the University Cayetano Heredia, Lima, Peru, and a Ph.D. in biophysics from the University of Virginia. His research work has been in the area of molecular biophysics, particularly in the development of new methods for the study of the energetics and thermodynamic mechanisms of protein folding, conformational equilibrium, and self-assembly of complex macromolecular systems.

Obdulio L. Mayorga is a visiting scientist in the Biocalorimetry Center at The Johns Hopkins University. He is a professor of physical chemistry at the University of Granada, Spain. He received a Ph.D. in physical chemistry from the University of Granada. His research work is in the area of calorimetric instrumentation development and in the analysis of biological systems using calorimetric techniques.

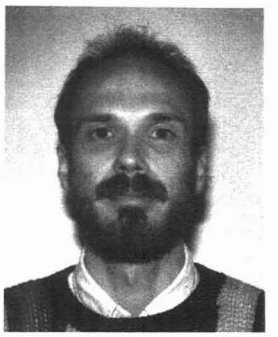

Martin Straume is the director of operations of the Biocalorimetry Center in the Department of Biology at The Johns Hopkins University. He received a B.S. degree in biochemistry and an M.S. degree in chemistry from Lehigh University and a Ph.D. in biochemistry from the University of Virginia. His research work has involved biophysical characterizaion of lipid–lipid and lipid–rhodopsin interactions, thermodynamic analysis of ligand binding to human hemoglobin, and development of high-sensitivity titration calorimetric instrumentation.


Automation
in the titration laboratory
Metrohm sample changers handle your routine titrations even during breaks and after work. Rapidly, reliably and reproducibly. Models exist
— for 10, 32, 64 or 96 samples (from 10 ... 250 mL)
— with single or double titration stations for complex analyses
— in several versions, e.g. for Karl Fischer water determinations and for COD determinations
They naturally also take over the sample preparation steps such as stirring, dissolution, dilution, pipetting, evacuation, gassing, degassing, etc.
Metrohm automation systems can be accommodated in the modern analytical laboratory with ease. They communicate and cooperate with PC, laboratory robots and LIMS.
Metrohm
Measurement in Chemistry
Worldwide with Metrohm
METROHM Ltd.
CH-9101 Herisau Switzerland
Phone 071 / 53 11 33
Telefax 071 / 52 11 14
Telex 88 27 12 metr ch
Brinkmann
INSTRUMENTS, INC.
Cantiague Rd., Westbury, New York 11590
(516) 334-7500 (800) 645-3050
CIRCLE 92 ON READER SERVICE CARD
Eckmayer + Schoch-ASW

Spectroscopy, Chromatography, and Laser-Induced Plasmas

Ion and Cluster Ion Spectroscopy and Structure. J. P. Maier, Ed. xiii + 483 pp. Elsevier Science Publishers, 52 Vanderbilt Ave., New York, NY 10017. 1989. $161

Reviewed by K-P. Wanczek, Department of Inorganic Chemistry, University of Bremen, Bremen, F.R.G.

The book contains 13 chapters on the theoretical and experimental study of ions and cluster ions in the gas phase. The editor has been very successful in bringing together authors who are among the leading scientists in the field. There have been substantial advances in this field, both in the experimental techniques and in the understanding of this type of compounds. This is well documented in the volume. The almost 1200 references include literature up to 1988.

In all the experimental chapters of the monograph the detailed description of experimental methods and instrumentation is of great value. Approximately half of the articles cover spectroscopy and structure of atomic and molecular ions and are centered around the experimental techniques. The coulomb explosion technique is described by Vager, Naamen, and Kanter. A chapter on microwave spectroscopy of small molecular ions by Woods follows. IR laser spectroscopy of the same type of compounds is described by Coe and Saykally. A chapter on high-resolution photodetachment of negative ions by Neumark and one on electronic spectroscopy of cations by the editor complete this part of the book.

Six papers deal with experimental studies of cluster ions. Kennedy, Kung, and Miller describe laser-induced fluorescence of ionic clusters; Bowers discusses photodissociation dynamics; and Chesnovsky, Pettiette, and Smalley deal with UV photoelectron spectroscopy of metal and semiconductor cluster ions. Photoelectron spectroscopy of negative cluster ions is described by Arnold, Eaton, Patel-Misra, Sarkas, and Bowen. Keesee and Castleman deal with structure elucidation of cluster ions from thermochemical and photodissociation data. Heinrich and Schwarz discuss ion–molecule complexes, which are a special type of cluster ion formed as intermediates in ion–molecule reactions.

The two papers by Botschwina and by Schaefer III describe the advanced theory of spectroscopic properties of ions. In many of the papers there is a detailed comparison of experiment and theory, which is especially useful in the case of the small ions and cluster ions discussed in the book.

The monograph is a progress report that is appropriate for the specialist in the field. However, the nonspecialist interested in fundamental properties also can get a lot from this book, because all the chapters are written very clearly and are comprehensible.

This book belongs in every library and on the shelf of any chemist or physicist interested in the field. However, the high price of this volume of directly reproduced manuscripts will severely limit circulation.

Chemiluminescence and Photochemical Reaction Detection in Chromatography. John W. Birks, Ed. 291 pp. VCH Publishers, 220 East 23rd St., New York, NY 10010-4606. 1989. $65

Reviewed by Cees Gooijer, Department of Analytical Chemistry, Free University, Amsterdam, De Boelelaan 1083, 1081 HV Amsterdam, The Netherlands

In this interesting book the authors have successfully covered the complex fields of gas-phase and liquid-phase chemiluminescence (CL) and liquid-phase photochemistry, with emphasis on detection in gas and liquid chromatography. The reader is assumed to be familiar with chromatographic principles. Five of the seven chapters have been written by researchers at the University of Boulder (J. W. Birks, R. E. Sievers, and co-workers); the other two are written by T. A. Nieman (University of Illinois) and R. S. Givens and R. L. Schowen (University of Kansas).

Each of the seven contributions has a strongly different character. The first one gives a comprehensive, clearly written overview of photophysical and photochemical principles. However, the number of subjects discussed in 37 pages is so overwhelming that the chapter will not be readily accessible for inexperienced chemists in this field.

Two chapters are devoted to CL detection in GC. Here the reagent gas (usually composed of highly reactive species generated in a gas discharge or a microwave bridge) is mixed with the GC effluent and, if the reaction is sufficiently exothermic, one or more of the products may be formed in electronically or high-vibrational excited states, subsequently losing their excess energy by luminescence (without substantially heating the detector cell). To date, three detectors have been commercialized, all based on the reaction between NO and O_3 producing NO_2*, which provides a broad emission at around 1200 nm—easily distinguishable from other CL signals. The most established one is the thermal energy analyzer for the selective analysis of nitroso compounds, which undergo catalyzed pyrolysis to produce NO.

Chapter 4 gives a clear, comprehensive overview of existing CL detection systems in liquid solutions and considers the most frequently studied reactions: luminol; lucigenin; peroxyoxalate and tris(2,2′-bipyridine)ruthenium(II); the possibility of electrochemiluminescence; and the bioluminescent luciferin/luciferase reaction, which gives the reader a good impression of the present accomplishments.

As such, the contents of the next chapter may be rather unexpected: an in-depth analysis of the peroxyoxalate CL reaction, not presented in the literature before. However, such a physical–organic approach is not only interesting to researchers studying reaction

mechanisms. To apply peroxyoxalate CL in HPLC detection at trace levels, the reaction variables have to be carefully defined and evaluated.

The most extensive chapter of the book is devoted to photochemical reaction (the counterpart of chemiluminescence) detection in HPLC. Obviously, it is advantageous to use photons as a "reagent" compared with chemical derivatization procedures, the most important point being that light can be introduced without additional pumps or mixing devices. Various practical applications are presented, emphasizing both the selectivity and the sensitivity of this detection mode.

Finally, an extensive treatment is given of photochemical reaction detection based on singlet oxygen sensitization. The basic idea is that analytes, upon being excited, decay at least partly via the electronic triplet state and subsequent reaction with molecular oxygen, thus producing singlet oxygen. This field is still hardly explored.

This book is of interest to chromatographers willing to try something a little out of the ordinary. Furthermore, it enables analytical chemists with research interest in CL (commonly confining their attention to a single CL reaction) to get involved in alternative reactions in a rather efficient way.

Packings and Stationary Phases in Chromatographic Techniques. Klaus K. Unger, Ed. viii + 836 pp. Marcel Dekker, 270 Madison Ave., New York, NY 10016. 1990. $150

Reviewed by Lane Sander, Organic Analytical Research Division, Center for Analytical Chemistry, National Institute of Standards and Technology, Gaithersburg, MD 20899

This book provides a comprehensive and well-balanced review of sorbents used in liquid, gas, and thin-layer chromatography. The 13 chapters by different authors each address a specific class of packings. Nine of the chapters are devoted to various packings used in LC, and the remaining chapters address subjects in GC and TLC as well as general issues.

Among the topics are discussions of packings used in reversed- and normal-phase separations; size exclusion chromatography; donor–acceptor complexation; ligand-exchange, ion-exchange, and affinity chromatography; and chemically bonded phases for chiral separations. The book is intended for chemists who are involved with separations and need to select, handle, or evaluate sorbents to solve separations needs. Although the topic of this book is too narrow for a primary text, it provides valuable supplementary reading for courses in separation science.

A particularly fascinating retrospective on the development of chromatographic concepts and methodology is provided by Ursula Wintermeyer. Readers may be surprised to learn that reports of separations involving gas and liquid adsorption and other techniques related to chromatographic processes were published long before Tswett's famous paper of 1903 (as early as 1657!). The evolution of chromatography is chronicled with a history of the researchers who were responsible for major advances in the field. Of particular interest are reproductions of figures from some of the original publications.

Stationary phases for GC are reviewed by Jürgen Pörschmann and W. Engewald. This chapter provides a discussion of basic concepts of GC, as well as a thorough review of the properties and typical applications of gas–solid and gas–liquid stationary phases. This review is supplemented with numerous figures and tabulations, and an extensive reference list (more than 500 citations) is provided.

The bulk of this book is composed of reviews of specific classes of stationary phases employed in column LC. Unger provides an introduction to the manufacture and properties of chromatographic substrates in his chapter on adsorbents in column LC. Commercial processes used to prepare silica, alumina, porous carbon, and polymer substrates are described, and a review of bonding procedures is presented. Perhaps the most useful section of this chapter is the discussion of techniques used to characterize stationary phases. Chromatographic tests for assessing column properties are tabulated, although this listing is incomplete. A tabulation of commercially available silicas and aluminas as well as reversed-phase packings is provided in the appendix.

A particularly comprehensive and useful review of ion exchangers is presented by Donald Pietrzyk. This chapter, which is essentially a monograph on ion-exchange chromatography, provides an excellent discussion of the theory of ion-exchange processes, the preparation and properties of organic and inorganic ion exchangers, and a generous section of examples and practical applications.

The task of covering the subject of packings and stationary phases is formidable; however, this book succeeds remarkably well. Although there are a few notable omissions (little emphasis is placed on biological applications or preparative separations; also, an index of applications is needed), this book provides a comprehensive examination of the major aspects of packing materials used in chromatography.

Laser-Induced Plasmas and Applications. Leon J. Radziemski and David A. Cremers, Eds. 464 pp. Marcel Dekker, 270 Madison Ave., New York, NY 10016. 1989. $100

Reviewed by E. H. Piepmeier, Department of Chemistry, Gilbert Hall 153, Oregon State University, Corvallis, OR 97331-4003

Since the first report of a plasma created by a focused laser beam in 1963, many reviews have been written on the subject. This book updates those reviews and presents new topics. In keeping with the philosophy of the Optical Engineering series, this book is not a research monograph. The approach is both tutorial and review: the book familiarizes the reader with the basic concepts and instrumentation used in each area discussed, reviews the state of the art, and provides sufficient references for an in-depth follow-up.

The emphasis is on the generation of laser-induced plasmas, their characteristics, and new applications. The authors frequently refer to monographs and reviews rather than duplicate previously published information.

The first part of the book reviews the basic physics of plasma initiation, growth, and decay. Initiation mechanisms in gases, including inverse bremsstrahlung and multiphoton ionization, are discussed in detail along with breakdown in liquids and solids. Dissipating and propagating plasmas are reviewed, including three plasma regimes with different absorption and hydrodynamic behavior: combustion, detonation, and radiation waves. Computer codes used to model plasma behavior are briefly described. The physical processes, plasma characteristics, and implementation of the continuous optical discharge are reviewed along with proposed applications to laser-based propulsion and spectrochemical analysis.

Diagnostics for high-energy, laser-induced plasmas are discussed, including new pulsed X-ray diagnostics applicable to energy transport, implosion hydrodynamics, and very dense plasmas. The first half of the book concludes with a chapter on the use of laser-driven ablation to induce fusion and includes recent and future implosion experiments.

A chapter on lasers in semiconductor

fabrication includes not only applications of laser plasmas, but also procedures that use lower laser irradiances, such as resistor trimming, redundancy and photomask repair, device marking, and drilling.

Recent advances in laser reproducibility and reliability have made laser microprobe methods of spectrochemical analysis more practical than the early literature would suggest. Still, the most successful applications involve problems that are difficult to handle by conventional methods. The next four chapters cover spectrochemical analyses where the laser vaporizes, atomizes, excites, and/or ionizes gas, liquid, and solid samples, including particles, aerosols, and molten metals. Applications include sampling in situ, in hostile environments, and in cases where the plasma is formed many meters away from the focusing and detection systems.

The use of laser-induced plasmas as vaporization and ion sources for MS is discussed, as are techniques in which atomic spectral information is not obtained directly from the laser plasma, but rather from another atomization and/or excitation source into which the laser-vaporized sample is transported. The emphasis is on methods of atomization and generating the analytical signal, rather than on such things as spectral interferences and nonlinear working curves.

The last chapter covers some of the newest applications, including the use of high-energy laser plasmas to produce pulsed X-rays and high-energy particles. The intriguing use of laser plasmas for particle accelerators is presented, followed by a discussion of laser-triggered, pulsed-power switching. Purposely omitted from the book, for lack of space, are laser welding and cutting as well as laser plasma applications in medicine.

There is a very helpful nine-page index, and each chapter has several pages of worthwhile references. There are many interesting figures. A few short sections have tedious equations that are of interest only to some readers, but they are easy to skim over. In an era of word-processor spelling checking, no misspelled words were expected or found. However, my train of thought was interrupted by three confusing word substitutions: contract was inadvertently substituted for contact, water for wafer, and turned for tuned.

This book is highly recommended for anyone with a basic background in plasmas who is interested in a better understanding of laser-induced plasmas, and for anyone who wants to know more about applications.

Before you go through another column, it pays to go through Whatman.

If you're not using the right sample prep with your HPLC system, you could be wasting valuable time and money. That's why it pays to go through the Whatman Sample Prep System.

Whatman sample prep filters help yield purer filtrates, to ensure reproducible results–which means *less* repeat testing for you and *more* life for your column.

The Whatman Sample Prep System includes:

Puradisc™ 25 (AS/TF/PP)–Syringe-tip filters are available with various membranes to help avoid generation of extractables: polysulfone, for aqueous applications (Puradisc 25 AS); PTFE, for solvent-based applications (Puradisc 25 TF); and polypropylene, for solvent/aqueous applications (Puradisc 25 PP).

SPEC–The only solid-phase extraction device that contains an integral 0.2 micron polypropylene membrane to eliminate the need for secondary filtration.

Solvent and Aqueous IFD™–The only filter device that filters and degasses mobile phases in-line to save time and extend the life of the HPLC column.

So before you go through another HPLC column, go through Whatman.

Contact Whatman Inc. for more information on receiving a FREE column.

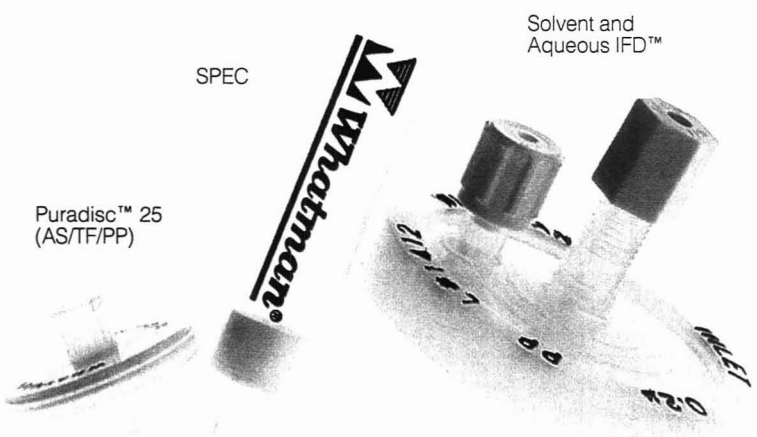

Whatman®

Whatman Laboratory Division

Whatman Inc., 9 Bridewell Place, Clifton, New Jersey 07014

Telephone: 201-773-5800 Telex: 133426 FAX: 201-472-6949

CIRCLE 144 ON READER SERVICE CARD

The Center for Process Analytical Chemistry

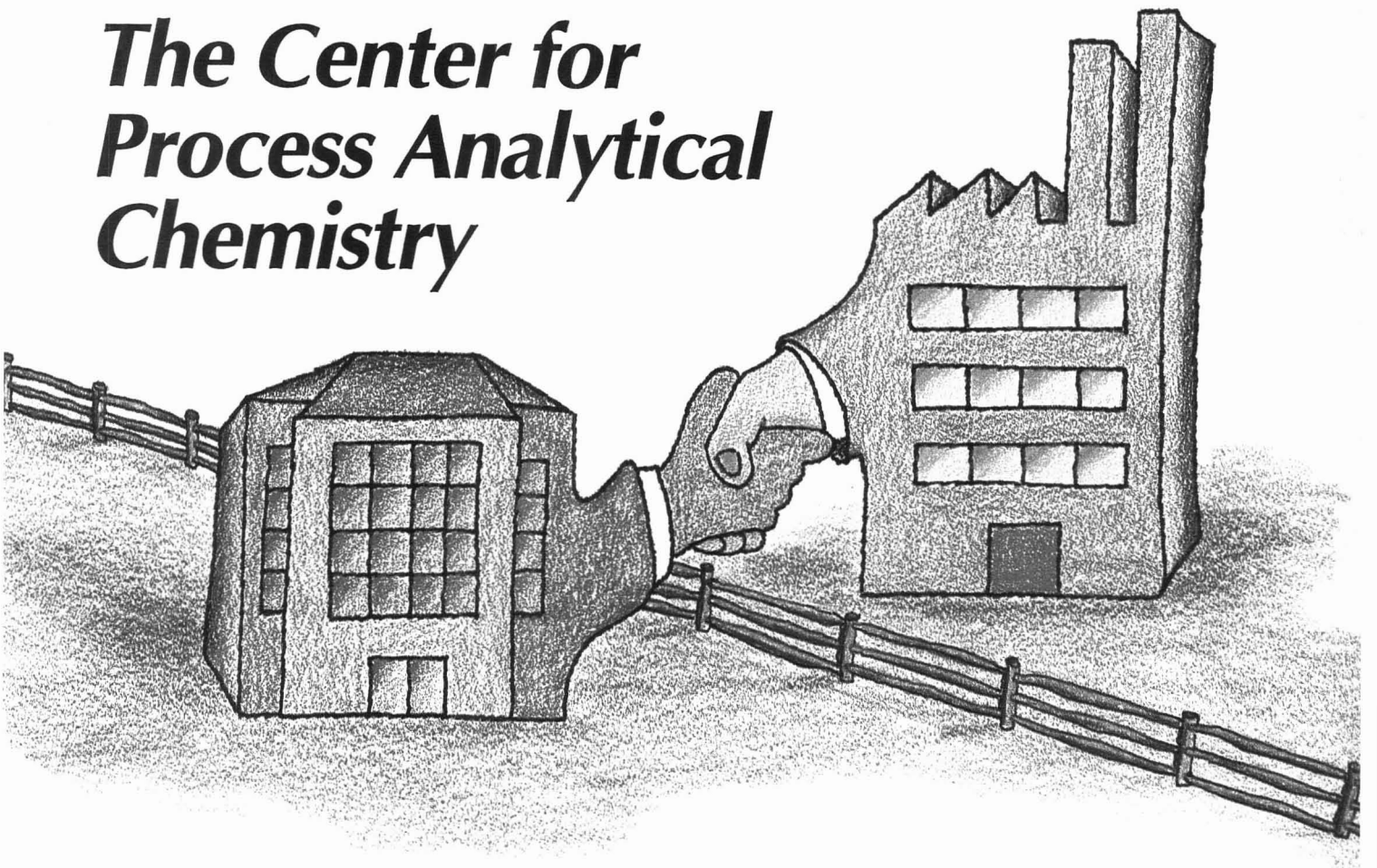

In many American universities, science departments are reaching across old boundaries to form cooperative centers of research. One such successful venture involving analytical chemists is the Center for Process Analytical Chemistry (CPAC) at the University of Washington in Seattle. Now beginning its seventh year, CPAC offers a unique model of how chemists can successfully forge bonds with industry, government, and allied academic disciplines to foster new ideas. At the same time, the center establishes a two-way flow of ideas between basic researchers in academia and scientists in industry and government—an important ingredient for U.S. companies fighting to remain economically competitive worldwide.

The center is the brainchild of Bruce Kowalski, an analytical chemist at the University of Washington who first proposed CPAC in 1982. Kowalski continues to promote the center eight years later with tireless enthusiasm. "It's like an active research collaboration," explains Kowalski. "It is all very exciting."

Kowalski recruited fellow analytical chemist James Callis to be co-director and postdoctoral associate Deborah Illman to be associate director of the center. Together with analytical chemists on the university faculty they form the core of CPAC's research staff. In addition, researchers from the departments of chemistry, chemical engineering, and electrical engineering participate in funded projects.

The goal of the center is to develop new methods of process analytical chemistry, considered by many to be an important approach for monitoring

FOCUS

and controlling chemical and material processes. Although the idea is not new, the technology to widely implement process analytical chemistry has not been available until recently.

Process analytical chemistry moves analysis out of the classic analytical laboratory and closer to or even into production lines or storage facilities. It offers the possibility of real-time and noninvasive chemical analysis and monitoring, rapid response to problems, lower production costs (because bad production batches are eliminated), and higher product quality.

However, achievement of these goals requires instruments that are rugged and compact, techniques that work with little or no sample preparation, and statistical methods that extract useful information from noisy and complex data. To tackle these demands, CPAC researchers and other process analytical chemists are developing a group of analytical tools that include in-line sensors, rapid separation techniques, chemometrics, and methods for nondestructive spectral determinations. Clearly these approaches are a partial outgrowth of advances in such areas as semiconductor devices, fiber optics, miniaturization, and computation.

Process analytical chemistry has also revolutionized how analytical chemists operate. Because analysis is becoming an integral part of production, chemists need to learn how to interact with engineers and production managers. Often, that means overcoming traditional habits and prejudices against doing things differently. "There are a lot of cultural differences between how analytical chemists and engineers work," says Kowalski. Joint planning is required to design or retrofit production

facilities for in-line sensors or flow cells. "It requires some champions on site," says Gene Coffey, Savannah River National Laboratory's representative to CPAC. "You need some support or at least someone to shield them while they are initially floundering around."

CPAC hopes to provide some of that support. "I view it [CPAC] as a source of ideas that have to be taken by us, developed, and applied to our needs," explains Ernie Baughman, Amoco's CPAC representative. "CPAC fills a unique niche."

Establishing CPAC required the efforts and ultimately the financial support of many institutions and businesses. The initial development was underwritten by a National Science Foundation (NSF) planning grant, with additional support from the University of Washington. The planning study conducted with these funds, under the coordination of Illman, helped to shape CPAC and identify the companies and laboratories that would become its constituency. Thus when CPAC was formally launched in 1984, it was funded with a five-year $550 000 NSF center grant and had 21 industrial and government sponsors. According to Kowalski, it was one of NSF's most successful center startups.

CPAC at that point made a strategic decision with respect to marketing the center. Says Kowalski, "We spent most of our effort on obtaining research results." The research effort set the tone for CPAC, although it meant that it would be years before some companies "discovered" the center.

Today, CPAC runs financially on its own although some NSF funds are used for specific programs such as visits by scientists from other institutions or graduate student training. The bulk of CPAC's research funds comes from about 50 sponsors who pay an annual membership fee that this year increased from $30 000 to $35 000. ("That," says Kowalski, "was done by the sponsors!") The university supplies additional operational support.

The sponsors represent a diverse collection of companies that include chemical, pharmaceutical, and instrument manufacturers; aerospace firms; petroleum companies; and food suppliers. In addition, the U.S. Air Force, Battelle's Pacific Northwest Laboratory, Los Alamos National Laboratory, and the Westinghouse-run Savannah River National Laboratory have joined CPAC.

In return for their support, sponsors gain an inside track on CPAC research. Research activities are regularly communicated through publications and CPAC's semiannual meetings. Sponsors learn about embryonic and continuing research at the university, and they have an opportunity to influence the direction of research projects. For instance, sponsors interested in flow-injection analysis encouraged Jaromir Ruzicka and Gary Christian to develop the technique to handle solutions with particulates, high salt concentrations, and nonaqueous solvents.

Sponsors are also invited to visit research laboratories and to send their own scientists to work with CPAC scientists. Furthermore, members can make appointments for CPAC faculty to visit their sites.

Equally important, sponsors are promised access to CPAC inventions, software, and patents. Patents arising from CPAC-funded research are available to sponsors through a nonexclusive, royalty-free license for in-house use. Additionally, sponsors review research papers based on CPAC-funded research prior to publication, and a sponsor can delay publication for up to one year to study potential patent applications from the work. Because the university holds title to the intellectual property, commercial use of patents would engender a negotiated royalty payment.

Have sponsors gotten their money's worth from this arrangement? "Yes, definitely," states Baughman. "It is hard to quantitate," says Alan Ullman of Procter & Gamble, "but there are tangible things we can show."

Most sponsors are reluctant to give specific details. However, from conversations with representatives of various companies, it appears that one of CPAC's most successful "products" to date has been chemometrics software, such as the partial least-squares multicomponent analysis program, from Kowalski's group.

In turn, Kowalski credits CPAC with some of the software's success. When he and former graduate student David Veltkamp developed the software, they decided to "make it a little better than a thesis project," according to Kowalski. Their discussions with sponsors about real-world problems associated with multivariate analysis—the statistical handling of several chemical and physical properties—helped to shape the software. The resulting program has been so successful that it has actually been used to control processes. "We never intended it to go that far," says Kowalski.

At the annual spring meeting, CPAC's principal investigators present research ideas that are evaluated by designated technical monitors from sponsoring organizations who are fa-

miliar with the research fields. The evaluations, in turn, are used by the Industrial Advisory Board—composed of one representative from each sponsor—to review and recommend how funds should be allocated.

As it has evolved, the Industrial Advisory Board has assumed a much more active role in running CPAC than was originally envisioned. "They have a real sense of ownership," says Kowalski. "We don't run their Industrial Advisory Board meeting anymore; we just sit on the sidelines."

As part of the board there is now an executive committee composed of the present, past, and future chairs, along with two other members. This committee meets on its own at different locations three to four times a year. Furthermore, some of the board members travel to Seattle several times a year to interact with CPAC faculty. Says Ullman, "The more you put into it, the more you get out of it."

Final decisions on funding rest with CPAC's directors. The directors support the advisory board by prescreening projects and recommending those to be presented at the meetings. There is also a Scientific Advisory Board, composed of university scientists who review projects and budgets. The group of funded investigators convenes periodically to brainstorm. Finally, to deal with center policies that may conflict with university rules, the university vice-provost, deans of engineering and arts and sciences, and the chairs of the participating departments meet with the advisory board and center directors to iron out problems.

In addition to its organizational presence, CPAC recently gained a significant physical presence. Offices and laboratories for the center now occupy a renovated wing of the university's chemistry library building. These facilities are in addition to the laboratory space already used by CPAC researchers as members of the faculty.

One of the advantages of CPAC has been its impact on graduate and postdoctoral students. Besides providing funds for training, CPAC encourages students to speak or present posters at sponsor meetings. There is even a designated time for sponsors to take a student to lunch, offering an opportunity for the young researchers to chat with prospective employers.

Kowalski also points out that because CPAC students are being trained in process analytical chemistry, they are better prepared for the workplace. "This is a real, sincere, authentic interdisciplinary program," he says. "These are students who know about engineering and require less retraining."

Chemistry students collaborate with engineers on projects and work with industry in a number of ways. For instance, a cooperative program offers chemistry students the chance to perform thesis-related research in an industrial setting. The center also affects the pace of research. On a number of occasions university researchers have used their CPAC connections to obtain materials that were still in development.

CPAC is not without some shortcomings. There is the old problem that solutions that work well in an academic laboratory may be impractical for real-world applications. Furthermore, some people question how CPAC will support the technology once it is transferred to industry.

Kowalski agrees. "A project that costs us $200 000 needs a minimum of five years and $2 million to develop." Even for instrument companies, these development costs are enormous. "Sponsors don't want us to build prototypes."

However, Kowalski sees this not as a CPAC problem, but rather as a national problem. "Our research is the envy of the world, but we don't take the technology far enough to use." According to Kowalski, the U.S. needs to address this missing step—something he says the Japanese do very well—if basic research ideas are going to revitalize the American workplace.

Despite all the discussion of products, much of CPAC's success lies in the allegiance that most sponsors feel with CPAC's faculty researchers. "It is the biggest part," says Baughman. "They are real colleagues of ours," adds Kowalski. "All of us could get funding with less hassle and less work, but it is the access that is important."

Kowalski calls CPAC an ongoing experiment: "We are trying to listen to companies about where they are going in the future." To maintain an edge CPAC has created an $N + 1$ research project that focuses on the center–university–industry relationship. "Everyone conducts the research—how can we do it better? We are continually in the quest," says Kowalski.

For more information on CPAC, contact the Center for Process Analytical Chemistry, BG-10, University of Washington, Seattle, WA 98195 (206-685-2326; FAX: 206-543-6506 or Bitnet: annalise@cpac.bitnet)

Alan R. Newman

Suggested reading

Callis, J. T.; Illman, D. L.; Kowalski, B. R. *Anal. Chem.* **1987,** *59,* 624 A.

Reibe, M. T.; Eustace, D. J. *Anal. Chem.* **1990,** *62,* 65 A.

NEW PRODUCTS

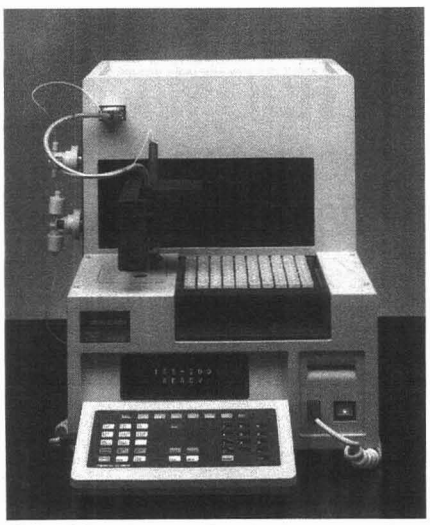

ISS-200 autosampler features random access programming and injection volumes as low as 1.0 μL. The system is compatible with narrow-bore columns and with high-speed LC. Perkin-Elmer **403**

Biotechnology. UMA ultrafast microprotein analyzer is a microbore HPLC system intended for use with a variety of specialty application packages, each containing columns, supplies, accessories, and documentation. Michrom BioResources **401**

Dissolved oxygen. Model 50B dissolved oxygen meter measures in two temperature-compensated modes: 0–19.99 mg/L dissolved oxygen, accurate to ±0.03 mg/L, or 199.9% air saturation, accurate to ±0.2%. Six alkaline cells power the meter for 1000 h of field use. YSI **406**

Spectrophotometers. Cary 4 and Cary 5 UV–vis–near-IR spectrophotometers feature a double monochromator with an out-of-plane Littrow design that reduces optical aberrations. The wavelength drive system eliminates peak shift or suppression with changes in scan speed. Varian **407**

LC/MS. LC system for MS includes a gradient solvent delivery system, three on-line UV–vis absorbance detectors, a postcolumn solvent addition pump, and an autosampler. The system is compatible with mass spectrometers and interfaces from any manufacturer. Waters Chromatography Division of Millipore **408**

Electron microscopy. MT-7 ultramicrotome, designed for the thin sectioning of specimens for analytical electron microscopy, produces single or serial sections in thicknesses from 10 nm to 10 μm in 1-nm increments. Features include stereo zoom optics, multifunction adjustable lighting, and a built-in digital section counter. RMC **409**

Ammonia. CFA-1010 analyzer is an on-line monitor for the continuous measurement of ammonia in water and wastewater. The instrument can be upgraded in the field from a single-stream monitor to a multistream analyzer capable of handling up to six different streams. Scientific Instruments **410**

Amino acids. Amino System 1 automates OPA and FMOC derivatization, performs sample cleanup using on-line membrane purification, and injects each sample onto a reversed-phase HPLC column. Both primary and secondary amino acids can be determined. Gilson Medical Electronics **411**

Software

Word processing. CCWORD revision 3.1, designed for HP 1000 and HP 9000 computer systems, provides full-function word processing and the ability to combine text with graphics. The software features self-recording macros for repetitive operations. Interactive Computer Technology **424**

Experimental design. Factorial-Design is a set of three programs for investigating two-, three-, and four-factor systems and response surfaces using full two-level factorial experimental designs. Output includes contour plots showing predicted response as a function of the factors. Statistical Programs **425**

Database. NIST Vibrational and Electronic Energy Levels of Small Polyatomic Transient Molecules Database (VEEL) contains data on transient molecules with 3–16 atoms. The program can be stored on a hard disk of any AT, XT, or PS/2 personal computer. NIST **426**

Scientific computing. DataWave is a software package that provides experiment design and execution, data analysis, data replay and editing, and hardcopy graphics. Data analysis functions include waveform averaging and smoothing, FFT analysis, x/y point plotting, and curve fitting. DataWave Technology, BrainWave Systems **427**

Manufacturers' Literature

Chromatography. Application note discusses basic methods and principles of radiochemical detection. Information on efficiency, minimum detectable activity, resolution, and data processing is provided. Radiomatic **422**

Gases. Brochure describes gas- and liquid-phase hydrocarbon calibration standards. Information on analytical accuracy and recommended equipment is provided. Alphagaz **432**

Newsletter. *Food and Beverage Notes*, Vol. 4, No. 1, includes information on the use of capillary electrophoresis for the determination of inorganic and organic ions. Waters Chromatography Division of Millipore **431**

Surface analysis. Booklet discusses surface modification and characterization of biomaterials. Included is information on ESCA, SIMS, FT-IR, SEM, XRF, and LAMMA techniques. Surface Science Laboratories **433**

For more information on listed items, circle the appropriate numbers on one of our Readers' Service Cards

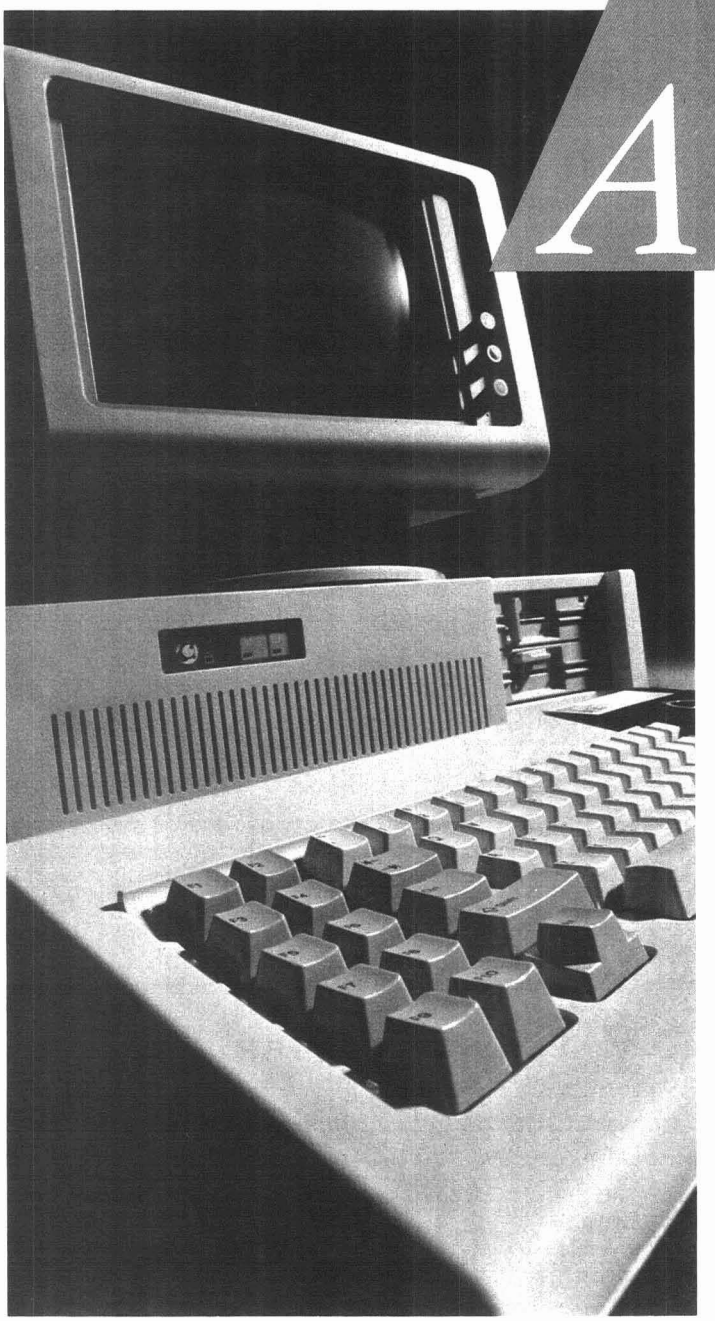

Access Elsevier Journals Online on STN International® !

On STN International, you can now access full-text articles from Analytica Chemica Acta, Journal of Organometallic Chemistry, Carbohydrate Research, and Applied Catalysis, four of the leading chemistry journals published by Elsevier Science Publishers B.V.

In the CJELSEVIER database, you'll find more than 2,400 citations added yearly, dating from 1990 to the present, with more than 50 new articles appearing weekly. The information in CJELSEVIER is some of today's most current — updates appear within the database BEFORE the journals are available!

On STN, the full-text articles in CJELSEVIER are both searchable and displayable without having to rely on an abstract or on keywords. You can quickly decide whether the material in the article is important to your work. In CJELSEVIER, you're getting complete information right from the start!

It's easy to begin searching the CJELSEVIER database on STN. Simply fill out the attached coupon and we'll send you a complete packet of information on all the full-text chemistry databases on STN and an STN sign-up kit.

☐ **YES! I'd like further information on full-text chemistry searching on STN. Please rush my information kit to me.**

Name _____

Title _____

Organization _____

Address _____

_____

Telephone _____

Mail to: STN International, c/o Chemical Abstracts Service, Marketing Dept. 39790, P.O. Box 3012, Columbus, OH 43202 USA.

STN®
INTERNATIONAL
The Scientific & Technical Information Network

Catalogs

Petroleum. Catalog features analytical standards for XRF determination of sulfur, lead, zinc, chlorine, bromine, and phosphorus in crude and refined petroleum products. Matrices include gasoline, kerosene, jet fuel, lube oil, and residual oil. Micrographics **439**

Scientific equipment. Catalog features products for biological and environmental analysis, including autoclaves, homogenizers, water baths, stirrers, automatic samplers, desorbers, flow meters, and purge-and-trap concentrators. Tekmar **440**

Computers. Catalog contains products for personal computer-based data acquisition and instrument control, including A/D converters, multiport serial boards, IEEE-488 interfaces, and digital oscilloscope boards. CyberResearch **441**

pH/conductivity. Catalog features products for pH and conductivity measurement, including field and laboratory instruments; custom electrodes and accessories; data acquisition systems; and pumps, valves, and mixers. Omega Engineering **442**

Chemicals. Catalog includes organic and inorganic chemicals; stains and dyes; deuterated and ^{13}C-labeled compounds; anhydrous, HPLC, and spectrophotometric solvents; organometallic reagents; gases; polymers; and ion-exchange resins. Aldrich **443**

Protein research. Catalog highlights products for protein purification, cell culture filtration, Western blotting, and laboratory safety. A minielectrophoresis system is described. Schleicher & Schuell **444**

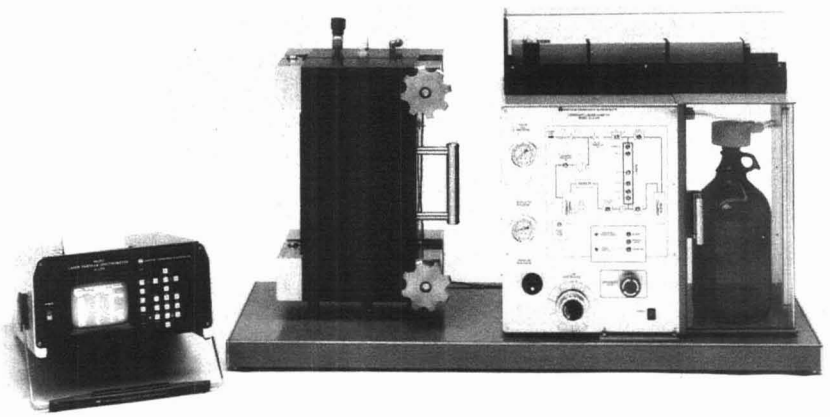

Model CLS-500 corrosive liquid sampler allows liquids to be sampled directly from containers through the use of volumetric or in situ sensors. Buret measurement and flow controller modes are available for sample volume determination. Particle Measuring Systems **402**

INDEX TO ADVERTISERS IN THIS ISSUE

Directory section, see page 970A.

** See ad in ACS Laboratory Guide.*

Advertising Management for the American Chemical Society Publications

CENTCOM, LTD

President
James A. Byrne
Executive Vice President
Benjamin W. Jones
Clay S. Holden, *Vice President*
Robert L. Voepel, *Vice President*
Joseph P. Stenza, *Production Director*

500 Post Road East
P.O. Box 231
Westport, Connecticut 06880
(Area Code 203) 226-7131
Telex No.643310
FAX: 203-454-9939

ADVERTISING SALES MANAGER
Bruce E. Poorman

ADVERTISING PRODUCTION MANAGER
Jane F. Gatenby

SALES REPRESENTATIVES

Philadelphia, PA . . . CENTCOM, LTD., GSB Building, Suite 405, 1 Belmont Avenue, Bala Cynwyd, Pa. 19004. Telephone: 215-667-9666, FAX: 215-667-9353.

New York, NY . . . John F. Raftery, CENTCOM, LTD., 60 East 42nd St., New York, N.Y. 10165. Telephone: 212-972-9660

Westport, CT . . . Edward M. Black, CENTCOM, LTD., 500 Post Road East, P.O. Box 231, Westport, Ct. 06880. Telephone: 203-226-7131, Telex 643310, FAX: 203-454-9939

Cleveland, OH . . . Bruce E. Poorman, John C. Guyot, CENTCOM, LTD., 325 Front St., Suite 2, Berea, Ohio 44017. Telephone: 216-234-1333, FAX: 216-234-3425

Chicago, IL . . . Michael J. Pak, CENTCOM, LTD., 540 Frontage Rd., Northfield, Ill. 60093. Telephone: 708-441-6383, FAX: 708-441-6382

Houston, TX . . . Michael J. Pak, CENTCOM, LTD. Telephone: 708-441-6383

San Francisco, CA . . . Paul M. Butts, CENTCOM, LTD., Suite 1070, 2672 Bayshore Frontage Road, Mountain View, CA 94043. Telephone: 415-969-4604

Los Angeles, CA . . . Clay S. Holden, CENTCOM, LTD., Newton Pacific Center, 3142 Pacific Coast Highway, Suite 200, Torrance, CA 90505. Telephone: 213-325-1903

Boston, MA . . . Edward M. Black, CENTCOM, LTD. Telephone: 203-226-7131

Atlanta, GA . . . John C. Guyot, CENTCOM, LTD. Telephone: 216-234-1333

Denver, CO . . . Paul M. Butts, CENTCOM, LTD. Telephone: 415-969-4604

United Kingdom

Reading, England . . . Malcolm Thiele, Technomedia Ltd., Wood Cottage, Shurlock Row, Reading RG10 OQE, Berkshire, England. Telephone: 073-434-3302, Telex #848800, FAX: 073-434-3848

Lancashire, England . . . Technomedia Ltd., c/o Meconomics Ltd., Meconomics House, 31 Old Street, Ashton Under Lyne, Lancashire, England. Telephone: 061-308-3025

Continental Europe . . . Andre Jamar, International Communications, Inc., Rue Mallar 1, 4800 Verviers, Belgium. Telephone: (087) 22-53-85, FAX: (087) 23-03-29

Tokyo, Japan . . . Sumio Oka, International Media Representatives Ltd., Room 100, 21 Bldg., 2-2-22 Okusawa, Setagaya-ku, Tokyo 158 Japan. Telephone: 502-0656, Telex #22633, FAX: 5706-7349

Get the Professional Know-How You Need to Do Your Job Better!

Register today for

ACS Short Courses at the Eastern Analytical Symposium

Somerset Marriott Hotel
November, 1990

Activated Carbon Adsorption: Principles & Applications ***New!***
Thursday-Friday, November 15-16, 1990

Chemical Engineering & Process Fundamentals for Chemists
Thursday-Saturday, November 15-17, 1990

Gas Chromatography
Monday-Tuesday, November 12-13, 1990

Gas Chromatography/Mass Spectrometry
Monday-Tuesday, November 12-13, 1990

Environmental Laboratory QA/QC Data Validation
Thursday-Friday, November 15-16, 1990

Interpretation of IR Spectra ***New!***
Tuesday-Thursday, November 13-15, 1990

Laboratory Information Management Systems: From Problem Definition to System Evaluation
Monday-Tuesday, November 12-13, 1990

New Sample Preparation Methods for Chemical Analysis ***New!***
Monday-Tuesday, November 12-13, 1990

Statistical Process Control ***New!***
Thursday-Friday, November 15-16, 1990

Thermal Analysis in Materials Characterization
Monday-Tuesday, November 12-13, 1990

☐ **Yes! Please send me more information about ACS Short Courses at the Eastern Analytical Symposium in Somerset, NJ in November 1990.**

Name _____
Title _____
Organization _____
Address _____
City, State, Zip _____

Mail to American Chemical Society, Department of Continuing Education, Meeting Code EAS90110, 1155 Sixteenth St., N.W., Washington, DC 20036, or call Toll Free at 1-800-227-5558.

ACS Satellite TV Seminar

Computer-Aided Genetic & Protein Engineering

Cosponsored by Digital Equipment Corporation

Friday, November 16, 1990
12:00 Noon-3:00 PM Eastern Time

Computer-aided genetic and protein engineering are among two of the most exciting and rapidly growing fields in science today. This unique ACS Satellite Television seminar offers an excellent opportunity to learn about the recent explosion of bioinformation—especially the information resulting from the Human Genome Initiative—and its impact on nucleic acid and protein R&D.

Leading experts in the field will discuss methods for obtaining and using information about DNA and protein sequences that can lead to better (and more efficient) design of new biologically active molecules. New ways to compare, characterize, and analyze gene sequences will also be covered.

Topics for this exciting event include:

- ✓ ***What is happening in computer-aided genetic and protein engineering?***
- ✓ ***Problems and Challenges***: Methods for Dealing with DNA Sequences, Methods for Dealing with Protein Sequences, Applications and the Future
- ✓ ***Explanations and Demonstrations of Computer-Based Tools***: Nucleic Acids Research, Protein Engineering Research, Sample Applications and the Future

Distinguished speakers

Joseph L. Modelevsky, John R. Devereux, Gregory Petsko, Charles Craik. Also, interviews with Leroy Hood, David Eisenberg, Tim Hunkapiller, James Ostell, John Wootton, Michael Waterman, and more.

Information/Enrollment

1-800-227-5558, ext. 31

ACS Satellite Television Seminars
1155 Sixteenth Street, NW, Room 809
Washington, DC 20036
Direct: (202) 872-8728
Fax: (202) 872-6336

Analytical CHEMISTRY

EDITOR: **GEORGE H. MORRISON**

ASSOCIATE EDITORS: **Catherine C. Fenselau, Georges Guiochon, Walter C. Herlihy, Robert A. Osteryoung, Edward S. Yeung**

Editorial Headquarters

1155 Sixteenth St., N.W.
Washington, DC 20036
Phone: 202-872-4570
Telefax: 202-872-4574

Managing Editor: Sharon G. Boots

Assistant Managing Editor: Mary Warner

Associate Editor: Louise Voress

Assistant Editors: Jane K. Baker, Grace K. Lee, Alan R. Newman

Editorial Assistant: Felicia Wach

Contributing Editor: Marcia Vogel

Director, Operational Support: C. Michael Phillippe

Head, Production Department: Leroy L. Corcoran

Art Director: Alan Kahan

Designers: Amy Meyer Phifer, Robert Sargent

Production Editor: Elizabeth E. Wood

Circulation: David Schulbaum

Editorial Assistant, LabGuide: Joanne Mullican

Journals Dept., Columbus, Ohio

Associate Head: Marianne Brogan

Journals Editing Manager: Joseph E. Yurvati

Senior Associate Editor: Rodney L. Temos

Published by the
AMERICAN CHEMICAL SOCIETY
1155 16th Street, N.W.
Washington, DC 20036

Publications Division

Director: Robert H. Marks

Journals: Charles R. Bertsch

Special Publications: Randall E. Wedin

Manuscript requirements are published in the January 1, 1990 issue, page 89. Manuscripts for publication (4 copies) should be submitted to ANALYTICAL CHEMISTRY at the ACS Washington address.

AUTHOR INDEX

Scanning Electrochemical Microscopy. Application to Polymer and Thin Metal Oxide Films

Chongmok Lee and Allen J. Bard*

Department of Chemistry, The University of Texas, Austin, Texas 78712

Scanning electrochemical microscopy (SECM) in the feedback mode, where the steady-state faradaic current at a microdisk electrode tip is measured as the tip is scanned close to a surface, was used to investigate several different polymer films on electrode surfaces: poly(vinylferrocene), *N,N'*-bis[3-(trimethoxysilyl)propyl]-4,4'-bipyridinium dibromide, and Nafion containing $Os(bpy)_3^{2+}$. The tip response (i.e., positive or negative feedback) depends upon the nature of the polymer, the substrate electrode potential, the identity of the solution redox species, and the tip potential. Studies carried out with polymer films on interdigitated array (IDA) electrodes with different redox species in the cell solution demonstrate that the SECM images can be used to distinguish chemically different sites on a substrate surface. It was also possible with similar methods to distinguish Au and oxide-covered Cr electrodes in an IDA.

INTRODUCTION

Previous studies from this laboratory have described the principles of scanning electrochemimcal microscopy (SECM), the theory of the feedback mode, and several applications (*1–5*). In SECM a microdisk electrode, with a tip radius of the order of a micrometer or less, is moved in close proximity to a substrate of interest that is immersed in a solution containing an electroactive species. The electrode reaction at the tip gives rise to a tip current that is affected by the presence of the substrate. In general, the steady-state tip current, i_T, is controlled by electrochemical reactions at the tip electrode and is a function of the tip–substrate distance, d, and the conductivity and the chemical nature of the sample substrate. The measurement of i_T can thus provide information about topography of the sample surface, as well as its electrical and chemical properties (*3–5*). In the feedback mode the magnitude of i_T increases with respect to its steady-state value at large distances from the substrate ($i_{T,\infty}$) (called positive feedback), when the tip electrode is moved close to a conductive substrate. $i_{T,\infty}$ is the steady-state disk ultramicroelectrode current given by (*6*, *7*)

$$i_{T,\infty} = 4nFDCr \qquad (1)$$

where n is the number of electrons in the electrode reaction, F is the Faraday constant, D is the diffusion coefficient, C is the concentration of electroactive species (O) in the solution, and r is the disk radius. Positive feedback arises because the tip reaction (e.g., $O + ne^- \rightarrow R$) generates a species, R, which is oxidized at the conductive substrate to produce O which then diffuses back to the tip. When the tip is moved close to an insulating substrate, i_T is decreased because the hemispherical diffusion to the tip is partially blocked; this can be termed negative feedback. Note that this feedback mode is different from the SECM generation/collection mode (*1*, *8*, *9*).

In this paper we focus on the variation of i_T caused by changing the chemical properties of sample substrates, e.g., films of redox polymers, whose redox properties and potentials can be changed electrochemically. This is related to, but different than, our previous study (*4*), where a variation of i_T was caused by changing the electrical conductivity of a sample substrate, a film of the electronically conductive polymer, polypyrrole. The difference between these two cases is shown schematically in Figure 1. The conductive substrate, i.e., the electronically conducting polymer, is shown in Figure 1A and the redox polymer film is shown in Figure 1B. In the latter, the feedback current increases because of the redox reaction at the interface of a solution and redox centers on the polymer film surface. This reaction depends on the oxidation state of redox centers in the film and the formal potential of the solution redox couple. The effects seen depend on the relative energy levels (redox potentials) of polymer and solution species (Figure 2) and are somewhat analogous to those observed with bilayer electrodes (*10*, *11*), where two redox polymer films (inner and outer) are coated on the surface of an electrode. With the SECM, the solution gap between the polymer film and the tip electrode plays the role of the outer film in the bilayer electrode. In this work, we employed three different redox polymers: poly(vinylferrocene) (PVF) (*12*) which was deposited from the dissolved polymer solution, a viologen-based polymer (*13*) which was deposited from the monomer solution, and a Nafion/$Os(bpy)_3^{2+/3+}$ film (*14*, *15*). We also show that SECM can provide information about the quality of the polymer film, i.e., whether leakage through pinholes in the film is significant. In a similar way, the effect of a thin oxide film on metal surfaces can be studied. This was used to distinguish different metal substrates, gold and chromium, by employing a solution containing different redox couples. Moreover, this study demonstrates that the SECM can be used to image chemically different sites on a substrate material, which shows apparently different topographic structures, by changing the substrate electrode potential and varying the electroactive species in the electrolyte solution (*4*).

EXPERIMENTAL SECTION

Materials. Milli-Q reagent water (Millipore Corp.) was used for all aqueous solutions, containing reagent grade $Ru(bpy)_3Cl_2 \cdot 6H_2O$, $K_4Fe(CN)_6$, $K_3Fe(CN)_6$, $Ru(NH_3)_6Cl_3$, methyl viologen (MV) dichloride hydrate, KCl, K_2SO_4, or Na_2SO_4, which were used as received. Acetonitrile (MeCN, spectrophotometric grade; Mallinckrodt, Inc.) was equilibrated with a molecular sieve (Mallinckrodt, grade 514GT 5Å) and was used for $Ru(bpy)_3(ClO_4)_2$, $MV(ClO_4)_2$, and tetrabutylammonium perchlorate (TBAP) solutions. Poly(vinylferrocene) (PVF) was 15 700 molecular weight and degree of polymerization 74 (*16*). *N,N'*-Bis[3-(trimethoxysilyl)propyl]-4,4'-bipyridinium (PQ^{2+}) dibromide was generaously provided by Professor M. S. Wrighton (MIT). A solution of Nafion (equivalent weight 1100, 5% (w/w) in an alcohol–water mixture) was obtained from Aldrich Chemical Co. (Milwaukee, WI) and was diluted with ethanol to give a 1% (w/w) solution. An interdigitated array (IDA) electrode consisting of 15 μm wide Au or Cr bands, with 15 μm spacing (30 μm periodicity) on a quartz substrate was obtained from Microsensor Systems, Inc. (Springfield, VA).

Preparation of Substrate. Before modified electrodes were prepared, the substrate electrodes were polished with alumina; the final polish was carried out with 0.05-μm particles. PVF was

0003-2700/90/0362-1906$02.50/0

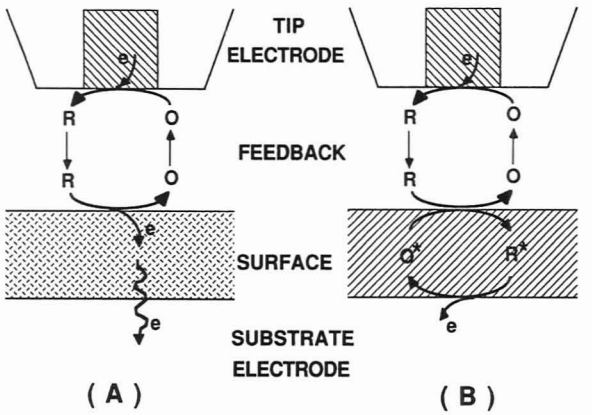

Figure 1. Comparison of positive feedback in SECM: (A) on an electrically conductive substrate, e.g., a conductive polymer (or just an extension of the solid electrode); (B) on a chemically modified substrate, e.g., a redox polymer.

electrodeposited by oxidation to poly(vinylferrocenium) perchlorate onto a Pt or Au electrode from a stirred CH_2Cl_2 solution containing 5 μM PVF at a potential of 0.7 V vs an oxidized silver wire quasi-reference electrode (AgQRE) (*12*). Electrolysis time was 1–2 min, yielding about 10^{-10} mol of PVF cm^{-2}. A $(PQ^{2+/+})_n$ film was grown on a 2 mm diameter Pt disk electrode, half of which was masked by Teflon tape, by applying cyclic potential sweeps (30 cycles, at a scan rate, v, of 100 mV/s) between 0.0 and −0.77 V vs SCE (*13*) from an aqueous solution containing ca. 3 mM PQ^{2+} monomer, 0.20 M KCl, and 0.10 M K_2HPO_4 (pH = 8.9) after presaturation with N_2. The thickness of this film was measured ellipsometrically and was 100 nm (assuming a refractive index of the oxidized form of 1.50–0.01*i*). To prepare a Nafion-modified electrode, a Pt disk electrode (5 mm diameter) was spin coated with 10 drops (ca. 10 μL/drop) of a Nafion solution (1% (w/w)) at 2000 rpm and dried in the air for 30 min. $Os(bpy)_3^{2+}$ cations were introduced into the Nafion film by immersing the coated electrodes in an aqueous solution containing 1 mM $Os(bpy)_3(ClO_4)_2$ and 0.1 M Na_2SO_4 (*15*, *17*). The measured thickness of a dry Nafion/$Os(bpy)_3^{2+}$ film was ca. 250 nm, obtained with an Alfa-step 200 profilometer (Tencor Instruments, Mountain View, CA) after partial removal of the film with a sharpened wooden stick.

SECM Experiments. Instrumental details and operational procedures for the SECM were as described previously (*3*). The bipotentiostat mode was used to apply potentials to the tip (E_T) and substrate (E_S). Two potential programmers, a PAR 175 universal programmer (Princeton Applied Research, Princeton, NJ) and a home-built bipotentiostat (*18*), were employed to control E_T and E_S independently. A microdisk carbon electrode tip (5.5 μm radius) was fabricated and used for SECM experiments (*1*). The rate of scanning of the tip over the substrate (S_T) was 23.7 μm/s for all experiments, except for measurements of ΔE_S where S_T was 0.66 μm/s. The distance between tip and substrate (d) was determined from the observed ratio of $i_T/i_{T,\infty}$ based on the theoretical curves (*2*), when d was of the order of the tip electrode radius, a. At larger distances, this was estimated from the calibration curve for the micropositioning device.

RESULTS AND DISCUSSION

We first describe SECM experiments on three different redox polymers where the results are discussed in terms of the SECM feedback principle and the polymer bilayer electrode model. We then present SECM experiments on an IDA with interdigitated gold and chromium electrodes with different redox couples and explain the results in terms of the properties of a thin passive oxide film on the chromium surface.

PVF Film. Several different forms of cyclic voltammetry (CV) can be carried out with SECM. In tip (T) CV, the tip potential (E_T) is scanned and the tip current (i_T) measured, with the substrate held at a potential E_S. Substrate (S) CV involves a scan of substrate potential (E_S) vs substrate current (i_S). These two CV modes (T-CV and S-CV) are used to check

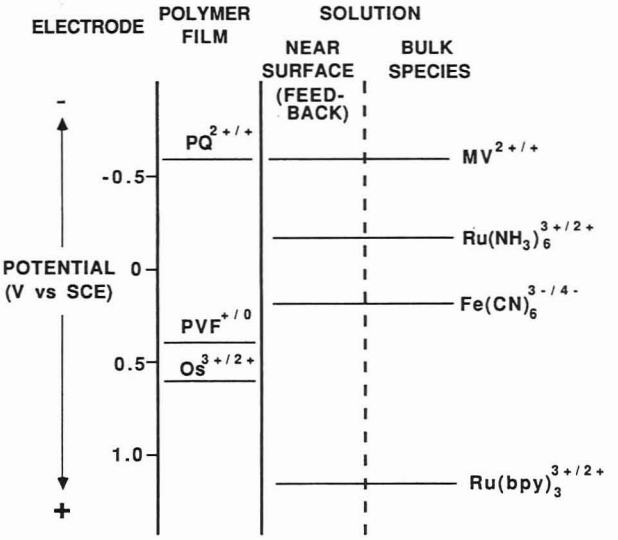

Figure 2. Potentials of redox species in this SECM system.

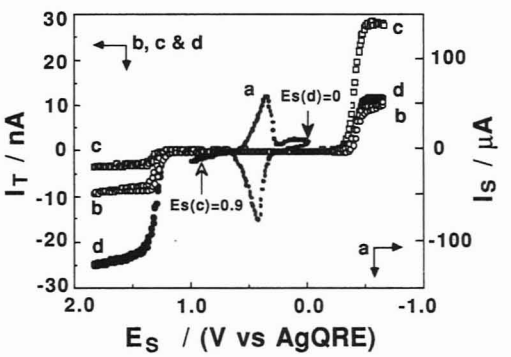

Figure 3. S-CV (curve a, v = 200mV/s) and T-CVs (curves b, c, and d, v = 1 V/s) on PVF-modified Pt electrode. In the T-CVs a solution of $MV(ClO_4)_2$ and $Ru(bpy)_3(ClO_4)_2$ was used: curve b, d = 98 μm; curve c, d = 2 μm, E_S = 0.9 V vs AgQRE; curve d, d = 2 μm, E_S = 0 V vs AgQRE.

the electrochemical response of the tip and substrate electrodes before topographic SECM scans. The S-CV of a PVF modified Pt disk electrode (2 mm diameter), at v = 200 mV/s, shows the usual surface redox waves for the $PVF^{+/0}$ couple (Figure 3, curve a) (*12*, *16*). When E_S is held negative of these waves, e.g., at 0 V vs AgQRE, the film will be in the reduced PVF^0 form. At potentials positive of the wave it will be in the PVF^+ form. The type of feedback current at the tip will depend on E_S, the redox couples in the solution, and E_T. Typical T-CVs at v = 1 V/s in a MeCN solution containing 10 mM each MV^{2+} and $Ru(bpy)_3^{3+}$ and 0.1 M TBAP are shown in Figure 3 (curves b, c, and d). When the tip electrode is far from the substrate (ca. 98 μm) (curve b), the currents are those of an unperturbed disk ultramicroelectrode. The limiting current plateaus, at both ends of the potential sweep range, yield the values of $i_{T,\infty}$ of ca.10 nA. The reaction at the tip at the negative end of the potential sweep range is

$$MV^{2+} + e^- \rightarrow MV^+ \quad (2)$$

At the positive end, the reaction is

$$Ru(bpy)_3^{2+} - e^- \rightarrow Ru(bpy)_3^{3+} \quad (3)$$

When T-CVs are carried out with the tip close to the PVF electrode (d = 2 μm), either positive or negative feedback effects arise that depend on the oxidation state of the PVF and tip electrode reaction, i.e., on E_S and E_T. The different possibilities can be understood by reference to the redox levels shown in Figure 2. When E_S = 0.9 V vs AgQRE (PVF^+ form), the limiting cathodic i_T is 2.5 times $i_{T,\infty}$ while the limiting anodic i_T is less than $i_{T,\infty}$ (Figure 3, curve c). The positive

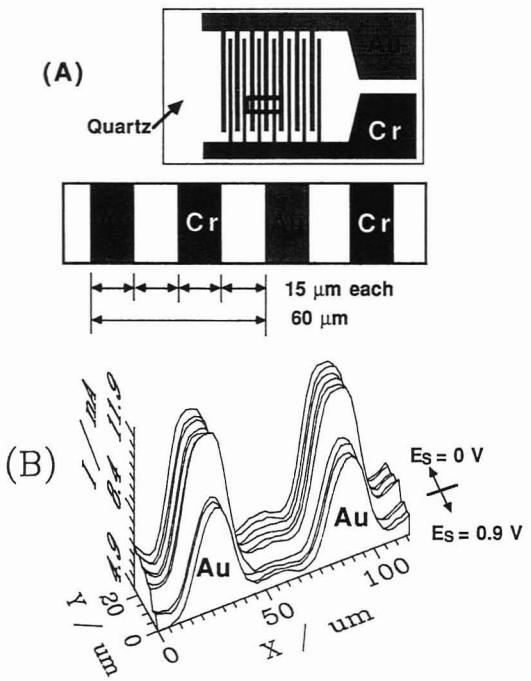

Figure 4. (A) Schematic structure of IDA (upper) and the enlargement of the boxed area (lower). (B) Scans of PVF-modified Au/Cr IDA electrodes (Au, 60 μm periodicity) in 8 mM $Ru(bpy)_3(ClO_4)_2$, 0.1 M TBAP/MeCN, E_T = 1.5 V vs AgQRE. E_S was changed from 0.9 V (front) to 0.0 V (rear) vs AgQRE; $|i_{T,\infty}|$ = ca. 8.6 nA.

feedback current, at the negative potentials, where tip electrode reaction (2) occurs, is the result of the reaction

$$MV^+ + PVF^+ \rightarrow MV^{2+} + PVF^0 \qquad (4)$$

at the solution/substrate interface, leading to regeneration of MV^{2+} in the gap region (see Figure 1B). On the other hand, when E_T is at the positive potential limit, reaction 3 occurs at the tip. Since $Ru(bpy)_3^{3+}$ does not react with PVF^+, the film behaves as an insulator and $i_T < i_{T,\infty}$. A similar interpretation can be given for the T-CV when E_S = 0 V vs AgQRE (PVF^0 form) (Figure 3, curve d). At positive E_T values, positive feedback occurs via the reaction

$$Ru(bpy)_3^{3+} + PVF^0 \rightarrow Ru(bpy)_3^{2+} + PVF^+ \qquad (5)$$

and $i_T > i_{T,\infty}$. Although i_T should be less than $i_{T,\infty}$ at negative E_T values, this was not observed, perhaps because the cell on the SECM mount could not be kept deaerated and some oxygen leaked into the cell and reacted with the tip-generated MV^+. The feedback behavior observed with a redox polymer like PVF can be contrasted with that of an electronic conductor, such as Pt, where i_T would be greater than $i_{T,\infty}$ with E_T at both the negative and positive limits, as long as E_S was in the zone between the $MV^{2+/+}$ and $Ru(bpy)_3^{3+/2+}$ waves or the Pt was at open circuit. By this selective feedback, which depends on the nature of the redox sites and the probing electroactive species, one can distinguish different sites on a substrate material by varying the electroactive species in the electrolyte solution. The behavior is somewhat analogous to that of polymer bilayer sandwich electrodes, where a redox reaction at the polymer/polymer interface controls the observed voltammetric response (*10*, *11*). In this case the thin solution layer plays the role of the outer polymer film. However in the SECM case, the potentials of both the polymer film and the solution can be controlled independently, so the situation is closer to that of the polymer film open-face sandwich or closely spaced interdigitated electrodes with two different polymers (*19–21*).

The topography and redox properties of the substrate can be probed by SECM x–y scans. For this purpose the PVF

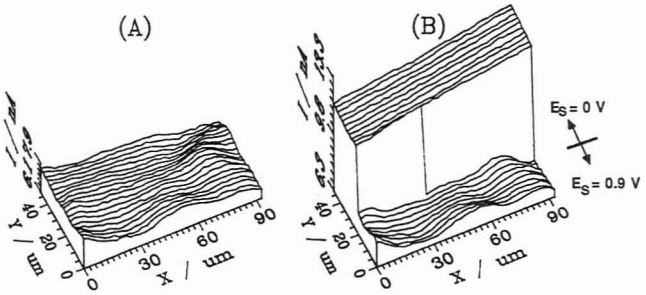

Figure 5. Scans of PVF-modified electrodes in 8 mM $Ru(bpy)_3(ClO_4)_2$, 0.1 M TBAP/MeCN, E_T = 1.5 V vs AgQRE: (A) on Pt disk electrode after OPD treatment, E_S = 0.9 V vs AgQRE; (B) same area as in part A except E_S was changed from 0.9 (front) to 0.0 V (rear) vs AgQRE, $|i_{T,\infty}|$ = ca. 7.4 nA.

was deposited on an Au/Cr IDA with the dimensions and configuration shown in Figure 4A. As described later, Au was removed from one of the sets of electrodes, leaving an array of interdigitated 15 μm wide Au and Cr bands spaced 15 μm apart. In the experiments described here, the Cr was in the oxidized form and behaved as an insulator (discussed below), so the array can be considered 15 μm wide Au bands separated by 45 μm spaces. PVF was electrodeposited on the Au bands of the array. For SECM studies, this Au IDA was immersed in a 8 mM $Ru(bpy)_3^{2+}$ and 0.1 M TBAP MeCN solution, where $i_{T,\infty}$ was 8.6 nA, at E_T = 1.5 V vs AgQRE. A topographic scan was then obtained by x–y rastering of the tip held close to the array at E_T = 1.5 V (Figure 4B). During the course of the scan E_S was switched from 0.9 V (PVF^+ form, which does not react with tip generated Ru(III)) to 0 V (PVF^0 form) where positive feedback is possible. Thus, from the T-CVs, one would expect to see a flat plane structure (insulating behavior) with E_S = 0.9 V ($i_T < i_{T,\infty}$) and the Au band structure (with a 60 μm periodicity) at E_S = 0 V with $i_T > i_{T,\infty}$. In SECM scans, the expected positive feedback at E_S = 0 V occurs, but negative feedback is not observed at E_S = 0.9 V. Instead i_T, when the tip is above the PVF-covered Au, is $\sim i_{T,\infty}$, and is much larger than i_T when the tip is over the truly insulating glass or chromium oxide zones. This is consistent with a PVF film that allows some leakage of solution to the underlying Au through pinholes in the film. Pinholes in PVF films have been observed in earlier studies and probed via chronoamperometry and rotating disk electrode voltammetry of appropriate solution species (*16*, *22*). The SECM feedback behavior for a leaky insulating film on a conductive substrate combines the blocking effect of the film ($i_T < i_{T,\infty}$) and the positive feedback effect of the conductive substrate through the pinholes ($i_T > i_{T,\infty}$). The overall i_T observed will be larger than i_T over an insulator and will depend upon the relative area of the pinholes and their size and distribution. The quantitative theory for this situation is not yet available and will be the subject of future SECM studies.

Another SECM study was carried out with a PVF film on a Pt electrode substrate. In this case we attempted to seal the pinholes by oxidizing *o*-phenylenediamine (OPD) in aqueous solution at the film-covered electrode. This treatment has been shown to deposit an insulating film on electrodes (*23*, *24*). The electrode was then transferred to the $Ru(bpy)_3^{2+}$–MeCN solution and SECM scans were carried out (Figure 5). A scan across the substrate at E_S = 0.9 V, where insulating behavior is expected, still showed larger i_T values than for a true insulator (Figure 5A). An apparently rough film structure is seen under these conditions. Thus the PVF film remains leaky after OPD treatment, perhaps because the film morphology changes upon moving the electrode from the aqueous to the MeCN solution. When E_S is switched to 0 V (Figure 5B), positive feedback behavior is observed. Note that under positive feedback conditions the film surface appears

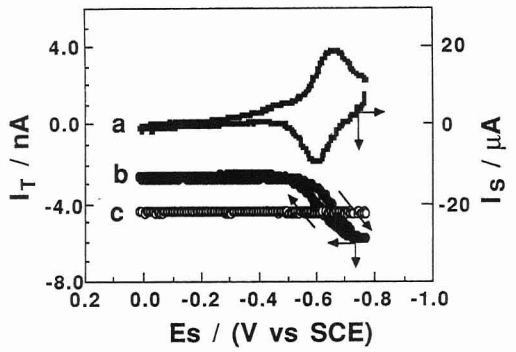

Figure 6. S-CV (curve a) and T/S CVs (curves b and c) on PQ-modified Pt electrode, v = 100 mV/s: T/S CVs in $K_4Fe(CN)_6$/KCl, E_T = 0.6 V vs SCE; curve b, d = 8 μm; curve c, d = 66 μm.

much smoother, suggesting that the variations noticed in the scan with E_S = 0.9 V represent variations in film porosity rather than actual film roughness.

$(PQ^{2+/+})_n$ Film. Studies were also carried out with a film of $(PQ^{2+})_n$ on a Pt substrate, prepared by reduction of the monomer (*13*). As shown below, this film showed behavior consistent with the absence of pinholes. The S-CV of $(PQ^{2+/+})_n$ film on a Pt disk electrode (2 mm diameter), at v = 100 mV/s in an aqueous solution containing only 0.1 M KCl, shows the usual surface redox waves for the $PQ^{2+/+}$ couple (Figure 6, curve a) (*13*). Thus when E_S is held negative of these waves, e.g., at −0.75 V vs SCE, the film will be in the reduced PQ^+ form. At potentials positive of the wave, it will be in the PQ^{2+} form.

A unique form of CV with the SECM is tip/substrate (T/S) CV (*4*). T/S CV involves monitoring i_T vs E_S with E_T maintained at a given potential and the tip held near the substrate. The tip monitors electrochemically induced changes in the substrate at locations immediately below the tip, shown by changes in the magnitude of the feedback current. This mode is different than operation in the collection mode (*1*, *8*), where products formed on the substrate are analyzed at the tip. In the T/S CV mode, the type of feedback current at the tip will depend on E_S, the redox couples in the solution, and E_T. Typical T/S CVs at v = 100 mV/s in an aqueous solution containing 5 mM $K_4Fe(CN)_6$ and 0.1 M KCl, at E_T = 0.6 V vs SCE, are shown in Figure 6 (curves b and c). When the tip electrode is far from the substrate (d = 66 μm) (curve c), i_T is that of an unperturbed disk ultramicroelectrode, i.e., $i_{T,\infty}$ = ca. 4.5 nA. The reaction at the tip is

$$Fe(CN)_6^{4-} - e^- \rightarrow Fe(CN)_6^{3-} \quad (6)$$

When T/S CV is carried out with the tip close to the $(PQ^{2+/+})_n$ electrode (d = 8 μm), either positive or negative feedback effects arise, depending on the oxidation state of the PQ. When E_S is moved negative of the surface $PQ^{2+/+}$ redox waves (PQ^+ form), $i_T > i_{T,\infty}$ (Figure 6, curve b). The positive feedback current, where the tip electrode reaction (6) occurs, is the result of the reaction

$$Fe(CN)_6^{3-} + PQ^+ \rightarrow Fe(CN)_6^{4-} + PQ^{2+} \quad (7)$$

at the solution/substrate interface leading to regeneration of $Fe(CN)_6^{4-}$ in the solution gap region (Figure 1B). On the other hand, when E_S is moved positive of the surface redox waves (PQ^{2+} form), the film behaves as an insulator and $i_T < i_{T,\infty}$ since $Fe(CN)_6^{3-}$ does not react with PQ^{2+}.

By use of SECM x–y scans above the region where the boundary between the Pt (left hand side) and the PQ film (right hand side) lies, both the topography and the conductive nature of the substrate can also be probed (Figure 7). In all cases in Figure 7, E_S was held at 0.0 V vs SCE (PQ^{2+} state) and the topography observed depended upon the redox couple

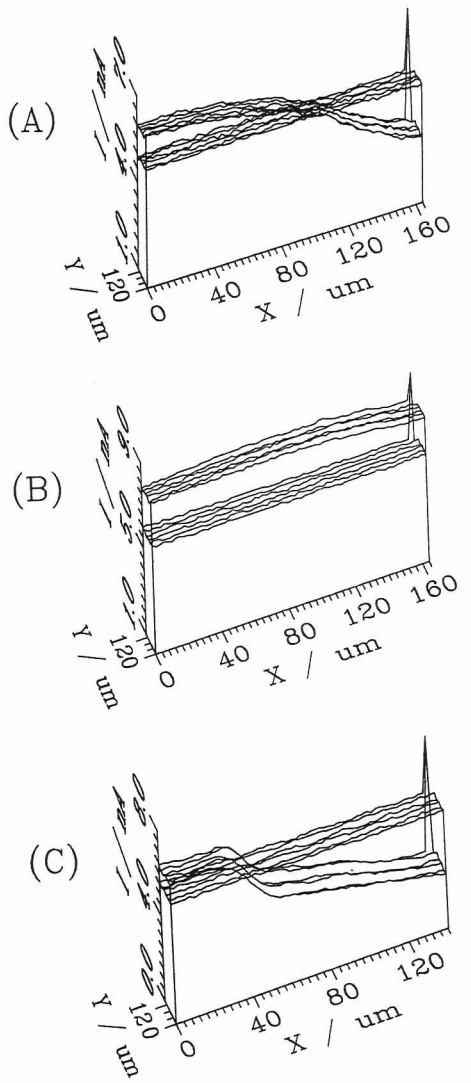

Figure 7. Scans of the boundary between Pt (left) and PQ film (right), E_S = 0.0 V vs SCE. Flat planes show $i_{T,\infty}$ planes: (A) in $K_4Fe(CN)_6$/KCl, E_T = 0.7 V; (B) in $MVCl_2$/KCl, E_T = −0.78 V; (C) in $Ru(NH_3)_6Cl_3/K_2SO_4$, E_T = −0.38 V.

in the electrolyte solution. When we scanned the polymer/Pt boundary region generating $Fe(CN)_6^{3-}$ at the tip (the same experimental conditions as in T/S CV), the $(PQ^{2+})_n$ film behaves as an insulator (Figure 7A). However when the boundary region is scanned with the film immersed in an aqueous solution containing 5 mM $MVCl_2$ and 0.1 M KCl at E_T = −0.78 V, the $(PQ^{2+})_n$ film acts as a conductor (Figure 7B). This positive feedback current, where the tip electrode reaction (2) occurs, is the result of the reaction

$$MV^+ + PQ^{2+} \rightarrow MV^{2+} + PQ^+ \quad (8)$$

at the solution/film interface leading to $i_T > i_{T,\infty}$. Here one does not see any defined Pt/film boundary; i_T is increased equally over Pt and (PQ^{2+}) compared to $i_{T,\infty}$. Results in Figure 7A,B are similar to those found previously with a PP film (*4*). Similar experiments were obtained for an SECM scan above the Pt/film boundary with an aqueous solution containing 5 mM $Ru(NH_3)_6Cl_3$ and 0.1 M K_2SO_4 at E_T = −0.38 V vs SCE. The tip electrode reaction is

$$Ru(NH_3)_6^{3+} - e^- \rightarrow Ru(NH_3)_6^{2+} \quad (9)$$

The film behaves as an insulator (Figure 7C), i.e., reaction

$$Ru(NH_3)_6^{2+} + PQ^{2+} \rightleftarrows Ru(NH_3)_6^{3+} + PQ^+ \quad (10)$$

(10) lies to the left (see Figure 2). In summary, the observed

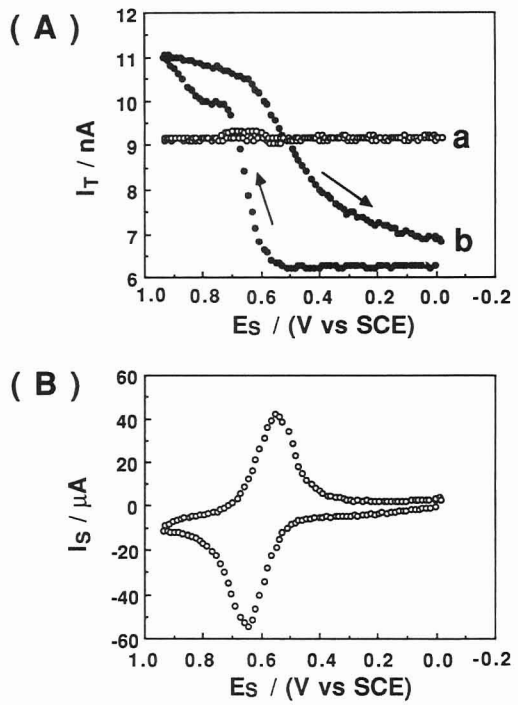

Figure 8. T/S CVs (A) curve a, d = 500 μm; curve b, d = 10 μm, and S-CV (B) on Nafion/$Os(bpy)_3^{3+/2+}$ electrode in $K_3Fe(CN)_6/Na_2SO_4$, v = 50 mV/s, E_T = −0.4 V vs SCE.

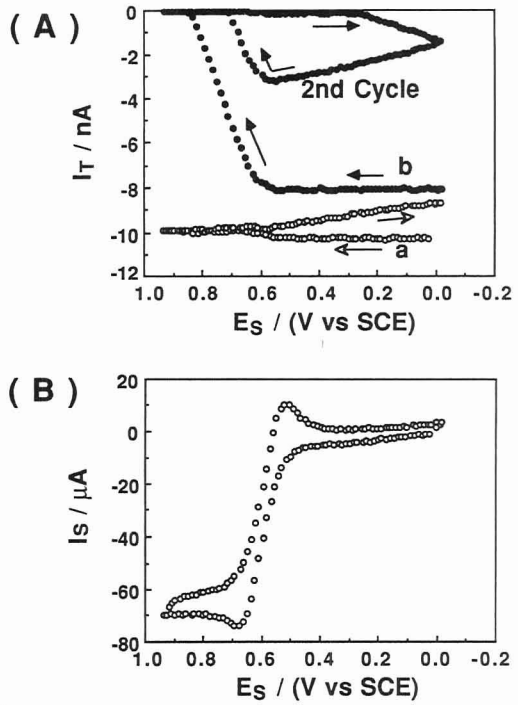

Figure 9. T/S CVs (A) curve a, d = 220 μm; curve b, d = 10 μm, and S-CV (B) on Nafion/$Os(bpy)_3^{3+/2+}$ electrode in $K_4Fe(CN)_6/Na_2SO_4$, v = 50 mV/s; E_T = 0.6 V vs SCE.

feedback response over a PQ film depends on the redox state of the film as well as the redox species in solution. The PQ film (~100 nm) shows much better blocking behavior (i.e., fewer pinholes) than the thicker PVF film.

Nafion/$Os(bpy)_3^{2+}$ Film. Films of the perfluorinated ionomer, Nafion, have been examined extensively (*11*, *14*) because of their utility in exchanging electroactive cations

$$M^{n+}_{soln} + n(SO_3^-Na^+)_{elec} \rightleftarrows [(SO_3^-)_nM^{n+}]_{elec} + nNa^+_{soln} \quad (11)$$

In this study, $Os(bpy)_3^{2+}$ cations were introduced into the Nafion films by immersing the Nafion-coated electrodes in an aqueous solution containing 1 mM $Os(bpy)_3(ClO_4)_2$ and 0.1 M Na_2SO_4. T/S and S-CV modes were used to check the electrochemical response of the tip and substrate electrodes before topographic SECM scans were carried out. T/S and S-CVs of a Nafion/$Os(bpy)_3^{3+/2+}$ substrate in an aqueous solution containing either 10 mM $K_3Fe(CN)_6$ and 0.1 M Na_2SO_4 or 10 mM $K_4Fe(CN)_6$ and 0.1 M Na_2SO_4 are shown in Figures 8 and 9, respectively. The $Fe(CN)_6^{3-/4-}$ couple was chosen because the high negative charge is known to prevent these ions from diffusing into the Nafion coating (*17*). Thus, reaction between $Fe(CN)_6^{3-/4-}$ and $Os(bpy)_3^{2+/3+}$ will be restricted to the solution/film interface, as found in a previous study with this couple and $Ru(bpy)_3^{2+}$. The S-CV of Nafion/$Os(bpy)_3^{3+/2+}$ film on a Pt disk electrode (5 mm diameter), at v = 50 mV/s in the $Fe(CN)_6^{3-}$ solution, shows the usual redox waves for the $Os(bpy)_3^{3+/2+}$ couple (Figure 8B). When E_S is held positive of these waves, the redox sites in the film will be oxidized to the $Os(bpy)_3^{3+}$ form; for E_S held negative of these waves, the redox sites will be in the reduced $Os(bpy)_3^{2+}$ form. Typical T/S CVs at v = 50 mV/s at E_T = −0.4 V vs SCE are shown in Figure 8A. When the tip electrode is far from the substrate (d = 500 μm), i_T shows $i_{T,\infty}$ (9.2 nA) independent of E_S (flat CV). The reaction at the tip is

$$Fe(CN)_6^{3+} + e^- \rightarrow Fe(CN)_6^{4-} \quad (12)$$

When T/S CV is measured with the tip close to the substrate electrode (d = 10 μm), either positive or negative feedback effects arise, depending on the oxidation state of the $Os(bpy)_3^{3+/2+}$ couple. When E_S is swept positive of the $Os(bpy)_3^{3+/2+}$ redox waves ($Os(bpy)_3^{3+}$ form), $i_T > i_{T,\infty}$. This positive feedback i_T, where the tip electrode reaction (12) occurs, is the result of the reaction

$$Fe(CN)_6^{4-} + Os(bpy)_3^{3+} \rightarrow Fe(CN)_6^{3-} + Os(bpy)_3^{2+} \quad (13)$$

at the solution/film interface leading to regeneration of $Fe(CN)_6^{3-}$ in the solution gap region (Figure 1B). When E_S is swept negative of the redox waves ($Os(bpy)_3^{2+}$ form), the film behaves as an insulator and $i_T < i_{T,\infty}$. $Fe(CN)_6^{3-}$ does not react with $Os(bpy)_3^{2+}$, since the reverse of reaction 13 is thermodynamically unfavorable (see Figure 2). The S-CV in Figure 8B in the presence of $Fe(CN)_6^{3-}$ is identical with that in an aqueous 0.1 M Na_2SO_4 solution regardless of the direction of E_S sweeping, because of this lack of reactivity.

Figure 9 shows T/S and S-CVs of a Nafion/$Os(bpy)_3^{3+/2+}$ substrate in an aqueous solution containing 10 mM $K_4Fe(CN)_6$ and 0.1 M Na_2SO_4, at v = 50 mV/s and E_T = 0.6 V vs SCE. As expected, the S-CV of the $Os(bpy)_3^{3+/2+}$ couple in the presence of $Fe(CN)_6^{4-}$ in solution (Figure 9B) shows the effect of reaction 13, i.e., the catalytic oxidation of $Fe(CN)_6^{4-}$ by the Os(III) form. For this solution the substrate reaction causes depletion of the bulk species [Fe(II)], rather than the tip-generated species [Fe(III)], and the extent of this depletion can be monitored by T/S CV (Figure 9A). When the tip is far from the substrate (d = 220 μm) and the substrate is at open circuit, $i_T = i_{T,\infty}$ = 10.2 nA, where E_T = 0.6 V and Fe(II) is oxidized to Fe(III) (reaction 6). However even at this relatively large distance, when E_S is cycled to more positive potentials where this same overall anodic reaction occurs (via reaction with Os(III)), i_T decreases because of depletion of Fe(II) in the solution region between substrate and tip (Figure 9A, curve a). The time, t_d, for i_T to decrease below $i_{T,\infty}$ in the cyclic scan represents the time needed for the diffusion layer to grow out from the substrate to the tip, i.e., $t_d \approx d^2/2D$. This "depletion effect" in SECM is different from the feedback modes, which require $d \approx 4a$, where a is the tip radius. The depletion effect can be seen for much larger tip distances, if sufficient time is allowed for substrate diffusion layer growth.

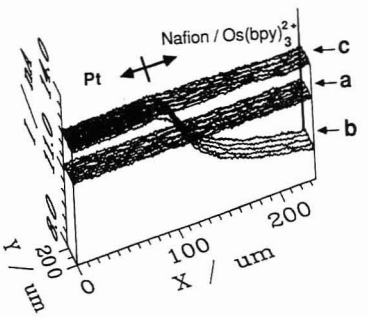

Figure 10. Scans of the boundary between Pt (left side) and Nafion film (right side) in $K_3Fe(CN)_6/Na_2SO_4$, E_T = −0.4 V vs SCE: (a) $i_{T,\infty}$ plane, d = 98 μm; (b) E_S = 0.42 V ($Os(bpy)_3^{2+}$ form), d = 10 μm; (c) E_S = 0.8 V ($Os(bpy)_3^{3+}$ form), d = 10 μm.

The same effect is seen in substrate–tip generation/collection experiments, where the diffusion layer of substrate-generated species grows out to the tip, e.g., as in the photogeneration of oxygen at a leaf (5).

When T/S CV is carried out with the tip close to the film surface (d = 10 μm) more rapid and greater depletion of the Fe(II) species at the substrate is detected at the tip (Figure 9A, curve b). i_T decreases rapidly to zero immediately after $Os(bpy)_3^{2+}$ oxidizes to $Os(bpy)_3^{3+}$, because the large modified substrate electrode (Pt disk, 5 mm diameter) depletes $Fe(CN)_6^{4-}$ near the surface of the film via reaction 13. The almost total depletion of Fe(II) is maintained until the substrate potential scan is reversed and the Os(III) in the Nafion is reduced. The tip current then increases because Fe(II) from the bulk solution diffuses into the gap region to the tip. This increase continues until i_T approaches the value characteristic of that over an insulator. However when E_S is scanned back into the region of Fe(II) oxidation, i_T decreases again via the depletion effect. Because the steady-state i_T in the depletion mode is essentially zero, this approach is not very useful as a steady-state mode, although it could be of interest in the electrochemical observation of a species at a tip in the presence of a larger concentration of another species which can be selectively depleted at the substrate. It could be useful in the transient mode, e.g., in estimation of diffusion coefficients.

Examination of the topography above the boundary region between Pt and the Nafion/$Os(bpy)_3^{3+/2+}$ film is useful in studying redox reactions at the film/solution interface, as well as to gauge the porosity and the quality of the film. The results of such topographic SECM scans are shown for a $Fe(CN)_6^{3-}$ solution (Figure 10). When the tip reaction is Fe(II) oxidation, reaction 12, and the tip is scanned far (98 μm) from the substrate, a flat response with $i_T = i_{T,\infty}$ over both polymer film and Pt is seen (curve a). When the tip is close to the substrate ($d \approx 10$ μm), the behavior depends upon E_S. At E_S = 0.42 V, the film acts as an insulator (curve b), and a clear boundary is seen between Pt and Nafion. When E_S = 0.8, V, positive feedback occurs over the film, and a flat response at $i_T > i_{T,\infty}$ is seen (Curve c). The good insulating behavior shown by Nafion with $Os(bpy)_3^{2+}$ demonstrates freedom from pinholes in the film and lack of penetration of $Fe(CN)_6^{3-}$ to the Pt substrate.

Au/Cr IDA Electrode. Topographic scans with the SECM were also carried out on an electrode array consisting of interdigitated Au and Cr bands (Figure 4A). This array was formed from an array of Au deposited over Cr with a bandwidth and spacing of 30 μm (Microsensor System, Inc., Part No. 302). PVF was deposited on one set of bands by electrochemical oxidation from a PVF solution in CH_2Cl_2, as described earlier. When the array was rubbed gently with a cotton swab (a Q-tip), the PVF and Au peeled from the bands with deposited polymer, but the Au on the other bands was not disturbed. This Au/Cr array was useful in probing the

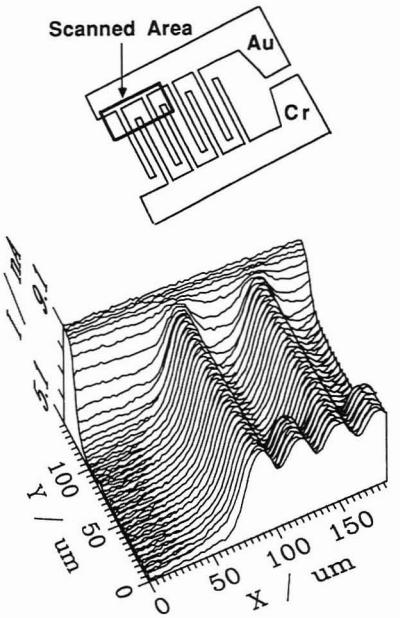

Figure 11. Schematic pictures of the scanned area of Au/Cr IDA (upper) and SECM scan of Au/Cr IDA at open circuit in $MVCl_2$/KCl (lower), E_T = −0.78 V vs SCE. Note, the first band from the left is an Au band.

effect of surface oxidation of the Cr on its electrochemical behavior by comparing its response to that of the neighboring Au bands. Figure 11 shows the characterization of this IDA at open circuit by SECM in an aqueous solution containing 5 mM $MVCl_2$ and 0.1 M KCl, where E_T was held at −0.78 V vs SCE, where MV^+ is generated ($i_{T,\infty}$ = 7.5 nA). Under these conditions Cr is maintained in the oxide-free (active) region of potentials and positive feedback is observed over both the Au and Cr bands. The average periodicity and structure observed was in good agreement with the manufacturer's specification. However, the current changes as the tip electrode moved across the bands showed a sinusoidal, rather than a step, shape, since the diameter of the tip disk electrode was 11 μm, which produces low resolution images of 30-μm bands and spaces. Higher resolution would be obtained with smaller tips scanned at smaller values of d, as discussed previously (*3*). Even at this resolution the structure is clearly shown and good gray-scale images could be obtained by suitably restricting the i_T range for maximum and minimum levels (e.g., between 8.1 and 9.1 nA). The topographic scans do show the effects of overlapping of the diffusion layers of the neighboring Au and Cr bands.

One can contrast the SECM behavior of the Au/Cr array at open circuit when different redox couples are employed (Figure 12). With MV^{2+} in solution and MV^+ generated at the tip, Au and Cr produce equal positive feedback currents (Figure 12A). However with $Ru(NH_3)_6^{3+}$ or $Fe(CN)_6^{4-}$ in solution, lower feedback responses were found with the tip over the Cr bands (Figure 12B–D). With $Ru(NH_3)_6^{2+}$ generated at the tip, a feedback response is still shown over the Cr, but at the potential of the $Ru(NH_3)_6^{3+/2+}$ couple, the rate of the oxidation of the Ru(II) on the oxidized Cr surface is slower than it is on Au (Figure 12B). With $Fe(CN)_6^{3-}$ generated at the tip, the Cr behaves as an insulator, i.e., reduction of Fe(III) to Fe(II) does not occur on the oxidized Cr (Figure 12C). The selectivity of response with E_T and redox couple is illustrated in Figure 12D, for a solution containing both MV^{2+} and $Fe(CN)_6^{4-}$. With E_T at −0.78 V, i_T is cathodic and conductive positive feedback is obtained over Cr; both Au and Cr bands are imaged. When E_T is switched to +0.7 V during the scan, i_T becomes anodic; the Cr is passivated and behaves as an insulator, so that only the Au bands are imaged.

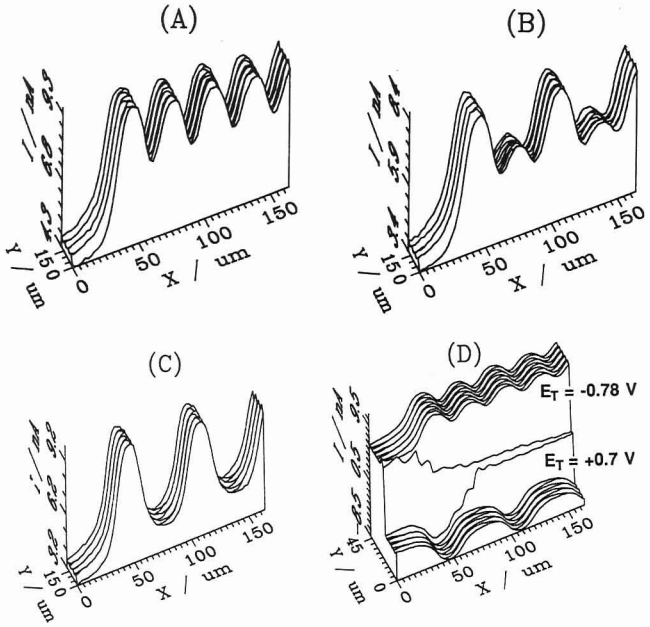

Figure 12. Scans of Au/Cr IDA in various electrolytes, where E_S was at open circuit and the first band from the left is an Au band: (A) in $MVCl_2$/KCl, E_T = −0.78 V; (B) in $Ru(NH_3)_6Cl_3/K_2SO_4$, E_T = −0.37 V; (C) in $K_4Fe(CN)_6$/KCl, E_T = 0.7 V; (D) in a mixture of [$K_4Fe(CN)_6$ and $MVCl_2$]/KCl, E_T was switched from 0.7 to −0.78 V vs SCE.

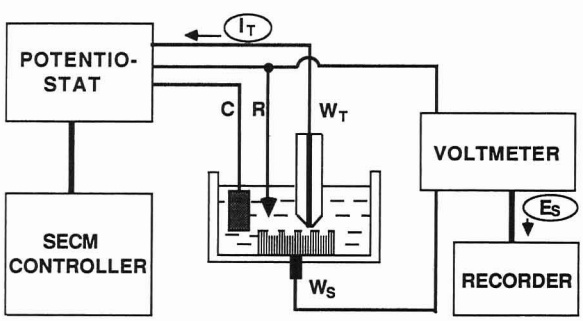

Figure 13. Schematic diagrams of experimental system for measuring ΔE_S simultaneously with scanning.

The potentials of the bands at open circuit, contacting both bulk solution species and tip-generated species, are mixed potentials. These were probed by measuring the change of E_S in the IDA at open circuit while simultaneously performing an SECM scan over this IDA (S_T = 0.66 μm/s). A schematic diagram for this experiment is shown in Figure 13. ΔE_S was measured with a high-impedance voltmeter connected between the reference electrode and the substrate. Typical results are shown in Figure 14, In Figure 14A, the electrolyte solution was an aqueous solution containing 5 mM $K_4Fe(CN)_6$, where ΔE_S of the Cr and Au bands was monitored separately. No clear change in ΔE_S was seen with the tip over the Cr bands, generating $Fe(CN)_6^{3-}$, as expected with an insulating substrate. However, with $Fe(CN)_6^{3-}$ generated above the Au bands, a significant change of E_S toward more positive values was seen. The change of ΔE_S correlated with that of Δi_T, showing that ΔE_S is a function of the flux density of oxidant impinging on the substrate surface. Movement of the sample during the scan caused the change in Δi_T and ΔE_S over Au during the two x–y scans. Different ΔE_S behavior was found when the electrolyte solution was an aqueous solution containing 5 mM $MVCl_2$, both Au and Cr bands were connected together, and ΔE_S of these bands was monitored simultaneously. ΔE_S changed to more negative values as the tip, generating MV^+ passed over either a Au or Cr band (Figure 14B). Note that the sign of ΔE_S was different in the two experiments and depended on whether i_T was cathodic or anodic. Again ΔE_S

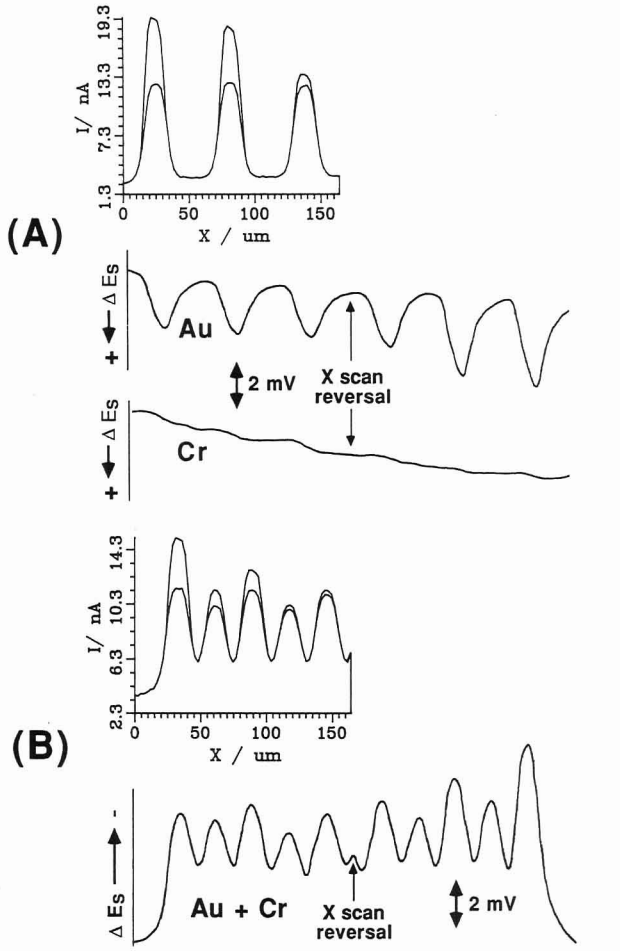

Figure 14. Experimental results on Au/Cr IDA using the system in Figure 13: (A) in $K_4Fe(CN)_6$/KCl, E_T = 0.7 V; (B) in $MVCl_2$/KCl, E_T = −0.78 V. Upper curves show Δi_T and lower curves show ΔE_S, for a scan of the tip across three Au lines followed by a reverse scan back across the same area. The change in current on reverse scan is caused by swelling of the tape holding sample and a decrease in the tip/substrate distance. In the lower curve of part B the Au and Cr lines were connected and the potential was measured.

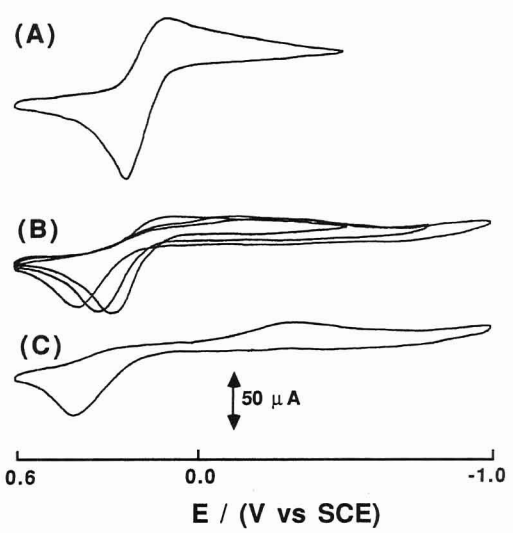

Figure 15. CV response of Cr electrode (v = 200 mV/s), in $K_3Fe(CN)_6$/KCl: (A) freshly sputtered Cr electrode; (C) CV after treatment of part B.

correlated with Δi_T, but in this case the potential of the Cr was in the active region.

Although it was beyond the scope of the present study to investigate the effect of an oxide film on Cr on the rate of electron transfer reactions to electroactive species, a few

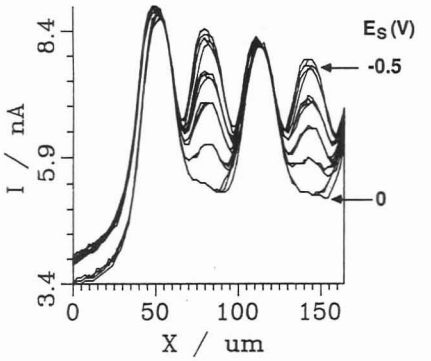

Figure 16. Scans of Au/Cr IDA in $K_4Fe(CN)_6$/KCl with changing E_S of Cr band. Four bands were scanned (Au, Cr, Au, and Cr from left to right), E_T = 0.69 V, E_S = 0.0, −0.2, −0.3, −0.4, and −0.5 V vs SCE from bottom to top.

preliminary experiments were carried out to demonstrate this effect. A fresh Cr layer, ca. 400 nm thick, was sputtered on a glass slide. The CV response of the fresh Cr electrode in an aqueous $K_3Fe(CN)_6$/KCl solution resembled that at an Au or a Pt electrode (Figure 15A). When the potential of the Cr was swept to increasingly more positive potentials (Figure 15B), the CV response of the $Fe(CN)_6^{3-/4-}$ couple became significantly less reversible (Figure 15C). We attribute this to the formation of an oxide film on the Cr surface, which decreases the heterogeneous rate constant for the $Fe(CN)_6^{3-/4-}$ reaction.

A similar effect can be seen at the Au/Cr IDA upon changing E_S, with substrate and tip controlled with a bipotentiostat (Figure 16). In this experiment with a redox couple the tip was held at a given potential and scanned over alternating Au and Cr bands connected together with E_S changed stepwise at the end of each x-scan. With a $Fe(CN)_6^{4-}$ solution and the tip generating the Fe(III) species (Figure 16), positive feedback was found at the Au bands for E_S values of 0 to −0.5 V. However the positive feedback observed for reduction of the Fe(III) species at −0.5 V became smaller as the potential was stepped to more positive values. This behavior was consistent with the CV behavior of $Fe(CN)_6^{3-}$ on an oxidized Cr substrate shown in Figure 15C. In this case the reaction is less reversible on the Cr electrode, except at the most extreme potentials.

CONCLUSIONS

SECM has been used to investigate films of electroactive polymers. The observed feedback response was a function of the nature of the redox sites in the polymer, the substrate potential, the redox species in solution, and the reaction at the tip electrode. The spatial distribution of polymer on the substrate could be probed by x–y scans, as shown by experiments with interdigitated electrode arrays. For a polymer in its insulating state, the observed SECM response could provide information about the presence of pinholes or porosity of the film. Thus PVF films were shown to be rather porous, in agreement with past studies, while $(PQ^{2+})_n$ and Nafion formed films that were free of pinholes. SECM can also be employed in studies where the rate of reaction between the substrate species and tip-generated species is finite, compared to the case of pure conductors (infinitely fast reaction) or pure insulators (infinitely slow reaction). A preliminary examination of this case was carried out with electrodes of Cr, where oxidation of the Cr surface decreases the rate of electrode reactions. Further theoretical and experimental studies of this case are under way in this laboratory.

ACKNOWLEDGMENT

The authors thank Professer M. S. Wrighton for providing the PQ monomer and Dr. H. Wohltjen for the donation of the IDA electrode.

LITERATURE CITED

(1) Bard, A. J.; Fan, F.-R. F.; Kwak, J.; Lev, O. *Anal. Chem.* **1989**, *61*, 132.
(2) Kwak, J.; Bard, A. J. *Anal. Chem.* **1989**, *61*, 1221.
(3) Kwak, J.; Bard, A. J. *Anal. Chem.* **1989**, *61*, 1794.
(4) Kwak, J.; Lee, C.; Bard, A. J. *J. Electrochem. Soc.* **1990**, *137*, 1481.
(5) Lee, C.; Kwak, J.; Bard, A. J. *Proc. Natl. Acad. Sci. U.S.A.* **1990**, *87*, 1740.
(6) Newman, J. *J. Electrochem. Soc.* **1966**, *113*, 501.
(7) Saito, Y. *Rev. Polarogr.* **1968**, *15*, 177.
(8) Engstrom, R. C.; Meany, T.; Tople, R.; Wightman, R. M. *Anal. Chem.* **1987**, *59*, 2005.
(9) Engstrom, R. C.; Pharr, C. M. *Anal. Chem.* **1989**, *61*, 1099A.
(10) Denisevich, P.; Willman, K. W.; Murray, R. W. *J. Am. Chem. Soc.* **1981**, *103*, 4727.
(11) Murray, R. W. In *Electroanalytical Chemistry*; Bard, A. J., Ed.; Marcel Dekker: New York, 1984; Vol. 13, and references therein.
(12) Merz, A.; Bard, A. J. *J. Am. Chem. Soc.* **1978**, *100*, 3222.
(13) Bookbinder, D. C.; Wrighton, M. S. *J. Electrochem. Soc.* **1983**, *130*, 1080.
(14) Rubinstein, I.; Bard, A. J. *J. Am. Chem. Soc.* **1980**, *102*, 6641.
(15) Chen, X.; He, P.; Faulkner, L. R. *J. Am. Chem. Soc.* **1983**, *105*, 685.
(16) Peerce, P. J.; Bard, A. J. *J. Electroanal. Chem. Interfacial Electrochem.* **1980**, *112*, 97.
(17) Krishnan, M.; Zhang, X.; Bard, A. J. *J. Am. Chem.* Soc. **1984**, *106*, 7371.
(18) Kwak, J., Ph.D. Dissertation, The University of Texas at Austin, Texas, 1989.
(19) Pickup, P. G.; Murray, R. W. *J. Am. Chem. Soc.* **1983**, *105*, 4510.
(20) Chidsey, C. E. D.; Murray, R. W. *Science* **1986**, *231*, 25.
(21) White, H. S.; Kittlesen, G. P.; Wrighton, M. S. *J. Am. Chem. Soc.* **1984**, *106*, 5375.
(22) Leddy, J.; Bard, A. J. *J. Electroanal. Chem. Interfacial Electrochem.* **1983**, *153*, 223.
(23) Lee, H. Y.; Adams, R. N. *Anal. Chem.* **1962**, *34*, 1587.
(24) White, H. S.; Abruna, H. D.; Bard, A. J. *J. Electrochem. Soc.* **1982**, *129*, 265.

RECEIVED for review March 26, 1990. Accepted June 18, 1990. The support of this research by NSF (CHE 8901450) and The Robert A. Welch Foundation is gratefully acknowledged.

Application of Information Theory to Electroanalytical Measurements Using a Multielement, Microelectrode Array

Robert S. Glass,* Sam P. Perone,[1] and Dino R. Ciarlo

Chemistry and Materials Science Department and Department of Electronics Engineering, Lawrence Livermore National Laboratory, Livermore, California 94550

Multielement microelectrode arrays have been developed for electrochemical sensors. The array sensors are fabricated on a single insulated silicon substrate (standard 2 in. wafer) using photolithographic methods. In the prototype devices, five different electrode materials have been included: Pt, Au, V, Ir, and carbon. One goal of this work was to quantitate the improvement in information content for voltammetric measurements with a matrix of different electrode materials relative to measurements made with a single electrode material. Additionally, we have developed fabrication methods for multielement microelectrode array detectors and evaluated their voltammetric characteristics. Ultimately, we are working toward the development of inexpensive and reproducible methods of producing these arrays so that they could be used in a disposable fashion. In order to accomplish our present goals, voltammetric data were obtained for a group of four explosive and four nonexplosive (but structurally similar) compounds in dimethyl sulfoxide using the microsensor array. The information content of these measurements was then evaluated by using the probabilistic model developed by Shannon. It was found that the information content was improved by using the multielement approach, with the average information content increasing by 25% relative to the case where a single platinum microelectrode array was used. Although their use thus far has been limited to laboratory applications, these disposable arrays could also be used in natural environments.

INTRODUCTION

A variety of chemical sensors are needed for use in environmental monitoring. Electrochemical sensors are very attractive for such applications because of their sensitivity, cost, size, and versatility. However, general selectivity has limited their development. Improvements in the performance of electrochemical sensors should be anticipated, however, through applications of chemically modified electrodes and through development and use of microelectrodes (especially when used in arrays).

When used in sensor devices, microelectrodes may offer new dimensions in experimental accessibility because they have the characteristics of (1) relative immunity from uncompensated resistance effects, (2) high rates of mass transfer and hence higher sensitivity, (3) high S/N ratio, (4) the possibility of extremely fast experiments, and (5) the extension of normal electrochemical background limits. Microelectrodes allow measurements to be made in unconventional environments without the intentional addition of supporting electrolyte (*1*). Particular electroanalytical advantages (i.e., improved signal-to-noise ratios) have been demonstrated when microelectrodes are used in arrays (*2–4*).

In our work we are attempting to combine the attractive features of microelectrode arrays with chemical modification of electrode surfaces to construct disposable electrochemical detectors which we can use in a variety of environments. The possibility of increasing the selectivity and sensitivity of electrochemical sensors through specific chemical modification of electrode surfaces has inspired an ever-widening area of research (for example, see ref 5–10). Advances clearly will be made as a result of greater insight into methods of creating electrochemical systems with tailored chemical and electrochemical properties, microstructures, etc.

Because we are trying to develop sensors capable of detection and identification of a variety of compounds, the required selectivity is often not attained by using a single type of detection element. This general problem has been addressed by Hirschfeld, Kowalski, and others (*11–13*) with regard to piezoelectric sensors, where a variety of coatings with different response factors have been applied in order to achieve overall improved selectivity through pattern recognition. Our approach is similar and involves the incorporation of a variety of electrode materials in an array of microelectrodes. Because each electrode material will display a somewhat different response to a given compound, information content is improved, leading to enhanced selectivity. Statistical methods that allow us to make appropriate choices of materials and measurement practice to maximize the information gain are clearly desirable, and this is the subject of the present communication. In the work reported here we will discuss the results of our studies obtained by using unmodified microelectrodes; studies using arrays containing both unmodified and chemically modified electrodes will be the subject of a future article.

A number of statistical approaches for the evaluation of chemical data and for the optimization of experimental protocols have been developed within the field of chemometrics, with application to a number of analytical methods (*14*). However, these methods have only infrequently been applied to electrochemistry (*15–17*). In the work described here, we have used the formalism of information theory, as introduced by Shannon (*18*), to quantify the information content of electroanalytical measurements and guide our selection of optimum sets of electrode materials. This theory is discussed in greater detail below.

For a given application, the choice of electrode materials will depend upon several electrochemical and materials considerations. In the work reported here we first evaluated the voltammetric properties of 10 different electrode materials [Ir, Pd, Ag, Cu, Au, Pt, V, AISI 304 stainless steel, C (graphite), and Ti] using electrodes of conventional size (about 0.1 cm^2 in area). From these measurements a set of five different materials was selected for incorporation into a microelectrode array device. Criteria for materials selection included voltammetric range, stability, varied response to compounds of interest, reproducibility, and ease of fabrication (using photolithography). From this study, the materials selected for

[1] Present address: Department of Chemistry, San Jose State University, San Jose, CA 95192.

0003-2700/90/0362-1914$02.50/0

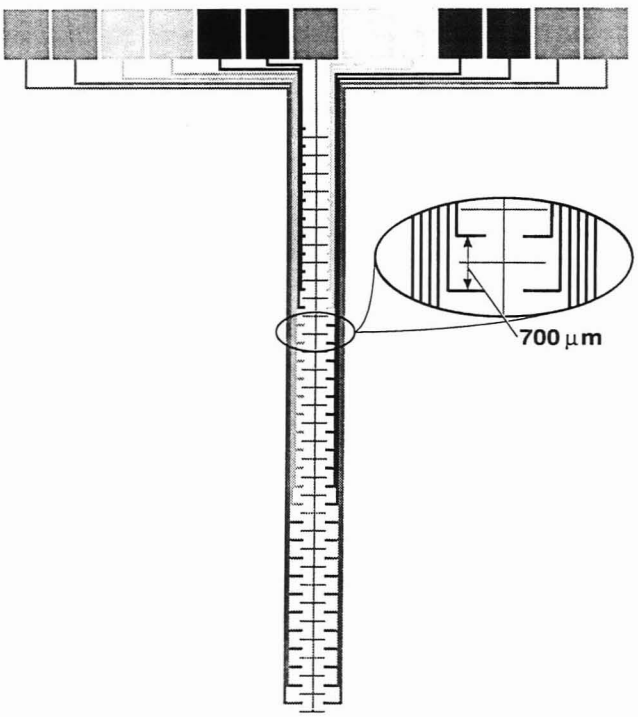

Figure 1. Diagram of microelectrode array. Insert shows spacings between working electrodes. Other details are provided in the text.

the prototype microelectrode array detectors were Pt, Au, V, Ir, and carbon.

By use of these array devices, cyclic voltammograms were obtained for a group of four high-explosive and four nonexplosive, structurally similar compounds. As discussed above, our goal was to ascertain whether a matrix of different electrode materials could improve the information content of electroanalytical measurements relative to measurements made with a single electrode material. Our efforts were directed toward obtaining a quantitative comparison and defining the most informative measurement strategy. It was found that we could indeed improve the information content of electroanalytical measurements in this specific case by using a matrix of measurements from the microelectrode array and that only a minimal set of measurements was required to achieve the informational goal. In a simple comparison, we found an enhancement of 25% in information content over a single electrode material (Pt) when an array of five different materials was used. The extension of this work to classification of unknowns using pattern recognition is underway.

EXPERIMENTAL SECTION

Microelectrode Array Fabrication. The microelectrode arrays used in this work were produced photolitographically, using a negative lift-off procedure. Because some of the features of multielement deposition are unique to this work, the details of our processing procedures are recounted here. The prototype array is shown in Figure 1. As mentioned above, the elements used in the array were Pt, Au, V, Ir, and carbon. A total of 66 microelectrodes were fabricated on each silicon substrate (standard 2-in. wafers of 12-mil thickness). In more recent work we have substituted a ceramic for the silicon substrate as it leads to greater durability. The individual materials are deposited sequentially in precise geometric registry. An outline of the overall procedure is given in Figure 2 and is described below:

(1) In all cases, we start with standard 2 in. diameter silicon wafers, (100) orientation, which are 12 mils in thickness.

(2) In the first step, in order to create a highly insulating substrate, a 1500-Å layer of silicon nitride is deposited onto the wafer using low-pressure chemical vapor deposition. This layer is then subjected to a plasma etch in oxygen at 300 W for 20 min, and then the chip is allowed to cool.

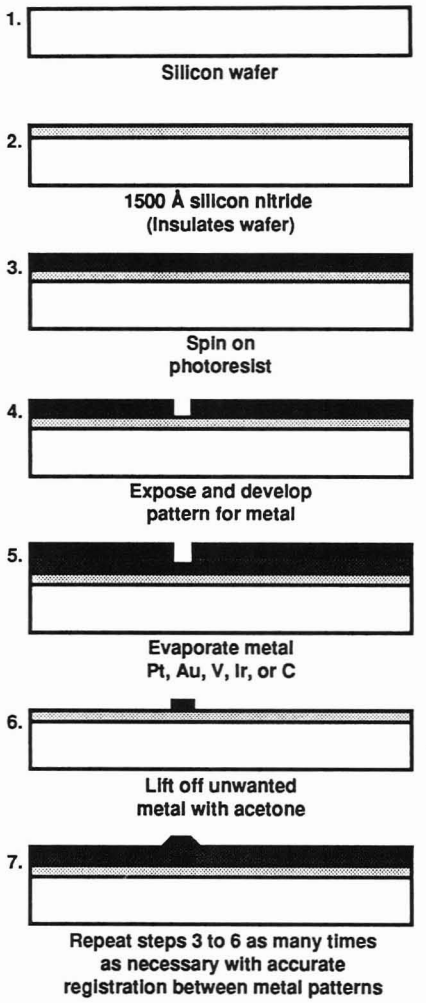

Figure 2. Photolithographic fabrication sequence for multielement microelectrode arrays.

(3) A layer of photoresist (AZ 1350J) is spun onto the wafer at 4000 rpm. This takes approximately 25 s and results in a layer 1.25 μm in thickness. The photoresist layer is then subjected to a soft bake at 85 °C for 25 min and then allowed to cool.

(4) The patterns for subsequent metal deposition are then generated. This is accomplished by first overlaying masks on the wafer and then exposing the wafer to UV irradiation (405 nm) using a power density of 148 mJ/cm^2. There are then five steps preceding metal deposition. These are (i) soak in chlorobenzene for 5 min at room temperature, then blow dry, (ii) spray develop for 1–1.5 min at 300 rpm to dissolve the photoresist that has been exposed to UV, (iii) spray rinse with deionized water at 500 rpm for 30 s to remove the developer, (iv) spin dry the wafer at 3000 rpm for 30 s, and, finally, (f) plasma etch the wafer at 100 W power in N_2 for 5 min, followed by treatment in O_2 for 3 min.

(5) A thin layer of niobium (100 Å) is deposited in order to increase adhesion of the sensor materials. The first sensor material is then deposited by electron-beam evaporation. In each case, the thickness of material was 0.1 μm.

(6) Unwanted metal is lifted off the wafer with acetone (which actually removes the photoresist underlying the unwanted metal).

(7) Steps 3–6 are now repeated in order to sequentially deposit the rest of the sensor materials (for total of five) with accurate registry between the metal patterns.

In a final step (not shown) once all the microelectrode arrays have been deposited, a layer of SiO_2 is then deposited through a mask so that all lead lines are masked and the exact microelectrode areas to be exposed to solution are defined. Besides SiO_2, other masking agents are also possible. Following the photolithographic fabrication procedure, the array is rinsed with deionized water, then acetone, and finally absolute ethanol and then allowed to dry prior to use.

The arrays shown in Figure 1 can be used in either a three- or two-electrode configuration. The essential feature of the arrays

Table I. Compounds Used in the Study

Set 1
2-methyl-1,3,5-trinitrobenzene (TNT)
octahydro-1,3,5,7-tetranitro-1,3,5,7-tetrazocine (HMX)
hexahydro-1,3,5-trinitro-1,3,5-triazine (RDX)
2,2-bis[(nitrooxy)methyl]-1,3-propanediol dinitrate (PETN)
Set 2
4-nitro-*o*-phenylenediamine
2,4-dinitrophenol
p-nitroaniline
2-nitroresorcinol

are the 66 working electrodes and the platinum auxiliary electrode which runs down the center and is interdigitated with the individual working electrodes. One way of using the center platinum electrode as a reference electrode would be to modify the surface with a redox polymer which has the capacity for the generation of a known distribution of redox states. This work is currently underway in our laboratory. Operation in the Pt quasi-reference mode is also possible.

Electrical contact to the microelectrodes is made on the pads at the top of the chip. A specially designed holder and connector pin fixture was used in our experiments. There are two pads shown for each electrode material. From left to right in Figure 1 the electrode materials are Pt (pads 1 and 2), carbon (pads 3 and 4), V (pads 5 and 6), Pt auxiliary (pad 7), Au (pads 8 and 9), Ir (pads 10 and 11), and Pt (pads 12 and 13). For each material one contact pad leads to a single microelectrode and the other leads to an array of ten electrically connected together. The individual working electrodes are configured as "tick marks" extending from the electrical lead lines from the contact pads. The width of the working electrodes is 5 μm, while that of the center platinum auxiliary electrode is 10 μm. After the microelectrodes are defined by masking with SiO_2, each individual microelectrode has an area exposed to solution of 104.5 μm^2. In each case, the SiO_2 masking procedure exposes only the last 20 μm of each microelectrode. This detail is shown in the insert to Figure 1. The vertical separation between the working electrodes is 700 μm. The interdigitated arms of the auxiliary electrode are placed centrally between the working electrodes.

Materials. The compounds used in this study are listed in Table I. Where commercially available, all chemicals used were of analytical reagent quality. The explosive compounds, TNT, RDX, HMX, and PETN were of commercial quality (approximately 98% purity). The solvent used was dimethyl sulfoxide (DMSO), with 0.1 M tetra-*n*-butylammonium tetrafluoroborate ($TBABF_4$) added as supporting electrolyte. Solutions were made 2.5 mM in each compound studied. The solutions were purged with argon prior to running a cyclic voltammogram. In addition, activated alumina was added just prior to each experiment to absorb as much residual water from solution as possible.

Safety. Although the high-explosive materials used here are definitely hazardous in large quantities (exceeding ca. 1 g), the dilute DMSO solutions used for chemical studies can be handled safely without concern for detonation. However, solid or concentrated samples should only be handled by authorized and trained personnel within qualified facilities. In our facility (LLNL), an authorized handler must pass an appropriate training course, and detailed laboratory operating procedures must be described and approved in advance. The normal precautions when handling DMSO, which can carry deleterious chemicals into the bloodstream, should be observed.

Procedures. In the work reported here we used a three-electrode configuration with the center Pt electrode as a counter electrode and a separate saturated calomel reference electrode. The reference electrode was used in conjunction with a salt bridge (containing 0.1 M $TBABF_4$ in DMSO) to make contact to the solution. All measurements were made by using the array of 10 microelectrodes for each material as the "working electrode". The arrays were accessed sequentially.

The cyclic voltammograms were obtained with the aid of a Princeton Applied Research Model 273 potentiostat/galvanostat which was interfaced to an IBM personal computer (AT). The software used to perform the cyclic voltammetric experiments were purchased from Covalent Associates (Woburn, MA). The scan rate in each case was 20 mV/s with the initial scan direction cathodic.

THEORY AND DATA ANALYSIS

Information content of our data was evaluated by using the formalism of information theory developed by Shannon for probabilistic models of communication (*18*, *19*). Simply stated, this theory says that the most information is provided by the event least likely to occur spontaneously. This principle is formalized by the concept of entropy which expresses increased information in terms of decreased uncertainty. The quantitative expression for the average information content is given as

$$H = -\sum_{i=1}^{N} p_i \log_2 (p_i) \qquad (1)$$

In this equation H is the entropy (or average information), N is the number of events (see below), and $p_i \ldots p_n$ are the probabilities of occurrence for each event in the system under consideration. Therefore, the average information is equal to a weighted average of the specific information, given as $-(\log_2 p_i)$, for each event in the system under consideration. When quantified by using this expression, information content is expressed in terms of "bits".

Strictly speaking, Shannon's formula is applicable only to random experiments, and does not mesh well with conventional electrochemical procedures. However, it is useful to use Shannon's concept of weighted averages of event probabilities to quantitate information content. Thus, we have attempted to construct electrochemical data arrays in a format that allows direct application of Shannon's formula. Although these arrays still do not fit all the boundary conditions assumed for a communications environment (Shannon's working domain), the computed values are at least useful for relative comparisons of information content in a chemical measurement domain, based on Shannon's definitions.

In order to apply Shannon's information theory concepts to electroanalytical data, cyclic voltammograms were run to establish the redox behavior of the subject group of compounds. Then, in order to simplify the analysis, tables were prepared which correspond to binary event markers which equate the measurement at a given potential of current exceeding background as the occurrence of an "event", whereas observance of no excess current is equated to the absence of an event. These states can be represented as "1's" and "0's", respectively, for each potential considered in the analysis. Thus, the occurrence of a "0" in the data array would correspond to an observation of only capacitative or impurity currents at a given potential. The occurrence of a "1" would correspond to the observation of currents exceeding the detection limit (+3 standard deviation units) at a given potential. (Refer to Tables II and III for typical data arrays.) Only reductions were considered in the analysis of data shown here, although oxidations could also have been considered.

It is important to note that the values obtained for the information content have strict validity only to the particular set of experimental conditions used—solution purities, electrode surface preparation (we used the microelectrode arrays essentially as received, polishing the surfaces was not possible), extent of deaeration and removal of moisture, etc. To determine whether or not faradaic current was observed at a given potential for a given compound, the voltammogram for the background (supporting electrolyte only) was subtracted from the voltammogram for each compound. Faradaic current levels exceeding background and clear inflection points corresponding to the reduction potential for a faradaic process were considered confirmatory. It is to be noted that in the results reported here, no serious attempts were made to op-

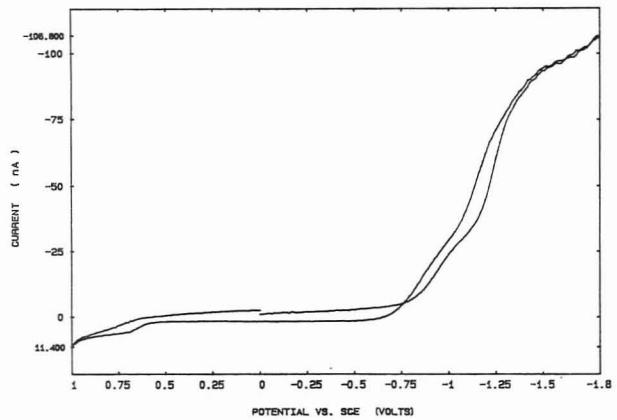

Figure 3. Cyclic voltammogram for RDX (2.5 mM) at the Au microelectrode array segment. A scan rate of 20 mV/s was used.

timize the experimental method (e.g., potential scan rate) or to account for the differences in reversibility of reductions for the various compounds (which influence curve shape).

RESULTS AND DISCUSSION

The group of chemical compounds used for this study was composed of two sets, listed in Table I. The first set consisted of explosives, while the second set included structurally similar nonexplosives.

Although electrodes of "conventional" size could have been used to obtain the electrochemical data for this particular study, microelectrode arrays were used because we wanted to demonstrate the feasibility of fabricating disposable detectors for compact sensor packages and because microelectrodes can yield data in a form convenient for the type of analysis we desired for this particular study. Depending upon electrode spacing and scan rates, sigmoidal curve shapes can be obtained with arrays of microelectrodes. In the work reported here, using arrays of 10 microelectrodes with each electrode having dimensions of 0.1 μm in height, 5 μm in width, and 20 μm in length (area 104.5 μm^2), and with electrode spacings of 700 μm, and using scan rates of 20 mV/s, quasi-steady-state shape of the voltammograms were generally obtained for the compounds listed in Table I. Similar quasi-steady-state behavior is predicted and has been observed for "microband" electrodes (*20*, *21*); although the electrodes used in this study cannot accurately be termed "microband" because of their relatively short length. An example of the response obtained is shown in Figure 3, which displays the cyclic voltammogram for RDX on the Au microelectrode segment.

As mentioned above, the experimental procedure can influence results. In our work, we took the as-received arrays and rinsed them with deionized water and acetone and then allowed them to dry in air before running repetitive voltammograms. Data were collected when an apparent steady-state surface condition had been achieved. As is well-known, electrode surface preparation can affect electrochemical results. If it were possible to polish the surfaces of the microelectrode arrays used in this work, such as vanadium (which forms oxides) or carbon (with surface functional groups) prior to making measurements, somewhat different results may have been obtained. However, since one long-term goal is to develop mass-produced disposable sensors for use under various conditions, including field work, our intention is to use the photolithographically produced arrays essentially as-received. The procedures used here are consistent with that goal.

In many situations there will be an optimum common potential at which to poise the different microelectrode materials for maximum information content. For the particular experiments reported here, it was found that the average information content was essentially the same for the array of materials at −1.0, −1.1, and −1.2 V. At potentials both lower and higher than this, the information content decreased. This is an expected result if one considers the basic tenant of information theory: "The more likely an event is to occur, the less information it conveys". Therefore, the more negative the potential, reduction becomes more likely to occur. Similarly, at the other end (less negative potentials), reduction becomes less likely. In either case, the information content is less.

Table II. Tabulation of Results Obtained by Using a Single Material (Pt) Microelectrode Array

	current at Pt microelectrode array				
	−0.2 V[a]	−0.5 V	−0.8 V	−1.0 V	−1.2 V
compound					
2,4-dinitrophenol	0	1	1	1	1
2-nitroresorcinol	0	0	1	1	1
4-nitro-*o*-phenylene-diamine	0	0	0	0	0
p-nitroaniline	0	0	0	0	0
TNT	0	0	1	1	1
HMX	0	0	0	0	0
PETN	0	0	0	0	1
RDX	0	0	0	0	1
P_i	0	0.12	0.38	0.38	0.62

[a] Potential, volts vs SCE.

The guidelines followed for obtaining voltammetric data arrays for information theory analysis have a significant impact on the information content calculations. It is important to point out that the data collection procedures and guidelines for construction of the data arrays were arbitrary. Alternative criteria lead to different numerical values for information content but do not significantly affect relative values for different systems, as long as the criteria are uniformly applied.

The guidelines applied here for constructing a data array for information theory analysis were as follows: (1) examine voltammetric currents at 0.1-V intervals; (2) select data from up to five information channels (e.g., current at five different potentials for a single electrode or current at one potential for five different electrode materials); (3) platinum was selected as the electrode material for multiple potential sampling; Pt, Au, C, Ir, and V were selected as the electrode materials for the single-potential sampling; (4) select data channels with the least probability of ambiguity regarding the detection of the presence or absence of the compounds of interest; (5) select channels providing the least redundant information (i.e., with greatest variety of response patterns).

Therefore, even though full cyclic voltammograms were run on all the compounds, for the purpose of demonstration we evaluated the information content using a single electrode potential (−1.2 V) for the array of five materials; for the platinum microelectrode array five different potentials were used (−0.2, −0.5, −0.8, −1.0, and −1.2 V). This analysis mimics the simplest electrochemical sensor design, a potentiostatic experiment. In the situation considered here, the same number of measurements were evaluated in each case and the information content can be directly compared. The data collected are summarized in Tables II and III. The probabilities of event occurrence are tabulated for each potential (when platinum alone is considered, Table II) or for each electrode material (Table III). Then, the average information content is evaluated by using Shannon's formula (eq 1), where the sum runs over N, the columns in Tables II or III.

For our experimental parameters, it was found that the average information content of our measurements using the single microelectrode material (Pt) and five different analysis potentials was 1.86 bits, while the average information content

Table III. Tabulation of Results Obtained Using Multimaterial Microelectrode Arrays

	current at −1.2 V vs SCE at various microelectrode arrays				
	Pt	Au	C	Ir	V
compound					
2,4-dinitrophenol	1	1	1	1	1
2-nitroresorcinol	1	1	1	1	0
4-nitro-*o*-phenylene-diamine	0	0	0	0	0
p-nitroaniline	0	0	0	0	0
TNT	1	1	1	1	0
HMX	0	0	0	0	0
PETN	0	1	0	1	0
RDX	1	1	0	0	0
P_i	0.50	0.62	0.38	0.50	0.12

using the full matrix detector with five different microelectrode materials and a single analysis potential (−1.2 V) was 2.32 bits. This simple analysis provides a quantitative figure of merit which clearly indicates enhanced information content using the multielement microelectrode array approach (by 25% in this case).

Closer examination of the data arrays in Tables II and III leads to some insight regarding differing information content. It is clear in Table II that there is inherent redundancy built in to each data row. This redundancy is related to the fact that faradaic currents observed at a lower potential are also observed at higher potentials. This inherent redundancy accounts for the diminished information content of Table II compared to Table III. The data array in Table III, because of different responses of different electrode materials to the same compounds, minimizes the redundancy in data rows.

Following this analysis, it is clear that Table II also includes some redundant information in column data for potentials −0.8 and −1.0 V. The patterns are identical, suggesting that one should be removed from the information content computation, as no real increase is obtained by including the redundant channel. When this elimination is done, the average information content is recalculated as 1.33 bits. If one channel (vanadium data) in the data array of Table III is likewise eliminated for a direct comparison of information content with only four measurements in each array, a value of 1.96 bits is obtained. Again, the comparison of information content between single-electrode and multielectrode measurements indicates a significant improvement with the multielectrode array (47% in this case).

These data analyses do not directly provide identification of analytes. However, the purpose of this study was to provide a quantitative comparison of information content for two different measurement approaches. The results of this study will allow us to fabricate microsensor devices with the most promising sensor materials and measurement strategy for achieving the ultimate goal of selective detection of various target analytes. These further studies will not be limited by the arbitrary data collection criteria applied here and will utilize pattern recognition for analyte identification. Thus we feel confident that the required information content will be obtained.

CONCLUSIONS

We have shown that the use of a variety of electrode materials in electrochemical microsensors can enhance the information content of voltammetric measurements, relative to a single electrode material, with the same number of measurements being made in each case. A quantitative figure of merit for the enhancement of information content was obtained by using Shannon's probabalistic model. Applied in this manner, information theory can be useful in providing experimental guidance as to how to optimize sensor design and experimental protocol. We have also shown that multielement microelectrode array sensors can be fabricated by using conventional photolithographic methods, which has potential applicability to the use of low-cost, disposable, mass-produced sensor arrays. These arrays can provide data in a form which is convenient for nonexpert analysis. Further work in our laboratory includes applying pattern recognition methods, such as artificial neural networks, to the analysis of full voltammetric curves obtained by using microsensor arrays for compound classification/identification.

ACKNOWLEDGMENT

The authors wish to thank Kenneth E. Vindelov for assistance in the fabrication of the array sensors, Jackson E. Harrar and David O. Jones for several useful discussions, and Cheryl L. Ham and Rebecca Hoff for assistance in the early stages of the experimental work.

LITERATURE CITED

(1) Bond, A. M.; Fleischmann, M.; Robinson, J. *J. Electroanal. Chem. Interfacial Electrochem.* **1984**, *168*, 299–312.
(2) Reller, H.; Kirowa-Eisner, E.; Gileadi, E. *J. Electroanal. Chem. Interfacial Electrochem.* **1984**, *161*, 247–268.
(3) Penner, R. M.; Martin, C. R. *Anal. Chem.* **1987**, *59*, 2625–2630.
(4) Weber, S. G. *Anal. Chem.* **1989**, *61*, 295–302.
(5) Ikariyama, Y.; Heineman, W. *Anal. Chem.* **1986**, *58*, 1803–1806.
(6) Patriarche, G. J. *J. Pharm. Biomed. Anal.* **1986**, *4*, 789–797.
(7) Wrighton, M. S.; Thackeray, J. W.; Natan, M. J.; Smith, D. K.; Lane, G. A.; Balanger, D. *Philos. Trans. R. Soc. London B* **1987**, *316*, 13–30.
(8) Ye, J.; Baldwin, R. P. *Anal. Chem.* **1988**, *60*, 1982–1984.
(9) Imisides, M. D.; Wallace, G. G.; Wilke, E. A. *TrAC, Trends Anal. Chem.* **1988**, *7*, 143–148.
(10) Whiteley, L. D.; Martin, C. R. *Mol. Cryst. Liq. Cryst.* **1988**, *160*, 359–376.
(11) Carey, W. P.; Beebe, K. R.; Kowalski, B. R.; Illman, D. L.; Hirschfield, T. *Anal. Chem.* **1986**, *58*, 149–153.
(12) Ballantine, D. S.; Rose, S. L.; Grate, J. W.; Wohltjen, H. *Anal. Chem.* **1986**, *58*, 3058–3066.
(13) Rose-Pehrsson, S. L.; Grate, J. W.; Ballantine, D. S., Jr.; Jurs, P. C. *Anal. Chem.* **1988**, *60*, 2801–2811.
(14) Brown, S. D.; Barker, T. Q.; Larivee, R. J.; Monfre, S. L.; Wilk, H. R. *Anal. Chem.* **1988**, *60*, 252R–273R.
(15) Stetter, J. R.; Jurs, P. C.; Rose, S. L. *Anal. Chem.* **1988**, *58*, 860–866.
(16) Byers, W. A.; Freiser, B. S.; Perone, S. P. *Anal. Chem.* **1983**, *55*, 620–625.
(17) Byers, W. A.; Perone, S. P. *Anal. Chem.* **1983**, *55*, 615–620.
(18) Shannon, C. E. *Bell Syst. Tech. J.* **1949**, 27, 379, and 623.
(19) Young, J. F. *Information Theory*; Butterworth: London, 1971.
(20) Aoki, K.; Tokuda, K. *J. Electroanal. Chem. Interfacial Electrochem.* **1987**, *237*, 163–170.
(21) Morris, R. B.; Franta, D. J.; White, H. S. *J. Phys. Chem.* **1987**, *91*, 3559–3564.

RECEIVED for review February 7, 1990. Accepted May 23, 1990. Work performed under the auspices of the U.S. Department of Energy by the Lawrence Livermore National Laboratory under Contract No. W-7405-ENG-48.

Optode for Bulk-Response Membranes

Peter C. Hauser, Philippe M. J. Périsset, Susie S. S. Tan, and Wilhelm Simon*

Department of Organic Chemistry, Swiss Federal Institute of Technology (ETH), Universitätstrasse 16, 8092 Zurich, Switzerland

A simple optical sensor based on photodiodes with built-in optical filters is described. The sensor is used with a new class of optode membranes recently introduced. These rely on ion extraction into the bulk of a polymeric membrane and therefore can yield relatively large absorbance changes that can be measured easily. Ambient light, whose intensity is monitored by a reference photodiode, is used as the light source. The membrane is placed directly on top of a second photodiode making the entire device very compact. The performance of the sensor with regard to fluctuations in the irradiation and the determination of nitrate in vegetable extracts, as an example, is described.

INTRODUCTION

A multitude of chemical sensors for liquid and gaseous samples with optical signal transduction has been reported very recently (*1–21*). For most of these sensors essentially a monolayer of reagent has been immobilized by covalent attachment (*1–3*), entrapment in a Langmuir–Blodgett film (*4–7*) or simple adsorption (*8–15*). The optical changes are therefore relatively weak and sensitive detection techniques have to be employed. Fluorescence measurements are very often used (*1, 2, 4–6, 8, 12–17*) and the light is commonly brought to the membrane by an optical fiber and returned to a spectrometer by the same way. If optical absorption is employed, multipath techniques such as attenuated total reflection (ATR) implemented on specially designed waveguides or optical fibers are usually needed (*7, 18, 19*). Immobilization can also be done on small beads to obtain a large surface area to be probed by one beam (*9–11*). Simple one-path absorbance measurements have been sufficiently sensitive in exceptional cases only (*3, 20, 21*).

A different class of membranes with optical signal transduction has been introduced recently. These membranes rely on the specific extraction of ions into the bulk of a thin lipophilic film, along solvent extraction principles, rather than reactions on the surface alone (*16, 22–26*). The measurable absorbance changes are therefore quite pronounced and the sensitive detection schemes mentioned above are not needed. It has been possible to evaluate these membranes by single path absorbance measurements in a conventional spectrophotometer (*23–26*). Specially designed flow-through cells onto whose windows the membranes were cast were used for these measurements (*25*). For the construction of an actual sensor, however, a relatively simple device should be adequate.

Optodes with single path absorbance measurements using light-emitting diode/photodiode pairs have been reported (*3, 20, 21*). Light-emitting diodes impart a degree of spectral selectivity because of their relatively narrow spectral bandwidth. However, ambient light interference is a problem with these devices, which had to be overcome, either by shielding the entire device (*3, 21*) or by modulating the light source (*20*), which requires the use of a relatively elaborate setup.

A device that is based on simple wavelength-selective detectors, solid-state silicon photodiodes with mounted optical filters, is reported here. The filters can be dye filters if a relatively wide spectral band-pass is sufficient, otherwise, interference filters are needed. Ambient light is made use of and a reference diode is employed to monitor fluctuations in the irradiation. The reference can be omitted if the ambient light is controlled as has been reported by the authors in a rapid communication (*27*). These optodes can be very compact, since no emission source is used and no shielding of the assembly or no modulation of the light source with consecutive lock-in amplification is necessary. The built-in reference element should also allow for an inherent compensation for color and turbidity of samples.

As an example of membranes that can be used, two types of anion responsive systems reported previously (*26*) were tested out in combination with the ion-selective photodiode (ISPD). These membranes rely on the coextraction of proton/anion pairs into a membrane. Selectivity is derived from the lipophilicity of the anions (Hofmeister series) and the optical transduction from the reversible protonation respectively deprotonation of a pH indicator.

Hofmeister optode systems of type I contain a lipophilized pH indicator (IND_{mem}), that is electrically neutral in its unprotonated form

$$IND_{mem} + H^+_{aq} + X^-_{aq} \rightleftharpoons INDH^+_{mem} + X^-_{mem} \quad (1)$$

Systems of type II contain a quaternary ammonium ion (R^+_{mem}) and a pH indicator (IND^-_{mem}) that is negatively charged in its unprotonated form

$$IND^-_{mem} + R^+_{mem} + H^+_{aq} + X^-_{aq} \rightleftharpoons INDH_{mem} + R^+_{mem} + X^-_{mem} \quad (2)$$

The degree of protonation of the pH indicator is dependent on the anion concentration in both cases. Determination of these concentrations can be carried out by buffering the samples at an adequate pH (*26*).

The performance of the ISPD with regard to ambient light fluctuation and in real sample measurements is reported here. Ion chromatographic and potentiometric measurements were carried out for comparison.

EXPERIMENTAL SECTION

Electronic Circuitry for the ISPD. A data acquisition system designed in-house for potentiometric measurements was adapted. The system consists of an analog multiplexer with front-end impedance conversion, a digital multimeter (Model 7150, Solartron Schlumberger Instruments, Farnborough, UK), and an Apple IIe personal computer (Apple Corp., Cupertino, CA) with a dot matrix printer (Model RX 80, Epson Corp., Nagano, Japan) and a plotter (Color Pro, Hewlett-Packard, San Diego, CA). Photodiodes were from Hamamatsu (Models S2684-560 and S2684-650, Hamamatsu Photonics Deutschland GmbH, Herrsching, Federal Republic of Germany) and Sharp (Model BS-500B; supplier, Omni Ray AG, Zurich, Switzerland). The photodiodes are biased with 5 V and their photocurrent is transformed into voltage by operational amplifiers (LF 356) in the current follower configuration. It was found that the sensitivity of photodiode pairs in some cases deviates slightly, so that it was necessary to compensate for this, as well as the tolerances of resistors, by adjusting the feedback resistors of the current followers. The output from these amplifiers is fed to the input of the data acquisition station. A program written in UCSD Pascal 1.3 was employed that samples both measuring and reference

0003-2700/90/0362-1919$02.50/0

channels alternatively (40 ms conversion time) 10 times to form averaged data points for the two channels as well as the ratio and its standard deviation. This conversion is carried out at predetermined intervals over a desired period of time and the result is graphically displayed on screen or plotted on paper.

Ion Chromatography and Potentiometry. A Dionex System 2000i/SP ion chromatograph equipped with a HPIC-AS4A column, a AG4A precolumn, a MicroMembrane suppressor, and a conductivity detector was employed (Dionex Corp., Sunnyvale, CA). The eluent was a solution of 0.375 M in $NaHCO_3$ and 1.0 M in Na_2CO_3, the flow rate was 2 cm^3/min, and the sample loop size was 50 μL. Ion-selective electrode measurements were carried out by direct potentiometry using a PVC-membrane electrode with methyltri-*n*-dodecylammonium chloride (Polysciences, Inc., Warrington, PA) as the anion exchanger (*28*) and a double junction reference electrode with lithium acetate solution (1 M) as bridging electrolyte.

Optode Membranes. The membrane mixtures were based on either lipophilized Nile Blue (ETH 5294 (*25*), 6 mg) alone (type I) or lipophilized Azo Violet (ETH 2412 (*26*), 6 mg) together with methyltri-*n*-dodecylammonium chloride (14.4 mg) as the active constituents (type II) and 160 mg of *o*-nitrophenyl octyl ether (Fluka AG, Buchs, Switzerland) as plasticizer and 80 mg of a vinyl chloride–vinyl alcohol copolymer (*29*). For the transmittance measurements with a conventional spectrophotometer these components were dissolved in 1.5 cm^3 of distilled tetrahydrofuran (Fluka AG) and cast onto the windows of a flow-through cell as described previously (*25, 26*). For use with the ISPD, the components were dissolved in about 10 cm^3 of tetrahydrofuran. A drop of this mixture was applied with a micropipet onto the glass carrier plate above the measuring diode to yield a membrane of an estimated thickness of about 5 to 10 μm after evaporation of the solvent.

Procedures. All standard solutions were made up from KNO_3 and were buffered in pH. The solutions for the acquisition of the transmittance spectra of the lipophilized pH indicators contained 0.1 M of KNO_3 and a universal buffer mixture at a 200-fold dilution. These solutions were adjusted to pH 2 and 12 with concentrated sulfuric acid and sodium hydroxide solutions, respectively. The stock of the universal buffer mixture consisted of 10 mM NaH_2PO_4, 6.6 mM citric acid, and 2.5 mM $Na_2B_4O_7$ (*30*). The transmittance spectra were acquired with a UV–vis spectrophotometer (UVIKON Model 810, Kontron AG, Zurich) as described previously (*26*). The nitrate standards for the ISPD measurements with the membrane of type I also contained the universal buffer mixture at a 200-fold dilution and were adjusted to pH 5.0. The nitrate standards for the ISPD system of type II contained Tris (tris(hydroxymethyl)aminomethane) at a concentration of 0.01 M and were adjusted to a pH of 7.5.

Vegetable extracts were obtained by mashing 20 g of plant material with 100 cm^3 of deionized water for 1 min in an electrical blender. The juices were then centrifuged, filtered, and divided into two parts. Half was diluted 1:1 (except samples 1, 3, and 6, which were diluted 1:9) with deionized water and used for the determination by ion chromatography. The other part was mixed 1:1 with a buffer solution. This buffer was 0.02 M in $Al_2(SO_4)_3$ (Fluka, p.A.) (to complex lipophilic organic ions (*31*)) and 0.02 M in acetic acid and adjusted to pH 3.9 with a concentrated sodium hydroxide solution. The samples were thus buffered at a pH of 4.0 after mixing. This pH was chosen to eliminate interference from bicarbonate (*31*). The samples with added buffer were used for both the ISPD and ISE measurements. Standards for these measurements were obtained from KNO_3 and in the case of the ISPD and ISE determinations were also mixed with the same buffer solution. All reagents were of analytical grade, and doubly quartz distilled water was used.

RESULTS AND DISCUSSION

Construction. The configuration of the ion-selective photodiode (ISPD) assembly is shown in Figure 1. A pair of photodiodes with built-in optical filters is mounted underneath a glass carrier. The optically ion-sensing membrane is placed on top of one of the diodes while the other serves as the reference. The sample solution is contained in a small cup formed by the thin glass plate and a plastic ring. The

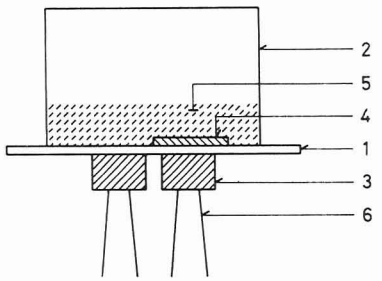

Figure 1. Schematic construction of the current ISPD: 1, thin glass carrier plate; 2, glass or plastic ring (diameter 35 mm, height 30 mm); 3, photodiodes with built-in optical filter; 4, bulk-response optode membrane; 5, sample solution; 6, connecting leads.

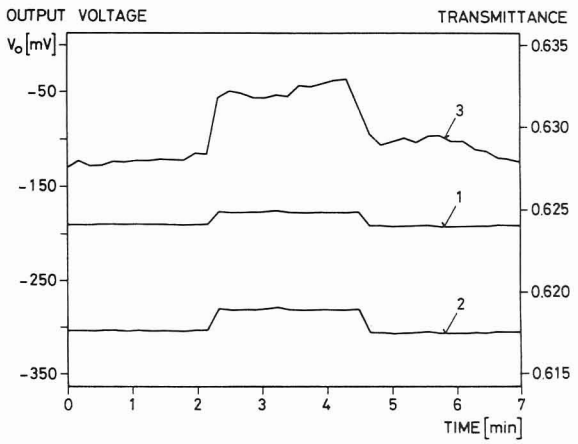

Figure 2. Output of the ISPD with a membrane at equilibrium: 1, measuring channel; 2, reference channel; 3, ratio or transmittance (T). The dip in intensity was caused by turning a lamp in the vicinity of the ISPD off and then on again.

output current (i) of the photodiodes, which is proportional to the light intensity (I) is fed individually to operational amplifiers in the current follower mode. Since the software routine of the data acquisition system forms the ratio of the two output voltages (V_o) of these amplifiers, a value proportional to the ratio of the light intensities (I/I_o) is obtained. This parameter corresponds to transmittance (T). The complete setup therefore resembles a conventional double beam spectrophotometer, except that only one sample container is needed rather then two cuvettes.

Response of the Detector to Changing Irradiation. The device, without an ion-selective membrane and the ring to contain a sample solution, was located in a typical laboratory with fluorescent tubes mounted at regular intervals on the ceiling. The influence of different light intensities and spatial distribution was studied with the help of a 60-W light bulb. A typical response to this additional light source is illustrated in Figure 2. The intensities measured for both channels and the resulting ratios are plotted. Note that the measured voltages (V_o) are negative. The drop of intensity between about the second and fifth minute was caused by turning the lamp in the vicinity off and then on again. The smaller fluctuations in V_o just recognizable on the scale of the plot can partly be traced to such reasons as movements of people in the room. As can be seen, the resulting ratio is also not perfectly constant. Noise with an amplitude of up to 0.002 in transmittance originates from the random fluctuations. This level was found to be very typical under ordinary laboratory conditions. A larger error of about 0.005 originates from the change in light intensity caused by the lamp. This points to an imperfect correction for changes in the irradiation which were thought to be due to two different causes. Firstly, a geometric error was expected, because the two diodes are not infinitely small. This causes slightly different distances and

angles to the light sources with corresponding differences in the irradiation. Secondly, slight nonlinearities in the response function of the two diodes will also lead to such an error.

To further investigate the behavior of the detector, the response to the 60-W lamp as additional light source mounted at different angles and distances was evaluated. This was carried out for both types of diodes used, the blue-sensitive diodes with built-in dye filter and the narrow bandwidth diodes with interference filter. It was found that the latter diodes were very sensitive to the direction of the light source. The lamp at 1 m distance caused an increase in measured light intensity of 123, 55, 5, and 1.4% for angles of impingement of 90, 60, 45, and 30°, respectively (diodes of type S2684-650). For the blue-sensitive diodes in contrast, the measured values were 23, 22, 19, and 16%, respectively. At a distance of 50 cm the values were 375, 177, 20, and 1.7% and 53, 48, 45, and 46% for the two types of diodes. The deviations in transmittance for the diodes with interference filter caused by turning the lamp on were found to be 0.009, 0.015, 0.013, and 0.001 for a distance of 1 m and angles of 90, 60, 45, and 30°, respectively. The corresponding values for the blue-sensitive diodes were 0.003, 0.009, and 0.009, and 0.005. Thus there appears to be some dependence on whether the light was impinging vertically or in an angle (relative to the vertical) and the light intensity itself. A similar but more pronounced pattern was found when the lamp was mounted at distances of 50 cm. The corresponding values were found to be 0.009, 0.04, 0.02, and 0.003 and 0.013, 0.005, 0.023, and 0.017 for the two diodes. All these values could be reproduced to better than 0.001. Interestingly, the values were similar regardless whether the light source was mounted to the front or the side of the two diodes. It was expected that the error would be more significant if the light was coming from the extension of the axis connecting the two diodes rather than if it was facing the two diodes evenly. No such pattern could be found. This indicates that most likely imperfections in mounting and possibly manufacturing tolerances in the geometry of the diodes themselves must cause slightly different spatial sensitivities.

No additional adverse effect was detected when the ring designated to hold the sample solution was mounted, unless when the angle from the light source was such that one diode was shaded but not the other.

The performance of the circuitry alone was tested by placing optical filters of different absorbances directly on top of the two photodiodes. No membrane was in place for this experiment. In this way the light intensity on both diodes was reduced stepwise and equally to about 40% of the original level. The transmittance values obtained in such a way were constant to within about 0.002 of unity. When an opaque piece of paper instead of an actual membrane was placed on the measuring diode, an error of up to 0.008 transmittance unit was found when the incident light intensities were reduced stepwise to the 40% on both channels. The reason for the difference in error must be a slight nonlinearity in the photodiode response, which however should be almost identical for the two channels. A similar performance was obtained with all types of photodiodes tested.

From these findings it follows, that the fluctuations in the measured ratio, as exemplified in Figure 2, must be caused by a combination of at least two factors, spatial sensitivity and nonlinearity of the response function. Often such light changes are of a temporary nature, so that an improvement can be made by averaging readings over a period of time. When the sensor is subject to normal conditions only, such as movements in the laboratory, the standard deviation of 10 transmittance values obtained in 10-s intervals were found to be about 0.0003 typically. The program always automatically returns the standard deviation of the measured transmittance values, so that any measurements showing excessive noise, due to unusual circumstances, can be rejected.

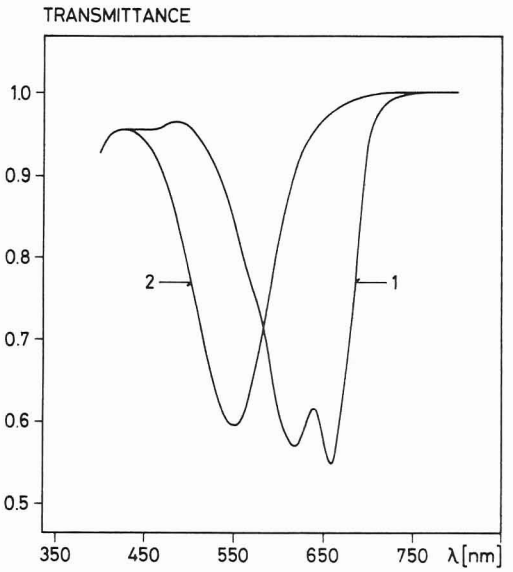

Figure 3. Transmittance spectra of lipophilized Nile Blue (ETH 5294) in a membrane of type I: 1, protonated (0.1 M KNO_3, pH 2); 2, deprotonated (0.1 M KNO_3, pH 12).

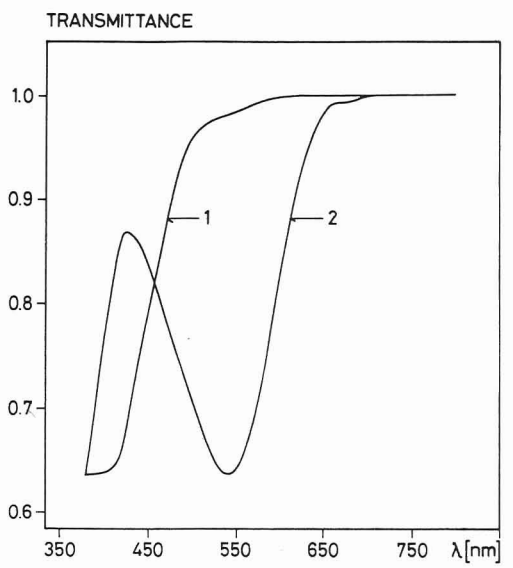

Figure 4. Transmittance spectra of lipophilized Azo Violet (ETH 2412) in a membrane of type II: 1, protonated (0.1 M KNO_3, pH 2); 2, deprotonated (0.1 M KNO_3, pH 12).

The most commonly encountered more permanent change in ambient light level was caused by the obscuration of the sun by clouds. This would cause an about 10% reduction in light intensity accompanied by an error in transmittance of about 0.0005. Under normal conditions, i.e. no strong fluctuating point sources are present in the vicinity, a precision of better then 0.0001 can be expected.

Application to the Determination of Nitrate Concentrations. Two different pH-indicator dyes were employed in the anion selective membranes, lipophilized Nile Blue (*25*) and Azo Violet (*26*). The transmittance spectra of these pH-indicator dyes in their protonated and unprotonated form are given in Figures 3 and 4. The blue-sensitive photodiode available has a spectral window ranging from about 400 to 650 nm, with its peak sensitivity at 560 nm (*32*), so that it matches reasonably well the broad absorbance band of the deprotonated form of the lipophilized Azo Violet. The diodes with built-in interference filters, with peak sensitivities at 560 and

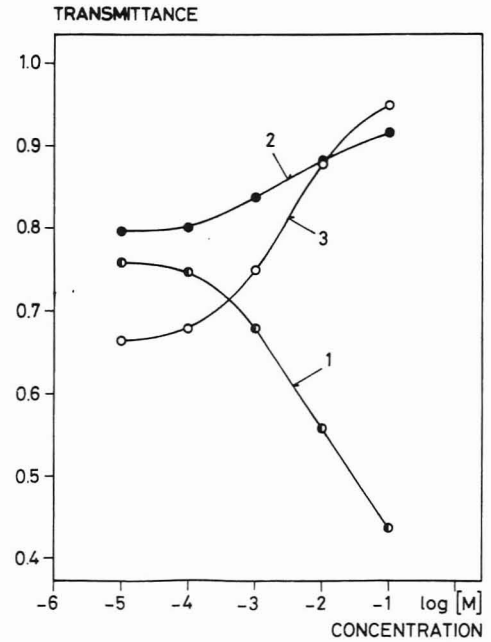

Figure 5. Calibration curves for nitrate obtained with the ISPD for different arrangements: 1, using a membrane containing lipophilized Nile Blue (ETH 5294) (type I) and a photodiode pair with interference filter (650 nm); 2, using a membrane containing lipophilized Azo Violet (ETH 2412) (type II) and a blue-sensitive photodiode pair; 3, same membrane as for curve 2, but using a photodiode pair with built-in interference filter (560 nm).

Table I. Precision Obtained with Different Optical Systems[a]

measurement	blue-sensitive diode		diode with interference filter		spectrophotometer[b]
	T	concn	T	concn	concn
		Membrane Type I			
0.001 M KNO_3			0.0023	±1.1%	±1%
0.01 M KNO_3			0.0014	±0.6%	±1%
		Membrane Type II			
0.001 M KNO_3	0.0012	±3%	0.0033	±3%	±4%
0.01 M KNO_3	0.0010	±3%	0.0007	±0.8%	±0.5%

[a] All values are standard deviations (n = 5). [b] Values taken from ref 26.

650 nm and a bandwidth of 10 nm, allow of course an almost perfect spectral match.

Calibration curves obtained for the two bulk membrane systems are given in Figure 5. The extent of the dynamic ranges agrees well with calibration curves obtained with a conventional UV–vis spectrophotometer (*26*). As can also be seen from the figure, the slope of the response curve for the system of type II based on lipophilized Azo Violet was better when the diode with interference filter was used. This must be due to an improved spectral match with this diode. The precision obtained when solutions 0.01 and 0.001 M in KNO_3 were measured alternatively is given in Table I. Note, that some care had to be taken to always use the same sample volume, as the surface was slightly concave. This causes a dispersion of incident light that may not be constant with changing level of the liquid. No such deviations could be detected when the liquid level was kept constant to within 1 mm. Better precision in concentration was obtained with the interference-filter-based diodes than with the blue-sensitive diode, as evidenced by the data in Table I. The precision in transmission is comparable for both types of diodes, however, so that this difference must be caused by the greater slope in the response curve obtained with the former detectors.

Table II. ISPD Measurement of Vegetable Extracts

sample	coloration	% light reduction on ref diode due to color and turbidity	precision in transmittance[a]
1	light brown	0	0.0013
2	light brown	0	0.0011
3	light brown	1	0.0019
4	green	8	0.0014
5	light green	9	0.0008
6	yellow	2	0.0012
7	yellow	1	0.0017

[a] Standard deviations (n = 4).

An increased slope could in principle also be obtained by increasing the total amount of indicator dye on the detector either by increasing the concentration of the active ingredients in the membranes or by making them thicker. The maximum concentrations however are limited by the solubility of the compounds and thicker membranes would lead to impractically long response times. Surprisingly, the precision in concentration for the interference-filter-based diodes is also comparable to the result obtained with conventional spectrophotometers. This indicates that the precision is limited by the membrane performance rather than the detectors themselves.

Response times depended on the thickness of the membrane, the concentration range, and the direction of the concentration change. It is mainly due to diffusion phenomena within the membrane phase which leads to response times in the order of seconds for a membrane of 4 μm thickness (*25*). With the device and membrane system (thickness about 5–10 μm for the ISPD) described here, the response times were less than 1 min. It was found that the membranes of both types could be used reversibly over a period of 10 h with no measurable loss in sensitivity. A detailed discussion of the lifetime of ISE's and optode membranes has been submitted for publication (*33*).

The combination of the ISPD detector with the anion sensitive membranes was tested in a practical application by measuring nitrate concentrations in extracts of different vegetables. The results are compared to those obtained by two independent methods, potentiometry and ion chromatography. Table II shows some parameters of these ISPD determinations. All the extracts were colored to some extent and also showed some turbidity which developed after adding the buffer solution to the extracts. The approximate reduction of light intensity on the reference diode caused by the color and turbidity of individual samples amounting to up to 10% is given in the table. The standard deviations of the transmittance values measured for each sample are given and match well the values obtained from aqueous standards given above. It should be noted, that the intensity of the incident light was gradually decreasing during the measuring period to a total of 15%. This was most likely caused by the sunset occurring during this time. The measured concentrations are given in Table III together with the values obtained by the independent methods. A reasonable agreement of the values was obtained, which demonstrates that an optical sensor based on ambient light can indeed give a performance comparable to established methods. The slightly lower slopes of the regression of ISPD vs ISE and IC measurements originate from a low bias of the four larger values found. There is no obvious reason for this and it might be purely coincidental.

CONCLUSIONS

The precision of the device reported was found to be excellent under conditions prevalent in an analytical laboratory.

Table III. Nitrate Concentrations (mM) in the Vegetable Extracts, Determined with the ISPD and by Potentiometry and Ion Chromatography

sample	ISPD	ion-selective electrode (ISE)	ion chromatography (IC)
1	11.5 ± 0.3	12.5 ± 0.5	13.0 ± 0.7
2	4.24 ± 0.06	4.4 ± 0.2	4.6 ± 0.3
3	8.9 ± 0.3	9.4 ± 0.4	9.6 ± 0.5
4	3.1 ± 0.1	2.6 ± 0.1	2.8 ± 0.2
5	4.0 ± 0.1	3.5 ± 0.2	3.8 ± 0.2
6	5.3 ± 0.1	7.0 ± 0.3	6.3 ± 0.3
7	1.55 ± 0.05	2.0 ± 0.1	1.5 ± 0.1

[a] The precision values given are standard deviations (n = 4) for the ISPD measurements, and estimates from two determinations for the other two methods. The correlation data for the combinations (ISPD/IC), (ISE/IC), and (ISPD/ISE) in the respective order are 0.853, 0.953, and 0.879 for the slope, 0.444, 0.252, and 0.315 for the y intercept, and 0.992, 0.989, and 0.967 for the correlation coefficient (r^2).

Transmittance values with a precision of up to 0.001 can be obtained, which corresponds to an error of about 1% in concentration. If strong light sources with fluctuating intensity are located in the vicinity of the present sensor, larger interferences might occur. The use of precision manufacturing techniques to assemble the sensors or of a series of measuring and reference pairs of diodes arranged in a regular pattern to average uneven irradiation and tolerances in diode response might alleviate this limitation.

ACKNOWLEDGMENT

The authors thank Beatrix Suter for help with the ion chromatograph.

LITERATURE CITED

(1) Fuh, M.-R. S.; Burgess, L. W.; Hirschfeld, T.; Christian, G. D.; Wang, F. *Analyst* **1987**, *112*, 1159–63.
(2) Urbano, E.; Offenbacher, H.; Wolfbeis, O. S. *Anal. Chem.* **1984**, *56*, 427–429.
(3) Goldfinch, M. J.; Lowe, C. R. *Anal. Biochem.* **1980**, *109*, 216–221.
(4) Schaffar, B. P. H.; Wolfbeis, O. S. *Anal. Chim. Acta* **1989**, *217*, 1–9.
(5) Schaffar, B. P. H.; Wolfbeis, O. S.; Leitner, A. *Analyst* **1988**, *113*, 693–697.
(6) Krull, U. J.; Brown, R. S.; DeBono, R. F.; Hougham, B. D. *Talanta* **1988**, *35*, 129–137.
(7) Smardzewski, R. R. *Talanta* **1988**, *35*, 95–101.
(8) Wolfbeis, O. S.; Weis, L. J.; Leiner, M. J. P.; Ziegler, W. E. *Anal. Chem.* **1988**, *60*, 2028–2030.
(9) Guthrie, A. J.; Narayanaswamy, R.; Welti, N. A. *Talanta* **1988**, *35*, 157–159.
(10) Ashworth, D. C.; Huang, H. P.; Narayanaswamy, R. *Anal. Chim. Acta* **1988**, *213*, 251–257.
(11) Alder, J. F.; Ashworth, D. C.; Narayanaswamy, R.; Moss, R. E.; Sutherland, I. O. *Analyst* **1987**, *112*, 1191–1192.
(12) Werner, T. C.; Cummings, J. G.; Seitz, W. R. *Anal. Chem.* **1989**, *61*, 211–215.
(13) Kawabata, Y.; Tahara, R.; Imasaka, T.; Ishibashi, N. *Anal. Chim. Acta* **1988**, *212*, 267–271.
(14) Bright, F. V.; Poirier, G. E.; Hieftje, G. M. *Talanta* **1988**, *35*, 113–118.
(15) Li, P. Y. F.; Narayanaswamy, R. *Analyst* **1989**, *114*, 1191–1195.
(16) Suzuki, K.; Tohda, K.; Tanda, Y.; Ohzora, H.; Nishihama, S.; Inoue, H.; Shirai, T. *Anal. Chem.* **1989**, *61*, 382–384.
(17) Carroll, M. K.; Bright, F. V.; Hieftje, G. M. *Anal. Chem.* **1989**, *61*, 1768–1772.
(18) Carey, W. P.; DeGrandpre, M. D.; Jorgensen, B. S. *Anal. Chem.* **1989**, *61*, 1674–1678.
(19) Cook, R. L.; Macduff, R. C.; Sammells, A. F. *Anal. Chim. Acta* **1989**, *226*, 153–158.
(20) Dickert, F. L.; Schreiner, S. K.; Mages, G. R.; Kimmel, H. *Anal Chem.* **1989**, *61*, 2306–2309.
(21) Posch, H. E.; Wolfbeis, O. S.; Pusterhofer, J. *Talanta* **1988**, *35*, 89–94.
(22) Gantzer, M. L.; Hemmes, P. R., Jr.; Wong, D. U.S. Pat. Appl. 583 127 (1984).
(23) Morf, W. E.; Seiler, K.; Lehmann, B.; Behringer, Ch.; Tan, S.; Hartman, K.; Sørensen, P. R.; Simon, W. In *Ion-Selective Electrodes*, *5*, *Proceeding of the Fifth Symposium held at Mátrafüred, Hungary, 9-13 October, 1988*; Pungor, E., Ed.; Pergamon Press: Oxford and New York, and Akadémiai Kiadó, Budapest, 1989; pp 115–140.
(24) Morf, W. E.; Seiler, K.; Lehmann, B.; Behringer, Ch.; Hartman, K.; Simon, W. *Pure Appl. Chem.* **1989**, *61*, 1613–1618.
(25) Seiler, K.; Morf, W. E.; Rusterholz, B.; Simon, W. *Anal. Sci.* **1989**, *5*, 557–561.
(26) Tan, S. S. S.; Hauser, P. C.; Chaniotakis, N. A.; Suter, G.; Simon, W. *Chimia* **1989**, *43*, 257–261.
(27) Perisset, P. M. J.; Hauser, P. C.; Tan, S. S. S.; Seiler, K.; Morf, W. E.; Simon, W. *Chimia* **1989**, *43*, 10–11.
(28) Wegmann, D.; Weiss, H.; Ammann, D.; Morf, W. E.; Pretsch, E.; Sugahara, K.; Simon, W. *Mikrochim. Acta* **1984**, *III*, 1–16.
(29) Dürselen, L. F. J.; Wegmann, D.; May, K.; Oesch, U.; Simon, W. *Anal. Chem.* **1988**, *60*, 1455–1458.
(30) Teorell, T.; Stenhagen, E. *Biochem. Z.* **1936**, *299*, 416–419.
(31) Paul, J. L.; Carlson, R. M. *J. Agric. Food Chem.* **1968**, *16*, 766–769.
(32) Data sheet for the Blue-Sensitive Photodiode Model No. BS-500B, Sharp Corporation, 1981, supplied by OmniRay AG, Zurich, Switzerland.
(33) Dinten, O.; Spichiger, U. E.; Chaniotakis, N.; Gehrig, P.; Rusterholz, B.; Morf, W. E.; Simon, W. Unpublished results.

RECEIVED for review February 22, 1990. Accepted June 18, 1990. The work was partly supported by the Swiss National Science Foundation.

Coated Amperometric Electrode Arrays for Multicomponent Analysis

Joseph Wang,* Gary D. Rayson, Ziling Lu, and Hui Wu

Department of Chemistry, New Mexico State University, Las Cruces, New Mexico 88003

This paper describes a sensor array of several amperometric electrodes, each coated with a different permselective film. Coatings with different transport properties, based on size (cellulose acetate), charge (Nafion, poly(vinylpyridine), poly(ester sulfonic acid)), and polarity (phospholipid) are employed in connection with a four-electrode thin-layer flow detector. With equipotential operation, the array's response pattern of each analyte provides a unique characterization of the individual components. Multicomponent analysis is obtained by taking advantage of the partial selectivity of the individual sensors and using a pattern recognition (multiple linear regression) method. Additional information is obtained by recording the complete hydrodynamic voltammogram at the individual sensors. The merits of the new array are illustrated for the quantification of neurologically significant catechol compounds.

INTRODUCTION

The use of chemically modified electrodes as chemical sensors is receiving considerable attention. The ability to deliberately control the manipulate the surface properties can lead to a variety of attractive effects. One promising avenue is coverage of the surface with an appropriate permselective membrane barrier. Coatings with different discriminative properties, such as size (*1–3*), charge (*4–6*), or polarity (*7, 8*) have been developed to yield significant improvements in in vivo monitoring of primary neurotransmitters (*9*), amperometric detection for liquid chromatography or flow injection systems (*1–6, 10, 11*), enzymatic and nonenzymatic sensing of glucose (*12–15*), or anodic stripping measurements of trace metals (*16*). The additional separation step, performed in situ at the surface, thus adds new dimensions of information that enhance the power of amperometric devices.

This paper describes the characterization and analytical utility of a novel array of partially selective amperometric electrodes based on coverage with different permselective coatings. Because of their great potential for practical analytical applications, sensor arrays are of considerable recent interest. The formation of such arrays brings an additional degree of information. Arrays based on different sensing principles have thus been described in past years. In particular, Kowalski and co-workers (*17, 18*) developed and characterized arrays of piezoelectric crystals, coated with different adsorbates, for detecting gaseous vapors in connection with environmental monitoring. An amperometric sensor array for detecting hazardous gases was developed by Stetter et al. (*19*). This array consisted of four uncoated electrodes, operated at different potentials and preceded by different heated filaments to treat the passing samples. Sparingly selective ion-selective electrode arrays were described by Otto and Thomas (*20*) and Beebe et al. (*21*). The coupling of these arrays with a chemometric (pattern recognition) approach has opened the door to multicomponent analysis. The partial selectivity of the individual sensing elements is particularly attractive for such use of multivariate calibration methods. Similar advantages accrue in the present study from the use of partially selective amperometric electrode arrays. Permselective coatings, with widely diverse transport properties, are used to obtain the pattern amperometric response of the array and hence to identify the analyte. We wish to report these features and advantages in the following sections in connection with flow-injection detection of neurochemically important compounds.

EXPERIMENTAL SECTION

Apparatus. The four-electrode thin-layer flow cell is shown in Figure 1. The body consisted of two dual electrode (glassy carbon) half cells (Model MF 1000, Bioanalytical Systems (BAS)). One of the blocks was drilled to accept the solution inlet and outlet tubings. The two blocks were separated by two Teflon gaskets (TG-15M, BAS). The Ag/AgCl (3 M NaCl) reference electrode and stainless steel auxiliary electrode were positioned downstream in the conventional manner. The flow injection system was described previously (*2*); a 20-μL sample loop was used. The electrodes were connected to an IBM instruments Model EC 220 voltammetric analyzer, the output of which was displayed on a Houston Omniscribe strip-chart recorder. The flow injection response of each electrode was recorded sequentially.

Reagents. Poly(vinylpyridine) (PVP, Polysciences, Inc.), Nafion (5% solution, Solution Technology, Inc.), cellulose acetate (Aldrich), Eastman AQ 55D (28% solution, Eastman Kodak Co.), ascorbic acid (Baker), and L-α-phosphatidylcholine (Type XI-E), cholesterol, catechol, epinephrine, norepinephrine, dopamine, (3,4-dihydroxyphenyl)acetic acid (DOPAC), and promethazine (Sigma) were used without further purification. All measurements were performed in 0.05 M phosphate buffer solution (pH 5.5). Solutions were prepared with doubly distilled water.

Surface Modification. Prior to their coating, the four glassy carbon surfaces were polished with 0.05-μm α-alumina particles, rinsed with doubly distilled water, and sonicated in a water bath for 5 min. The different coatings were applied at the individual electrodes by placing 5 μL of the corresponding solutions to cover the active disk and allowing to air-dry. The individual films did not overlap. The different solutions were prepared by (a) dissolving PVP in methanol (0.5% solution), (b) diluting the Nafion solution 10-fold in ethanol, (c) dissolving cellulose acetate in 1:1 acetone:cyclohexanone solution (2% solution), (d) adding water (at 1%) to the Eastman AQ 55D solution and diluting it 20-fold in methanol, and (e) adding 12 mg of cholesterol to 1 mL of chloroform solution containing 10 mg of phosphatidylcholine. The cellulose acetate coating was hydrolyzed in 0.07 M KOH, prior to coverage of the other disks.

Procedure. Flow injection analysis, with equipotential operation and flow rate of 1.0 mL/min, was used for demonstrating the merits of the arrays. Working potentials (in the plateau regions) were applied sequentially at the individual electrodes. Some experiments were performed by recording the complete hydrodynamic voltammograms at the individual sensors.

CALCULATIONS

The current response, i_I, of a coated electrode can be generalized in the following equation (*22*):

$$i_I = nFA\frac{P_m}{b}C \qquad (1)$$

where n is number of electrons in the reaction, F is the value of Faraday, A is the electrode area, P_m is the film permeability

0003-2700/90/0362-1924$02.50/0

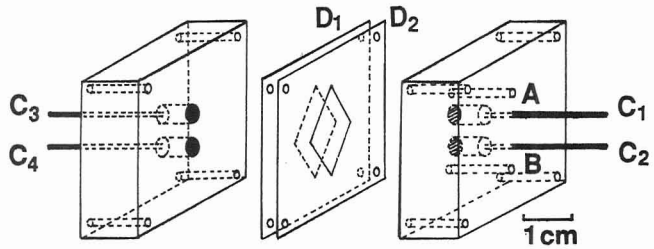

Figure 1. Expanded view of the thin-layer flow cell: (A, B) solution inlet and outlet; (C_1–C_4) working electrodes; (D_1, D_2) spacers.

for the electroactive species, b is the film thickness, and C is the bulk concentration of this species. Consider the case in which several oxidizable species (A, B, etc.) are present in the same solution, so that the redox processes $R_A \rightarrow O_A + n_Ae^-$, $R_B \rightarrow O_B + n_Be^-$, etc. occur at the operating potential. The measured current is thus given by

$$i_I = \frac{FA}{b}(n_AP_{m,A}C_A + n_BP_{m,B}C_B + ...) \quad (2)$$

Multiple linear regression (MLR) is employed to predict a component's concentration in a sample mixture. By use of several coated electrodes for every calibration mixture, a set of linear equations is obtained that can be expressed in matrix notation as follows:

$$\mathbf{I} = \mathbf{CR} \quad (3)$$

where **I** is the matrix of transformed current valued with n rows (number of mixtures) and p columns (number of electrodes), **C** is the matrix mixture concentration having n rows and m columns (number of analytes), and **R** is the response parameter matrix with m rows and p columns. In the most general case of overdetermined systems, the response parameters are obtained according to

$$\mathbf{R} = (\mathbf{C}^t\mathbf{C})^{-1}\mathbf{C}^t\mathbf{I} \quad (4)$$

where the superscript t indicates the transpose of a matrix. The matrix of response parameters, **R**, is then used to analyze unknown mixtures by measuring their current values and substituting the transformed values into

$$\mathbf{c} = \mathbf{eR}^t(\mathbf{R}\cdot\mathbf{R}^t)^{-1} \quad (5)$$

where **c** is the vector of the m sought-for concentrations and **e** is the vector of current values at the p different electrodes.

RESULTS

The concept of partially selective electrode arrays is illustrated in the following sections for assays of mixtures of catechol compounds, of great relevance to neurochemical studies. Figure 2 shows flow injection peaks recorded at a three-channel coated amperometric electrode array for dopamine (a), DOPAC (b), and catechol (c). Despite the structural similarities of these analytes and the use of the *same* operating potential, the different coated electrodes exhibit distinctly different response peaks. The size-exclusion cellulosic film (A) exhibits higher permeability toward the smaller catechol molecules. These neutral molecules readily transport through the cationic PVP film (B), that also yields enhanced response toward the anionic DOPAC. On the other hand, facile transport through the negatively charged poly(ester sulfonic acid) Eastman-AQ layer (C) is observed for the cationic dopamine; this film effectively excludes the DOPAC anions. All coatings thus exhibit the expected permselective response, as well as fast response to dynamic changes in concentrations. As will be illustrated in the following sections, the partial (rather than total) selectivity of the individual coatings is advantageous for the use of such arrays for multicomponent analysis.

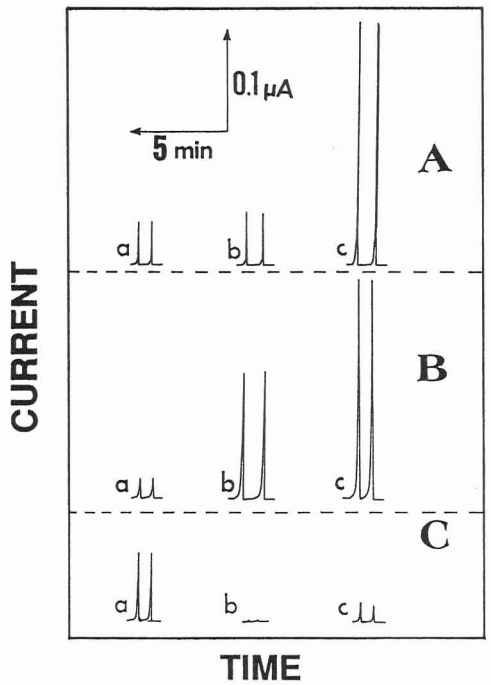

Figure 2. Flow-injection peaks for 2×10^{-5} M dopamine (a), DOPAC (b), and catechol (c) at the 25-min hydrolyzed cellulose acetate (A), PVP (B), and Eastman-AQ55D (C) coated electrodes: flow rate, 1.0 mL/min; applied potential, +0.95 V; 0.05 M phosphate buffer (pH 5.5).

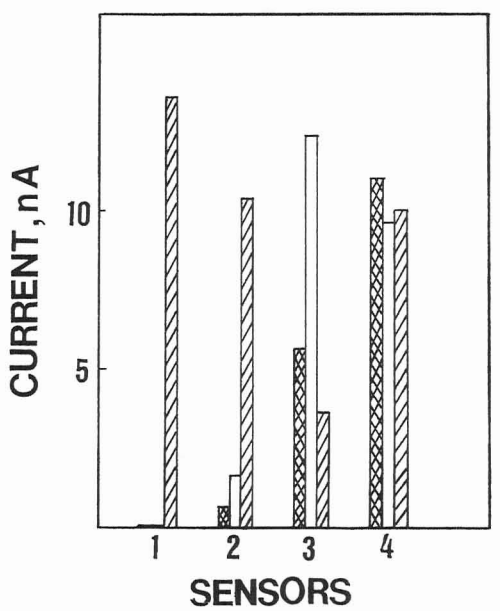

Figure 3. Sensor array response pattern for 2×10^{-6} M promethazine (crosshatch), dopamine (open), and catechol (hatch): sensors, 20-min hydrolyzed cellulose-acetate (1), PVP (2), Nafion (3), and lipid (4) coated electrodes; flow injection operation with detection at +0.80 V. Other conditions are given in Figure 2.

The multielectrode operation, based on different transport properties, can be used to generate the array's response of each analyte. For example, Figure 3 shows the array response pattern for dopamine, promethazine, and catechol at a four-channel array with permeabilities based on size, charge, or polarity. For each analyte, the amperometric array response is unique from the response pattern of the other species. For instance, the large hydrophobic promethazine molecules are readily detected at the hydrophobic lipid- and Nafion-coated electrodes, while being excluded from the cellulose acetate and PVP coated elements. The structurally similar dopamine and catechol exhibit a relatively similar response at the cellulose acetate and lipid-coated electrodes but differ largely in their behavior at the charged PVP and Nafion coated surfaces.

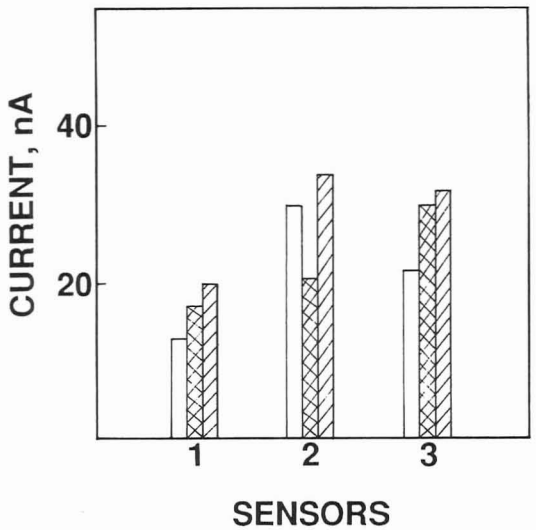

Figure 4. Sensor array response pattern for 2×10^{-6} M epinephrine (crosshatch), norepinephrine (open), and dopamine (hatch): sensors, 30-min hydrolyzed cellulose acetate (1), Nafion (2), and Eastman AQ55D (3) coated electrodes; flow injection operation with detection at +0.90 V. Other conditions are given in Figure 2.

Table I. Multivariate Prediction for Two-Component Mixtures

1. ascorbic acid + epinephrine[a]	6.0 + 2.0	6.09 + 1.97
2. ascorbic acid + epinephrine[a]	2.0 + 6.0	1.48 + 5.62
3. catechol + DOPAC[b]	2.0 + 6.0	2.35 + 5.02

[a] Sensors: Nafion, PVP, and 30-min hydrolyzed cellulose acetate coated electrodes, held at +0.8 V. [b] Sensors: as in Figure 2, held at +0.8 V.

Another response pattern of great significance for neurochemical studies is shown in Figure 4. While negatively charged coatings (e.g. Nafion) allow discrimination against anionic species (e.g., DOPAC, ascorbic acid), they lack the desired resolving power between cationic neurotransmitters with similar redox properties, e.g. dopamine, epinephrine, and norepinephrine. As shown in Figure 4, small variations in the transport of these compounds through charge- and size-exclusion coatings can be combined and exploited for generating a characteristic array's response for each cationic neurotransmitter. For transport through ion-exchange polymers the permeability of the electroactive species (P_m in eq 1) is given by $P_m = K_d D_f$, where K_d is the distribution constant and D_f the diffusion coefficient in the film. Differences in the K_D and D_f values of cationic neurotransmitters in Nafion films have been elucidated recently (*11*). For the array shown in Figure 4, the sulfonated Nafion and Eastman AQ coatings exhibit different trends in the permeability (Nafion, dopamine > norepinephrine > epinephrine, vs Eastman AQ, dopamine > epinephrine > norepinephrine). In the case of the cellulosic film the trend is dopamine (molecular weight 153) > epinephrine (molecular weight 183) > norepinephrine (molecular weight 169). The latter indicates that molecular weight is not the sole factor affecting the transport through the cellulosic layer. Overall, the characteristic signature patterns as shown in Figures 3 and 4 can be used to "fingerprint" and identify the individual components and to predict their concentrations in simple mixtures. (Because of the increased similarity of cationic neurotransmitters, additional sensors may be needed to increase the prediction capability.)

The ability of the amperometric array/chemometric approach to perform multicomponent analysis is illustrated in Table I, using different sample sets. The MLR prediction results follow closely the actual concentration of ascorbic acid, epinephrine, catechol, and DOPAC. The relative predictive errors range from 1 to 26%, with an average value of 11%. In addition to the use of additional sensors, the predictive ability should be improved by employing a partial least-squares calibration technique (which addresses more successfully errors created by collinearity (*17*)).

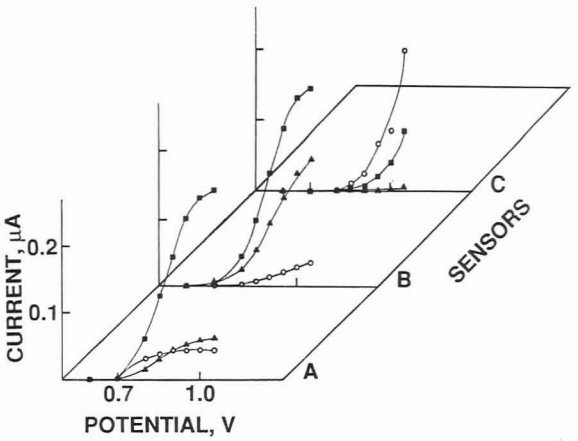

Figure 5. Hydrodynamic voltammograms for 2×10^{-5} M dopamine (○), DOPAC (▲) and catechol (■) at the 25-min hydrolyzed cellulose acetate (A), PVP (B), and Eastman-AQ 55 (C) coated electrodes. Other conditions are given in Figure 2.

Further improvement in the power of the partially selective electrode array can be achieved by providing an additional (third) dimension of information to the sensor array pattern. In particular, it is possible to apply different potentials to each electrode of the array and to register the corresponding individual currents (i.e. recording the complete hydrodynamic voltammogram). An example of such a three-dimensional (potential–current–sensor) display of data is illustrated in Figure 5, using cellulose acetate (A), PVP (B), and Eastman AQ 55D (C) coated electrodes and dopamine, DOPAC, and catechol as model analytes. Since each of the three electrodes is operated at eight different potentials, 24 channels of data are obtained for each analyte. Although beyond the scope of the present study, these provide extremely useful qualitative information, based on the coupling of redox and transport properties of the individual solutes. An even further strengthening of the qualitative information could be achieved by adding a fourth (time) dimension—in connection with liquid chromatographic detection—based on the retention properties of the analytes. Such ability to obtain multiple-dimension array patterns can be beneficial for more complex samples. Since the individual points are obtained at constant potential, no loss in sensitivity is observed (as compared to potential scanning schemes, that suffer from charging-background current contributions).

DISCUSSION

We have demonstrated that an array of partially selective coated electrodes, in connection with a chemometric approach, can greatly enhance the power of amperometric sensing. One important requirement for the chemometric MLR approach is linear additivity with respect to analyte concentration. In accordance with eq 1, the amperometric response of each coated electrode is expected to be linear. For all analytes tested, the concentrations used in this study were within the dynamic range of the individual electrodes. However, deviation from linearity may occur due to factors such as surface passivation (via adsorption of reactants, reaction products or electroinactive surfactants), chemical reactions between the individual solutes, and ohmic losses (associated with the resistance of the thin-layer cell). For example, most analytes tested exhibit a curvature in their calibration plots at concentrations higher than 1×10^{-4} M. Such deviations from linearity, which are independent of coexisting constituents,

may be addressed by other mathematical treatments. For example, curved concentration dependences may be modeled by quadratic or mixed concentration terms with alternative chemometric approaches. The individual sensors must also be highly stable. The more reproducible the results are, the more reliable is the mathematical model. While (as expected) the film-to-film reproducibility is 3–6% (in terms of relative standard deviation of the response), the individual films maintain their permselective transport properties over long periods and thus offer excellent reproducibility (1–2% relative standard deviation). This was indicated from repetitive flow injection analysis measurements, performed in 15-min intervals over several (3–5) hours. (In addition to their permselective properties, these coatings possess antifouling properties which further enhance the sensor lifetime.)

While the concept is presented within the framework of biomedical (neurochemical) applications, similar amperometric-electrode arrays could be beneficially employed for environmental monitoring or industrial process control. The array also provides a rapid estimate of the discriminative capability of each element (as desired for developmental work) and obviates the needs for developing totally selective coatings. The use of pattern recognition techniques can facilitate the selection of coatings for amperometric arrays, in a manner analogous to the selection of adsorbates for piezoelectric crystal arrays (*23*). Additional improvement can be achieved by expansion of these arrays to include additional partially selective electrodes (based on different discriminative properties, e.g. shape, or various molecular weight cutoffs). The latter may be accomplished from size-exclusion electropolymerized films (e.g., polyaniline, polyphenol (*3*)) deposited for different times. Improvements in the collection and displaying of the individual current signals can be achieved by using a multipotentiostat with individual working-electrode terminals.

LITERATURE CITED

(1) Sittampalam, G.; Wilson, G. S. *Anal. Chem.* **1983**, *55*, 1608.
(2) Wang, J.; Hutchins, L. D. *Anal. Chem.* **1985**, *57*, 1536.
(3) Wang, J.; Chen, S. P.; Lin, M. S. *J. Electroanal. Chem. Interfacial Electrochem.* **1989**, *273*, 231.
(4) Steck, A.; Yeager, H. L. *Anal. Chem.* **1980**, *52*, 1215.
(5) Wang, J.; Tuzhi, P.; Golden, T. *Anal. Chim. Acta* **1987**, *194*, 129.
(6) Wang, J.; Golden, T.; Tuzhi, P. *Anal. Chem.* **1987**, *59*, 740.
(7) Chastel, O.; Kauffmann, J. M.; Patriache, G. J.; Christian, G. *Anal. Chem.* **1989**, *61*, 170.
(8) Garcia, O. J.; Quintela, P. A.; Kaifer, A. E. *Anal. Chem.* **1989**, *61*, 979.
(9) Gerhardt, G. A.; Oke, A. F.; Nagy, G.; Moghaddam, B.; Adams, R. *Brain Res.* **1984**, *290*, 390.
(10) Hutchins-Kumar, L. D.; Wang, J.; Tuzhi, P. *Anal. Chem.* **1986**, *58*, 1019.
(11) Tüdös, A. J.; Ozinga, W. J. J.; Poppe, H.; Kok, W. Th. *Anal. Chem.* **1990**, *62*, 367.
(12) Harrison, D. J.; Turner, R. F. B.; Baltes, H. P. *Anal. Chem.* **1988**, *60*, 2002.
(13) Amine, A.; Kauffmann, J. M.; Patriarche, G. J.; Guilbault, G. G. *Anal. Lett.* **1989**, *22*, 2403.
(14) Gorton, L.; Karan, H. E.; Hale, P. D.; Inagaki, T.; Okamoto, Y.; Skotheim, T. A. *Anal. Chim. Acta* **1990**, *228*, 23.
(15) Bindra, D.; Wilson, G. S. *Anal. Chem.* **1989**, *61*, 2566.
(16) Hoyer, B.; Florence, T. M.; Batley, G. E. *Anal. Chem.* **1987**, *59*, 1608.
(17) Carey, W. P.; Beebe, K. P.; Kowalski, B. R. *Anal. Chem.* **1987**, *59*, 1529.
(18) Carey, W. P.; Kowalski, B. R. *Anal. Chem.* **1988**, *60*, 541.
(19) Stetter, J. R.; Jur, P. C.; Rose, S. L. *Anal. Chem.* **1986**, *58*, 860.
(20) Otto, M.; Thomas, J. D. R. *Anal. Chem.* **1985**, *57*, 2647.
(21) Beebe, K.; Uerz, D.; Sandifer, J.; Kowalski, B. R. *Anal. Chem.* **1988**, *60*, 66.
(22) Smart, R. B.; Dormond-Herrera, R.; Mancy, K. H. *Anal. Chem.* **1979**, *51*, 2315.
(23) Carey, W. P.; Beebe, K. P.; Kowalski, B. R.; Illman, D. L.; Hirschfeld, T. *Anal. Chem.* **1986**, *58*, 149.

RECEIVED for review March 27, 1990. Accepted June 19, 1990. This work was supported by the donors of the Petroleum Research Fund, administrated by the Americal Chemical Society, and by the National Institutes of Health (Grant No. GM 30913-06).

Role of Selective Sorption in Chemiresistor Sensors for Organophosphorus Detection

Jay W. Grate,* Mark Klusty, William R. Barger, and Arthur W. Snow

Chemistry Division, Naval Research Laboratory, Washington, D.C. 20375-5000

Nickel, palladium, platinum, and copper tetrakis(cumylphenoxy)phthalocyanines were combined with an elastomeric, oligomeric fluoropolyol material in mixed Langmuir–Blodgett films on chemiresistor sensors for organophosphorus vapors. The phthalocyanine carried the electronic current, while the fluoropolyol improved the sorption characteristics of the film. This strategy produced sensors with improved response and recovery times and high sensitivity. Factors influencing the selectivity of the sensor responses were analyzed in terms of two steps: sorption and transduction. Sorption was shown to be the primary determinant of selectivity among the organic vapors tested.

INTRODUCTION

The use of Langmuir–Blodgett (LB) films on chemical sensors is now well established (*1–12*). This technique is used to apply thin films of the materials which must interact selectively with the chemical environment. Upon interaction with the species to be detected, the film material undergoes a change that is detected by the transducer to which the film has been applied. This could be a mass change, a change in electrical conductivity, or a change in optical properties, to name just three. Changes in electrical conductivity are the basis for the chemiresistor sensors illustrated in Figure 1 (*5–8*). A set of interdigital electrodes on an insulating substrate is covered by a thin film of a weakly conducting organic material. A constant bias voltage is applied and the current through the sensor is measured. Changes in current measure the change in film conductivity which occurs in response to interactive vapors.

The advantage of the LB technique in preparing films for these and other sensors is the ability to prepare very thin films which are continuous. In addition, application of the film one layer at a time affords precise control of film thickness. These

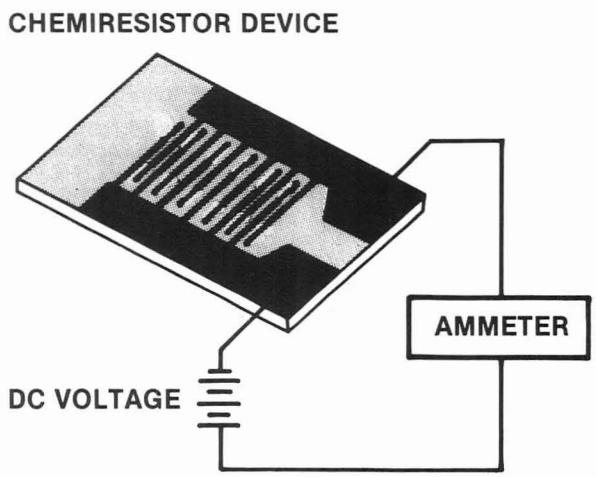

Figure 1. Schematic diagram of a chemiresistor sensor.

advantages often outweigh the principal disadvantage of this technique, which is that it places stringent requirements on the film material. The material must be insoluble in water, soluble in an organic spreading solvent, form a film on the air–water interface, and transfer from the interface to the surface of the sensor. These requirements preclude many materials or require synthetic modification to make them compatible with the technique. Even materials that meet the solubility requirements and form films may be difficult to transfer. When all is optimal, highly ordered structures a single molecule thick can be obtained.

A technique used in our laboratory to improve the transfer of organic semiconductors to sensor substrates has been to mix the semiconductor with an amphiphile such as stearyl alcohol (*8*, *13*). The mixed films transfer effectively, yielding film structures that are not the classical LB monolayers but retain the functional advantages of being very thin and continuous. Mixed films containing phthalocyanines and stearyl alcohol have been investigated for their structures, properties, and uses for chemical sensors (*6–8*, *13–17*). Recently, mixed films of nickel dithiolenes with stearyl alcohol have been used on chemiresistor sensors for hydrazine (*5*).

In these sensors, the only known function of stearyl alcohol has been to facilitate their fabrication. It was not intentionally included to facilitate or influence any aspect of vapor detection. Indeed, the waxy character of this material could conceivably impede vapor transport within the film. For these reasons, we considered the possibility of preparing mixed films wherein the organic semiconductor would carry the current and the second component would play an active role in the sorption of vapor into the film.

This strategy is based on a two-step analysis of sensor response. First, the vapor must sorb onto or into the film on the sensor in order to be detected. Second, the sorbed vapor influences the electronic conductivity of the film. For vapors that influence film conductivity, the hypothesis is that the more vapor sorbed, the greater the sensor's response will be. Deliberate selection of the second film component to optimize sorption of the vapor to be detected should favorably influence the sensitivity and selectivity of the sensor.

In this study, we examine chemiresistor sensors for organophosphorus compound detection, focusing on the design of the chemically selective layer, and the factors influencing its selectivity. The best sensor performance was obtained by using films consisting of a phthalocyanine and a soft oligomeric material we refer to as fluoropolyol. The structures of these materials are shown in Figure 2. The phthalocyanines were the metal-substituted tetrakis(cumylphenoxy)phthalocyanines, which we have studied in previous investigations, and served as the current carrying components of the films (*6–8*, *13–18*).

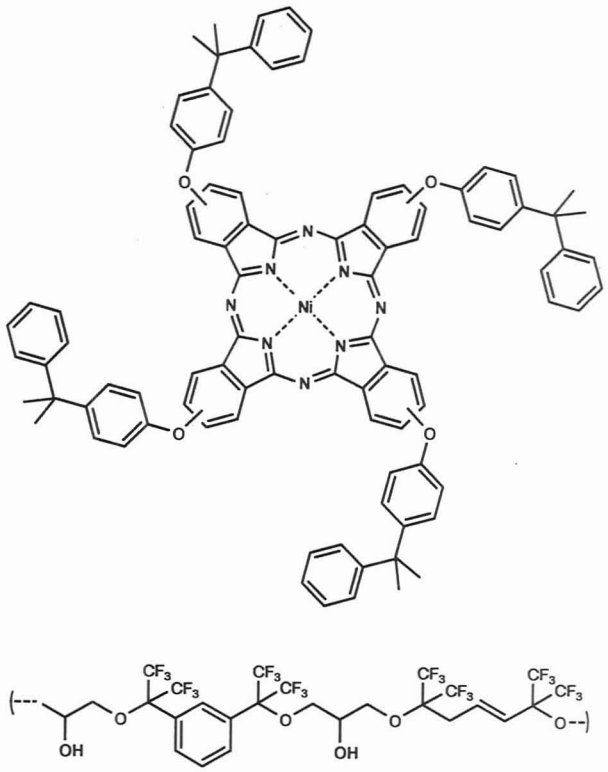

Figure 2. Structure of a metal-substituted tetrakis(cumylphenoxy)-phthalocyanine (PcCP) (above) and the repeat unit of fluoropolyol (below). The PcCPs are isomeric mixtures, resulting in structural disorder in the solid state. The double bond in the fluoropolyol can be cis or trans.

The fluoropolyol was selected because it is well established from investigations on surface acoustic wave (SAW) vapor sensors to be an excellent sorbent for organophosphorus compounds (*19–21*). It is a soft oligomer above its glass transition temperature, which facilitates vapor transport in and out of the film. Strongly hydrogen bond donating sites in fluoropolyol contribute to the sorption of organophosphorus compounds, since the P=O groups in such compounds are strong hydrogen bond bases. Mixed films of phthalocyanines and fluoropolyol did not transfer to sensor substrates as efficiently as mixed films with stearyl alcohol, but they yielded sensors with greater film conductivity, and significantly improved response and recovery characteristics.

EXPERIMENTAL SECTION

Materials. Metal-substituted tetrakis(cumylphenoxy)-phthalocyanines (PcCP) were synthesized and purified as described previously (*18*). The fluoropolyol was the same material used in previous studies on surface acoustic wave vapor sensors (*19–21*). It is a transparent, very viscous, elastomeric, oligomeric material whose repeat unit is illustrated in Figure 2. Fluoropolyol was provided by Dr. Jim Griffith of the Naval Research Laboratory Polymeric Materials Branch. These types of materials are prepared by methods described by Field (*22*).

The liquid solvents used to generate vapor streams were commercial materials of greater than 99% purity, except diethyl sulfide (98%, Aldrich) and dimethyl methylphosphonate (DMMP) (97%, Aldrich).

Sensor Substrates. Chemiresistor sensors were fabricated by using 52-MHz SAW devices (Microsensor Systems, Inc., SD-52-B). These devices contain four pairs of gold interdigital fingers (IDTs), each of which can be used as a chemiresistor sensor after coating with a chemically selective conductive film. The SAW devices used are essentially identical with those in ref 6, except that the four IDTs were fabricated with separate ground connections, rather than the common ground connection shown in Figure 3 of ref 6. Each IDT consisted of 50 finger pairs with finger width 15 μm, finger spacing 15 μm, and overlap length 4800 μm. Sensors were prepared by coating the entire device with a

chemically sensitive LB film. Electrical connections were made to one of the IDTs for sensor response measurements. Devices were cleaned by Soxhlet extraction with chloroform prior to the application of the LB film.

Langmuir–Blodgett (LB) Apparatus and Method. Film pressure vs area isotherm measurements and film depositions were carried out at 25 °C by using a thermostated, paraffin-coated Langmuir trough constructed in our laboratory and interfaced with an Apple IIe microcomputer. Surface tension measurements were made with a Gould UC-2 strain gauge carrying a 1.7-cm-wide platinum foil Wilhelmy plate. Motors for controlling bar movement (to put pressure on the film) and for substrate dipping were operated automatically with the computer. More details on the trough can be found in ref 13.

Sensor Fabrication. Mixed LB films were applied to the sensor substrates using the vertical dipping technique. Solutions containing a mixture of the metal phthalocyanine and the second component were prepared in Fisher ACS chloroform (used as received). The ratio of phthalocyanine to stearyl alcohol, stearoyl amide, or stearyl amidoxime was a 1:1 molar ratio. This corresponds to 85% phthalocyanine by weight. Films containing poly(ethylene maleate) were 75% by weight phthalocyanine.

The fluoropolyol-containing LB films described in this investigation were 60% by weight phthalocyanine and 40% by weight fluoropolyol. Initial studies showed that fluoropolyol-containing films of 40% phthalocyanine by weight had poor electrical conductivity, while films of 80% phthalocyanine by weight were not substantially more conductive than those with 60% by weight phthalocyanine. However, films with 80% by weight phthalocyanine transferred to substrates less reliably than those with 60%. Typical solution concentrations were in the range of 0.2–0.5 mg/mL in each component.

Water used as the subphase was triply distilled, with the last two distillations from an all-quartz still. All film transfer operations began with the substrate submerged. The dipping velocity was 4.2×10^{-4} m/s, with the device being coated allowed to dry in air for 5 min after each down–up cycle.

Transfer ratios for these mixed films (phthalocyanine/fluoropolyol, 60:40 by weight) were typically 50–60%. Although this is a less than ideal 100% transfer, sensors with very thin films could be consistently fabricated by this method.

Electrical Measurements. All current measurements were made with a Keithley 617 programmable electrometer and a Keithley 705 scanner equipped with a Model 7058 low current scanner card. These instruments were connected to a microcomputer via the IEEE-488 bus. Sensors were connected via gold-plated clips and triaxial cables to the low current card in the scanner, whose single output was connected via triaxial cable to the electrometer. The electrometer was operated in AMPS mode. Bias voltage to the sensors was supplied by the electrometer via BNC cable. One contact pad of the sensor IDT was connected to the bias voltage, and the other to the Input HI lead of the triaxial cable. The Input LO and ground leads were grounded. Sensors were operated at a constant bias of 1 V during vapor exposures. Current–voltage characteristics of the sensors were determined in the range of ±1.25 V as described in ref 5.

A chamber capable of holding up to five sensors was constructed from a molded PFA Teflon digestion vessel. Two holes were drilled, tapped, and fitted with molded PFA tube fittings for the gas inlet and outlet. Each sensor was held in the chamber by two gold-plated clips fashioned from the parts of a wire-wrap edge connector. The posts of these clips were press-fit through predrilled holes in the Teflon vessel. In addition to holding the sensors in place, the clips were electrical connections between the contact pads on an IDT of the chemiresistor sensors inside the chamber and wires to the leads of the triaxial connectors outside the chamber. The sensors, chamber, and connections were shielded in a closed die-cast aluminum chassis box connected to ground.

Vapor Stream Generation. Vapor streams for testing sensors were generated from gravimetrically calibrated permeation tubes or gravimetrically calibrated bubblers using an automated vapor-generation instrument described in ref 23. This instrument generates selected vapor streams, dilutes them, and delivers a programmable flow rate of either clean carrier gas or the diluted vapor stream to the sensor. The instrument is controlled with a microcomputer, which communicates with the data collection microcomputer to synchronize data collection with vapor stream operations.

For these studies the carrier gas was dry air delivered to the sensor at ambient pressure. Dimethyl methylphosphonate vapor streams were generated by using permeation tubes and the remaining vapor streams were generated from bubblers. Vapor streams from bubblers were diluted to 10% of saturation prior to delivery to the sensors. The flow rate of vapor stream to the sensor was 100 mL/min.

Data Collection and Handling. Each vapor experiment consisted of two consecutive 15-min exposures to the test vapor, alternated with periods under clean air. The test sequence was air–vapor–air–vapor–air for time intervals of 18, 15, 60, 15, and 60 min. An interval of 33 min ellapsed between consecutive experiments, during which time the sensor remained under clean air. The four sensors in the test chamber were exposed simultaneously to the same vapor stream. The time interval between data points for each sensor was 45 s. Collecting a data point consisted of connecting the sensor to the electrometer via the scanner, waiting 8 s (during which the electrometer settled on the current reading), reading the electrometer, and disconnecting the sensor from the electrometer via the scanner.

The two consecutive vapor exposures gave similar results; current readings related to the response were determined from the first exposure. Representative data points were selected at the baseline and at the top of the response curve. This procedure was appropriate because (1) the baseline noise was much smaller than the responses, so that averaging several baseline points to exposure was unnecessary, and (2) drift, when present, was much slower than the response, so that it could be ignored in determining the response. A linear regression was performed on 24 baseline points prior to the first exposure to determine the baseline noise, taking the standard deviation of the residuals as the noise. Baseline current, response current, and baseline noise, in picoamps, were recorded for use in further calculations.

RESULTS

Selection of Film Materials. The selection of film materials for these studies was based on a variety of criteria and screening experiments. The results from these experiments formed the basis of our choice of fluoropolyol as the second component in our mixed phthalocyanine-containing LB films. After the experiments that led to this choice are outlined, the remainder of the paper will focus entirely on sensors with phthalocyanine/fluoropolyol films.

Our accumulated experience with tetrakis(cumylphenoxy)phthalocyanines (PcCP) indicated that metal substitution with Ni, Pd, Pt, and Cu produced sensors with measurable conductivity which responded to vapors. A series of second components were examined, including stearyl alcohol, stearoyl amide, stearyl amidoxime, poly(ethylene maleate), and fluoropolyol. Stearoyl amide and stearyl amidoxime were considered because their structures are analogous to the stearyl alcohol utilized previously, and because their higher melting points might afford some advantages in film stability under severe conditions. The polymers poly(ethylene maleate) and fluoropolyol were both considered because they are sorbents for organophosphorus vapors (*19*, *21*). Mixed films of the blue PcCPs with stearyl alcohol or stearoyl amide transferred efficiently to sensor substrates with transfer ratios near 100%. These films were a uniform blue color. Mixed films with the other second components transferred less efficiently, with transfer ratios in the 50–60% range. The films with stearyl amidoxime were visibly blotchy. The films with the polymers were uniform but paler in intensity than those with stearyl alcohol or stearoyl amide that had been prepared by an equal number of dipping cycles.

The intrinsic conductivity of the metal-substituted PcCPs were compared in a series keeping the second film component constant as stearoyl amide. Conductivity was determined from the current–voltage (I–V) characteristics, which also confirmed

Table I. Response Data for PcCP/Fluoropolyol Chemiresistor Sensors

		Ni PcCP			Pt PcCP		
vapor	concn, mg/m^3	noise,[a] pA	I_0,[b] pA	I,[c] pA	noise, pA	I_0, pA	I, pA
water	2880	0.006	46.33	53.69	0.010	70.16	73.97
DMMP	51	0.009	45.55	64.55	0.011	68.67	81.42
isooctane	52300	0.007	40.28	44.90	0.010	62.2	65.97
toluene	23000	0.003	41.03	52.13	0.003	63.23	75.6
water	2880	0.013	26.33	28.39	0.021	50.47	52.55
DMMP	51	0.004	27.48	39.64	0.004	51.94	59.53
1-butanol	3490	0.003	27.46	34.78	0.003	50.58	59.57
2-butanone	61000	0.005	28.00	96.57	0.005	50.93	119.4
water	2880	0.018	17.95	19.32	0.004	45.28	46.98
DMMP	51	0.008	19.53	27.75	0.018	47.7	52.51
dichloroethane	72200	0.004	20.12	25.81	0.007	48.1	62.88
diethyl sulfide	56000	0.004	19.09	26.05	0.002	46.63	57.07
water	2880	0.018	17.37	18.54	0.026	39.53	40.87
DMMP	51	0.009	18.33	25.43	0.007	40.65	45.05
DMMP	82	0.021	18.91	30.09	0.041	39.28	46.72
DMMP	51	0.012	16.44	23.13	0.031	35.08	39.48
DMMP	35	0.005	16.18	21.41	0.012	34.3	37.72
DMMP	17	0.005	17.72	21.20	0.010	35.37	37.65
		Pd PcCP			Cu PcCP		
vapor	concn, mg/m^3	noise, pA	I_0, pA	I, pA	noise, pA	I_0, pA	I, pA
water	2880	0.015	112.7	114.7	0.260	2422	2448
DMMP	51	0.018	108.2	132.8	0.403	2382	2658
isooctane	52300	0.015	96.67	101.5	0.330	2126	2216
toluene	23000	0.005	98.43	128.1	0.117	2153	2719
water	2880	0.037	87.98	90.38	0.744	2098	2090
DMMP	51	0.004	89.26	107.9	0.178	2109	2323
1-butanol	3490	0.004	80.67	94.67	0.171	1991	2180
2-butanone	61000	0.009	79.52	155.6	0.265	1990	2659
water	2880	0.005	65.04	66.97	0.059	1149	1163
DMMP	51	0.026	68.22	78.91	0.373	1236	1321
dichloroethane	72200	0.008	63.09	85.58	0.114	1177	1462
diethyl sulfide	56000	0.003	60.48	72.93	0.049	1179	1372
water	2880	0.027	41.27	42.47	0.521	1046	1051
DMMP	51	0.007	42.57	49.61	0.162	1085	1170
DMMP	82	0.037	33.29	41.44	0.923	1011	1125
DMMP	51	0.022	22.41	26.97	0.569	831.9	904.0
DMMP	35	0.007	20.47	23.87	0.201	802.8	859.2
DMMP	17	0.006	19.59	21.61	0.209	837.7	877.0

[a] Baseline noise. [b] Baseline current. [c] Response current.

that the coated devices were functioning as resistors. Films with Cu PcCP were the most conductive, with conductivity decreasing in the order Cu > Pd > Pt > Ni. This same order was later observed for films using fluoropolyol as the second component.

The influences of the second components on conductivity were determined for stearyl alcohol, stearoyl amide, poly(ethylene maleate), and fluoropolyol keeping the phthalocyanine constant as Cu PcCP. Films with fluoropolyol were ca. 100 times more conductive than the other three, which were comparable. The I–V characteristics for fluoropolyol-containing films were linear with no hysteresis. By contrast, those for poly(ethylene maleate)-containing films exhibited substantial hysteresis. The I–V characteristics for stearoyl amide containing films were linear without hysteresis, while those with stearyl alcohol showed slight hysteresis, as had been observed previously (*7*). A series comparing these second components with the phthalocyanine kept constant as Pt PcCP gave similar results, with the fluoropolyol-containing film again having substantially greater conductivity.

Sensors were also screened for the nature of their responses to dimethyl methylphosphonate (DMMP), an organophosphorus compound we use in our laboratory as a simulant for more hazardous organophosphorus vapors (*20, 21*). The Cu PcCP-containing films described above were challenged with 15-min exposures to DMMP at 13 mg/m^3. The Cu PcCP/stearyl alcohol and Cu PcCP/stearoyl amide films responded with decreases in current, whereas the Cu PcCP/fluoropolyol and Cu PcCP/poly(ethylene maleate) films responded with increases in current. This interesting result is apparently related to the physical characteristics of the films' second components. Stearyl alcohol and stearoyl amide are both waxy materials, whereas fluoropolyol and poly(ethylene maleate) are both elastomers.

The most important result of these experiments, however, is illustrated in Figure 3. The film with stearyl alcohol does not reach a steady-state conductivity during the 15-min vapor exposure, nor does it completely recover. By contrast, the film with fluoropolyol responds rapidly, reaches a maximum response during DMMP exposure, and rapidly recovers upon removal of the DMMP.

As noted in the introduction, our objective was to investigate films with good sorption characteristics for organophosphorus compounds. Of the two polymers considered for this purpose, fluoropolyol is the better sorbent (*20, 21*). Fortuitously, the LB films with fluoropolyol have superior electrical conductivity to the other films, and the I–V characteristics are linear and without hysteresis. The further result that fluoropolyol yielded sensors with superior response and recovery characteristics made a compelling case for the selection of PcCP/fluoropolyol films for more detailed study.

On this basis, sensors were prepared with Ni, Pd, Pt, and Cu PcCPs as the organic semiconductor, and fluoropolyol as the second component. The sensors were challenged with

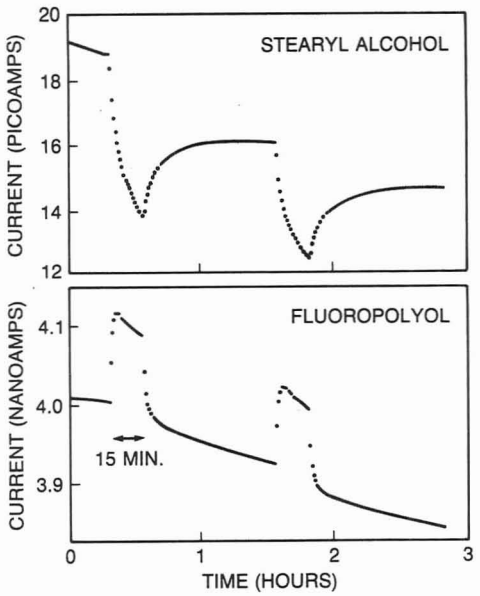

Figure 3. Comparison of the responses of Cu PcCP/stearyl alcohol and Cu PcCP/fluoropolyol LB films to two 15-min exposures to 13 mg/m^3 DMMP.

water and several organic vapors in addition to DMMP. The primary data are presented in Table I, where the baseline noise, baseline current (I_0), and the steady-state response current (I) are given for each sensor. The vapors are listed in the order in which the sensors were exposed to them. Approximately $3^1/_2$ h elapsed between the beginning of one experiment and the beginning of the next. The precise timing is described in the Experimental Section; the four sensors were tested simultaneously. The first 14 experiments were done consecutively, requiring just under 2 days. The last four experiments were begun a day later. The design of the data set allows a variety of comparisons to be made, which will be considered individually below. Note, for example, that DMMP was repeated throughout the data set in order to establish the reproducibility of these sensors.

Two types of baseline drift were seen during these experiments. The first was a consistent drift to lower baseline currents, as has been described previously for these types of sensors (7). The consequences of this type of baseline drift on the calculation of sensor responses will be considered in detail below. The second type of drift consisted of small short-term drifts in either direction. Because these drifts occurred simultaneously for all four sensors, these must be due to some change in environmental conditions (perhaps temperature).

The responses observed when the test gas stream was changed from clean carrier gas (dry air) to carrier gas containing the test vapor, and vice versa, approximated step functions, as seen in the second plot of Figure 3. The exceptions to this behavior are noted here. The current observed under the 2-butanone was particularly noisy during the steady-state response. For a few of the vapors, the sensor drifted during the vapor exposure in a manner that was not related to the baseline drift. This effect was largest for Cu PcCP exposed to the highest concentration of DMMP, 82 mg/m^3. The response rose from a flat baseline, then drifted down linearly. On removal of the DMMP, the current dropped by an amount equivalent to the original response, coming to a new lower baseline. This effect decreased with lower test concentrations of DMMP. In addition, responses of the Cu PcCP sensor to water vapor were erratic.

The responses of the Ni PcCP sensor were the most consistently behaved, and drift during DMMP exposure was least for this sensor. For these reasons, and because it was the most

Table II. Responses of the Ni PcCP Sensor to the Test Vapors

vapor	concn, mg/m^3	$(I - I_3)$, pA	$(I - I_0)/I_0$	log I/I_0	S/N
water	2880	7.35	0.159	0.064	1200
DMMP	51	19.00	0.417	0.151	2090
isooctane	52300	4.62	0.115	0.047	651
toluene	23000	11.10	0.271	0.104	3470
water	2880	2.05	0.078	0.033	163
DMMP	51	12.16	0.442	0.159	3200
1-butanol	3490	7.31	0.266	0.103	2150
2-butanone	61000	68.57	2.449	0.534	13400
water	2880	1.37	0.076	0.032	77
DMMP	51	8.22	0.421	0.153	1070
dichloro-ethane	72200	5.69	0.283	0.108	1350
diethyl sulfide	56000	6.97	0.365	0.135	1660
water	2880	1.17	0.067	0.028	64
DMMP	51	7.09	0.387	0.142	780
DMMP	82	11.18	0.591	0.202	535
DMMP	51	6.69	0.407	0.148	582
DMMP	35	5.24	0.324	0.122	1050
DMMP	17	3.49	0.197	0.078	684

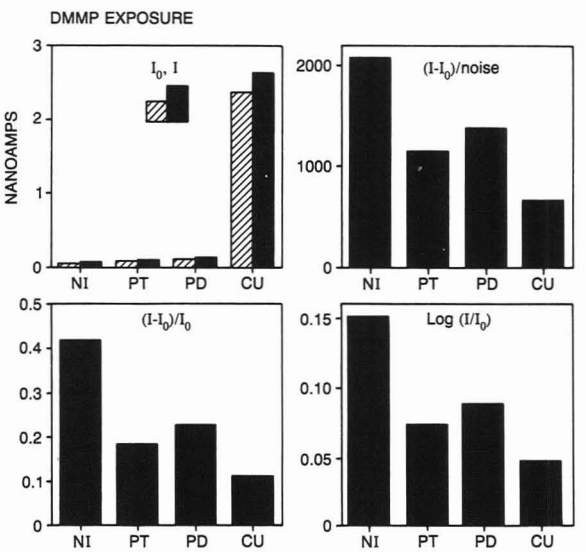

Figure 4. Effect of the metal-substituted phthalocyanine on chemiresistor sensitivity to 51 mg/m^3 DMMP. Clockwise from the upper left, the plots give the baseline (I_0) and response (I) currents, the signal-to-noise ratios ($I - I_0$)/noise), the responses normalized to the baseline according to $(I - I_0)/I_0$, and the responses normalized to the baseline according to log (I/I_0).

sensitive sensor for DMMP, the data from this sensor were examined in the greatest detail. Values for the responses of the Ni PcCP sensor to the test vapors, expressed in several ways, are given in Table II.

Influence of the Central Metal Atom on Sensitivity. The four sensors were compared for their sensitivity to DMMP by examining the data for the first 51 mg/m^3 exposure. The baseline currents and response currents are plotted together in the first plot in Figure 4. This plot raises the question of how to properly express sensor response and to compare sensors with varying baseline currents. We do not have guidance from an analytical expression which relates some function of the sensor current to the vapor concentration. Therefore, a number of alternatives are considered and compared below.

If the response is simply expressed as the change in current, I–I_0, then Cu PcCP would clearly have the largest response. However, normalization to the baseline current by the expressions $(I - I_0)/I_0$ or log (I/I_0) indicates that the Ni PcCP sensor gives the greatest response. Results for the latter two

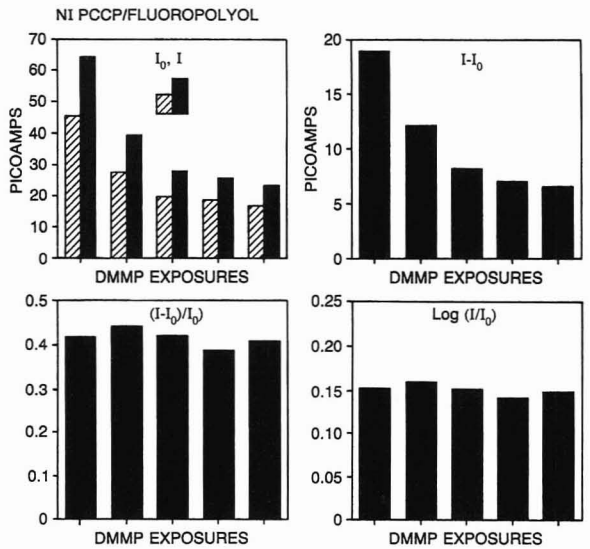

Figure 5. Reproducibility of the response of the Ni PcCP sensor to 51 mg/m^3 DMMP exposures throughout the data set. Clockwise from the upper left, the plots give the baseline (I_0) and response (I) currents, the responses expressed as $I - I_0$, the responses normalized to the baseline according to $(I - I_0)/I_0$, and the responses normalized to the baseline according to log (I/I_0).

expressions are shown as the lower two plots in Figure 4. We have also plotted the signal-to-noise ratio, taken as $(I - I_0)$/noise, for comparison. The signal-to-noise ratio is the rigorous test for sensitivity and agrees with the baseline normalization expressions in selecting the Ni PcCP as the most sensitive sensor. These results suggest that the appropriate method of expressing the responses of these sensors will be a function with I_0 in the denominator.

Reproducibility of the DMMP Response. The reproducibility of the sensor responses to DMMP is illustrated by comparing the responses of the Ni PcCP sensor to the 51 mg/m^3 exposures to DMMP which were repeated throughout the data set (see Table I). Five such experiments were included in the data set and the results are shown in chronological order in the bar graphs in Figure 5. The time interval in between these DMMP experiments was approximately 11 h, except for the last such interval, when it was approximately 24 h. In between the DMMP experiments, the sensors were exposed to other vapors.

The first bar graph illustrates the baseline and response currents. Expressing the response as the current change, $I - I_0$, as shown in the second bar graph, suggests that the sensor is losing sensitivity over time. However, the first bar graph reveals that the baseline was drifting to lower currents at the same time. Normalization to the baseline, as shown in the lower two bar graphs, indicates that the responses were actually consistent and reproducible. They also indicate that exposures to other vapors at much higher concentrations did not cause significant hysteresis.

These normalization procedures, i.e. expressions such as $(I - I_0)/I_0$ or log (I/I_0), serve as a simple and practical method of compensating for baseline drift. These results also suggest that the rigorous analytical expression for sensor response, if known, would include I_0 in the denominator.

DMMP Calibration Curves and Sensitivity. The last four experiments in the data set were exposures to DMMP at various concentrations to determine the calibration curve. The results for the Ni PcCP sensor are plotted in Figure 6, as $(I - I_0)/I_0$ and as log (I/I_0). For both expressions, the sensor response as a function of gas-phase vapor concentration fails to go through zero if extrapolated linearly. The result is not surprising, however, because the sorption isotherm of DMMP in fluoropolyol is nonlinear and curved concave downward (*19*).

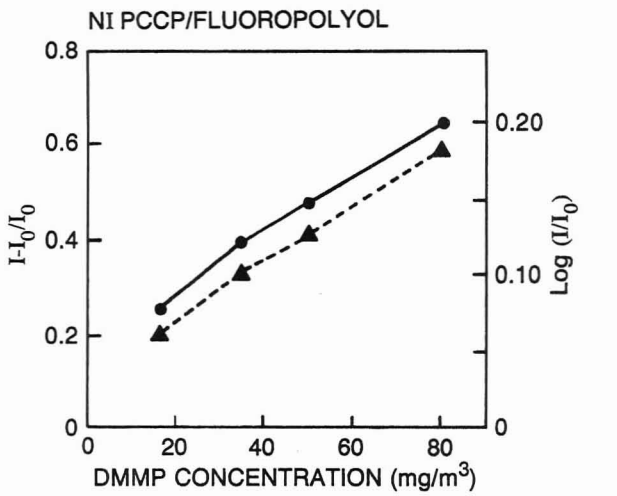

Figure 6. Calibration curves for DMMP on the Ni PcCP sensor, plotted in terms of the normalized responses, $(I - I_0)/I_0$ (dashed line) and log (I/I_0) (solid line).

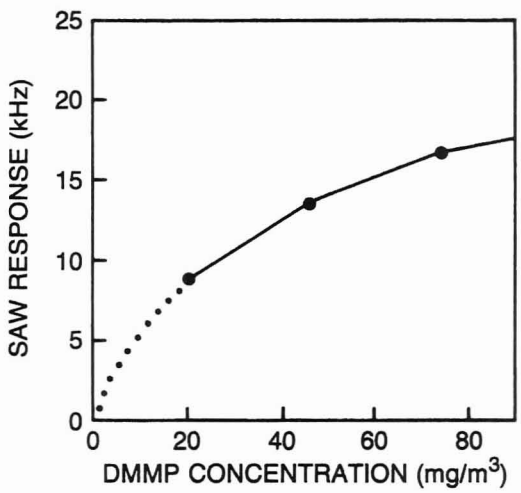

Figure 7. Sorption isotherm of DMMP into fluoropolyol determined from the response of a fluoropolyol-coated surface acoustic wave sensor.

It is a typical type II sorption isotherm (*24*). Since the sensor response is expected to be more directly related to the vapor concentration in the LB film than to the vapor concentration in the gas phase, the curved sorption isotherm for DMMP should result in a nonlinear chemiresistor response.

For comparison, the responses of a fluoropolyol-coated SAW vapor sensor to DMMP in the same concentration range are plotted in Figure 7 (*19*). Because the SAW sensor acts as a microbalance in this case, the plot is essentially the sorption isotherm for DMMP in fluoropolyol. The experimentally determined data points in this plot would also fail to intersect zero if extrapolated linearly. The similarity of the chemiresistor and SAW calibration curves demonstrates the importance of sorption characteristics in determining the behavior of these chemiresistor sensors.

The ultimate sensitivity of these chemiresistors to DMMP can be determined from the signal-to-noise ratios of the DMMP exposures given in Table II for Ni PcCP. These values range from approximately 500 to 4000, indicating that DMMP could be detected at much lower concentrations than those tested in this data set. By linear extrapolation of the results to lower concentrations, which should underestimate the sensitivity for these nonlinear sensors, the concentrations predicted to be detectable at a signal-to-noise ratio of 3 are in the range of 0.05–0.5 mg/m^3 DMMP. (To obtain these values, the signal-to-noise ratio of 3 is divided by the observed signal-to-noise ratio, and the quotient is multiplied times the

Table III. Relative Vapor Sensitivities of the Ni PcCP/Fluoropolyol Chemiresistor Compared to Vapor Sorption in Fluoropolyol

vapor	rel sensitivity[a]	log (rel sensitivity)[b]	log K_{SAW}[c]
DMMP	1000	6.0	6.3
1-butanol	9.3	4.0	3.8
2-butanone	4.9	3.7	3.4
water	3.3	3.5	3.2
toluene	1.4	3.2	2.9
diethyl sulfide	.80	2.9	2.7
dichloroethane	.49	2.7	2.5
isooctane	.27	2.4	2.1

[a] Relative sensitivity: responses were taken as $(I - I_0)/I_0$, divided by the vapor concentration, and scaled to make DMMP = 1000. [b] Relative sensitivity was rescaled to make DMMP = 10^6, and the logarithm was taken. [c] log of the partition coefficient for the vapor in fluoropolyol, measured on a SAW vapor sensor, taken from ref 19.

test concentration.) Actual tests against other organophosphorus vapors in this concentration range confirmed sensitivity below 0.5 mg/m^3.

Relative Sensitivities to Other Organic Vapors. The vapors tested in addition to DMMP were selected to represent a wide range of potential interferents. The actual responses to 51 mg/m^3 DMMP, taken as $(I - I_0)/I_0$ or log (I/I_0), were greater than the responses to any other vapor except 2-butanone, even though the interferent vapors were tested at much higher concentrations (by factors of 100–2000). Relative sensitivities were compared by dividing the responses $(I - I_0)/I_0$ of the Ni PcCP sensor by the test vapor concentrations. These numbers were then arbitrarily scaled to make DMMP equal to 1000. The results are shown in the second column (entitled relative sensitivity) of Table III. The sensitivity to DMMP was 100 to nearly 4000 times greater than the sensitivities to the other vapors. In particular, the most common interferents anticipated in a field environment are water (humidity) and hydrocarbon fuels. Sensitivity to DMMP was 150 times greater than the sensitivity to water, 700 times greater than the sensitivity to toluene, and 3700 times greater than the sensitivity to isooctane.

The order of vapor sensitivity is remarkably similar to the order observed for fluoropolyol-coated SAW devices (*19*). Relative vapor sensitivity of SAW vapor sensors can be expressed using the partition coefficient, K, which is the ratio of the vapor concentration in the sorbent stationary phase sensor coating to the vapor concentration in the gas phase. The logs of these partition coefficients are listed in the fourth column of Table III. In order to compare the chemiresistor responses to these numbers, the relative sensitivities in column 2 of Table III were rescaled with DMMP equal to 1 000 000. The logs of these relative sensitivities are reported in the third column of Table III. The close correspondence between how the vapors are ranked by chemiresistor response and how they are ranked by the strength of sorption is quite striking.

A similar analysis of the other PcCP/fluoropolyol sensors produces a similar ranking of vapors with DMMP detected with the greatest sensitivity and isooctane with the least. For the Pt, Pd, and Cu PcCP sensors, the sensitivities to diethyl sulfide and dichloroethane are reversed, but the values are so close as to be essentially the same. For the Pd PcCP sensor the sensitivity to toluene is greater than that to water, and for the Cu PcCP sensor, toluene ranks higher than butanone and water.

In summary, the overall trend for the four PcCP/fluoropolyol sensors is to rank vapors according to their sorption in fluoropolyol, with a secondary influence of the particular phthalocyanine. The order of chemiresistor relative sensitivity is identical with the order of sorption for the Ni PcCP, essentially identical for the Pt PCCP, and very similar for Pd PcCP. Cu PcCP follows the trend least rigorously, but it also gave the least consistently behaved response curves.

DISCUSSION

This study has demonstrated that the second component in mixed phthalocyanine-containing LB films has a substantial influence on sensor response. The plots in Figure 3 illustrate the profound effect that the nature of this component can have; the responses of films containing the same organic semiconductor exposed to the same vapor, but differing in their second components, went in opposite directions. The deliberate selection of a second component with good sorption characteristics for the analyte of interest yielded chemiresistor sensors with excellent response and recovery characteristics, substantial selectivity, and high sensitivity.

The physical properties of the second component are an important factor in determining the interactions of the mixed films with vapors. Stearyl alcohol and stearoyl amide are both solid, waxy, and relatively impermeable materials. By contrast, the fluoropolyol and poly(ethylene maleate) materials are elastomeric and are very permeable. Vapors can diffuse through these materials readily because of the thermal mobility of the polymer chain segments.

The structures of pure and mixed films of PcCPs have been determined from transmission electron micrographs and are reported in ref 14. The phthalocyanine component forms small disklike aggregates on the order of 50 to 500 nm in diameter and 5 nm in height. These aggregates are contiguous, and the spaces between them are presumed to be filled with the second component when mixed films are made. Such structures may have certain advantages for application in vapor sensors. If the second component is highly permeable, the mixed film can be regarded as "porous", with rapid vapor transport to and from the phthalocyanine aggregates. This may account for the greatly improved response and recovery times observed when fluoropolyol is the second film component.

In addition, the small particle sizes of the phthalocyanine aggregates may be advantageous in providing large surface areas with which the vapors may interact. Direct current conductivity through microcrystalline materials is often discussed in terms of limiting charge transport across grain boundaries. In our mixed LB films, adsorption of organic vapors at the interfaces between contiguous aggregates may alter the mobility of charge carriers across those interfaces.

The close correspondence between the relative sensitivities of the chemiresistor sensors and the partition coefficients for vapor sorption in fluoropolyol confirmed the importance of sorption in determining sensor responses. The conductivity change observed was primarily dependent upon the amount of vapor sorbed, and much less dependent upon the chemical composition of the vapor or the metal substitution of the phthalocyanine. Thus, selectivity among the vapors tested is attributable to the interactions which influence sorption, rather than specific interactions which directly alter the current.

The factors determining the amount of vapor sorbed are the exoergic attractive interactions between the vapor (solute) and the sorbent (solvent) which promote sorption, minus the endoergic cost of forming a cavity in the sorbent (*19*, *25*, *26*). The attractive interactions, defined as solubility interactions, include dispersion, dipole/induced-dipole, dipole/dipole, and hydrogen bonding interactions. Dispersion interactions always occur between a solute and a solvent and contribute significantly to sorption. In general, larger less volatile organic vapors will be capable of greater dispersion interactions and be more strongly sorbed. DMMP is the least volatile (satu-

ration vapor pressure ca. 1 Torr at room temperature) of the vaors tested.

The roles of polar and hydrogen bonding interactions in the sorption of vapors into fluoropolyol are illustrated by the order of the log K_{SAW} values in Table III (*19*). The least strongly sorbed vapor is isooctane, which is only capable of dispersion interactions. More polarizable vapors such as diethyl sulfide, dichloroethane, and toluene are more strongly sorbed. The most strongly sorbed are those which are capable of hydrogen bonding interactions. Significantly, the vapor with the largest K_{SAW}, DMMP, is the strongest hydrogen bond base. Hydrogen bond basicities of organic solutes can be compared by using Abraham's solvation parameter for basicity, β_2^H (*27*, *28*). Phosphonates have β_2^H values near 0.8, compared to values near 0.5 for ketones, values near 0.45 for primary alcohols, and values of 0 for nonbasic compounds such as alkanes. Basic vapors interact with fluoropolyol via its hydroxyl groups, whose hydrogen bond acidity is enhanced by the proximity of electron-withdrawing oxygen and fluorine atoms along the polymer chain.

In the Introduction, we proposed that sensor responses be analyzed in terms of two steps: sorption and transduction. This method of analyzing sensor response can be generalized to all point vapor sensors using a thin organic film to interact with the chemical environment. The second step, transduction, will vary with the type of sensor, but in all cases the vapor must first be sorbed. Separately considering the factors influencing selectivity for each of these two steps can lead to improved understanding of the mechanism of sensor response. Carefully tailoring the properties of the film material to interact with the solubility properties of the analyte (and thus promote its sorption) can lead to improved sensor performance.

In this study, we chose to incorporate a sorbent for organophosphorus vapors in our chemiresistor sensor coatings. Other sorbents could be utilized to prepare phthalocyanine-based chemiresistor sensors which have chemical selectivity for other applications. An array of chemiresistor sensors for use in a chemical sensor array detector using pattern recognition (*20*, *21*) could be logically designed by varying the sorbent characteristics of the LB films on those sensors via the second film component.

ACKNOWLEDGMENT

The authors acknowledge Michael H. Abraham for many stimulating discussions on solubility interactions and the sorption of vapors into sensor coatings.

LITERATURE CITED

(1) Morizumi, T. *Thin Solid Films* **1988**, *160*, 413–429.
(2) Snow, A. W.; Barger, W. R. In *Phthalocyanines Principles and Applications*; Lever, A. B. P., Leznoff, C. C., Eds., in press.
(3) Roberts, G. G. *Sens. Actuators* **1983**, *4*, 131–145.
(4) Roberts, G. G.; Petty, M. C.; Baker, S.; Fowler, M. T.; Thomas, N. J. *Thin Solid Films* **1985**, *132*, 113–123.
(5) Grate, J. W.; Rose-Pehrsson, S.; Barger, W. R. *Langmuir* **1988**, *4*, 1293–1301.
(6) Snow, A. W.; Barger, W. R.; Klusty, M.; Wohltjen, H.; Jarvis, N. L. *Langmuir* **1986**, *2*, 513–519.
(7) Wohltjen, H.; Barger, W. R.; Snow, A. W.; Jarvis, N. L. *IEEE Trans. Electron Devices* **1985**, *ED-32*, 1170–1174.
(8) Barger, W. R.; Wohltjen, H.; Snow, A. W. *Proc. Int. Conf. Solid State Sens. Actuators—Transducers '85* Philadelphia, PA, June 11–14, 1985; pp 410–413.
(9) Baker, S.; Roberts, G. G.; Petty, M. C. *Proc. Inst. Electr. Eng.* **1983**, *130*, 260–263.
(10) Tredgold, R. H.; Young, M. C. J.; Hodge, P.; Hoorfar, A. *Proc. Inst. Electr. Eng. Part I: Solid State Electron Devices* **1985**, *132*, 151–156.
(11) Holcroft, G.; Roberts, G. G. *Thin Solid Films* **1988**, *160*, 445–452.
(12) Henrion, L.; Defrost, G.; Ruaudel-Teixier, A.; Barraud, A. *Sens. Actuators* **1988**, *14*, 251–257.
(13) Barger, W. R.; Snow, A. W.; Wohltjen, H.; Jarvis, N. L. *Thin Solid Films* **1985**, *133*, 197–206.
(14) Barger, W. R.; Dote, J.; Klusty, M.; Mowery, R.; Price, R.; Snow, A. *Thin Solid Films* **1988**, *159*, 369–378.
(15) Dillella, D. P.; Barger, W. R.; Snow, A.; Smardzewski, R. R. *Thin Solid Films* **1985**, *133*, 207–217.
(16) Kutzler, F. W.; Barger, W. R.; Snow, A. W.; Wohltjen, H. *Thin Solid Films* **1987**, *155*, 1–16.
(17) Pace, M. D.; Barger, W. R.; Snow, A. W. *J. Magn. Reson.* **1987**, *75*, 73–82.
(18) Snow, A. W.; Jarvis, N. L. *J. Am. Chem. Soc.* **1984**, *106*, 4706–4711.
(19) Grate, J. W.; Snow, A. W.; Ballantine, D. S., Jr.; Wohltjen, H.; Abraham, M. H.; McGill, R. A.; Sasson, P. *Anal. Chem.* **1988**, *60*, 869–875.
(20) Rose-Pehrsson, S. L.; Grate, J. W.; Ballantine, D. S., Jr.; Jurs, P. C. *Anal. Chem.* **1988**, *60*, 2801–2811.
(21) Ballantine, D. S., Jr.; Rose, S. L.; Grate, J. W.; Wohltjen, H. *Anal. Chem.* **1986**, *58*, 3058–3066.
(22) Field, D. D. *J. Paint Technol.* **1976**, *48*, 43.
(23) Grate, J. W.; Ballantine, D. S.; Wohltjen, H. *Sens. Actuators* **1987**, *11*, 173–188.
(24) Rodgers, C. E. In *Polymer Permeability*; Comyn, J., Ed.; Elsevier: New York, 1985; pp 29–34.
(25) Kamlet, M. J.; Doherty, R. M.; Abboud, J.-L. M.; Abraham, M. H.; Taft, R. W. *CHEMTECH* **1986**, *16*, 566–576.
(26) Abraham, M. H.; Doherty, R. M.; Kamlet, M. J.; Taft, R. W. *Chem. Br.* **1986**, *22*, 551–554.
(27) Abraham, M. H.; Grellier, P. L.; Prior, D. V.; Morris, J. J.; Taylor, P. J.; Lawrence, C.; Berthelot, M. *Tetrahedron Lett.* **1989**, *30*, 2571.
(28) Abraham, M. H.; Grellier, P. L.; Prior, D. V.; Morris, J. J.; Taylor, P. J. *J. Chem. Soc., Perkin Trans. 2*, in press.

RECEIVED for review November 17, 1989. Accepted June 19, 1990. This work was supported with funds from the Office of Naval Technology administered by the U.S. Naval Surface Warfare Center, Dahlgren, VA.

Amperometric Microsensor for Water

Huiliang Huang and Purnendu K. Dasgupta*

Department of Chemistry and Biochemistry, Texas Tech University, Lubbock, Texas 79409-1061

A thin film of a perfluorosulfonate ionomer (PFSI) is supported upon two electrodes. The positive electrode is composed of a noble metal. The polymer film has high affinity for water and certain other highly polar molecules, notably alcohols. When a voltage above the threshold of electrolytic breakdown potential of such a compound is applied across the film, the compound partitioned into the film can be electrolytically decomposed. Provided that the electrolytic breakdown products have a high enough vapor pressure to spontaneously leave the film, a versatile sensor, with a current output related to the analyte concentration, is formed. Sensors fabricated from available PFSI materials and functioning in this manner behave essentially as sensors specific for water and the lower alcohols.

Water is omnipresent on this planet. In our present state of existence, the determination of water in a variety of matrices is routinely necessary. Volumes have been written regarding the measurement of water, whether present as a major or a trace constituent (*1*, *2*). Among chemical methods, the Karl Fischer reaction is the best known; new improvements in exploiting this chemistry continue to be reported (*3*, *4*). A plethora of physical methods has been utilized for the measurement of water: IR and near-IR absorption spectroscopy including the use of diode laser sources, photoacoustic detection of surface plasmon resonance (*5–8*), Kr or H glow-tube hygrometry (*9*), thermooscillometry (*10*), direct potentiometry (*11*), cyclic voltammetry (*12*), etc. represent some recent examples. With some samples, direct determination is impossible and prior chromatographic separation from the sample matrix is essential (*13–15*); another often used approach is to generate acetylene by reaction with CaC_2, followed by chromatographic determination of the evolved gas (*16–18*). The reaction of dimethoxypropane with water to form acetone and methanol is well-known and has been utilized in the past for dehydrating various samples (*19–22*). In favorable cases, the products can be measured directly by absorption spectroscopy (*23*); otherwise chromatographic separation is necessary (*24*, *25*). The enthalpimetric sensing of the dimethoxypropane reaction was first developed by Wilson (*26*) and has since been widely exploited in commercial thermometric titrators (*27*). In many cases, direct measurement of water is possible. Chilled mirror hygrometry (*28*) is widely believed to be the most reliable approach but cannot be applied in condensed phases or when other condensable species are present in large concentrations. Reported optical fiber based sensors generally involve a sensing element based on a phase-transition (accompanied by a change of color or opacity) (*29–31*) but such sensors are still to be proven commercially viable. One particularly interesting approach utilized perfluorosulfonate ionomer (PFSI) immobilized Rhodamine 6G; an increase in fluorescence intensity and decrease in fluorescence lifetime are observed with increasing humidity (*32*). Surface acoustic wave moisture sensors, regarded as holding much promise (*33*), are also in the experimental stage.

In presently popular water sensors, one of two basic principles is exploited. Typically, two electrodes are in contact with a substrate with a high affinity for water. Synthetic organic polymers or inorganic ceramic type materials are used as substrates. Sorption of water causes a change in electric properties of the polymer, such as the capacitance, which may be measured by determining the ac impedance of the device. Aluminum oxide is best known for this application (*34*); however, because of superior performance characterics, a silicon-based sensor is rapidly gaining popularity (*2*, *35*). Many other substrates have also been described (*36–42*). With some substrates, it is possible to use the change in dc resistance, rather than ac impedance, as an index of moisture content. However, such an approach is meritorious only if sufficient potential can be applied to the sensor to electrolytically decompose the sorbed water. The solid electrolyte substrate must resist electrolytic breakdown; only two substances have been shown to be applicable for this purpose. Phoshorus pentoxide is well-known for its affinity for water. The electrolysis of syrupy H_3PO_4 as a film between two electrodes yields P_2O_5 as a paste with HPO_3 presumably formed as the intermediate product. The present commercially available versions of this sensor have changed little from the original description by Keidel (*43*); the principle was shown to be applicable to the measurement of moisture in organic liquids as well (*44*). While its ability to measure trace levels of water is an attractive feature, the relative fragility of the P_2O_5 film is a problem. The sensor is generally irreversibly affected upon exposures to high levels of humidity. The search for a better sensor therefore continues.

Within a decade of commercialization of Nafion by Du Pont, this PFSI was shown to be applicable as a solid electrolyte substrate material for an electrolytic water sensor (*45*). Aside from tubular membranes attached to coillike electrodes on the interior and exterior (*45*), planar Nafion membranes have been used with painted-on or pressed-on electrodes (*46*, *47*). Because of the thick film characteristics intrinsic to these designs, the response time to a step change in humidity is diffusion limited to several minutes. The attainable detection limit for water with such sensors or the effects of other compounds or temperatures are not known. Similar devices are, however, being explored for commercial use as a "microdryer", designed to electrolytically "burn off" the water (*48*). In recent years, a new cation exchanger PFSI with properties significantly different from Nafion has been reported by Dow scientists (*49*, *50*). In particular, this PFSI can be synthesized with much lower equivalent weights than Nafion, with correspondingly higher water absorption (*49–51*). In this paper, we report a new class of inexpensive, sensitive, and fast, thin film sensors made from the Dow PFSI and Nafion and characterize them in detail.

EXPERIMENTAL SECTION

Reagents and Supplies. Nafion was obtained as a 5 wt % solution (equivalent weight (EW) ~ 1100, in a medium of 90% lower alcohols/10% water, Aldrich). The solution was diluted 1:1 with 95% ethanol before use. The Dow PFSI, 1,1,2,2-tetrafluoro-2-((trifluoroethenyl)oxy)ethanesulfonic acid, was obtained either as a film (EW ranging from ~600 to ~1200) or as a 2.5 wt % solution in alcohols as a gift from the Dow Chemical Co., Freeport, TX. The sulfonyl fluoride form, the precursor form of the Dow ionomer, was also obtained as a powder. Like Nafion, only the sulfonyl fluoride form can be extruded or pressed into

0003-2700/90/0362-1935$02.50/0

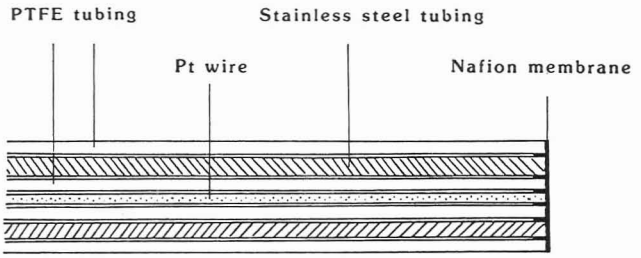

Figure 1. Needle-type RH sensor.

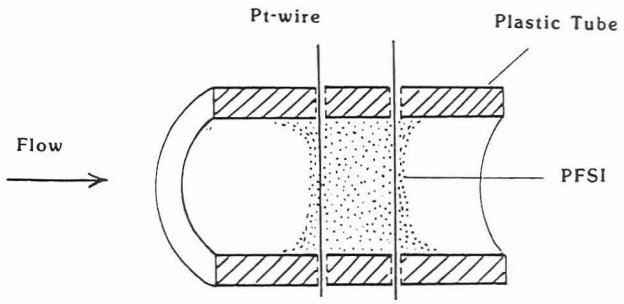

Figure 2. Cross section of flow-through RH sensor. A longitudinal cutaway view is shown. The gas flow is horizontal, along the plane of the paper.

a film. Attempts to form films at the tip of needle type microsensors (vide infra) by thermoforming the sulfonylfluoride powder did not lead to good sensors and this approach was not further pursued. The sulfonic acid polymer was used in solution form, after dilution with 95% ethanol to ≤1.25 wt %. The preformed film material was put in solution essentially following the procedure of Martin et al. (52): weighed amounts of the polymer were dissolved in ethanol–water mixtures by prolonged heating in a poly(tetrafluoroethylene) (PTFE) high pressure bomb (Paar Instrument Co.) at temperatures of 150–240 °C depending on the EW of the polymer.

Noble metal wires (e.g., platinum wires in diameters of 25, 50, and 100 μm) were obtained from Aesar, Inc. Stainless steel needle tubing (type 304) was obtained either in the form of standard hypodermic needles or as lengths of tubing (Small Parts, Inc., Miami, FL).

Instrumentation. Potenial applied to the sensor was supplied from 9-V alkaline batteries, a Harrison 6106A dc power supply (0–120 V, Hewlett-Packard), or an electrophoresis dc power supply (25–310 V, Fotodyne, Inc.). The current flowing through the sensor was monitored in a variety of ways: measuring the voltage drop on a resistor connected in series to the sensor, using an operational amplifier based current → voltage converter, or using a Model 421 picoammeter or a Model 427 current amplifier (both from Keithley instruments). Sensor output was recorded on a multichannel strip chart recorder (Knauer, FRG). The effect of temperature upon the sensor response was determined by locating the sensor (and a length of $^1/_8$ in. diameter copper tubing upstream of the sensor for thermal equilibration of the test gas) inside a liquid chromatography column heater (Model CH-30, Fiatron Systems, Inc., Oconomowoc, WI). Commercial capacitance or ac impedance type sensors were tested respectively with their own electronics or were connected to a Model 213 conductivity detector (Wescan Instruments, Santa Clara, CA) for excitation at 10 kHz.

Sensor Fabrication. Although a number of different sensor configurations were explored, two designs emerged as preeminent and are described here. The first, hereinafter called the needle sensor, utilizes a coaxial design as shown in Figure 1. The end of a hypodermic needle (18–22 gauge) is cut to a blunt terminus and a snugly fitting PTFE insulator tubing is inserted within. A platinum wire, 100 μm in diameter, forms the central electrode. At the rear end of the needle (e.g., inside the hub), an insulating epoxy-based adhesive is applied to hold these components in place and a sturdier lead wire is also soldered to the central Pt conductor and held in place by the adhesive. A PTFE sleeve is then placed outside the needle, this fits snugly around the needle and nearly flush with the needle terminus. A small amount (typically 3 μL) of the PFSI solution is then applied to the top of the needle assembly with a microliter syringe. After the solvent evaporates at room temperature, it is thermally treated by placing in an oven at 70–100 °C for 4–12 h. It has been previously noted that unless thermally cured, solution cast PFSI films of this type can have considerably different properties from films obtained by thermoforming the sulfonyl fluoride and subsequent hydrolysis (*53*). Accordingly, we noted that without the thermal treatment step the sensor response may initially be higher but tends to continually decrease during operation. The thermal treatment step was therefore incorporated in all subsequent experiments. As shown in Figure 1, the PFSI film is formed not just as a planar sheet at the tip of the sensor but also between the outer sleeve and the needle and inside the inner PTFE sleeve. While these aggregations improve the integrity of the sensor by increasing the adherence of the film to the electrodes, it becomes difficult to exactly estimate the mean thickness of the planar portion of the film. On the basis of microscopic examination, we estimate that the aggregate areas can contain as much as 50% of the applied PFSI, the other half being responsible for the planar film. The reported film thickness data are based, however, on the assumption of a planar film only and assumes a polymer density of 2 g/cm^3 (*54*). Sensors with increasing film thicknesses are fabricated by repeating the steps of coating, room temperature evaporation, and thermal treatment. Unless otherwise stated, the results reported are for a needle sensor.

The second design, hereinafter called the flow-through sensor, is shown in cross section in Figure 2. This design utilizes a 1.5 mm i.d., 3 mm o.d. polyurethane tube segment, ca. 2 cm in length. A narrow gauge (≥27) hypodermic needle is used to puncture the wall of the tubing radially. A segment of 50 or 25 μm diameter Pt wire is inserted through the bore of the needle and the needle is then removed. The process is then repeated to place a second wire parallel to and as close to the existing wire as possible. The excess lengths of platinum wires are wrapped around the polymer tube, lead wires are attached to each platinum wire electrode, and the assembly is secured and insulated with parafilm. As with needle sensors, the PFSI film is formed by applying a microaliquot (2–5 μL) of the PFSI solution on the electrode wires inside the tube. As the solvent evaporates, the surface tension of the film pulls the wire electrodes closer; the typical distance between the wires after the film is thermally cured is 100–300 μm. Microscopic examination indicates that much of the polymer material aggregates near the supporting peripheries of the film structure, resulting in a particularly thin central film. In use, the test gas flows through the tube around the sensing film.

The results from two other designs are briefly cited in this work. One design utilizes intedigitated rhodium film electrodes spaced 150 μm apart, deposited on a 1 × 1 cm alumina wafer. The second design contains a cylindrical ceramic element (6.3 mm diameter) on which two rhodium wires (0.2 × 200 mm) are wound in parallel without contacting each other (center-to-center spacing 320 μm). The film was formed on both of these sensors by dip coating several times. The film thickness of these sensors was ≥100 μm. The first of these is referred to as the wafer-type sensor and the second as the cylindrical sensor. The base material for these devices was obtained from EG&G, Inc., Environmental Equipment Division (Burlington, MA) and Chandler Engineering Division (Tulsa, OK), respectively. Low-level humidity testing of these sensors was carried out at these respective facilities.

Test Arrangements. Preliminary results have indicated that while the sensor can be deployed in liquid samples, film adhesion needs to be improved for reproducible results. In the present paper only gas-phase applications of the sensor will be reported. Experiments to determine sensor longevity, stability, response times, etc. were conducted by using the test setup shown in Figure 3. Compressed house air dried through silica gel (relative humidity (RH) ca. 5%) or cylinder nitrogen passed through $Mg(ClO_4)_2$ (RH ~ 0%) flows, regulated by regulator R, through two metallic solenoid-operated three-way valves, V1 and V2 (12 V dc, Skinner valve MBD 002). These valves are controlled by a microprocessor-driven process controller (Micromaster LS, 100 ms resolution, Minarik Electric, Los Angeles, CA); the value acutation time is <25 ms. In one position, the stream flows directly to a serial bank of sensors (flow-through sensors or needle sensors sealed through tee ports). The gas flow (typically ≤ 100 mL/min)

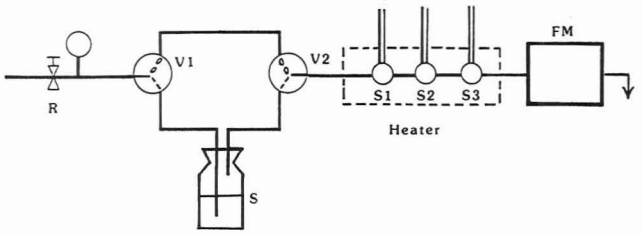

Figure 3. Sensor testing arrangement: R, flow controller; V1, V2, solenoid valves; S, constant humidity solution; S1, S2, S3, sensors; FM, flow meter.

is measured by a digital soap bubble meter. When the valves are actuated, the gas stream bubbles through (or flows close to the surface of) a solution which is known to generate a constant humidity effluent. Saturated NaCl and LiCl solutions were used to generate 75 and 15% RH values (at ca. 25 °C) and solutions of H_2SO_4 of known concentration (*55*) were used to generate all other humidity levels, the lowest test RH being 3.2% corresponding to a H_2SO_4 solution of density 1.70 (~78% by weight). In some experiments, where speed of actuation was not critical, valves V1 and V2 were replaced with an electrically actuated six-port rotary valve (type HVLX 6-6, Hamilton Co.).

Gas chromatography was conducted with a GC–8A gas chromatograph (Shimadzu Scientific) using a homemade 2.5 × 2000 mm PTFE column packed with Chromosorb R (100 mesh, Supelco). Unless otherwise stated, the column and injector temperatures were 110 and 130–140 °C, respectively, with a N_2 carrier gas flow of 20 mL/min. The flowthrough sensor functioned as a detector and was located at ambient temperature outside the oven. Locating the sensor inside the oven results in lower signals. The detector output was acquired by a Shimadzu C-R3A Chromatopac data acquisition system which provided both peak height and area information. The primary consideration in these experiments was to evaluate detector performance; no attempts were made to optimize chromatographic parameters. Unless otherwise stated, the voltage applied to the sensor for all test arrangements was 10 V dc.

RESULTS AND DISCUSSION

Principle of Operation. The first step in sensor operation is the partitioning of water from the surrounding environment into the polymer film

$$H_2O(g) \underset{}{\overset{k_1}{\rightleftharpoons}} H_2O(\text{film}) \qquad (1)$$

The voltage applied to the sensor, E_{app}, is the sume of three components

$$E_{app} = iR + E_a + E_c \qquad (2)$$

where E_a and E_c are the anode and cathode potentials. The resistance of a PFSI film can be quite large at very low humidity levels. Unless E_{app} is sufficiently high to overcome the iR drop, the current through the device can be limited by applied voltage. In other words, the process

$$H_2O(\text{film}) \xrightarrow[k_E]{} H_2(\text{cathode}) + \tfrac{1}{2}O_2(\text{anode}) \qquad (3)$$

may be limited by the applied voltage such that $k_E < k_1$. However, since the exact electrical resistance of the film is a function of the water content, the current through the device is still a measure, albeit not necessarily linear, of the humidity surrounding the device. In the situation that sufficient voltage is applied to the device and the sensor current is not voltage limited, $k_E > k_1$. In this case, the water arriving into the film is electrolyzed almost as soon as it partitions into the film. Under this condition, the sensor current is dependent on the rate of arrival of water into the film, which at any given temperature is a linear function of the water activity of the surrounding environment.

Sensor Design. The difference in overvoltage for hydrogen evolution among different electrode materials is slight compared to the typical voltage applied to the sensor. Stainless steel is an excellent cathode material for the fabrication of needle sensors because of good film adhesion, low cost, and availability in a variety of sizes. On the other hand, the anode must be resistant to oxidation. Stainless steel or gold was found to be unacceptable. Platinum and rhodium both performed well; the former was chosen because of lower cost.

In the needle-type sensor, at a fixed diameter of the cathode, an increase in anode diameter leads to a larger current. However, beyond a certain point, film integrity appears to be adversely affected by increasing anode size, resulting in noise and poor reproducibility. The maximum diameter of the anode used for this sensor was therefore limited to 100 μm and the data reported are for sensors fabricated from this size anode. At a fixed anode diameter, the response increases with a decreasing inside diameter of the cathode. In going from 18 gauge (0.84 mm i.d.) to 22 gauge (0.41 mm i.d.), the response increased, for example, from a few percent to more than an order of magnitude, the difference increasing with decreasing RH. At a fixed applied voltage, this behavior may be attributed to the increasing field strength (vide infra). Unless otherwise stated, the data are reported for sensors fabricated from 18 gauge cathode tubing although the narrower bore sensors yield superior results.

In the flow-through sensor, we observe that although the fabrication becomes an increasingly delicate task, smaller electrode diameters lead to more responsive sensors; this is possibly due to the smaller electrode spacings that are typically obtained when finer wires are used.

Effect of Polymer Type and Film Thickness. The EW of the three different Dow PFSI samples used were approximately 600, 850 and 1150. When fabricated in an otherwise identical manner, sensor response increased with decreasing EW of the PFSI. However, sensors made from the lowest EW film showed a consistent decrease in response with time and microscopic examination suggested that the structural integrity of the film is a problem. On the basis of a systematic study of these ionomers, Moore and Martin (*51*) have found the extent of the water absorption to be inversely proportional to the degree of crystallinity. The lowest EW polymer studied by them (EW 635) was atypical from the rest (the next higher congener studied had an EW of 803) in having essentially no crystallinity, very large ionic cluster size, and equilibrium water absorption nearly twice the weight of the dry polymer itself (an order of magnitude higher than the 1176 EW polymer). It is reasonable that the extent of water absorption determined (under saturation conditions) is related to the intrinsic affinity of the polymer for water, albeit the relationship may not be linear. Water absorption by Nafion is also similarly related to its EW (*56*, *57*). Nafion is inherently less crystalline than the Dow PFSI at comparable EW levels and actually absorbs more water (*50*, *51*). However, Nafion is not available at EW levels below 1100 and it is possible to have lower EW Dow PFSI's with much greater water absorption than the available Nafion material.

The stabilities and relative responses of seven different kinds of needle and flow-through type sensors are shown in Figure 4. The amount of polymer present in each sensor type varies and is indicated; this should be taken into account in considering the relative response. The test arrangement exposes the sensor to a background RH of 5%, with a 2-min exposure to 75% RH every 10 min. At a 75% RH level, the applied voltage (10 V) is sufficient to keep the sensor current from becoming voltage limited. First, the difference in response between the needle and the flow-through type sensors is immediately apparent. With flow-through sensors, increasing the tubing diameter markedly increases the response, presumably due to a larger film area. The current level

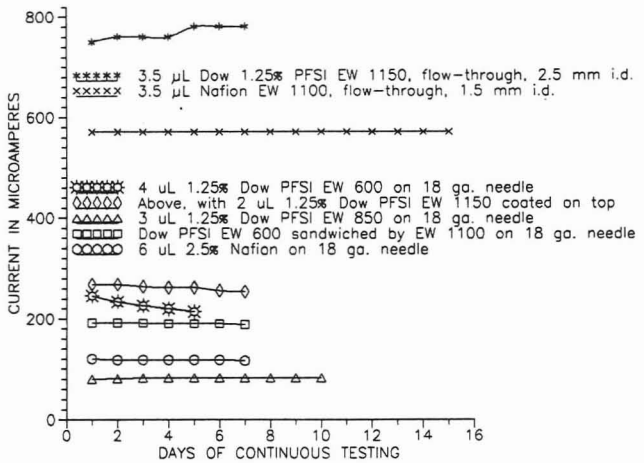

Figure 4. Relative response and stability of different sensors studied.

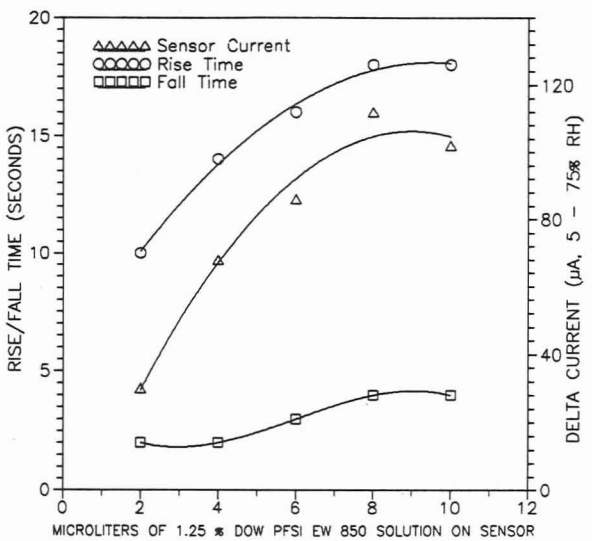

Figure 5. Sensitivity and response time as a function of the amount of polymer on a needle-type sensor.

produced by devices of such size (active film area $\ll 1$ mm^2) is quite remarkable—current levels considerably in excess of 1 mA are elicited by exposing such a sensor to human breath. This corresponds to an electrolysis rate of ~ 6 μg of water/min or nearly 30% of the mass of the polymer per minute.

Among the needle sensors, the response from the Dow PFSI EW 600 film decays over a period of days. A higher EW Dow PFSI film (EW 1150, not shown) yields stable but quite low response levels (<30 μA sensor current). It is reasonable to expect that for layered composite thin films, the ultimate water affinity (or the extent of the response) will be controlled by the layer with the most affinity, within limits of water transport rates through the layer with less affinity. Meanwhile, the structural integrity can be provided by the polymer with the greater crystallinity. Based on these expectations, needle sensors were fabricated by (a) first forming a Dow PFSI EW 600 film followed by a EW 1150 PFSI film on top of it and (b) sandwiching a EW 600 PFSI film between EW 1150 PFSI films. Good response with excellent stability resulted with the sandwich film. Nafion EW 1100 and Dow PFSI EW 850 (note the difference in the amount of polymer used) both yield sensors of excellent stability.

The current observed for any given sensor increases with the amount of polymer present in the sensor, up to a point, for either Nafion or the Dow PFSI. This is illustrated in Figure 5. Response times (10–90% rise time, 90–10% fall time) as a function of film thickness are also shown in this figure. Note that for our sensors the rise time, which is

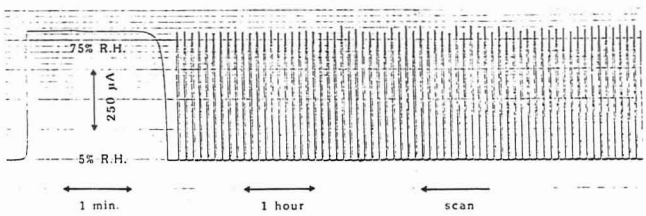

Figure 6. Short- and long-term output of a flow-through type sensor using a 5–75% RH test swing.

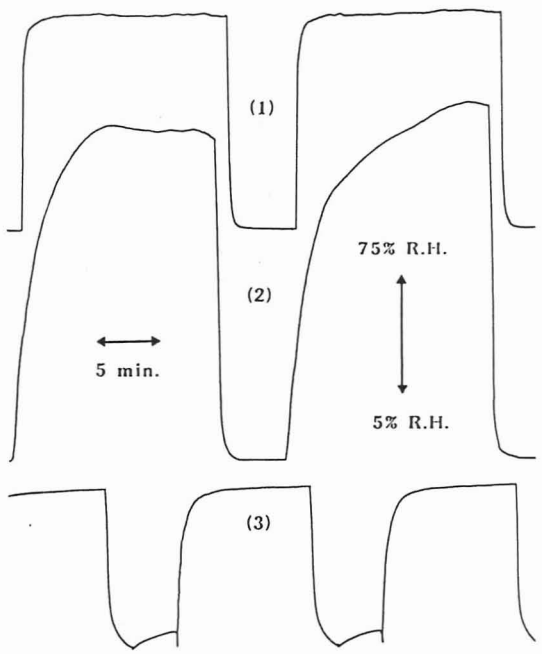

Figure 7. Response behavior of a needle type sensor (1) compared to a commercial ac impedance type sensor (2) and a capacitive sensor (3); 5–75% RH test swing.

controlled both by the resistance to interfacial mass transfer and mass transfer within the film, is always substantially greater than the fall time, which is controlled by the second factor alone. In the following, otherwise unspecified sensors are of the 18 gauge needle type with a ~ 15 μm thick Dow PFSI EW 850 film (3 μL of 1.25% polymer solution used for fabrication).

Response Speed and Reproducibility: Comparison with Commercial Sensors. The uniformity of response of sensors fabricated in an identical manner can be an indication of how uniformly such sensors can be mass produced. With a film thickness of ~ 15 μm, five different sensors yielded a response of 83.2 ± 16.6 μA (5 ↔ 75% RH), a rise time of 9.0 ± 1.6 s, and a fall time of 1.0 ± 0.0 s (each given as mean ± standard deviation). With the sensors recoated a second time in the same manner, the respective figures were 162.4 ± 43.3 μA, 13.2 ± 2.6 s, and 1.5 ± 0.1 s. It is interesting to note that when the same total amount of polymer was coated at a time, the corresponding figures ($n = 5$) were 155.2 ± 11.3 μA, 18.0 ± 5.6 s, 3.0 ± 1.0 s; a significant increase in the response time is evident. For Nafion EW 1100, with a film thickness of ~ 60 μm (6 μL of 2.5% solution), the response amplitude was 132.8 ± 10.0 μA ($n = 5$).

We have not tested a sufficient number of the flow-through sensors under uniform conditions to present statistically meaningful results. However, these sensors are substantially faster than their needle-type counterparts. Fall time is uniformly ≤1 s and the rise time at ambient humidity levels is ~ 2 s with 25-μm electrodes. This is fast enough for the device to function effectively as a detector in gas chromatography with conventional packed columns. Figure 6 shows

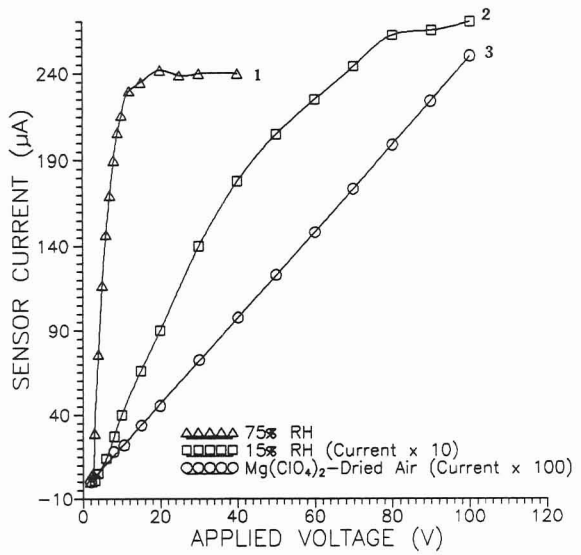

Figure 8. Current–voltage behavior of a needle-type sensor at three different humidities.

the sensor output for a flow-through sensor fashioned from 100-μm electrodes an Dow PFSI EW 850 using a 5–75% RH test swing. Both fast and slow scans are depicted to indicate response times and longer term reproducibility, respectively. Figure 7 shows the performance of two commercial sensors compared to the needle-type sensor (trace 1). Trace 2 is from a quaternary ammonium functionality polymer film sensor (RH-8, General Eastern, Inc.), and trace 3 is from a capacitive element sensor (HP-1, Jenway, Inc.). Rise time for the RH-8 sensor is >5 min and is obviously variable; for the HP-1 sensor it is 1.5 min. Both of these are much slower than the ca. 20 s rise time the needle-type sensor shown in this trace exhibits. Fall times are much shorter and comparable for the different sensors, but even in this case the presently developed sensor is clearly superior. Further, the HP-1 sensor exhibits marked hysteresis and the long-term output precision of the RH-8 sensor upon repeated cycling (not shown) is poor.

Current–Voltage Relationship and Calibration Behavior. Figure 8 shows the current–voltage relationship for the same needle sensor exposed to (1) 75% RH, (2) 15% RH, and (3) <5% RH ($Mg(ClO_4)_2$-dried air). As indicated in the figure, relative to trace 1, the ordinate for traces 2 and 3 are respectively 10- and 100-fold magnified for visual clarity. In trace 1, the plateau voltage is reached by ca. 12 V. The plateau voltage is 95–100 V for trace 2 and in the lowest relative humidity trace, a voltage-independent current region could not be reached at all within an applied voltage of 100 V. Parallel data from an identical sensor, except for a smaller cathode (19 gauge), also indicate that large ohmic drops are involved. The reduced interelectrode distance resulted in a lower plateau voltage for both the 75% and 15% RH cases; for the lowest RH case, the plateau voltage was still unattainable but the slope of the i–V curve became perceptibly lower, suggesting a current plateau at applied voltages $\gtrsim$200 V. At even lower humidities (with a stream of cylinder N_2 dried through $Mg(ClO_4)_2$), a plateau was not reached even with a 22-gauge cathode and an applied voltage of 310 V.

It is well-known that the ionic functionalities in PFSI membranes occur in clusters where the sorbed water accumulates (*53*, *56–58*). The system may be envisioned as islands of water in a matrix of the fluoropolymer backbone. Even in the 75% RH case, the value of the plateau voltage suggests that such islands are not interconnected: if a single water-bearing patch could be traced to both electrodes, the plateau voltage would likely have been attained at lower values. At the considerable field strengths involved (even at an applied voltage of 10 V, the small interelectrode distances of 400–100 μm mean a field strength of 0.25–1 kV/cm), we suggest that the current is carried between the islands of water by H^+ and/or OH^- (or possibly by the aquated electron, see e.g., ref 59); the charge transport is controlled by the electrical field strength between the islands. At high humidity levels, the aqueous cluster areas are large and the interisland hopping distances are small (*58*). Even at modest applied voltages, the field strength across the intervening regions is large enough to permit the current to be limited by the rate of water influx from outside the sensor. In contrast, at very low humidity levels, the water clusters are much smaller with relatively large distances between the clusters (*58*); even at relatively high applied voltages, the overall current conduction is charge transport/field strength limited. This model is supported by the observation that at any given RH value, the minimum voltage necessary to attain the plateau region decreases with decreasing interelectrode distance. It is also noteworthy that the wafer and cylindrical type sensor, with their substantially thicker film coating, attain plateau currents at voltages significantly smaller than their needle-type counterparts. These devices can appropriately be considered as multiple sensors operating in parallel within a three-dimensional polymer film network; the pathways available for charge transport are concomitantly more numerous. The overall resistance is governed by the path of least resistance which is maintained in a dynamic eqiulibrium state by the diffusive transport of water to this region. This is consistent with the three-dimensional percolation models fowarded by Gierke and Hsu (*58*).

This allows us also to make qualitative predictions about the response behavior. As previously stated, for operation under conditions in which the current conduction is not voltage limited, the response should be linearly related to the humidity level to which the sensor is exposed. A needle-type sensor (10 V dc applied) was subjected to a multipoint ($\geq$5) calibration between 0 and 100% RH (at 22 ± 1 °C) on four different days. The entire data set between 20 and 100% RH can be represented by the linear equation

$$\text{current } (\mu A) = (\%\ \text{RH} - 14.24\ (\pm 1.60)) \times 2.245\ (\pm 0.054)$$

with a coefficient of correlation >0.99. The data in Figure 8 clearly indicate that 10 V is not nearly sufficient to attain the plateau current at the low RH end of the above range. Consequently, the above line does not pass through the origin but instead intersects the RH axis at a value of ~14% RH. In reality, of course, the response does not drop to zero at this RH, rather the response below 20% RH deviates from the linear behavior at higher RH levels. As may be expected, a higher applied voltage results in reducing the intercept on the RH axis to lower values and extends the lower limit of the linear range of operation. It is practical to attain linear response over essentially the full meaningful range of ambient humidity levels by a combination of sensor design and operating voltage.

It may not be practical, however, to operate in the voltage-independent response region at levels between 0 and 5% RH (at 25 °C, this corresponds approximately to gas-phase water concentrations of 0–1500 parts per million by volume, ppmv). Although the exact distribution of the water clusters in the film is probably chaotic, let us consider a simplified situation of two point-electrodes x cm apart imbedded in a three-dimensional polymer matrix with a single spherical (*58*) water cluster of diameter l cm ($x \gg l$) present in the straight line connecting them. (It can be easily shown that the specific number of clusters considered in such a model is immaterial.) Let the field strength across the water cluster be E_1 and the field strength across the polymer backbone be E_2. We assume

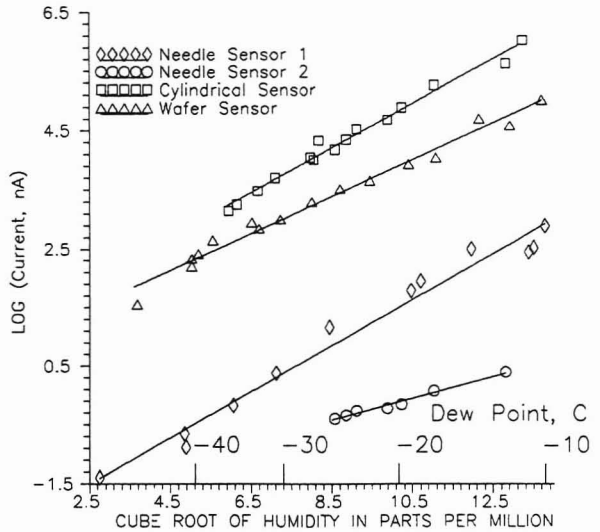

Figure 9. Response of four different electrolytic thin film PFSI sensors at low humidity levels.

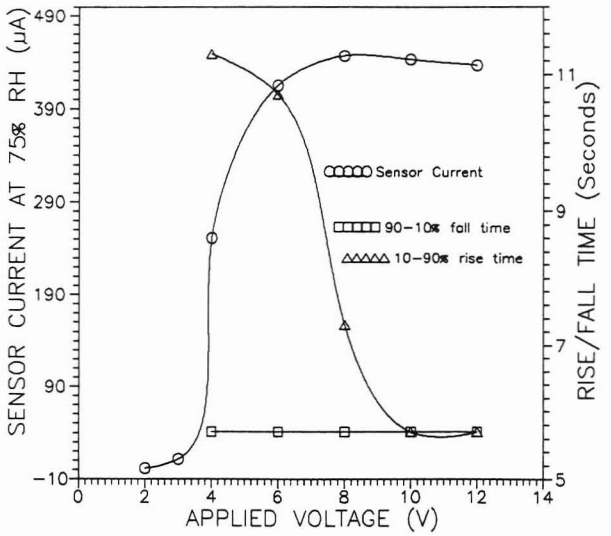

Figure 10. Response times and sensitivity for a needle-type sensor as a function of applied voltage.

that the current is linearly proportional to the field strength across the polymer backbone

$$i = KE_2 \tag{4}$$

where i is the current and K is a constant of proportionality. The dimension of the water cluster is dependent on the humidity level. The total applied voltage V is given by

$$V = lE_1 + (x - l)E_2 \tag{5}$$

When the first term in eq 5 is negligible

$$V = (x - l)E_2 \tag{6}$$

Equations 4 and 6 yield

$$i = KV/(x - l) \tag{7}$$

A logarithmic transformation of eq 7 yields

$$\ln i = \ln (KV/x) - \ln (1 - l/x) \tag{8}$$

since $l/x \ll 1$, $\ln (1 - l/x) \simeq -l/x$ and eq 8 takes the form

$$\ln i = \text{constant} + l/x \ldots \tag{9}$$

For spherical water clusters (*58*), l would be linearly related to the cube root of the humidity level, if a straightforward partition model prevails. Thus, we expect a linear dependence between the logarithm of the response and the cube root of the humidity at low humidity levels. Figure 9 shows the response of four different sensors at low humidity levels. In a three-dimensional model of truly chaotic distribution of the water clusters, it is likely that a fractal relationship may be more applicable. Such a general case requires that the logarithm of the current be linearly related to the logarithm of the water concentration. The plot shown in Figure 9 is a specially constrained case of the above general relationship.

While the data in Figure 9 provide some general confirmation of the model represented by eqs 4–8, it can be equally well argued that phenomenologically the resistance of the film is a function of its water content because the latter may control the ionization of the $-SO_3H$ group in the polymer. Present experimental approaches cannot provide an unequivocal solution as to the correctness of this explanation.

Although the current–humidity relationship does not remain the same over the entire range of operation,the dynamic range of the sensor is competitive with existing alternatives. With the same applied voltage, the cylindrical and wafer sensors tend to produce more reproducible readings at very low humidities than the needle sensor. As previously noted, these macrosensors behave as an assemblage of microsensors in parallel. This essentially results in statistical consequences. The larger fluctuations observed for an individual single needle-type microsensor are understandable in that there are likely a multitude of cluster sites where water aggregation can occur. If this occurs in a chaotic manner, specific sites which are occupied (the geometric location of which, vis-a-vis the electrodes, governs the resistance) may not be the same each time the device is brought from a drier to a wetter environment. At higher humidities this does not pose a problem because of the much larger number of clusters (and hence the statistically larger number of pathways for current conduction) that exist. An assessment of the preliminary reproducibility data indicates that at an applied voltage of 15 V, the lower practical limit of an 18 gauge needle sensor is likely to be a dew point of −40 °C (~130 ppm H_2O) and that for a macrosensor like the wafer sensor is likely to be −55 °C (~20 ppm H_2O). These figures should improve with higher applied field strengths (reduced interelectrode distance and/or higher applied voltage. It is possible that a constant current mode of operation with a series resistor for safety protection, with the applied voltage being the output parameter, may have advantages for low humidity sensing. The performance of the thin film electrolytic PFSI sensors is notable especially in view of Huang's recent assessment, based on his long-standing work at NIST in this area, of the present status of polymeric RH sensors—such sensors are "generally characterized by low sensitivity at high levels of relative humidity" (*60*).

The magnitude of the applied voltage has consequences on the response time as well. This is true even at relatively high RH. The current level, rise time and fall time for a 19-gauge needle sensor is shown for a 5 ↔ 75% RH test cycle in Figure 10 as a function of applied voltage. It seems that the ultimate response times are obtained only at applied voltages large enough to reach the plateau current and this is consistent with the general model. Although Figure 10 does not show any marked change in the fall time, the fall time is also a function of applied voltage at lower humidity levels.

Thermodynamic Behavior. Effect of Temperature. Huang (*40*, *41*, *60*) has studied thin film capacitive sensors fabricated from PVC–styrenesulfonate and PFSI's bearing both sulfonic and carboxylic acid groups. In particular, response to different water vapor concentrations was tested at various temperatures and the values of ΔG, ΔH, and ΔS for the process of water sorption by the polymer thence computed. ΔH was found to be essentially temperature independent but strongly dependent on the water vapor concentration, de-

creasing with increasing humidity. The heat of adsorption per mole of water ranged from ~16.8 kJ/mol at 5% RH for the PVC–styrenesulfonate film to 2.3 kJ/mol at 97% RH for the PFSI bearing $-SO_3H$ and $-CO_2H$ groups. The general problem with this type of sensor was hysteresis. Huang felt that this would be solved by systems exhibiting increased enthalpy and entropy changes (*40*). Further, although detailed data were not presented, Nafion films were found to exhibit drastically decreased sensitivity at RH values greater than 40–50% (*41*, *60*). The hysteresis problem in capacitive sensors has much to do with desorption kinetics. This does not apply to the present sensors because the adsorbed water is electrolytically decomposed. As previously shown in Figures 6 and 7, even when cycled over a large RH range, there is no evidence of detectable hysteresis in these sensors.

However, the partition equilibrium given by eq 1 is affected by temperature regardless of the measurement principle. The response of the present sensors decreases with increasing temperature at constant water vapor pressure. The response to 75% RH (referred to 25 °C) for a number of different sensors was tested at 25–150 °C at 25 °C intervals. All Arrhenius type plots (ln i vs $1/T$) exhibited linear correlation coefficients better than 0.99 and the mean ΔH values obtained for the Dow PFSI EW 850, Nafion EW 1100, and Dow PFSI EW 850 sandwiched by Nafion on either side were respectively 18.3, 10.7, and 11.6 kJ/mol respectively. Considering that this test was conducted at a high RH of 75%, the ΔH value for the Dow PFSI is significantly higher than those determined by Huang for PFSI's and other polymers, granted that we assume no temperature dependence for ΔH. It should also be reported here that the ΔH values reported above are significantly smaller than those reportedly obtained for Nafion by direct calorimetry (*61*). In any case, the relative order for the ΔH values reported above should be correct regardless of the exactness of the absolute values. The larger enthalpy changes for the low EW Dow PFSI's are consistent with a greater intrinsic affinity for water. While intrinsic sensitivity should be better therefore for the low EW Dow PFSI, a high ΔH value also means increased temperature dependence. However, most absolute humidity measurement schemes do require temperature measurement. Correction in the present case is simple inasmuch as the system exhibits Arrhenius behavior. Because the thermal mass of the needle sensor is very small, we are also presently experimenting with sensors containing integral Peltier heat pumps to provide thermostating.

Temperature also affects the response times. The rise time is affected somewhat more than the fall time; the exact degree is dependent on the film thickness. For a needle sensor with a ~30-μm film and a test RH swing of 5 ↔ 75% (referred to 25 °C), the response times decreased by ~50% in going from 25 to 50 °C; no further significant decrease occurred thereafter.

Effect of Flow Rate. As tested with the needle-type sensor located in the short arm of a 2 mm i.d. tee, the response is insensitive to test gas flow rate at least down to 10 mL/min.

Response to Other Compounds. Gas Chromatographic Experiments. Polymeric capacitive or resistive sensors are generally not specific for water. Usually, such sensors are calibrated over saturated salt solutions of known humidity (*55*). However, most users know that commercial sensors of this type cannot be reliably calibrated over salt solutions which contains a significant vapor pressure of a substance other than water. For example, a saturated solution of potassium acetate is a good low RH calibrant but cannot be used because the sensors respond to acetic acid. Such interferences are inconsequential in applications involving the measurement of ambient humidity, where water vapor is by far the predominant species to which the sensor responds. In many other

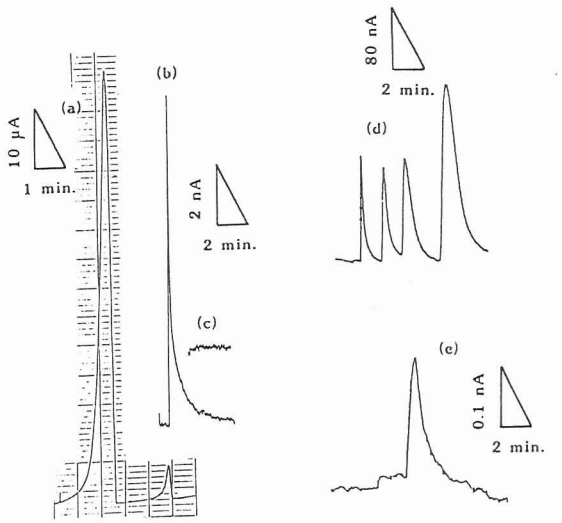

Figure 11. Sensor as a detector specific for water and alcohols: (a) 2 μL of 99% ethanol–1% water, (b) 2 μL of benzene containing 250 ppm water, (c) 50 μL of Na-dried benzene, (d) 4 μL of 1% methanol, 1% ethanol, 5% 2-propanol, and 5% 1-propanol in *n*-heptane, (e) 58 ng of water in dry nitrogen. For multiple peaks, all are cited in order of elution. The carrier gas is dry nitrogen.

applications, it is essential that the extent of sensor response to other compounds be known. We can divide potential test compounds in four general classes: acids, bases, neutral polar, and apolar. The general experimental strategy followed in this work was to inject a liquid test sample into a gas chromatograph under conditions that will separate the water present in the sample from the sample matrix (the separation being verifiable by a general detector such as a thermal conductivity detector) using the flow-through sensor as the principal detector. The detector response to water under the precise experimental conditions could be determined by directly injecting a microsample of water or, more accurately, by performing a series of standard additions of water to the sample. The response ratio (in terms of peak area counts) per unit mass of water injected relative to unit mass of the matrix constituent, as well as the initial water content of the sample, could thus be calculated. The approach is experimentally straightforward because rigorous drying of the test sample is not necessary.

As may be expected, no response whatsoever was observed from nonpolar hydrocarbons like benzene, toluene, xylene, heptane, etc. Figure 11b shows a chromatogram of a 2-μL injection of a benzene sample containing 250 ppm water. The matrix response is below the noise level. Only higher polar compounds partition into the PFSI films. Compounds of intermediate polarity, e.g., diethyl ether or dichloromethane, produced no response either. In order to produce a response, the test substance not only must partition into the PFSI film but must also to be electroactive. No response was observed from highly polar neutrals such as acetonitrile. Acids such as acetic or formic can be electrolyzed but are inhibited from partitioning into the strongly acidic PFSI film due to the Donnan barrier. The sensor was selective by a factor of >2700 and >3100 for water over HCOOH and CH_3COOH, respectively. No response was observed from weakly acidic ethyl mercaptan or H_2S (direct gas injection). Electroactive polar neutrals also respond. The most significant response is observed from alcohols which are discussed separately below. Other compounds in this class include, for example, acetone, formaldehyde, etc. The mass selectivity of the sensor for water is ~8800 over acetone in terms of area counts; it was not possible to accurately determine the corresponding selectivity for water over formaldehyde because of experimental difficulties. Based on the vapor pressure, formaldehyde may not

partition into the film as well as acetone and results indicate that the value of the selectivity factor is at least comparable to that for acetone. Most basic compounds of potential importance are not electroactive. Dimethylformamide, for example, elicited no response. One potential concern with a basic gas, e.g., ammonia, methylamine, or diethylamine, is that it may irreversibly change the sensor response by occupying the cation exchange sites. Fortunately, this has proved not to be a problem. Presumably the cations migrate to the cathode where an excess of OH^- forms the free base and the free base is then desorbed. Exposure to high levels of a base, e.g., putting the sensor over a bottle of concentrate NH_4OH, does change the sensor response, but the effect is reversible. To date we have not found any compound that irreversibly poisons the sensor.

Other than water, alcohols represent the most important class of compounds to which the present sensor responds. The area response ratio of water and various alcohols was in the order 26:2.5:2.8:1.0:2.0:1.9 for water, methanol, ethanol, 2-propanol, 1-propanol, and 1-butanol. The sensor response to methanol is lower than that to ethanol probably due to a lower tendency of the former to partition into the film. The response then decreases slowly along the series of *n*-alcohols; it is notable that 2-propanol responds much less than 1-propanol. The sensor also responds to glycerol and ethylene glycol but it was not possible to obtain reliable response factors because of the low vapor pressures of these compounds. The sensor can be effectively used as a chromatographic detector for the lower alcohols. Some examples are shown in Figure 11. Obviously, reliable values for either alcohols or water are not possible to obtain without chromatographic separation if both are present in significant amounts. Identification of the products is necessary for a full elucidation of the mechanism of response to alcohols. With an appropriate molecular-sieve-packed cartridge at the front end to remove water, it is possible that the present device can be configured into an attractive sensor for the measurement of breath alcohol levels.

Limit of Detection. Figure 11e shows the response of a needle sensor (background $Mg(ClO_4)_2$-dried N_2) when 58 ng of water in 100 μL of N_2 is injected over a period of 200 ms. Obviously, the base width of the peak ($\sim$150 s) is much greater than the injection period. It is both a consequence of operation at a voltage (10 V) much lower than the plateau voltage and adsorption/desorption from the connecting tubing. This makes it difficult to obtain an accurate estimate of the limit of detection. However, we conservatively estimate that the detection limit should be $\leq$10 ng/s with a quality measuring instrument (a Keithley Model 427 current amplifier was used to obtain the results in Figure 11e). While operation at a higher field strength is expected to improve the detection limit further, an alternative approach is to modify the PFSI film to increase its intrinsic affinity for water. We hope to report on such sensors in the future.

ACKNOWLEDGMENT

We acknowledge the interest and assistance of Stanley Ronchinsky and Prabhakar Rao of EG&G, Inc., in characterizing the sensor. We are indebted to David A. Babb, Dow Chemical (Freeport, TX), for the gift of the Dow PFSI material and to the Division of Analytical Sciences, Dow Chemical (Midland, MI), for active encouragement. We thank Douglas L. Strong for a meticulous review of this manuscript.

LITERATURE CITED

(1) Mitchell, J. Jr.; Smith, D. M. *Aquametry*, Parts I–III, Wiley: New York, 1977–1984.
(2) Carr-Brion, K. *Moisture Sensors in Process Control*; Elsevier: New York, 1986.
(3) Dahms, H. U.S. Patent 4,786,602, November 22, 1988.
(4) Liang, C.; Vacha, P.; Van der Linden, W. E. *Talanta* **1988**, *35*, 59–61.
(5) Mucha, J. A.; Barbalas, L. C. *Instrum. Soc. Am. Trans.* **1986**, *25*, 25–30.
(6) Ludvik, J.; Hilgard, S.; Volke, J. *Analyst* **1988**, *113*, 1729–1731.
(7) Dec, D. A. *Annu. Meet.—Air Pollut. Contr. Assoc.* **1986**, *5*, 86/71.4 (79th Annual Meeting, 1986).
(8) Matsubara, K.; Kawata, S.; Minami, S. *Appl. Spectrosc.* **1988**, *42*, 1375–1379.
(9) Campbell, G. S.; Tanner, B. D. *Moisture Humidity: Proc. Int. Symp.* **1985**, 609–614 (Instrument Society of America, Research Triangle Park, NC).
(10) Gast, T.; Talebi, R. *Thermochim. Acta* **1987**, *119*, 37–45.
(11) Karim, M. R. O. *Analyst* **1987**, *112*, 1369–1371.
(12) Atanasoski, R. T.; Law, H. H.; McIntosh, R. C.; Tohias, C. W. *Electrochim. Acta* **1987**, *32*, 877–886.
(13) Popescu-Dimofte L. M. Romanian Patent 90,834. January 30, 1987.
(14) Stevens, T. S.; Small, H. U.S. Patent 4,696,904, September 29, 1987.
(15) Yamaguchi, K.; Shibamoto, T. *J. Chromatogr. Sci.* **1988**, *26*, 588–590.
(16) Sarafyan, G. D.; Ovsepuan, A. M.; Ter-Stepanyan, E. S.; Ter-Gevorkyan, S. T. *USSR Prom-St. Stroit Arkhit. Arm.* **1988**, (8), 67–68.
(17) Loeper, J. M.; Grob, R. L. *J. Chromatogr.* **1988**, *457*, 247–256.
(18) Loeper, J. M.; Grob, R. L. *J. Chromatogr.* **1989**, *463*, 365–374.
(19) Beckman, H. J.; Dierichs, R. *Histochemistry* **1982**, *76*, 407–412.
(20) Truter, E. J.; Davids, S.; Williams, E. D. F. *Proc. Electron. Microsc. Soc. S. Afr.* **1980**, *10*, 13–14.
(21) Bredeweg, R. A.; Rothman, L. D.; Pfeiffer, C. D. *Anal. Chem.* **1979**, *51*, 2061–2063.
(22) Postek, M. T.; Tucker, S. C. *Can. J. Bot.* **1976**, *54*, 872–875.
(23) Critchfield, F. E.; Bishop, E. T. *Anal. Chem.* **1961**, *33*, 1034–1037.
(24) Martin, J. H.; Knevel, A. M. *J. Pharm. Sci.* **1965**, *54*, 1464–1470.
(25) Dix, K. D.; Sakkinen, P. A.; Fritz, J. S. *Anal. Chem.* **1989**, *61*, 1325–1327.
(26) Wilson, E. W. Ph.D. Dissertation, University of Alabama, Tuscaloosa, AL, 1968.
(27) SANDA, Inc., Philadelphia, PA. Application Note on the Thermometric Titration of Water, 1989.
(28) Clevett, K. J. *Process Analyzer Technology*; Wiley: New York, 1986; pp 420–424.
(29) Boltinghouse, F.; Abel, K. *Anal. Chem.* **1989**, *61*, 1863–1866.
(30) Elliott, S. B. Int. Patent Appl. WO 87 00 925, February 1987.
(31) Elliott, S. B. *Moisture Humidity: Proc. Int. Symp.* **1985**, 717–728 (Instrument Society of America, Research Triangle Park, NC).
(32) Zhu, C.; Bright, F. V.; Wyatt, W. A.; Hieftje, G. M. *Proc. Electrochem. Soc.* **1987**, *87*-9, 476–483.
(33) Huang, P. H. *IEEE Trans. Electron Devices* **1988**, *35*, 744–749.
(34) Fong, V. *Moisture Humidity: Proc. Int. Symp.* **1985**, 345–358 (Instrument Society of America, Research Triangle Park, NC). Chleck, C. *Ibid.* 615–621; Hammond, R. H. *Ibid.* 843–848; Cucchiara, O.; Mittelman, M. *Ibid.* 895–902.
(35) Stephen, S. A. *Res. Dev.* **1989**, (2), 169–170.
(36) Uchikawa, F. Eur. Patent Appl. EP 191 627, February 14, 1985.
(37) Madou, M.; Sher, A.; Spindt, C.J. Int. Patent Appl. WO 88 00 341, January 14, 1988.
(38) NEC Corporation. Japanese Patent JP 60 27 850, July 25, 1983.
(39) Lusakszewicz, J. P.; Siedelewski, J. *Springer Ser. Solid-State Sci.* **1987**, *76*, 428–431.
(40) Seiyama, T. *Kinzoku Hyomen Gijutsu* **1986**, *37*, 724–732.
(41) Huang, P. H. *Sensors Actuators* **1985**, *8*, 23–28.
(42) Huang, P. H. U.S. Patent 4,681,855, July 21, 1987.
(43) Keidel, F. A. *Anal. Chem.* **1959**, *31*, 2043–2048.
(44) Cole, L. G.; Czuha, M.; Mosley, R. W.; Sawyer, D. T. *Anal. Chem.* **1959**, *31*, 2048–2050.
(45) Lawson, D. D. U.S. Patent 4,083,765, April 11, 1978.
(46) Ishifuku Metal Industry Co., Ltd., Japanese Patent JP 60 36 947, February 26, 1985.
(47) Yamanaka, A.; Kodera, T.; Fujikawa, K.; Kita, H. *Denki Kagaku* **1988**, *56*, 200–201.
(48) Hirschfeld, T. *CHEMTECH* **1986**, *16*, 118–123.
(49) Ezzell, B. R.; Carl, W. P.; Mod, A. U.S. Patent 4,417,969, November 29, 1983.
(50) Ezzell, B. R.; Carl, W. P., Mod, W. A. *AIChE. Symp. Ser.* **1986**, 82 (248), 45–50.
(51) Moore, R. B., III; Martin, C. R. *Macromolecules* **1989**, *22*, 3594–3599.
(52) Martin, C. R.; Rhoades, T. A.; Ferguson, J. A. *Anal. Chem.* **1982**, *54*, 1639–1641.
(53) Moore, R. B., III; Martin, C. R. *Macromolecules* **1988**, *21*, 1334–1339.
(54) E. I. du Pont de Nemours and Co., Product Information Literature, Nafion Perfluorosulfonic Acid Products, 1976.
(55) Weast, R. C., Astle, M. J., Eds. *CRC Handbook of Chemistry and Physics*, 62nd ed., CRC Press: Boca Raton, FL, 1981.
(56) Gierke, T. D.; Munn, G. E.; Wilson, F. C. *J. Polym. Sci. Polym. Phys. Ed.* **1981**, *19*, 1687–1704.
(57) Fujimura, M.; Hashimoto, T.; Kawai, H. *Macromolecules* **1981**, *14*, 1309–1315.
(58) Gierke, T. D.; Hsu, W. Y. *ACS Symp. Ser.* **1982**, *No. 180*, 283–307.
(59) Walker, D. C. *Can. J. Chem.* **1967**, *45*, 807–811.
(60) Huang, P. H. *Sensors Actuators* **1988**, *13*, 329–3379
(61) Escoubes, M.; Pineri, M. *ACS Symp. Ser.* **1982**, *No. 180*, 9–23.

RECEIVED for review April 16, 1990. Accepted June 26, 1990. This work was supported partially by an unrestricted grant from Dow Chemical Co., Midland, MI, and partially by the Office of Basic Energy Sciences, U.S. Department of Energy, through DE-FG05-84ER-13281.

Effect of Particle Size and Modulation Frequency on the Photoacoustic Spectra of Silica Powders

Raghoottama S. Pandurangi and Mohindar S. Seehra*

Physics Department, West Virginia University, Morgantown, West Virginia 26506

Investigations of the infrared spectra of crystalline and amorphous silica particles of different sizes (0.05, 5, 10, 15, 30, 45, and 260 μm) in the range of 400–4000 cm^{-1} using Fourier transform infrared/photoacoustic spectroscopy are reported. The change in the intensity I of the signal with porosity ϵ of powders follows the $\epsilon/(1-\epsilon)$ dependence for strong bands and ϵ dependence for weaker bands as predicted by the theory of McGovern et al. For strong bands, I also follows the empirical relation $I \sim D^{-n}$, where D is the particle diameter in cm and $n = 0.34$–0.42. The anomalous positive frequency dependence of I on the modulation frequency f observed for the stronger bands in the 45-μm and 260-μm particles is believed to result from saturation. Some observations on the effect of changing the background from (carbon black) powder to pellet are also made.

INTRODUCTION

Since the publication of the Rosencwaig–Gersho (RG) theory on the photoacoustic effect in solids (*1*, *2*), Fourier transform infrared/photoacoustic spectroscopy (FTIR/PAS) has become an important technique for obtaining the IR spectra of surfaces and materials in their natural state (*1–12*). In the one-dimensional RG theory, the incident radiation, modulated at frequency f, is absorbed by the material to a depth $\mu_\beta = 1/\beta$ (β = absorption coefficient), thus setting up temperature variations in the material. These variations heat the adjacent gas/solid interface leading to the pressure fluctuations of the gas above the sample, which in turn is detected by microphone as a PA signal. The thermal wave originating from no deeper than the thermal diffusion length $\mu_s = (2k/\pi\rho cf)^{1/2}$ in the material contributes to the PA signal (here k, ρ, and c are respectively the thermal conductivity, density, and specific heat of the material). Since μ_s can be varied by varying the experimental parameter f, depth profiling by PAS is possible and a number of papers on this subject have appeared in recent years (*2–10*). Another important phenomenon is saturation which occurs when the material thickness $l > \mu_s > \mu_\beta$ (*1–12*).

The original promise of PAS for use with powder samples, without the need to "prepare" samples as in FTIR spectroscopy, has not yet been fully realized because of several complications. Theoretical works by Monchalin et al. (*13*) and McGovern et al. (*14*) showed that the interstial gas in the voids of the powders can act as amplifier and that, for the same mass, a finer powder is expected to yield higher PA signal than a coarser powder. Although in a number of earlier studies (*15–21*) an increase of PA signal with decreasing particle size has been observed, a quantitative check on the equations developed by McGovern et al. (*14*) has not yet been made. It is necessary to understand the particle size effects in PAS if the promise of PAS for IR spectroscopy of powders is to be realized. In this paper, we report results of a detailed study on the PAS of silica powders for the particle size range of 0.05–260 μm and compare the results with theory (*14*). We have also investigated the frequency dependence of the various IR modes in these powders and show that the saturation phenomenon affects at least some of the observations. Some observations on the effects of pellet vs powder background are also reported (*22–24*). Details of these findings are presented and discussed in this paper.

* Author to whom correspondence should be addressed.

Table I. Tabulation of the Porosity ϵ and $\epsilon/(1-\epsilon)$ for Different Particle Sizes

particle diameter, μm	porosity ϵ	$\epsilon/(1-\epsilon)$
0.05 (powder)	0.97	32.33
0.05 (pellet)	0.66	1.94
5 (powder)	0.79	3.76
5 (pellet)	0.61	1.56
10 (powder)	0.78	3.55
30 (powder)	0.64	1.78
45 (powder)	0.48	0.92
260 (powder)	0.46	0.85

EXPERIMENTAL SECTION

Here, measurements are reported on Min-U-Sil, a crystalline form of SiO_2, and Cab-O-Sil, an amorphous form of SiO_2. In a recent paper (*24*), we have given the details of our studies on the electron microscopy, FTIR spectroscopy, and cytotoxicity of these two forms of silica. For the work reported here we used Min-U-Sil particles of mean size 5, 10, 15, 30, 45, and 260 μm, and these samples were obtained from several sources (U.S. Silica Inc., Berkely Springs, WV, and Mill Creek, OK; Alfa Products; 88316 and 88777). Cab-O-Sil, of mean particle size 0.05 μm (*25*), was obtained from Cabot Corp. of Tuscola, IL.

All the spectra reported here were taken with a Mattson Instruments Cygnus-100 FTIR spectrometer, equipped with an MTEC photoacoustic cell. The spectrometer and the sample zone are flushed continuously with dry air using the Balston air filter system, in order to avoid interference from carbon dioxide and water bands. Typically 32 scans at resolution of 4 cm^{-1} were used to collect the spectra from 400 to 4000 cm^{-1} range. The spectra are modulated with different mirror speeds v ranging from 0.08 to 0.18 cm/s, leading to modulation frequency $f = 2v\bar{\nu}$. This gives, e.g., $f = 1.44$ kHz for $\bar{\nu} = 4000$ cm^{-1} at $v = 0.18$ cm/s.

In the theory by McGovern et al. (*14*), porosity ϵ of the powders defined by $\epsilon = (\rho_s - \rho)/\rho_s$ is important where ρ is the apparent density of the powder and ρ_s is the density of silica in solid state ($\rho_s = 2.65$ g/cm^3). To measure ρ and hence ϵ, we measured masses of different powders in a standard 1-mL flask, and these values of ϵ for different powders are given in Table I. For Cab-O-Sil, our measured value of $\epsilon = 0.97$ agrees very well with the value given by McGovern et al. (*14*). For pellets, volumes were easily measured by measuring physical dimensions with a micrometer.

THEORY OF PAS OF POWDERS

The main result of the calculations by McGovern et al. (*14*), which in turn were based on the theory by Monchalin et al. (*13*), is that for powders with porosity ϵ, there are two contributions to the intensity of the PA signal: the thermal signal from the solid which is well described by the RG theory and a pressure signal due to the interstitial gas which acts as an amplifier. The pressure signal depends on the porosity ϵ and the total signal I can be written in a simple form (*14*) as

$$I = A\left\{1 + B\frac{\epsilon}{(1-\epsilon)}(1 - \exp[-(1-\epsilon)\beta l])\right\} \qquad (1)$$

0003-2700/90/0362-1943$02.50/0

Table II. Values of μ_s, β, and μ_β for Different Bands and for Different Modulation Frequencies

band, cm^{-1}	frequency, Hz	μ_s, μm	β,[a] cm^{-1}	$\mu_\beta = 1/\beta$ (μm)
1080	173	85	960	10.4
	260	70		
	389	56		
797	126	100	294	34
	190	85		
	284	68		
693	111	107	53	189
	166	92		
	249	73		
1875	300	67	25	400
	450	54		
	675	44		
3750	600	46	*b*	
	900	38		
	1350	31		

[a] Spitzer, W. G.; Kleinman, D. A. *Phys. Rev.* **1961**, *121*, 1324. [b] Not known.

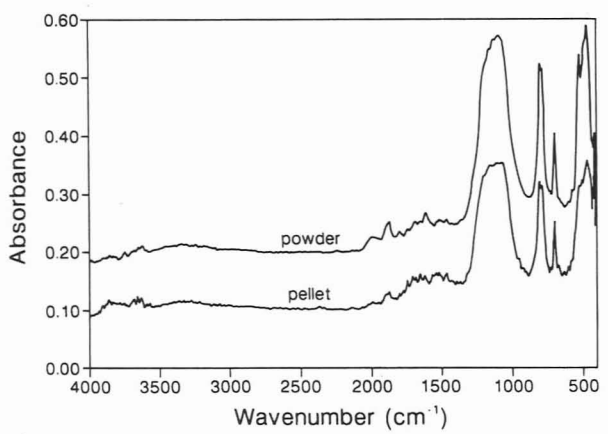

Figure 1. PA spectra of 5-μm particles of 3.5 mg of silica, both in the powder and the pellet form.

where the second term in eq 1 is the pressure term and A and B are constants depending upon the properties of the solid and the gas. If $(1 - \epsilon)\beta l \ll 1$ (weak absorption), then the pressure term reduces to $B\beta l\epsilon$ (proportional to ϵ). On the other hand, for strongly absorbing IR modes, $(1 - \epsilon)\beta l \gg 1$ and the exponential term in eq 1 $\rightarrow$ 0. This leads to $\epsilon/(1 - \epsilon)$ dependence of I. Note that in the limit $\epsilon \rightarrow 0$, $I = A$, the thermal signal. We will check the validity of eq 1 with the observations reported here on silica particles and with the data on other materials reported in literature (*21*).

In Table II, we list the calculated values of the thermal diffusion length μ_s and the optical absorption length $\mu_\beta = 1/\beta$ for different bands of silica at different modulation frequencies (see Figure 1). These quantities are important for discussing the saturation phenomenon for various bands in particles of different sizes.

RESULTS

The PA spectra of the 5-μm particles of Min-U-Sil, both in the powder and pellet forms, with carbon black powder as background, are shown in Figure 1. In this case, 3.5 mg of silica is used and the pellet was made under a pressure of 1500 lb/in.^{2} (1.03×10^7 N/m^2). It is clear that the intensity of all the bands is higher for the powder sample as compared to the pellet, increase being of the order of 75%. Also some of the weaker bands, viz. the 1875- and 1609-cm^{-1} bands, are well-defined only for the powder sample. By use of the porosity values of Table I, it is clear that the above difference may simply be related to the pressure signal due to the interstial gas which is lowered in the pellet.

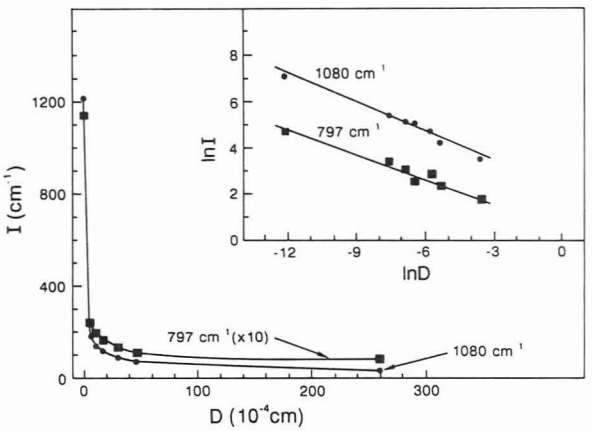

Figure 2. Intensity I of the 797- and 1080-cm^{-1} bands plotted as a function of mean particle diameter D. Inset: ln I vs ln D for the same data. The solid lines are fits to the empirical eq 2, with $n = 0.42$ and 0.34 for the 1080- and 797-cm^{-1} bands, respectively.

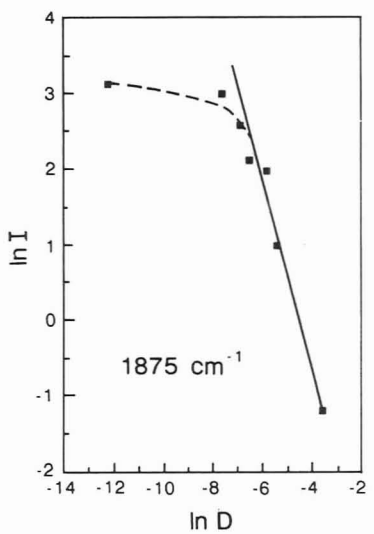

Figure 3. Plot of ln I vs ln D (similar to inset of Figure 2) for the 1875-cm^{-1} band. The solid line is a least-squares fit to the data for the six larger particles with $n = 1.06$, whereas the dashed curve is drawn by connecting the data points.

To compare the signal I for different particle sizes and porosity values, we used 1 mg of each sample to take the spectra. The intensity I of each band was computed in inverse centimeters by computing the area under each band with a computer option available on the Cygnus-100. In Figure 2, we have plotted I for two intense bands, viz. 797 and 1080 cm^{-1}, against the mean diameter D of the particles. (The data for the 693-cm^{-1} band is not plotted because this band is absent in amorphous silica (*24*) and its intensity is too weak for the larger particles of 45 and 260 μm size). The increase in I with decreasing D is qualitatively similar to some earlier reports (*16–18*). However a quantitative understanding of this kind of data has been lacking so far.

In the inset of Figure 2, ln I vs ln D is plotted. The excellent fit obtained suggests that I varies with D as

$$I \sim D^{-n} \qquad (2)$$

The solid lines are the least-squares fit to the data with $n = 0.34 \pm 0.04$ for the 797-cm^{-1} band and $n = 0.42 \pm 0.03$ for the 1080-cm^{-1} band. These values of n are intriguingly close to 1/3. However for the weaker 1875-cm^{-1} band (Figure 3), the data fit eq 2 only if the 0.05-μm Cab-O-Sil particles are excluded and magnitude of $n = 1.06 \pm 0.11$ is much larger.

The results presented above were all taken at the lowest mirror velocity $v = 0.08$ cm/s and the spectra are ratioed against carbon black spectra taken at the same velocity. The

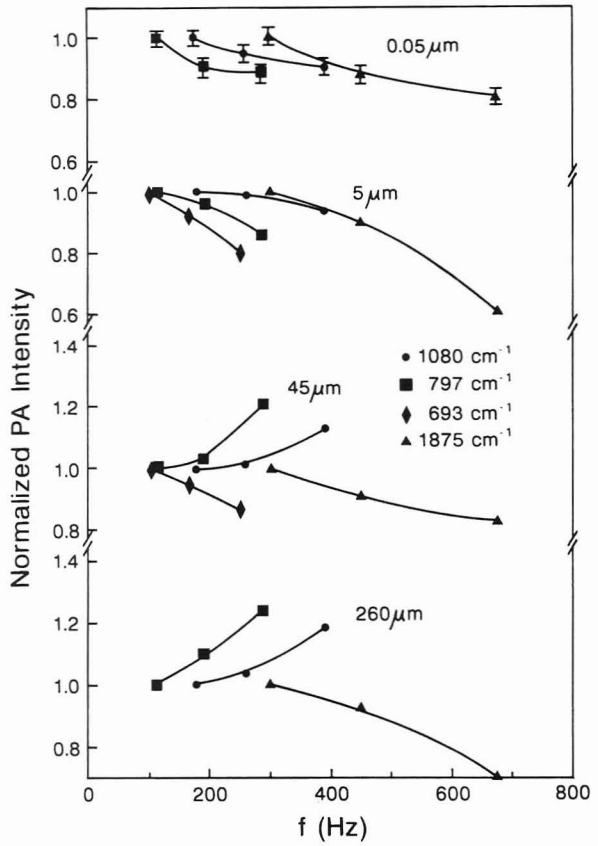

Figure 4. Effect of modulation frequency f on the intensity of the PA signal of various bands for four particle sizes. The PA signals are normalized to unity at the lowest f. The solid lines are drawn connecting the data points.

normalized PA intensities of various bands at other velocities (i.e. at different modulation frequencies) are shown in Figure 4 for particles of 0.05-, 5-, 45-, and 260-μm sizes. Again, the spectra are ratioed against carbon black at each new velocity. A systematic trend is evident from these observations. For the smallest particles (0.05 and 5 μm), the frequency dependence is similar to the predictions of the RG model in that the intensities of all the bands decrease as the modulation frequency f increases. However, for the larger 45- and 260-μm particles, the intense bands at 797 and 1080 cm^{-1} have now a positive frequency dependence (I increases as f increases) whereas the weaker bands at 693 cm^{-1} and 1875 cm^{-1} retain the negative frequency dependence as expected from the RG theory (*1*, *2*). In the discussion section below, we argue that this phenomenon arises from the saturation of the intense bands for the larger particles.

The question of a proper background reference material in PAS has been raised in several recent papers (*22–24*). In Figure 5, we show the effect of changing the background from powder carbon black to pelletized carbon black. Note that the intensities of all the bands are enhanced with the pellet as the background compared to the powder background. Measurements of I show that all bands are enhanced by exactly the same factor. In Figure 6, we have plotted the frequency dependence of the 1080-cm^{-1} band for the 0.05-μm particles with carbon powder and carbon pellet as backgrounds. The frequency dependence is different in the two cases, although in both cases the signal decreases as the frequency increases. A discussion of these and other results is presented below.

DISCUSSION

In order to check whether eq 1 describes our data of Figure 2, we have plotted the intensity I of the 797-, 1080-, and 1875-cm^{-1} bands as a function of porosity ϵ in Figure 7 and

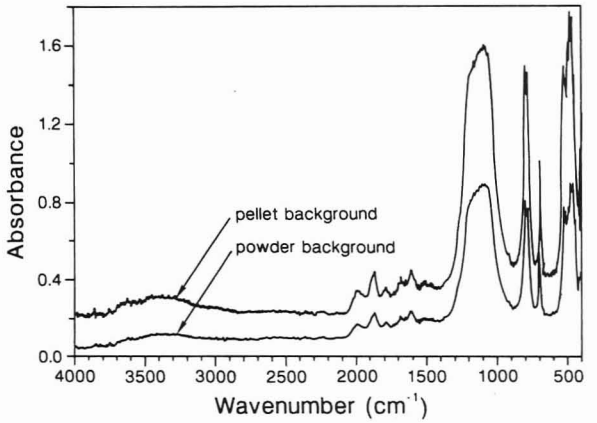

Figure 5. Effect of changing the background (from powder to pelletized carbon-black) on the PA spectra of 5-μm particles.

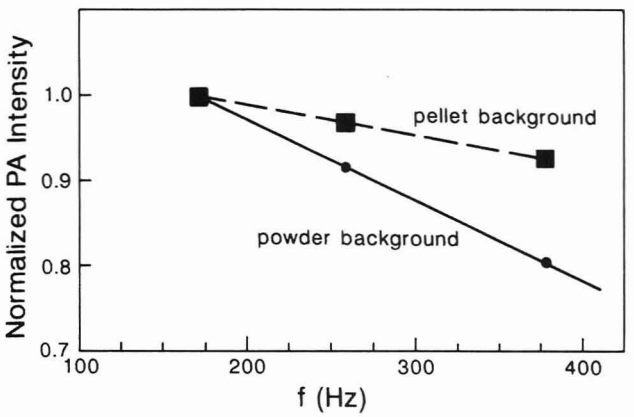

Figure 6. Effect of changing the background (from pellet to powder of carbon black) on the frequency dependence of the 1080-cm^{-1} band of 0.05-μm particles of silica.

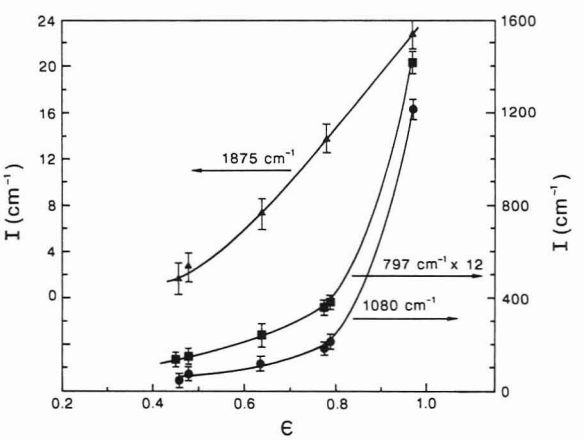

Figure 7. PA intensity I plotted against porosity ϵ for three bands. The solid curves are drawn connecting the data points for visual aid. However note the near linear dependence on ϵ for the weaker 1875-cm^{-1} band.

as a function of $\epsilon/(1-\epsilon)$ in Figure 8. It is clear that for the stronger bands at 797 and 1080 cm^{-1}, I varies very nearly as $\epsilon/(1-\epsilon)$, and for the weaker 1875-cm^{-1} band, I varies as ϵ. This is what is predicted by eq 1. This verification of the calculations by McGovern et al. (*14*) is a major result of this work and provides a quantitative estimate of the amplification factor of the PA signal in powders by the pressure term. For powders for which $\mu_s > D$, considerable amplification of the PA signal results.

It is noted that in the recent work of Belton et al. (*21*) on the PA spectroscopy of sucrose and carbon black powders of particle size ranging between 28 and 212 μm, a near linear dependence of the intensity of several relatively weaker bands

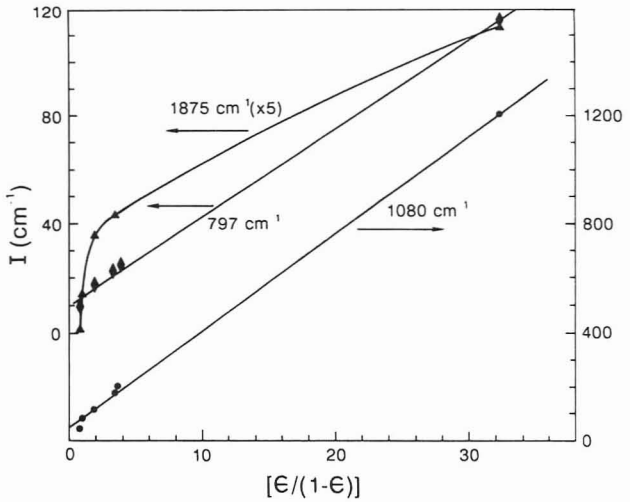

Figure 8. Data of Figure 6 replotted against $\epsilon/(1 - \epsilon)$. Now for the 797- and 1080-cm^{-1} bands, the solid lines are least-squares linear fits, whereas for the 1875-cm^{-1} band, the solid curve is drawn connecting the data points for visual aid.

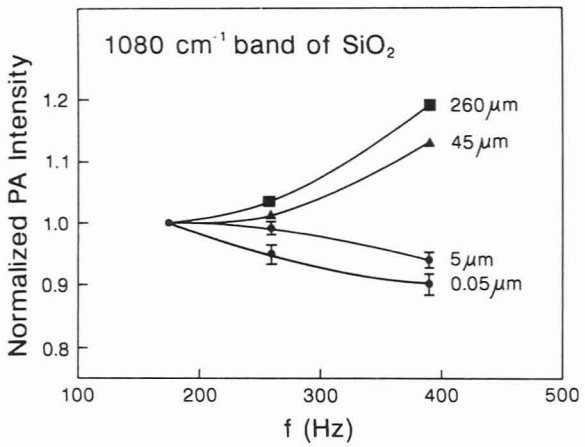

Figure 9. Effects of modulation frequency f on the PA intensity of the 1080-cm^{-1} bands for several particle sizes.

on porosity ϵ is evident from their plots. Although they did not interpret their results in terms of the calculations of McGovern et al. (*14*), we believe that their observations are also supportive of this theory. It would, however, be of interest to extend their measurements to smaller particles.

The empirical relation, eq 2, equally well fits our data for the stronger bands (Figure 2) and it allows a very convenient description of the intensity of the signal on the particle size D. However why the exponent n is close to 1/3 for the stronger bands and much different for the weaker band at 1875 cm^{-1} (Figure 3) is not clear at present. An interpretation of the empirical eq 2 is highly desirable.

The dependence of the PA intensity on the modulation frequency f (normalized to that at the lowest f) for different bands and different particle sizes (Figure 4) is considered next. For smaller particles (0.05 and 5 μm), $\mu_s \gg D$ and the volumes occupied by the interstial gas are much larger than those occupied by the particles. Hence the pressure term in eq 1 dominates. Decrease of μ_s by increasing f decreases the signal but mainly because of the decrease in the pressure term. As discussed by McGovern et al. (*14*), the frequency dependence is then similar to that of homogeneous samples, following the prediction of the RG theory (*1*, *2*).

For the larger particles of 45 and 260 μm, the frequency dependence of the intensity for the strong bands at 797 and 1080 cm^{-1} does not follow the prediction of the RG theory. Instead the signal increases as f increases (Figures 4 and 9). However the weaker band at 1875 cm^{-1} follows the normal behavior of the decrease in I with an increase in f (Figure 4). Although we do not have a quantitative interpretation of this anomalous result, the following argument is advanced as an explanation. Consider the relative magnitude of μ_s, μ_β, and D (Tables I and II). Note that for the larger particles $D \sim \mu_s$ but $\mu_\beta < \mu_s$ for the stronger bands and $\mu_\beta > \mu_s$ for the weaker bands. The condition for saturation is that $\mu_\beta < D$. The crux of the argument is that the 797- and 1080-cm^{-1} bands are severely saturated and the contribution of the pressure term to the signal for larger particles is also negligible. As f increases, μ_s decreases leading to a less severe condition for the inequality $\mu_\beta < \mu_s$. The increase of I with increasing f then results as we move from a more severe condition of saturation to one of less severity. For the nonsaturated bands such as that at 1875 and 693 cm^{-1}, the normal frequency dependence is observed.

The effect of background on the PA signal is considered next in light of several recent publications (*22–24*) and the data presented in Figures 5 and 6. As noted earlier, our measurements show that with carbon black *pellet* as a background (vis-a-vis carbon black *powder*), the intensities of all the bands are enhanced by exactly the same factor. This enhancement results from the reduction in the carbon background signal in the pellet compared to that in the powder because of reduction in porosity upon pelletizing. Note that the PA signal is ratioed against the background signal so that the above observation is completely understandable. We have also observed that pelletizing the carbon black for reference material reduces the errors due to the pressure signal in the finely divided powder when the finely divided powder is redistributed in repeated measurements. Carter et al. (*22*, *24*) have suggested other solid materials (such as painted substrates, carbon-filled rubber, and solid graphite) as reference materials for PAS. These findings suggest that reference material in PAS may not be limited just to carbon black powder.

The frequency dependence of the PA signal for a particular band, viz. that at 1080 cm^{-1} for the 0.05 μm particles, with carbon black powder and pellet as background, was presented in Figure 6. Although in both cases the signal decreases as the frequency increases, the magnitude of the decrease is less with the pellet as the background, probably because the pressure term is reduced in the pellet at all frequencies.

In conclusion, the intensity of PA signal for powders is strongly dependent on the particle size (or equivalently the porosity of the sample), and we have demonstrated that this dependence is satisfactorily explained by the theory McGovern et al. Also the effect of modulation frequency on the PA signal of various particle sizes has been explained qualitatively. We have also shown that pelletized carbon black gives higher PA intensity and it may be a better reference material for a number of cases. From this work it is evident that quantitative analysis of powders by PAS is possible only by properly taking into account the particle size dependence of the PA signal or by using powders of exactly the same particle size. The latter situation poses a major experimental difficulty so that recourse to the analysis by using the theory of McGovern et al., as e.g. done here, appears unavoidable.

ACKNOWLEDGMENT

Several useful discussions with Dr. W. E. Wallace are gratefully acknowledged.

Registry No. SiO_2, 7631-86-9; vitreous silica, 60676-86-0.

LITERATURE CITED

(1) Rosencwaig, A.; Gersho, A. *J. Appl. Phys.* **1976**, *47*, 64–69.
(2) Rosencwaig, A. *Photoacoustics and Photoacoustic Spectroscopy*; John Wiley and Sons: New York, 1980.
(3) Low, M. J. D.; Parodi, G. A. *Appl. Spectrosc.* **1980**, *34*, 76–80.

(4) Yang, C. Q.; Ellis, T. J.; Bresee, R. R.; Fateley, W. G. *Polym. Mater. Sci. Eng.* **1985**, *53*, 169–175.
(5) Teramae, N.; Tanaka, S. *Appl. Spectrosc.* **1985**, *39*, 797–799.
(6) Urban, M. W.; Koenig, J. L. *Appl. Spectrosc.* **1986**, *40*, 994–997.
(7) Yang, C. Q.; Bresee, R. R.; Fateley, W. G. *Appl. Spectrosc.* **1987**, *41*, 889–896.
(8) Zerlia, T. *Appl. Spectrosc.* **1986**, *40*, 214–217.
(9) Carter III, R. O.; Paputa Peck, M. C. *Appl. Spectrosc.* **1989**, *43*, 468–473.
(10) Michaelian, K. H. *Appl. Spectrosc.* **1989**, *43*, 185–190.
(11) McClelland, J. F.; Kniseley, R. N. *Appl. Phys. Lett.* **1976**, *28*, 467–469.
(12) Krishnan, K. *Appl. Spectrosc.* **1981**, *35*, 549–556.
(13) Monahalin, J.-P.; Bertrand, L.; Rousset, G.; Lepoutre, F. *J. Appl. Phys.* **1984**, *56*, 190–210.
(14) McGovern, S. J.; Royce, B. S. H.; Benziger, J. B. *J. Appl. Phys.* **1985**, *57*, 1710.
(15) King, D.; Davidson, R. S.; Phillips, M. *Anal. Chem.* **1982**, *54*, 2191–2194.
(16) Davidson, R. S.; King, D. *Anal. Chem.* **1984**, *56*, 1409–1411.
(17) Rockley, N. L.; Woodard, M. K.; Rockley, M. G. *Appl. Spectrosc.* **1984**, *38*, 329–334.
(18) Yang, C. Q.; Fateley, W. G. *J. Mol. Struct.* **1986**, *141*, 279–284.
(19) McGovern, S. J.; Royce, B. S. H.; Benziger, J. B. *Appl. Surf. Sci.* **1984**, *18*, 401–413.
(20) Seehra, M. S.; Pandurangi, R. S. *J. Phys.: Condens. Matter* **1989**, *1*, 5301–5304.
(21) Belton, P. S.; Wilson, R. H.; Saffa, A. M. *Anal. Chem.* **1987**, *59*, 2378.
(22) Carter III, R. O.; Paputa Peck, M. C.; Samus, M. A.; Killgoar, P. C., Jr. *Appl. Spectrosc.* **1989**, *43*, 1350–1354.
(23) Vidrine, D. W. *Appl. Spectrosc.* **1980**, *34*, 314–319.
(24) Carter III, R. O.; Paputa Peck, M. C. *Appl. Spectrosc.* **1989**, *43*, 468–473.
(25) Pandurangi, R. S.; Seehra, M. S.; Razzaboni, B. L.; Bolsaitis, P. *Environ. Health Perspect.* in press.

RECEIVED for review February 1, 1990. Accepted May 31, 1990. This work was supported in part by grants from the U.S. Bureau of Mines under the Generic Technology Center for Respirable Dust (Grant No. G1135142).

Chemical Control of Reaction Time in an Enzyme Assay and Feasibility of Enzyme Spot Tests

Jane N. Valenta[1] and Stephen G. Weber*

Department of Chemistry, University of Pittsburgh, Pittsburgh, Pennsylvania 15260

Robert C. Elser

York Hospital, 1001 South George Street, York, Pennsylvania 17405

There are many circumstances in which the understanding of a patient's status would be improved by knowing one or more enzyme activities. Such data are routinely produced in clinical laboratories, but simple, noninstrumental tests for enzymes are a rarity, so their extralaboratory determination is also rare. The essential problem is that effective clinical determinations of enzyme activities are typically carried out by measuring reaction rates, so the reaction time needs to be controlled. The reaction time of a sample can be controlled by using a passive, ion exchange-based titration. In this work, OH^-, H^+, and quinidine have been used to stop the enzymes LDH (EC 1.1.1.27) (with H^+ and OH^-) and cholinesterase (EC 3.1.1.8) (with quinidine). The ion exchange material containing the enzyme-stopping ion is separated from the sample by a filter. The sample contains ions that can exchange with the enzyme-stopping ion in the ion exchange material, and it may contain species that buffer the enzyme-stopping ion. The reaction time is governed by the exchanging ion's concentration in the sample, the quantity of buffer in the sample, the thickness of the filter between the ion exchange material and the sample, and the temperature. A test for LDH requiring 50 μL of serum and no instrumentation can be made so that results from sera with elevated levels appear different than those with normal levels.

INTRODUCTION

The philosophy behind the development of sensors and spot tests is that analyses can be performed by nonprofessionals. Functions ordinarily carried out instrumentally should be carried out chemically in an extralaboratory analytical device (EXLAD). For example, the sequence of mixing reagents, ordinarily carried out by other means in clinical laboratory apparatus, can be achieved by creating a series of reagent layers through which sample seeps (*1–3*).

In order to perform quantitative determinations of catalysts, and in particular enzymes, with an EXLAD, a means for the control of timing is required. This is in distinct contrast to the situation for most analytes; EXLAD's for noncatalytic solutes yield a steady signal (e.g., color) after a brief incubation period and during some long time determined by the stability of the signal. What would be ideal for catalyst EXLAD's is some method that irreversibly destroyed the catalyst after a certain time. Physical methods, such as heating or cooling, have the advantage of being conceptually simple, electronically controllable, and fast. On the other hand they would draw considerable power and would influence other reactions, such as color-forming reactions. Such means would also be reasonably expensive to the user.

Enzymes typically have pH optima, and there are generally ranges of pH over which an enzyme activity is much less than the maximum. This leads to a method for turning off enzyme activity after a certain time—the addition of acid or base. The slow addition of H^+ or OH^- to a buffered solution containing an enzyme will gradually alter the pH of the solution, thus causing the activity of the enzyme to decrease. The ultimate goal of an EXLAD requires that the addition be simple, safe, and operable under a variety of environmental conditions with low power. A noninstrumental, passive acid–base titration has been developed for such devices. The source of H^+ or OH^- for the passive titration is an ion exchange material.

There are cases in which an alteration in pH would be inappropriate, for example in a case where the substrate,

[1] Current address: PPG Industries, Inc., Research Center, P.O. Box 9, Allison Park, PA 15101.

0003-2700/90/0362-1947$02.50/0

product, or color reagent is pH sensitive. In such a case, an ionic inhibitor could be used to accomplish the desired reduction in activity.

The purpose of this paper is to illustrate that passive ion exchange can be used to stop enzyme activity in the cases investigated. The parameters that control the time that the enzyme is active have been determined. Because a single method for stopping an enzyme will not work for all enzymes, the three potentially most widely useful have been investigated. Hydroxide ion has been used to stop LDH (EC 1.1.1.27) catalysis of pyruvate to lactate; quinidine has been used to stop the cholinesterase (EC 3.1.1.8) catalyzed hydrolysis of the pH sensitive acetylthiocholine, and protons have been used to stop LDH catalysis of lactate to pyruvate.

The latter reaction was studied in detail to determine the parameters controlling the time that the enzyme has to catalyze the substrate to product conversion. Conditions have been determined that allow semiquantitative visual estimation of the LDH activity in 50 μL of blood serum.

EXPERIMENTAL SECTION

A. Materials. Ion exchange resins were Rexyn 101 H^+ (Fisher Scientific, Fair Lawn, NJ) and Dowex 1-XB (Cl^-) (Baker). The latter resin was converted to OH^- form by washing with NaOH solution until no cloudiness was induced in the supernatant from the addition of $AgNO_3$. Ion exchange membranes were H-form Nafion 117 (Plastics Department, Du Pont Co., Wilmington, DE) with an equivalent weight of 1100, nominal capacity of 0.91 mequiv/g, and thickness of 0.017 cm. Equivalent weight is defined as the mass in grams of dry polymer in the acid form to neutralize 1 equiv of base (*4*). This membrane was received in the form of a sheet and pieces were cut from this sheet for the experiments. The membranes were regenerated to the H-form by soaking each membrane in a glass jar containing approximately 0.1 M HCl for at least a day. Before these membranes were used, they were rinsed with doubly deionized water and wiped dry.

Magna Nylon 66 filters (MSI, Honeoye Falls, NY) of pore size 0.22 and 0.45 μm were used as received. The filters have a thickness of 120 μm and a pore density of 5×10^8 pores/cm^2.

All chemicals used were reagent grade; all water was doubly deionized. The water was first passed through an organic removal cartridge and then passed through a high-purity ion exchange cartridge with a 1-MΩ automatic cutoff. The water was finally distilled in an all-glass still and stored in a Pyrex glass vessel.

Two buffer systems were employed. A phosphate buffer of pH 8 was prepared by mixing 2.65 mL of 0.2 M monobasic sodium phosphate, NaH_2PO_4 (Fisher), with 47.35 mL of 0.2 M dibasic sodium phosphate, Na_2HPO_4 (Mallinckrodt, Inc., Paris, KY), and diluting to 100 mL. Tris(hydroxymethyl)aminomethane hydrochloride (Tris) solutions, 0.10 M (Sigma, St Lous, MO), was also prepared and was adjusted to pH 9 with a 6 M NaOH solution. Potassium chloride (EM Science, Cherry Hill, NJ) was reagent grade.

The diagnostic kit for LDH, kit no. 228-UV was purchased from Sigma. This test kit provides 153 μM solutions of β-NAD and of 60 mM L-lactate in 106 mM Tris buffer. Also purchased from Sigma were test kits containing control serum and diluent (type I-A and type II-A); these were used as directed. Type I-A control serum contains 150 units/L of lactate dehydrogenase while type II-A contains 350 units/L of lactate dehydrogenase. One international unit of activity is defined as the quantity of enzyme that will catalyze the reaction of 1 μmol of substrate per minute at a specified temperature (*5*). The reagents for the color reaction were nitro blue tetrazolium, NBT (Sigma), phenazine methasulfate, PMS (Sigma), and Triton X-100 (Rohm & Haas, Philadelphia, PA).

B. Spectrophotometric Observations. *Apparatus.* The floor of a 1 cm × 1 cm polystyrene cuvette (Fisher) was removed, and a 2-mm-thick glass frit was glued into place so that its top surface was 9–10 mm above the cuvette base. This effectively produced a two-compartment cell. An IBM 9420 UV–vis spectrophotometer was modified by drilling a hole in the bottom of the sample chamber large enough to accommodate the cylindrical magnet of a magnetic stirrer. Spectrophotometric observations were made in the top part of the cell while the solution therein was stirred.

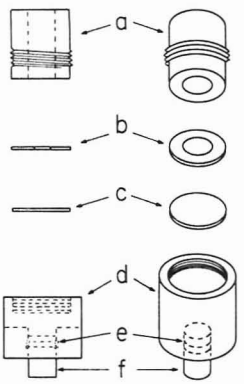

Figure 1. Exploded diagram of cell A: a, chamber for sample; b, Teflon ring; c, filter; d, chamber for ion exchange resin; e, O-ring; f, plunger.

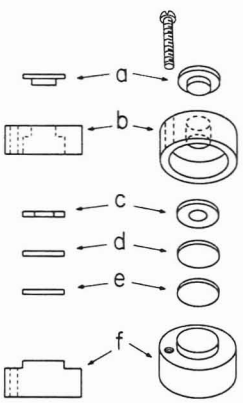

Figure 2. Exploded diagram of cell B: a, cover; b, body; c, Teflon ring; d, filter; e, Nafion; f, base.

Procedure. Ion exchange resin was placed in the lower compartment with enough water to fill the compartment. A 1 cm × 1 cm × 3 mm piece of silicone rubber was used to cap the bottom. The cuvette was placed in the spectrophotometer, reagents and stir bar were added to the top, and measurement of pH and/or absorbance was initiated.

C. Prototype Devices. *Apparatus.* Two cells were used. The first, cell A, was a more controllable version of the cuvette–cell without the optical qualities. It is diagrammed in Figure 1. The volume of the lower compartment is adjustable through the operation of a plunger. It is separated from the upper compartment by one or more microporous membranes with nominally 0.22- or 0.45-μm pores. This cell was used with relatively large volumes of solution (>1 mL) in the upper compartment and ion exchange resin in the lower one.

Another cell, cell B, Figure 2, was built for work with Nafion membranes as the source of protons. The cell consists of three parts: a Lucite top piece, a Teflon ring, and a Lucite base in which a stainless steel plug has been inserted. The Teflon ring prevents the nylon filter from tearing when the assembly is clamped together. The exposed area of the cell base is approximately 1.77 cm^2.

The acid–base titration was monitored by recording the pH changes in solution. A pH meter, an Orion Ionanalyzer Model 701 (Cambridge, MA), was calibrated daily with buffer solutions of pH 4 and 7 (Fisher). A Sargent-Welch recorder, Model XKR (Cleveland, OH), was calibrated to ensure that pH readings coincided with the markings on the chart paper. The contents of cell A were often transferred to a spectrophotometer for quantitation at the end of the titration. Because the second cell is only capable of holding a small volume of solution, pH and reference electrodes were used (Lazar Research, Inc., Los Angeles, CA) that had low volume requirements. These electrodes can measure the pH in samples as small as 10 μL.

Procedure. Cell A was used analogously to the cuvette–cell. For cell B, a pool of water was placed on the plateau of the base

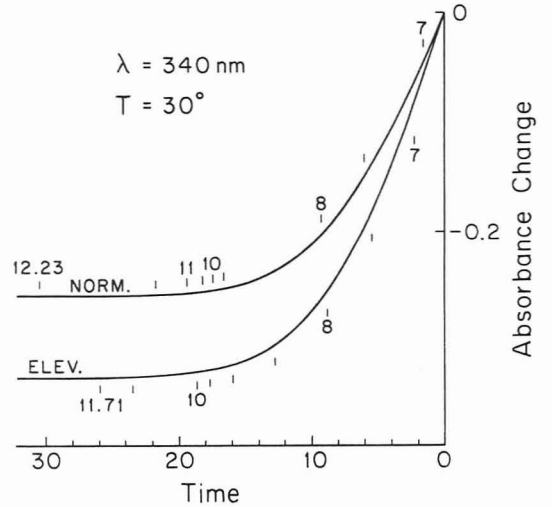

Figure 3. Absorbance from NADH as the pH in the cuvette cell becomes more basic. Numbers along the curves are the pH of the solution at that time. Tick marks are separated by 0.5 pH units.

piece of the cell and one piece of Nafion was placed into the pool of water. To prevent the membrane from curling, additional water was placed on the membrane. A nylon filter and the Teflon ring were placed into the assembly. The top piece of the cell was inserted and the entire cell was secured into place by screws. The exposed area was rinsed with water. The electrodes were placed in the cell so that they sat flush against the surface of the filter. The pH meter and recorder were then turned on. A sample solution (100–500 μL) was injected into the cell and the pH of the solution was recorded until the solution reached a pH of 2.5.

RESULTS AND DISCUSSION

LDH + Hydroxide. Figure 3 shows representative data obtained by using the cuvette–cell for normal and elevated control sera. The absorbance of NADH is monitored at 340 nm in the upper part of the cuvette. Measurements of pH were made simultaneously, and these are indicated on Figure 3. The reaction is described by eq 1. It is stopped by an

$$\text{pyruvate} + \text{NADH} \xrightarrow{\text{LDH}} \text{lactate} + \text{NAD}^+ + \text{H}^+ \qquad (1)$$

alkaline excursion caused by the exchange of Cl^- for OH^- on the resin. The OH^- titrates the Tris and other buffers that may be present with the result that enzyme activity ceases and a constant absorbance is established. Note that the final absorbance is correlated with the initial reaction rate, which would ordinarily be measured instrumentally. Repetitive experiments with both basic and acidic resins have yielded essentially the same result. The details of the acid resin reaction will be taken up in considerable detail below so they will not be discussed here.

Cholinesterase + Quinidine. Acidic and basic excursions are generally useful to stop the activity of a variety of enzymes of clinical importance. However, alteration of pH may not be an appropriate choice and another means of stopping the enzyme activity is required. One example is that of the enzyme cholinesterase (EC 3.1.1.8). In the most widely used reaction, the substrate, acetylthiocholine iodide, is hydrolyzed and the liberated thiol reacts with the reagent dithiobis(2-nitrobenzoic acid) (DTNB) to form a yellow compound. The absorbance at 412 nm due to the presence of this compound is used to estimate enzyme activity. Acetylthiocholine and DTNB are hydrolytically unstable in acidic or basic solutions (*6*). As a consequence, alteration of pH by H^+ or OH^- would be a poor choice to stop this reaction. The enzyme is inhibited by quinidine, a tertiary amine which exists as the ammonium ion in neutral solution.

For these investigations, cell A was used. The lower compartment contained ion exchange resin H^+ form, with an overlayer of quinidine free base. The free base is not soluble, but exists as a paste over the resin. A microporous membrane separates the lower compartment from the upper one. The upper compartment contained the reagents and sample which were added in the following way. All reagents, 1.5 mL of 0.01 M pH 7 phosphate buffer, 0.5 mL of 2.5×10^{-4} M DTNB, 0.5 mL of 0.018 M acetylthiocholine iodide, and 0.5 mL of 0.2 M KCl, were mixed in a test tube. Serum, 50 μL, was added and the combination poured into the upper chamber of cell A. Cell A does not allow continuous observation of the optical absorbance of the sample. On the basis of the results found with the cuvettes, examples of which are shown in Figure 3, 20 min was chosen as the reaction time. Therefore, 20 min after the sample was mixed with the reagents, the mixture was transferred to a 1 cm path length cuvette and the absorbance at 412 nm was determined. Table I shows absorbance values for such experiments. There are four sets of conditions, two using normal serum (N) and two using elevated serum (E). In each pair of trials, the upper chamber of the cell was stirred in one trial, but not the other. The initial pH in all cases was 7.00 ± 0.01. A control experiment was run in which no resin or quinidine was present under the membrane (last two lines of the table). Evidently, sufficient quinidine was liberated by the resin to inactivate the enzyme and stop the reaction. Absorbance measurements of samples from both stirred and unstirred cells were constant. In contrast, the reactions done without quinidine continued to produce product with a concomitant increasing absorbance. This demonstrates the successful cessation of the reaction by introduction of quinidine. UV absorbance at 235 nm confirmed the presence of quinidine (absorbance > 3) in the upper chamber. We speculate that cations in the upper chamber displace protons from the resin, which then protonate quinidine which in turn is transported back to the upper chamber. Stirring seems to improve reproducibility. There is a clear difference between the elevated and normal controls. Because there is no "buffer" for the enzyme deactivating ion to titrate, the control of reaction time must be through control of the ion flux. That this can be accomplished is evidenced by the data. Increasing the number of filters separating the upper and lower compartments (data not shown) increased the ultimate absorbance.

In these experiments about 15 mg of quinidine was used. When that value is increased to about 50 mg, the pH drift is less severe (Table II). Thus it is possible to stop the enzyme in a controlled fashion with an ionic inhibitor while keeping the pH stable.

Table I. Absorbance at 412 nm after 20 min in Cell A

conditions			two membranes		two membranes	
serum	stir	resin	abs	pH	abs	pH
N	+	+	0.205	6.35	0.199	5.37
N	–	+	0.258	6.48	0.306	–[a]
E	+	+	0.396	6.34	0.402	5.30
E	–	+	0.397	6.50	0.398	6.21
N		–	0.530[b]	7.03		
E		–	1.02[b]	6.99		

[a] Not measured. [b] And still increasing.

Table II. Absorbance at 412 nm and pH after 20 min

trial	N[a]	E[b]	pH E
1	0.174	0.365	6.90
2	0.184	0.350	6.98
3	0.207	0.295	6.99

[a] Absorbance from the sample with the normal level. [b] Absorbance from the sample with the elevated level.

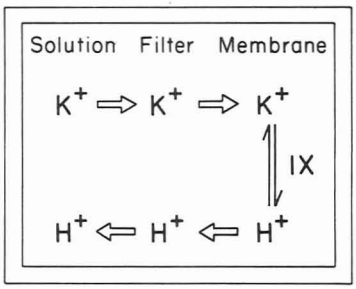

Figure 4. Schematic diagram of the possible rate-controlling steps in the flux of H^+ into the sample compartment.

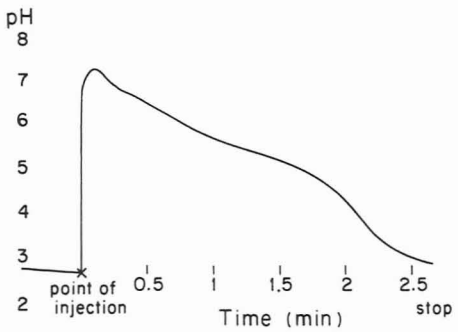

Figure 5. Titration curve for 100 μL of a solution 0.2 M in KCl and 0.04 M in phosphate.

Evidence has been given that convincingly illustrates that simple ion exchange can be used to stop enzyme activity. Two different ions, one the generally useful OH^- and the other the selective inhibitor quinidine, have been used. In neither case, however, is the apparatus or procedure employed anything like what an enzyme spot test would be like. Moreover, a quantitative understanding of how one can control the time for any enzyme reaction is not in hand. A cell that more closely resembles the volume and physical dimension of an enzyme spot test was used for the next set of experiments. Attention now turns not to stopping enzymes, for this has been demonstrated, but to how to control the rate of enzyme-stopping-ion transport so that the time of the process is controlled. This has been done by using the ion H^+.

Controlling Time by Controlling H^+ Flux. In this set of studies, the proton was used as the enzyme stopping ion. The driving force for the titration is the unequal chemical potentials of H^+ between phases and of K^+ between phases. Coupled by electrical potential, they exchange across the passive diffusion barrier as shown in Figure 4. It is straightforward to predict the influences on the time taken to reach a particular value of pH in the sample. The ion exchange capacity of the Nafion must be sufficient to titrate the sample; the concentration of the competing counterion to the Nafion (K^+ in Figure 4) (which will simply be called "counterion"), the buffer capacity of the sample, the thickness of the passive barrier, and temperature will all influence the titration time.

These experiments were carried out with cell B, so spectroscopic evaluation was precluded. The pH was followed as a function of time. A typical plot of pH vs time for cell B is shown in Figure 5.

Ion Exchange Capacity. The influence of the total number of ion exchange sites on titration time was determined. Each membrane was weighed before each run. The cell (type "B") was assembled and 100 μL of 1:1 0.6 M KCl/0.4 M phosphate buffer were injected into the cell. A plot of titration time to pH 2.5 versus Nafion weight can be found in Figure 6. There is no dependence of the titration time on the weight of Nafion for the given set of experimental conditions. Each membrane contains a sufficient quantity of H^+ to titrate completely the

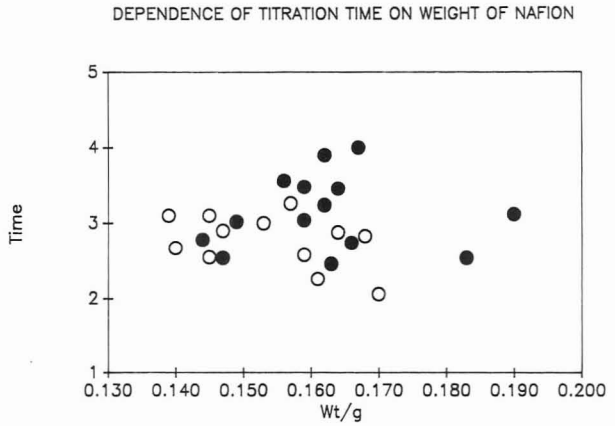

Figure 6. Titration time to pH 2.5 as a function of the mass of Nafion used under the filter. Open and closed circles represent experiments done on different days.

Table III. Influence of [KCl] on Average Titration Time

[KCl]/M	time/min	[KCl]/M	time/min
0.3	1.97	0.12	3.61
0.24	2.34	0.06	4.08
0.18	3.05		

Table IV. Influence of Type and Amount of Buffer on Titration Time

	time/min	
quantity of buffer, μmol	phosphate	Tris
5	2.12	–
4	1.97	2.31
3	1.58	2.09
2	1.40	1.64
1	1.09	1.10

buffered solution. Even though the titration was monitored to a pH of 2.5, the titration continued on to lower pH values confirming that the proton reservoir was not being depleted. The scatter in the data is also important to note. A relative standard deviation of 15% is typical. Reproducibility will be discussed later.

Counterions. The influence of the concentration of exchangeable cation in solution was investigated. Experiments using KCl with a concentration range between 0.06 and 0.30 M were performed. The expected outcome is that as the concentration of KCl increases, the rate of ion transfer increases as well. Some of the results are shown in Table III. Each point represents the average for at least five successive runs. From these data, it can be concluded that if a short titration is desired, a high concentration of exchangeable cation is required and longer titration times can be obtained by using dilute solutions of the cation. Serum contains cations, and these cations will make a contribution to the driving force in the ion exchange process that increases the rate of exchange.

Buffer Capacity. Although the quinidine experiments demonstrate that the filters influence the titration time, the quantity of buffer must also exert an influence. From the data found in Table IV, it can be seen that as the quantity of buffer is lowered, less H^+ is needed to titrate the buffer. This is expected because of the similarity of this system to volumetric quantitative analysis.

It was of interest to examine buffers that are cationic because a cationic buffer may partake in the ion exchange process as well as buffering the solution. A comparison study was done with 0.1 M phosphate buffer and 0.1 M Tris buffer. Since the selectivity coefficient is not known for Tris, it is a possibility that Tris-H^+ would compete with K^+ for the ion

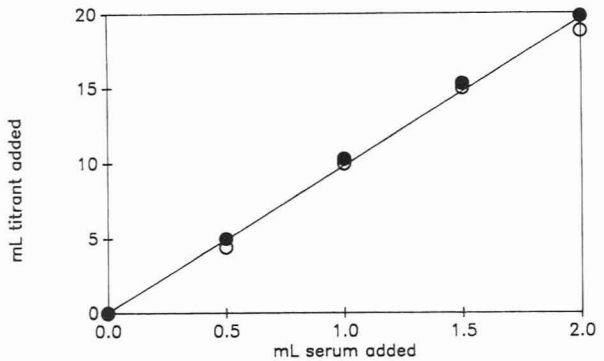

Figure 7. Increase in milliliters of titrant required to titrate buffer + control serum as a function of milliliters of control serum added: open circles, phosphate buffer; closed circles, Tris buffer.

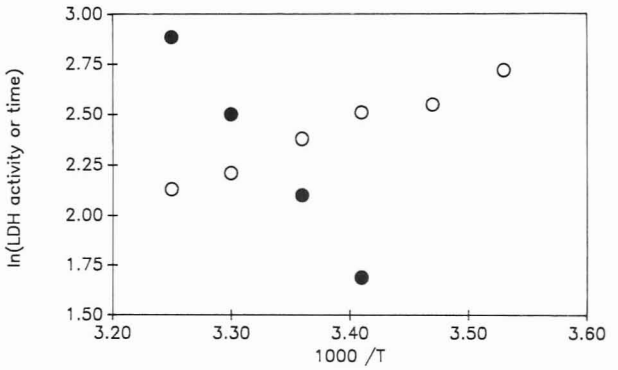

Figure 8. Temperature dependence of titration time (O) and of the LDH activity (●) (*7*).

exchange sites. Some of the results are shown in Table IV. These numbers are averages taken from at least five successive runs. The conclusion is that the difference in the buffers is not significant even though the buffer ions differ in charge.

A series of volumetric potentiometric titrations was performed to examine serum effects on buffer capacity. To 5 mL of 0.1 M phosphate and Tris buffers, additions of 0.5, 1.0, 1.5, and 2.0– mL of serum were made, and the solution was titrated. As the volume of serum is increased, a larger volume of 0.0192 M HCl is required to reach a pH of 3.00 in comparison to the buffered solutions containing no serum. The serum's buffer capacity can be calculated from the slope of the line in Figure 7 and is 0.18 mequiv/mL serum. This leads to the conclusion that serum makes a significant contribution to the buffering capacity of the system.

Mass Transfer. There are two limiting cases for diffusion through a passive barrier, the microporous filters, such as has been employed in these studies. In one, the transient approach to steady state is rapid, and the flux is governed by direct application of Fick's first law to the problem

$$J = \epsilon D \frac{\Delta C}{ml} \tag{2}$$

where J is the ion flux, ϵ is the membrane porosity ($\sim$0.19), D is the diffusion coefficient of the ions in the film (e.g. H^+ and Na^+ electrostatically coupled), ΔC is the concentration difference of the limiting reagent, equal to the added concentration of the cations in the sample chamber, l is the membrane thickness, and m is the number of membranes. The other extreme case is that in which the entire titration occurs during the transient, that is before the establishment of a steady state in the membrane. In this case the mathematical behavior is complex, but to a first approximation one can apply Einstein's relationship to find

$$t = m^2 l^2 / 2D \tag{3}$$

In the first case (steady state), the titration time is given by

$$t = \mathrm{mol_B}/JA \tag{4}$$

where $\mathrm{mol_B}$ is moles of buffer and A is the area through which the flux occurs. Then, for the steady state

$$t \propto m \tag{5}$$

In the transient case

$$t \propto m^2 \tag{6}$$

Another way to look at this in the transient case is to suggest that eq 4 holds but J is time dependent. Other processes, such as diffusion in the sample cell, diffusion in the Nafion, and ion exchange kinetics, would all be independent of the number of membranes used to separate the Nafion from the sample compartment.

Cell B was used with 0.03 M KCl, 0.05 M phosphate, 100 μL total volume, and within one or two filters. With one filter the time was 4.08 min (s = 0.40, n = 5) and with two filters it was 13.4 min (s = 1.5, n = 5). With the approximations and uncertainties involved, quantitative analysis is not justified. However, this experiment and the quinidine experiment indicate that the processes occurring in the membrane are important, and the transient phase of the mass transfer process may be the most important; i.e. eq 6 is probably applicable. It is important to note that membrane thickness, counterion concentration, and buffer quantity all can be manipulated to control titration time.

Temperature Dependence. The temperature dependence of the titration time for a buffer was determined. Results are shown for cell A in Figure 8. Also shown in Figure 8 is the temperature dependence for the enzyme reaction of LDH (*7*). As expected for a process governed largely by diffusion, the higher the temperature the more rapid the titration. The data fit the Eyring model (*8*) for diffusion as an activated process. This is fortunate. Because of the exponential dependence of both the enzyme rate and the diffusion rate on $1/T$, the net result is an approximate cancellation of effects. In fact, one can write for diffusion (*8*)

$$D = D_0 \exp(-\Delta G_D^{\ddagger}/RT) \tag{7}$$

and for the enzyme reaction

$$k = k_0 \exp(-\Delta G_E^{\ddagger}/RT) \tag{8}$$

The overall color change that would be produced in an enzyme reaction is proportional to time t_D, where

$$t_D \sim l^2/D \tag{9}$$

and l is the thickness of the diffusional barrier. If the enzyme were active for the time t_D, producing at a rate k, and then the enzyme were stopped, the yield of product, q, would be

$$q = kt_D \tag{10}$$

$$= l^2(k_0/D_0) \exp[-(\Delta G_E^{\ddagger} - \Delta G_D^{\ddagger})/RT] \tag{11}$$

Thus, if the activation free energy of diffusion were identical with that for the enzyme rate, the temperature effect would disappear. If ethylene glycol, glycerol, or even borate cross-linked poly(vinyl alcohol) ("slime") were used as a matrix in the filters, the activation barrier for diffusion may be increased enough to exactly offset the T-dependent rate increase the enzyme experiences. This is extremely important for an EXLAD which may be used anywhere from Ulan Bator to Singapore.

Model. A plausible model that can be used to predict the titration time for the behavior of these devices can be constructed. We assume that the driving force for the titration is the cation concentration in the sample compartment, the proton source is inexhaustible, and the time is linearly related to the amount of buffer. A function of concentrations and

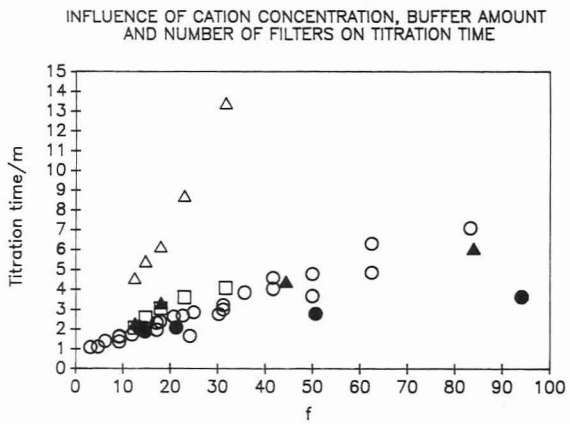

Figure 9. Plot of titration time versus model parameter f in eq 12. Experiments with one filter: phosphate buffer without (□) and with (▲) serum; Tris buffer, without (○) and with (●) serum; phosphate without serum, two filters (△).

volumes that contains the driving force and equivalents of buffer titrated is shown in eq 12. This equation is the total

$$f = \frac{(0.18V_S + V_B[\text{Buf}])}{(0.15V_S + [\text{KCl}]V_X + [\text{Buf}]V_B\alpha)/(V_S + V_X + V_B)} \quad (12)$$

amount of buffer divided by the *total concentration* of cations. V_S, V_X, and V_B are the volumes of serum, salt, and buffer, respectively. The number 0.15 is used to approximate the number of microequivalents per microliter of cations in serum, 0.18 is from experimental data for serum's buffer capacity. The number of nonproton cation equivalents per buffer molecule is α. For the $Na_2HPO_4/NaHPO_4$ buffer used in these studies, $\alpha = 1.95$. For Tris about 0.08 mol of NaOH is required to bring 1 L of 0.1 M Tris·HCl to pH 9.0, so $\alpha = 0.8$. Titration times vs f are shown for a variety of experiments in Figure 9. Each point represents the average of four to six determinations. There are several important conclusions to be taken from this collection of data. Most obviously, the model, which is based on diffusion flux, ion exchange, and mass balance, works. Careful inspection points out some finer points. The Tris data, no serum, are the most numerous, and the correlation between titration time and f is substantially linear over a wide range (factor of 30) of f. The data for phosphate show a distinct curvature. In the noise of the combined experiments done over weeks, it seems small, but either curve taken in isolation is significantly nonlinear. The serum–Tris data show a significantly different slope than the other data. The slope for the data taken with two membranes is about 5 times the slope of the one-membrane data. The difference caused by the number of membranes is clearly predicted in eq 9.

We speculate that the chief cause of the differences mentioned is the failure of the model to account for activity coefficients. Phosphate is highly charged and anionic, while Tris is less charged and may exist as a cationic species. Albumin is anionic when the titration begins (pH ~ 9) and cationic when it is finished. Clearly the many complex interactions between ions can play a role in the processes governing titration time. In fact, the diffusive flux is driven by a chemical potential gradient, which depends on ionic activity coefficients. Thus the assumption that the flux is concentration dependent, made for practical reasons, is really incorrect to begin with, but it is convenient.

These differences aside, it is clear that the model, which is physically sound, is in general correct. It shows that gross changes in time are achievable by varying the number of filters, while fine-tuning of the time can be accomplished by changing f.

Table V. Analysis of Variance H_0: Individual Cells Are Identical

number of obs	29	R^2	0.4525
root MSE	0.624	Adj R^2	0.4323

source	partial SS	df	MS	F	Prob > F[a]
cell	8.687	1	8.687	22.32	0.0001
residual	10.50	27	0.389		
total	19.196	28	0.68		

[a] Probability that the value of F, 22.32, occurs by chance alone, is lower than 0.0001.

Note the intercept at $f = 0$ (corresponding to no buffer) is nonzero. This represents the transient period during which protons are first diffusing through the filter.

Reproducibility. In any clinical test, it is desirable to distinguish activities of enzyme corresponding to a state of good health from those indicating a pathological condition. Imprecision in the measurement will only blur the distinction between the sick and the well. Because of this, some probable sources of error were investigated.

The procedure for constructing the device uses wet films (Nafion and filters). The volume of distilled water used is not well controlled. To investigate the importance of this, several tests were run with dry filters and compared to wet filters. Conditions were as follows: total volume, 200 μL; [KCl], 0.5 mM; phosphate buffer, 1.0 μmol. For the wet filters the average titration time was 13.0 min ($s = 0.82$, $n = 5$), where s is standard deviation, while for the dry filters it was 6.93 min ($s = 1.24$, $n = 5$). Thus there is a considerable difference because of this. This would clearly be an important variable to control in an actual device.

The titrations were followed to pH 2.5. This was convenient for use with Tris but, in retrospect, was a poor choice for use with phosphate buffer or serum-containing samples. In this range of pH, buffers are being titrated. Because the pH changes slowly, the exact time at which the pH reaches a value of 2.5 is somewhat difficult to determine. It would be easier to determine the time for a pH that occurred in a more poorly buffering region like pH 4. A set of 29 titrations was performed, and the times taken to reach pH 4.0 and pH 2.5 were recorded. In each of the 29 experiments, the same cell was used (type B). The total volume was 100 μL: [KCl], 50 mM; phosphate buffer, 5 μmol. The data are as follows: pH 2.5, average time 4.79 min ($s = 0.63$, $n = 29$); pH 4.0, average time 3.17 min ($s = 0.46$, $n = 29$). The relative standard deviations are as follows: pH 2.5, 0.13; pH 4.0, 0.14. Clearly the precision is the same for both of them.

An experiment was performed to determine whether the individual cell used (of type B) made a difference. In any one experiment up to six nominally identical cells were used. The same solutions and conditions were used as those described in the previous paragraph. Table V shows results of an analysis of variance for the variable "cell" which represents individual cell difference. The data show a highly significant effect due to the individual variations among cells. This was discovered after the results, for example shown in Figure 9, were taken. This is probably a major contribution to irreproducibility.

Color Reaction. The ultimate indicator of enzyme activity is the appearance of product. The color reaction used for LDH with an acidic titration is the redox reaction between NADH and nitro blue tetrazolium (NBT) mediated by phenazine methasulfate. A clear difference in color between the control serum and the elevated serum is obtained when using the conditions shown in Table VI. It is obvious that the chemical timing process is essential, for without it both normal and

Table VI. Conditions for LDH Spot Test

serum		50 μL
buffer	(60 mM L-lactate, 106 mM Tris, pH 9.0)	25 μL
PMS	(0.81 mM in 0.6 M KCl)	5 μL
NBT	(0.46 mM in 0.6 M KCl)	20 μL

elevated control serum samples cause conversion of a large quantity of substrate to product which results in a very dark, almost black, solution for both elevated and normal sera.

CONCLUSIONS

Three different ways of turning enzymes off chemically have been shown in three different cells. OH^- was used in a cell that allowed simultaneous photometric observation of the course of the reaction and the pH, quinidine was used in a cell that employed large volumes, and H^+ was used in a cell that used small volumes. The latter cell was made of materials that are stable and consequently good candidates for use in an actual device. The latter case was investigated in detail; it was found that the diffusional barrier thickness has a dramatic, perhaps quadratic, influence on time. More subtle alterations in the time are possible by varying the solution composition. Cell B allows visual discrimination between normal and elevated levels of LDH in control sera with H^+ as the enzyme stopping ion.

ACKNOWLEDGMENT

The enthusiastic laboratory assistance of Alvin Murn (now Alvin Murn, M.D.) is gratefully adknowledged.

Registry No. LDH, 9001-60-9; OH^-, 14280-30-9; H^+, 12408-02-5; cholinesterase, 9001-08-5; quinidine, 56-54-2.

LITERATURE CITED

(1) Emancipator, K.; Deutsch, D. G. *Chem. Anal.* **1989**, *100*, 203.
(2) Skarstedt, M. T.; Usmani, A. M. *Polym. News* **1989**, *14*, 38.
(3) Walter, B. *Anal. Chem.* **1983**, *55*, 498A.
(4) Yeo, R. S. *J. Electrochem. Soc.* **1983**, *130*, 534.
(5) Kaplan, L. A.; Pesce, A. J. *Clinical Chemistry*; C. V. Mosby, Co.: St. Louis, MO, 1984; p 5.
(6) Riddles, P. W.; Blakely, R. L.; Zerner, B. *Methods Enzymol.* **1983**, *91*, 49.
(7) Sigma Technical Bulletin No. 226-UV (August 1982).
(8) Glasstone, S.; Laidler, K. J.; Eyring, H. *The Theory of Rate Processes*; McGraw-Hill, New York, 1941; p 516 and following.

RECEIVED for review February 15, 1990. Accepted May 31, 1990. Financial support from Med-Chek Laboratories and the Ben Franklin Partnership of Western Pennsylvania are also gratefully acknowledged.

Sensitized Phosphorescence with Anchored Naphthoate Energy Donors in Reverse Micelles

L. A. Blyshak and I. M. Warner*

Department of Chemistry, Emory University, Atlanta, Georgia 30322

A series of cetyltrimethylammonium (CTA^+) surfactants with naphthoate counterions have been used as donors of triplet-state energy for the acceptor biacetyl in reverse micelles of Aerosol OT (AOT). Microviscosities obtained by using fluorescence polarization measurements have been employed to describe the relative binding of different naphthoate counterions to the interfacial region of the micelle. Since the naphthoate moieties are associated with the CTA^+ surfactant, they are anchored to the head groups in reverse micelles of AOT where biacetyl is solubilized. Therefore, cetyltrimethylammonium naphthoate acts as a more efficient energy donor than the corresponding sodium salt that is not bound as effectively to the micelle interface. Counterion binding and several other parameters that affect the intensity of sensitized phosphorescence have been examined.

INTRODUCTION

The utility of micellar media for luminescence enhancement has been outlined by several investigators (*1–9*). In particular, the molecular organization and protection afforded by micellar media for solubilized luminophores has been used to minimize nonradiative decay (*1*), to prevent triplet–triplet annihilation (*3*), and to bring luminophores and heavy atoms into close proximity (*4*). In addition, micelles have been used to organize energy donors and acceptors for more efficient triplet–triplet energy transfer (*5, 6*).

Since triplet–triplet energy transfer or sensitized phosphorescence only occurs over short distances (typically 10–15 Å), observation of this phenomenon in homogeneous fluid solution is often limited by the necessity of using extremely large donor and acceptor concentrations to facilitate collisions between donor and acceptor. The molecular organization available for solubilized analytes in micelles can be used to bring interactants into close proximity, thereby increasing the collisions between donor and acceptor (*3, 6*). Under these circumstances, lower analyte concentrations may be used because the effective concentration of donors and acceptors in the micelle is high. Enhanced sensitization for solubilized analytes has been observed in both normal and reverse micellar solutions (*7–9*).

Careful control of the binding site for energy donors and acceptors in micellar solution may be useful for enhancing sensitized phosphorescence signals. In this study, energy transfer is examined in normal and reverse micelles containing anchored energy donors. Several cetyltrimethylammonium naphthoate (CTA^+N^-) surfactants that have been previously characterized as normal micelles and as probes in reverse micelles of Aerosol OT (AOT) (*10*) are used as bound energy donors in reverse micellar solutions containing solubilized biacetyl. Biacetyl was chosen as a triplet energy acceptor due to its high phosphorescence quantum efficiency ($\phi \cong 1$) (*11*) and its expected solubilization site at the interfacial region of the reverse micelle.

Energy transfer between the bound naphthoate counterion and biacetyl is expected to be more efficient in reverse micellar solutions than in fluid solutions due to the localization of both the donor and acceptor species at the interfacial region of the reverse micelle. The CTA^+N^- counterions will be anchored at the head group–water interface in AOT reverse micelles

0003-2700/90/0362-1953$02.50/0

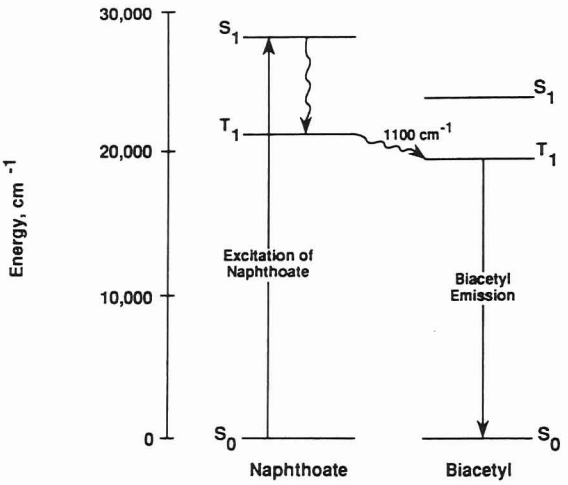

Figure 1. Relative energy levels for naphthoate and biacetyl. The difference between the triplet energies of naphthoate and biacetyl (ΔE) equals 1100 cm^{-1}.

as a result of the associated cetyltrimethylammonium cation (CTA^+). In fact, the counterions of CTA^+N^- are expected to show stronger binding to the interfacial region than the counterions of sodium 2-naphthoate (SN). Therefore, comparison of energy transfer using these two species in reverse micelles is expected to show that the surfactant probe will be a more effective sensitizer for biacetyl than SN.

Observation of exchange energy transfer also requires that the triplet state of the donor possess a greater energy than the triplet state of the acceptor. A diagram of the relative energy levels for the naphthoate/biacetyl pair is shown in Figure 1. Clearly, the triplet energy of naphthoate lies above the triplet for biacetyl with an energy difference (ΔE) of approximately 1100 cm^{-1} between the triplet states. This arrangement is ideal for sensitized phosphorescence since temperature-dependent energy transfer from T_1 of the acceptor back to T_1 of the donor is negligible for systems with triplet-state energy differences greater than 1000 cm^{-1} (*12*).

In addition to the spacing of triplet energy levels and the required proximity of interactants, the characteristics of the donor and acceptor luminescence also contribute to the observed sensitized phosphorescence as shown by

$$I_{sp} = 2.303kI_o\epsilon_D bC_D(\phi_t^D)\phi_{et}(\phi_p^A) \quad (1)$$

In this equation, I_{sp} represents the intensity of sensitized phosphorescence, ϵ_D is the molar absorptivity for the donor in M^{-1} cm^{-1}, b is the pathlength in cm, C_D is the molar concentration of donor, ϕ_t^D is the quantum efficiency of intersystem crossing for the donor, ϕ_{et} is the quantum efficiency of energy transfer from donor to acceptor, and ϕ_p^A is the quantum efficiency of acceptor phosphorescence. The terms k and I_0 represent an instrumental correction factor and the intensity of the incident light, respectively. The term, ϕ_{et}, is defined by

$$\phi_{et} = \frac{k_{et}C_A}{k_{et}C_A + (\tau_0^D)^{-1}} \quad (2)$$

where k_{et} is the rate constant for triplet–triplet energy transfer, C_A is the molar concentration of the acceptor and $(\tau_0^D)^{-1}$ is the reciprocal of the phosphorescence lifetime of the donor in the absence of the acceptor (*5*). Clearly, the observed sensitized phosphorescence intensities depend on many parameters of the naphthoate/biacetyl pair.

In this study, sensitized phosphorescence in reverse micelles containing the bound naphthoate donors and solubilized biacetyl is examined. Parameters including the concentrations of AOT and solubilized water have been varied and the effects of these parameters on the biacetyl-sensitized phosphorescence are observed. The relative binding of the naphthoates, predicted from microviscosity data, is used in conjunction with the absorption and luminescence characteristics of the naphthoates to elucidate the factors that affect sensitized phosphorescence when using CTA^+N^- energy donors. Sensitized phosphorescence observed in the reverse micelles containing CTA^+N^- probes is compared to sensitized phosphorescence observed in normal CTA^+N^- micelles and in homogeneous fluid solution.

EXPERIMENTAL SECTION

Materials. The surfactants cetyltrimethylammonium 2-naphthoate (CTA^+N^-), bis(cetyltrimethylammonium) 2,3-naphthalenedicarboxylate ($[CTA^+]_2NDC^{2-}$), cetyltrimethylammonium 2-naphthylacetate (CTA^+NA^-) and cetyltrimethylammonium 1-hydroxy-2-naphthoate (CTA^+HN^-) were prepared as described previously (*10*) and stored in a heated vacuum desiccator over P_2O_5 at 40 °C. The surfactant AOT (Sigma) was purified according to a procedure outlined by Menger et al. (*13*) and dried in a heated vacuum desiccator at 40 °C over P_2O_5. Methanol and cyclohexane (Burdick and Jackson) were used. Cyclohexane was dried with 4-Å molecular sieves prior to use in reverse micellar preparations. Biacetyl (2,3-butanedione, Aldrich, 99+%) was used as a triplet energy acceptor.

Methods. Aqueous samples were prepared with type I reagent grade water (MilliQ, Continental Water Systems). Reverse micellar solutions of AOT were prepared by dissolving solid AOT in cyclohexane to give a concentration of 0.1 M unless otherwise specified. Then, the concentration of water required to give a specified $[H_2O]/[AOT]$ ratio, designated by W, was dissolved in the solution by using a sonicating bath until the solution was optically clear. The W was equal to 10 unless otherwise noted. Solutions of $AOT/C_6H_{12}/H_2O$/naphthoate were prepared by adding solid CTA^+N^- to $AOT/C_6H_{12}/H_2O$. Solutions of $AOT/C_6H_{12}/H_2O$/biacetyl were prepared by evaporating methanol from an aliquot of biacetyl stock solution and dissolving the biacetyl in $AOT/C_6H_{12}/H_2O$. Changes in the absorbance of 2×10^{-4} M naphthoate as a function of AOT concentration were observed by preparing a series of samples with different AOT concentrations and a fixed W equal to 10.

Polarization values were obtained by using 3. In this equation,

$$P = \frac{(I_\parallel)_v - (I_\perp)_v G_f}{(I_\parallel)_v + (I_\perp)_v G_f} \quad (3)$$

$(I_\parallel)_v$ and $(I_\perp)_v$ are the intensities of fluorescence emission parallel and perpendicular to vertically polarized excitation light. The G_f is a wavelength-dependent correction factor that describes the relative sensitivity of the detection system to vertically and horizontally polarized light. Polarization values were converted to microviscosities by using the Perrin equation

$$\frac{(1/P - 1/3)}{(1/P_0 - 1/3)} = 1 + \frac{kT\tau_f}{\eta V} \quad (4)$$

In this equation, P is the observed polarization, P_0 is the limiting value of polarization when no molecular rotation occurs, T is the temperature in Kelvin, τ_f is the fluorescence lifetime of the fluorophore, η is the microviscosity, V is the volume of the fluorophore, and k is the Boltzmann constant. Polarization values for the sodium salt of each naphthoate were obtained in a series of glycerol–water mixtures of known viscosity. Then, calibration curves for each counterion were constructed by plotting $(1/P - 1/3)$ versus T/η.

Reverse micellar solutions for sensitized phosphorescence studies were prepared by mixing portions of the stock solutions $AOT/C_6H_{12}/H_2O$/naphthoate and $AOT/C_6H_{12}/H_2O$/biacetyl to give bulk concentrations of 2.0×10^{-4} and 1.4×10^{-6} M for naphthoate and biacetyl, respectively. For sensitized phosphorescence in normal micelles, an aliquot of a concentrated aqueous biacetyl solution was added to an aliquot of concentrated aqueous CTA^+N^- solution and the sample was diluted with water. Aqueous samples containing SN and biacetyl were prepared in the same manner. The final bulk concentrations of naphthoate

Table I. Characteristics of Naphthoate Probes in AOT Reverse Micelles

naphthoate probe	η, cP	ϵ_a[a]	τ_f, ns	τ_P, ms
CTA^+N^-	17.0	6540	10	1.3
SN	15.3	6750	10	1.3
CTA^+NA^-	7.3	6540	5.7	1.6
$[CTA^+]_2NDC^{2-}$	6.5	400	23	2.6
CTA^+HN^-	13.2	2820	1.3	1.3

[a] Absorbance measured at 280 nm for all species except CTA^+HN^-, which was measured at 340 nm.

and biacetyl in aqueous solution were 2×10^{-4} and 1.4×10^{-6} M, respectively.

Instrumentation. All phosphorescence spectra were obtained by using a Perkin-Elmer LS-5 fluorescence spectrophotometer with a 20-μL flow cell. Samples were purged with extra-dry nitrogen (Specialty Gas) prior to phosphorescence measurement. The counterions of CTA^+N^-, $[CTA]^+]_2NDC^{2-}$, and CTA^+NA^- were selectively excited at 280 nm. The counterion of CTA^+HN^- was selectively excited at 340 nm. Sensitized phosphorescence of biacetyl was monitored from 450 to 700 nm. Absorbance spectra were obtained by using a Perkin-Elmer Lambda 3 spectrophotometer with 1-cm absorbance cuvettes.

Fluorescence lifetime measurements were obtained by using a PRA System 2000. Phosphorescence lifetimes were obtained by using the Perkin-Elmer LS-5 and eq 5. In this equation, ln

$$\ln I_t = -k(t_d) + \ln I_0 \quad (5)$$

I_t is the natural log of the phosphorescence intensity at a delay time t_d, k is the rate constant for the phosphorescence decay, ln I_0 is the natural log of the phosphorescence intensity with zero delay time. A plot of ln I_t versus t_d gives a straight line with a slope of $-2.303\tau_p$.

RESULTS AND DISCUSSION

Polarization Studies of the CTA^+N^- Probes. In order to examine naphthoate counterion binding in $AOT/C_6H_{12}/H_2O$, polarization of the fluorescent naphthoate counterions was employed to determine the relative naphthoate microviscosities in the reverse micelle. Polarization values were converted to microviscosities by using the calibration curves for the naphthoates described in the Experimental Section. The relative microviscosities, fluorescence lifetime, and several other characteristics for the naphthoate counterions in $AOT/C_6H_{12}/H_2O$ are provided in Table I. The short lifetimes of the naphthoates make them useful probes of their own microenvironments.

Assuming the rotational rate of the AOT micelle is the same in the presence of each naphthoate probe, several important observations concerning naphthoate binding can be made from these data. First, the counterion of CTA^+N^- is present in a more structured microenvironment than the counterion of the corresponding sodium salt SN. Since CTA^+N^- orients according to the AOT reverse micellar structure with its hydrocarbon tail extended, the quaternary ammonium head groups and naphthoate counterions will be anchored at the head group–water interface of the reverse micelle. As a result, the counterion of CTA^+N^- binds easily to the sulfonate head groups, resulting in a more rigid microenvironment than that observed for SN. The naphthoate counterion of SN can rotate more freely within the reverse micelle due to the smaller associated sodium ion. As indicated by the smaller microviscosity for SN, this orientational freedom probably results in a decrease in binding of the SN counterion to the sulfonate head groups of AOT.

The microviscosities obtained in this study can be used to elucidate the relative binding of the different counterions in the reverse micelles. Examination of the data indicates that the counterion binding order is $N^- > HN^- > NA^- > NDC^{2-}$. Although the probes N^- and NA^- are similar, greater binding for N^- is expected since the methylene unit in NA^- fixes the naphthyl group at a position further from the sulfonate head group region. The observed binding order may be useful for predicting the utility of each naphthoate as a triplet energy donor for biacetyl in sensitized phosphorescence.

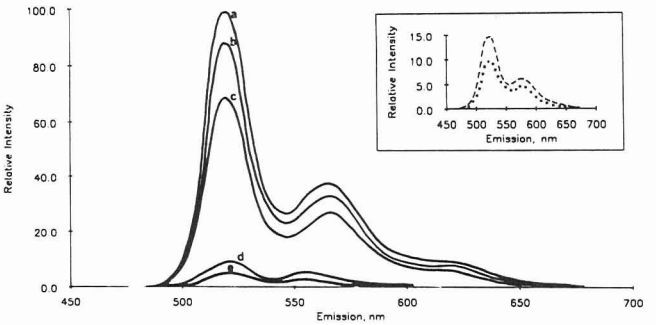

Figure 2. Relative phosphorescence spectra of 1×10^{-6} M biacetyl sensitized by 2×10^{-4} M (a) CTA^+N^-, (b) SN, (c) CTA^+NA^-, (d) $[CTA^+]_2NDC^{2-}$, and (e) CTA^+HN^-. The phosphorescence spectra for 1×10^{-6} M biacetyl sensitized by aqueous 2×10^{-4} M CTA^+N^- (– – –) and SN (• • •) are shown in the insert.

Sensitized Phosphorescence Using CTA^+N^- Donors. In micellar media in the absence of naphthoate, biacetyl phosphorescence was not observed when using an excitation wavelength of 280 nm. Excitation at 280 nm in micellar solutions containing both naphthoate ion and biacetyl resulted in the observation of the characteristic biacetyl phosphorescence. In fact, biacetyl phosphorescence was observed over the range of wavelengths at which the naphthoate absorbs. Since changes in the naphthoate absorbance spectrum are not observed in the presence of biacetyl, the observed biacetyl phosphorescence results from the transfer of triplet energy from naphthoate to biacetyl.

Sensitization of biacetyl phosphorescence with the CTA^+N^- and SN in $AOT/C_6H_{12}/H_2O$ and in aqueous solution was examined to determine the parameters that control energy transfer. The relative emission of biacetyl when sensitized by the naphthoate donors is shown in Figure 2. The insert shows the intensity of sensitized phosphorescence (I_{sp}) for the CTA^+N^-/biacetyl pair in normal CTA^+N^- micelles and for the SN/biacetyl pair in aqueous solution with the same concentrations of donor and acceptor.

Several observations can be made by examining the spectra of Figure 2. First, the I_{sp} for biacetyl in both normal and reverse micellar systems is greater than the I_{sp} observed in aqueous SN. Since micellar assemblies can be used to compartmentalize interactants, collisional interactions between naphthoate and biacetyl are increased in micelles. The I_{sp} of biacetyl in reverse micelles containing the CTA^+N^- probe is about 7 times greater than the I_{sp} observed in aqueous CTA^+N^- micelles. In normal micelles where biacetyl is solubilized at the head group–water interface (5), energy transfer is weak since the counterions are distributed between the bulk aqueous solvent and the Stern layer of the micelle. This counterion distribution decreases the probability of collisional interactions between naphthoate and biacetyl. Conversely, naphthoate and biacetyl are both restricted to the interfacial region of the reverse micelle and, therefore, are probably located within collisional diameters of one another. The result is enhanced energy transfer in the reverse micelle.

Another observation that can be made by examining Figure 2 is that variability in the I_{sp} of biacetyl is observed when using the different CTA^+N^- energy donors. The I_{sp} follows the order $CTA^+N^- > SN > CTA^+NA^- > [CTA^+]_2NDC^{2-} > CTA^+NH^-$. This order may be related to several characteristics of the naphthoate donors in reverse micellar systems. As discussed in the Introduction, several parameters of the donor and acceptor may affect the observed sensitized phosphorescence.

Assuming the solubilization site of biacetyl is unchanged in the presence of each naphthoate surfactant, then the molar absorptivity, the molar concentration, and the phosphorescence lifetimes of the naphthoate counterion will affect the I_{sp}. The binding of the naphthoate counterions will also contribute to the observed sensitized phosphorescence. In Table I, these parameters are compiled for the naphthoates in $AOT/C_6H_{12}/H_2O$.

The most efficient donors, CTA^+N^-, SN, and CTA^+NA^-, have similar molar extinction coefficients and phosphorescence lifetimes in reverse micellar solution. For these probes, the controlling factor appears to be the strength of binding for the naphthoate counterion. The microviscosity study of $AOT/C_6H_{12}/H_2O$ indicated that the relative binding of these three naphthoates is $CTA^+N^- > SN > CTA^+NA^-$. This same order is observed for the I_{sp}, indicating that the binding of the probe to the head groups of the reverse micelle is an important variable in sensitized phosphorescence for the naphthoate/biacetyl pair. The lower energy transfer of CTA^+NA^- compared to CTA^+N^- is expected since the presence of the methylene group in NA^- pushes the naphthyl moiety further from the interface where biacetyl is solubilized. In fact, similar observations have been made in other energy transfer studies where the number of methylene units between the carbonyl group and the naphthalene moiety has been varied (7).

For the surfactants CTA^+HN^- and $[CTA^+]_2NDC^{2-}$, considerably weaker energy transfer is observed. This result can be attributed predominantly to the small molar absorptivities for the HN^- and NDC^{2-} counterions. Although CTA^+HN^- binds more strongly to the sulfonate head groups and has a larger molar absorptivity, $[CTA^+]_2NDC^{2-}$ sensitizes biacetyl somewhat more effectively than CTA^+HN^-. Possibly, the larger phosphorescence lifetime of NDC^{2-} offsets the greater binding and larger molar absorptivity for HN^-. The longer phosphorescence lifetime for the NDC^{2-} counterion provides additional time for energy transfer to occur and, as shown by eq 1 and 2, this results in an increase in I_{sp}.

From the data provided for the CTA^+N^- probes, it is clear that the absorption and luminescence characteristics of the naphthoates are valuable parameters for determining the I_{sp} for biacetyl. Additionally, the binding of the naphthoate probes to the interfacial region in the reverse micelle is also crucial for the observation of triplet energy transfer to biacetyl. In fact, when the absorption and luminescence characteristics are similar for a series of naphthoate donors, the I_{sp} is related directly to the naphthoate binding at the interface. For the remaining studies, CTA^+N^- is used as a triplet energy donor since this probe proved to be the most effective sensitizer for biacetyl.

Variation in the AOT Concentration. The effect of AOT concentration on I_{sp} at a fixed $[H_2O]/AOT]$ ratio, or W, equal to 10 was examined to elucidate the effect of this parameter on sensitized phosphorescence. A plot showing I_{sp} of biacetyl versus the AOT concentration at a fixed CTA^+N^- donor concentration is provided in Figure 3. The I_{sp} of biacetyl increases in the concentration range from 0.01 to 0.075 M AOT and shows no further increases above 0.075 M AOT. These data indicate that the change in AOT concentration can be used to control I_{sp}.

Examination of the insert in Figure 3 shows that the naphthoate absorbance gives the same profile as a function of AOT concentration. As shown in eq 1, an increase in absorbance (ϵbC) corresponds to an increase in I_{sp}. This change in absorbance may correspond to a change in the binding of the naphthoate counterion to the sulfonate head groups of AOT. To examine this possibility in greater detail, a series of absorbance spectra for CTA^+N^- were obtained with

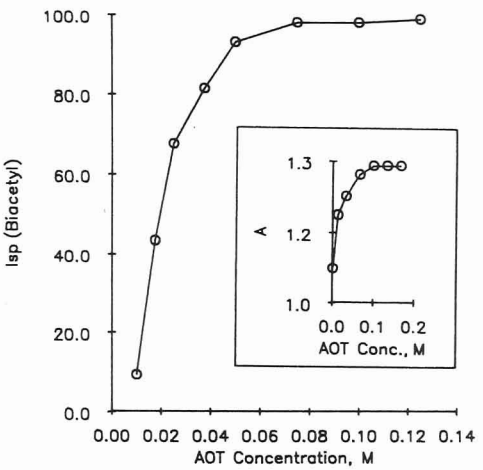

Figure 3. Relationship between sensitized biacetyl phosphorescence and the concentration of AOT. Concentrations of CTA^+N^- and biacetyl are 2×10^{-4} and 1.4×10^{-6} M, respectively. The insert shows the change in absorbance for 2×10^{-4} M CTA^+N^- as a function of the AOT concentration. For all measurements W is equal to 10.

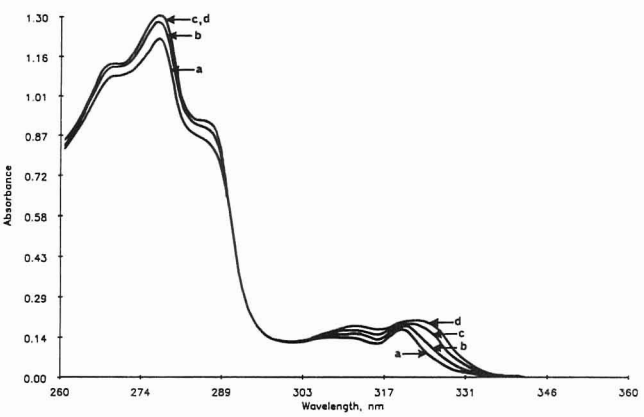

Figure 4. Absorbance spectra of 2×10^{-4} M CTA^+N^- with (a) 0.01 M, (b) 0.05 M, (c) 0.075 M, and (d) 0.10 M AOT. The peaks from 340 to 310 nm result from the $n\pi^*$ absorbance of the carbonyl group while the peaks from 295 to 270 nm result from the $\pi\pi^*$ absorbance of the naphthyl moiety.

different AOT concentrations and a fixed W equal to 10. Although CTA^+N^- is insoluble in cyclohexane in the absence of AOT, it is soluble at low AOT concentrations (0.01 M) in the presence of water. Therefore, the effect of consecutive additions of AOT on naphthoate absorbance can be followed.

The naphthoate absorbance spectra are shown in Figure 4. In addition to the increase in absorbance at 280 nm, a shift in the bands located from 340 to 300 nm, resulting from the $n\pi^*$ absorbance of the carbonyl is observed. Shifts in absorbance for $n\pi^*$ transitions are typically solvent-dependent and usually show a shift to shorter wavelengths with an increase in solvent polarity (14). The observed shift to longer wavelengths for naphthoate with increasing AOT concentration is indicative of an increasingly nonpolar microenvironment for the carbonyl group. These data indicate that the changes observed in the sensitized phosphorescence with addition of AOT most likely result from the increase in CTA^+N^- binding to the interface of the AOT reverse micelle. At low AOT concentrations, the carbonyl groups are solubilized by the water pool; however, the carbonyl groups become firmly bound to the sulfonate head groups as the concentration of AOT increases.

On the basis of these results, the most intense sensitized phosphorescence is expected at high AOT concentrations because the naphthoate is bound to the head groups where biacetyl is solubilized, resulting in an increase in absorbance. Interestingly, many studies that describe energy transfer in

Table II. Variation in Sensitized Phosphorescence of Biacetyl with Changes in W

W^a	relative I_{sp} biacetyl[b]	R,[c] Å
2.5	0.98	3.72
5.0	1.01	7.43
10	1.00	14.9
15	0.95	22.3
20	0.87	29.7
25	0.31	37.1

[a] Performed with [AOT] = 0.1 M. [b] Performed with [biacetyl] = 1.4×10^{-6} M and $[CTA^+N^-] = 2 \times 10^{-4}$ M. Values are given relative to 1.00 for $W = 10$. [c] Radius of the water pool calculated from eq 6.

AOT reverse micelles use AOT concentrations well below 0.1 M (*15*). In these studies, aromatic acids are presumed to be sufficiently bound to the reverse micellar interface. Depending on the binding constants for the particular analytes involved in the energy transfer scheme, it may be possible to enhance the measured sensitized phosphorescence by increasing the AOT concentration as shown for the naphthoate/biacetyl pair.

Variation in Water Content. The effect of the water pool size on I_{sp} was examined by altering W at a fixed AOT concentration of 0.1 M. An increase in W may decrease the probability of sensitized phosphorescence by providing a larger effective volume for solubilization of naphthoate and biacetyl. Additionally, beyond W equal to 6, an increase in W contributes to an increase in the fluidity of the head group–water interface (*16*). Changes in either of these parrameters may alter the intensity of the observed sensitized phosphorescence by changing the microenvironments for the donor and acceptor.

Approximate radii of the water pool in $AOT/C_6H_{12}/H_2O$ have been calculated at varying water contents. Reasonable estimates of the water pool radii can be made by using eq 6 which is shown below (*16*). In this equation, R is the radius

$$R = 36.65v/w_t \qquad (6)$$

of the water pool, v is the percent (volume/volume) of water, and w_t is the percent (weight/volume) of AOT. The calculated radii are shown in Table II along with the relative I_{sp} at various W.

It is clear that, as the radius of the water pool exceeds 29 Å, energy transfer declines rapidly. Since no changes in the absorbance maximum and luminescence lifetime for naphthoate are observed as the micellar water content is increased, the observed decrease in I_{sp} probably results from changes in the proximity of naphthoate and biacetyl when the water pool becomes sufficiently large. Naphthoate is expected to be solubilized at the head group–water interface regardless of the water content, so that the nonpolar naphthyl moiety can be solubilized in a more nonpolar environment. Biacetyl may become more freely soluble in the water core with increasing W; however, the lack of a sharp decrease in I_{sp} as the water pool radius exceeds 15 Å suggests that biacetyl also remains bound at the head group–water interface as W is increased.

In order to evaluate the microenvironment for naphthoate at different W, the shifts of the $n\pi^*$ absorbance bands of naphthoate were examined. The absorption energies for naphthoate in chloroform, methanol, and water were plotted versus the dielectric constants for the solvents as shown in Figure 5a. Then, the absorption energies for naphthoate in $AOT/C_6H_{12}/H_2O$ with different W were extrapolated to the line to give approximate dielectric constants for the naphthoate microenvironments in each micelle. As shown in Figure 5a, the $n\pi^*$ absorption energy of naphthoate increases as W increases, approaching a more aqueous microenvironment. At W equal to 10, the dielectric constant calculated from the plot

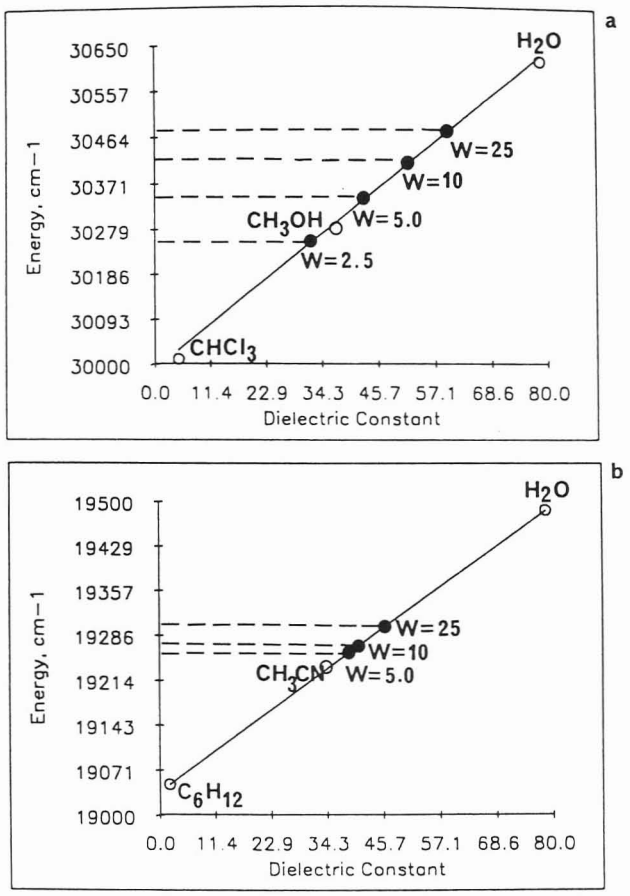

Figure 5. Relationship between dielectric constant and (a) energy of the $n\pi^*$ absorbance of naphthoate and (b) energy of the $n\pi^*$ phosphorescence of biacetyl. The darkened circles show where the absorption and phosphorescence energies observed in the reverse micelles would fall on the line. These values can be extrapolated to the x axis to give approximate dielectric constants for the microenvironments of naphthoate and biacetyl in reverse micelles with varying water content.

is 49.5 and the calculated dielectric constant increases to 54.7 when W reaches 25. Thus, the naphthoate microenvironment becomes more water-permeable as the concentration of solubilized water is increased in the reverse micelle.

Similar absorbance studies for biacetyl cannot be conducted since biacetyl has a low molar absorptivity; however, the $n\pi^*$ phosphorescence of biacetyl is solvent sensitive and shows a shift to shorter wavelengths with an increase in solvent polarity (*17*). The biacetyl phosphorescence energies in water, acetonitrile, and cyclohexane, along with the dielectric constants for these solvents, were used to construct a plot similar to the one shown in Figure 5a. From this plot for biacetyl (Figure 5b), dielectric constants for the biacetyl microenvironment in the reverse micelle with W equal to 10 and W equal to 25 are estimated at 43.5 and 49.0, respectively. Thus, the microenvironment of biacetyl also becomes more water-permeable as W is increased.

Examination of the respective absorbance and phosphorescence data for naphthoate and biacetyl shows that the dielectric constants for both species at W equal to 10 and W equal to 25 are similar. Therefore, both species are expected to reside in a similar microenvironment, probably at the interfacial region of the reverse micelle. At W equal to 6, sufficient water is present to hydrate the head groups and counterion of AOT (*16*). Beyond this value, "free" water that contributes to the fluidity of the head group–water interface is available in the reverse micelle. Since this interface becomes more fluid with increasing W, greater freedom of movement within the interfacial region becomes possible for both

naphthoate and biacetyl. Therefore, collisions between these interactants become less probable as the water content increases. The result is a decrease in I_{sp} when the fluidity of the interface becomes sufficiently large. For this reason, sensitized phosphorescence between naphthoate and biacetyl can be maximized by using low water content so that the proximity of these interactants can be maintained.

CONCLUSION

The energy transfer scheme used here effectively illustrates the utility of bound CTA^+N^- donors for sensitized phosphorescence in micellar media. On the basis of the data for triplet energy transfer from naphthoate to biacetyl in both normal and reverse micelles, reverse micelles containing the CTA^+N^- probes provide a more structured microenvironment for effective sensitized phosphorescence. The greater sensitization possible in reverse micelles results from the efficient restriction of the solubilized probes within a small volume at the interfacial region of the reverse micelle. The probe CTA^+N^- is a more effective sensitizer than SN as a result of the greater binding of CTA^+N^- to the micelle. Specifically, the CTA^+ chain acts as an "anchor" to control the solubilization site for the naphthoate counterion.

The relative sensitized phosphorescence intensities can be predicted for the various naphthoate counterions. The microviscosity data, as well as the absorption and luminescence characteristics of the donor, are useful for predicting the relative intensities of sensitized phosphorescence in reverse micelles. When absorbance and luminescence characteristics are similar, the binding order anticipated from microviscosities can be used alone to accurately predict the relative sensitized phosphorescence intensities.

When energy transfer in AOT reverse micelles is examined, several factors can be manipulated to enhance the luminescence signal. Specifically, the water content of the micelle can be altered to enhance the proximity of donor and acceptor species. Typically, low water content provides more intense sensitized phosphorescence since donors and acceptors can be maintained within collisional diameters of one another. The binding of the probe can also be controlled by using an AOT concentration at which the probe is sufficiently bound to the micelle interface. A greater knowledge of these factors may be useful when examination of energy transfer in reverse micelles is desired. Ultimately, the use of anchored energy donors may provide more sensitive analyses for small quantities of aromatic pollutants found in aqueous systems.

Registry No. CTA^+N^-, 127317-35-5; $[CTA^+]_2NDC^{2-}$, 127317-37-7; CTA^+NA^-, 127317-39-9; CTA^+HN^-, 127317-40-2; AOT, 577-11-7; biacetyl, 431-03-8.

LITERATURE CITED

(1) Hinze, W. L. In *Solution Chemistry of Surfactants*; Mittal, K. L., Ed.; Plenum: New York, 1979; Vol. 1, p 79.
(2) Pelizzeti, E.; Pramauro, E. *Anal. Chim. Acta* **1985**, *169*, 1.
(3) Weinberger, R.; Rembish, K.; Cline Love, L. J. In *Advances in Luminescence Spectroscopy*; Cline Love, L. J., Eastwood, D., Eds.; American Society for Testing Materials: Philadelphia, PA, 1985; p 40.
(4) Humphry-Baker, R.; Moroi, Y.; Gratzel, M. *Chem. Phys. Lett.* **1978**, *58*, 207.
(5) DeLuccia, F. J.; Cline Love, L. J. *Anal. Chem.* **1984**, *56*, 2811.
(6) Cline Love, L. J.; Grayeski, M. L.; Noroski, J. *Anal. Chim. Acta* **1985**, *170*, 3.
(7) Gelade, E.; De Schryver, F. C. *J. Am. Chem. Soc.* **1984**, *106*, 5871.
(8) Correll, G. D.; Cheser, R. N.; Nome, F.; Fendler, J. H. *J. Am. Chem. Soc.* **1978**, *100*, 1254.
(9) Almgren, M.; Svensson, A. Ch. *Chem. Scr.* **1976**, *9*, 145.
(10) Blyshak, L. A.; Rollie-Taylor, M.; Underwood, A.; Patonay, G.; Warner, I. M. *J. Colloid Interface Sci.* **1990**, *108*, 509.
(11) Turro, N. J. *Modern Molecular Photochemistry*; Benjamin/Cummings: Menlo Park, CA, 1978; Chapter 9.
(12) Wilkinson, F. In *Luminescence in Chemistry*; Bowen, E. J., Ed.; D. Van Nostrand: Princeton, NJ, 1968; Chapter 4.
(13) Menger, F. M.; Saito, G. *J. Am. Chem. Soc.* **1978**, *100*, 4376.
(14) Herkstroeter, W. G. In *Creation and Detection of the Excited State* Lamola, A. A., Ed.; Marcel Dekker: New York, 1971; Vol. 1A, Chapter 1.
(15) Eicke, H.-F.; Shepherd, J. C. M.; Steineman, A. *J. Colloid Interface Sci.* **1976**, *56*, 168.
(16) Wong, M.; Thomas, J. K.; Nowak, T. *J. Am. Chem. Soc.* **1977**, *99*, 4730.
(17) Wilkinson, F.; Horrocks, A. R. In *Luminescence in Chemistry*; Bowen, E. J., Ed.; D. Van Nostrand: Princeton, NJ, 1968; Chapter 7.

RECEIVED for review December 28, 1989. Revised manuscript received May 30, 1990. Accepted June 1, 1990. This work was supported in part by the National Science Foundation (CHE-8609372) and the Office of Naval Research. Isiah M. Warner acknowledges support from a National Science Foundation Presidential Young Investigator Award (CHE-8351675).

Flow Injection Analysis and Real-Time Detection of RNA Bases by Surface-Enhanced Raman Spectroscopy

Fan Ni, Rongsheng Sheng, and Therese M. Cotton*

Department of Chemistry, Iowa State University, Ames, Iowa 50011

Surface-enhanced Raman scattering (SERS) spectroscopy has been successfully interfaced with a flow injection analysis system to detect RNA bases in real time. Four of the major base components of RNA, uracil, cytosine, adenine, and guanine, were introduced into the flow injection system and were mixed with a Ag sol prior to SERS measurements. Several experimental parameters including pH, temperature, flow rate, and tubing materials were examined, and their impact on the SERS spectra is presented here. The feasibility of interfacing flow injection based SERS detection methods with liquid or high-performance liquid chromatography for the detection of individual components in a complex mixture is also assessed.

* Author to whom correspondence should be addressed.

INTRODUCTION

Surface-enhanced Raman scattering (SERS) has been used to detect nucleic acid bases, the building blocks of DNA and RNA, as well as several of their derivatives (*1–12*). The experimental results have revealed that the interfacial behavior of the individual bases is dependent on the adsorbate orientation, concentration of the base in bulk solution, and the pH of the surface (if a metal colloid is used as the SERS-active substrate) or the applied potential (if an electrode is used as the SERS-active substrate) as well as other physical and chemical parameters (*1–12*). So far, most SERS studies have been concerned with the individual compounds rather than a mixture of bases. A number of studies have also been concerned with intact DNA and RNA and have shown that the SERS spectra are dominated by the characteristic SERS

0003-2700/90/0362-1958$02.50/0

bands of individual nucleic acid bases (*1*, *2*). Thus, these spectra can be used to identify the individual components of DNA and RNA when they are in contact with the metal surface.

Koglin et al. (*2*) reported that the SERS spectrum of a mixture containing adenine, guanine, cytosine, and thymine was dominated by vibrational bands attributed to the adenine base. Bands due to thymine and/or cytosine were also observed.

Direct analysis of mixtures of two or three components other than RNA or DNA bases has been achieved by using SERS (*13*, *14*). Carrabba et al. (*13*) found that SERS selectivity for each component could be achieved by modulating the potential of the electrode and the excitation wavelength. The requirement for potential control and variation of the excitation wavelength adds considerable complexity to the procedure. Also, because no prior separation step was used, overlapping and nondifferentiable SERS bands were observed. In another report, Laserna et al. (*14*) used SERS to identify three nitrogen-containing organic molecules adsorbed on silver-coated filter paper. An excess of one component in the mixture led to, at most, a weak SERS signal from the other two components. In addition, overlapping and unidentified SERS bands were also present in the spectra. It appears that prior separation of a mixture of components is advantageous, or essential in some cases, for the application of SERS to the analysis of a mixture of compounds.

High-performance liquid chromatography (HPLC) as well as other chromatographic techniques have the desired high-resolution separation capability. In recent years, analytical applications of SERS have been concerned with combining the selectivity and sensitivity of the technique with the separation power of HPLC (*12*, *15–17*). Séquaris and Koglin (*12*) used SERS to detect purine and nine purine derivatives that were separated by high-performance thin-layer chromatography (HPTLC). Detection limits for individual compounds were estimated to be 5 ng/spot when the sample was excited with 10 mW of 514.5 nm light from an Ar^+ laser. A similar study has also been conducted by Tran (*17*), who used SERS to identify three dyes separated by paper chromatography. Recently, Freeman et al. (*16*) successfully interfaced an HPLC system and a Raman spectrometer. A common organic dye, pararosaniline hydrochloride, was chosen as a test analyte. A detection limit near 100 ppb was achieved. Several SERS spectra of pararosaniline hydrochloride were obtained under flow-stopped conditions (*16*). This approach appears to be promising, although only a single compound was tested rather than a mixture. Ni et al. (*15*) used SERS as an off-line ancillary HPLC detector for a mixture of nitrophenol compounds. The detection limits were near the 14 ppb level and the SERS spectra were recorded under static conditions.

Although several attempts have been made to combine SERS with HPLC (*15*, *16*), thus far most SERS measurements were taken under static conditions. Obviously, there are additional problems associated with obtaining SERS under flowing conditions.

To a certain extent, the postcolumn conditions of LC and HPLC methods can be simulated by a flow injection analysis (FIA) system. Several researchers (*18–20*) have interfaced SERS with a FIA system as a real time detector. Under continuous flow conditions, a major difficulty encountered is the maintenance of an active and clean SERS substrate, especially when several compounds are subsequently introduced into the FIA system. By using a short electrochemical roughening procedure, Forcē (*20*) was able to regenerate a SERS-active Ag electrode surface under flowing conditions. However, only pyridine was tested and the method required a reproducible roughening procedure, as well as a potential step to remove the adsorbate resulting in a cumbersome procedure.

Ag sols have several obvious advantages as SERS substrates in a continuous flow system. These include the mobility of the sol and the availability of a fresh silver surface for each of the separated analytes. Berthod et al. (*19*) reported the SERS spectrum of *p*-aminobenzoic acid (PABA) after it was mixed with a Ag sol and passed through a FIA system.

The literature indicates that very few SERS studies have utilized flowing systems. The paucity of experimental results in this area reflects the degree of experimental difficulty associated with flowing systems.

The purpose of this study is to develop SERS as a real-time detector for a FIA system and to test the feasibility for interfacing SERS to an HPLC system. Several experimental parameters for optimizing SERS signals will be discussed in detail. Four RNA bases were chosen for study because of their biological significance, their well-characterized SERS spectra, and the wealth of available HPLC data concerning their separation. The results extend the original studies by Winefordner et al. (*18*, *19*) to include direct detection of analytes in a flowing solution.

EXPERIMENTAL SECTION

Reagents. All chemicals, including ethylenediaminetetraacetate (EDTA), sodium citrate, silver nitrate, uracil, cytosine, adenine, and guanine were purchased from Sigma Chemical Co. (St. Louis, MO) (reagent grade) and were used without further purification. The water was deionized and twice-distilled.

Silver Sol Preparation. Silver sols were prepared by two different procedures as described below.

(*1*) *EDTA Reduction Procedure* (*5*). One milliliter of 0.1 M EDTA tetrasodium salt and 1.3 mL of 0.1 M $AgNO_3$ were added to 100 mL of boiling water with vigorous stirring. Upon cooling, the solution's color changed gradually from colorless to light yellow and, finally, to golden yellow. When the solution became golden yellow, 0.3 mL of 0.1 M HCl was added, at which point the solution became yellow-brown. The Ag sol was aged for a few days prior to use.

(*2*) *Citrate Reduction Procedure* (*21*). Five hundred milliliters of a 1.0×10^{-3} M $AgNO_3$ was brought to the boiling point. Ten milliliters of 3.4×10^{-2} M sodium citrate was added dropwise to the solution with vigorous stirring. The mixture was maintained at the boiling point for 1 h and the final volume was adjusted to 500 mL with distilled water. The Ag colloid was transferred to a graduated cylinder, the cylinder was covered, and the colloid was allowed to fractionate by sedimentation. Successive 50-mL aliquots were carefully withdrawn from the cylinder. The fraction with the maximum enhancement was used as the SERS substrate, as described in ref 21.

RNA Base Stock Solution. Solutions of uracil, cytosine, adenine, and guanine were prepared at a concentration of 1×10^{-3} M. The final solutions were prepared by serial dilution from the stock solution.

Mobile Solutions. Two mobile solutions that were used previously for HPLC separation of RNA bases were prepared as described (*22*): (1) 5×10^{-5} M sodium citrate, 5×10^{-3} M K_2HPO_4 (pH = 9.00) and 50% ethanol; (2) 5×10^{-5} M sodium citrate, 5×10^{-3} M phosphate buffer and 50% ethanol (pH = 7.25).

Flow System. A schematic diagram of the flow system used in this study is shown in Figure 1. The Ag sol, sample solution, and mobile solution are pumped by a peristaltic pump (Buchler Instruments), through a T-joint at a flow rate of 1 mL/min and mixed together. The slowest flow rate per minute attainable with this system is 1 mL/30 min at room temperature and 0.1 mL/min at 70 °C. The mixture next flows through a constant temperature water bath. A capillary sample cell (1.5–1.8 mm i.d.) is used to obtain the SERS spectra.

Raman Instrumentation. The 457.9-nm line of an Ar^+ laser was used as the excitation source for the SERS measurements. A two lens collection system was used to collect and focus the Raman scattering light onto the entrance slit of the monochromator/spectrograph (Spex Triplemate 1877), which is coupled to a Model 1420 intensified Si photodiode detector (Princeton

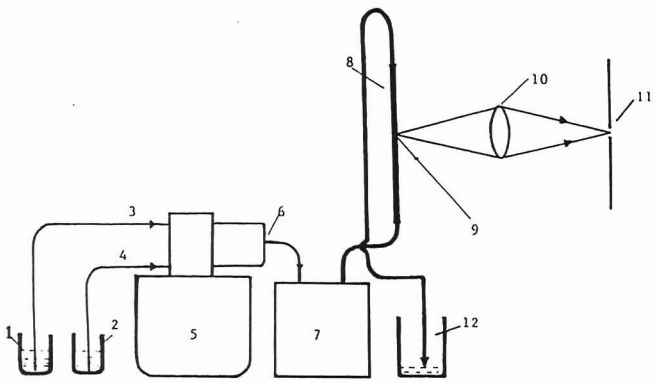

Figure 1. Schematic diagram of the flow injection system used for SERS analysis: (1) sample solution or mobile solution; (2) Ag sol; (3) injection tubing for sample solution or mobile solution; (4) injection tubing for Ag sol; (5) peristaltic pump; (6) T-joint; (7) temperature-controlled water bath; (8) capillary sample cell; (9) laser excitation beam; (10) collection lens; (11) monochromator slit; (12) waste beaker.

Applied Research Corp.). The Raman spectra were recorded and processed with an optical multichannel analyzer (OMA-2, Princeton Applied Research Corp.). Eighteen spectra were recorded consecutively as the four bases were injected sequentially. The acquisition time per spectrum was 30 s and the total elapsed time for the complete analysis of all four bases was 9 min. In some cases, two sets of 18 spectra were measured during a longer injection process. Between the acquisitions of the two sets of 18 spectra, the flow was halted briefly (about 1 min) in order to store the first 18 spectra.

RESULTS AND DISCUSSION

Consideration was given to the selection of tubing material and cleaning of the tubing in a recent study of a SERS/FIA system (*16*). Because Ag sols are unstable, aggregation or even deposition of silver particles can be induced when analytes are added to the sol and the mixture is heated. The deposition of silver particles on the inner wall of the tubing used in the FIA system can create undesirable "memory effects". The "memory effects" are due to the presence of adsorbed sample molecules on the silver particles that are deposited on the tube walls. Hence, the SERS signal from the initially injected compound persists for a longer period than that of the subsequent compounds, until the deposited particles are dislodged or replaced by the continually flowing stream. This also produces tailing, overlapping, or even disappearance of SERS spectra from some of the injected samples, particularly when poly(vinyl chloride) (Tygon) tubing is used. Cleaning the tubing with nitric acid is an effective method to remove the deposited silver particles from the inner walls of glass tubing. However, Tygon tubing is attacked by nitric acid and forms a nitrated product that cannot be rinsed out by water. The nitrated product can interact with sample molecules in the eluent or can itself adsorb on the silver particles. To complicate matters further, the acid-reacted Tygon tubing causes increased silver particle deposition on the inner wall as compared with the original tubing. Consequently, an unusual SERS spectrum (not shown), associated with the nitrated species and a more pronounced "memory effect" or overlapping of SERS spectra for different compounds was observed when Tygon tubing was used. Therefore, glass tubing was chosen for all experiments reported in this paper. It is essential that the glass tubing is cleaned daily with nitric acid to ensure the quality of SERS spectra.

Figure 2 illustrates the SERS spectra of the four RNA bases obtained at room temperature in the stopped-flow or static condition. Each base can be distinguished from the others by the band positions and relative intensity patterns. The bands corresponding to the ring breathing mode for adenine (A), cytosine (C), uracil (U), and guanine (G) are at 727, 798,

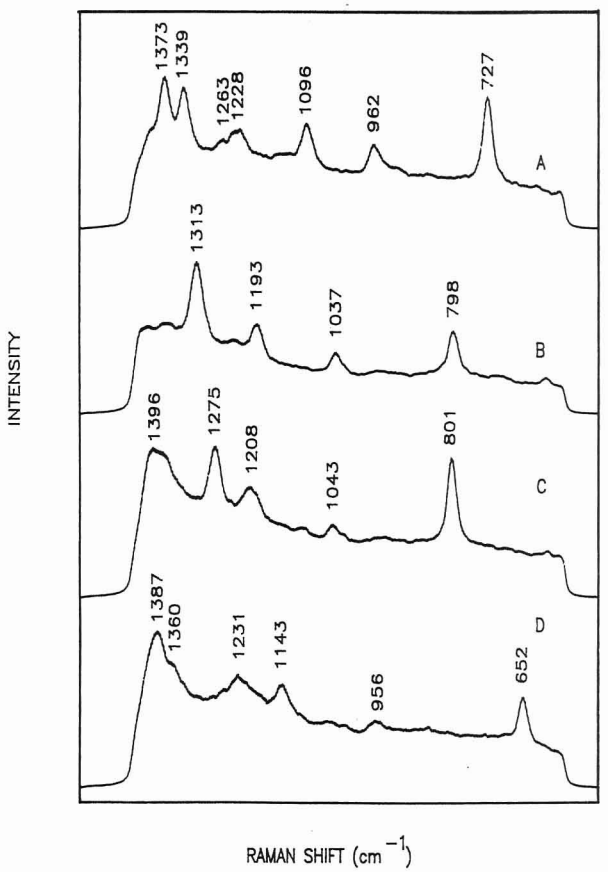

Figure 2. SERS spectra of four RNA bases obtained at room temperature: (A) 5×10^{-4} M solution of adenine at pH 3.0; (B) 5×10^{-4} M cytosine; (C) 5×10^{-4} M solution of uracil; (D) 3.3×10^{-4} M solution of guanine at pH 3.0. The sample was dissolved in distilled water and the pH adjusted with HCl. The laser power was 20 mW and the spectral acquisition time was 33 s.

801, and 652 cm^{-1}, respectively (*23*, *24*). C and U have almost the same band position for the ring breathing mode, but the two spectra can still be distinguished by the differences in the 1200–1400-cm^{-1} region. Thus, these four SERS spectra serve as a fingerprint for identifying each RNA base.

A major concern when using SERS as a detector for FIA is the reproducibility of the SERS substrate for consecutively introduced samples. Forcé (*20*) used a Ag electrode as a SERS substrate for FIA detection. The electrode was initially activated by an oxidation–reduction cycle (ORC) prior to introduction of the sample. The potential was adjusted to −1.2 V to remove the first adsorbate via the H_2 produced on the electrode surface. However, H_2 evolution deactivated the surface. Before the second sample was introduced, the activity of the Ag surface was regenerated by stepping the potential back and forth for another ORC. The use of a Ag sol as a mobile SERS substrate eliminates the necessity for activation and potential changes that are required when a silver electrode is used as the SERS substrate. Sols are replenishable and can provide active surfaces for a series of samples following their introduction into a FIA system.

Although Ag sols are advantageous as SERS substrates in a FIA system, they also present difficulties. Figure 3A shows a SERS spectrum of U obtained under static conditions at room temperature, whereas spectrum Figure 3B was taken under flowing conditions at room temperature and at the slowest flow rate attainable from the peristaltic pump (1 mL/30 min). With higher flow rates (as little as 2 mL/30 min), the signal arising from uracil was nearly indistinguishable from the background. It is clear that the faster the flow rate of the sample, the weaker the SERS spectrum. The two spectra were plotted with the same scale in Figure 3 and from

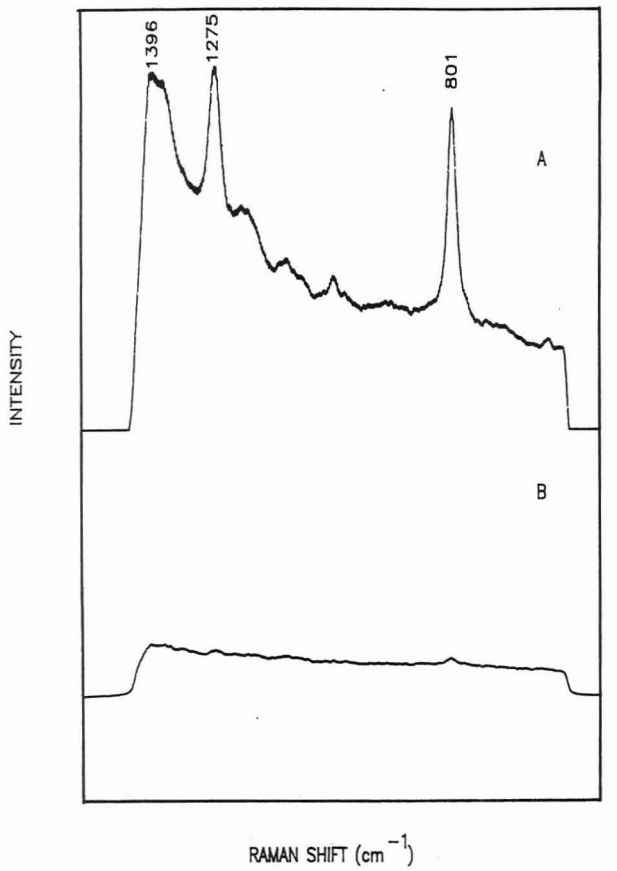

Figure 3. (A) SERS spectrum of a 5 × 10^{-4} M solution of uracil obtained under static conditions at room temperature. (B) SERS spectrum of a 5 × 10^{-4} M solution of uracil obtained under flowing conditions at room temperature. The laser power was 105 mW and the spectral acquisition time was 33 s.

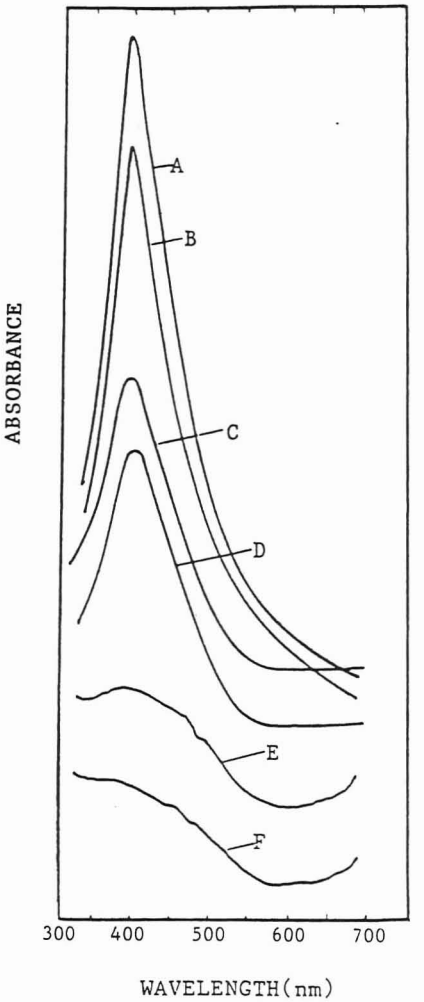

Figure 4. UV absorption spectra of a Ag sol mixed with a 5 × 10^{-4} M uracil solution at various temperatures: (A) 20 °C; (B) 30 °C; (C) 45 °C; (D) 55 °C; (E) 65 °C; (F) 75 °C.

the measurement of the relative peak heights, it can be seen that the intensity of the 801-cm^{-1} band in Figure 3A is about 25 times greater than that in Figure 3B.

Several factors could contribute to the poor quality of the SERS spectra under flowing conditions. It has been shown (*25*) that the degree of aggregation of the Ag sol influences the observed enhancement factor; i.e. the greater the extent of aggregation, the greater the enhancement. This fact may explain the observation (*21*) that a highly flocculated Ag sol that has been aged for a few days produces more intense SERS than an unaggregated sol. Under static conditions, laser irradiation at a single spot on the sample produces localized thermal aggregation of the Ag sol, and thus gives a good SERS spectrum. Laser irradiation may also contribute to photoreactions at the Ag surface as well. In contrast, photoreactions and photothermally induced aggregation of the Ag sol do not occur as readily in a flowing system under the very short transit times in the laser beam. Freeman et al. (*16*) appear to have observed the same effect when they interfaced SERS with stopped-flow HPLC. They recorded SERS spectra under stopped-flow conditions.

It is known that aggregation of a silver sol can be monitored by visible absorption spectroscopy (*25*). The unaggregated form of the sol used in this study had a strong absorption peak in the 400-nm region at room temperature (see Figure 4A,B). With increased aggregation at higher temperatures, this peak becomes weaker and broadens and is accompanied by a red shoulder (see Figure 4C–F). These results demonstrate that aggregation of the silver sol can be induced by thermal effects.

Several other explanations could also account for the strong SERS intensity under laser irradiation. First, each base usually exists in a hydrated state. The hydration shell of the base may hinder its direct interaction with the silver surface. Laser irradiation could cause dehydration of the base and, thereby, enable it to adsorb more strongly to the silver surface. Second, some RNA bases tend to form hydrogen-bonded dimers or polymers. The polymeric form may be more sterically hindered, as compared with the monomer of dimer, and unable to interact with the silver surface. Thermal disruption of the hydrogen bonds by laser irradiation produces more monomer species and, hence, facilitates adsorption of the base at the metal surface. Third, the adsorption–desorption equilibrium is reached more quickly at the higher temperatures produced by laser irradiation. Although less adsorbate may be bound to the surface at higher temperatures, the equilibrium between surface and bound species is achieved much more rapidly. In summary, under static conditions, adsorbates can be activated by a localized heating of the sol resulting from laser irradiation. In contrast, under flowing conditions, each fraction of Ag sol/sample mixture is irradiated for a very short period. Photothermal effects on the Ag sol and the sample are negligible.

An extension of this logic predicts that raising the temperature of the sol/analyte mixture may provide a means for improving the quality of the SERS spectrum under flowing conditions. Figure 5 illustrates the SERS spectra of U at different temperatures under flowing conditions. From Figure 5, it can be concluded that the SERS intensity is strongly dependent on temperature. The higher the temperature, the greater the extent of aggregation of the silver sol, and the stronger the peak intensity. At 76 °C the intensity of the 801-cm^{-1} band is stronger than that obtained under static conditions at room temperature.

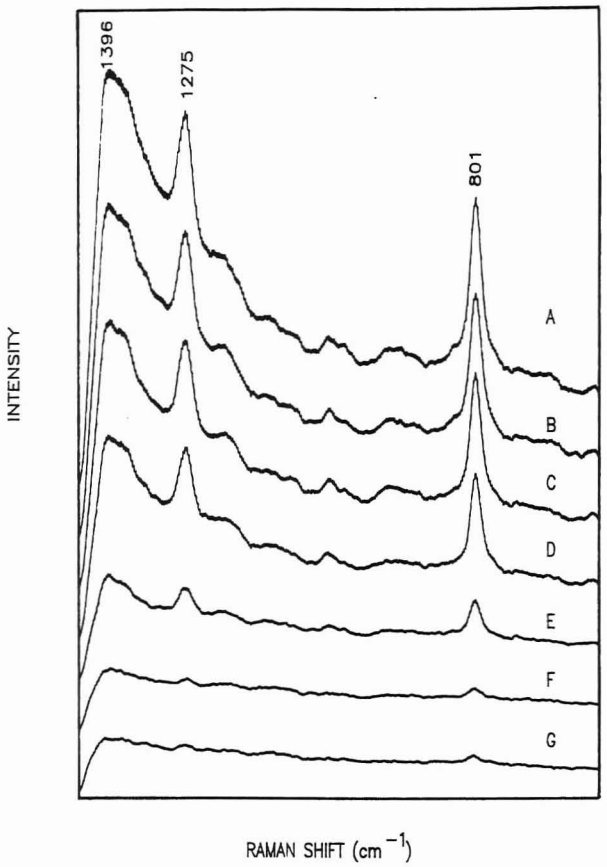

Figure 5. SERS spectra of a 5 × 10^{-4} M uracil solution obtained under flowing conditions at various temperatures: (A) 76 °C; (B) 71 °C; (C) 62 °C; (D) 53 °C; (E) 46 °C; (F) 36 °C; (G) 23 °C. The laser power was 105 mW and the spectral acquisition time was 33 s.

Because the boiling point of the mobile phase used for HPLC is approximately 76 °C, the temperature of the water bath was set below 76 °C to avoid vaporization of the mobile phase solution. Thus, unless indicated otherwise, the remainder of the experimental results presented here were obtained with the temperature of the water bath set at 70 °C (±1 °C).

The pH of the sample solution is another critical parameter for obtaining high-quality SERS spectra (*18*). When isolated samples are tested under the static conditions, optimization of the pH can be performed as desired. But when several samples are introduced consecutively into a flowing system, the situation is not as simple. Figure 6 illustrates the pH effect on the SERS spectrum of each RNA base studied in this work. Due to their similar pyrimidine structure, the SERS spectra of U and C show a comparable pH dependence in that the strongest spectra are obtained at neutral pH or above. Whereas, due to their purine skeleton, the SERS spectra of A and G are strongest under acidic conditions. However, if the pH is made too acidic, the SERS spectrum of adenine becomes slightly less intense, as can be seen from the plot of the 727-cm^{-1} peak height versus pH (Figure 6). As a compromise, the pH of the Ag sol was adjusted to 6.8. Other changes in the SERS spectra as a function of pH also occur. A doublet is observed for A and G in the 1350-cm^{-1} region, and the relative intensity of the two bands is dependent on pH. Further study of the pH effect on the SERS spectra of RNA bases is currently underway. If a group of compounds with similar pK_a values are to be tested, the optimum pH value for the eluent can readily be selected, as the maximum SERS enhancement can be obtained within a narrow pH range.

Figure 7 displays a three-dimensional plot of the SERS spectra obtained from the FIA system. The absolute amount of each base injected was about 100 nmol. The flow rate was

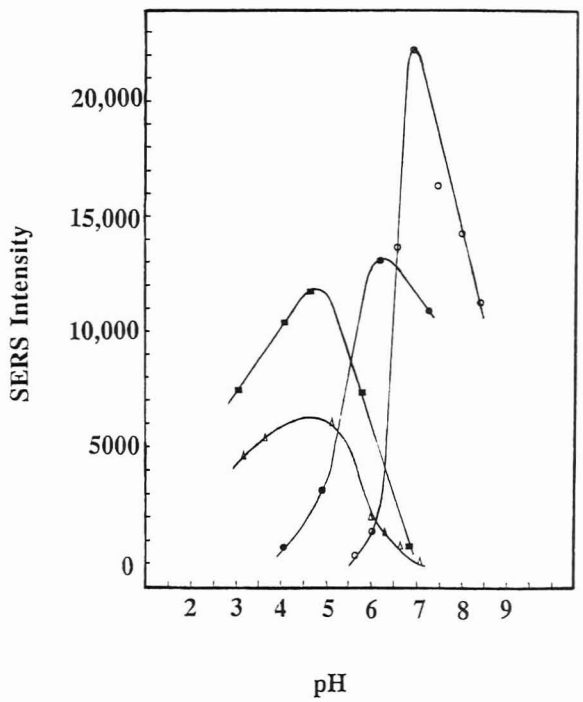

Figure 6. pH-dependent SERS intensities of a 5 × 10^{-4} M solution of adenine (△, 727-cm^{-1} band), cytosine (●, 798 cm^{-1}), guanine (■, 652 cm^{-1}), and uracil (○, 801 cm^{-1}). Spectra were obtained under static conditions. The laser power was 20 mW at 457.9 nm and the spectral acquisition time was 33 s.

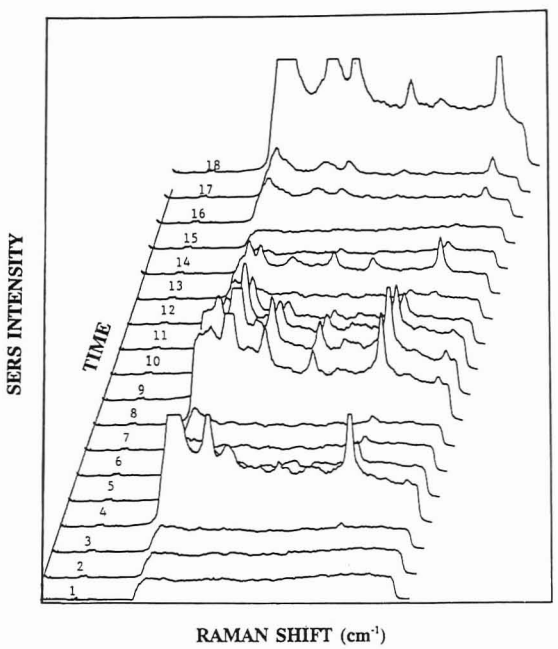

Figure 7. Three-dimensional SERS spectra of uracil, cytosine, adenine, and guanine (18 traces). About 100 nmol of each base was injected. The acquisition time for each spectrum was 30 s and the laser power was 10 mW. See text for experimental conditions.

0.1 mL/min and samples were injected at 1.5-min intervals. The bath temperature was set at 70 °C. Four RNA components, U, C, A, and G were detected consecutively. The acquisition time for each spectrum was 30 s and the laser power was 10 mW. Even though very low laser power was used, the fourth spectrum of U and the final spectrum of G in the series were quite intense. In contrast, the SERS spectra of A were relatively weak and persisted for only two successive scan periods. This is due to the pH effect. At neutral pH, A exhibits only a small enhancement factor as discussed previously. Unlike A, G was prepared in a strongly acidic solution

because of its poor solubility in neutral solution. When the solution was mixed with Ag sol at neutral pH, the eluent became acidic, which resulted in a greater enhancement of the Raman spectrum of G.

The distribution of each sample in the eluent may be represented by a skewed Gaussian curve. As can be seen from Figure 7, the intensity of the initial spectrum of a given base rises abruptly above background, but the intensity of the subsequent spectra decreases slowly. Also, the separation of each injected sample is not as complete as desired in this figure (e.g. a peak at 1396 cm^{-1} due to U can be seen in the spectrum of C). The reasons for spectral overlap are 2-fold. First, the path length from the T joint to the SERS capillary cell is too long. Second, raising the temperature of the mixture produces longitudinal dispersion of the sample along the tubing. Elongation of a 1 cm long plug of crystal voilet into a 4 cm long plug was observed after it had passed from the T-joint to the capillary tube. To reduce or eliminate sample overlap, more time (2.5 min) was allowed to elapse between successive injections. Under these conditions, all of the base pairs were well-separated.

CONCLUSIONS

SERS has been successfully interfaced with a FIA system for real time detection of four RNA bases. It appears this is the first successful application of SERS to the analysis of a group of compounds which were successively introduced into a FIA system. Several experimental parameters that affect the SERS intensity were investigated. These include the pH and temperature of the mobile phase, as well as the solution flow rate and the tubing material used for the construction of the FIA system. Raising the temperature of the mixture of the silver sol and the analyte produced aggregation of the sol and significantly improved the SERS intensities in the flowing system. The temperature of the water bath was maintained at 70 °C to minimize vaporization of the eluent. The pH effect on the SERS spectra of the RNA bases is opposite for the purines as compared to the pyrimidines. A compromise value (6.8) for the silver sol/analyte mixture was used to ensure detection off the SERS spectrum of each RNA base in the flowing system. Several different tubing materials were tested and the glass was chosen for its chemical stability and ease with which it can be cleaned. The results of this study provide a foundation for interfacing SERS as a real time detection method for HPLC analysis of nucleic acid bases.

ACKNOWLEDGMENT

We thank Dr. Bernard Rospendowski for his critical reading of the manuscript.

Registry No. Ag, 7440-22-4; adenine, 73-24-5; cytosine, 71-30-7; uracil, 66-22-8; guanine, 73-40-5.

LITERATURE CITED

(1) Cotton, T. M. *Spectroscopy of Surfaces*; Clark, R. J. H., Hester, R. E., Eds.; Wiley: New York, 1988; Vol. 16, p 91.
(2) Koglin, E. and Séquaris, J. M. *Topics in Current Chemistry*; Springer-Verlag: New York, 1986; Vol. 134.
(3) Koglin, E. *J. Mol. Struct.* **1988**, *173*, 369.
(4) Suh, J. S.; Moskovits, M. *J. Am. Chem. Soc.* **1986**, *108*, 4711.
(5) Xiong, J.; Sheng, R.-S. *Chin. J. Chem. Phys.* **1989**, *2*, 59.
(6) Kim, S. K.; Joo, T. H.; Suh, S. W.; Kim, M. S. *J. Raman Spectrosc.* **1986**, *17*, 381.
(7) Koglin, E.; Séquaris, J. M.; Valenta, P. *J. Mol. Struct.* **1980**, *60*, 421.
(8) Koglin, E.; Séquaris, J. M.; Valenta, P. *J. Mol. Struct.* **1982**, *79*, 185.
(9) Koglin, E.; Séquaris, J. M.; Valenta, P. *J. Mol. Struct.* **1984**, *114*, 219.
(10) Ervin, K. M.; Koglin, E.; Séquaris, J. M.; Valenta, P.; Nürnberg, H. W. *J. Electroanal. Chem. Interfacial Electrochem.* **1980**, *114*, 179.
(11) Oh, W. S.; Suh, S. W.; Kim, M. S. *J. Raman Spectrosc.* **1988**, *19*, 261.
(12) Séquaris, J. M.; Koglin, E. *Anal. Chem.* **1987**, *59*, 527.
(13) Carrabba, M. M.; Edmonds, R. B.; Rauh, R. D. *Anal. Chem.* **1987**, *59*, 2259.
(14) Laserna, J. J.; Campiglia, A. D.; Winefordner, J. D. *Anal. Chem.* **1989**, *61*, 1697.
(15) Ni, F.; Thomas, L.; Cotton, T. M. *Anal. Chem.* **1989**, *61*, 888.
(16) Freeman, R. D.; Hammaker, R. M.; Meloan, C. E.; Fateley, W. G. *Appl. Spectrosc.* **1988**, *42*, 456.
(17) Tran, C. D. *J. Chromatogr.* **1984**, *292*, 432.
(18) Berthod, A.; Laserna, J. J.; Winefordner, J. D. *Appl. Spectrosc.* **1987**, *41*, 1137.
(19) Laserna, J. J.; Berthod, A.; Winefordner, J. D. *Talanta* **1987**, *41*, 1137.
(20) Forcé, R. K. *Anal. Chem.* **1988**, *60*, 1989.
(21) Sheng, R. S.; Zhu, L.; Morris, M. D. *Anal. Chem.* **1986**, *58*, 1116.
(22) Eksteen, R.; Kraak, J. C.; Linssen, P. *J. Chromatogr.* **1978**, *148* (2), 413.
(23) Lord, R. C.; Thomas, G. J., Jr. *Spectrochim. Acta* **1967**, *23A*, 2551.
(24) Susi, H.; Ard, J. S. *Spectrochim. Acta* **1974**, *30A*, 1843.
(25) Creighton, J. A.; Blatchford, C. G.; Albrecht, M. G. *J. Chem. Soc., Faraday Trans. 2* **1979**, *75*, 790.

RECEIVED for review February 21, 1990. Accepted May 31, 1990. The authors are grateful to the National Institutes of Health (GM 35108) for the support of this work. T.M.C. is the recipient of an NIEHS Career Development Award (ES 00169).

Optical Sensor for Calcium: Performance, Structure, and Reactivity of Calcichrome Immobilized at an Anionic Polymer Film

Lai-Kwan Chau and Marc D. Porter*

Ames Laboratory—USDOE and Department of Chemistry, Iowa State University, Ames, Iowa 50011

A calcium-selective optical sensor has been fabricated by the electrostatic immobilization of calcichrome at a porous anion-exchange polymer film. The change in the optical properties of the bound indicator as a function of Ca(II) concentration was monitored in a single-beam diffuse reflection mode at a pH of 12.1. Advantageous features of this design include a short response time (<15 s), high selectivity, facile construction, and compatibility with commercially available instrumentation. The rapid response results from the porous microstructure of the anion exchange polymer, which facilitates the mass transport of analyte and counterions between solution and polymer film. The optical response is linear for a Ca(II) concentration between 3 and 30 mM with a detection limit of 3 mM. Immobilization alters both the acid and chelation strength of the indicator. Possible causes of these reactivity differences are discussed, based on insights provided by infrared internal reflection and photoacoustic spectroscopies. Equations to determine the metal complex formation constant and acid dissociation constants of the immobilized agent from diffuse reflectance spectra are developed.

INTRODUCTION

Thin films of organic polymers have been used extensively for the development and construction of a wide variety of sensors based on either electrochemical or optical detection schemes (*1–4*). Central to both of these schemes is the control of the selectivity and/or sensitivity of an analysis by the synthetic manipulation of the chemical and physical properties of the polymeric film. For electrochemical sensors, strategies to control the composition of "redox" and ion exchange polymers have been employed to mediate the electron-transfer of large biomolecules (*5–7*) and to preconcentrate metal ions (*8, 9*). One approach to control selectivity has focused on the careful alteration of the permselectivity of cellulosic polymers (*10–12*). Permselective films have the additional advantage of precluding the adsorption of macromolecules that may foul the electrode surface, enhancing the long-term stability of the sensor.

As has been briefly summarized (*12*), the design and construction of optical sensors have focused to a large degree on approaches for the attachment of a colorimetric reagent to a host polymeric support. Immobilization schemes include the attachment of acid–base and metallochromic indicators with a covalent linkage (*13–16*), the electrostatic immobilization of sulfonate- and carboxylate-functionalized indicators at ion exchange polymers (*17*), and the adsorption of dyes onto cellulosic films (*18*). Such sensors have exhibited a wide range of performance characteristics (e.g. sensitivity, stability, and response time), which are intimately linked to the composition and microstructure of the polymeric film. It is therefore apparent that the optimization of the performance characteristics of both optical and electrochemical sensors represents a complex mixture of fundamental and practical issues. To this end, future progress will require an increasingly interdisciplinary research strategy, drawing from specialties such as synthesis, materials characterization, theory, and instrumentation.

This paper describes the construction, performance characteristics, and structural and reactivity details of an optical sensor for the selective determination of Ca(II). The sensor was fabricated by the electrostatic immobilization of calcichrome (2,8,8′-trihydroxy-1,1′-azonaphthalene-3,6,3′,6′-tetrasulfonic acid) at a *porous* anion exchange polymer film. The changes in the optical properties of the immobilized reagent were monitored in a diffuse reflection mode in the visible spectral region. Relevant features of this design include a short equilibration time (<15 s), high selectivity, facile construction, and compatibility with commercially available instrumentation. The rapid response results from the porous microstructure of the anionic polymer which facilitates the mass transport of analyte and counterions between solution and polymer film. Immobilization, however, alters both the acid and chelation strength of the indicator. Possible causes of the reactivity differences are discussed and substantiated by structural descriptions of the bound indicator that are deduced from infrared internal reflection and photoacoustic spectroscopic data. Equations to determine the metal complex formation constant and acid dissociation constants of the immobilized reagent from diffuse reflectance spectra are developed and used to assist the characterization of the chemical properties of the sensor. Considerations for the application of this sensor to environmental, industrial, and clinical purposes are also briefly discussed.

THEORY

This section describes the requisite formulization for obtaining the conditional formation constants and acid dissociation constants for immobilized colorimetric indicators with diffuse reflection spectroscopy in both single- and double-beam modes. It begins with use of Kubelka–Munk theory (*19*) to develop equations that relate the experimentally measured intensities of the diffusely reflected light to the equilibrium between a solution phase metal ion and an immobilized metallochromic indicator. An analogous method for the determination of the acid dissociation constant(s) of an immobilized indicator is also presented.

Determination of the Formation Constant for a Metal Complex with Diffuse Reflection Spectroscopy. The general reaction for the equilibrium between a solution phase metal ion, M^{n+}, and an immobilized ligand, L^{m-}, is

$$M^{n+} + L^{m-} = ML^{n-m} \quad (1)$$

where ML^{n-m} is the immobilized metal complex. Assuming activity coefficients of unity for both solution and immobilized species, the conditional formation constant, K_f, for the che-

* Author to whom correspondence should be addressed.

0003-2700/90/0362-1964$02.50/0

lation of the metal and ligand is

$$K_f = \overline{ML}/[M]\bar{L} \quad (2)$$

where [M] is the equilibrium solution concentration of the metal ion, and $\bar{L}$ and $\overline{ML}$ are the respective equilibrium concentrations of the immobilized ligand and the immobilized metal complex. Equation 2 can also be written with respect to $\overline{ML}$ and the initial concentrations of the metal ion in solution, $[M]_0$, and the immobilized ligand, $\bar{L}_0$, to give

$$K_f = \frac{\overline{ML}}{([M]_0 - \overline{ML})(\bar{L}_0 - \overline{ML})} \quad (3)$$

Upon expansion and rearrangement, eq 3 yields

$$\frac{1}{K_f} = \frac{[M]_0\bar{L}}{\overline{ML}} - [M]_0 - \bar{L}_0 + \overline{ML} \quad (4)$$

If experimental conditions are such that

$$\bar{L}_0 - \overline{ML} \ll \frac{[M]_0\bar{L}_0}{\overline{ML}} - [M]_0$$

i.e. $\overline{ML} \ll [M]_0$, then eq 4 reduces to

$$\frac{1}{K_f} = \frac{[M]_0\bar{L}_0}{\overline{ML}} - [M]_0 \quad (5)$$

For diffuse reflection measurements, the Kubelka–Munk (K-M) function provides an empirical approach for relating the observed signal quantitatively to the sample concentration. The K-M function, $f(R_\infty)$, is defined as

$$f(R_\infty) = \frac{(1 - R_\infty)^2}{2R_\infty} \quad (6)$$

where R_∞ is the absolute diffuse reflectance of an infinitely thick sample. This function is related to the concentration of an absorbing sample species, C, by

$$f(R_\infty) = \epsilon C/s \quad (7)$$

where ϵ is the molar absorptivity of the sample species and s is the scattering coefficient. For a nonabsorbing M^{n+}, $f(R_\infty)$ can be expressed by using eq 7 as

$$f(R_\infty) = \frac{\epsilon_{\overline{ML}}\overline{ML}}{s} + \frac{\epsilon_{\bar{L}}(\bar{L}_0 - \overline{ML})}{s} \quad (8)$$

where $\epsilon_{\overline{ML}}$ and $\epsilon_{\bar{L}}$ are the molar absorptivities of $\overline{ML}$ and $\bar{L}$, respectively. If $f(R_\infty')$ represents the K-M function for $\bar{L}_0$, eq 8 becomes

$$f(R_\infty) = \frac{(\epsilon_{\overline{ML}} - \epsilon_{\bar{L}})\overline{ML}}{s} + f(R_\infty') \quad (9)$$

The general expression for the Kubelka–Munk function in eq 6 can also be used to formulate $f(R_\infty)$ in terms of $f(R_\infty')$, which through subtraction of $f(R_\infty')$ and rearrangement gives

$$f(R_\infty) - f(R_\infty') = \frac{(R_\infty' - R_\infty)(1 - R_\infty R_\infty')}{2R_\infty R_\infty'} \quad (10)$$

For measurements that result in $R_\infty R_\infty' \ll 1$, eq 10 simplifies to

$$f(R_\infty) - f(R_\infty') = \frac{R_\infty' - R_\infty}{2R_\infty R_\infty'} \quad (11)$$

Combining eqs 9 and 11 then results in an expression that relates R_∞ and R_∞' with $\overline{ML}$

$$\frac{R_\infty' - R_\infty}{2R_\infty R_\infty'} = \frac{(\epsilon_{\overline{ML}} - \epsilon_{\bar{L}})\overline{ML}}{s} \quad (12)$$

To relate eqs 5 and 12 to measurements in a single-beam mode, a comparison to a reference intensity is necessary to compensate for instrument fluctuations (e.g. long-term drift of the intensity of the light source). One approach for compensation is to use the reflected intensity at an isosbestic point as a reference (*16*). For a diffuse reflectance measurement, the diffuse reflectance ratios for the free (R_n') and complexed (R_n) forms of an immobilized indicator can be expressed as

$$R_n = J_n/J_r \quad (13)$$

$$R_n' = J_n'/J_r \quad (14)$$

where J_n, J_n', are the experimentally measured intensities of the diffusely reflected light at the sampling wavelength and J_r is that at an isosbestic point. Additionally, as most experimental measurements do not determine the absolute diffuse reflectance of a sample, it is usual to relate the observed signal to a suitable reference material (*20*). These relative quantities are given as

$$r_\infty = R_\infty/\sigma_{std} \quad (15)$$

$$r_\infty' = R_\infty'/\sigma_{std} \quad (16)$$

where σ_{std} is the absolute diffuse reflectance of the reference material and is equal to unity for a perfect diffuse reflector. Dividing both the numerators and denominators in eqs 13 and 14 by σ_{std} yields

$$R_n = R_\infty\sigma_{std}/J_r \quad (17)$$

$$R_n' = R_\infty'\sigma_{std}/J_r \quad (18)$$

Combining eqs 5, 12, 17, and 18 results in

$$\left(\frac{1}{R_n} - \frac{1}{R_n'}\right)^{-1} = \frac{s\sigma_{std}}{2(\epsilon_{\overline{ML}} - \epsilon_{\bar{L}})J_r\bar{L}_0K_f[M]_0} + \frac{s\sigma_{std}}{2(\epsilon_{\overline{ML}} - \epsilon_{\bar{L}})J_r\bar{L}_0} \quad (19)$$

In the conventional double beam mode, a comparable derivation gives

$$\left(\frac{1}{r_\infty} - \frac{1}{r_\infty'}\right)^{-1} = \frac{s}{2(\epsilon_{\overline{ML}} - \epsilon_{\bar{L}})\sigma_{std}\bar{L}_0K_f[M]_0} + \frac{s}{2(\epsilon_{\overline{ML}} - \epsilon_{\bar{L}})\sigma_{std}\bar{L}_0} \quad (20)$$

In both instances, a plot of $(1/R_n - 1/R_n')^{-1}$ or $(1/r_\infty - 1/r_\infty')^{-1}$ vs $1/[M]_0$ is linear, which allows the calculation of K_f by dividing the y intercept by the slope.

Determination of Acid Dissociation Constants for an Immobilized Species with Diffuse Reflection Spectroscopy. The general reaction for the acid dissociation of an immobilized ligand is

$$\overline{H_nL^{m-}} = \overline{H_{n-1}L^{(m+1)-}} + H^+ \quad (21)$$

where $\overline{H_nL^{m-}}$ and $\overline{H_{n-1}L^{(m+1)-}}$ are the immobilized forms of a conjugate-acid-base pair, respectively. The acid dissociation constant for eq 21 can be written as

$$K_a = \frac{[\overline{H_{n-1}L^{(m+1)-}}][H^+]}{[\overline{H_nL^{m-}}]} \quad (22)$$

Since eq 7 shows that concentration is proportional to $f(R_\infty)$, the pK_a for eq 22 can then be expressed as

$$pK_a = pH - \log\left(\frac{f(R_{\infty 1}) - f(R_\infty)}{f(R_\infty) - f(R_{\infty 2})}\right) \quad (23)$$

where $f(R_{\infty 1})$ and $f(R_{\infty 2})$ are the K-M function at pH values

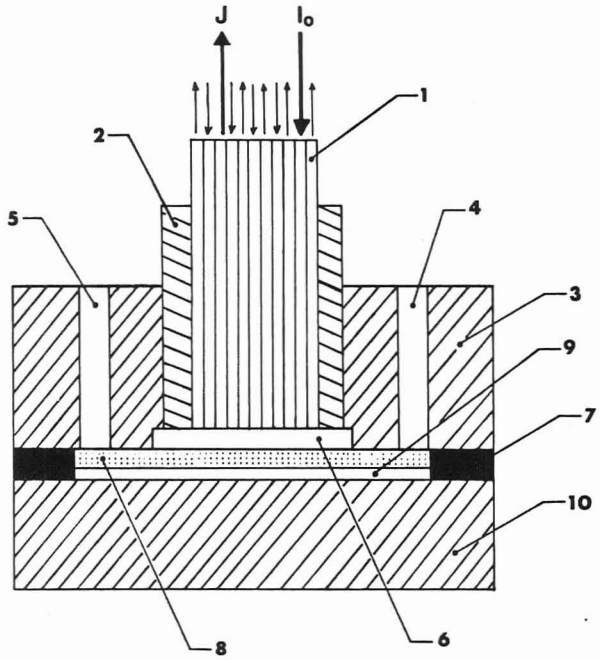

Figure 1. Flow cell construction: (1) optical fiber, (2) fiber mounting cylinder, (3) front plate, (4) solution inlet channel, (5) solution outlet channel, (6) front window, (7) slotted gasket, (8) thin film Ca(II) sensor, (9) diffuse white reflector, (10) back plate.

which result only in $\overline{H_nL^{m-}}$ or $\overline{H_{n-1}L^{(m+1)-}}$, respectively, and $f(R_\infty)$ is the K-M function at intermediate pH values where both $\overline{H_nL^{m-}}$ and $\overline{H_{n-1}L^{(m+1)-}}$ are present.

If one or more sets of isosbestic points exist, eq 22 can be expressed following earlier arguments as

$$pK_a = pH - \log\left(\frac{1/R_{n1} - 1/R_n}{1/R_n - 1/R_{n2}}\right) \qquad (24)$$

where R_{n1} and R_{n2} are the diffuse reflectance ratios at pH values which result only in $\overline{H_nL^{m-}}$ and $\overline{H_{n-1}L^{(m+1)-}}$, respectively, and R_n is that at intermediate pH values where both $\overline{H_nL^{m-}}$ and $\overline{H_{n-1}L^{(m+1)-}}$ are present.

EXPERIMENTAL SECTION

Sensor Construction. The sensor was constructed by the electrostatic immobilization of calcichrome at a N-0030 anion exchange film (RAI Research Corp., Hauppauge, NY). This film is a porous (pore size ≥ 10 μm) organic polymer with ~1.5 meq/g of quaternary ammonium cationic exchange sites. The films scatter light analogously to the mats commonly employed as references for diffuse reflection spectroscopy. Immobilization was accomplished by immersing a film into an aqueous 0.1 mM calcichrome solution for 24 h at 25 °C. Under these conditions, the concentration of immobilized calcichrome was ~6 mM (1.2 mmol/g of dry film). This value was determined by the optical quantitation of the difference in the amount of colorimetric reagent in solution before and after immobilization. The thickness of an immersed membrane was ~800 μm.

Flow Cell. The optical sensor and flow cell are shown in Figure 1. The incident light was carried to the cell through 400-μm-diameter optical fibers (Ensign-Bickford Optics Co., Avon, CT). The fiber diameter with cladding is ~730 μm. Optical fibers also collected and transmitted the diffusely reflected light to the entrance slit of a monochromator. The optical fiber bundle consisted of 10 fibers, which were arranged in a vertical orientation, with half used to transmit the incident light to the thin film and half used to transmit the diffusely reflected light to the entrance slit of a monochromator. The optical fibers were sealed into slotted Plexiglas cylinders and mounted to the cell with setscrews. The solution cavity was defined by the front window of the cell, the silicone rubber gasket, and the thin film sensor. The window was sealed into place with silicone rubber cement. The front and back plates of the cell were machined from Plexiglas to respective thickness of 1.2 and 2.0 cm. The solution inlet and outlet channels were drilled to a diameter of 0.2 cm and connected to Teflon tubing with flanged fittings. The cell was sealed with a 0.15 cm thick silicone rubber gasket of which an inner portion was removed to define the solution channel. The time required to affect a complete change (99.9%) of the solution in the cell was 1.22 ± 0.18 s (standard deviation, n = 17).

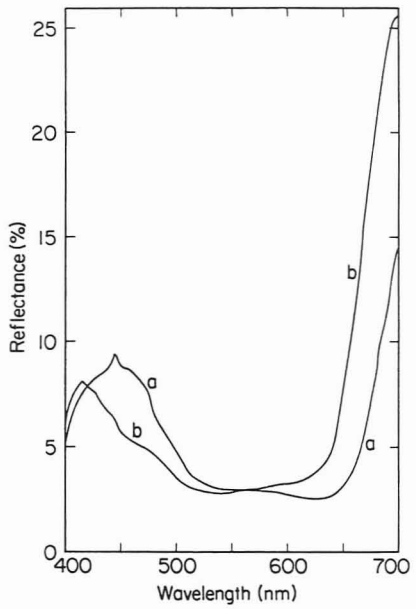

Figure 2. Diffuse reflectance spectra of (a) immobilized calcichrome, (b) immobilized Ca(II)–calcichrome complex ([Ca(II)] = 0.2 M, at pH 12.1 in the flow cell).

Under these experimental conditions, values for $R_\infty R_\infty'$ were less than 0.01, which corresponds to an error of less than 1% for the approximation in developing eq 11 from eq 10. In addition, by using calcium concentrations greater than 0.06 M, the approximation in arriving at eq 5 from eq 4 results in an error of less than 10% in the determination of K_f.

Instrumentation. A xenon arc lamp (Oriel Corp., Stamford, CT) was used as a light source. The collected light was dispersed with a 0.22-m grating monochromator and monitored with a digital photometer (Spex DPC-2, SPEX, Edison, NJ) in a photon counting mode. The pH of the solutions was measured with a 140 A Accumet pH meter (Fischer Scientific, Pittsburgh, PA). Infrared spectra of solid and dissolved calcichrome were collected with a Nicolet 740 Fourier transform infrared spectrometer (Madison, WI). A CIRCLE cell (Spectra Tech, Inc., Stamford, CT) with a ZnSe internal reflection element was used to acquire the solution IR spectra. The y axis of the solution spectra is given as $-\log(R/R_0)$, where R is the single beam spectrum of calcichrome at a given pH and R_0 is that of the same solution without calcichrome. This method of data presentation effectively compensates for small changes in the absorptivity of the aqueous solvent as a function of pH below ~1550 cm^{-1}; however, the large absorbance of the solvent precluded an effective compensation at the higher energies of the carbonyl and C=C stretching regions. Photoacoustic spectra of both the calcichrome modified film and the unmodified film were collected with a Perkin-Elmer 1800 Fourier transform infrared spectrometer (Norwalk, CT) and a MTEC 200 photoacoustic detector (Ames, IA).

Reagents. The pH values of the solutions were controlled by varying the amounts of NaOH or HCl or by citrate or phosphate buffers (McIlvaine buffers). All solutions were prepared with deionized water. Calcichrome (Pfaltz and Bauer, CT) was used as received. The ionic strength of the solutions was maintained with 0.2 M KCl.

RESULTS AND DISCUSSION

Diffuse Reflectance Spectra of the Sensor. Diffuse reflectance spectra of immobilized calcichrome before and after complexation with Ca(II) are shown in Figure 2. Both

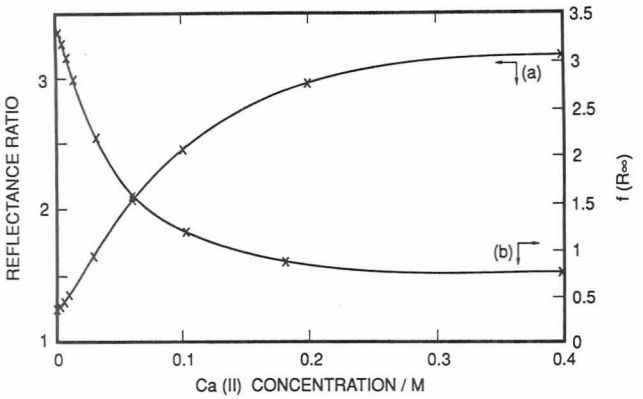

Figure 3. (a) Diffuse reflectance ratio and (b) K-M function of the Ca(II) sensor as a function of Ca(II) concentration at pH 12.1.

spectra were taken at pH 12.1 and are given as relative reflectances, i.e. R_s/R_u, where R_s is the diffuse reflectance of the free or complexed forms of the immobilized indicator and R_u is that of the unmodified film. The free form of immobilized calcichrome exhibits a reflectance minimum near 620 nm, whereas that for the immobilized Ca(II)–calcichrome complex is slightly above 540 nm. These reflectance minima are red shifted about 20 nm relative to the absorbance maxima of their solution analogues (*21*). On the basis of a comparison to the transmission spectra of the solution form of the indicator (*21*), a set of isosbestic points in the reflectance spectra were also observed at 556 and 425 nm. The shifts in the reflectance minima for immobilized calcichrome arise primarily from optical dispersion effects that are inherent to diffuse reflection measurements (*19*).

Response to Ca(II). Both the K-M function and the diffuse reflectance ratio of the sensor as a function of Ca(II) concentration at 670 nm are shown in Figure 3. The reflected intensity at the isosbestic point at 556 nm was used as the reference. The K-M function is linear up to a Ca(II) concentration of ~30 mM, leveling off at higher concentrations because of saturation of the chelating sites of the thin film sensor. The plot of diffuse reflectance ratio vs Ca(II) concentration is sigmoidal, also exhibiting a linear region approximately between 3 and 30 mM. The detection limit, defined as the concentration which gave a signal that was 4 times the standard deviation of the blank, was estimated at 3 mM. Efforts are currently underway to lower the detection limit both by increasing the light collection efficiency and by reducing stray light (*22*). The latter improvement should also increase the dynamic range of the measurement (*23*).

Response Time. The optical response of the sensor to a rapid change in Ca(II) concentration is shown in Figure 4. The wavelength used for these measurements was 670 nm. Both the blank ([Ca(II)] = 0.0 M) and calcium-containing solution ([Ca(II)] = 0.20 M) were buffered at pH 12.1. Upon injection of analyte solution, the diffuse reflectance ratio increases rapidly, corresponding to the formation of the immobilized metal complex. Equilibration (99.9% completion) is achieved in ~13 s, with the response reaching 63% of the maximum value in less than 4 s. The response of this sensor is 5–10 times more rapid than those for other metal ions (*24–29*) and is roughly 20 times more rapid than those of other Ca(II) sensors (*30, 31*). Comparable improvements in response times have been observed for pH sensors that were constructed at a porous microstructure (*18*), further demonstrating an advantage of designing sensors based on porous polymeric materials.

Interferences. In addition to Ca(II), the solution form of calcichrome complexes with a variety of other metal ions, including Cu(II), Cd(II), Zn(II), V(IV), Mg(II), and Ba(II) (*32*). However, near pH 12 calcichrome complexes only with Mg(II), Ba(II), and Ca(II). Tests for the possible interference of each of the latter metal ions with the response from the sensor were conducted over a broad range of concentrations (up to saturated solutions) at pH 12.1. In all instances, the response of the sensor was virtually indistinguishable (<1% change in reflectance at 670 nm) from that obtained with a blank pH 12.1 solution. Thus, the sensor exhibits a high selectivity for Ca(II), suggesting its applicability to a variety of applications (vide infra).

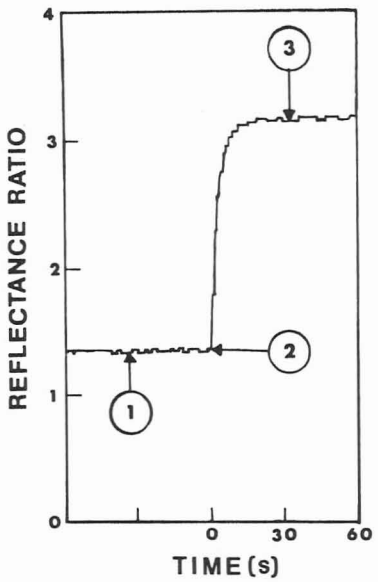

Figure 4. Response time of the Ca(II) sensor: (1) equilibrated response at a pH 12.1 solution, (2) injection of a 0.2 M Ca(II) solution at pH 12.1, (3) equilibrated response at the 0.2 M Ca(II) solution at pH 12.1.

Stability. The stability of the sensor was tested by the replicate injection of a calcium-containing solution under constant irradiation at 670 nm. Freshly prepared sensors were subject to photobleaching during the first few minutes of light exposure which was accompanied by a small decrease in the intensity of the diffusely reflected light. However, the signal stabilized after the first few minutes of light exposure, with no observable degradation in response to calcium over a period of several weeks. Other variables that may affect the response of the sensor, such as temperature, will be tested in the near future.

Reactivity of the Solution Form of Calcichrome. In several instances, the complexation of a metallochromic indicator with a metal ion proceeds with the loss of one or more protons from the indicator. The design of optical sensors for metal ion determinations therefore requires a detailed understanding of those factors that can influence both the acid–base reactivity and chelation capability of an immobilized indicator. One approach for gaining insights into the molecular level details of such interfaces is through a comparison of the structures and reactivities of the solution and immobilized forms of the indicator. This and the next section examine the details of the reactivities of the solution and immobilized forms of calcichrome through measurements of acid dissociation and metal association constants and through structural information provided by infrared internal reflection and photoacoustic spectroscopies.

In aqueous solution, calcichrome has two titratable naphtholic protons with pK_a values of 7.19 ± 0.05 and 11.63 ± 0.05 at 25 °C (*21*). The reaction scheme is given in eq 25 and includes both the acid–base and the tautomeric equilibria for each proton dissociation step. On the basis of considerations of intramolecular hydrogen bonding, which is revealed by ^1H and ^{13}C NMR (*21*) and supported by molecular models, acid dissociation proceeds by the successive loss of protons from

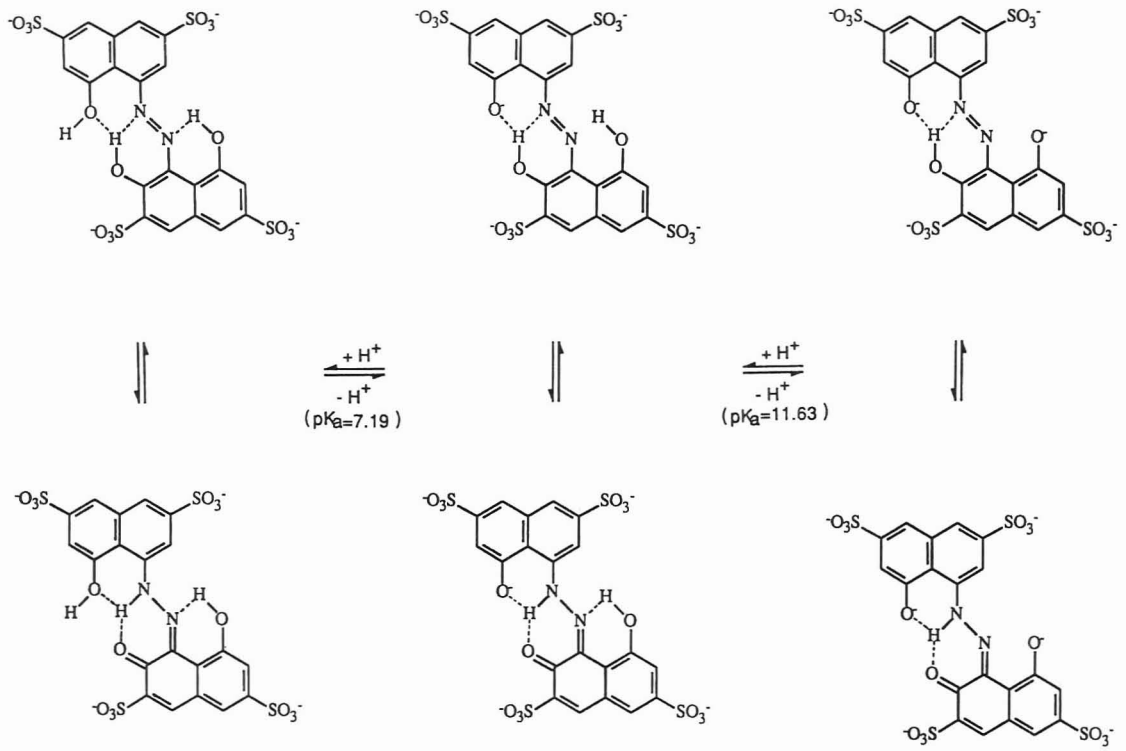

(25)

Table I. Peak Positions (cm^{-1}) and Vibrational Mode Assignments for the Solution and Immobilized Forms of Calcichrome[a]

solution form						
pH 5.1	pH 8.2	pH 12.0	Ca(II) complex (pH 12.0)	solid form (Na salt)	immobilized form	band assignment[b]
1042	1040	1040	1039	1044	1037	$\nu_s(SO_3^-)$
1196	1196	1195	1207	1193	1202	$\nu_a(SO_3^-)$
	1270	1268	1263		1269	δ'(NH)
1293	sh			1277		δ(OH)
1335	1334			1335	1322	δ(OH)
1371	1368	1365	1363	1367	1342	
	1392	1391	1379		1384	ν_s(C=N—N)
	1442	1438	1419		1425	ν_a(C=N—N)
1474					1475	ν(C=C)
				1519	1501	ν(C=C)
					1567	δ(NH)
				1603	1599	ν(C=C)
				1635	1645	ν(C=O)

[a] Band assignments based on those reported in refs 33–35. [b] Key: ν_a, asymmetric stretch; ν_s, symmetric stretch; δ, bending; δ', deformation; sh, shoulder.

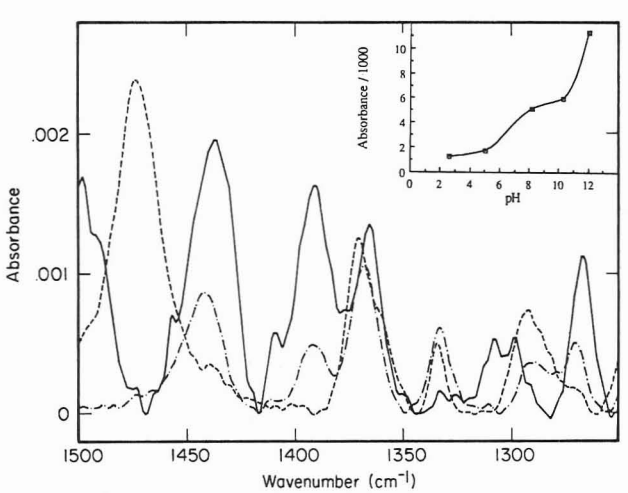

Figure 5. Infrared internal reflection spectra of calcichrome solution at (a) pH 5.1 (- - -), (b) pH 8.2 (– • –), and (c) pH 12.0 (——). Inset: absorbance of δ'(NH) as a function of pH.

the hydroxy groups at the 8′ and 8 positions. The naphtholic proton of the hydroxy group at the 2 position does not dissociate in aqueous solution as a result of extensive hydrogen bonding with the azo nitrogen at the 1′ position and possibly with the oxygen of the hydroxy group at the 8′ position. Both resonance stabilization and hydrogen bonding contribute to the differences in the acid strengths of the naphtholic protons at the 8′ and 8 positions.

Identification of the predominant tautomeric species of dissolved calcichrome was aided by the analysis of the infrared internal reflection spectra shown in Figure 5. These spectra were taken at pH values representative of each of the protonated forms of the indicator. As such, the spectra at pH 5.1 and 8.2 are essentially those of the triprotic and diprotic forms of the indicator, respectively. The spectrum at pH 12.1 represents a mixture of the diprotic and monoprotic forms of the indicator. Peak positions and band assignments for these spectra are given in Table I.

All of the bands shown in Figure 5 are affected to varying degrees by a change in pH, complicating the mode assignments

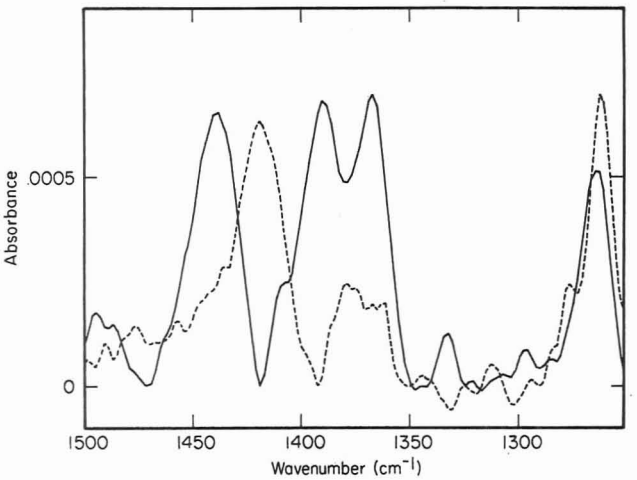

Figure 6. Infrared internal reflection spectra of solutions of (a) calcichrome (——) and (b) Ca(II)–calcichrome (- - -), at pH 12.0.

and subsequent molecular level interpretation. The bands at ~1290 and 1335 cm^{-1} and the shoulder on the low energy side of an unassigned band slightly above 1350 cm^{-1} are attributed respectively to the O-H bending modes (δ(O–H)) of the naphtholic protons at the 2, 8, and, tentatively, 8′ positions. Changes in these bands reflect the deprotonation process as well as conformational rearrangements about the azo linkage and/or alterations in intramolecular hydrogen bonding. For example, δ(O–H) for the naphtholic proton at the 8 position shifts to slightly lower energies between a pH of 5 and 8, whereas its absorbance decreases to a level only slightly distinguishable from the background noise at pH 12. The absorbance decrease is caused by the loss of a proton from the diprotic form of calcichrome. Shifts in peak position are ascribed to the changes in conformation and hydrogen bonding that arise from the stepwise deprotonation process (vide infra). Decreases in the absorbance of the δ(O–H) of the hydroxy group at the 2 position reflect the transfer of the proton from the hydroxy group to an azo nitrogen as a result of the increased formation of the hydrazone form. The disappearance of δ(OH) for the naphtholic proton at the 8′ position between a pH of 5 and 8 is consistent with the loss of a proton from the triprotic form of calcichrome.

Several of the bands shown in Figure 5 exhibit changes that arise from alterations in the relative amounts of the azo and hydrazone forms in each of the tautomeric equilibria. The increase in the absorbance of the N–H deformation mode (δ'(N–H)) at 1270 cm^{-1} with increasing pH, as shown in the inset of Figure 5, indicates a shift toward the hydrazone form of the indicator. The appearance and subsequent growth with increasing pH of the bands at ~1440 and 1390 cm^{-1}, which are assigned respectively to the asymmetric (ν_a(C=N—N)) and symmetric (ν_s(C=N—N)) stretching modes, further confirm the increasing presence of the hydrazone form of the indicator. The structural implications of the pH dependence of the band at 1475 cm^{-1} are as yet unclear.

The change from the azo to hydrazone form of calcichrome is induced by an alteration in the hybridization of the azo nitrogen at the 1′ position from sp^2 to sp^3. This rehybridization leads to a nonplanar structural arrangement of the two naphthalene rings (*36*), an arrangement which is required for the formation of the Ca(II)–calcichrome complex. The conditional formation constant for the complex at pH 12.3 is 8.0×10^3 (*21*). Evidence for the nonplanar structure of the metal complex is provided by the presence of δ'(N–H) in the infrared spectrum of the Ca(II)–calcichrome complex in Figure 6. The shifts of δ'(N—H), ν_a(C=N—N), and ν_s(C=N—N) toward lower energies are consistent with the donation of electron density for the formation of the complex. From these data,

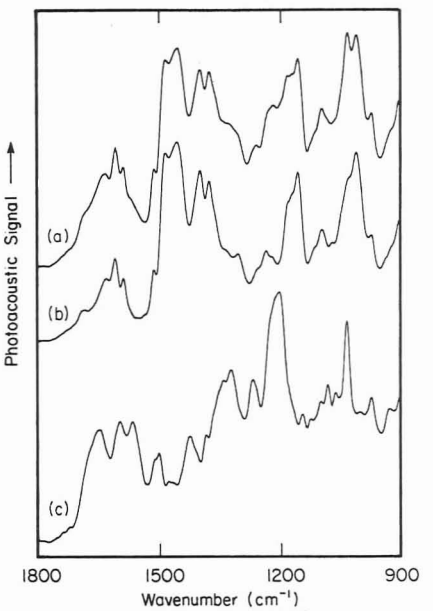

Figure 7. Infrared photoacoustic spectra of (a) calcichrome modified anion exchange membrane, (b) unmodified anion exchange membrane, and (c) immobilized calcichrome at the anion exchange membrane. The *y* axis for part c is 3 times that of parts a and b.

I is proposed as the structure for the Ca(II)–calcichrome complex.

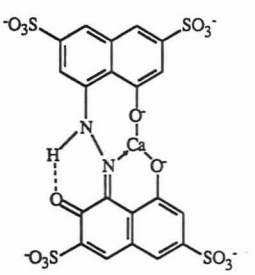

I

Reactivity of Immobilized Calcichrome. The reactivity of the immobilized form of calcichrome at the anion exchange film was determined by the approaches described in the theory section. Plots of the relevant data for eqs 19 and 24 gave K_f' for the Ca(II)–calcichrome complex of 32 ± 8 at pH 12.3 and pK_a values of 5.3 ± 0.3 and 10.7 ± 0.3. In both complexation and acid–base dissociation, the immobilized and solution forms of the indicator are markedly different, with immobilized calcichrome acting as a stronger acid but weaker ligand than its solution analogue. Such differences can arise from a variety of effects. For instance, the cation exchange polymer film known as Nafion acts as a strong acid with a strength that is comparable to CF_3SO_3H (*37*). This leads to the complete protonation of bases such as *p*-nitroaniline (pK_a = 1.0) upon their incorporation into the Nafion matrix. By analogy, an anion exchange polymer based on quaternary amines will behave as a strong base, promoting the acid dissociation of an immobilized reagent as observed for calcichrome. The lower pK_a values of immobilized calcichrome suggest that the complexation process may be facilitated at a lower pH in the anion exchange film.

Another factor that may influence the reactivity of the immobilized indicator is the hydrophobic/hydrophilic nature of the polymeric support. Hydrophobic environments have been shown to favor hydroxyl forms of tautomeric equilibria for azo structures comparable to calcichrome, whereas hydrophilic environments favor keto forms (*36*). For example, upon incorporation into the hydrophobic cavity of α- and

β-cyclodextrins from aqueous solutions, the tautomeric equilibrium of 4-phenylazo-1-naphthol (as the 4-phenylsulfonic acid) shifts from the less acidic hydrazone form to the more acidic azo form (*38*). This change results in a structure with lower polarity and is induced by the nonpolar microenvironment of the cyclodextrin cavity. In contrast, hydrophilic environments, such as that of a quaternized polymer film, favor the more polar, less acidic hydrazone form of the tautomeric equilibrium. The presence of the hydrazone form of calcichrome in the anion exchange resin is supported by the three infrared photoacoustic spectra (IR-PAS) shown in Figure 7. Parts a and b of Figure 7 are IR-PAS for the calcichrome-modified anion exchange membrane and the unmodified anion exchange membrane, respectively. Figure 7c is the difference spectrum for the subtraction of Figure 7b from Figure 7a. The presence of the hydrazone form of calcichrome is indicated by δ'(N–H) at 1269 cm^{-1}, δ(N–H) at 1567 cm^{-1}, and ν(C=O) at 1645 cm^{-1}. Additionally, a transmission spectrum of a thin-sectioned dry film in the visible region exhibited an absorbance maximum at 593 nm, indicating nearly full conversion of the immobilized calcichrome to its hydrazone form. Hence, immobilized calcichrome has the same hydrazone form as its Ca(II) complex. These interactions between calcichrome and the anion exchange resin appear to favor the formation of the Ca(II)–calcichrome complex.

The above discussion, although providing a qualitative explanation for the apparent increase in the acid strength of the immobilized form of calcichrome, fails to accounts for the low K_f' for the sensor. However, an examination of the mode of attachment between the indicator and support provides a plausible explanation. Calcichrome contains four sulfonic acid groups, each of which are capable of binding electrostatically with a cationic site of the polymeric support. Since immobilized calcichrome molecules may exist in different conformations in the matrix, rotation about the C–N axis may be necessary to achieve a conformation that is favorable for complex formation. Hence, tethering by more than one linkage would markedly hinder complexation. By the same reasoning, metallochromic reagents which are tethered through a single linkage may more readily undergo the structural rearrangements required for complexation, exhibiting more comparable reactivities of the solution and immobilized forms. More comparable reactivities have been observed for the binding of Mg(II) and Zn(II) by the solution and immobilized forms of quinolin-8-ol-5-sulfonate (*24*), a ligand which is naturally fixed in a configuration favorable for complex formation.

CONCLUSIONS

The construction of an optical sensor with a variety of attractive performance characteristics for the determination of Ca(II) has been demonstrated. Both the sensitivity and rapid response suggest several interesting applications (e.g. clinical assays, compliance environmental monitoring, and control of industrial processing). However, most of these situations will require that the composition of the analyte solution be altered to a more basic pH. One approach for accomplishing a change in pH would be to couple the sensor with instrumentation for flow injection analysis (FIA). With FIA, the pH of the analyte can be readily manipulated by premixing the analyte solution with a small volume of a buffer solution. Premixing of analyte with FIA has been successfully employed in the development of instrumentation for pH measurement in solutions with low ionic strengths (*39*). These and other opportunities are presently under investigation and should offer a facile means to adjust the pH to the level needed for the functioning of the calcichrome-based Ca(II) optical sensor.

This study also points to the need to consider the influence of immobilization on the reactivity of an indicator. Both the apparent acid–base and chelation strengths for an indicator can be markedly altered by immobilization (*12*). The apparent acid–base reactivity for calcichrome is affected by the basic nature of the anion exchange film, whereas immobilization appears to hinder the structural rearrangement necessary for chelation. The latter suggests the possible use of a calcichrome analogue with fewer sulfonic acid moieties as an approach for enhancing the reactivity and, hence, sensitivity of the sensor. The flexibility to tune the reactivity of immobilized calcichrome by using a calcichrome analogue with fewer sulfonic acid moieties and/or adjusting the number of cationic sites in the polymeric matrix may enable the design of a sensor to suit the needs of a specific application. Efforts to develop further insights into the fundamental interactions that govern reactivity of such sensors are currently underway.

ACKNOWLEDGMENT

Acquisition of infrared photoacoustic spectra by R. Jones is acknowledged.

LITERATURE CITED

(1) Durst, R. A.; Blubaugh, E. A. In *Fundamentals and Applications of Chemical Sensors*; Schuetzle, D., Hammerle, R., Butler, J. W., Eds.; ACS Symposium Series 309; American Chemical Society: Washington, DC 1986; Chapter 14.
(2) Seitz, W. R. *CRC Crit. Rev. Anal. Chem.* **1988**, *19*, 135–173.
(3) Janata, J.; Bezegh, A. *Anal. Chem.* **1988**, *60*, 62R–74R.
(4) Johnson, D. C.; Ryan, M. D.; Wilson, G. S. *Anal. Chem.* **1988**, *60*, 147R–162R.
(5) Lau, A.; Miller, L. *J. Am. Chem. Soc.* **1983**, *105*, 5271.
(6) Lundrum, H. L.; Salmon, R. T.; Haukridge, F. M. *J. Am. Chem. Soc.* **1977**, *99*, 3154–3158.
(7) Degani, Y.; Heller, A. *J. Am. Chem. Soc.* **1989**, *111*, 2357–2358.
(8) Guadalupe, A.; Abruna, H. *Anal. Chem.* **1985**, *57*, 142.
(9) Baldwin, R. P.; Christensen, J. K.; Kryger, L. *Anal. Chem.* **1986**, *58*, 1790–1798.
(10) Sittampalam, G.; Wilson, G. S. *Anal. Chem.* **1983**, *55*, 1608–1610.
(11) Wang, J.; Hutchins, L. D. *Anal. Chem.* **1985**, *57*, 1536–1541.
(12) Stole, S. M.; Jones, T. P.; Chau, L. K.; Porter, M. D. In *Chemical Sensors and Microinstrumentation*; Murray, R. W., Dessy, R. E., Heineman, W. R., Janata, J., Seitz, W. R., Eds.; ACS Symposium Series 403; American Chemical Society: Washington, DC, 1989; Chapter 19.
(13) Saari, L. A.; Seitz, W. R. *Anal. Chem.* **1982**, *54*, 823–824.
(14) Munkholm, C.; Walt, D. R.; Milanovich, F. P.; Miller, S. M. *Anal. Chem.* **1986**, *58*, 1427–1430.
(15) Kawabata, Y.; Tsuchida, K.; Ishibashi, N. *Anal. Sci.* **1987**, *3*, 7–9.
(16) Peterson, J. I.; Goldstein, S. R.; Fitzgerald, R. V.; Buckhold, D. K. *Anal. Chem.* **1980**, *52*, 864–869.
(17) Zhujun, Z.; Seitz, W. R. *Anal. Chim. Acta* **1984**, *100*, 47–55.
(18) Jones, T. P.; Porter, M. D. *Anal. Chem.* **1988**, *60*, 404.
(19) Wendlandt, W. W.; Hecht, H. G. *Reflectance Spectroscopy*; Interscience: New York, 1966; Chapter III.
(20) Guthrie, A. J.; Narayanaswamy, R.; Russell, D. A. *Analyst* **1988**, *113*, 457–461.
(21) Chau, L. K.; Pruski, M.; Porter, M. D. *Anal. Chim. Acta* **1989**, *217*, 31.
(22) Skogerboe, K. J.; Yeung, E. S. *Anal. Chem.* **1987**, *59*, 1812–1815.
(23) Coleman, J. T.; Eastham, J. F.; Sepaniak, M. J. *Anal. Chem.* **1984**, *56*, 2246–2249.
(24) Saari, L. A.; Seitz, W. R. *Anal. Chem.* **1983**, *55*, 667–670.
(25) Saari, L. A.; Seitz, W. R. *Analyst* **1984**, *109*, 655–657.
(26) Zhujun, Z.; Weitz, W. R. *Anal. Chim. Acta* **1985**, *171*, 251–258.
(27) Zhujun, Z.; Mullin, J. L.; Seitz, W. R. *Anal. Chim. Acta* **1986**, *184*, 251–258.
(28) Alder, J. F.; Ashworth, D. C.; Narayanswamy, R.; Moss, R. E.; Sutherland, I. O. *Analyst* **1987**, *112*, 1191–1192.
(29) Carroll, M. K.; Bright, F. V.; Hieftje, G. M. *Anal. Chem.* **1989**, *61*, 1768–1772.
(30) Ashworth, D. C.; Huang, H. p.; Narayanaswamy, R. *Anal. Chim. Acta* **1988**, *213*, 251–257.
(31) Suzuki, K.; Tohda, K.; Tanda, Y.; Ohzora, H.; Nishihama, S.; Inoue, H.; Shirai, T. *Anal. Chem.* **1989**, *61*, 382–384.
(32) Close, R. A.; West, T. S. *Talanta* **1960**, *5*, 221–230.
(33) Socrates, G. *Infrared Characteristic Group Frequencies*; Wiley: New York, 1980.
(34) Nolting, F.; Zetzsch, C. *Spectrochim. Acta* **1988**, *44A*, 845–848.
(35) Jones, T. P.; Porter, M. D. *Appl. Spectrosc.* **1989**, *43*, 908–911.
(36) Zollinger, H. *Color Chemistry: Syntheses, Properties and Applications of Organic Dyes and Pigments*; VCH: Weinheim, 1987; Chapter 7.
(37) Sondheimer, S. J.; Bunce, N. J.; Lemke, M. E.; Fyfe, C. A. *Macromolecules* **1986**, *19*, 339–343.

(38) Ball, P.; Nicholis, C. H. *Dyes and Pigm.* **1982**, *3*, 5–26.
(39) Woods, B. A.; Ruzicka, J.; Christian, G. D.; Carlson, R. J. *Anal. Chem.* **1986**, *58*, 2496–2502.

RECEIVED for review April 9, 1990. Accepted June 6, 1990. M.D.P. gratefully acknowledges the support of a Dow Corning Assistant Professorship and a Society of Analytical Chemists for Pittsburgh Starter Grant Award. Ames Laboratory is operated for the U.S. Department of Energy by Iowa State University under Contract No. W-7405-eng-82. This work was supported by the Office of Basic Energy Sciences, Chemical Science Division.

Selective Determination of Histamine by Flow Injection Analysis

James M. Hungerford,*[1] Kevin D. Walker,[1] Marleen M. Wekell,[1] Jack E. LaRose,[2] and Harold R. Throm[2]

Seafood Products Research Center and Science Branch, Food and Drug Administration, Bothell, Washington 98041-3012

A flow injection analysis (FIA) method for the determination of histamine is described. Control of reaction timing allows exploitation of a transient, chemical-kinetic increase in selectivity that occurs when *o*-phthalaldehyde reacts with histamine. The molar fluorescence ratio (selectivity) of histamine/histidine reaches a maximum value of 800 in 32 s, precluding the need for separation of histamine from histidine, spermidine, and other potential interferences in biological samples. On-line dilution prevents matrix effects and affords a linear response up to approximately 4.45 mM histamine, or 500 mg of histamine free base/100 g. Under these conditions the detection limit (3 times peak-to-peak baseline noise) is 5.5 pg (corresponding to 0.60 mg of histamine free base/100 g of sample) and throughput is 60 injections per hour. The high sensitivity and high selectivity of the method allow the rapid determination of histamine in fish with minimal sample conditioning and will find application in the determination of endogenous histamine as well, such as in blood plasma and brain tissue.

Histamine is a potent mediator of physiologic processes. In the hypersensitivity reaction, histamine is released from mast cells (*1*) and has a central role in the secretion of gastric acid (*2*, *3*). Histamine is also associated with decomposition in fishery products. For example, the occurrence of high levels of histamine in decomposed fish correlate well with outbreaks of scombroid poisoning. Histamine is produced in tissues by decarboxylation of free histidine, although endogenous, physiologic histamine is produced by a different pathway (*4*) than histamine produced by microbes in decomposed fish. Fish with high levels of free histidine, including scombroid fish (tuna, mackerel, jacks) and others (mahi-mahi) are most often implicated in scombroid-poisoning incidents (*5*). Thus there is a need for chemical methods that allow the rapid determination of histamine in biological materials.

Existing methods for determining histamine in biological samples are based on bioassay (*6*), thin-layer chromatography (*7*), gas chromatography (*8*), gas chromatography/mass spectrometry (9), and high-performance liquid chromatography (HPLC) (*10–12*). Wet chemical methods are also available. These include an isotopic-enzyme method (*13*) an immunoassay (*14*), and many (batch) fluorometric methods (*15–21*). Among the fluorometric methods, one (*19*) has been refined (*21*) and collaborated (*22*) and is now the official method (*23*) most widely used. Since the discovery of the reaction by Shore, Burkholder, and Cohn (*15*), it is now recognized that the histamine/*o*-phthalaldehyde (OPT) condensation reaction used in the fluorescence methods, while much more specific than amine/OPT/thiol condensation, is affected by many interferences in biological matrices. As with all of the batch methods that are now available for determining histamine, the official fluorometric method (*23*) requires time-consuming sample conditioning prior to the determinative step. In tuna, histidine and perhaps histidyl peptides are the most serious interferences with the OPT chemistry. This led Luten (*24*) to modify a clinical autoanalysis procedure (ref 25, based on the OPT/condensation) to allow for automation of both histidine removal and the determination of histamine in fish. The only drawback of the method is the requirement for 15 pump channels.

The need for sample conditioning can be eliminated if the selectivity of the OPT–histamine condensation can be increased to the point where histidine does not interfere in the direct determination of histamine. However, only modest improvements in the selectivity of the histamine–OPT condensation are achieved by manipulating pH, by masking the reaction, or by running the reaction at reduced temperature (*16*).

Activation energies are quite sensitive to subtle differences in molecular structure (*26*), such as those that exist between histamine and histidine, and yet only limited attention has been given to the relative dynamics of the histamine–OPT and histidine–OPT reactions. Exploitation of the chemical kinetics of moderately fast reactions (such as the OPT reaction) to yield enhanced chemical selectivity requires careful control of reaction timing. Many chemistries have been automated, and their reaction dynamics brought under rigid control, using flow injection analysis (FIA).

Facile control of timing is the hallmark of FIA practice, and this makes FIA an attractive method for systems in which chemical kinetics could be exploited, either to analyze for multiple components or to suppress interferences. Described here is an FIA method that greatly enhances the selectivity of the histamine–OPT reaction, allowing determination of histamine in tuna, mackerel, and mahi-mahi without removal

[1] Seafood Products Research Center.
[2] Science Branch.

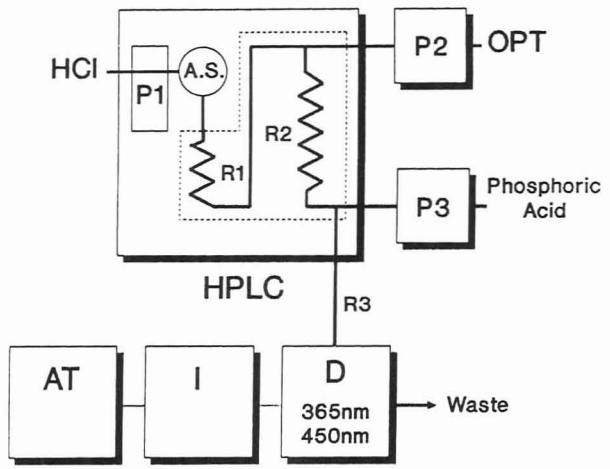

Figure 1. Experimental arrangement for the determination of histamine in fish. P1 and A.S. are the HPLC pump and autosampler, respectively, R1 and R2 are Teflon reactors mounted within the oven of the HPLC, P2 and P3 are pulse-dampened reciprocating pumps, R3 is a connecting tube between the outlet of the final mixing tee and the flow cell within the fluorescence detector, (D), I is an integrator, and AT is an IBM-AT computer, respectively.

of histidine. The method is sensitive enough to allow its application to other biological samples as well, such as plasma and brain tissue.

EXPERIMENTAL SECTION

Standards and Reagents. All standards and reagents used were of analytical-reagent grade (Aldrich Chemical Co., Milwaukee, WI) and used without further purification. All methanol used was HPLC grade (Fischer Scientific, Pittsburgh, PA) and deionized water was used throughout. Histamine stock solutions (15.9 mM) were prepared from the dihydrochloride salt in methanol. Stock histamine solution was diluted with methanol to yield working standard solutions in the range 1.00×10^{-5} to 1.59×10^{-2} M; this range corresponds to 1.11 mg/100 g to 1770 mg/100 g of histamine free base in a fish sample. For interference studies, methanolic solutions of cadaverine, cysteine, histidine, indole, octopamine, putrescine, spermidine, spermine, tryptamine, and tyramine were prepared at 1.00×10^{-3} M. Solutions of cadaverine and putrescine were prepared from their dihydrochlorides and spermidine and spermine from their tri- and tetrahydrochlorides, respectively. Tryptamine, tyramine, and octopamine were all prepared from their hydrochlorides, and histidine, cysteine, and indole were prepared from their neutral forms. Solubility limitations required that histidine working solutions were prepared in 90% methanol by dilution from an aqueous stock (10.0 mM) solution. All of the above working-standard solutions were stable for 1 week at 4 °C. Solutions of *o*-phthalaldehyde (OPT) were prepared on the day of analysis by dilution of a 1% (w/w) stock solution (in HPLC grade methanol) with deionized water and aqueous sodium hydroxide stock. Sodium hydroxide stock solutions (0.080–0.40 M) were prepared weekly from freshly boiled (deionized) water and standardized by titration prior to preparation of OPT reagent solutions. Phosphoric acid reagent (0.37 M) was prepared each week by dilution of 85% (w/w) concentrated acid with deionized water. The hydrochloric acid carrier stream (6.0×10^{-3} M by titration) was prepared fresh each week by dilution of the concentrated acid in deionized water. Both the hydrochloric acid carrier and the phosphoric acid reagent were stored at 4 °C when not in use.

Instrumentation. During initial studies, peristaltic pumps were used to propel the reagent stream. Excessive back pressure generated by the fluorescence detector (Perkin-Elmer, Norwalk, CT, Model LS-4, designed for microbore-HPLC compatibility) restricted the range of flow rates available. Modification of the detector would have prevented its use in other projects and so high-pressure propulsion was chosen. The reactors and tees used in the remainder of the FIA system are all compatible with low-pressure operation, and the system described here could easily be implemented by using peristaltic pumps if a fluorescence detector of lower pressure drop were available. The instrumentation used, including the HPLC (Hewlett-Packard, Palo Alto, CA, Model 1090) and two reciprocating pumps (Eldex, San Carlos, CA) equipped with pulse dampeners, was arranged as shown (Figure 1). A Model 4270 Spectra Physics (San Jose, CA) integrator, Spectra-Physics Chromstation-AT computer, and associated softward were used for data reduction and storage. One channel of the HPLC was used to propel the HCl stream and the two postcolumn reactor pumps were used to push the OPT and phosphoric acid reagent streams. The detector was operated at excitation and emission wavelengths of 365 and 450 nm, respectively, both at 10 nm band-pass. These conditions were chosen as a compromise between the sensitivity and the selectivity of the method for histamine versus histidine. The mixing tees used were stainless steel (SSI/Alltech, Deerfield, IL) with 0.4 mm i.d. passages in a standard 90–90 configuration. All reactor tubing was PTFE of 1.5 mm o.d. and 0.6 mm i.d. (OPT reactors), 0.30 mm i.d. (low-dispersion HCl reactor), or 0.9 mm i.d. (high-dilution HCl reactor). The reagent concentrations, flow rates, reactor dimensions, and other conditions used in the optimized procedure are given in Table I.

Table I. Operating Conditions for Maximum Selectivity

reactor	dimensions[a]	reactor geometry
R1 (HCl reactor, low-dilution)	0.3 mm × 100 cm	coiled or straight
R1 (HCl reactor, high-dilution)	0.9 mm × 40 cm	coiled or straight
R2 (OPT reactor)	0.6 mm × 250 cm	knotted
R3 (phosphoric acid reactor)	0.4 mm × 70 cm	connecting tube

solution	pump; flow rate, mL/min	concentrations
HCl	P1; 1.0	6.0×10^{-3} M HCl in deionized water
OPT	P2; 0.3	5.9×10^{-4} M OPT, 1.5×10^{-1} M NaOH in 1% (v/v) MeOH/deionized water
phosphoric acid	P3; 0.9	3.7×10^{-1} M phosphoric acid in deionized water
temperature	30 °C[b]	
injection volume	1 μL[c]	

[a] For maximum selectivity, the residence time in reactor R2 must be 30–35 s; the internal volume of R2 and the flow rate of P2 should be adjusted accordingly. The dimensions of R1 influence sensitivity and linear range but not selectivity; the length of R1 should be adjusted to yield overall dilution factor of 450. See definition of D^{max} in ref 27. [b] The temperature of reactor R2 is most crucial; maintaining a 30 °C temperature in R1 and in the equilibration coil (see text) is recommended. [c] Larger sample volumes may be used; dilution with 6.0 mM HCl prior to injection will then be necessary. An x-fold increase in sample volume must be offset by at least an x-fold dilution of extract prior to injection.

Since free histidine and small histidyl peptides are believed to comprise the most serious interferences in fish, most of the effort in developing the FIA method was directed toward solving this problem. At first interfering histidine and peptides were to be removed by an anion-exchange minicolumn placed in-line with the carrier stream. In the course of this work it was found that the selectivity of the OPT–histamine reaction was influenced by the OPT reagent flow rate and that major improvements in selectivity could be made by controlling reaction timing. Changes in the OPT reagent flow rate affect several variables, and a detailed study of the factors affecting the selectivity of the OPT–histamine reaction was conducted. The OPT reaction time was studied by varying the length of the OPT reactor. Knotted reactors of 0.6 mm i.d. were constructed with lengths between 25 and 750 cm. The NaOH concentration was varied between 0.080 and 0.40 M, and the OPT concentration from 195 to 1200 μM. The phosphoric acid reagent concentration and flow rate affected peak height and sample throughput, but not the selectivity of the determination, and so the phosphoric acid concentration was fixed at 0.37 M.

The HCl concentration of the carrier stream was fixed at 6.0 mM for reasons given below. The effect of the temperature within the OPT reactor was also investigated. For these studies, temperatures between 30 and 55 °C were maintained (within 0.1 °C) using the (fan-equipped) column oven of the chromatograph. When room temperatures were 20 °C or lower, temperature control at 30 ± 0.2 °C could be achieved by using a postcolumn heater (Model PCRS 510, Applied Biosystems, Ramsey, NJ) surrounding the reactor coil. In order to improve temperature equilibration, a 200-cm coil of 0.6 mm i.d. Teflon tubing was placed in the column oven (or postcolumn heater) between the postcolumn pump used to propel the OPT reagent and the inlet of the OPT mixing tee. The selectivity of the reaction was determined by comparing peak heights generated by injecting solutions of histamine before and after addition of interferand and by comparing peak heights due to separate histamine and interferand solutions.

Experiments with separate solutions gave comparable selectivities, and so the selectivity data reported below was determined conveniently by comparing the response of the system to separate histamine dihydrochloride (1.00×10^{-5} M) and interferand 1.00×10^{-3} M) standards. The flow rates of the HCl and OPT reagent streams were chosen to yield a combined flow rate that was high enough (1.3 mL/min) to augment radial mixing by secondary flow (*28*) within the knotted reactor and yet low enough to avoid excessive back pressure.

Fish Samples. Acceptable and decomposed samples of Atlantic Mackerel (*Scomber scombrus*) were generated by time–temperature abuse of whole fresh fish followed by filleting, while decomposed mahi-mahi (*Coryphaena hippurus*) samples were obtained by time–temperature abuse of 30-g segments of a fresh, skin-on fillet. Other fish samples used were quality-assurance composites, commercially obtained (canned) samples, and consumer-complaint (fresh or canned) samples implicated in scombroid poisoning incidents.

Extraction. Fresh fish fillets or canned fish were handled and extracted as described in ref 23, 18.001 and paragraph 1, 18.066. Briefly, 10.0-g samples of ground composite were blended with 50 mL of HPLC grade methanol for 2 min, heated for 15 min at 60 °C, cooled, diluted with methanol to 100 mL, and gravity filtered. Extracts were stored at 4 °C and, if precipitate appeared following storage, were filtered through 0.45-μm nylon syringe filters prior to injection.

Procedure. After optimum conditions were established, the solutions and operating conditions listed in Table I were used to determine the selectivity of the FIA method for histamine (versus several interferands). With these same conditions, the performance of the FIA method in determining histamine in fish was evaluated by comparing FIA-derived histamine levels in fish extracts with data obtained by using the AOAC fluorometric method (*23*).

When the same extracts were analyzed by the official AOAC (fluorometric) method, all samples were analyzed in duplicate and, if possible, in triplicate; samples found to be higher in histamine than the linear range of the method were diluted with 0.1 N HCl following the column cleanup step. Recoveries using the FIA method were determined by spiking 10.0 g of composite with the appropriate amount of a methanolic solution of histamine dihydrochloride to yield spike levels of 12 mg/100 g, 20 mg/100 g, and 50 mg/100 g histamine as the free base. Extractions were performed in triplicate and the FIA determinative step was performed in triplicate on each extract.

RESULTS AND DISCUSSION

The FIA method described here can be divided into four stages. First, the extract is injected into a flowing stream of aqueous HCl where it is diluted within the HCl reactor. This step in the scheme replaces the manual dilution and pipetting step in batch procedures. Greater on-line dilution can be achieved by decreasing the volume of sample injected, by using an HCl reactor with greater band broadening, or by decreasing the HCl–OPT flow-rate ratio. On entering the first mixing tee, acidified and diluted sample encounters alkaline OPT reagent, and the alkaline part of the histamine–OPT reaction proceeds for a time determined by the OPT reactor volumn. The knotted reactor-geometry of the OPT reactor ensures efficient radial mixing (and reduced dispersion of sample and product) within the reactor. The alkaline part of the reaction is stopped downstream of the second mixing-tee when phosphoric acid reagent drops the pH below 2. The acidic and final part of the reaction proceeds very rapidly in the transfer tubing between the second mixing tee and the detector. Finally, fluorescence due to the product is detected within the flow cell. Conditions within the OPT reactor had the greatest influence on the selectivity of the reaction.

Selectivity Studies. The selectivity, S, of the OPT–histamine reaction in the presence of an interferand (such as histidine) is defined here by a ratio obtained on dividing the molar peak height, generated by injecting histamine, by the molar peak height due to injection of the interferand:

$$S = \mathrm{Hm(histam)}/\mathrm{Hm(interf)} = H(\mathrm{histam})C(\mathrm{interf})/H(\mathrm{interf})C(\mathrm{histam}) \quad (1)$$

where Hm(histam) and Hm(interf) are the molar peak heights due to injection of histamine and interferand, respectively, and H(histam) and H(interf) are the absolute peak heights at (moles per liter) concentrations C(histam) and C(interf) of histamine and the interferand.

Many of the variables studied affected the selectivity of the reaction. As the NaOH concentration was increased above 0.080 M, the molar selectivity increased until a plateau was reached near 0.20 M. However, the best reproducibility was observed at a NaOH concentration of 0.15 M, and this concentration was used in all further work. The HCl concentration in the carrier stream affected selectivity (and sensitivity) only by its effect on the OPA reaction pH. The HCl concentration used (6.0 mM) was sufficient to prevent excessive dispersion due to adsorption of histamine on the walls of the HCl (dilution) reactor. Changes in the phosphoric acid concentration or flow rate had no effect on selectivity but affected peak height. Thus, the 0.37 M concentration of phosphoric acid and 0.9 mL/min phosphoric acid flow rate were chosen for optimum sensitivity.

Transient Selectivity. The effect of both reaction time and OPT concentration (at an OPT reactor temperature of 30 °C) on the selectivity of the method for histamine over histidine is shown in Figure 2. Note that the selectivity reaches a maximum value after 32 s of reaction time and then decreases with additional reaction time and that the selectivity of the method was a function of the OPT concentration. The reaction is more selective for histamine at lower OPT concentrations. System selectivity was also a function of the OPT reactor temperature. As shown in Figure 3, the molar response ratio histamine/histidine attains a much higher value at 30 °C than at 60 °C. Note that maximum selectivity is attained earlier at the higher temperature.

The selectivity of the optimized FIA procedure for histamine versus all the compounds tested is summarized in Table II. Solutions of indole, octopamine, putrescine, tryptamine, and tyramine give no detectable response, even at millimolar levels, and cadaverine and cysteine produced only weak response. On a molar basis, spermidine and spermine produced the highest response when tested. Spermiding has not been detected in either fresh or decomposed tuna at levels higher than about 7 ppm, and for spermine the upper limit in tuna is 19 ppm (*10*). At these low levels neither spermidine nor spermine constitute a significant interference in the determination of histamine in tuna, given the high selectivity of the method for histamine. Free histidine is present in much higher concentrations than the other compounds tested. Free histidine levels of 4000 ppm have been found in the muscle tissues of mackerel (*29*). In skipjack tuna, 11 000 ppm free histidine has been found (*30*). The histamine/histidine molar selectivity ratio of the FIA method is 800; free histidine levels of 4000 ppm and 11 000 ppm free histidine would give re-

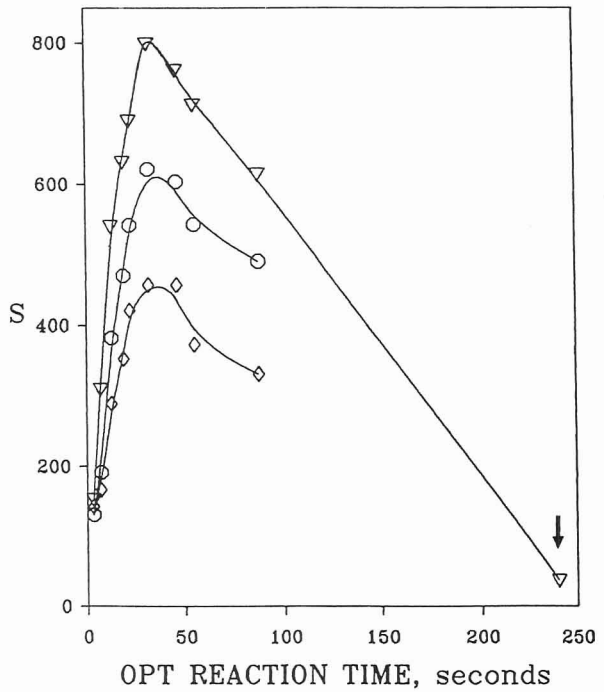

Figure 2. Effect of reaction time in reactor R2 and OPT concentration on the selectivity, S, of the method for histamine over histidine: diamonds, 1.2 mM OPT; circles, 0.89 mM OPT; inverted triangles, 0.59 mM OPT. Reaction temperature is 30 °C. Arrow indicates data determined by manually stopping all flow to arrest the sample zone within reactor R2 for ~4 min. S was calculated by using eq 1.

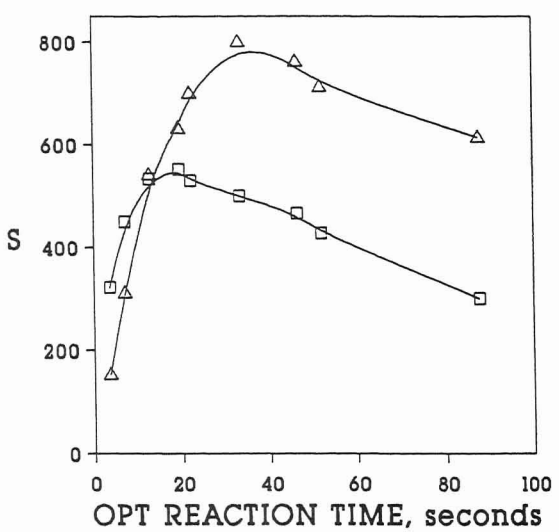

Figure 3. Effect of reaction time and temperature in R2 on the selectivity of the method for histamine over histidine: squares, 60 °C; triangles, 30 °C. Concentration of OPT was 0.59 mM; other conditions were as in Table I.

Table II. Selectivity of the Optimized Method[a]

compound	selectivity (molar response ratio, S)[b]
histidine	800
cadaverine	4707
cysteine	3661
indole	NR
octopamine	NR
putrescine	NR
spermidine	525
spermine	741
tryptamine	NR
tyramine	NR

[a] Values reported from data obtained by using operating conditions given in Table I. [b] Calculated by using eq 1. NR = no response was detectable.

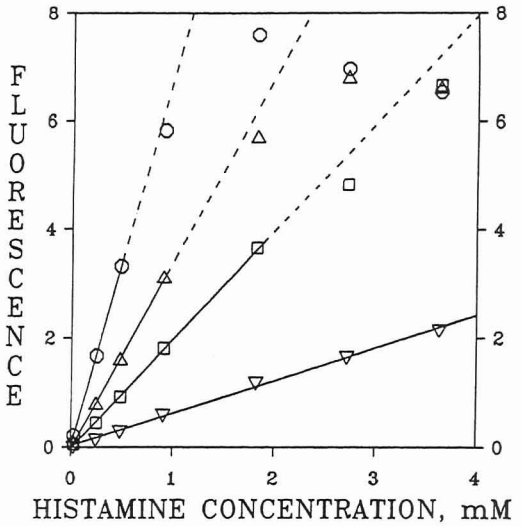

Figure 4. Effect of sample volume on linearity and sensitivity of response using high dispersion reactor R1: inverted triangles, 1 μL; squares, 3 μL; triangles, 5 μL; circles, 10 μL. Regions of nonlinearity indicated by dotted lines. Other conditions were as in Table I.

sponses equivalent to 0.36 mg % histamine and 0.98 mg % histamine, respectively. Therefore, the interference from histidine is negligible at the levels approaching regulatory significance (20 mg %). The FIA-controlled OPT reaction is about 27 times more selective than the lengthy low-temperature procedure described by Haakenson and Ronnberg (*16*). When the determinative step used in the official method (*23*) was used without the ion-exchange cleanup step, selectivity for histamine was about 20 times less (S = 39) than the FIA-controlled reaction.

The increase in selectivity of the optimized FIA procedure is transient and appears to be due to reaction dynamics. When the FIA-controlled OPT reaction was allowed to proceed for 4 min (by stopping the flow to arrest the sample zone was within the OPT reactor) the reaction was again far less selective for histamine. This long reaction time brings the selectivity back down to S = 36 (point indicated by arrow in Figure 2), a value more typical of the batch procedures.

Reagent Concentration. Peak heights obtained in injection of histamine were a strong function of the concentrations of both NaOH and OPT. Increasing the concentration of either above the values shown in Table I resulted in higher peaks, but this increase in absolute response was accompanied by a loss of selectivity and precision. Higher concentrations of OPT decreased the selectivity of the reaction and higher concentrations of NaOH gave erratic response. Sensitivity also increased with reaction time; at a fixed flow rate, longer reactors gave higher response than shorter reactors. A reaction time of 4 min (at stopped flow) resulted in peaks that were 100 times higher than those obtained under the conditions given in Table I.

Effect of On-Line Dilution on Sensitivity, Response Linearity, and Matrix Effects. The linear range, sensitivity, and susceptibility of the method to matrix effects was a function of dilution occurring within the system, especially within the HCl and OPT reactors. The major function of the HCl reactor was to level the pH of the injected sample zone to that of the HCl stream by dispersing the sample within this stream. Both on-line sample dilution and pH adjustment occurred concurrently and were conveniently achieved through control of the volume of sample injected and the HCl reactor dimensions.

As shown in Figure 4, lower sample volumes resulted in responses that retained their linearity at high histamine levels. At high concentrations of histamine and sample volumes greater than 1 μL, the observed fluorescence response leveled

Table III. Recovery of Histamine from Fish Tissues with FIA Method

species	histamine spike level (mg of free base/100 g)	% av recovery
albacore tuna	12	93
	20	94
	50	90
skipjack tuna	12	92
	20	97
	50	89
yellowfin tuna	12	100
	20	93
	50	105
Atlantic mackerel	12	101
	20	103
	50	97
mahi-mahi	12	102
	20	103
	50	99
all species[a]	12	98
	20	98
	50	96

[a] Overall relative standard deviation of extraction was 5%, averaged over all 45 extractions.

off as a result of the reagent consumption. The histamine/OPT ratio was made smaller to prevent this reagent depletion and consequently the range of linearity was increased. This could have been achieved by increasing the OPT concentration. However, the low (590 μM) OPT concentration enhanced the selectivity of the reaction (Figure 2), and so the ratio of histamine to OPT was reduced by increasing sample dilution on-line, within the FIA system. Since the OPT reactor dimensions cannot be changed without also effecting the OPT reaction time, the original, low dispersion, R1 reactor (0.3 mm i.d., 125 cm long) was replaced with an R1 reactor of 0.9 mm i.d. and 40 cm length to increase sample dilution by band broadening. This modification extended to the upper limit of linearity to histamine concentrations to 4.5 mM (500 mg of histamine free base/100 g of tissue) at 1 μL sample volume. Dispersion experiments using fluorescein showed that the sample was diluted by a factor of 450 when the high-dilution reactor was used in combination with a 1-μL sample volume. Under these (high dilution) conditions, the detection limit (3 times peak-to-peak baseline noise) was 5.5 pg, corresponding to 0.60 mg of histamine free base/100 g of sample. This sensitivity is more than adequate for the purpose of screening fish tissues for histamine at levels of regulatory interest.

Extracts of decomposed mackerel and mahi-mahi showed evidence of matrix effects if they were injected directly when the low dispersion HCl reactor was used. Recoveries were low and histamine levels determined by FIA were significantly lower than AOAC values, even when the histamine levels were well within the linear range indicated by calibration. Substitution of the high-dispersion HCl reactor for the low dispersion reactor eliminated the apparent matrix effects, as did manual dilution of the extracts with 6.0 mM HCl prior to injection.

The high-dilution HCl reactor had a throughput of 60 injections/h, which can be contrasted with 120 injections/h with the low-dilution reactor. Thus the choice between on-line dilution (using the high-dilution HCl reactor) or manual dilution prior to injection is a trade-off between reduced sample throughput (due to band broadening) during the determinative step or increased sample manipulation. In food analysis, sample compositing and extraction are the most time-intensive steps in the analytical process. The primary advantage of automating the determinative step is to increase the ruggedness of the method by reducing the number of manipulations required to perform it.

Table IV. Histamine Levels in Fish by Flow Injection and Official[b] Methods

sample	source	histamine level, mg(free base)/100 g FIA	AOAC[b]
	Albacore Tuna (*Thunnus alalunga*)		
1	QA composite, high quality	0.4	ND
2	canned in broth, commercial	2.6	1.3
3	canned in broth, commercial	2.5	4.4
4	canned in broth, commercial	0.9	1.3
	Skipjack Tuna (*Euthynnus pelamis*)		
5	canned in oil, high quality	0.9	0.5
6	canned in oil, low quality	4.0	2.7
7	canned in oil, decomposed	71	72
	Yellowfin Tuna (*Thunnus albacares*)		
8	QA composite, high quality	0.9	0.5
9	QA composite, decomposed	20	18
10		27	28
11		37	40
12	frozen, decomposed	432[a]	450
	Canned Light Tuna		
13	canned in oil, commercial	4.8	4.3
14	canned in broth, commercial	4.2	4.3
	Atlantic Mackerel (*Scomber scombrus*)		
15	fresh, commercial	2.5	0.5
16	fresh, commercial, TTA[c]	2.5	1.0
17		15.5	16.3
18		256[a]	244
	Mahi-Mahi (*Coryphaena hippurus*)[a]		
19	fresh, commercial	2.5	1.0
20		0.9	0.2
21		1.0	0.5
22		2.7	2.7
23	fresh, commercial, TTA[c]	4.9	3.6
24		3.7	2.8
25		2.6	1.7
26		12.0	8.4
27	fresh, commercial, TTA (decomposed)[c]	208	195
28		212	196
29		211	196
30		184	173
31		153	138
32		111	111
33		112	90.4
34		172	169
35		197	201
36		190	169
37		192	177
38		192	188
39		208	195

[a] Using high-dilution version of R1 and other conditions in Table I. [b] Reference 23. [c] TTA = samples generated by time-temperature abuse. See text.

Recovery Studies. Histamine recoveries were very good (89–105%) at the 12, 20, and 50 mg % levels for all five species tested (see Table III). Relative standard deviations for the triplicate extractions ranged from 4% to 6%. When all spike-and-recovery data are combined, an average recovery (n = 45) of 97% is obtained. This average value, when considered together with the average 5% variability in the extraction step, indicates that recovery is essentially quantitative.

Method Comparison. When extracts were diluted manually or on-line as discussed above, the histamine levels determined in fish using the FIA method compared well (see Table IV) with data obtained by using the official (fluorometric) method. Regression analysis of the FIA data against

the AOAC data (n = 39) yields r = 0.997, slope (FIA/AOAC) = 1.02, and a Y intercept of 2.5 mg/100 g.

The FIA method is more precise than the official fluorometric method. In our hands and in a collaborative study (*22*) the official fluorometric method has (within laboratory) relative standard deviations of about 5% at high histamine levels and relative standard deviations in excess of 30% at low histamine levels. The corresponding relative standard deviations in the FIA method are 2% and 5%.

When the t test was used to compare the two methods, only one extract (sample 15 in Table IV) yielded FIA and AOAC histamine levels that were significantly different at the 95% confidence level.

The transient selectivity observed and exploited in this work is a special case of kinetic enhancement of selectivity. Straka (*31*) and Pacey et al. (*32*, *33*) were first to point out that differences in the physical- or chemical-kinetic behavior of an analyte, and a potential interference can be used to enhance the selectivity of an FIA method. There are probably many more chemistries in the analytical chemistry literature that have not been studied from the standpoint of boosting their performance through control of reaction dynamics.

Analysis of biological materials is perhaps the ultimate test of the performance of a new analytical method. This is especially true in the determination of toxins and decomposition products in seafoods, where many potential interferences are present within the tissues of a variety of species. Described here is the first application of flow injection analysis and chemical-kinetic enhancement of selectivity to the analysis of a biological sample. The flow injection analysis method for determining histamine has advantages in rapidity, simplicity, and precision. These advantages derive from the high selectivity of the method for histamine, which eliminates the need for extensive sample cleanup. Selectivity for histamine versus spermidine, histidine, and cysteine is high enough to indicate that the method could be applied to other biological samples (brain tissue, plasma) in addition to fish tissues. The method can be implemented by using a single peristaltic pump (with variable pump-tube sizes) when a fluorescence detector of low pressure drop is available.

ACKNOWLEDGMENT

The authors wish to acknowledge Thomas A. Hollingworth, Jr., for advice and helpful discussions and Nancy Hill for preparing the manuscript.

Registry No. OPT, 643-79-8; histamine, 51-45-6.

LITERATURE CITED

(1) Wasserman, S. I. In *The Mast Cell-Its Role in Health and Disease*; Pepys, J., Edwards, A. M., Eds.; Pitman Medical: Turnbridge Wells, 1979; pp 9–20.
(2) Grossman, M. I.; Konturek, S. J. *Gastroenterology* **1974**, *66*, 517–521.
(3) Soll, A. H. *Gastroenterology* **1982**, *83*, 216–223.
(4) Kierska, D.; Sasiak, K.; Maslinski, C. *Agents Actions* **1981**, *11*, 28–32.
(5) Karolus, J. J.; LeBlanc, D. H.; Marsh, A. J.; Mshar, R.; Furgalack, T. H. *J. Food Prot.* **1985**, *48* (2), 166–168.
(6) Williams, D. W. *J.—Assoc. Off. Anal. Chem.* **1954**, *37* (3), 567–572.
(7) Lin, J. S.; Baranawski, J. D.; Olcott, H. S. *J. Chromatogr.* **1977**, *130*, 426–430.
(8) Navert, H. *J. Chromatogr.* **1975**, *106*, 218–224.
(9) Payne, N. A.; Zirrolli, J. A.; Gerber, J. G. *Anal. Biochem.* **1989**, *178*, 414–420.
(10) Mietz, J.; Karmas, E. *J. Food Sci.* **1977**, *42*, 155–158.
(11) Ronnberg, A. L.; Hansson, C.; Hakanson, R. *Anal. Biochem.* **1984**, *139* (2), 338–344.
(12) Pozo, R. G.; Saitua, E. S. *Alimentaria* **1988**, *25* (196), 27–29.
(13) Snyder, S. H. In *Methods of Enzymology*; Tabor, H., Tabor, C. W., Eds.; Academic Press: London, 1971; Vol. 17B, pp 838–841.
(14) Mita, H.; Yui, Y.; Yasueda, H.; Shida, T.; Tagawa, M. *Jpn. J. Allergol.* **1987**, *36* (3), 121–129.
(15) Shore, P. A.; Burkhalter, A.; Cohn, V. H. *J. Pharmacol. Exp. Ther.* **1959**, *127*, 182–186.
(16) Hakanson, R.; Ronnberg, A. L. *Anal. Biochem.* **1974**, *60*, 560–567.
(17) Lerke, P. A.; Bell, L. D. *J. Food Sci.* **1976**, *41*, 1282–1284.
(18) Edmunds, W. J. E.; Eitenmiller, R. R. *J. Food Sci.* **1975**, *40*, 516–519.
(19) Weissbach, H.; Lovenberg, W.; Udenfriend, S. *Biochim. Biophys. Acta* **1961**, *50*, 177–179.
(20) Gutierrez, M. D.; Gomez-Hans, A.; Valcarcel, M. *Anal. Chim. Acta* **1986**, *185*, 83–89.
(21) Staruszkiewicz, W. F.; Waldron, E. M.; Bond, J. F. *J.—Assoc. Off. Anal. Chem.* **1977**, *60* (5), 1125–1130.
(22) Staruszkiewicz, W. F. *J.—Assoc. Off. Anal. Chem.* **1977**, *60* (5), 1131–1136.
(23) Williams, S., Ed. *Official Methods of Analysis*; Association of Official Analytical Chemists: Arlington, VA, 1984; Sections 18.067–18.071, pp 341–342.
(24) Luten, J. B. *J. Food Sci.* **1981**, *46*, 958–959.
(25) Siraganian, R. P. *Anal. Biochem.* **1974**, *57*, 383.
(26) Mark, H. B. In Instrumental Analysis; Bauer, H. H., Christian, G. D., O'Reilly, J. E., Eds.; Allyn and Bacon: Boston, MA, 1979.
(27) Ruzicka, J.; Hansen, E. H. *Flow Injection Analysis*, 2nd ed.; Wiley: New York, 1988; pp 299–302.
(28) Selarko, C. M.; Jiao, K. S.; Drull, I. S. *Anal. Chem.* **1987**, *59*, 2221–2224.
(29) Mackie, I. M.; Fernandez-Salguero, J. *J. Sci. Food Agric.* **1977**, *28*, 935–940.
(30) Foo, L. Y. *J.—Assoc. Off. Anal. Chem.* **1977**, *60*, 183–185.
(31) Straka, M. R. *Diss. Abstr. Int., B* **1986**, *46*, 3421.
(32) Pacey, G. E.; Hollowell, D. A.; Miller, K. G.; Straka, M. R.; Gordon, G. *Anal. Chim. Acta* **1986**, *179*, 259.
(33) Pacey, G. E. *Anal. Chim. Acta* **1986**, *180*, 30.

RECEIVED for review April 16, 1990. Accepted June 8, 1990.

Noninvasive Method for Monitoring Ethanol in Fermentation Processes Using Fiber-Optic Near-Infrared Spectroscopy

Anna G. Cavinato, David M. Mayes, Zhihong Ge, and James B. Callis*

Center for Process Analytical Chemistry, Department of Chemistry, BG-10, University of Washington, Seattle, Washington 98195

Short-wavelength near-infrared (SW-near-IR) spectroscopy (700–1100 nm) is used for the determination of ethanol during the time course of a fermentation. Measurements are performed noninvasively by means of a photodiode array spectrometer equipped with a fiber-optic probe placed on the outside of the glass-wall fermentation vessel. Pure ethanol/water and ethanol/yeast/water mixtures are studied to establish the spectral features that characterize ethanol and to show that determination of ethanol is independent of the yeast concentration. Analysis of the second-derivative data is accomplished with multilinear regression (MLR). The standard error of prediction (SEP) of ethanol in ethanol/water solutions is approximately 0.2% over a range of 0–15%; the SEP of ethanol in ethanol/yeast/water solutions is 0.27% (w/w). Results from the mixture experiments are then applied to actual yeast fermentations of glucose to ethanol. By use of a gas chromatographic method for validation, a good correlation is found between the intensity of backscattered light at 905 nm and the actual ethanol. Additional experiments show that a calibration model created for one fermentation can be used to predict ethanol production during the time course of others with a prediction error of 0.4%.

INTRODUCTION

The need for real-time monitoring of the chemical and physiological status of fermentation processes and the lack of suitable sensors for this purpose have long been recognized (*1*, *2*). For the case of alcohol fermentations, measurements are limited to the determination of physical parameters which only give indirect estimates of ethanol production. Recently, efforts have been made to develop direct analyses for ethanol in fermentation broths (*3*, *4*). Unfortunately, most of these techniques require sample removal and preparation. A noninvasive method would be desirable, because sterility problems can be avoided and sampling is simplified (*2*). While there are a number of potential noninvasive analytical techniques such as X-ray, ultrasound, nuclear magnetic resonance, and infrared emission, the most readily implemented one is short-wavelength near-infrared (SW-near-IR) spectroscopy, which lies between 700 and 1100 nm (*5*). For the most part, absorptions in this spectral region arise from the second and third overtones of CH, OH, and NH stretches together with combination bands from other types of vibrations. The exact position of the bands depends on the chemical environment giving rise to a reasonably high degree of uniqueness of the spectra for different organic mulecules.

Although the low extinction coefficients of these highly forbidden transitions may seem a disadvantage, they can actually be of great utility for analysis of major constituents in the 0.1–100% concentration range. First, long path lengths are used, ensuring that a spectrum is more representative of the bulk and that a thin layer of adsorbed materials on the optical window will not fatally degrade the results. Second, quantitative measurements can be made on highly scattering materials. Both diffuse transmittance and diffuse reflectance geometries can be used. Additionally, the hardware in this region is very inexpensive and employs readily available fiber-optic components, conventional monochromators, tungsten lamps, and silicon detectors. Even with use of inexpensive components, signal-to-noise ratios on the order of 10000:1 can be obtained. Thus, very subtle changes in the spectra can be reliably used for analysis. Because this sensing technology is readily implemented in multichannel form (*6*), multiple characteristics of a bioprocess can be potentially monitored simultaneously.

One apparent disadvantage of SW-near-IR spectroscopy is that the spectral resolution in condensed phase is not high enough to ensure that the absorption bands arising from the different species in a mixture will be free of interferences. This necessitates the use of multivariate statistical calibration (*7*). Results obtained by Alberti et al. (*4*) using Fourier transform infrared (FT-IR) data show the advantages of this quantitation technique. These authors measured the infrared spectra of fermentation broths and extracted quantitative information about glucose, ethanol, and glycerol, using multivariate analysis. At the Center for Process Analytical Chemistry, SW-near-IR spectroscopy and multivariate calibration have been used for gasoline quality evaluation, making simultaneous measurement of octane numbers, API density, bromine number, total aromatics, olefins, and aliphatics (*8*) and for measurement of caustic and caustic brine (*9*). Near-IR technology is well established as an analytical method in the agricultural commodities industries (*10*) and has already been used to follow solid-phase fermentations (*11*).

The above review serves as a powerful rationale for the use of the SW-near-IR spectroscopy and multivariate statistical calibration as a noninvasive means of monitoring biofermentations. In this work, the feasibility of continuous analysis of ethanol production directly through the walls of a glass fermentation vessel is demonstrated. Monitoring and control of ethanol production are of obvious interest in the beer and wine industry and distilleries. Officially, alcohol in beverages is measured by specific gravity (picnometry and hydrometry) or refractometry (*12*). Although these methods are reproducible to 0.1–0.2%, they suffer from several drawbacks such as a long and complicated analysis and large sample size (*13*). A number of other analytical methods have been proposed for determination of ethanol in beverages and fermentation broths. These include gas chromatography (*14*), Fourier transform infrared spectroscopy (*4*, *15*), nuclear magnetic resonance (*16*), near-infrared spectroscopy (*17*, *18*), laser Raman spectrometry (*19*), immobilized enzymes (*20*, *21*), and flow injection analysis (*22*, *23*). Some of these techniques do not have enough precision, while others are lengthy and/or expensive; most have no potential for noninvasive analysis.

MATERIALS AND METHODS

Biofermentation. The yeast *Saccharomyces cerevisiae* was grown anaerobically on the defined medium listed in Table I with glucose as the carbon source. The fermentation was carried out

0003-2700/90/0362-1977$02.50/0

Table I. Defined Medium for *Saccharomyces cerevisiae* Fermentation

component	amt, g/L
glucose	150–200
yeast extract	10.4
ammonium sulfate	9.2
potassium hydrogen phosphate	2.9
magnesium sulfate	1.25

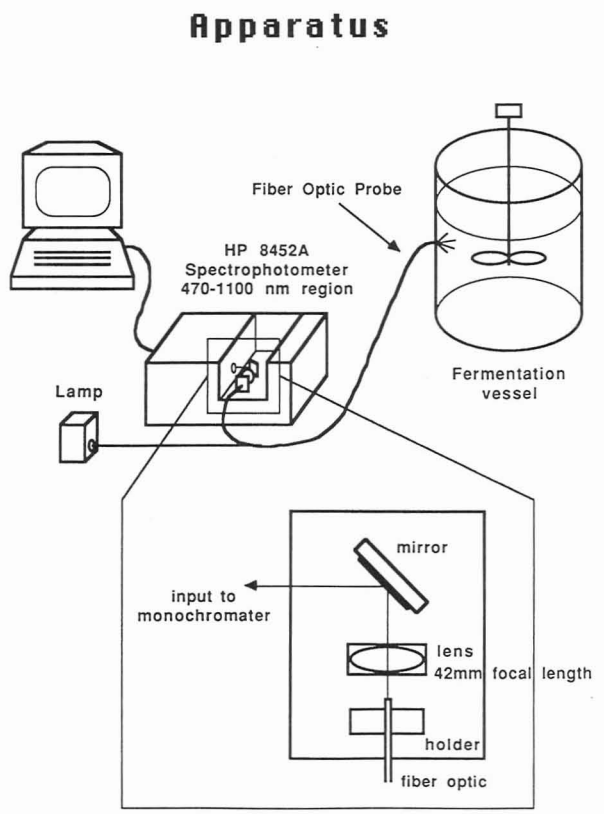

Figure 1. Schematic diagram of the instrument.

in a Bioflow I reactor from New Brunswick Scientific, Inc., of 2-L capacity. The culture was maintained at room temperature with an agitation speed of 300 rpm. Samples of 2-mL volume were withdrawn periodically for ethanol analysis by GC.

Ethanol Analysis. Ethanol analysis was performed on a Hewlett-Packard Model 5880A gas chromatograph equipped with a flame ionization detector (FID) (*24*). The column was a 6 ft × 20 mm i.d. glass 5% Carbowax 20M on 60/80 mesh Carbopack B. The chromatograph was operated under the following conditions: column temperature, 80 °C; injector temperature, 125 °C, FID temperature, 125 °C; carrier gas flow rate, 20 mL/min. The injection volume was 0.5 μL. Prior to injection, each sample was diluted with an equal volume of 2% by weight 1-propanol solution as an internal standard. The chromatograph was calibrated with aqueous ethanol samples diluted with the internal standard.

Near-IR Spectroscopy. SW-near-IR spectroscopy was carried out by means of a Hewlett-Packard 8452A photodiode array based spectrophotometer with the near-infrared option. The instrument was modified for use with a bifurcated fiber-optic probe (Sterngold Corp; 1 m in length, 6 mm outside bundle diameter, 2 mm inside bundle diameter) (Figure 1). As a light source a tungsten/halogen lamp (Osram 64635), operated from a stable dc power supply, was employed. It was focused on the outer bundle and guided to the sample. Light backscattered from the sample was collected by the inner bundle and directed to the monochromator. A 42-mm focal length asymmetric lens was used to collimate the light from the inner fiber bundle. This collimated light impinged on the collecting lens supplied by the manufacturer, which focused it on the entrance slit. With this configuration, the instrument retains the factory spectral resolution of 4 nm and a peak-to-peak

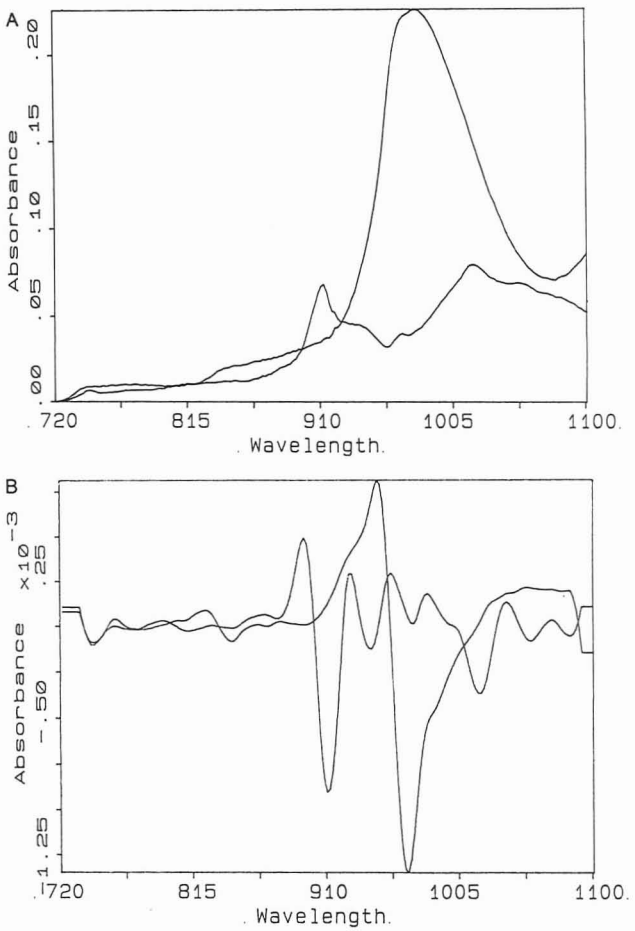

Figure 2. Absorbance spectra of pure water and pure ethanol (A). Second derivative spectra of pure water and pure ethanol (B). Spectra taken in transmission geometry in a 1-cm cuvette.

signal-to-noise ratio of 10^4:1 at zero absorbance with a 25-s averaging time and a 0.1-s acquisition time (*25*). Similar modifications of the HP8452A for use with fiber optics have been reported (*26*). The ethanol/water mixtures were analyzed in transmission mode using a 1-cm quartz absorption cell. In this configuration, an additional fiber bundle was used to convey the transmitted light to the collimating lens. The ethanol/yeast/water mixtures, as well as the fermentation, were monitored by placing the bifurcated fiber-optic probe (*6*) up to the side of a 1 × 1 × 4 cm quartz cuvette (1 cm path length) or the fermentor glass vessel wall. Spectra were obtained from the light scattered back to the fiber bundle from the scattering particles in the medium.

Data Analysis. Data analysis was carried out on an IBM PC-AT. Spectra were first smoothed and a second derivative transformation was calculated using a 26-nm window with in-house-developed software. In the analysis and comparison of spectral data from different experiments, the same smoothing and second derivative parameters were used. For calibration and prediction of ethanol content in a sample, stagewise multiple linear regression (MLR) provided by Pacific Scientific Co. (NIRS, Inc., Silver Spring, MD) was used. The standard error of prediction was from a cross validation estimate (*27*) that uses all but one sample as a calibration set to form a prediction equation, and then a prediction is made of the remaining sample. This "leave-one-out" exercise was repeated for each sample in the training set and the standard error of prediction was determined from the predicted and actual values for samples omitted.

RESULTS AND DISCUSSION

Basic Spectroscopy. The spectra of pure water and pure ethanol in the spectral region 700–1100 nm in a 1-cm cuvette are shown in Figure 2A. For water the most prominent band is at 960 nm. As previously noted (*9*) this band arises from the overtone combination motion ($2\nu_1 + \nu_3$) where ν_1 is the symmetric OH stretch and ν_3 the bending mode. The band

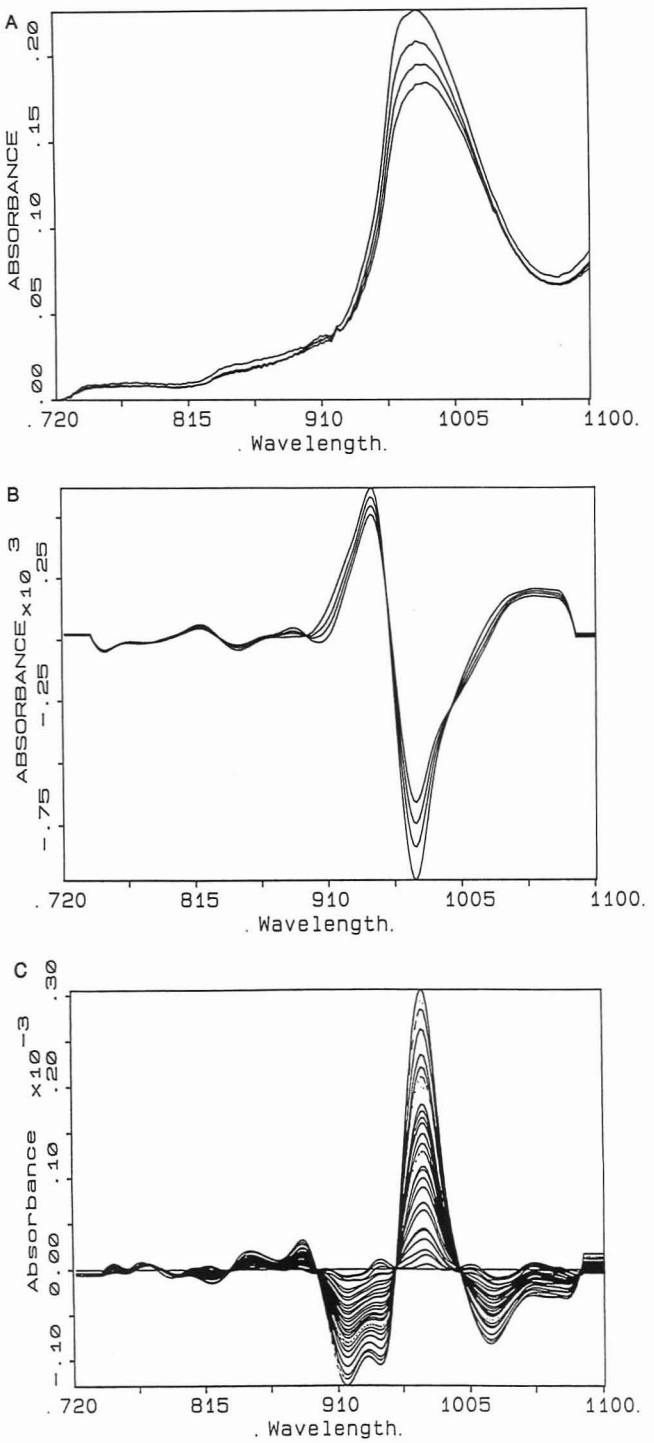

Figure 3. Absorbance spectra of water/ethanol mixtures (0–15% (w/w)) (A). Second derivative spectra of 3A (B). Second derivative difference spectra of 3B (C). Spectra taken in transmission geometry in a 1-cm cuvette.

is particularly broad due to the presence of two or more types of hydrogen bonded molecular complexes (*28*). In addition, weaker absorptions at 829 and 730 nm can be distinguished. The ethanol spectrum is more complex due to the presence of three near-IR-active functional groups (methyl, methylene, and hydroxide). The band at 905 nm is particularly important to this study and is assigned to the third overtone of the CH stretch on the methyl group. The shoulder at 935 nm is assigned to the third overtone CH stretch on the methylene group. The band at 960 nm is assigned to the OH stretch. This band becomes more evident when ethanol is diluted in carbon tetrachloride due to lack of hydrogen bonding. The first two assignments are consistent with those previously

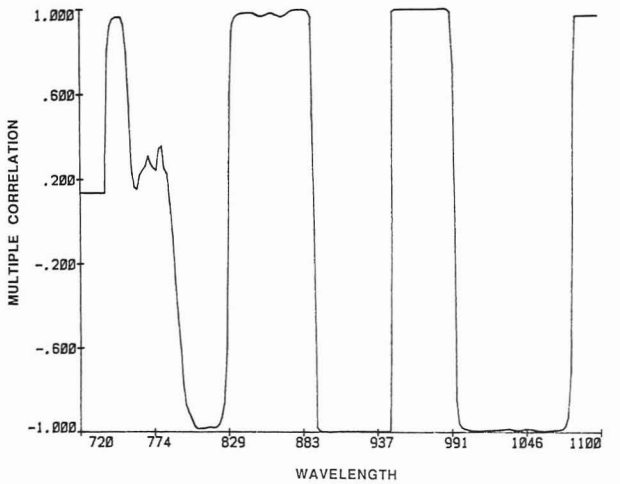

Figure 4. Multiple R plot vs wavelength of water/ethanol mixtures using one wavelength.

made for hydrocarbons (*29*) and the ratio of intensities reflects the ratio of protons on the methyl and methylene functional groups, respectively.

Calculation of the second derivative eliminates baseline offsets due to cuvette placement in the single-beam spectrophotometer and provides better spectral resolution. The second derivative spectra of pure water and ethanol are shown in Figure 2B. The ethanol second derivative intensities are considerably increased relative to those of water. In the zero derivative spectrum the maximum extinction coefficient of water is more than 4 times that of ethanol, whereas in second derivative the absorption intensities are about equal. This is a result of the ethanol bands being sharper than those of water. In addition, the 935-nm methylene band is fully resolved from the methyl band.

Analysis of Ethanol/Water Mixtures. The basic concepts of the use of SW-near-IR spectroscopy and multivariate calibration are well illustrated by the study of simple mixtures of ethanol and water and provide a basis for analysis of the more complex fermentation broths. Accordingly, a series of ethanol/water mixtures in the 0–15% (w/w) concentration range were prepared and their spectra taken (Figure 3A). The major spectroscopic feature in this data set is the water band at 960 nm while the methyl stretch of ethanol at 905 nm is present as a minor shoulder. The artifact at 915 nm is instrumental and arises from a filter placed over the photodiode array. Oscillations in the data arise from the "odd–even" readout scheme for this detector. The disappearance of the 960-nm water band is the most prominent spectral change as a result of the dilution of water with ethanol addition. After calculation of the second derivative (Figure 3B), the methyl stretch of ethanol is much more prominent. To further enhance the spectral features for observation purposes, the second derivative spectrum of pure water is subtracted from the data set. Now, in the second derivative difference spectra (Figure 3C), both the methyl and methylene stretches are well resolved.

The second derivative spectra of the ethanol/water mixtures (Figure 3B) were analyzed by stagewise MLR. A very high correlation (correlation coefficient $R = 0.999$) was obtained with just one wavelength, 905 nm. The plot of multiple R vs wavelength (Figure 4) shows a region of high correlation corresponding to the methyl band. An additional wavelength does not improve the correlation significantly, as expected for an ideal two-component mixture. Therefore, a model using $\lambda = 905$ nm was constructed. The standard error of estimate (SEE) with this model was 0.17% (w/w). The standard error of prediction (SEP) obtained from a cross validation estimate was 0.19% (w/w) ($R = 0.998$) (Figure 5).

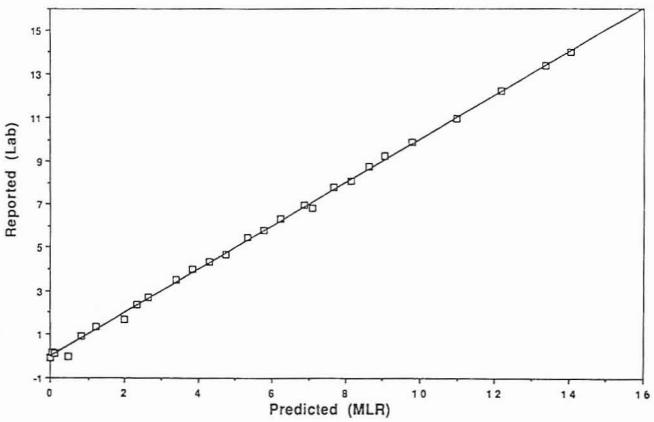

Figure 5. SEP correlation of water/ethanol mixtures using MLR and the 905-nm wavelength.

Effect of Light Scatter. During the time course of a fermentation, the number of yeast cells may increase by several orders of magnitude. This will result in greater light scattering, which may either increase or decrease the apparent absorbance through changes in the effective path length (*30*). This path length change could also affect ethanol determination. In order to investigate the influence of cell mass, a series of water/ethanol/yeast mixtures were analyzed in which the ethanol was varied between 0 and 7% (w/w) and the yeast concentrations varied between 0 and 17 g/L.

Figure 6A shows spectra recorded in a 1 × 1 × 4 cm cuvette in diffuse reflectance geometry. These spectra appear very similar to those recorded directly on the fermentation vessel (see Figure 9A). The major features are the water band at 960 nm and a decrease in relative absorbance baseline due to changes in yeast concentrations.

Figure 6B shows how the second derivative transformation corrects for baseline offset, and Figure 6C shows the second derivative difference, where a spectrum of a mixture containing no ethanol was subtracted from the set. Changes in the band at 905 nm with different ethanol concentrations are now clearly visible, while the overall change in the water band is due to displacement of water by yeast and ethanol. In fact, all spectra with pronounced changes in the 935-nm band correspond either to high yeast or high ethanol concentrations. These changes are not regular as in the fermentation spectra (compare Figure 9C) because ethanol and yeast are changing randomly with respect to each other. A one-wavelength (λ = 905 nm) model similar to that constructed for the ethanol/water solutions, but with different slope and offset, successfully predicts ethanol concentration despite the presence of yeast. This result is supported by the multiple R plot (Figure 7), which shows a good correlation in the spectral region corresponding to the methyl band.

However, the SEP of 0.27% (w/w) (R = 0.980) obtained from a cross-validation analysis was significantly greater than that of the ethanol/water mixtures (Figure 8). This is not entirely unexpected because the presence of these highly scattering organisms contribute considerable noise to the measurements.

Quantitative Determination of Ethanol in Fermentation. The production of ethanol in the medium defined in Table I was followed in real time. Spectra were taken at half-hour intervals for a 30-h period. A representative set of spectra is shown in Figure 9A. The most obvious change in the spectra is the decrease in relative baseline absorbance with increased time of the reaction. With increased scattering material, relative reflectance increases, causing more light to return to the detector (*30*), thus decreasing the relative absorbance. At the beginning of the fermenation, when yeast production is very slow, the baseline offset remains constant.

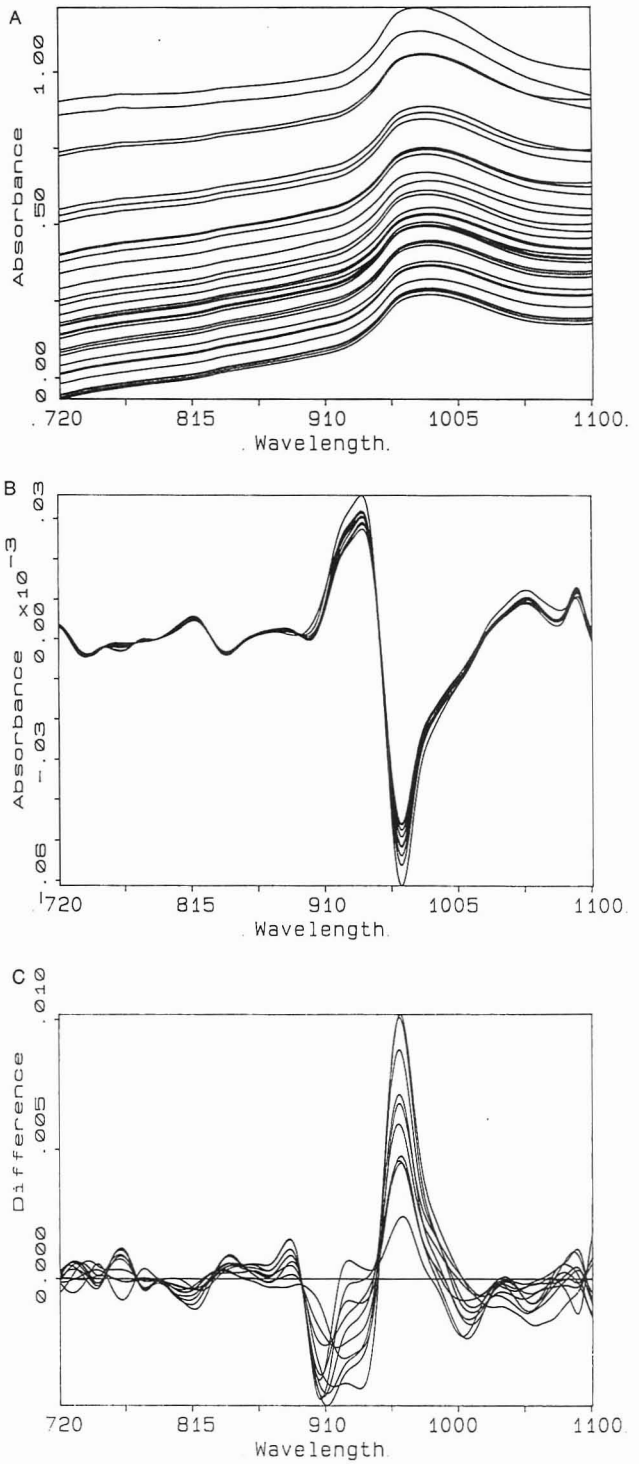

Figure 6. Absorbance spectra of water/ethanol/yeast mixtures: ethanol concentration 0–7% (w/w), yeast concentrations 0–17 g/L (A); second-derivative spectra of 7A (B), second-derivative spectra of 7B (C). Spectra taken in backscattering geometry.

However, as the yeast cells begin to rapidly reproduce, the baseline offset decreases, and when yeast reproduction stops, the offset again becomes constant. While there is no evident ethanol information in this set of spectra because of the baseline offset variation and the large size of the water peak, calculation of the second derivative enhances the third overtone methyl CH stretch (Figure 9B). Again, the spectral information is further enhanced by subtraction of a spectrum, from early in the fermentation process (Figure 9C). By comparing Figure 9C to Figure 3C and Figure 6C, it is evident that the signal to noise ratio (S/N) achieved in the fermentation broth is not as good as in the artificial mixtures. This is due in part to a greater extent of noise rising from stirring and

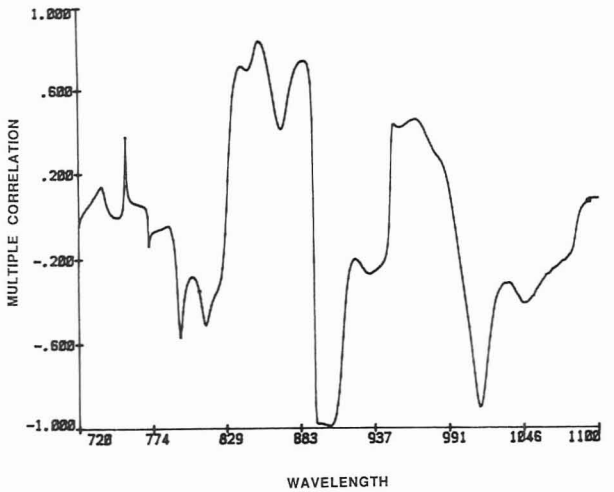

Figure 7. Multiple R plot vs wavelength of water/ethanol/yeast mixtures using one wavelength.

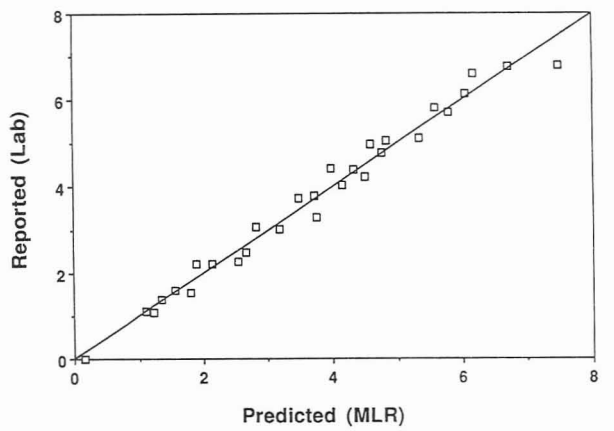

Figure 8. SEP correlation of water/ethanol/yeast mixtures using MLR and the 905-nm wavelength.

bubbling and in part to a reduced signal from the backscattered light compared to the transmission cell used for the ethanol/water experiments. Correlation between the GC reference analysis and the SW-near-IR second derivative spectra at 905 nm resulted in a SEE of 0.19% (w/w) (R = 0.993). A linear regression model was constructed by using a single wavelength (905 nm) of the second derivative spectra from this fermentation experiment as a calibration set. Prediction of ethanol production over the time course of the fermentation is shown in Figure 10. Also shown is the concentration of ethanol measured by GC on samples withdrawn from the reaction vessel immediately after the recording of a spectrum. The shape of this curve follows the ethanol production pattern of a typical batch fermentation (*31*).

Applicability of Calibration Constants to Succeeding Fermentation. The final series of studies was designed to investigate whether a model developed for one fermentation could be applied to succeeding runs. Accordingly, two further experiments were undertaken, which were reasonable duplications of the first. Figure 11 shows that the model developed on the first fermentation could be successfully applied to the second and third fermentations. The linear regression equation for the production of ethanol was

$$\%\ \text{ethanol (w/w)} = K(0) + K(1)\,A_{2\text{nd}}(905) \qquad (1)$$

where $K(0)$ = 2.82 and $K(1)$ = −70 888 and $A_{2\text{nd}}$ is the second derivative absorbance value. The standard error of prediction was 0.42% (w/w) and R = 0.95. Conversely, models constructed with either the second or third fermentations could be used to predict the other two with similar values of SEP

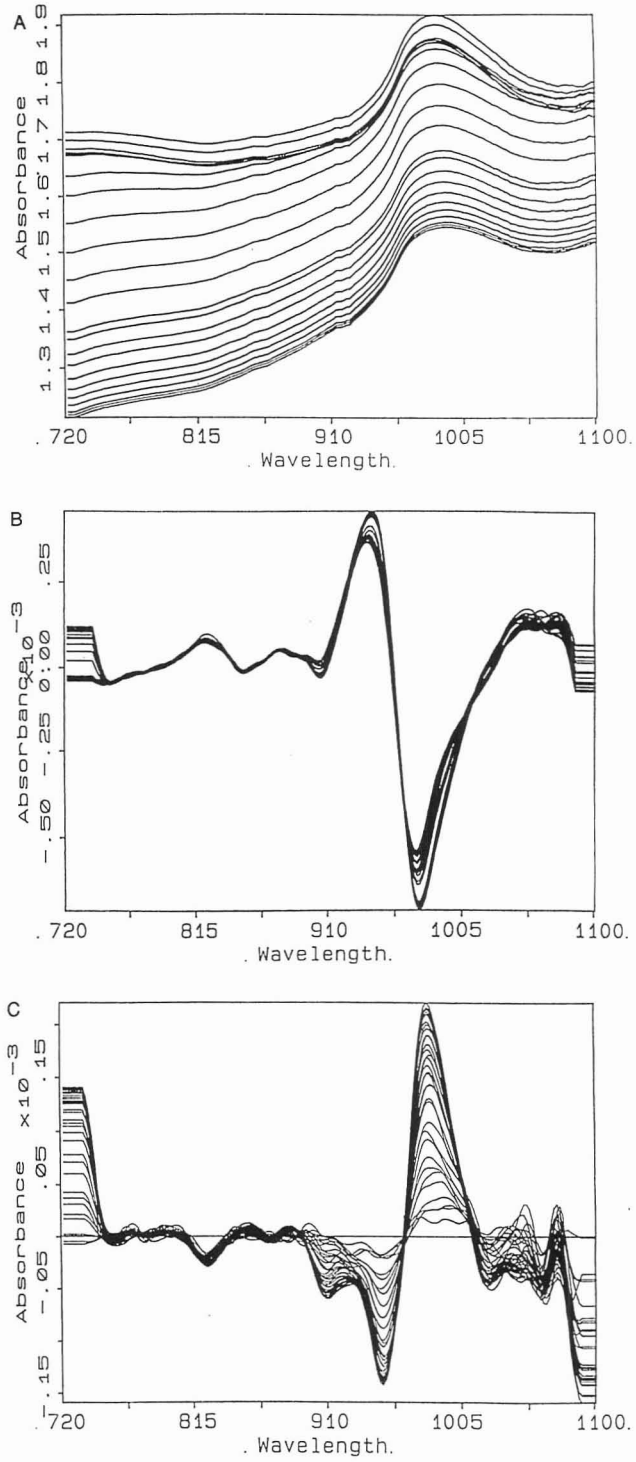

Figure 9. Absorbance spectra of fermentation over time (A). Second derivative spectra of 9A (B). Second derivative difference spectra of 9B (C). Spectra taken in backscattering geometry.

and R. These results are all the more remarkable when one considers that the probe was removed and replaced between each fermentation.

CONCLUSION

We have successfully demonstrated the potential of SW-near-IR spectroscopy for monitoring of a bioprocess for ethanol concentration. The major advantage of this technique is that it is noninvasive and requires only that the reactor vessel have a quartz or glass window. Thus, the need for elaborate sterile sampling systems and antifouling probes is eliminated. In its present form the cost of the instrumentation (~$10 000) may seem high. However, inexpensive instruments based upon light-emitting diodes have been constructed for agricultureal

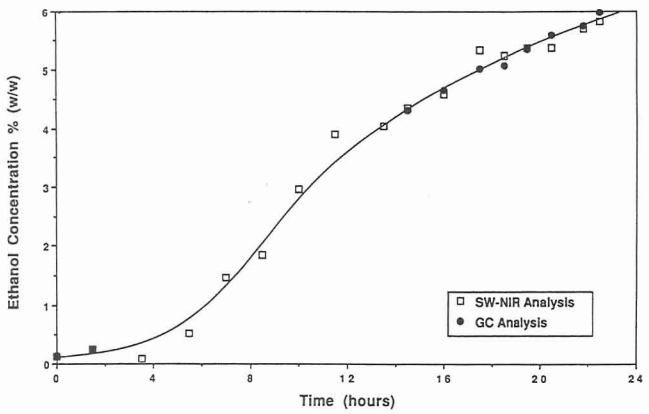

Figure 10. Prediction of ethanol production during the time course of a fermentation using the 905-nm second derivative wavelength value.

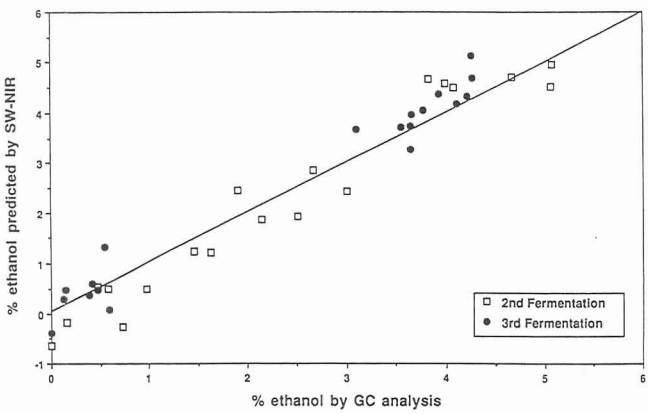

Figure 11. Prediction of ethanol content during other fermentations using SW-near-IR compared to GC analysis.

product analysis and could be adapted for use here (*10*). Another advantage of this approach is the apparent robustness of the calibration, as shown by the ability to apply a model developed on one fermentation to succeeding fermentations. This method represents an excellent tool for monitoring and control of ethanol production fermentations. However, the present technology does not yet allow monitoring of ethanol at trace level, as in the case of aerobic fermentations.

The current major drawback to the SW-near-IR method is its precision (SEP = 0.42%). While it is more reproducible than other reported spectroscopic methods (*15*, *19*), the detection limits and precision of gas chromatography, flow injection analysis, and enzyme-based electrodes are superior and this may be of importance in certain applications. One of our research goals is to improve the S/N of our measurements and decrease detection limits proportionally.

The final advantage of our technique is the potential for simultaneous multiparameter analysis. Current research is directed toward demonstration of SW-near-IR methods for glucose, cell density, and aerobic/anaerobic status.

ACKNOWLEDGMENT

We are grateful to David Burns for use of his data-analysis software, John Beale for useful discussions, Heinz Floss for encouragement, Rod Fisher for loan of the bioreactor, and Stephan Whitley for experimental assistance.

Registry No. EtOH, 64-17-5.

LITERATURE CITED

(1) Humphrey, A. E. *Chem. Eng.* **1974**, *81* (26), 98–112.
(2) Clark, D. J.; Calder, M. R.; Carr, R. J. G.; Blake-Coleman, B. C.; Moody, S. C. M.; Collings, T. A. *Biosensors* **1985**, *1*, 213–320.
(3) Dinwoodie, R. C.; Mehuert, D. W. *Biotechnol. Bioeng.* **1985**, *26*, 1060–1062.
(4) Alberti, J. C.; Phillips, J. A.; Fink, D. J.; Wacasz, F. F. *Biotechnol. Bioeng. Symp.* **1985**, *15*, 689–722.
(5) Callis, J. B.; Illman, D. L.; Kowalski, B. R. *Anal. Chem.* **1987**, *59*, 625A–637A.
(6) Mayes, D. M.; Callis, J. B. *Appl. Spectrosc.* **1989**, *43*, 27–32.
(7) Beebe, K. R.; Kowalski, B. R. *Anal. Chem.* **1987**, *59*, 1007A–1017A.
(8) Kelly, J. J.; Barlow, C. H.; Jinguji, T. M.; Callis, J. B. *Anal. Chem.* **1989**, *61*, 313–320.
(9) Phelan, M. K.; Barlow, C. H.; Kelly, J. J.; Jinguji, T. M.; Callis, J. B. *Anal. Chem.* **1989**, *61*, 1419–1424.
(10) Norris, K. H. *NATO Adv. Study Inst. Ser.*, **1983**, *46*, 471–484.
(11) Norris, K. H. *Biotechnol. Bioeng.* **1983**, *25*, 603–607.
(12) *Official Methods of Analysis of the Association of Official Analytical Chemists*; William Hormitz, Ed.; Association of Official Analytical Chemists: Washington, DC, 1980.
(13) Kovar, J. *J. Chromatogr.* **1985**, *333* (2), 389–403.
(14) Cutaia, A. J. *J. Assoc. of Anal. Chem.* **1984**, *67*, 192–193.
(15) Kuehl, D.; Crocombe, R. *Appl. Spectrosc.* **1984**, *38*, 907–909.
(16) Guillou, M.; Tellier, C. *Anal. Chem.* **1988**, *60*, 2182–2185.
(17) Buchanan, B. R.; Honigs, D. E.; Lee, C. J.; Roth, W. *Appl. Spectrosc.* **1988**, *42*, 1106–1111.
(18) Halsey, S. A. *J. Inst. Brew.* **1985**, *91*, 306–312.
(19) Gorny, C.; Jouan, M.; Quy Dao, N. *C. R. Hebd. Seances Acad. Sci.* **1988**, *306* (II), 417–422.
(20) Wiseman, A. *TrAC, Trends Anal. Chem.* **1988**, *7*, 5–7.
(21) Walters, B. S.; Nielsen, T. J.; Arnold, M. A. *Talanta*, **1988**, *35*, 151–155.
(22) Worsfold, P. J.; Ruzicka, J.; Hansen, E. H. *Analyst* **1981**, *106*, 1309–1317.
(23) Lazaro, F.; Luque de Castro, M. D.; Valcarcel, M. *Anal. Chem.* **1987**, *59*, 1859–1863.
(24) Martin, G. E.; Burggraff, J. M.; Dyer, R. H.; Buscemi, P. E. *J. Assoc. Off. Anal. Chem.* **1981**, *64*, 186–193.
(25) Owen, A. J. *The Diode-Array Advantage in UV/Visible Spectroscopy*; Hewlett-Packard Publication No. 12-5954-8912; Hewlett-Packard: Palo Alto, CA, 1988.
(26) Van Hare, D. R.; O'Rourke, P. E.; Prather, W. S.; Bowers, M. B.; Hovanec, M. J. *On-Line Fiber Optic Spectrometry*; Du Pont Publication DP-MS-88-186; Du Pont: Wilmington, DE, 1989.
(27) Sharaf, M. A.; Illman, D. L.; Kowalski, B. R. Chemometrics, In *Chemical Analysis: A Series of Monographs on Analytical Chemistry*; Elving, P. J., and Winefordner, J. D., Eds.; Kolthoff, I. M., Editor Emeritus; John Wiley and Sons: New York, 1986; Vol. 82.
(28) Scherer, J. R. In *Advances in Infrared and Raman Spectroscopy*; Clark, R. J. H., Hester, R. E., Eds.; Heyden: London, 1979; Vol. 5, Issue 3, pp 149–216.
(29) Weyer, L. G. *Appl. Spectrosc. Rev.* **1985**, *21*, 1–43.
(30) Reynolds, L.; Johnson, C.; Ishimaru, A. *Appl. Opt.* **1976**, *15*, 2059–2067.
(31) Wang, D. I. C.; Cooney, C. L.; Demain, A. L.; Dunnill, P.; Humphrey, A. E.; Lilly, M. D. *Fermentation and Enzyme Technology*; John Wiley & Sons: New York, 1979; p 79.

RECEIVED for review January 30, 1990. Revised manuscript received May 29, 1990. Accepted June 6, 1990. Funding for this research was provided by the Center for Process Analytical Chemistry. We are indebted to the Instrumentation Donation Committee of Hewlett-Packard for the gift of the near-IR spectrophotometer.

Continuum-Source Atomic Absorption Spectroscopy with an Echelle Spectrometer Adapted to a Charge Injection Device

Chunming Hsiech, Steven C. Petrovic, and Harry L. Pardue*

Department of Chemistry, Purdue University, West Lafayette, Indiana 47907

An instrumental system for continuum-source atomic absorption spectroscopy has been developed for simultaneous multielement determinations. The system consists of an electrothermal atomizer and a charge injection device adapted to an echelle spectrometer to achieve multiplex detection. A continuous 40-nm spectral range in the two-dimensional echelle spectrum was acquired simultaneously through the capability of the charge injection device to integrate signals in its MOS capacitors. Novel methods were developed to compute absorbances by "scanning" through all orders in the entire echelle spectrum or selecting absorption lines randomly. In the range 300–430 nm, characteristic concentrations (1% absorption) were 1.6, 2.6, 2.9, and 3.8 ng mL^{-1} respectively for Cu, Mn, and two Cr lines; these values are similar to those (1.3, 2.2, 1.2, and 3.6 ng mL^{-1}) obtained for single-element detection with an image-dissector system.

INTRODUCTION

Since the early work of Fassel et al. (*1*) there have been many studies of continuous-source atomic absorption spectroscopy (CS-AAS), most of which have been discussed in recent reviews (*2–5*). Although many of these studies have involved the use of conventional optics with conventional detectors, some more recent studies have combined conventional and echelle spectrometers with one- and two-dimensional imaging detectors (*6–8*).

In the work of Masters et al. (*6*, *7*), an image dissector was adapted to an echelle spectrometer to obtain high resolution with moderately broad spectral range. Although good sensitivity was obtained for a variety of elements, it was difficult to quantify multiple elements simultaneously because the image dissector is not an integrating detector. In a more recent study (*8*), a higher (fifth) order of a conventional grating was used with a cross-dispersion grating and a one-dimensional photodiode array. Use of the higher order of the grating provided improved resolution (0.01 nm) and use of the integrating feature of the photodiode array permitted multiple elements to be quantified simultaneously. The principal problem with this system was the rather limited spectral range of 2.5 nm for each atomization step.

The present study was undertaken to determine to what extent these problems could be resolved by adapting an echelle spectrometer to a two-dimensional integrating detector. Special features of the system described here involve use of an echelle grating with a blaze angle of 76° used in an off-Littrow configuration (*9*) with a charge injection device (CID) and an electrothermal atomizer. This system offers advantages relative to all those reported previously. Relative to the echelle spectrometer/image dissector system (*6*, *7*), it permits simultaneous multielement quantification with similar sensitivies and detection limits. Relative to the conventional-grating/one-dimensional photodiode array system (*8*), it combines a 2.5- to 3-fold improvement in spectral resolution with a 16-fold improvement (2.5–40 nm) in spectral range. Because this is the first application of the CID for CS-AAS, some of its salient features are discussed below.

The CID is a solid-state imaging device that uses charge injection and intracell charge transfer to transduce image information (*10*). Each element in the two-dimensional sensor consists of a pair of metal-oxide semiconductor (MOS) capacitors which are reverse biased to collect and store photon-generated charge signals. The major advantage of the CID over the image dissector in detection of transient signals, such as those from an electrothermal atomizer, is the integrating capability. Consequently, spectral information at many different resolution elements can be measured and stored simultaneously in the CID. The image dissector has no integration capability and accordingly it is not possible to store signals at different locations simultaneously. Also, the electron beam from a selected pixel of the image dissector is focused onto the amplifying dynodes by electrical fields; accordingly, stray or drifting electric fields can cause inaccuracies in the addressing process in the image dissector. Because addressing in CID is achieved with solid-state electronics, the CID is less sensitive to electrical fields.

Considerations that influence the choice of a detector and optical configuration are very different for absorption studies relative to emission studies. Whereas wide dynamic range is required for emission studies, the nature of the absorption process imposes inherent limitations on the dynamic range for which acceptable errors are obtained (*11*, *12*). Accordingly, in the choice of a detector for atomic absorption spectroscopy, it is a reasonable compromise to sacrifice dynamic range in favor of improved spectral resolution. In addition to choosing a CID that emphasized spatial resolution, we also used the off-littrow configuration of the echelle spectrometer (*9*) to further enhance spectral resolution. Results are reported for simultaneous multielement quantification in the spectral range from 300 to 430 nm.

EXPERIMENTAL SECTION

Reagents. All solutions were prepared by using distilled, deionized water and certified atomic absorption standards (Alfa Products, Danvers, MA). Multielement solutions were prepared by mixing aliquots from the stock solutions of the elements of interest and diluting to appropriate volumes. Concentrations for calibration studies were in the range from 0.1 ng mL^{-1} through 10 μg mL^{-1} with four standards in each 10-fold range.

Instrumentation. A diagram of the instrumentational setup is depicted in Figure 1. The system consists of a xenon-arc lamp, an electrothermal atomizer, an echelle spectrometer, a charge injection device, an interface unit, and a microcomputer.

The xenon-arc lamp (Model L2479, Hamamatsu Corp., San Jose, CA) was located in an air-cooled housing and powered by a current-regulated power supply (Model 533, Optical Radiation Corp., Azusa, CA) operated at 15 A and 20 V. The intensity of the continuum radiation was higher than that available from hollow cathode lamps at wavelengths above 350 nm.

The electrothermal atomizer (Model HGA2100, Perkin-Elmer, Norwalk, CT) was equipped with pyrolytically coated graphite tubes. The temperature cycle was set to evaporate the solution at 100 °C for 20 s, char the residue at 1000 °C for 10 s, and atomize the sample at 2700 °C for 10 s. The atomization temperature was optimized for the least volatile element (vanadium) among those

0003-2700/90/0362-1983$02.50/0

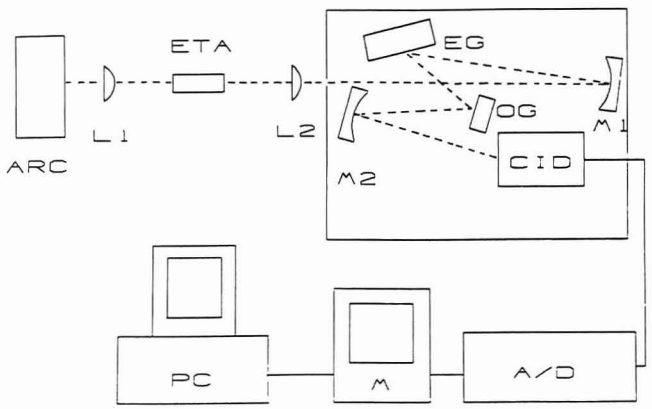

Figure 1. Diagram for instrumentation setup: ARC, xenon-arc lamp; L1, L2, imaging lens; ETA, electrothermal atomizer; M1, M2, collimating and focusing mirrors; EG, echelle grating; OG, order-sorting grating; CID, charge injection device; A/D, interface unit; M, monitor; PC, microcomputer.

being studied. The flow rate of argon gas was 60 mL min^{-1}, which was interrupted during atomization. To reduce memory effects, the atomizer was heated at 2800 °C for 10 s and cooled with argon and running water for 2 min between samples.

The echelle spectrometer was modified to achieve 3-fold image reduction because the size of the CID was about one-third that of the image dissector used in the previous study (*7*). This was accomplished by replacing the original 75-cm focal length (fl) mirror (M2) with a 25-cm fl mirror. Orders in the echelle spectrum were separated by using an order-sorting grating (OS, first-order diffraction grating, 600 grooves mm^{-1}). The positions of the echelle grating (EG) and order-sorting gratings were rearranged to eliminate aberrations. The width and height of the entrance slit for the spectrometer were set to 100 and 200 μm, respectively.

The charge-injection device (Model TN2250, General Electric, Liverpool, NY) has a resolution of 512 rows by 512 columns. Each square pixel in the CID has the dimension of 15 μm × 15 μm. The surface of the CID sensor is covered with a fused-silica plate instead of regular glass to improve ultraviolet transmittance. The signal, photon-generated charge, was integrated by setting the CID to the injection-inhibit mode to enhance the signal-to-noise ratio. In this study, signal integration periods between 0.3 and 0.8 s were used. The selection of these operational conditions is discussed in a later section.

The interface unit (Model PC-512, Poynting Products, Oak Park, IL) consists of a camera-support module and a memory buffer. The CID-support module provides power and timing pulses and converts analog signals from the CID to digital form. The analog-to-digital converter (ADC) has 8-bit resolution and a 14-MHz conversion rate. A display monitor was used to inspect the echelle spectrum visually and a microcomputer was used for communication, control, data collection, and data processing.

Data Processing. The conversion of signals from the stored charges to the absorbances of spectral lines involved the following procedures. First, the stored charges in the entire CID were injected sequentially, converted to digital form, and stored in a 256K memory buffer located in the camera support module. Second, signals were then transferred from the 256K buffer to a 1-Mbyte buffer located in the microcomputer I/O slot. In this process, the image data representing dark current and light intensities before and during atomization were saved in separate locations of the 1-Mbyte memory buffer for computation of absorbances in a latter step. The image data transferred could be saved with reduced spatial resolution when more than four frames of images were needed to meet the required resolution in time. The resolution format for the transferred data is loaded into the control registers before the data acquisition. The timing of those processes is controlled by a clock in the camera-support module and the signal conversion has a frame rate of 30 Hz.

The last step of data processing is to transform data that represents the integral of spectral signals into data that represents the absorbances of spectral lines. This can be done either by a random-access algorithm to obtain absorbances of selected absorption lines or by a sequential-access algorithm to obtain the entire absorption spectra. In the sequential method, an image resolution format of 512 by 240 pixels is used and eight frames of spectral images are stored in the 1-Mbyte image buffer.

The procedure for measuring signals in the sequential access algorithm is as follows. The dark current and signal at 100% T were measured in advance and stored in the first and second frames of the memory buffer. Then, the signals obtained for atomized samples were stored in the other frames of the buffer. After the data were stored in the memory buffer, the data were processed according to the following method. First, the 100% T signals were "scanned" vertically to locate the center of each order and to determine the total number of orders covered. The entire echelle spectrum was then scanned from the lowest order toward the highest order. Each order was scanned from the left to the right edge of the CID. Because the echelle spectrum was somewhat slanted, the center of each order was determined at every pixel scanned and assigned to the appropriate position. The absorbance (A) was computed as $A = \log [(I_0 - I_d)/(I - I_d)]$, where I_0 is the 100% T signal, I is the absorption signal, and I_d is the dark current.

In the random-access method, the data retrieved to compute absorbance were only those from the pixels for preselected absorption lines. The time required to compute absorbances for the selected absorption lines was in the range of milliseconds and absorbances could be computed in real time. Also, it was possible to resolve the full 512 by 480 pixel array because it was necessary to store only one frame of image in the memory buffer when absorbances were computed in real time.

RESULTS AND DISCUSSION

Unless stated otherwise, results were obtained with an electrothermal atomizer and uncertainties are reported at the level of one standard deviation.

Echelle Spectrometer. Use of an echelle grating differs from conventional gratings in that high resolution is achieved by using high orders (10–1000) rather than high-density ruling. Because the different orders are superimposed on each other, they are separated into a two-dimensional pattern by using a second grating or prism to disperse the radiant energy at 90° relative to the dispersion axis of the echelle grating. In order to reduce the dimensions of the dispersed spectrum so that a complete free spectral range could be monitored along one dimension of the CID, the 63° 21′ echelle grating used in earlier studies was replaced by a 76° grating. The 76° grating provides a free spectral range that is 4-fold smaller than the 63° 21′ grating. The resulting improvement of the spectral coverage in the horizontal direction results in a trade-off of the spectral coverage in the vertical direction. In the same spectral range, the number of orders generated from the 76° echelle is 4-fold that from the 63° 26′ echelle, thus requiring greater dispersion in the vertical direction to reduce overlap among diffraction orders. The greater dispersion was achieved by using a 600-groove/mm first-order grating and by replacing the 75-cm fl focusing mirror (M2, Figure 1) used earlier (*6*, *7*) with a 25 cm fl mirror. This change resulted in a reduction of the spectral range that can be monitored simultaneously and an increase in the aberration due to the increase in the solid angle (β) between the incident and the reflecting rays to M2. We were able to reduce the aberration by placing the smaller order-sorting grating next to the CID. This resulted in absorption profiles with very small asymmetric deviations. With this configuration, including a 25-cm focusing mirror and a 100-μm slit, the resolution in vertical dispersion was 1.1 nm at 300 nm. At this wavelength, the overlap among orders was about 15% of the peak height. At longer wavelengths, the free spectral range and the spacing between orders increased, so that overlap among orders was reduced.

Charge Injection Device. The dark current in a CID mainly results from thermally generated charges in the depleted storage regions of the semiconductor. This process competes with the photon-generation charges and reduces the

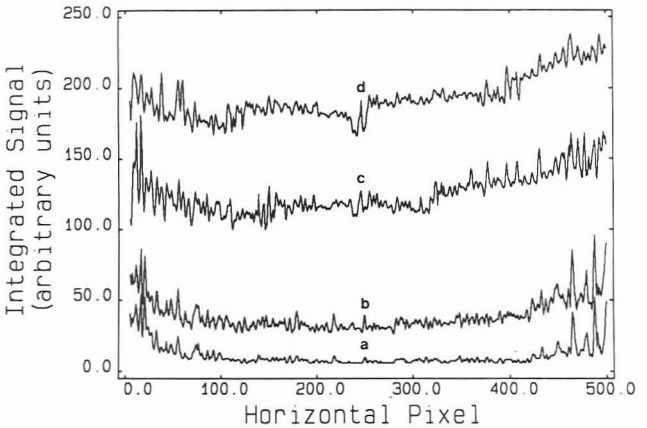

Figure 2. Integrated signals (300 ms) across a row in the middle of sensor: (a) dark current; (b) at 300 nm; (c) at 350 nm; (d) at 400 nm.

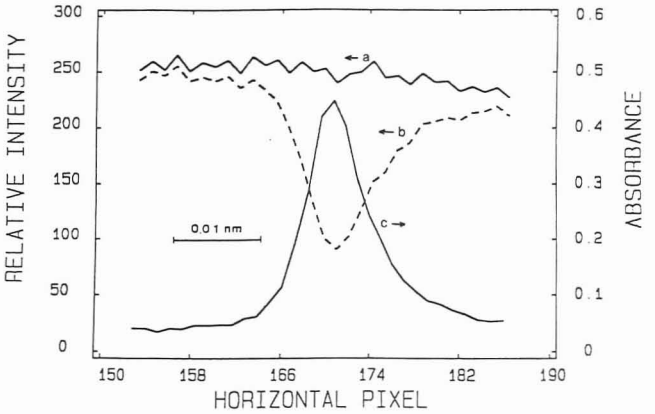

Figure 3. Spectral response near 422.7 nm without and with calcium in a flame atomizer: (a) 100% T; (b) intensity with calcium; (c) absorbance.

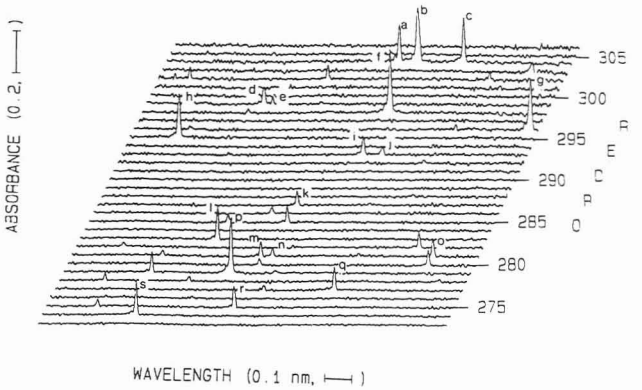

Figure 4. Absorption spectra between 315 and 355 nm with the signals nm with the signals integrated between 3.2 and 4.0 s from the start of atomization (element and absorption wavelength, nm): (a) V, 318.3; (b) V, 318.4; (c) V, 318.5; (d) Li, 323.3; (e) Ni, 323.3; (f) Cu, 324.8; (g) Cu, 327.4; (h) Cu, 327.4; (i) Na, 330.2; (j) Na, 330.3; (k) Ni, 337.0; (l) Ni, 341.5; (m) Al, 343.9; (n) Fe, 344.0; (o) Al, 344.4; (p) Yb, 346.4; (q) Ni, 349.3; (r) Ni, 351.5; (s) Ni, 352.5.

dynamic range and signal-to-noise ratio (S/N). In applications to atomic emission spectroscopy the intensity is usually quite low and it is frequently necessary to cool the detector in order to reduce thermally generated dark current. However, because the xenon-arc lamp used in this study produces much higher intensities, the dark current represents a smaller fraction of the signal and we chose to evaluate the CID at room temperature.

Dark Current/Wavelength Dependency. Figure 2 shows some results for the CID operated at room temperature with an integration time of 300 ms. The spectral range covered by each plot is about 1.3 nm and the spectral resolution varies from about 0.003 nm at 300 nm to about 0.004 nm at 400 nm. The jagged nature of the plots represents variations among the various pixels in each row. The dark current (curve a) represents about 27, 7, and 4% respectively, of the signal amplitudes at 300, 350, and 400 nm, respectively. It is probable that improved results could be obtained, especially at shorter wavelengths, with a cooled detector. However, as noted above, our objective in this study was to evaluate the performance of the detector at room temperature.

The results in Figure 2 also show how the combined effects of the source and detector influence the 100% T signal level at different wavelengths; the 100% T signal at 400 nm is about 3-fold that at 300 nm. To compensate for these variations, we used different integration times in different wavelength regions. For example, integration times varied from 800 ms at 300 nm to 300 ms at 400 nm. For the 40 nm monitored by the CID at any one time, the variation of intensity with wavelength was relatively small and fixed integration times could be used within each of the 40-nm ranges.

Linearity. The linearity of the CID response was evaluated by using neutral density filters to vary the light intensity reaching the sensor. Transmittances of the filters were calibrated with a diode-array based spectrophotometer (Hewlett-Packard 4850A). For five transmittances between 20 and 100%, least-squares fits of CID values (y) vs results with the spectrophotometer (x) yielded

$$y = (1.03 \pm 0.02)x - (3.9 \pm 0.8)$$

with $S_{yx} = 0.47$ and $r = 0.9997$ at 340 nm

and

$$y = (1.05 \pm 0.06)x - (4.9 \pm 0.5)$$

with $S_{yx} = 0.68$ and $r = 0.9999$ at 400 nm

Plots of log y vs log x were linear with slopes of 1.00 ± 0.01 at both 340 and 400 nm, respectively. The scatter about the least-squares lines as reflected by the standard errors of the estimates (S_{yx}) and the values of unity for the log/log plots illustrate good agreement between the two instruments and confirm a linear relationship between integrated current and light intensity. We were somewhat surprised by the negative intercepts for the linear least-squares fits; we are uncertain about the origin of these nonideal in intercepts, but a possible reason is that some of the photon-generated charge was not injected into the substrate during the readout period.

Fixed Pattern Noise. As noted earlier, the jagged shapes of plots in Figure 2 reflect different sensitivities of the different pixels in each row. Figure 3 shows analogous data for the 100% T signal and absorption by calcium near 422.7 nm. The fixed-pattern noise in the transmittance data (curves a and b) is reduced substantially in the absorbance data (curve c). There is less fixed pattern noise in the absorbance plot (curve c) than the transmittance plots (curves a and b), suggesting that the pixel-to-pixel variations are partially canceled by the ratios of intensities used to compute absorbance.

Atomic Absorption Spectra. *Typical Spectrum.* Figure 4 shows typical absorption spectra between 315 and 355 nm for several elements. Positions of spectral lines were calculated by using the equation

$$\lambda = \lambda_0 + (d\lambda/dX)\,(X - X_0) + (d\lambda/dY)\,(Y - Y_0)$$

where λ and λ_0 are computed and reference wavelengths, respectively, X and X_0 are the horizontal coordinates of the computed and reference wavelengths, respectively, Y and Y_0 are the vertical coordinates of the computed and reference wavelengths, respectively, and $d\lambda/dX$ and $d\lambda/dY$ are the horizontal and vertical reciprocal dispersion factors, respectively. The vertical reciprocal dispersion factor was found to

Table I. Comparisons of Computed and Expected Wavelengths for Selected Absorption Lines

	wavelengths, nm			
element	computed	expected	difference	order
V	318.173	318.341	0.168	304
V	318.340	318.398	0.058	304
V	318.414	318.540	0.126	304
Li	323.162	323.261	0.099	299
Ni	323.176	323.296	0.120	299
Cu	324.580	324.754	0.174	298
Cu	327.246	327.396	0.150	296
Cu	327.219	327.396	0.177	295
Na	330.124	330.232	0.108	293
Na	330.155	330.299	0.144	293
Ni	336.825	336.957	0.132	287
Ni	341.412	341.477	0.065	283
Al	343.921	343.935	0.014	281
Fe	343.061	344.939	0.122	281
Al	344.239	344.364	0.125	281
Yb	346.318	346.436	0.118	279
Ni	349.269	349.296	0.027	277
Ni	351.379	351.505	0.126	275
Ni	352.447	352.454	0.007	274
		av	0.108	
		std dev	0.052	

be virtually constant at a value of 0.1735 nm per pixel. The horizontal reciprocal dispersion factor varied from order to order, as expected, as was computed as $d\lambda/dX = 0.605/m$, where m is the diffraction order.

Results for computed and expected wavelengths are presented in Table I. The average of differences among computed and expected values is 0.108 nm with a standard deviation of 0.05 nm. The observed bias probably results from the facts that the reference absorption line was not located at the center of the reference pixel and that coordinates of pixels were in integer values. A program is being developed to address coordinates of absorption lines as floating point numbers in the effort to improve the accuracy with which wavelength locations are predicted.

The appearance of the Cu line at 327.4 nm in both the 295th and 296th orders (see Table I) shows that the free spectral range is fully covered in the horizontal direction.

Time Dependencies. In addition to the multielement capabilities of systems that include imaging detectors, these systems also permit more efficient studies of effects of variables. For example, Mones et al. (*8*) used their system to evaluate effects of temperature on the atomization process. In this study we chose to examine effects of time on the atomization process.

Figure 5 illustrates some time dependencies of the absorption spectra in the range from 395 to 435 nm. The signals for volatile elements (potassium, manganese, and gallium) appeared at about 0.6 s after the start of atomization (Figure 5A). Signals for less-volatile elements (aluminum, calcium, and chromium) appeared at about 1.2 s after the start of atomization (Figure 5B) at about the same time that the signals for the more volatile elements reached their maxima. After 1.8 s (Figure 5C) the signals for the less-volatile elements were still increasing, while signals for the more volatile elements were decreasing. After 2.4 s (Figure 5D), signals for all elements except calcium were decreasing. More complete time dependencies are illustrated in Figure 6. The latter data were collected and processed with the random-access algorithm.

Calibration Results. The quantification of multielement samples was done by evaluating both the heights and areas of the absorption peaks from the electrothermal atomizer. Some typical calibration plots for peak height and peak area

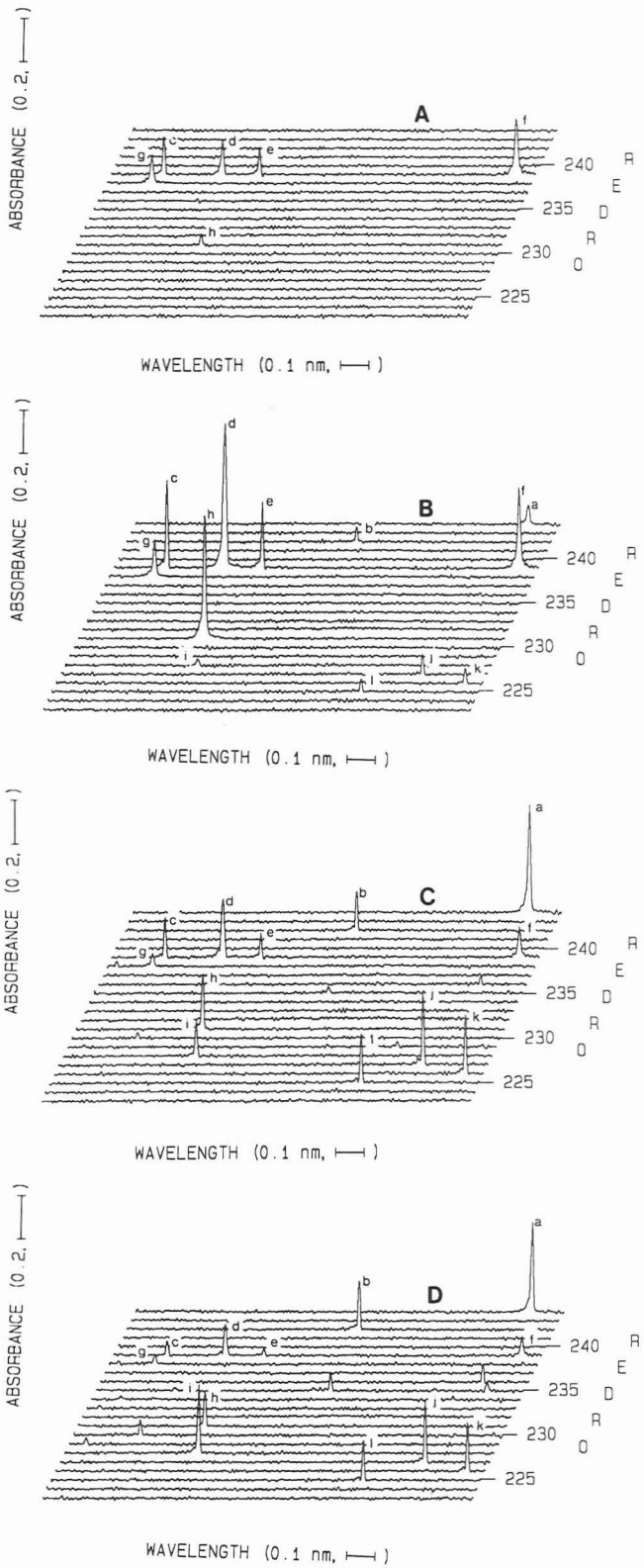

Figure 5. Absorption spectra at different times for several elements in an electrothermal atomizer. Time (s) after start of atomization: A, 0.6; B, 1.2; C, 1.8; D, 2.4. Sample concentration (ng mL^{-1}), absorption wavelength (nm): (a) Al, 200, 396.2; (b) Yb, 20, 398.8; (c) Mn, 100, 403.1; (d) Mn, 100, 403.3; (e) Mn, 100, 403.4; (f) K, 600, 404.4; (g) K, 600, 404.7; (h) Ga, 400, 417.2; (i) Ca, 20, 422.7; (j) Cr, 800, 425.4; (k) Cr, 800, 427.5; (l) Cr, 800, 429.0.

vs concentration are shown in Figure 7 and numerical data are summarized in Table II. These results were obtained by the random-access method by combining signals from three consecutive pixels along the vertical axis of the order for each absorption line. Characteristic concentrations were computed as $0.0044/S$, where S is the slope of each calibration curve

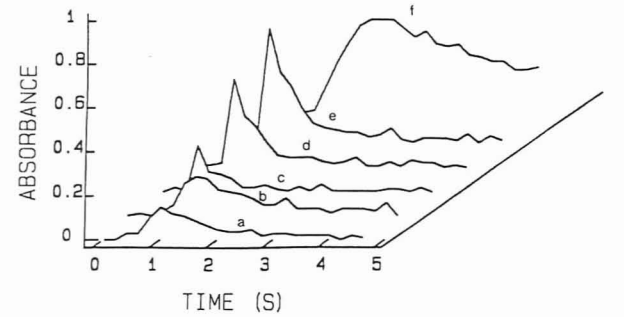

Figure 6. Absorbance vs time traces of representative elements obtained by the random-access method with 0.3-s integration periods (sample concentration, ng mL^{-1}, absorption wavelength, nm): (a) Cr, 800, 427.5; (b) Cr, 800, 425.4; (c) Mn, 100, 403.4; (d) Mn, 100, 403.1; (e) Mn, 100, 403.3; (f) Ca, 20, 422.7.

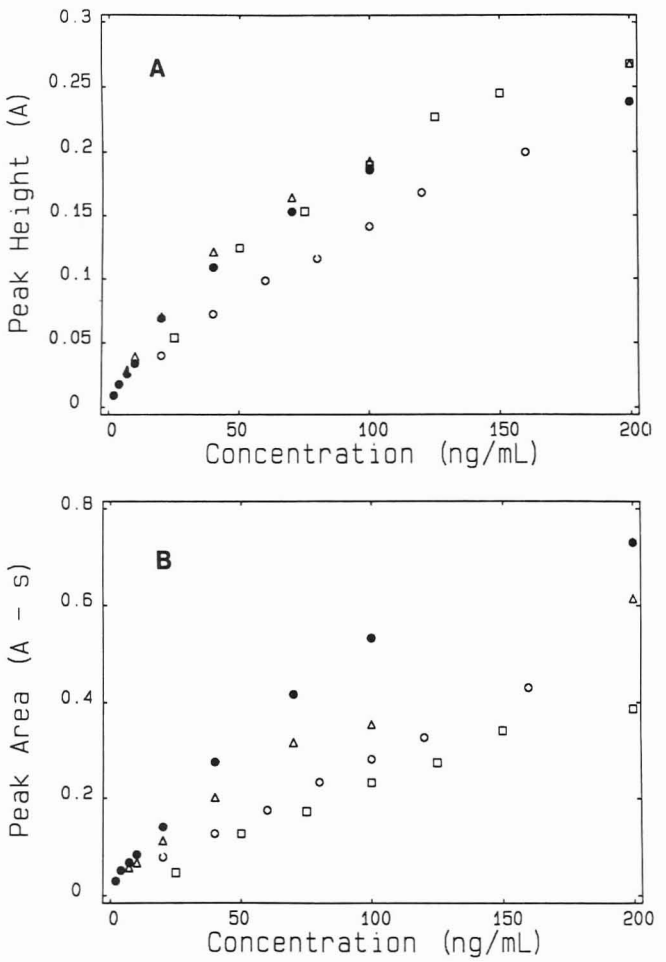

Figure 7. Calibration curves for representative absorption lines in both peak-height (A) and peak-area (B) methods (element and absorption line, nm: (△) Cu, 324.8; (●) Cr, 357.9; (□) Mn, 403.1; (○) Cr, 425.4.

within the linear range (see Figure 7). Detection limits (DL) were computed as $DL = E_{i0}/2.3i_0S$, where E_{i0} is three standard deviations in i_0, i_0 is the signal at 100% T, and S is the slope of the calibration curve at low concentrations.

Standard deviations ($n = 50$) for most elements/lines were in the range of 3% T, characteristic concentrations (corresponding to 1% absorption) were in the range of 1–25 ng mL^{-1}, and detection limits (except potassium at 404.7 nm) were in the range of 3 ng mL^{-1}. The high values of the detection limits for potassium probably result from the very high charring temperature (1000 °C) used. It is probable that some of the potassium was lost before the absorption measurements were made. Comparisons among these data show that peak areas give better linearity and detection limits than peak heights

Table II. Performance Characteristics for Selected Elements Absorption Lines

element	absorption wavelength, nm	integrated signal at 100% T[a]	characteristic concentration,[b] ng mL^{-1} peak height	characteristic concentration,[b] ng mL^{-1} peak area	detection limit,[c] ng mL^{-1} peak height	detection limit,[c] ng mL^{-1} peak area
V	318.341	300 ± 3	22	7.0	38	32
V	318.398	282 ± 4	25	7.7	73	59
V	318.540	261 ± 2	24	8.2	46	40
Cu	324.754	293 ± 3	1.6	1.0	3.4	6.1
Cu	327.396	374 ± 2	4.6	2.8	5.1	8.2
Yb	346.436	514 ± 3	5.8	3.5	6.0	9.6
Ni	352.454	506 ± 3	26	14.	27	38
Cr	357.869	329 ± 3	1.6	0.85	2.9	2.5
Cr	359.349	341 ± 2	2.6	0.95	3.0	3.0
Cr	360.533	334 ± 3	3.5	1.4	5.3	5.7
Fe	371.994	316 ± 3	19	7.6	31	31
Fe	385.991	548 ± 3	28	19.	26	45
Al	394.409	600 ± 3	16	10.	43	18
Al	396.153	616 ± 3	5.2	4.8	4.6	11
Yb	398.799	419 ± 3	1.5	0.49	2.0	1.7
Mn	403.076	445 ± 3	2.9	2.7	3.7	9.2
Mn	403.307	427 ± 3	1.8	1.6	2.3	5.5
Mn	403.449	416 ± 3	4.3	3.7	5.7	13
K	404.414	384 ± 3	26	18.	40	71
K	404.720	412 ± 7	83	49.	290	450
Ga	417.205	418 ± 2	9.0	7.2	10	21
Cr	425.435	478 ± 3	3.8	1.7	4.5	5.2
Cr	427.480	510 ± 3	5.4	2.2	6.9	7.4
Cr	428.972	471 ± 3	6.3	3.0	6.8	8.5

[a] In arbitrary units. Mean and standard deviation from 50 replicates. Integration times: 315–355 nm, 0.8 s; 355–395 nm, 0.5 s; 395–435 nm, 0.3 s. [b] The concentration corresponding to 1% absorption. [c] The lowest concentration that can be determined at the 99.7% confidence level.

Table III. Comparison of Characteristic Concentrations for Results Obtained with Image Dissector and CID Systems

element	wavelength, nm	characteristic concentration,[a] ng mL^{-1} image dissector[b]	CID[c]
Cu	324.754	1.3	1.6
Cr	357.869	2.2	1.6
Mn	403.076	1.2	2.9
Cr	425.435	3.6	3.8

[a] Concentration which gives 1% absorption. [b] From ref 5. [c] This study.

for the less volatile elements, whereas peak heights give as good or better results for more volatile elements. Peak areas have higher nominal sensitivities (slopes) for all elements, though it is not very useful to compare sensitivities for different types of responses. A serious limitation of CS-AAS is the stray light which causes reduced sensitivities at higher concentrations. This was manifested in this work as well as that described earlier (*8*) by calibration plots that curved toward the concentration axes at absorbances as low as 0.10. A solution to this problem is discussed later.

Table III compares results of characteristic concentrations obtained for selected elements by using the CID and an image dissector (*7*). Results with the image dissector were obtained in a single-element mode, whereas results with the CID were obtained in a multielement mode as described above. These and other results indicate that the CID/echelle combination can provide simultaneous multielement determinations with quantitative characteristics similar to results obtained by single-element methods with an image dissector. This is

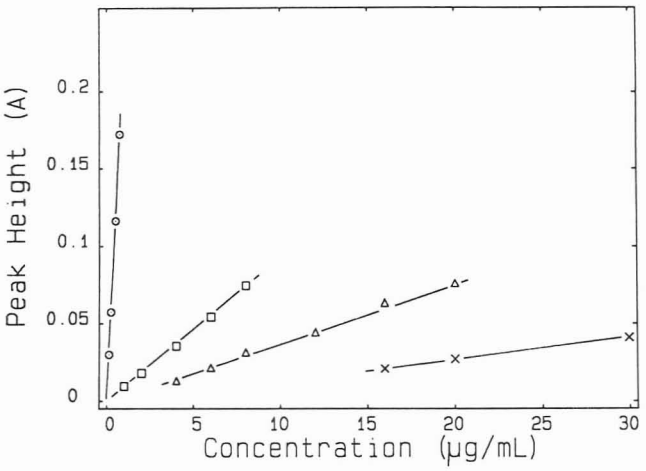

Figure 8. Calibration plots for a wide range of iron concentrations by using wavelengths with different sensitivities: O, 372.0; □, 390.0; △, 382.1; ×, 385.9 nm.

particularly gratifying in view of the fact that it was necessary to reduce the echelle image 3-fold to adapt it to the CID. The most probable reason why results were not degraded is that the physical size (15 μm) of each pixel in the CID is about 2.5-fold smaller than the aperture (38 μm) in the image dissector. Consequently, the reduced image in the CID system did not seriously reduce the spectral resolution. Two of the detection limits in Table III (Cr, 357.9 nm and Cu, 324.7 nm) can be compared directly with results reported by Jones et al. (*12*). By taking account of the 20-μL sample sizes used in this study, the concentration detection limits for Cr and Cu reduce to mass values of 60 and 68 pg, respectively, compared to values of 30 and 3 pg reported earlier (*8*). Our value for Cr is about 2-fold higher than the earlier while our value for Cu is about 23-fold higher than that reported earlier.

Extended Concentration Range. As noted earlier, a serious limitation of continuous source atomic absorption is the limited linear range which is caused primarily by stray light. One possible solution to this problem is to use different lines with different sensitivities for different concentration ranges. Figure 8 shows calibration data at four different wavelengths for a wide range of iron concentrations. By using these different wavelengths, it is possible to quantify iron concentrations over a range of at least 3 orders of magnitude.

Admittedly, iron is a special case in that it has a very rich spectrum from which one can choose lines with widely varying sensitivities. However, to the extent that other elements have analogous distributions of absorption sensitivities, the same procedure can be used to extend the concentration range for other elements. The larger range available with the echelle/CID combination relative to a one-dimensional detector is very useful in this regard.

DISCUSSION

This study has elucidated advantages and limitations of the use of a two-dimensional charge injection device with an echelle grating spectrometer for elemental determinations by continuous-source atomic absorption spectroscopy. Some advantages include the ability to quantify multiple elements simultaneously by virtue of the integrating character of the CID, the ability to address different pixels randomly, the ability to use different integration times to compensate for different responses in different regions of the spectrum, the ability to monitor the time course of several responses simultaneously, the ability to extend the useful concentration range by using lines with different sensitivities for different concentration ranges, and simplified background correction.

Although the spectral range covered for a given optical setting is only 40 nm, this is 16-fold better than that described in the most recent application of an imaging detector for CS-AAS (*8*). Also, the spectral resolution of 0.003 to 0.004 nm at 300 and 400 nm, respectively, is a 2.5- to 3-fold improvement over the 0.01-nm resolution reported with a one-dimensional array detector. A mechanized system analogous to that described earlier (*13*) could be used to address different segments of the spectrum sequentially.

LITERATURE CITED

(1) Fassel, V. A.; Mossotti, V. G.; Grossman, W. E. L.; Kniseley, R. N. *Spectrochim. Acta* **1966**, *22*, 347–357.
(2) O'Haver, T. C. *Analyst* **1984**, *109*, 211–217.
(3) Marshall, J.; Ottaway, B. J.; Ottaway, J. M.; Littlejohn, D. *Anal. Chim. Acta* **1966**, *180*, 357–371.
(4) Harnly, J. M. *Anal. Chem.* **1986**, *58*, 933A–943A.
(5) O'Haver, T. C.; Messman, J. D. *Prog. Anal. Spectrosc.* **1986**, *9*, 483–503.
(6) Masters, R.; Hsiech, C.; Pardue, H. L. *Anal. Chim. Acta* **1987**, *199*, 253–257.
(7) Masters, R.; Hsiech, C.; Pardue, H. L. *Talanta* **1989**, *36*, 133–139.
(8) Jones, B. T.; Smith, B. W.; Winefordner, J. D. *Anal. Chem.* **1989**, *61*, 1670–1674.
(9) Masters, R.; Hsiech, C.; Pardue, H. L. *Appl. Opt.* **1988**, *27*, 3895–3897.
(10) Burke, H. K.; Michon, G. J. *IEEE J. Solid State Circuits* **1976**, *SC11*, 121–127.
(11) Willard, H. H.; Merritt, L. L., Jr.; Dean, J. A. *Instrumental Methods of Analysis*; D. Van Nostrand Co., Inc.: New York, 1965; p 90.
(12) Pardue, H. L.; Hewitt, T. E.; Milano, M. J. *Clin. Chem.* **1974**, 1028–1042.
(13) Karanassios, V.; Horlick, G. *Appl. Spectrosc.* **1986**, *40*, 813–821.

RECEIVED for review February 2, 1990. Revised manuscript received June 6, 1990. Accepted June 8, 1990. This work was supported by Grant No. GM13326-20,21 from the National Institutes of Health.

Scanned Laser Fluorescence Line Narrowing Spectroscopy of Photosensitive Organic Chromophores

Bradford B. Price and John C. Wright*

Department of Chemistry, University of Wisconsin—Madison, Madison, Wisconsin 53706

Inhomogeneous broadening typically interferes with the observation of sharp featured fluorescence from organic chromophores dispersed in glasses and polymers. Fluorescence line narrowing (FLN) and nonlinear spectroscopic techniques can be used to obtain site selective spectra in photochemically stable systems but produce ambiguous results when the incident laser induces frequency domain hole burning. The effects of hole burning on the observed line narrowed fluorescence signal are described by introducing a time-dependent site distribution. To overcome the limitations of hole burning, FLN spectra are acquired while scanning both the laser and monochromator wavelengths. The requisite laser scan rate is predicted from the kinetics of the hole burning. Feasibility of the technique is demonstrated in the system of octaethylporphine in poly(methyl methacrylate). It is postulated that unlike previous methods of circumventing site depletion, this approach should be readily applicable to our experiments in nonlinear spectroscopy.

INTRODUCTION

Fluorescence line narrowing (FLN) and hole burning are two widely used techniques for site selective spectroscopy in inhomogeneously broadened systems where chromophores are dispersed in organic glasses and polymers (*1–5*). The single site spectrum consists of a sharp, purely electronic transition of the chromophore (zero phonon line) and a relatively broad phonon sideband. The sideband is the result of the interaction of the chromophore electronic transition with the host material lattice dynamics and will vary in intensity relative to the zero phonon feature for different host–guest systems. Both FLN and hole burning techniques rely on the static site distribution in low-temperature systems but are complementary both in the method of site selection and in the resulting information. In FLN a subset of sites is selectively excited and the fluorescence of this subset is monitored. In hole burning a subset of photolabile chromophore sites is excited, producing a site-selective depletion. The resulting change in absorption is site specific assuming the zero phonon condition of Burland (*6*) is fulfilled. The complementary nature of the two techniques leads to conflict when FLN is applied to systems where hole burning can occur. Since hole burning processes deplete resonant sites, fluorescence signal intensities are dramatically decreased. This decrease distorts the observed spectrum and ultimately eliminates the sharp-featured fluorescence.

Several methods have been developed to circumvent the problems of site depletion during a fluorescence scan. By increasing the sample temperature, Friedrich and Haarer (*7*) decreased site depletion at the cost of less intense, broader fluorescence signals. In the case of reversible hole burning, Bykovskaya (*8*) applied intense white light pulses between laser pulses to reverse the selective depletion. More recently, Hoftstradt et al. (*9*) and Cooper et al. (*10*) have used a solid-state array detector to perform spectral acquisition on a time scale faster than the rate of hole burning.

Methods involving synchronous scanning have been developed to perform spectral scans in both fluorescence spectroscopy (*11*) and nonlinear spectroscopy (*12*). In their application of FLN to the ultratrace level detection of DNA–PAH adducts, Cooper et al. (*10*) and Jankowiak et al. (*13*) have suggested and demonstrated that synchronously scanning the laser and monochromator enhances the sensitivity of FLN in systems which exhibit nonphotochemical hole burning. Further enhancements in spectral discrimination against broad phonon sideband emission can be achieved by acquiring both brief (minimal hole burning) and extended (severe hole burning) excitation time spectra and performing a spectral subtraction (*10*, *14*).

Both site restoration and array detectors are successful for the majority of fluorescence experiments but require a reasonable investment to modify the standard laser fluorescence system. In addition, neither approach has proven feasible in our efforts to extend site-selective four-wave mixing (*15*) to systems that undergo hole burning. The four-wave mixing technique uses intense optical fields in a small sample volume with a single output frequency defined by the input frequencies, conditions which decrease the effectiveness of site restoration and remove the advantages of multichannel detection.

In this paper we discuss the distortions observed in FLN spectroscopy of photolabile systems and modify the practice of synchronous scanning to circumvent the problems of hole burning in FLN and, presumably, four-wave mixing. The approach we have developed is to scan both the excitation laser and the detection monochromator, but to scan them at different rates. With the laser scanning at a rate faster than the rate of hole burning, new unburned sites are the source of the line-narrowed fluorescence which is detected by the monochromator. The scan rate of the monochromator is selected to cover the spectral region of interest as in conventional fluorescence line narrowing.

The utility of the scanned laser fluorescence (SLF) approach is demonstrated on the system of octaethylporphine in poly(methyl methacrylate), a system which undergoes rapid photochemical hole burning (*4*, *16*). Vibrational energies are consistent with previously reported values, demonstrating the applicability of the technique to the fluorescence line narrowing spectroscopy of photolabile systems.

EXPERIMENTAL SECTION

Sample Preparation. 2,3,7,8,12,13,17,18-Octaethyl-21*H*,23*H*-porphine (OEP) was obtained from Aldrich Chemical Co. and used without further purification. 2,2′-Azobis(2-methylpropionitrile) (AIBN) (Alfa Products, Danvers MA) was recrystallized from ethanol prior to use. Methyl methacrylate monomer (Alfa Products) was vacuum distilled immediately prior to use to remove inhibitors.

Sample preparation involved the polymerization of methyl methacrylate in the presence of the initiator AIBN and the desired chromophore. Methyl methacrylate monomer is vacuum distilled and combined with 1% (w/w) AIBN and an appropriate amount of OEP to give a concentration of 10^{-5} M. The resulting solution

* Author to whom correspondence should be sent.

0003-2700/90/0362-1989$02.50/0

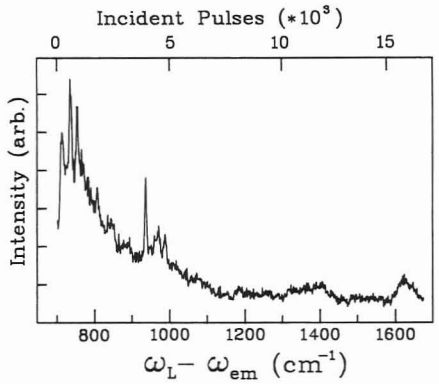

Figure 1. Static excitation fluorescence of porphine in PMMA at 2 K. Excitation at ω_L = 16 375 cm^{-1}, scan emission, ω_{em}.

is degassed and sealed under vacuum prior to polymerization at 40 °C. After 3 h, the viscous solution is transferred to a template held between two glass plates and polymerization is continued at 75 °C for 8 h. Resulting samples can be several millimeters thick and have excellent optical quality. There is no significant alteration of the OEP absorbance spectrum as a result of the polymerization although less robust porphyrins, such as porphine, do exhibit some degradation.

Experimental Apparatus. Fluorescence is excited by a XeCl excimer pumped home-built dye laser operating in ninth order at a 13 Hz repetition rate with DCM dye (Exciton Chemical Co.). Typical output characteristics include a 5-ns pulse duration, 0.2-cm^{-1} (0.07 Å) bandwidth (fwhm), and 100 μJ per pulse at 620 nm. The excitation laser is attenuated and directed to a 2 mm diameter spot on the sample which is immersed in superfluid liquid helium. Fluorescence is collected from the face of the sample and monitored by a 0.85-m double monochromator with an EMI 9658R photomultiplier and associated electronics.

The wavelength position of both the dye laser and the monochromator is monitored and controlled by a computer-based data acquisition system. Both components are scanned linearly in wavelength using a traditional sine-bar drive. For all the experiments discussed the monochromator (ω_{em}) is scanned at 0.1 Å/s while the excitation laser (ω_L) scan rates varied over the range of 0–0.02 Å/s. A typical fluorescence scan requires 10–15 min with 1 cm^{-1} resolution. The experiments have been performed with comparable success using the laser system, omitting the computer-based acquisition and control.

THEORY

Excitation of a photolabile chromophore will ultimately lead to site depletion. As expected, the total fluorescence intensity decreases as a result of resonant site depletion. However, in FLN this depletion has the observed effect of preferentially removing the sharp spectral features with broad, phononlike features dominating the spectrum after prolonged irradiation at a fixed wavelength. Figure 1 illustrates the distortions typically observed when hole burning interferences occur in FLN and spans the range from short to prolonged illumination. At short times sharp peaks corresponding to the chromophore vibrational energies are observed superimposed on a relatively intense background. At longer times both the background and sharp feature intensities decrease. Once the background broad-band emission reaches a stable value, no vibrational lines are observed. Most noteworthy is the absence of the 1316-cm^{-1} line and 1600-cm^{-1} multiplet, which are the dominant features in the absence of hole burning (*8*). Throughout the scan, sharp feature intensities are decreasing, prohibiting accurate estimates of relative line intensities. While line-narrowed features decay rapidly, phonon sideband emission features show a slow decay (*9*) and dominate the fluorescence after prolonged irradiation.

Although these observations have been previously documented (*7–9*), models for FLN have not been expanded to include the effects of site depletion. To explain the features of the time varying emission spectrum, we will combine the time-dependent behavior of spectral hole burning as developed by Friedrich (*7*) with the convolution model for fluorescence line narrowing, initially proposed by Abram (*17*). The resulting equation demonstrates a decay rate that is strongly dependent on both the Debye–Waller factor and the breadth of the spectral feature and is in good agreement with the observations associated with Figure 1.

This approach, while lacking the generality to permit rigorous extension to systems which undergo nonphotochemical hole burning, permits a qualitative understanding of the interfering effects of hole burning on FLN spectra and quantitatively is in good agreement with our data. In addition, the implicit assumptions of Friedrich (*7*) regarding weak, linear electron phonon coupling have been adopted since this approach provides a tractable, analytic solution. Recently Hayes and Lee (*16*, *18*) have generalized the description of hole burning spectra to systems with arbitrarily strong electron phonon coupling. Incorporating the strong coupling model may be appropriate for many biologically significant systems but is not necessary to demonstrate the efficacy of scanned laser excitation on the enhancement of FLN spectral features. Since porphyrins dispersed in polymers generate a broad distribution of antiholes (*18*), effects due to site restoration will be minimal and are not included in the analysis.

A single site in the inhomogeneous distribution with a zero phonon energy of ω_0 will have the intrinsic peak normalized absorption and emission given by

$$S_{ab}(\omega,\omega_0) = \alpha Z_{ab}(\omega,\omega_0) + [1-\alpha]P_{ab}(\omega,\omega_0) \quad (1a)$$

$$S_{em}(\omega,\omega_0) = \alpha Z_{em}(\omega_0,\omega) + [1-\alpha]P_{em}(\omega_0,\omega) \quad (1b)$$

where Z represents the homogeneous line shape of the zero phonon line, P the spectral profile of the associated phonon sideband, and α the Debye–Waller factor for the site (*17*). The relative shift of the phonon sideband is implicit in the functionality of P (*19*).

For a sample volume containing N molecules, we can express the number of sites centered at ω_0 as $N(\omega_0)$ and will represent the inhomogeneously broadened site distribution as an area normalized probability distribution function, $D(\omega_0) = N(\omega_0)/N$. When a photostable sample is excited with a laser with an area normalized frequency profile $L(\omega',\omega_L)$ centered at ω_L, the fluorescence spectrum can be written as the convolution

$$S(\omega) = \int_{-\infty}^{+\infty}\int_{-\infty}^{+\infty} S_{ab}(\omega',\omega_0)\, D(\omega_0)\, L(\omega',\omega_L)\, S_{em}(\omega,\omega_0)\, d\omega'\, d\omega_0 \quad (2)$$

In a photolabile system the site distribution is altered by the incident laser and frequency domain hole burning occurs. The rate of change of $N(\omega_0)$ over the interval $d\tau$ is given by

$$\frac{dN(\omega_0)}{d\tau} = \int_{-\infty}^{+\infty} \frac{I}{\hbar\omega_L} L(\omega,\omega_L)\, \sigma\, S_{ab}(\omega,\omega_0)\, \eta_{hb}\, N(\omega_0)\, d\omega \quad (3)$$

where I, σ, and η_{hb} are the laser intensity, absorption cross section, and hole burning quantum efficiency, respectively. Friedrich (*7*) considered a laser with a δ function frequency dependence to derive eq 4 for the relative number of molecules remaining at ω_0 after an irradiation time τ

$$\frac{N_\tau(\omega_0)}{N} = C_\tau \frac{N_0(\omega_0)}{N} = C_\tau D(\omega_0))$$

$C_\tau = \exp\{-\tau(I/\hbar\omega_L)\sigma\eta_{hb}S_{ab}(\omega_L,\omega_0)\}$ and $N_0(\omega_0)$ is the number of sites centered at ω_0 at time $\tau = 0$. Equation 2 must be

modified for a time-dependent site distribution since $N(\omega_0)/N$ is now time dependent. The time dependent analogue to eq 2 is

$$S_\tau(\omega) = \int_{-\infty}^{+\infty}\int_{-\infty}^{+\infty} S_{ab}(\omega',\omega_0)\, C_\tau\, D(\omega_0)\, L(\omega',\omega_{L_2})\, S_{em}(\omega,\omega_0)\, d\omega'\, d\omega_0 \quad (5)$$

where the laser frequency ω_L induces the site depletion and ω_{L_2} is the laser frequency generating the fluorescence spectrum. For brevity we will consider the typical case of $\omega_{L_2} = \omega_L$ where the excitation source simultaneously induces hole burning and fluorescence.

The form of C_τ prohibits the analytic solution of eq 5 without approximation. To generate a useful form, we consider the case of a laser with a δ-function frequency dependence and the short burn time limit where C_τ is expanded in a Taylor series, truncating after the linear term. These approximations transform eq 5 into

$$S_\tau(\omega) = \int_{-\infty}^{+\infty} S_{ab}(\omega_L,\omega_0)\, D(\omega_0)\, S_{em}(\omega,\omega_0)\, d\omega_0 + \quad (6a)$$

$$\int_{-\infty}^{+\infty} \frac{-I}{\hbar\omega_L}\sigma\,\eta_{hb}\,\tau\, S_{ab}^2(\omega_L,\omega^0)\, D(\omega_0)\, S_{em}(\omega,\omega_0)\, d\omega_0 \quad (6b)$$

Considering the two terms in eq 6, the first term is equivalent to eq 2 in the limit of an infinitely narrow laser, a case which has been previously addressed (*17*, *19*). The second term represents a first-order correction for resonant site depletion and is accurate to a few percent for $C_\tau \geq 0.8$.

To evaluate the depletion term (6b), we substitute eq 1a-b for the absorption and emission features, expand the products, and combine terms of comparable spectral breadth. In the case of weak electron–phonon coupling we can consider $D(\omega_0)$ to be broad enough relative to the single site features to be considered a constant and 6b becomes

$$\frac{-I}{\hbar\omega_L}\,\sigma\,\eta_{hb}\,\tau\, D(\omega_0)[\alpha^3\int_{-\infty}^{+\infty} Z_{ab}^2(\omega_L,\omega_0)\, Z_{em}(\omega,\omega_0)\, d\omega_0 + \quad (7a)$$

$$\alpha^2(1-\alpha)\int_{-\infty}^{+\infty}[Z_{ab}^2(\omega_L,\omega_0)\, P_{em}(\omega,\omega_0) + 2Z_{ab}(\omega_L,\omega_0)\, P_{ab}(\omega_L,\omega_0)\, Z_{em}(\omega,\omega_0)]\, d\omega_0 + \quad (7b)$$

$$\alpha(1-\alpha)^2\int_{-\infty}^{+\infty}[P_{ab}^2(\omega_L,\omega_0)\, Z_{em}(\omega,\omega_0) + 2Z_{ab}(\omega_L,\omega_0)\, P_{ab}(\omega_L,\omega_0)\, P_{em}(\omega,\omega_0)]\, d\omega_0 + \quad (7c)$$

$$(1-\alpha)^3\int_{-\infty}^{+\infty} P_{ab}^2(\omega_L,\omega_0)\, P_{em}(\omega,\omega_0)\, d\omega_0] \quad (7d)$$

Each term in eq 7 takes the general form $-I\sigma\eta\tau f(\alpha)\, g(Z,P)$ where $g(Z,P)$ indicates the breadth of the spectral feature being observed. In the situation where the zero phonon line is sharp relative to the phonon sideband, the breadth of the depleted features becomes apparent. All terms other than 7a have a significant phononlike contribution to their FLN breadth and represent the depletion of relatively broad spectral features while 7a represents the decay of the zero phonon fluorescence.

The nature of $g(Z,P)$ is defined by the breadth of the individual features involved in the hole burning, absorption, and emission processes. Each term contains the product of two absorption profiles and an emission profile. The fluorescence intensity is determined by the absorption and emission profile and the hole burning is determined by the absorption profile. The different terms result because the zero phonon feature and the phonon sideband can participate in all combinations.

The enhanced decay of zero phonon features relative to phonon sideband features can be explained by eq 7. By expanding the convolution integrals analogous to those in eq 7, Friedrich (*7*) examined the rate of hole formation in absorption experiments and demonstrated an inverse relationship between the width of the absorbing feature and the rate of hole burning. Since the dominant perturbation is due to site depletion, Friedrich's analysis can be applied directly. Taking the homogeneous line width of porphine in PMMA of 0.016 cm^{-1} (*4*) and a the phonon sideband width of 30 cm^{-1} as representative values, we would initially predict the depletion due to zero phonon absorption occurs 2000 times faster than that expected for phonon sideband absorption. Since 7a–b will be affected by zero-phonon hole burning, these terms will cause depletion at a rate 3 orders of magnitude faster than the depletion due to 7c–d. Term 7a will deplete the entire zero-phonon feature (ref 15, eq 4a) while 7b will only be capable of rapidly depleting one-third of the total observed phonon sideband feature (ref 15, eq 7b–d) which is observed in FLN.

In addition, the dependence of each term on the Debye–Waller factor will further enhance the sharp feature's relative depletion. Taking the estimate of Kador et al. (*20*) of $\alpha = 0.77 \pm 0.1$ for phthalocyanine in PMMA to be comparable to that expected for OEP in PMMA, we calculate the $f(\alpha)$ for terms 7a–d to be 0.45 ± 0.2, 0.13 ± 0.04, 0.04 ± 0.01 and 0.012 ± 0.002, respectively, further enhancing the relative depletion due to term 7a. This effect is less dramatic than the line breadth contribution from $G(Z,P)$, especially considering the fact that there are three contributions from each term 7b and 7c due to the summation of the three convolution integrals. In situations of weak electron-phonon coupling as $\alpha \rightarrow 1$, the contributions from $f(\alpha)$ will become more significant.

Given the assumptions of eq 7 and the estimates for the line widths and the Debye–Waller factor, we would expect the depletion of zero phonon features to be approximately 3 orders of magnitude faster than that observed for the phonon sideband features. This discrepancy in decay rates adequately explains the observations in Figure 1 where sharp features are short lived under prolonged irradiation at a fixed frequency.

SCAN RATE DEPENDENCE

To predict the effect of scanned laser excitation on the observed spectra, eq 3 is evaluated for the case of a time varying ω_L. By considering a δ-function laser scanned linearly with a scan rate r, the energy at any time τ can be written as $\omega_L = \omega_L^\circ + r\tau$. Under these conditions, eq 3 can be rewritten in the time-dependent form

$$\frac{dN(\omega_0)}{d\tau} = -\frac{I}{\hbar\omega_L}\sigma\,\eta_{hb}\, N(\omega_0)\, S_{ab}((\omega_L^\circ + r\tau) - \omega_0) \quad (8)$$

Since eq 7 indicates that $Z_{ab}(\omega_L,\omega_0)$ is the dominant line shape affecting sharp feature depletion, we can consider S_{ab} to be a single Lorentzian with a half width at half maximum of $\Delta\omega$, $S_{ab}(\omega_L,\omega_0) = \Delta\omega^2/[(\omega_L^\circ + r\tau - \omega_0)^2 + \Delta\omega^2]$. In this discussion, we have only considered the laser with a δ-function frequency dependence where $\Delta\omega$ reflects the homogeneous line width of the zero phonon line $S_{ab}(\omega,\omega_0)$. An equivalent result would be achieved by treating $S_{ab}(\omega,\omega_0)$ as a δ function in frequency space. In practice, $\Delta\omega$ reflects the width of the convolution of the zero phonon line and the laser profile.

To perform the integration of eq 8, we assume that the photon flux, $I_L = I/\hbar\omega_L$, is a slowly varying function over the laser scan range and treat it as a constant. This approximation is reasonable considering the 200–400 cm^{-1} tuning range of typical laser dyes which emit in the vicinity of 16000–20000 cm^{-1}. If the excitation laser were scanned across the entire tuning curve, the change in I_L would be predominantly due

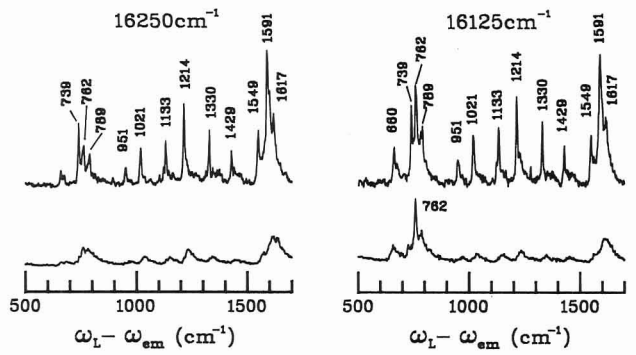

Figure 2. Comparison of static (lower) and scanned laser excited fluorescence of OEP in PMMA at 2 K. Excitation at two positions in the inhomogeneous absorption profile. Laser scan rate of 1.6 cm^{-1} per minute gives upper spectra.

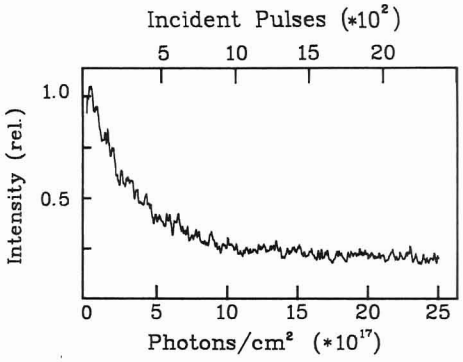

Figure 3. Signal decay of 1214-cm^{-1} vibrational feature under static 1.5 μJ per pulse excitation.

to the decreased laser intensity, I, rather than the change in photon energy, $\hbar\omega_L$.

Considering the case where σ, and η_{hb} are constant over the scan range, it is possible to analytically solve eq 8. Integrating eq 8 from $\tau = 0$ to $\tau = (\omega_0 - \omega_L^\circ)/r$ when the laser will be centered on the site at ω_0 gives

$$I_F \approx C_\tau = \exp\left[-I_L\sigma\eta_{hb}\frac{\Delta\omega}{r}\tan^{-1}\left(\frac{\omega_0 - \omega_L^\circ}{\Delta\omega}\right)\right] \quad (9)$$

Since C_τ is directly related to the number of molecules remaining at ω_0, the fluorescence signal intensity is proportional to eq 9. For a rapid laser scan rate, $C_\tau \rightarrow 1$ indicating the absence of hole burning and an unaltered fluorescence spectrum. Similarly for a laser scan rate which is slow compared to the rate of hole burning $I_L\sigma\eta_{hb}$, $C_\tau \rightarrow 0$ and the sharp features due to selective excitation at ω_0 will not appear. For the case of pulsed laser excitation in the absence of saturation effects, I_L can be rewritten as the product of the pulse energy per cm^2, I_P, and the repetition rate, R, where $I_L = I_P R/\hbar\omega_L$, and we are able to consider the scan rate of the dye laser not just in terms of laser bandwidths scanned per second but can introduce the units of bandwidths scanned per pulse.

RESULTS AND DISCUSSION

The improvements in sharp featured signal intensity which result from scanned laser FLN are shown in Figure 2. The lower spectra demonstrate the fluorescence obtained with static excitation at the indicated frequency. Broad ($\sim$50 cm^{-1}) emission features are seen over the entire range with a single, sharp feature at 762 cm^{-1} in the case of 16 125-cm^{-1} excitation. In contrast, the upper spectra were obtained by scanning the excitation laser at 1.6 cm^{-1}/min while the monochromator is scanned at a rate 10 times faster. The vibrational energies indicated are corrected for the scanning of the laser and are within a few wavenumbers of the values reported by Bykovskaya for OEP in a polystyrene host. This agreement indicated at most a weak dependence of the porphyrin vibrational energy on the choice of host material.

Comparable features are seen for the two excitation regions with the exception of the peak enhancement for the 762-cm^{-1} vibration in the case of the red-shifted excitation. The persistence of the 762-cm^{-1} feature in both static and scanned laser excitation indicates that it is associated with a relatively photostable molecule, presumably an impurity or aggregate which absorbs at a lower energy than the majority of OEP molecules. Spectral contributions from stable impurities are readily removed by a spectral subtraction in a manner analogous to that of Hoftstradt (*9*) and Zamzow (*14*), revealing the spectrum of the photolabile chromophore.

In experiments where the excitation was varied across the entire inhomogeneous absorption profile, no significant changes in the OEP fluorescence spectrum were observed other than overall intensity, indicating that the shape $S_{em}(\omega,\omega_0)$ is not a strong function of ω_0. In systems with stronger electron–phonon coupling, the intensity of phonon sidebands relative to zero phonon features will typically increase as the excitation energy is increased (blue shifted). In addition, it is possible that different sites within an inhomogeneous distribution may show an alteration in the relative line intensities. These complications are not expected to diminish the analytical utility of the scanned laser technique since the excitation energy is scanned over a small interval (<10 cm^{-1} in this work) relative to the inhomogeneous width and the anticipated weak energy dependence of the two effects.

By use of a fixed frequency at 16 175 cm^{-1}, the time-dependent fluorescence to a vibrational level can be monitored. Figure 3 is typical of the signal depletion caused by prolonged irradiation at a fixed frequency where the ordinate is the cumulative intensity and the abscissa is the relative signal intensity measured at 14 961 cm^{-1}, corresponding to the 1214-cm^{-1} vibrational level. A single exponential decay is observed, reaching a constant, low intensity within 2000 pulses at 1.5 μJ per pulse. Fitting the data to a single exponential decay, we can extract an effective decay cross section of 3×10^{-18} cm^2.

Considering eq 3 and 4, the decay cross section corresponds to $\sigma\eta_{hb}$ summed over the frequency spread of the laser and the homogeneous line shape. One can estimate the quantum efficiency of hole burning once the absorption cross section is determined. Considering the comments of Moerner et al. (*21*) regarding estimating σ in inhomogeneously broadened systems, the laser bandwidth defines an effective homogeneous line width and we apply eq 3 of ref 21 directly, inserting 1.50 for the refractive index of PMMA (*20*). The oscillator strength for the $Q_{(0,0)}$ transition of porphine and etioporphine has been previously calculated (f = 0.019) and estimated from experimental data (f = 0.0058–0.025) by Gouterman (*22*). The average of the experimental values corresponds to an absorption cross section of 1.2×10^{-13} cm^2. Thus, one would estimate η_{hb} is ca. 2×10^{-5}. While this method of measuring the quantum efficiency is dramatically different than the more conventional technique of measuring the change in transmittance extrapolated to zero time and in the low power limit, it is encouraging that the value is comparable to that observed for other systems which undergo rapid photochemical hole burning (*20*). Since the product $\sigma\eta_{hb}$ will depend on both the chemical and instrumental systems, in further discussions we will treat it as a single parameter and use the observed value to illustrate the effects of scan rate and laser power on the observed spectra.

The laser scan rate required to observe sharp-featured spectra with a laser of given power and bandwidth is determined by eq 8 which depends on the product $I_L\sigma\eta_{hb}\Delta\omega$ and the arctangent function which describes the cumulative la-

Table I. Scan-Rate Dependence of Normalized Signal

scan rate, (Å/s) × 10^3	pulses (hwhm)	$r\tau$, Å	calcd eq 10	exptl
0.33	11000	0.12	0.20	0.27 ± 0.13
0.55	6400	0.20	0.35	0.35 ± 0.18
1.1	3200	0.40	0.57	0.56 ± 0.21
3.3	1100	1.2	0.82	0.89 ± 0.15
6.7	520	2.4	0.91	0.91 ± 0.09
17.0	210	6.1	0.96	1.00

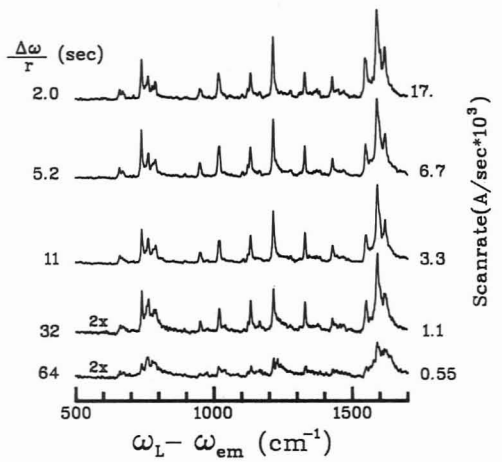

Figure 4. Line narrowed fluorescence with scanned laser excitation at various laser scan rates, 0.5 μJ per pulse.

ser-line-shape overlap caused by scanning across a Lorentzian line shape. Considering typical experimental conditions and a pulse energy of 0.5 μJ, eq 9 for the predicted normalized peak intensity will take the form

$$I_F \approx \exp\left[-0.012\,\frac{\Delta\omega}{r}\,\tan^{-1}\left[\frac{\omega_0 - \omega_L^\circ}{\Delta\omega}\right]\right]$$

Evaluating eq 10 for the case of $r\tau = \omega_0 - \omega_L^\circ \gg \Delta\omega$ and with $\Delta\omega = 0.035$ cm^{-1}, we expect the sharp-featured fluorescence to increase with laser scan rate following $I_F = \exp[(-6.6 \times 10^{-4})/r]$, where the scan rate r is expressed in angstroms per second. For slow scan rates, where $r\tau$ becomes comparable to the bandwidth $\Delta\omega$, the arctangent term must be explicitly included to correctly represent the signal growth. Without the arctangent correction, an anomalously low signal would be predicted. In essence, for small values of $r\tau$, the time integrated intensity at ω_0 has not attained the steady-state value before the site fully resonant with the laser. To avoid distortions in the relative peak intensities in long spectral scans, it is important to scan greater than two bandwidths prior to resonant excitation so that peaks which appear at the beginning of the scan are not enhanced relative to those at the end of the scan.

To display the data in a format compatible with eq 10, the peak intensity at the maximum laser scan rate is assigned the value 1.0 and all other intensities are normalized to this value. Table I indicates good agreement between the predicted and experimentally observed data where the normalized intensity from three sets of scans is averaged to yield the experimental data. The large relative uncertainties associated with the low intensity signals are predominantly caused by baseline noise. In all cases the calculated intensities are within the experimental error.

Examples of fluorescence spectra acquired with various laser scan rates are shown in Figure 4. With the initial excitation position at 16 150 cm^{-1}, the scan rates chosen cover the span from 0.0005 to 0.02 Å s^{-1}. This range is sufficient to demonstrate the behavior from the case of extensive site depletion

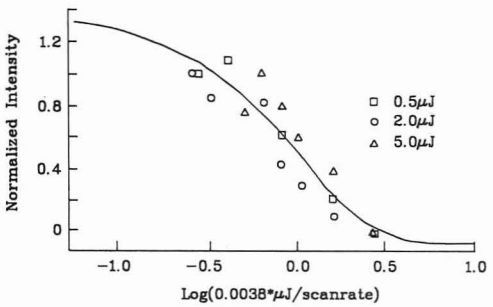

Figure 5. Enhancement of 1214-cm^{-1} vibrational feature as a function of laser power and scan rate.

to that of minimal depletion. At a scan rate of 0.0005 Å s^{-1}, the spectra are indistinguishable from those obtained under static excitation. A continuous enhancement of the sharp features is seen with increasing scan rate until 0.0067 Å s^{-1} where scanning has reduced the site depletion to the level of the pulse to pulse fluctuations in signal intensity. This general trend is predicted by eq 10 where, for small scan rates, the number of resonant centers approaches 0. Similarly, as $r/\Delta\omega$ becomes greater than the decay rate, the number of centers asymptotically approaches the no hole burning case where $C_t = 1$.

One of the concerns about scanned laser excitation is the influence of exciting sites with different intrinsic spectra and incorporating the information from these various sites into a single spectrum. At 0.02 s^{-1} the laser has scanned <15 cm^{-1}, which does not appear to introduce any significant skew in the spectrum. Over longer scan ranges variations in the spectrum may be significant as has been demonstrated in Figure 2 and by Abram (*17*).

A second concern regarding scanned excitation is the influence of changes in $D(\omega_0)$ over the scan range. As $D(\omega_0)$ decreases, the absorption and fluorescence intensity will decrease, introducing a bias in the relative intensities over a long scan range. The critical parameters in this effect will be the scan range and the frequency dependence of the inhomogeneous absorption profile $\delta A/\delta\bar{\nu}$. The absorption spectrum for the sample used in Figure 4 indicates $\delta A/\delta\bar{\nu} = 0.003$, which is less than 1% per cm^{-1} over the excitation range. We would expect this to skew the observed spectra in the case of the fastest scan rates; however over the scan range there is a comparable laser power increase due to the choice of laser dye and the dye laser tuning curve. The net result is that the fluorescence intensity is stable over the entire excitation scan range.

To verify the effects of incident power on the scanned laser fluorescence, a series of spectra analogous to those in Figure 4 was collected with 0.5, 2.0, and 5.0 μJ pulse energies. Figure 5 illustrates the coupled effects of scan rate and pulse energy on the normalized peak intensity for the 1214-cm^{-1} vibrational feature. Over the range of powers the sharp feature intensity at maximum scan rate scaled linearly with pulse energy, indicating the absence of saturation effects at the tested power densities.

The normalized intensity for all points shows a log–linear increase with the ratio of the pulse energy to scan rate (I_P/r) as predicted by eq 4. While increases in incident power enhance the fluorescence signal, there is a concomitant increase in site depletion, requiring a more rapid scan rate to minimize the effects of depletion on the observed signal.

Under the axis transformation of Figure 5 the linear fit of eq 9 to the data yields the sigmoidal trace which mimics the observed data. For large values of I_P/r extensive site depletion occurs and the observed spectra have low intensity, broad features which are indistinguishable from those observed under static excitation. Decreasing I_P/r produces only mar-

ginal improvements until a threshold is reached where spectral features increase dramatically, then asymptotically approach a constant, high intensity. Although a log–linear increase in signal is observed, a practical region for observing the signal enhancement is limited by pulse to pulse variations in laser intensity. Although deviations from the fit occur, all three powers demonstrate the same basic functionality and are in good agreement with eq 9. This agreement indicates that in the absence of saturation effects, the line-narrowed fluorescence intensity as a function of laser scan rate and incident power can be predicted by eq 9, once the appropriate value for $\sigma\eta_{hb}$ has been calculated.

As the incident power is increased to the point where the absorption begins to saturate, further increases in scan rate would not be required. At saturation the population of the 0′ level reaches a steady-state value and no further enhancement in either the fluorescence intensity or one-photon photoconversion depletion is expected since both processes exhibit kinetics which are first order in the population of 0′.

CONCLUSIONS

Resonant hole burning effects interfere with fluorescence line narrowing spectroscopy of photolabile low-temperature organic systems, preferentially depleting the sharp spectral features. Significant improvements in signal intensity can be achieved by scanning both the excitation source and the monochromator. The requisite scan rate for the excitation source is readily predicted from the measured decay rate of the fluorescence signal and scales inversely with the laser power and the convolution width of the laser frequency profile and the homogeneous line shape. The technique requires no equipment other than that used in the conventional fluorescence line narrowing experiment and is capable of producing high-resolution spectra of organic chromophores in low-temperature glasses. This technique can be extended for line narrowed fully resonant four-wave mixing spectroscopy.

LITERATURE CITED

(1) Brown, J. C.; Duncanson, J. A., Jr.; Small, G. J. *Anal. Chem.* **1980**, *52*, 1711–1715.
(2) Small, G. J. In *Spectroscopy and Excitation Dynamics of Condensed Molecular Systems*; Agranovich, V. M., Hochstrasser, R. M., Ed.; North Holland: Amsterdam, 1983; pp 515–554.
(3) Personov, R. I. In *Spectroscopy and Excitation Dynamics of Condensed Molecular Systems*; Agranovich, V. M., Hochstrasser, R. M., Ed.; North Holland: Amsterdam, 1983; pp 555–617.
(4) Thijssen, H. P. H.; Volker, S. *J. Chem. Phys.* **1986**, *85*, 785–793.
(5) Jankowiak, R.; Small, G. J. *Anal. Chem.* **1989**, *61*, 1023A–1032A.
(6) Burland, D. M.; Haarer, D. *IBM J. Res. Dev.* **1979**, *23*, 534–540.
(7) Friedrich, J.; Haarer, D. *J. Chem. Phys.* **1982**, *76*, 61–67.
(8) Bykovskaya, L. A.; Gradyushko, A. T.; Personov, R. I.; Romanovskii, Y. V.; Solov'ev, K. N.; Starukhin, A. S.; Shul'ga, A. M. *Zh. Prikl. Spektrosk.* **1978**, *29*, 1088–1098.
(9) Hofstraat, J. W.; Engelsma, M.; De Roo, J. H.; Gooijer, C.; Velthorst, N. H. *Appl. Spectrosc.* **1987**, *41*, 625–631.
(10) Cooper, R. S.; Jankowiak, R.; Hayes, J. M.; Pei-qi, L.; Small, G. J. *Anal. Chem.* **1988**, *60*, 2692–2694.
(11) Suter, G. W.; Kallir, A. J.; Wild, U. P. *Chimia* **183**, *37*, 413–421.
(12) Nguyen, D. C.; Wright, J. C. *Anal. Spectrosc.* **1985**, *39*, 230–243.
(13) Jankowiak, R.; Cooper, R. S.; Zamzow, D.; Small, G. J.; Doskocil, G.; Jeffrey, A. M. *Chem. Res. Toxicol.* **1988**, *1*, 60–68.
(14) Zamzow, D.; Jankowiak, R.; Cooper, R. S.; Small, G. J.; Tibbels, S. R.; Cremonesi, P.; Devanesan, E. G.; Rogan, E. G.; Cavalieri, E. L. *Chem. Res. Toxicol.* **1989**, *2*, 29–34.
(15) Lee, S. H.; Steehler, J. K.; Nguyen, D. C.; Wright, J. C. *Appl. Spectrosc.* **1985**, *39*, 243–253.
(16) Lee, In-Ja; Hayes, J. M.; Small, G. J. *J. Chem. Phys*, **1989**, *91*, 3463–3469.
(17) Abram, I. I.: Auerbach, R. A.; Brige, R. R.; Kohler, B. E.; Stevenson, J. M. *J. Chem. Phys.* **1975**, *63*, 2473–2478.
(18) Hayes, J. M.; Gille, J. K.; Tang, D.; Small, G. J. *Biochim. Biophys. Acta* **1988**, *932*, 287–305.
(19) McColgin, W. C.; Marchetti, A. P.; Eberly, J. H. *J. Am. Chem. Soc.* **1978**, *100*, 5622–5626.
(20) Kador, L.; Schulte, G.; Haarer, D. *J. Phys. Chem.* **1986**, *90*, 1264–1270.
(21) Moerner, W. E.; Gehrtz, M.; Huston, A. L. *J. Phys. Chem.* **1984**, *88*, 6459–6460.
(22) Gouterman, M. J.; Wagiere, G. H.; Snyder, L. C. *J. Mol. Spectrosc.* **1963**, *11*, 108–127.

RECEIVED for review January 30, 1990. Accepted June 7, 1990. We gratefully acknowledge the support of the Analytical Chemistry Program of the National Science Foundation under Grant CHE-8903556.

Preconcentration of Copper on Algae and Determination by Slurry Graphite Furnace Atomic Absorption Spectrometry

Mo Shengjun[1] and James A. Holcombe*

Department of Chemistry and Biochemistry, The University of Texas at Austin, Austin, Texas 78712

Unicellular green algae are utilized to preconcentrate Cu ions from seawater and riverine water samples. Studies show that after the algae are rinsed with 1% HCl, Cu adsorption on the algae is improved. The addition of sodium citrate and dodecyl sulfate can also improve Cu adsorption. The algae weight and the solution pH are not critical. The seawater matrix does not affect the adsorption efficiency for Cu. Cu preconcentration can be achieved by mixing 6 mg of algae with 10–100 mL of sample and subsequently separating by centrifugation. The algae pellet is then resuspended in 1 mL of 0.5% HNO_3 and analyzed as a slurry by graphite furnace atomic absorption spectrometry. The determined values of Cu in riverine (SLRS-1) and seawater (CASS-1) standard reference materials are within the limits of certification.

* Author to whom correspondence should be addressed.
[1] On leave from the Department of Chemistry, South China Normal University, Guangzhou, People's Republic of China.

Preconcentration techniques are often necessary in ultratrace analysis. Ion exchange, solvent extraction, coprecipitation, electrodeposition, and osmosis are extremely useful preconcentration methods. However, they are often time-consuming, involve complex procedures, or are not sufficiently selective to prevent preconcentration of an undesirable matrix component.

In general, biological organisms have the ability to selectively adsorb a specific element without preconcentrating the matrix (*1–4*). Previous studies (*5–7*) have demonstrated the ability of severl algae strains to separate and preconcentrate Cu. Mahan and co-workers (*5*) have studied the ability of three unicellular algae strains to adsorb 13 elements, including Cu. Gardea-Torredey and co-workers (*6*) also demonstrated the analytical utility of the algae by constructing an algae-modified carbon paste electrode for determination of Cu in aqueous solution. Ferguson and Bubela (*7*) studied the reactions of Cu(II), Pb(II), and Zn(II) in aqueous solutions with

0003-2700/90/0362-1994$02.50/0

Table I. Furnace Operating Conditions

step no.	temp. °C	ramp time, s	hold time, s	argon flow, L/min	read
1	70	5		3	
2	90	60		3	
3	130	10	40	3	
4	1100	10	40	3	
5	1100		5	0	
6	2500	1.1	3	0	*
7	2500		3	3	

several algae. Their data showed that Zn adsorption, as compared with Pb and Cu adsorption, is considerably more sensitive to the presence of added salts in the solution. On the other hand, Cu adsorption is only marginally decreased by the addition of up to 200 mmol/L NaCl in the solution. However, none of the above studies used algae to analyze complex samples. Majidi and Holcombe (*4*) attempted the use of these algae for preconcentrating Cd and were successful with a 16.6 ± 1.9 ng/L of riverine sample but saw a reduced recovery for Cd in a seawater matrix.

In this paper conditions for the preconcentration of Cu by algae and subsequent analysis by slurry graphite furnace atomic absorption spectrometry have been studied. This method has been used to determine Cu in complex environmental samples.

EXPERIMENTAL SECTION

Preparation of Algae. The algae strain used in this study was a form of unicellular green *Chlorella*. Preparation and cultivation of the algae have been described previously (*3*, *5*). To remove trace amounts of Cu indigenous to the algae, 6 mg of algae is added to 10 mL of 1% HCl. The mixture is agitated and centrifuged and the supernatant is decanted and discarded. The algae pellet is then washed with 5 mL of deionized water and centrifuged again. After the washing solution is discarded the algae are used.

Apparatus. All experiments were performed with AA-875 spectrophotometer equipped with a GTA-95 graphite furnace atomizer (Varian Techtron). The operational conditions and temperature programs are listed in Table I. The wavelength and the spectral bandpass of the monochromator were set to 324.7 and 0.5 nm, respectively. All studies were performed with deuterium lamp background correction and wall atomization with a 10-μL aliquot of the slurry suspension or supernatant. All data were recorded as peak areas.

Procedure. The sample was prepared by adding 6 mg of algae to 10 mL of a solution containing 4 ng/mL Cu. The pH values of all solutions were adjusted to between 3.5 and 6.5 by the dropwise addition of nitric acid and sodium hydroxide after the algae were added. The mixture then was agitated for 20 min and centrifuged. The supernatant was decanted and the algae pellet was resuspended in 2 mL of a solution of 0.5% HNO_3. This slurry was then transferred to the autosampler sampling vial for analysis. Three replicates were carried out for each experiment. A blank was run for all experiments, and the blank value was subtracted from the corresponding sample. Typical blank values are shown later in this paper. Once the algae had been washed with HCl, the procedure required about 40 min for the preconcentration of six samples. All extraction efficiencies are based on concentrations derived from calibration curves prepared for Cu standards prepared in 0.5% HNO_3.

RESULTS AND DISCUSSION

Effect of pH on Cu Adsorption. Figure 1 demonstrates the effect of pH on Cu adsorption by the algae. In this figure, curves a and b denote the algae that were cleaned by washing in 1% HCl; curves c and d represent algae that were not cleaned. Curves a and d designate experiments when $CuCl_2$ was used to prepare the standard solution and HCl and/or NaOH used to adjust the solution pH to approximately 5. Curves b and c designate the use of $Cu(NO_3)_2$ as the analyte-containing compound with HNO_3 and/or NaOH for adjustment to pH ~5. After centrifugation all solutions were brought to 2 mL final volume in 0.5% HNO_3, resuspended, and analyzed.

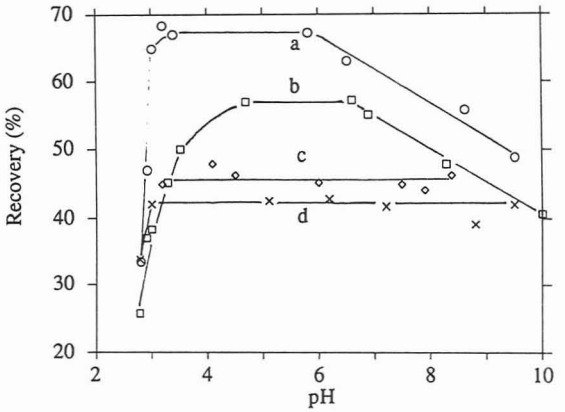

Figure 1. Effect of pH on Cu absorption by algae. The algae were initially rinsed in 1% HCl (a, b) or not acid washed (c, d). Both $Cu(NO_3)_2$ (b, c) and $CuCl_2$ (a, d) were considered in the analytical solution. The copper concentration was 4 ng/mL for all solutions initially and all final suspensions were 0.5% in HNO_3.

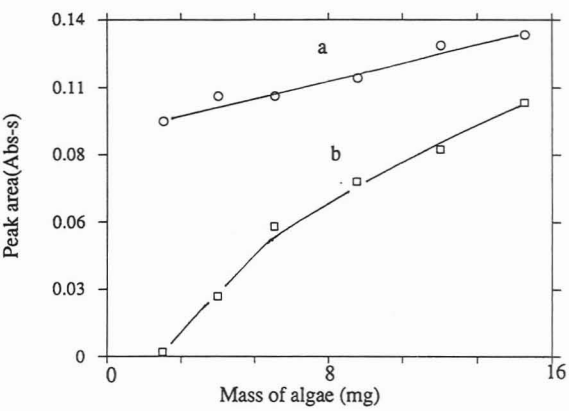

Figure 2. Effect of algae mass on (a) the Cu adsorption signal and (b) the background signal (10 mL of 4 ng/mL Cu solution).

This figure shows that the effect of pH on Cu adsorption by the algae is dependent on the use of a preliminary wash in HCl. It can be seen in this figure that the pH range for optimum Cu adsorption is narrower with the acid-washed algae while the extraction efficiency over the pH range from 3 to 9 is relatively constant for the unwashed algae. With the acid-washed algae, Cu adsorption decreases for pH values greater than 6.5. This is in contrast to earlier work with *Vlothrix* (*6*) and *Eisenia bicyclis* (*7*), which exhibited a stronger pH dependence.

After the algae were cleaned with 1% HCl, the properties of Cu adsorption appear changed with the maximum extraction efficiency being 67% for $CuCl_2$ and 57% for $Cu(NO_3)_2$. This is in contrast to 42% and 46%, respectively, for the same compounds on the unwashed algae.

Effect of Algae Mass on Cu Adsorption and Background Signal. In order to investigate the effect of algae mass, 2, 4, 6, 9, 12, and 15 mg of algae were added to 10 mL of solution containing 4 ng/mL Cu. After 20 min of agitation, the mixture was centrifuged. The algae pellet then was mixed with 2 mL of 0.5% HNO_3 and this slurry suspension was subsequently analyzed by GFAAS. The results are shown in Figure 2. The background was measured by using the "background only" mode of the instrument. The Cu adsorption increases gradually and slowly with increasing mass of algae. When the algae weight is increased from 2 to 15 mg, the Cu recovery is increased by less than 38%, i.e., from 40% to 55%.

Table II. Effect of the Solution Matrix on Copper Adsorption by Algae for 4 ng/mL Cu Concentrations (% Cu Recovery)

10 mg/mL NaCl	0.5 mg/mL KCl	0.5 mg/mL $Ca(NO_3)_2$	1 mg/mL $MgCl_2$	NaCl KCl[b] $Ca(NO_3)_2$ $MgCl_2$	no matrix[c]	
					$Cu(NO_3)_2$	$CuCl_2$
65	67	57	63	66	57	67

[a] Approximate seawater concentrations for NaCl, KCl, $Ca(NO_3)_2$, and $MgCl_2$ are 26.7, 0.72, 1.64, and 5.34 mg/mL (*8*). [b] Mixed matrix concentration is the same as in individual solutions. [c] The respective salts were used in preparing the solution without any added matrix.

While the algae mass does not appear to be critical for reproducible adsorption efficiencies, the GFAA background signal shows a stronger dependence (Figure 2). In addition, when the algae mass exceeds 12 mg/10 mL, the algae suspension is not stable, clustering of the algae occurs and, after 20 min, visible settling of these clusters has taken place.

The pH of the suspension increases with increasing mass of algae. For example, when 4, 6, 9, 12, and 15 mg of algae were mixed with 10 mL of solution containing 0.1 mL of 0.5% HNO_3 and 4 ppb Cu, the pH values of the solutions were 5.5, 6.1, 6.3, 6.5, and 6.7, respectively. This points out existence of weak acid/base functionalities present on the algae.

Thus, increasing the amount of algae shows no significant advantage in extraction efficiency while background absorption and algal clumping does occur at higher masses. Six milligrams of algae was selected as a good compromise and was used in the balance of the experiments conducted.

Effect of the Matrix. Data in Table II show that Cu adsorption on the algae is not very sensitive to the presence of simple alkali of salts in solution, unlike the results shown previously for Cd (*4*). For example, Cd adsorption was interfered with seriously by a seawater matrix and preconcentration was not successful (*4*). In Table II the salt concentration is approximately half that found in seawater (*8*) and the uptake was virtually unchanged. These results suggest that the primary concomitants of seawater will not affect Cu adsorption by the algae. It is interesting to note that when $Ca(NO_3)_2$ matrix is added, Cu adsorption is reduced to the level observed for the simple $Cu(NO_3)_2$ solution.

Copper was preconcentrated from a sample whose concentrations of NaCl, KCl, $MgCl_2$, and $Ca(NO_3)_2$ are given in Table II. The determined value of 5.9 ± 0.6 ng/mL was in good agreement with the Cu added (5.5 ng/mL) to this matrix. This is consistent with the general results of Ferguson and Bubela (*7*).

Since anionic complexes of copper may bind to the algae surface, the effects of several organic complexing agents on Cu adsorption were considered. After addition of ethylenediaminetetraacetic acid (EDTA, 0.1%), sodium citrate (0.2%), and sodium dodecyl sulfate (0.01%), Cu recovery was found to be 10, 76, and 78%, respectively. Cu adsorption is improved slightly by the presence of sodium citrate and dodecyl sodium sulfate, but EDTA seriously attenuates the Cu adsorption. While one is tempted to ascribe EDTA's effect to the stability of the Cu–EDTA complex ($K_f = 6.3 \times 10^{18}$), the citrate complex is also quite stable ($K_f = 1.5 \times 10^{14}$). This obviates the simple explanation that the stable complexation of Cu by EDTA prevents Cu^{2+} adsorption. It also fails to explain why an enhanced extraction efficiency is detected with the addition of the citrate. Dodecyl sulfate addition also improves Cu adsorption on the algae. It may be possible that both the dodecyl sulfate and citrate modify the algae surface to enhance the Cu adsorption while this mechanism is not available for EDTA due to charge distribution or steric effects. Certainly, additional studies are needed before any definitive conclusion can be reached.

The aforementioned observations show that the mechanisms of Cu adsorption on algae are complex. At least two types of adsorption sites are suggested. One may involve the direct interaction between the Cu cation (i.e., the aquo complex) and the algae, while the other may be adsorption of a neutral or anionic Cu complex.

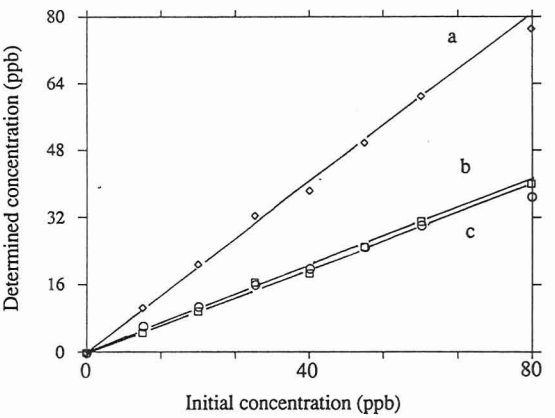

Figure 3. Concentration-dependent uptake of Cu by algae: (a) the total concentration, (b) the supernatant, (c) the suspended algae. The algae were not cleaned.

Concentration-Dependent Uptake of Cu. A series of Cu solutions (1–8 ng/mL) were prepared, and a 10-mL volume of each of these solutions was preconcentrated in 1 mL. The concentration of Cu in this 1-mL volume was then determined by using a working curve prepared from aqueous standards. Figure 3 displays the concentration of Cu determined in the suspension, the supernatant or the total of these two systems as a function of the total concentration of Cu in the original solution. The results show that the Cu adsorbed on the algae does not depend on the concentration of Cu in any periodic fashion. The extraction efficiency of Cu ranges from 45% to 50% in these experiments since the algae were not acid washed before use. By considering the amount adsorbed on the algae and that recovered from the supernatant, all Cu in the system was accounted for.

Calibration curves can be constructed by treating standards in the same way as sample (i.e., via algal preconcentration) or by using simple standards and then accounting for the preconcentration factor and the extraction efficiency. The latter approach was used because of its simplicity, less stringent requirements in standard preparation (e.g., ng/mL in place of pg/mL concentrations), and the relatively reproducible extraction efficiency values obtained for Cu under a variety of conditions.

Effect of Thermal Pretreatment Temperature on Cu Absorbance and Background Signal. Figure 4 shows the thermal pretreatment curve for Cu in the algal slurry. The shape suggests that thermal pretreatment at 1100–1200 °C minimizes the background without attenuating the Cu signal. Oxygen (i.e., air) ashing at temperatures between 600 and 900 °C was also considered but generally gave comparable or higher background readings than those obtained with Ar and was not used in this study. Since the algae have the ability to preferentially adsorb the analyte, much of the sample solution matrix is not included in the final algal suspension being analyzed. As a result, the *analytical* matrix is nearly independent of the original *sample* matrix and consists only of the algae. Thus, any thermal pretreatment or matrix modification developed becomes broadly applicable and inde-

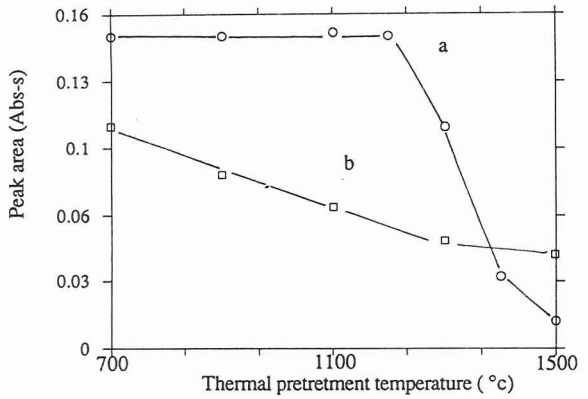

Figure 4. Effect of thermal pretreatment temperature on (a) Cu absorbance, and (b) background signal.

Table III. Effect of Sample Volume on Cu Adsorption

initial sample vol, mL	final sample concn vol, mL	concn factor	% Cu recovery
10	2	5	67
25	2	12.5	71
25	1	25	65
50	1	50	63
100	1	100	68
average			67 ± 3[a]

[a] Standard deviation.

pendent of the *original* sample.

Preconcentration Factor and Sampling Volume. Extracting the Cu from a sample solution can be used to reduce the complexity of the original sample matrix and/or to preconcentrate the Cu to improve the analytical precision and accuracy. As a result, the degree of preconcentration desired depends on the Cu concentration in the original solution. It remains to determine the variation in extraction efficiency as a function of preconcentration factor.

To obtain this information, 6-mg portions of algae were added to 10, 25, 50, and 100 mL of a solution containing a total of 40 ng of Cu. The solutions were preconcentrated to a final slurry volume of either 1 or 2 mL. The extraction efficiency results are given in Table III and show that with different sample volumes and different preconcentration factors, the Cu recovery is nearly constant with no obvious dependency on the sample volume used.

Riverine and Seawater Samples Analysis. To verify the capability of this algae for preconcentrating Cu in environmental samples, two standard reference solutions were preconcentrated and analyzed. They are nearshore seawater (CASS-1) and riverine water (SLRS-1) from the National Research Council of Canada. The algae were acid washed in 1% HCl in batches by the procedure described previously. This provided algae with the lowest Cu blank level and an average uptake efficiency of 67%. Before preconcentration, the samples (which are in a dilute HNO_3 solution) were neutralized by dropwise addition of a NaOH solution to raise the pH to approximately 5. The sample volumes were 100 mL for the seawater and 10 mL for the riverine water, resulting in preconcentration factors of 100 and 10, respectively.

Table IV. Concentration of Copper in the Riverine Water and Seawater Reference Samples

sample	determined values, ng/mL	certified values, ng/mL
CASS-1	0.302 ± 0.011	0.291 ± 0.027
SLRS-1	3.54 ± 0.09	3.58 ± 0.30

There is a residual Cu blank in the algae even after acid washing that is likely due to trace Cu on the cell interior. As a result, a copper-free aqueous solution blank was carried through the preconcentration step with every batch of samples, and the peak area of this blank subtracted from the sample signal. Typical values for the signal and blank are 8.0 ± 0.4 ng/mL and 0.079 ± 0.004, respectively, for the 100-fold preconcentration of the seawater and 4.6 ± 0.22 ng/mL and 0.066 ± 0.003 ng/mL for the 10-fold preconcentration of the riverine water. In Table IV five replicates for riverine water (SLRS-1) and three replicates for seawater (CASS-1) were carried out. The average values, standard deviation, and certified values are shown. As shown in Table IV, the determined values are in good agreement with the certified values for these two diverse water samples.

CONCLUSION

This study has demonstrated that unicellular *Chlorella* algae can be used to separate and preconcentrate Cu from seawater and riverine water samples. The Cu recovery is constant at least to a 100-fold preconcentration factor.

The extraction efficiency appears relatively insensitive to (a) solution pH in the pH range of 3–6, (b) solution volume-to-algal mass ratio at least up to a 16 mL/mg ratio, (c) algal mass used in preconcentration, and (d) interferences by many of the alkali and alkaline-earth metal salts. The presence of complexing agents does affect the preconcentration efficiency, although the cause of their influence has not been clearly delineated.

ACKNOWLEDGMENT

The authors express their appreciation to Cynthia Mahan and Vahid Majidi for the useful discussions regarding this research.

Registry No. Cu, 7440-50-8; water, 7732-18-5; sodium citrate, 994-36-5.

LITERATURE CITED

(1) Sakaguchi, T.; Tsuji, T.; Makajima, A.; Horikoshi, T. *J. Appl. Microbiol. Biotechnol.* **1979**, *41*, 207–215.
(2) Nakamima, A.; Sakaguchi, T. *Appl. Microbiol. Biotechnol.* **1986**, *24*, 59–64.
(3) Majidi, V.; Holcombe, J. A. *Spectrochim. Acta* **1988**, *43B* (12), 1423–1429.
(4) Majidi, V.; Holcombe, J. A. *J. Anal. At. Spectrom.* **1989**, *4*, 439–442.
(5) Mahan, C. A.; Majidi, V.; Holcombe, J. A. *Anal. Chem.* **1989**, *61* (6), 624–627.
(6) Gardea-Torredey, Jorge; Darnall, Denni; Wang, Joseph *Anal. Chem.* **1988**, *60*, 72–76.
(7) Ferguson, J.; Bubela, B. *Chem. Geol.* **1974**, *13*, 163–186.
(8) Rodier, J. *Analysis of Water*; Keter Publishing House: Jerusalem, 1975; p 891.

RECEIVED for review March 26, 1990. Accepted June 22, 1990. M.S. gratefully acknowledges the financial assistance of the State Educational Commission of the People's Republic of China. This work was supported in part by the Robert A. Welch Foundation, Grant F1108.

Correction for Fluorescence Response Shifts in Polyaromatic Hydrocarbon Mixtures with an Innovations-Based Kalman Filter Method

Todd L. Cecil and Sarah C. Rutan*

Department of Chemistry, Virginia Commonwealth University, Box 2006, Richmond, Virginia 23284

A Kalman filter based method for the correction of spectral response shifts in overlapped fluorescence spectra of polycyclic aromatic hydrocarbons (PAHs) has been developed. An iterative approach is shown to correct spectral response shifts of PAHs in methanol, acetonitrile, and tetrahydrofuran hydro–organic solvent mixtures. It is also shown that correction for shifts in overlapped spectral responses consisting of up to three components is feasible. The correction of shifts of up to 10 nm in severely overlapped spectra is shown to be possible, as well. The use of this method is shown to significantly improve the quality of the fit and yields more accurate concentration estimates of the individual contributions of overlapped fluorescence responses as compared to a regular Kalman fit.

INTRODUCTION

Fluorescence spectroscopy is an extremely sensitive and selective method for the detection of many biologically and environmentally significant compounds. Many of these are members of a class of compounds known as polycyclic aromatic hydrocarbons (PAHs). PAHs are significant because they are combustion products of fossil fuels and many are known or suspected carcinogens. However, there are several problems associated with the measurement of PAH fluorescence spectra. These problems include quenching, spectral distortion, and spectral response shifts.

Many species can cause quenching of the fluorescence response of PAH molecules. Common quenchers include oxygen, halides, and various paramagnetic species. The attenuation of the response caused by quenching can cause substantial errors in quantitative analysis if variable concentrations of quenchers are present in the sample matrix. Demas has shown that the effects of quenching can be minimized by using phase-resolved spectrofluorometers (*1*). However, no convenient corrections are available for steady-state instrumentation.

Spectral distortions can also affect qualitative and quantitative analysis in fluorescence spectroscopy. There are many different origins of spectral distortion, including variable background and drift, variations in individual instrumental characteristics, and unmodeled fluorophore contributions. Some of these difficulties can be circumvented with the use of appropriate data analysis methods. Recent research has demonstrated that unknown fluorophores can be present in the sample without corrupting the concentration estimates for the known components. Generalized rank annihilation and adaptive Kalman filter methods have been shown to be useful in this regard (*2–5*). In addition, both derivative methods and factor analysis methods have been used in conjunction with the adaptive Kalman filter to correct for the presence of a variable background contribution (*6*, *7*).

Another source of spectral distortion comes from solvent-induced spectral response changes. These solvent effects can cause changes in the relative intensities of different spectral features. An excellent example of this type of solvent-induced spectral distortion can be seen in spectra of pyrene collected in solvents of differing polarity. In fact, pyrene has been used as a solvent polarity indicator based on changes in observed band intensity ratios (*8*). Other PAHs show this type of distortion, and related solvent polarity scales have been developed based on observed distortions (*9–13*).

Spectral response shifts, like the distortions described above, are usually caused by differences in solvent polarities. The following explanation is based on a discussion by Lackowicz (*14*). The diagram in Figure 1 describes, qualitatively, how fluorescence spectral response shifts can be caused by changes in solvent polarity. In this diagram, the dipole moments are represented by the arrows and the electronic configurations of the solvent molecules are represented by the surrounding ovals. Initially, the solute and solvent molecules are in the ground electronic level (S_0) and in the ground-state configuration. In the ground-state, time averaged configuration, the dipole moments of the solvent molecules in the solvation sphere are aligned with the dipole moment of the solute. Upon absorption of a photon, the molecule is excited to the S_1' electronic level. When the solute is excited, the dipole moment of the solute changes. This change has been portrayed by a lengthening of the dipole moment vector and a change in the direction of the dipole moment. In the case of PAHs, the ground-state dipole moment is usually very small and excitation to the S_1' level can induce a dipole moment. On the same time scale as the absorption of the photon (the transition from S_0 to S_1'), there is a redistribution of the electrons in the molecules in the solvation sphere to better align with the solute's new dipole moment. However, the time scale of the absorption of a photon of light is too short to allow the physical reorientation of the molecules in the solvation sphere. The relaxation from the excited S_1' level to the excited S_1 level is called solvent relaxation and occurs when the solvent molecules rotationally reorient to a more stable configuration over the lifetime of the excited state. After the emission of a photon resulting in a return to the ground state, S_0' from the excited state S_1, the dipole moment of the solute and the electronic configuration of the molecules in the solvation sphere return to the ground state. The solvent molecules, however, have not returned to the ground-state spatial orientation. The molecules will subsequently rotate to the ground-state orientation, thereby returning the system to the ground energy state. The mechanism of fluorescence is the same for every molecule in every solvent, but the separation between the energy levels varies with each solute and solvent. The size of the energy stabilization that occurs during solvent relaxation appears to be the most important factor in determining the size of fluorescence spectral response shifts. Therefore, when a fluorescence spectrum of a PAH is collected in a polar solvent, the energy stabilization caused by solvent relaxation is larger than the stabilization found for a nonpolar solvent. This gives rise to fluorescence emission at longer wavelengths, or a red shift, for PAHs in polar solvents.

0003-2700/90/0362-1998$02.50/0

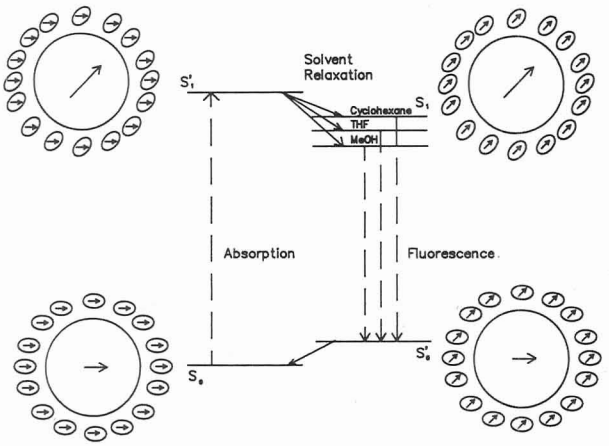

Figure 1. Jablonski diagram showing solvent relaxation process: (- - -) radiative process; (——) nonradiative process.

This type of spectral response shift is often found in the solvent systems used in gradient liquid chromatography (LC). However, in gradient LC separations, it is very difficult to predict the actual solvent composition at any point in the chromatographic profile, especially as the column ages. Thus, the unknown and the standard spectral responses may be measured in solvents with differing polarities, which leads to spectral response shifts. These shifts can cause erroneous concentration estimates to be reported when fitting overlapped spectral responses (obtained from diode array instrumentation) with a curve resolution procedure. PAHs are particularly susceptible to solvent-dependent spectral response shifts in the solvent systems used for LC. Even a small change in solvent polarity can cause significant errors in the concentration estimates obtained from curve resolution procedures (*15*).

We therefore address in this paper, the significant remaining difficulties with quantitative analysis of overlapped fluorescence spectral responses, namely, problems due to solvent dependent distortions and spectral shifts. To our knowledge, no other existing data analysis method can correct for spectral shifts. We have extended a method, based on the Kalman filter, which corrects for shifts in single-component Gaussian spectra, described previously (*15*), to correct for spectral response shifts of overlapped PAH fluorescence spectra. Although the detection of a spectral response shift of a single Gaussian peak is trivial, the detection of multiple response shifts in an overlapped, multiple component system is not as straightforward. An iterative approach was found to be necessary to obtain accurate fits of overlapped spectra of PAHs. The approach has been developed by using PAH fluorescence spectra that have been shifted by a computer algorithm and has been applied to mixtures of PAHs in hydro–organic solvent mixtures. We have also examined the sensitivity of the Kalman filter to solvent-dependent response distortions.

THEORY

Kalman Filter. The Kalman filter is a recursive, digital filtering algorithm developed in the 1960s for engineering applications (*16*, *17*). This mathematical method allows the estimation of system parameters in the case of noisy and/or overlapped spectral responses. For this study, the system parameters that are being estimated are the concentrations of the fluorophores contributing to an overlapped fluorescence response. For this system the Kalman filter measurement model is expressed as

$$z(k) = \mathbf{H}^{\mathrm{T}}(k)\cdot\mathbf{X}(k) + v(k) \quad (1)$$

where $\mathbf{X}(k)$ is the vector that contains the parameters to be estimated, $z(k)$ is the kth measured response, and $\mathbf{H}^{\mathrm{T}}(k)$ is the measurement function vector, which relates the system states to the measured response (i.e., fluorescence sensitivity values). Finally, $v(k)$ is the measurement noise contribution to the kth measurement. The central equation of the Kalman filter algorithm is the measurement update equation

$$\mathbf{X}(k) = \mathbf{X}(k-1) + \mathbf{K}(k)\cdot[z(k) - \mathbf{H}^{\mathrm{T}}(k)\cdot\mathbf{X}(k-1)] \quad (2)$$

where $\mathbf{K}(k)$ is the Kalman gain vector. Because the Kalman filter is a recursive algorithm, an initial guess is required for the parameters and their covariance before the filter can begin processing the data. Equation 2 is then implemented repetitively until all the measured responses, $z(k)$, have been processed. The bracketed portion of the Kalman filter update equation is called the innovations sequence ($\nu(k)$), and is given as follows

$$\nu(k) = z(k) - \mathbf{H}^{\mathrm{T}}(k)\cdot\mathbf{X}(k-1) \quad (3)$$

The innovations sequence is the point-by-point residuals of the fit obtained while the data is being processed or, equivalently, the difference between the predicted measurement value and the actual measurement value at point k. When the model is accurate, the innovations sequence should consist of zero-mean white noise. Earlier work has shown that the innovations sequence can be used as an indicator of the presence and magnitude of a spectral peak shift between the spectrum of a known compound of unknown concentration and a corresponding spectrum of a standard solution (*15*). The Kalman algorithm can be employed to filter a spectrum from high to low wavelengths (reverse filter) or from low to high wavelengths (forward filter). The forward and reverse innovation sequences obtained from the corresponding filter passes are significantly different if a modeling error, such as a spectral peak shift, has occurred. When the reverse innovations sequence is subtracted from the forward innovations sequence, the difference innovations sequence (ν_{diff}) is obtained

$$\nu_{\mathrm{diff}}(k) = \nu_{\mathrm{fwd}}(k) - \nu_{\mathrm{rev}}(k) \quad (4)$$

From the difference innovations sequence it is possible to determine whether a shift has occurred and, if so, the direction and magnitude. The shift direction is ascertained by identifying the sign of the peak in the difference innovations sequence which is associated with the component of interest. For instance, if this peak in the difference innovations sequence is positive, then it can be concluded that a positive (or red) shift, relative to the model fluorescence response, has occurred. In order to accurately determine the magnitude of the shift, it is necessary to compute a D^* value for this system. The D^* value is an empirically determined, normalized difference and is defined by the following equation (*15*):

$$D^* = (\nu_{\mathrm{diff}}(k_{\mathrm{max/min}})\, w\, X_{\mathrm{i,s}})/(X\, h) \quad (5)$$

where $\nu_{\mathrm{diff}}(k_{\mathrm{max/min}})$ is the peak height of the appropriate peak in the difference innovations sequence, w is the peak width (approximated by estimating the standard deviation of the largest peak in the pure component response), h is the peak height of the model response, and $X_{\mathrm{i,s}}$ and X_{i} are the concentration of the pure component model and the final concentration estimate returned by the Kalman filter, respectively. Previous studies have found that this D^* value varies linearly with peak shift for single Gaussian peaks (*15*).

EXPERIMENTAL SECTION

The PAHs used in this study, benzo[*a*]pyrene (B[*a*]P), perylene (PER), anthracene (ANT), pyrene (PYR), benzo[*ghi*]perylene (B[*ghi*]P), and phenanthrene (PHE), were purchased from Analabs, Inc. (Foxboro Co., North Haven, CT), and were of at least 98% purity. The solvents used were all EM Science OmniSolv grade (VWR Scientific, Bridgeport, NJ) and included methanol,

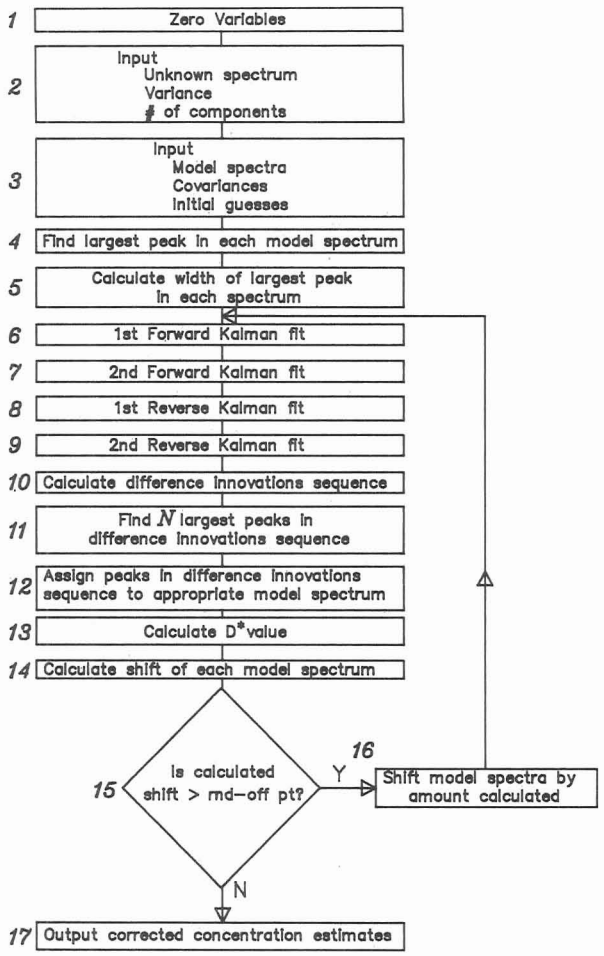

Figure 2. Flow chart of shift correction program.

acetonitrile, and tetrahydrofuran (THF). The solvents were used as received.

The PAH fluorescence spectral data were acquired from a Farrand MK-1 spectrofluorometer (Optical Technology Devices, Inc., Elsmford, NY). This fluorometer and an 80386-based PC-type computer were interfaced via the analog chart-recorder output on the fluorometer and a Metrabyte Dash-16 A/D board (Metrabyte Corp., Taunton, MA) in the computer. Data collection was accomplished with Labtech Notebook software (Laboratory Technologies Corp., Wilmington, MA). Data points were collected at 1-nm intervals. All other programs, including the data analysis programs, were written with the PASCAL programming language and were compiled using the TURBO Pascal programming environment (Borland International, Scotts Valley, CA).

The program used in these studies utilizes an iterative approach to allow a better approximation of the spectral response shifts and concentration estimates from overlapped spectra. Figure 2 is a simplified flow chart of the program. In step 4 of the flow chart the largest peak in each of the pure component model spectra is determined. In step 5, the standard deviation of the largest peak for each component is determined, by assuming a Gaussian peak profile for the peaks in the PAH fluorescence spectrum. However, most PAH spectra are not single peak systems and many have multiple peaks which are not baseline resolved. Since baseline resolution is often unattainable, another method of peak width determination is necessary. The peak width at half-height is often utilized for the determination of the standard deviation of Gaussian peak shapes. Initially, the peak height (y axis) and peak position (x axis) of the largest peak in each model spectrum are determined. The peak height is then divided by 2 to calculate the half-height intensity value. Then all the x axis values (within 40 nm of the peak maximum) corresponding to the half-height intensity value are found. If none are found, then an error message is returned. The distance (in nanometers) between the peak position and the half-height crossing point closest to the peak maximum position is calculated. This distance is then multiplied by (2/2.354) to calculate the corresponding peak standard deviation, w (based on the assumption of Gaussian peak shape).

Steps 6 through 9 consist of four Kalman filter fits of the unknown spectrum. The first forward and reverse fits are assigned initial guesses for the concentrations of 0 and initial guesses for the diagonal elements of the covariance matrix of 1 (off-diagonal elements are set to 0). For the second forward and reverse fits, the initial guesses for the concentration and covariance are the final estimates of these values from the previous Kalman fit. The difference innovations sequence is calculated (step 10) from the innovations sequences obtained from the second forward and reverse fits using eq 4. In this step, the N largest peaks in the difference innovations sequence are determined, where N is the number of pure component spectra used to fit the unknown spectrum. However, any peaks that are smaller than one-tenth of the square root of the variance of the measurement noise are not recorded as they are most likely due to noise. The factor of one-tenth can be used, as significant smoothing of the noise occurs when subtracting the forward and reverse innovations sequences. The peaks in the difference innovation sequence are then assigned to the appropriate model spectrum based on the relative peak positions (step 12). The difference innovations peak at the shortest wavelength is assumed to correspond to the pure component spectrum with the largest peak at the shortest wavelength. Once the peaks are assigned, the D^* values for each of the model spectra are calculated (step 13) using eq 5. From the D^* values the approximate spectral shifts are calculated (step 14) by using the following calibration equation:

$$\text{peak shift} = (D^* - (0.0002 \pm 0.008)) \times (0.3761 \pm 0.0002) \quad (6)$$

This equation is simply the straight line calibration equation that was reported previously (*15*) for a shifted, single-component Gaussian peak system. If the shifts are greater than a preset round-off point (step 15), then the model spectra are shifted by the amounts calculated above (step 16) and the Kalman fit procedure is repeated. The round-off point is empirically determined and is simply the point at which a shift is either rounded up to a one point shift or rounded down to a zero point shift. The shift in step 16 is carried out by manipulating the array that contains the fluorescence intensity values. Since shifting leads to some empty array elements at the beginning (or end) of the array, the average of the first (or last) 10 values of the baseline is used to fill the array. In all cases, the original model spectra are shifted by the sum of the shifts calculated in all of the previous iterations. The original data are used to prevent cumulative errors caused by repetitive shifts of the models. If all of the shift values are less than the round-off point, the estimates for the concentration and variance for each component in the mixture are reported, as well as the correlation coefficient and the variance of fit. If this does not occur within 75 iterations, the program halts execution.

The synthetic shift studies with mixtures of B[*a*]P and PER and ANT and B[*a*]P were accomplished with data collected in cyclohexane from a previous study (*18*).

A study of the spectra of PER in THF/water mixtures was conducted, where a spectrum of PER in pure THF was obtained, and the solvent polarity was changed by the addition of water in 10% (v/v) portions. The spectrum of PER in each of the aqueous–organic solutions was then measured. The same study was also conducted with methanol and acetonitrile.

Next, standard solutions of PYR, B[*ghi*]P, and PHE were prepared in methanol/water and THF/water solvent mixtures. Each of the solutions had the same concentration of PAH for a series of solutions with compositions of 60%, 70%, 80%, 90%, and 100% methanol or THF. Thus there were no dilution effects. The spectrum of each of the PAHs in each of the solvents was then obtained.

Finally, mixtures of B[*a*]P and PER were prepared in a 1:1 ratio (i.e., 1 mL of the 60/40 MeOH/H_2O solution of B[*a*]P was added to 1 mL of the 60/40 MeOH/H_2O solution of PER). These studies were done in methanol/water solvent mixtures. All spectra were obtained with an excitation wavelength of 254 nm.

RESULTS AND DISCUSSION

The D^* value discussed in the theory section has been shown to provide an accurate method for the detection and

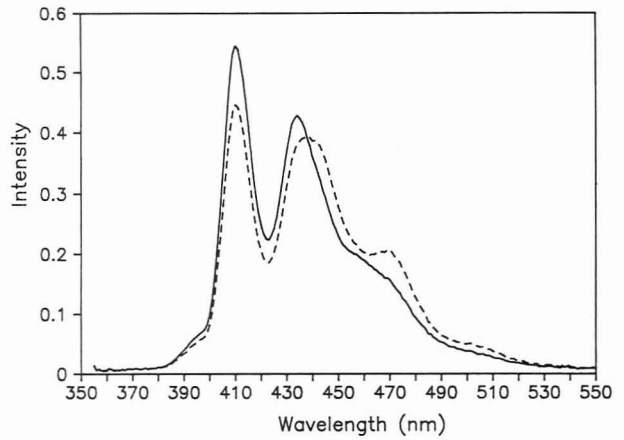

Figure 3. (– – –) Shifted mixture containing B[*a*]P and PER. (——) Kalman filter fit with no shift correction.

quantification of shifts in single-component Gaussian peak systems. The D^* value was also found to be applicable to a shifted spectrum of B[*a*]P if a new shift calibration curve based on B[*a*]P shifts was used. However, the spectral response shifts predicted by the Gaussian-based shift calibration curve were generally found to be smaller than the actual spectral shift of a PAH spectrum. It was possible to significantly improve the concentration estimates using these underestimated calculated spectral shift values (*15*).

For example, in Figure 3, curve a is a mixture spectrum of artificially shifted B[*a*]P and PER. Both of the PAH spectra were shifted 5 nm to the red relative to the pure component model spectrum. Curve b is a Kalman fit of the spectrum without correction for these spectral response shifts. The fit is poor and results in concentration estimation errors for B[*a*]P and PER of 18% and 38%, respectively. By use of a single iteration of the Gaussian-based D^* method a shift of 2.65 nm is calculated for B[*a*]P and a shift of −0.7 nm is calculated for PER. When the model spectra are shifted by the amounts calculated and the Kalman filter is again employed, the errors are reduced to 1.4% and 9.6% for B[*a*]P and PER, respectively.

The reduction in the concentration estimate errors indicates that the D^* method is capable of correcting spectral response shifts to some degree. However, the fact that the calculated shift is not equal to the actual shift suggests that there is a factor missing from the D^* equation that could improve the shift estimates. In order to identify the missing factor or factors, a study involving artificial mixtures of shifted B[*a*]P and PER spectra was conducted.

In this study, a spectrum of B[*a*]P and a spectrum of PER were shifted in 1-nm increments to both higher and lower wavelengths, with the largest shift of 10 nm. These shifted B[*a*]P and PER spectra were then combined in every possible permutation. The D^* values for each of these combinations were then calculated.

The D^* values calculated as described above showed a significant deviation from the predicted values using the Gaussian calibration curve. A number of correction factors were investigated, including normalizations for relative concentration differences, for relative spectral peak separations (to correct for cross-talk between overlapped responses), and logarithmic transformations. The relative peak height and relative peak separation of the two components were found to be important in determining the magnitude of the D^* values. However, all correction terms devised to compensate for these errors were ineffective.

Finally, the iterative D^* approach was examined. The iterative D^* method consists of three primary steps. The first step involves calculating the D^* value of each of the components of the unknown spectrum. From the D^* values, an approximate shift is calculated, using the Gaussian-based calibration curve, for each of the pure component spectra. In the second step, these spectra are shifted by the calculated amount. The third step involves obtaining the concentrations and D^* values calculated with the shifted pure component spectra. From the D^* value, an approximate spectral shift is again calculated and the cycle is repeated. The procedure is repeated until the calculated shift falls below some critical value (the round-off point) which indicates that the calculated shift is correct. By allowing the round-off point to be varied from the standard value of 0.5 points, additional flexibility is obtained. This flexibility gives the analyst the ability to scan a spectrum rapidly for significant peak shifts or accurately determine very small shifts. For example, if the round-off point is set to 1, then only spectral response shifts of greater than 1 point will cause an iteration. This will have two main effects, accurate calculations of the peak shift and concentration will not be possible, but, very few iterations will occur and therefore the determination of the existence of a significant shift can be made very rapidly. On the other hand, if a round-off value of less than 0.5 is used, the number of iterations increases but improved accuracy is afforded, especially for multicomponent systems where the D^* values for the different components are not completely independent. For these experiments the round-off point is set at 0.4, unless otherwise noted. This procedure is summarized in the flow chart given in Figure 2 and is described in more detail in the Experimental Section. Using this method, it is possible to reduce the errors in the estimated concentration of the compounds in Figure 3 to 0.0% in five iterations. There is no error because the noise contributions to the pure component spectra and the unknown spectrum are identical.

Table I. Summary of Results for Shift Corrections for B[*a*]P/PER System[a]

total number of cases tested	441
average number of iterations	5.3
cases with incorrect shift(s) and concentrations	24.3%
average error in concentration of B[*a*]P	0.3%
average error in concentration PER	0.7%
average shift error for B[*a*]P	0.2 nm
average shift error for PER	1.3 nm
cases with shift errors for B[*a*]P	4.1%
cases with shift errors for PER	24.1%
cases with greater than 75 iterations	4.1%

[a] Conditions: measurement variance, 1.0×10^{-6}; round-off point, 0.4.

This iterative D^* method was automated and the entire series of shifted two-component B[*a*]P and PER spectra was analyzed. The results are summarized in Table I. Of the 441 cases examined, only 4.1% failed to converge within 75 iterations. In these instances, the use of a different rounding point (0.7) gave convergence. For those cases where convergence was obtained, the average number of iterations required was 5.3, which is particularly small as compared to the number of iterations that would be necessary to obtain the same goodness of fit via a simplex optimization routine. For 76% of these cases, the exact shift was correctly determined. For the situations where the exact shift was not obtained, the shift errors were typically less than 2 nm. In fact, only 10% of the cases showed shift errors of greater than 1 nm, where shifts of 1 nm or less cause very minor errors in the concentration estimation in these systems. The average concentration estimation error for B[*a*]P was 0.3% and for PER was 0.7%. The smaller error for B[*a*]P is most likely due to the fact that portions of the B[*a*]P response are well-resolved from the PER response, while the PER response is virtually completely overlapped by the B[*a*]P. The results of this study are summarized in Table I.

Table II. Summary of Results for Shift Corrections for ANT/B[*a*]P System[a]

total number of cases tested	441
average number of iterations	11.0
cases with incorrect shift(s) and concentrations	51.2%
average error in concentration of ANT	3.5%
average error in concentration B[*a*]P	5.1%
average shift error for ANT	2.0 nm
average shift error for B[*a*]P	1.8 nm
cases with shift errors for ANT	51.1%
cases with shift errors for B[*a*]P	41.7%
cases with greater than 75 iterations	16.3%

[a] Conditions: measurement variance, 1.0×10^{-6}; round-off point, 0.7.

In order to more thoroughly test the performance of the method under different conditions, artificially shifted combinations of ANT and B[*a*]P were also studied. This system shows strong overlap, where the largest peak in the ANT spectrum is in close proximity to the largest peak in the B[*a*]P spectrum. The same permutations were obtained for this system as for the B[*a*]P/PER system, and the results are summarized in Table II. This system showed behavior similar to the first system, but when the largest peak in one model spectrum completely overlapped the largest peak in the other spectrum, the iteration algorithm began to cycle through a series of identical shifts and failed to converge. In order to minimize the cycling and obtain an accurate concentration estimation, the round-off point was increased to 0.7 for those cases that failed to converge. In this study, incorrect shifts were more likely than for the previous study and the average concentration errors in these cases were 3.5% and 5.1% for ANT and B[*a*]P, respectively. Even though a large portion of the shift estimates were incorrect, only 17% of them were large enough (>1 nm) to cause significant concentration estimation errors.

Several artificially shifted three-component mixtures (composed of ANT, B[*a*]P, and PER) were also examined at this point, and the algorithm was able to correct for moderate shifts in this system as well. Having found a method that successfully corrects for spectral response shifts in an artificially shifted PAH systems, it was next necessary to test the procedure with a case more representative of actual shifts observed in LC mobile phases.

Single-Component PAH Study. The next series of experiments were done by using spectra of PER in various LC mobile phase solvent mixtures, as described in the Experimental Section. In all systems studied here, the fluorescence sensitivities were highly variable. No simple correlation of peak height with concentration and/or solvent composition was found. The cause of this variability is currently under investigation. In order to test the performance of the peak shift algorithm independently of these variations, all data were normalized, and only peak height estimation errors (rather than concentration errors) are reported. These results are summarized in Table III. As illustrated in the table, good fits are obtained except for cases where significant spectral distortion occurred. In the case of methanol, the distortion effects seem to become significant with a solvent composition of 70% methanol relative to pure methanol. PER in THF and acetonitrile appears to be less susceptible to distortions with the addition of water. In each of the cases without significant distortions, the shift was correctly identified within 1.0 nm, and in three iterations or less. In addition, the shift correction algorithm yields smaller peak height estimation errors for the peak height for all cases, relative to a simple Kalman filter fit. One point to note about Table III is that the estimated shifts from the Kalman filter shift algorithm appear to be much more accurate than the shifts obtained from the simple peak location method that was used to find the "true" peak shift. The largest intensity value was assumed to correspond to the wavelength of the peak maximum. Any displacement of the peak maximum of an unknown spectrum relative to the model spectrum was considered the "true" shift. However, when the model spectrum was shifted by the "true" shift amount and the fit quality was compared to the fit quality obtained from the iterative D^* method, it was found that the latter method gave a lower variance of fit in every case. This indicates that even for single-component systems, it is advantageous to use the shift-correction algorithm.

To determine the effects of variable solvent polarity upon the fluorescence spectra of other PAHs, a study of PYR, PHE, and B[*ghi*]P in methanol/water solvent systems was undertaken. The PYR and B[*ghi*]P showed no significant shifts. These are PAHs for which the band intensity ratios have been used as solvent polarity indicators. For the relatively small solvent polarity variations studied here, however, the intensity ratio changes were not large enough to affect the fitting process. In contrast, PHE showed shifts in the range of 2–3 nm which are large enough to cause fitting errors to occur if the shifts are not corrected. An example of the type of shift found is shown in Figure 4. As an extension of this study, the spectra of B[*a*]P, PER, PYR, and B[*ghi*]P in THF/water mixtures were obtained. The results are tabulated in Table IV. In all of the cases, the spectrum of the PAH in pure THF was used as the model. The spectral shifts do not seem to follow a progression of larger red shifts with increasing water content in the solvent system. However, all of the spectral shifts are red shifts with the exception of PER in 70% THF. The blue shift found in that spectrum is probably associated

Table III. Results for Shift Correction for PER in Hydro–Organic Solvents[a]

organic modifier[b]	% organic composition	true shift,[c] nm	estimated shift, nm	errors in Kalman fit, %	no. of iterations	variance of fit		*F* ratio[f]
						Kalman	iterative	
MeOH	100	−2.0	−2.0	1.2	2	6.20×10^{-5}	6.85×10^{-6}	9.06
MeOH	80	5.0	4.0	4.4	3	2.19×10^{-4}	9.74×10^{-6}	22.38
MeOH	70	2.0	8.0	−7.1	*d*	4.82×10^{-5}	1.77×10^{-4}	0.27
MeOH[e]	60	0.0	−4.0	−51.4	*d*	7.83×10^{-6}	1.27×10^{-5}	0.62
THF	100	−1.0	−1.0	0.5	1	1.42×10^{-5}	4.74×10^{-6}	3.01
THF	80	2.0	1.0	0.6	1	1.49×10^{-5}	3.37×10^{-6}	4.43
THF	70	−2.5	−3.0	1.9	3	4.26×10^{-5}	1.36×10^{-6}	31.28
THF	60	−4.0	−4.0	4.7	3	8.84×10^{-5}	9.55×10^{-6}	9.25
ACN	100	−4.0	−4.0	4.5	3	2.08×10^{-4}	8.77×10^{-6}	23.62
ACN	80	−1.0	−1.0	0.3	1	1.43×10^{-5}	8.03×10^{-6}	1.78
ACN	70	1.0	0.0	0.0	0	5.41×10^{-6}	5.41×10^{-6}	1.00
ACN	60	−2.0	−2.0	0.9	2	3.35×10^{-4}	3.16×10^{-4}	1.07

[a] Conditions: measurement variance, 1.0×10^{-5}; round-off point, 0.4. [b] MeOH, methanol; THF, tetrahydrofuran; ACN, acetonitrile. [c] Shift relative to 90% organic modifier spectrum, in nm. [d] Did not converge. [e] Signal strongly quenched. [f] $F\alpha_{=0.1,198,198} = 1.2$.

Table IV. Results for Shift Correction for PAHs in Hydro–Organic Solvent Mixtures

PAH	% organic modifier	estimated shift, nm	no. of iterations	errors in Kalman fit, %	variance of fit		F ratio[c]
					Kalman	iterative	
PHE	100/MeOH[a]	−1.8	2	2.0	4.23×10^{-4}	1.79×10^{-5}	23.59
PHE	80/MeOH[a]	0.7	2	0.7	5.29×10^{-5}	1.05×10^{-5}	5.02
PHE	70/MeOH[a]	−0.9	1	0.7	8.62×10^{-5}	1.29×10^{-5}	6.65
ANT	90/THF[b]	0.0	0	0.0	8.60×10^{-6}	8.60×10^{-5}	1.00
ANT	80/THF[b]	5.1	3	10.6	1.73×10^{-4}	3.85×10^{-6}	44.94
ANT	70/THF[b]	0.0	0	0.0	1.88×10^{-6}	1.88×10^{-6}	1.00
ANT	60/THF[b]	0.0	0	0.0	3.19×10^{-6}	3.19×10^{-6}	1.00
ANT	50/THF[b]	2.3	2	3.1	7.85×10^{-5}	6.28×10^{-6}	12.50
B[a]P	90/THF[b]	2.3	2	6.1	3.75×10^{-4}	2.43×10^{-5}	15.43
B[a]P	80/THF[b]	1.8	2	2.9	1.84×10^{-4}	9.39×10^{-6}	19.59
B[a]P	70/THF[b]	3.2	2	14.0	7.56×10^{-4}	1.45×10^{-5}	52.14
B[a]P	60/THF[b]	0.9	1	0.5	5.49×10^{-5}	1.31×10^{-5}	4.22
B[a]P	50/THF[b]	3.2	2	9.3	1.96×10^{-3}	6.02×10^{-5}	316.99
PER	90/THF[b]	0.0	0	0.0	1.74×10^{-6}	1.74×10^{-6}	1.00
PER	80/THF[b]	0.9	3	0.0	4.92×10^{-6}	1.05×10^{-6}	4.71
PER	70/THF[b]	−0.5	1	0.0	2.45×10^{-6}	1.13×10^{-6}	2.16
PER	60/THF[b]	1.8	4	0.5	2.46×10^{-5}	2.04×10^{-6}	10.46
PER	50/THF[b]	0.0	0	0.0	2.20×10^{-6}	2.20×10^{-6}	1.00
PYR	90/THF[b]	1.9	3	3.7	6.74×10^{-4}	1.67×10^{-4}	4.03
PYR	80/THF[b]	0.0	0	0.0	1.79×10^{-4}	1.79×10^{-4}	1.00
PYR	70/THF[b]	1.4	2	2.7	6.15×10^{-4}	2.19×10^{-4}	2.81
PYR	60/THF[b]	0.0	0	0.0	9.46×10^{-5}	9.46×10^{-5}	1.00
PYR	50/THF[b]	1.9	3	3.6	5.65×10^{-4}	1.54×10^{-4}	3.66

[a] Conditions: measurement variance, 1.0×10^{-5}; round-off point, 0.3. [b] Conditions: measurement variance, 1.8×10^{-7}; round-off point, 0.4. [c] $F\alpha_{=0.1,198,198} = 1.2$.

Table V. Results for Shift Correction for B[a]P and PER in Methanol/Water Solvents[c]

% methanol	shift, nm		% errors in Kalman fit[a]		no. of iterations	variance of fit		F ratio
	B[a]P	PER	B[a]P	PER		Kalman	iterative	
100	−0.9	−2.8	3.3	−5.8	3	8.13×10^{-5}	1.05×10^{-5}	7.74
90	−0.9	2.3	2.4	−5.4	4	3.45×10^{-5}	7.23×10^{-6}	11.39
80	−0.5	−1.3	1.3	−3.1	14	6.53×10^{-5}	1.85×10^{-5}	13.53
70	2.1	1.5	−7.7	18	53	1.03×10^{-3}	4.10×10^{-5}	25.07
60	−1.4	−1.5	0.7	−7.9	46	1.63×10^{-4}	3.06×10^{-5}	5.36
50	2.3	−0.2	−0.9	5.6	75	1.31×10^{-4}	3.44×10^{-5}	3.80

[a] Peak height estimation error for regular Kalman filter. [b] $F\alpha_{=0.1,198,198} = 1.2$. [c] Conditions: measurement variance, 1.0×10^{-5}; round-off point, 0.3.

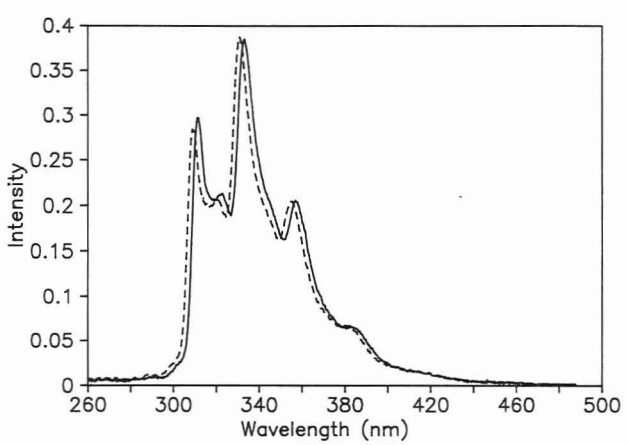

Figure 4. (– – –) Spectrum of PHE in 100% MeOH. (——) Spectrum of PHE in 90% MeOH/water.

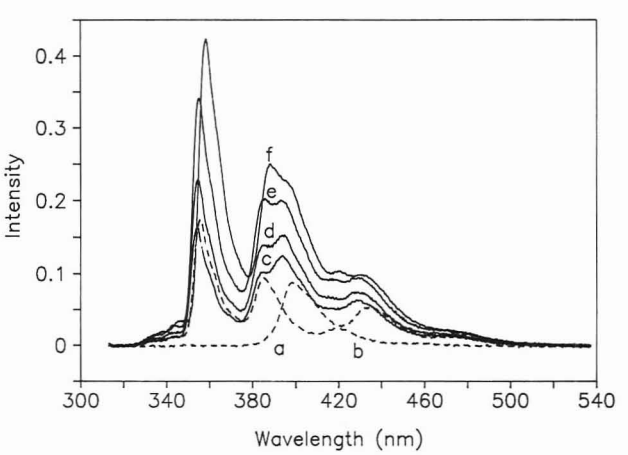

Figure 5. (– – –) Pure component spectra, (a) B[a]P, (b) PER. (——) Mixture spectra, (c) 100% methanol/water, (d) 90% methanol/water, (e) 80% methanol/water, (f) 70% methanol/water.

with instrumental variations, as explained below. In all cases where a shift was detected, the iterative method showed a significantly improved fit as compared to the regular Kalman fit. The improved fit is shown in Table IV by comparing the variances of fit resulting from the two methods, with an F test used to determine the significance of the observed differences.

These data indicate that spectral shifts can cause large errors and that this method can correct for them.

Two-Component PAH Study. In this study B[a]P and PER were added in equal proportions to methanol/water mixtures as described in the Experimental Section. The

results of this study are compiled in Table V and the spectra are shown in Figure 5. The overlapped fluorescence spectra that were obtained in solvents with compositions ranging from 50% to 100% methanol/water were analyzed with the spectra obtained in pure methanol as the model spectra. The results from the shift correction algorithm were compared to the results from a regular Kalman filter fit. The values for the F ratio indicate that a significantly improved fit is obtained. Peak height estimation errors for the regular Kalman fit ranged from 0.7% to 17%. The variance of fit indicated that significant spectral distortions were occurring in the 50% and 60% methanol mixtures. Recent studies have found that these can be minimized by using an excitation wavelength greater than 300 nm.

While the methanol/water study described above was conducted, it was noted that some of these shifts may have been caused not by chemical interactions but by irreproducibility in the data collection system. To examine the possibility of shifts caused by nonchemical factors, 15 replicates of the PER spectrum in MeOH were obtained. Upon analysis of these data, a standard deviation in the peak position of 1 nm was found. This indicates that anything less than a nanometer shift may not be due to chemical effects in these studies. In Table V, most of the shifts are greater than 1 nm and therefore indicate that these shifts are caused, at least in part, by the chemical interactions outlined in the theory section. The implementation of a diode array detector and accompanying data collection software is not susceptible to this type of irreproducibility. Preliminary studies with diode array instrumentation have shown that spectral response shifts are still found.

CONCLUSIONS

It is clear from the results presented above that variations in solvent composition have a wide range of complex effects on the observed fluorescence responses of PAHs. We observed variations in peak positions, peak intensity ratios, and fluorescence sensitivities. We have developed an algorithm that successfully corrects for the peak response shifts observed in typical reversed-phase LC solvent mixtures. The changes in the peak intensity ratios (spectral distortions) can be accommodated in some of the cases studied here, however, severe distortions can cause the algorithm to iterate indefinitely. It is evident that fluorescence response shifts caused by changes in the solvent polarity do cause significant problems in concentration calculations. It is further evident that the algorithm reported in this paper does correct for a large majority of the response shifts and therefore gives significantly improved concentration estimations. In cases where there are overlapped shifted responses, the algorithm was a more reliable method for the determination of the peak shifts than any other method available. The shift correction algorithm described here is potentially applicable to other instrumental methods besides fluorescence analysis, including atomic emission spectroscopy and infrared spectroscopy.

ACKNOWLEDGMENT

We thank Philip Morris, Inc., for the donation of the Farrand MK-1 spectrofluorometer.

LITERATURE CITED

(1) Demas, J. N.; Jones, W. M.; Keller, R. A. *Anal. Chem.* **1986**, *58*, 1717.
(2) Sanchez, E.; Ramos, L. S.; Kowalski, B. R. *J. Chromatogr.* **1987**, *385*, 151.
(3) Ramos, L. S.; Sanchez, E.; Kowalski, B. R. *J. Chromatogr.* **1987**, *385*, 165.
(4) Rutan, S. C.; Brown, S. D. *Anal. Chim. Acta* **1984**, *160*, 99.
(5) Rutan, S. C.; Brown, S. D. *Anal. Chim. Acta* **1985**, *167*, 39.
(6) Gerow, D. D.; Rutan, S. C. *Anal. Chim. Acta* **1986**, *184*, 53.
(7) Gerow, D. D.; Rutan, S. C. *Anal. Chem.* **1988**, *60*, 847.
(8) Dong, D. C.; Winnik, M. A. *Photochem. Photobiol.* **1982**, *35*, 17.
(9) Carr, J. W.; Harris, J. M. *Anal. Chem.* **1986**, *58*, 626.
(10) Waris, R.; Rembert, M. A.; Sellers, D. M.; Acree, W. E., Jr.; Street, K. W., Jr.; Poole, C. F.; Shetty, P. F.; Fetzer, J. C. *Appl. Spectrosc.* **1988**, *42*, 1525.
(11) Waris, R.; Rembert, M. A.; Sellers, D. M.; Acree, W. E., Jr.; Street, K. W., Jr.; Fetzer, J. C. *Analyst* **1989**, *114*, 195.
(12) Tucker, S. A.; Acree, W. E., Jr.; Street, K. W., Jr.; Fetzer, J. C. *Appl. Spectrosc.* **1989**, *43*, 162.
(13) Waris, R.; Street, K. W., Jr.; Acree, W. E., Jr.; Fetzer, J. C. *Appl. Spectrosc.* **1989**, *43*, 845.
(14) Lakowicz, J. R. *Principles of Fluorescence Spectroscopy*; Plenum Press: New York, 1983.
(15) Webster, G. H.; Cecil, T. L.; Rutan, S. C. *J. Chemom.* **1988**, *3*, 21.
(16) Brown, S. D. *Anal. Chim. Acta* **1986**, *181*, 1.
(17) Rutan, S. C. *J. Chemom.* **1987**, *1*, 7.
(18) Rutan, S. C.; Gerow, D. D.; Hartmann, G. E. *Chemom. Intell. Lab. Sys.* **1988**, *3*, 61.

RECEIVED for review April 27, 1990. Accepted June 26, 1990. This work was supported by the U.S. Department of Energy (Grant DE-FG05-88ER13833).

Resolution of Multicomponent Fluorescence Emission Using Frequency-Dependent Phase Angle and Modulation Spectra

Joseph R. Lakowicz,* Ranjith Jayaweera, Henryk Szmacinski, and Wieslaw Wiczk

Department of Biological Chemistry, School of Medicine, University of Maryland at Baltimore, 660 West Redwood Street, Baltimore, Maryland 21201

We describe a new fluorescence method that allows the resolution of both the decay times and emission spectra of mixtures of fluorophores. This method is completely general and does not require any assumptions or knowledge of the decay times or emission spectra of the individual fluorophores. We use the phase angle spectra and modulation spectra of the mixture, measured over a range of suitable light modulation frequencies and emission wavelengths. These data are analyzed by nonlinear least-squares analysis to recover the emission spectra and the associated decay times. The principle of the method and the nature of the data are illustrated by using two-component mixtures with increasing spectral overlap. We then demonstrate the recovery of minor components, of structure emission spectra, and of a three-component mixture with completed overlapping emission spectra. And finally, we describe the resolution of a two-component mixture with decay times of 0.8 and 1.4 ns using modulation frequencies up to 774 MHz.

INTRODUCTION

Fluorescence spectroscopy is a widely used methodology in biochemical research (*1–5*), in chemical analysis (*6*) and in clinical research (*7, 8*). Until recently the analytical applications fluorescence were limited to the use of the steady-state intensities, this being the result of the complex and/or expensive instrumentation required for time-resolved measurements. However, there are many advantages in the use of time-dependent fluorescence data. The emission spectra of most fluorophores are broad, unstructured, unusually overlap on the wavelength scale. In such cases the decay times of the fluorophores are often distinct and can provide the basis for resolution of the individual components. Additionally, fluorescence decay times are largely independent of the total fluorophore concentration and/or signal intensity. Consequently, decay times can be accurately determined in absorbing and/or scattering media such as cell cultures, body fluids or tissues. Consequently, time-resolved measurements can be accomplished for complex samples, whose optical properties preclude the use of the steady-state intensities.

There are two dominant methods of obtaining time-dependent data. These are the time-domain (TD) methods, most commonly time-correlated single-photon counting (*9, 10*), and the frequency-domain (FD) method (*11, 12*). In the latter FD method the more familiar pulsed excitation is replaced with an intensity modulated light source. The measured values are the phase lag and modulation of the emission, relative to the incident light, measured over a range of modulation frequencies. The frequency-domain method is now widely used in chemical and biochemical research (*13–16*). The FD measurements provide resolution of mixtures of fluorophores (*17, 18*), excited-state reactions (*19, 20*), solvent relaxation (*21, 22*), time-dependent anisotropy decays (*23–26*), lifetime distributions (*27–29*), distance distributions (*30, 31*) and transient effects in diffusive quenching (*32, 33*). These advanced applications have been made possible by the development of the frequency-domain instruments, which allow measurement over a wide range of modulation frequencies (*11, 12, 34*). However, comparatively little effort has been directed toward the use of these modern instruments to recover the emission spectra and decay times of components present in mixtures of fluorophores.

Prior to the introduction of the variable-frequency FD instruments, the only available phase-modulation fluorometers operated at one to three fixed modulation frequencies. Weber devised an analytical solution to obtain the decay times of N components from data measured at N frequencies (*35, 36*). This method appears to be unstable (*37, 38*) and sensitive to the small systematic errors which were present in data obtained from the fixed-frequency instruments (*38–40*). This method has not been used to recover the emission spectra of the components.

The usefulness of the fixed-frequency instruments for the resolution of emission spectra was enhanced by the use of phase-sensitive detection (*41, 42*). This method was described initially by Vesolova and co-workers for the resolution of a two-component mixture of fluorophores (*43*) and was later used for the resolution of fluorescence and phosphorescence (*44*). This method was made considerably simpler by performing the phase-sensitive detection on the low-frequency cross-correlation signals (*41, 42*). Following this innovation there was rapid development of this method in a number of laboratories. The method was used for suppression of background fluorescence in Raman spectroscopy (*45, 46*), for studies of ligand binding to macromolecules (*47, 48*), and for resolution of mixtures with more than two components (*49, 50*). The method was also modified to allow decomposition of the emission spectra using known decay times (*51*) or to allow recovery of the decay times and fraction intensities of the components using the known shapes for the emission spectra (*52, 53*).

While the phase-sensitive methods described above have found some utility, they are all limited by the need to know either the emission spectrum or the decay times of the individual fluorophores. This is because the measurements are performed at a single modulation frequency, which does not provide adequate information content to recover both the decay times and the spectral shapes. Additionally, the phase-sensitive intensities are stationary values that do not reveal the phase angle or modulation of the emission, unless the data are measured over a range of detector phase angles. Even then the data at a single modulation frequency reveal only a single weighted phase angle for the total emission, which is not adequate to recover both the phase angles and the relative intensities of the components in the mixture. Hence, measurement of the phase-sensitive intensity results in loss of the phase and modulation information, which must then be recovered by multiple measurements at various detector phase angles. Additionally, recovery of the modulation information requires the assumption that each component

* To whom correspondence should be addressed.

0003-2700/90/0362-2005$02.50/0

displays a single exponential decay and that there are no excited-state reactions. And finally, the method of phase suppression to record the individual emission spectra is only possible for two-component mixtures because only one emission can be suppressed in a single phase-sensitive emission spectrum.

The limitations described above can be circumvented to modern phase fluorometers which allow measurements over a wide range of modulation frequencies. In the present report we describe an extension of the frequency-domain method to provide resolution of both the emission spectra and the decay times of the individual fluorophores, without any assumptions about the spectra shapes, fractional contributions, decay times, or phase angles. In this method we scan the emission wavelength while simultaneously recording wavelength-dependent phase angle and modulation. The phase angle and modulation spectra (PM Spec) are recorded over an appropriate range of modulation frequencies. Nonlinear least-squares analysis yields the individual emission spectra and the decay times of each component in the mixture. To demonstrate the resolution available using this method, we report the resolution of three completely overlapping emission spectra for fluorophores with only a 3-fold range of decay times (3.7–11.7 ns). Additionally, we describe the resolution of two structured emission spectra for fluorophores with decay times of 0.8 and 1.4 ns. These results demonstrate that PM Spec is a powerful method for the resolution of multicomponent mixtures of fluorophores.

THEORY

Time and Frequency Domain Expressions. The sample is assumed to consist of a mixture of fluorophores, each of which displays a single exponential decay time. The time-dependent emission of each wavelength (λ) is then a multiexponential decay

$$I(\lambda, t) = \sum_i \alpha_i(\lambda) e^{-t/\tau_i} \tag{1}$$

where the preexponential factors ($\alpha_i(\lambda)$) depend on emission wavelength. The decay times (τ_i) are assumed to be characteristic of each component in the mixture and to be independent of wavelength for each component. At each emission wavelength the fractional intensity of each component is given by

$$f_i(\lambda) = \frac{\alpha_i(\lambda)\tau_i}{\sum_j \alpha_j(\lambda)\tau_j} \tag{2}$$

The fractional contribution of each component to the total emission is given by

$$F_i = \frac{1}{N}\sum_\lambda f_i(\lambda) \tag{3}$$

where N is the number of emission wavelengths.

The frequency-domain data consist of phase ($\phi_{\omega\lambda}$) and modulation ($m_{\omega\lambda}$) values, each measured over a range light of modulation frequencies (ω) and emission wavelengths (λ). For a multiexponential decay these values are given by

$$\tan \phi_{\omega\lambda} = N_{\omega\lambda}/D_{\omega\lambda} \tag{4}$$

$$m_{\omega\lambda} = [N_{\omega\lambda}^2 + D_{\omega\lambda}^2]^{1/2} \tag{5}$$

where

$$N_{\omega\lambda}J_\lambda = \sum_i \frac{\alpha_i(\lambda)\omega\tau_i^2}{1 + \omega^2\tau_i^2} \tag{6}$$

$$D_{\omega\lambda}J_\lambda = \sum_i \frac{\alpha_i(\lambda)\tau_i}{1 + \omega^2\tau_i^2} \tag{7}$$

and

$$J_\lambda = \sum_j \alpha_j(\lambda)\tau_j$$

The data consist of multiple sets of phase and modulation spectra, each measured at a single modulation frequency. These data sets are fit by using nonlinear least squares (*54*). The goodness-of-fit is given by

$$\chi_R^2 = \frac{1}{\nu}\sum_{\omega,\lambda}\left(\frac{\phi_{\omega\lambda} - \phi_{\omega\lambda}^c}{\delta\phi_{\omega\lambda}}\right)^2 + \frac{1}{\nu}\sum_{\omega,\lambda}\left(\frac{m_{\omega\lambda} - m_{\omega\lambda}^c}{\delta m_{\omega\lambda}}\right)^2 \tag{8}$$

where c indicates the values calculated for the assumed parameter values (τ_i and $\alpha_i(\lambda)$) and ν is the number of degrees of freedom. In our analysis the decay times (τ_i) and amplitudes ($\alpha_i(\lambda)$) are floating parameters, with the restriction that $\sum_i \alpha_i(\lambda) = 1.0$. At the beginning of the analysis the values of $\alpha_i(\lambda)$ are set equal to 0.5 for a two-component mixture and 0.33 for a three-component mixture. The weighting factors ($\delta\phi_{\omega\lambda}$ and $\delta m_{\omega\lambda}$) are given by the actual standard deviations found for each measurement, typically after 10–30 individual measurements at a single wavelength and modulation frequency. The values ($\delta\phi_{\omega\lambda}$ and $\delta m_{\omega\lambda}$) are written to the same data file which contains the phase and modulation data.

Emission Spectra of Components. The emission spectrum of each component ($I_i(\lambda)$) is calculated from its fractional intensity at each wavelength ($f_i(\lambda)$ from eq 2) and the steady-state emission spectrum ($I_{ss}(\lambda)$) of the sample

$$I_i(\lambda) = f_i(\lambda) I_{ss}(\lambda) \tag{9}$$

Apparent Decay Times. Irrespective of the complexity of the decay at each wavelength, it is possible to interpret the phase and modulation values in terms of apparent decay times

$$\tau^\phi_{app}(\lambda) = \frac{1}{\omega}\tan \phi_\omega \tag{10}$$

$$\tau^m_{app}(\lambda) = \frac{1}{\omega}\left[\frac{1}{m_w^2(\lambda)} - 1\right]^{1/2} \tag{11}$$

While this can be a useful representation of the data, it should be remembered that these are only apparent values, which are the result of a complex frequency-dependent weighing of the individual decay times. Furthermore, it is these weighted values that define the data measured at a single modulation value. There is no general method to recover the component decay times ($\tau_i(\lambda)$) and amplitudes ($\alpha_i(\lambda)$) from these limited data ($\tau^\phi_{app}(\lambda)$ and $\tau^m_{app}(\lambda)$). These apparent values have been used occasionally to fit the data in terms of the multiexponential model (*40*, *55*). While this approach, when used with caution, may yield acceptable results, the fitting to apparent lifetimes should be discouraged. Constant errors in ϕ_ω or m_ω do not translate linearly into errors in τ_ϕ and τ_m. Hence, it is difficult to even approximately estimate the uncertainties, which is necessary for the least-squares analysis. Importantly, the single frequency measurements do not contain adequate information to recover multiexponential decay parameters.

EXPERIMENTAL SECTION

Phase and modulation spectra were obtained by using the frequency-domain fluorometer described previously (*12*, *34*), with the data acquisition being controlled by a DEC Minc 11/23. An emission monochromator with automatic scanning was added to obtain the wavelength-dependent data. At each modulation frequency we first measured the phase and modulation of the reference, which was typically scattered light from a Ludox suspension at the excitation wavelength. This instrument, when used with the microchannel plate detector, displays no measurable wavelength dependence and hence it was not necessary to use reference fluorophores (*39*). The emission wavelength is then

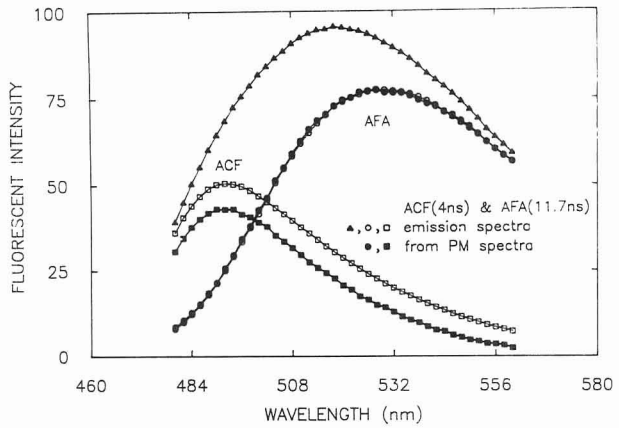

Figure 1. Emission spectra and recovered spectra from a mixture of ACF and AFA in propylene glycol at 20 °C. Emission spectra are shown for the mixture (▲), of the individual components (□, ○), and recovered from the phase-modulation spectra (■, ●). [ACF] = 5×10^{-7} M, [AFA] = 2×10^{-5} M.

scanned, with continuous recording of the phase and modulation values. The emission bandwidth was 8 nm. At each wavelength we typically measure 10 to 30 phase and modulation values. Additionally, we record the standard deviations of these values ($\delta\phi_{\omega\tau}$ and $\delta m_{\omega\lambda}$), which are used for weighing the data during least-squares analysis (eq 8). After completion of the scan, the reference is again measured, and the scan accepted or rejected based on the stability of the reference values. For measurements performed with the R928 squirrel-cage photomultiplier tube (PMT), we occasionally recorded phase and modulation spectra using lifetime standards, followed by appropriate correction for the decay time of the standard.

The light source and method of obtaining modulated light was varied to suit the absorption spectra and decay times of the fluorophore. For mixtures containing acriflavin (ACF), acridine orange (AO), 3-aminofluoranthene (AFA) and 7-(benzylamino)-4-nitrobenz-2-oxa-1,3-diazole (BBD), we used the 442-nm line from a HeCd laser. The intensity was modulated by using a Lasermetrics 1024 electrooptic modulator (*12*), and the emission was detected with an internally cross-correlated Hamamatsu R928 PMT (*12*). For mixtures containing perylene (Per) and 9-aminoacridine (9-AA), we used the harmonic content of a pyridine-2 dye laser, frequency doubled to 375 nm. For diphenyloxazole (PPO) and *p*-quaterphenyl (*p*-QP) we used the output of a R6G dye laser, frequency-doubled to 300 nm. Both dye lasers were cavity-dumped at 3.79 MHz and were synchronously pumped with a mode-locked argon ion laser. For these measurements the detector was an externally cross-correlated R1564 microchannel plate PMT, also from Hamamatsu (*34*). Magic angle polarizer orientations were used to avoid the effects of Brownian rotation.

For comparative purposes the decay times of the individual compounds and the mixtures were also recovered from the more usual frequency-domain (FD) method (*17*, *18*). In this case the phase and modulation of the sample were measured using wideband emission filters over a range of modulation frequencies, followed by least-squares analysis as described previously (*17*, *18*). Solutions in ethanol or cyclohexane were purged with N_2 to remove dissolved oxygen. Propylene glycol solutions were not purged. The total optical density in the longest absorption band was near 0.1.

RESULTS

Partially Overlapping Two-Component Mixture. The nature of the phase and modulation spectra is best illustrated for a mixture of fluorophores with incomplete spectral overlap and a large difference in the decay times. Partial overlap of the emission spectra allows one to visualize the contributions of each component on the sides of the emission from the mixture. These conditions were satisfied using a mixture of acriflavin (ACF) and 3-aminofluoranthen (AFA), which display decay times of 4.0 and 11.7 ns, respectively. The ACF (□) emission is centered near 490 nm and that of AFA (○) near

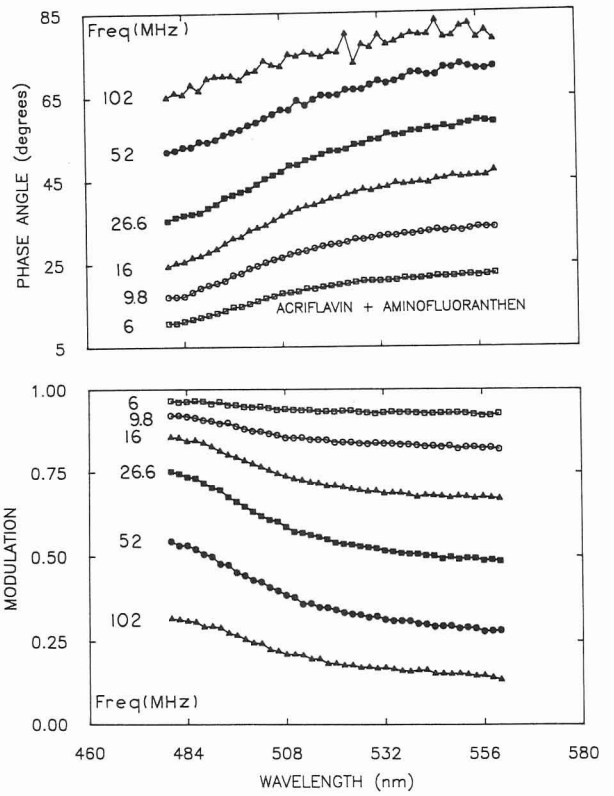

Figure 2. Representative phase angle (top) and modulation spectra (bottom) for a mixture of ACF and AFA. The complete data set consisted of PM Spec at 20 modulation frequencies.

530 nm (Figure 1). Also shown is the emission spectrum of the mixture (▲) which contains equivalent amounts of each of the single-component solutions.

Phase angle and modulation spectra at representative frequencies are shown in Figure 2. The phase angles increase and the modulation decreases with increasing emission wavelength. This is due to the longer decay time of the AFA whose emission becomes more dominant at longer emission wavelengths. The wavelength-dependence of $\phi_\omega(\lambda)$ and $m_\omega(\lambda)$ is monotonic because the fractional contribution of AFA to the emission increases monotonically with increasing wavelength. The increased uncertainty in the phase angles at 102 MHz is due to the lower amplitude of the modulated emission.

It is also possible to present the data in terms of the apparent phase and modulation lifetimes (eqs 10 and 11). The apparent lifetimes increase with increasing emission wavelength (Figure 3). At high frequencies the apparent phase lifetimes display considerable uncertainty, which illustrates how uncertainties in the phase angles can be amplified when presented in terms of apparent phase lifetimes. Additionally, there are greater uncertainties in the apparent modulation lifetimes at 6 MHz, which is the result of the small amount of demodulation at this frequency. While such a presentation of the data is informative with regard to the time scale of the emission, it should be recalled that these values are interpretations of the experimentally measured values. For this reason we prefer the direct presentation of the phase and modulation spectra (Figure 2). It should be noted that the apparent decay times show $\tau_m > \tau_\phi$, as is expected for a multiexponential decay with positive preexponential factors (*56*, *57*).

The decay times and amplitudes recovered for the pure compounds and for this mixture are summarized in Table I. We recovered essentially the same decay times from ACF and AFA from the PM Spec analysis and from the more common frequency-domain measurements. Also, there is no decrease in χ_R^2 when the PM Spec of each pure compound are analyzed

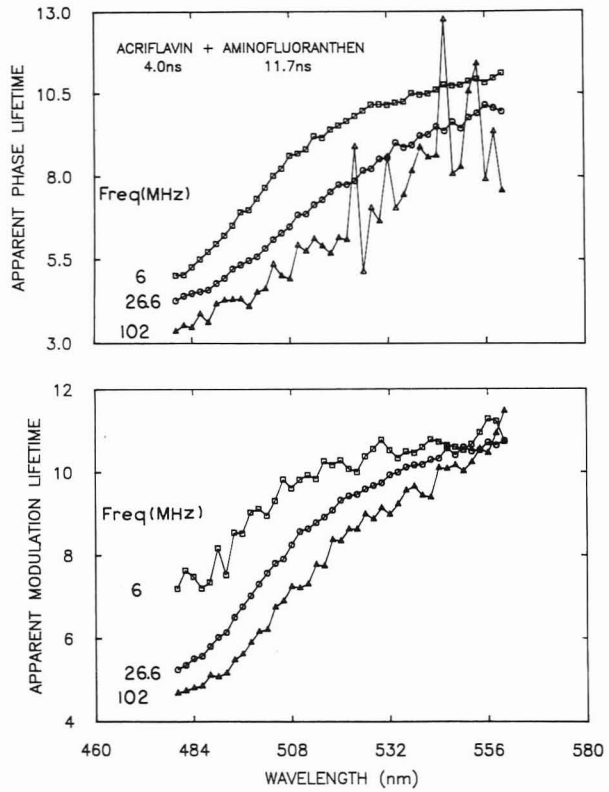

Figure 3. Apparent phase (top) and modulation (bottom) lifetimes for a mixture of ACF and AFA.

Table I. Decay Times and Amplitudes for ACF, AFA, and AO, and for Two-Component Mixtures of ACF, AFA, and AO

	τ_1, ns		F_1		χ_R^2	
sample	expected[a]	found	expected[b]	found	FD	PM Spec
ACF	3.95	3.98	1.0	1.0	0.3	0.6
AFA	11.72	12.04	1.0	1.0	0.5	0.8
AO	3.69[c]	3.73	1.0	1.0	0.1	1.2
ACF &	8.98[d]	8.47	1.0	1.0	46.7	79.3
AFA[e]	3.95	3.79	0.32	0.31		0.5
	11.72	11.19	0.68	0.69		
AO &	7.29[c,d]	7.34	1.0	1.0	23.1	29.9
AFA[f]	3.69	3.90	0.41	0.38		1.6
	11.72	12.35	0.59	0.62		

[a] The lifetime values are the results from the usual FD measurements, where the emission is observed through a band-pass filter (Corning 3-71). [b] The fractional intensity values are the results from steady-state measurements. [c] The FD measurements were performed with an emission wavelength of 522 nm. [d] The results of the forced single exponential fits are not necessarily the same for the FD and PM Spec data. [e] [ACF] = 5×10^{-7} M and [AFA] = 2×10^{-5} M. [f] [AO] = 1.25×10^{-6} M and [AFA] = 2×10^{-5} M.

using the two-component model, as is illustrated for the attempted two-component analysis of AFA (Table I). This is an important result because it indicates that the PM Spec data do not contain systematic errors which result in the apparent presence of a second component.

It should be emphasized that the recovered emission spectra and amplitudes are in agreement with the known emission spectra of the pure components and the known composition of the mixture (Figure 1). It is also important to note that the value of χ_R^2 decreases 230-fold for the two-component analysis. Such a large decrease in χ_R^2 implies certainty in the presence of at least two components in the mixture.

Strongly Overlapping Two-Component Mixture. We next examined a mixture with similar decay times, but one

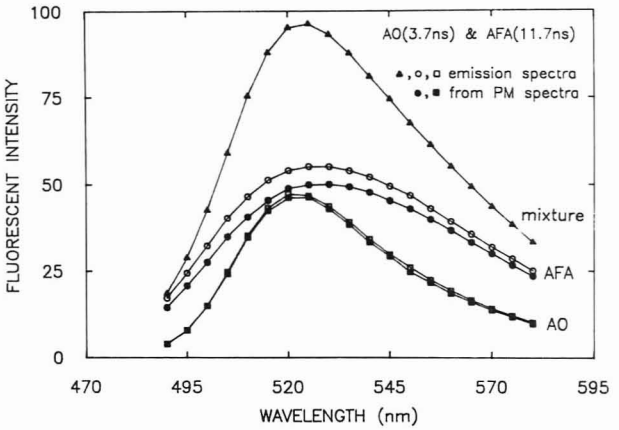

Figure 4. Emission spectra and recovered spectra from a mixture of AO (○) and AFA (□), in propylene glycol at 20 °C. Emission spectra are shown for the mixture (▲), the individual components (□, ○) and recovered from the phase-modulation spectra (■, ●). [AO] = 1.25×10^{-7} M, [AFA] = 2×10^{-5} M.

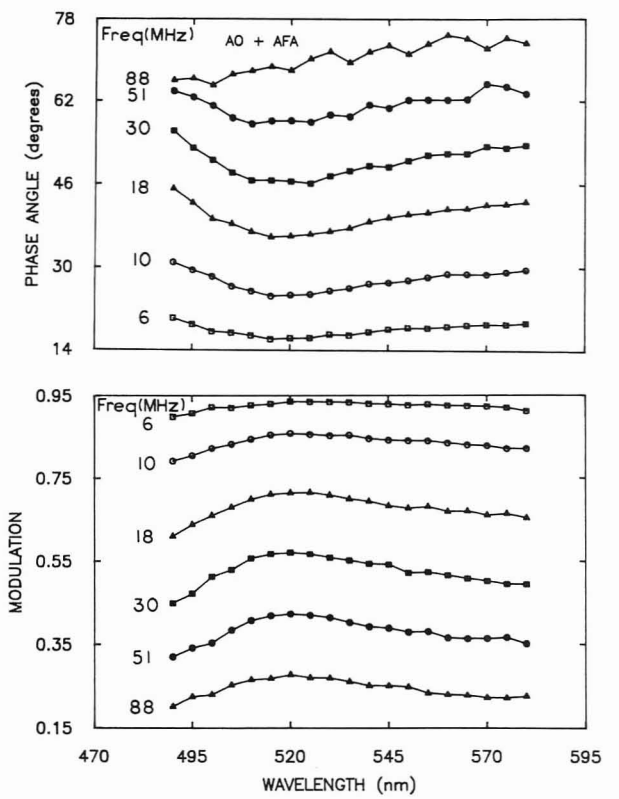

Figure 5. Phase angle (top) and modulation spectra (bottom) for a mixture of AO and AFA.

with the completely overlapping emission spectra. Such a sample is more difficult to resolve because the two components contribute more equally at all emission wavelengths, which results in more redundancy in the data. Overlapping emission spectra were obtained by using acridine orange (AO, 3.7 ns) and AFA (11.7 ns), both of which display emission maximum near 520–530 nm (Figure 4). The emission spectrum of AFA is more broadly distributed on the wavelength scale than is the spectrum of AO, so that the longer decay time is expected to be most evident on the blue and red sides of the emission.

The phase modulation spectra for the AO–AFA mixture are shown in Figure 5. The phase angles display a minimum, and the modulation a maximum, in the central region of the spectra. This effect is due to the higher contribution of AO (with its shorter decay time) in the central region of the emission. The spectra profiles and amplitudes (Figure 4) recovered from the data (■, ●) were found to be in precise

Table II. Decay Times and Amplitudes for a Three-Component Mixture of AO, BBD, and AFA and for the Individual Compounds

sample	τ_i, ns		F_i		χ_R^2	
	expected	found	expected	found	FD	PM Spec
AO	3.69 (0.01)[a]	3.73	1.0	1.0	0.1	1.2
BBD	6.15 (0.04)	6.08	1.0	1.0	0.6	1.9
AFA	11.75 (0.4)	12.04	1.0	1.0	0.2	0.8
AO + BBD + AFA[e]	6.76[c]	6.08[b]	1.0	1.0	56.2	5.0
	⟨3.5⟩[d]	3.05 (0.2)[b]	0.23	0.19	0.5	0.6
	7.9 (1.2)	6.58 (0.5)	0.40	0.45		
	12.7 (3.8)	10.78 (0.7)	0.37	0.36		

[a] Estimated uncertainty in the recovered values (*54*). [b] The number of decay times in an entry indicates the number of decay times used in the analysis. [c] The results of the forced single exponential fits are not necessarily the same for the FD and for the PM Spec data. [d] It was necessary to fix this decay time to obtain a stable solution. The emission was observed through a Corning 3-71 filter. [e] [AO] = 6×10^{-7} M, [BBD] = 1.3×10^{-6} M, and [AFA] = 2×10^{-5} M.

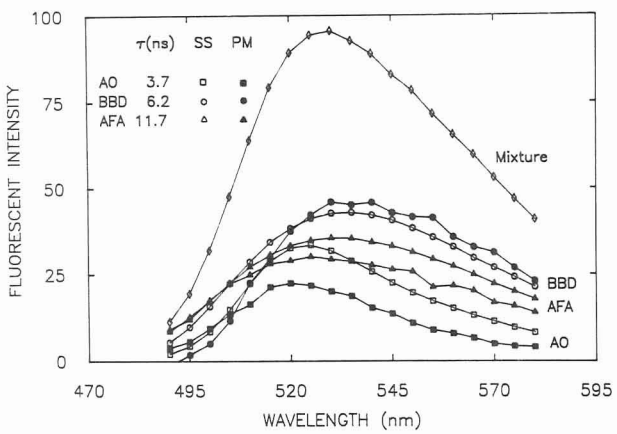

Figure 6. Emission spectra of a mixture (◇) of AO, AFA, and BBD, in propylene glycol at 20 °C. Also shown are the spectra of the individual components, AO (□), AFA (△), and BBD (○), and the spectra recovered from the phase-modulation spectra (solids). [AO] = 6×10^{-7} M, [BBD] = 1.3×10^{-6} M, and [AFA] = 2×10^{-5} M.

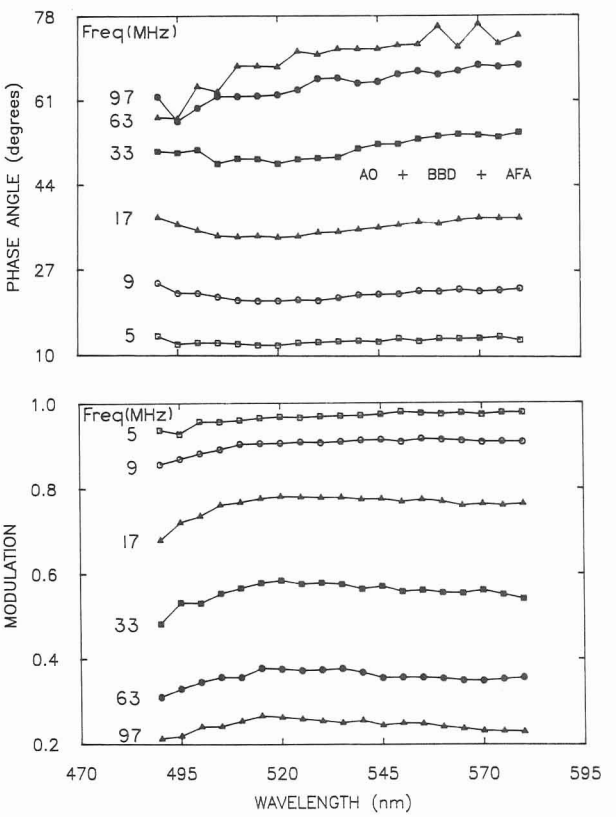

Figure 7. Representative phase-modulation spectra for a mixture of AO, AFA, and BBD. The complete data set consisted of PM Spec at 20 modulation frequencies.

agreement with those expected from the control solutions which contained a single component (□, ○). The decay times (Table I) were also in agreement with the expected values (expected for AO and AFA, 3.69 and 11.72; found, 3.90 and 12.35 ns). These results demonstrate that even complete spectral overlap does not have a significant effect on the ability to recover the spectral parameters. However, it is important to recognize that the components could not be resolved if the decay times were identical, even if the emission spectra were distinct. This is because resolution of the decay times and spectra depends on a difference in the decay times. From this perspective it would be challenging to resolve a mixture of AO and ACF, where the decay times are 3.69 and 3.95 ns, respectively.

Three Overlapping Components. To further evaluate the resolution obtainable using the phase-modulation spectra, we examined a mixture of three fluorophores whose emission spectra overlap completely and with a total lifetimes range of only 3-fold. The emission spectra of these components (AO, 3.7 ns; BBD, 6.2 ns; and ACF, 11.7 ns) are shown in Figure 6. The phase and modulation spectra (Figure 7) show little detail.

The spectra recovered from the mixture are shown in Figure 6. In spite of the complexity of this mixture, the emission spectra and amplitudes were recovered with reasonable precision. Additionally the decay times and total amplitudes (F_i) are in good agreement with the expected values (Table II). We note that this mixture was also difficult to resolve by the FD method. In fact, it was necessary to fix one of the decay times to obtain a reliable minimization (Table II). These results demonstrate that even three strongly overlapping spectra and closely spaced decay times can be recovered by using our method.

Structured Emission Spectra and Minor Components. It is instructive to examine the resolution of overlapping spectra, each of which contains vibrational structure. Such an experiment tests whether the amplitudes at adjacent wavelengths are well determined by the data. Such a sample was provided in a mixture of perylene (per, 5.1 ns) and 9-aminoacridine (9-AA) (14.2 ns). Their emission spectra overlap (Figure 8), with the peaks and valleys being interlaced. The phase angle and modulation spectra show maximum and minimum dependent upon whether perylene or 9-AA is the dominant emitter, respectively (Figure 9). The solid line shows the best fit to the data using the two decay time model. While the fit is not perfect at all wavelengths, the data were adequate to yield excellent recovery of the spectra (Figure 8), decay times, and amplitudes (Table III).

We also examined the usefulness of the phase-modulation spectra for recovery of a minor component in the emission.

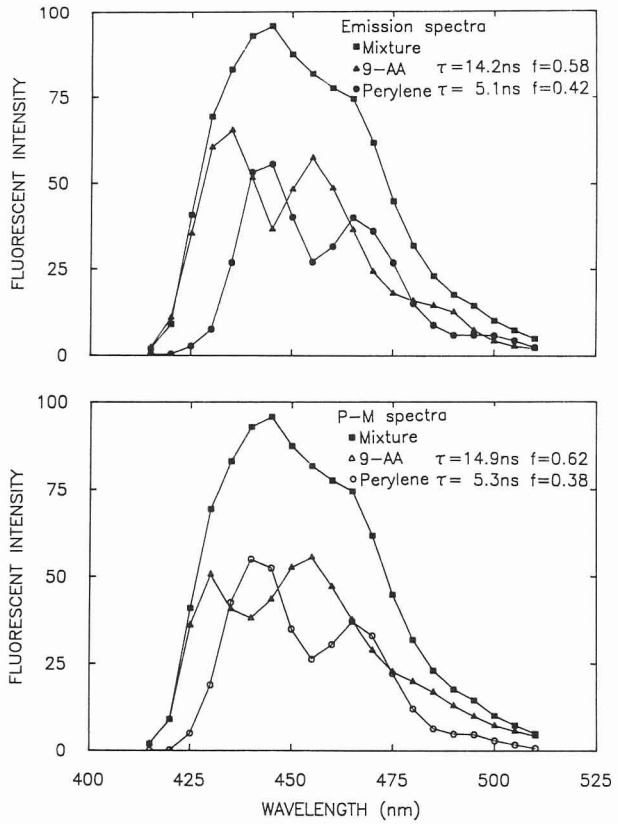

Figure 8. Emission spectra (top) and recovered spectra (bottom) from a mixture of perylene and 9-AA, in ethanol at 20 °C. [9-AA] = [perylene] = 5×10^{-6} M.

Table III. Decay Times and Amplitudes for Two-Component Mixtures

sample	τ_i, ns expected[a]	τ_i, ns found	F_i expected[b]	F_i found	χ_R^2
Per + 9-AA[c] (50/50)		8.95		1.0	38.0
	5.07[c]	5.26[d]	0.42	0.38	
	14.18	14.89	0.58	0.62	2.9
Per + 9-AA[e] (07/93)		13.31		1.0	4.0
	5.07	5.50	0.07	0.05	
	14.18	13.94	0.93	0.95	2.3
p-QP + PPO[c,g] (50/50)		1.12[f]		1.0	7.7
	0.80	0.81	0.48	0.46	
	1.42	1.53	0.52	0.54	2.5

[a] From the usual FD measurements. [b] From the steady-state spectra normalized to 1.0. [c] The FD measurements of Per + 9-AA were performed using a Corning 3-74 emission filter, and of *p*-QP + PPO using a WG filter. [9-AA] = [Per] = 5×10^{-6} M. [d] Measured at 12 modulation frequencies. [e] [9-AA] = 1×10^{-5} M, [Per] = 1×10^{-6} M. [f] Measured at 16 modulation frequencies. [g] [*p*-QP] = [PPO] = 3×10^{-6} M.

For this purpose we used a solution that contained dominately 9-AA (≈93%) and a small amount of perylene (≈7%). In spite of the small amplitude due to perylene, its spectrum and intensity were recovered from the data (Figure 10 and Table III).

Subnanosecond Components. And finally we questioned our ability to resolve fluorophores with decay times near 1 ns. We chose a mixture of 2,5-diphenyloxazole (PPO, 1.42 ns) and *p*-quarterphenyl (*p*-QP, 0.80 ns), whose emission spectra are structured and overlap nearly completely (Figure 11). The phase and modulation spectra were collected at frequencies ranging to 774 MHz (Figure 12). These spectra show modest peaks and valleys corresponding to the emission of PPO and *p*-QP. The dashed lines in Figure 12 show the

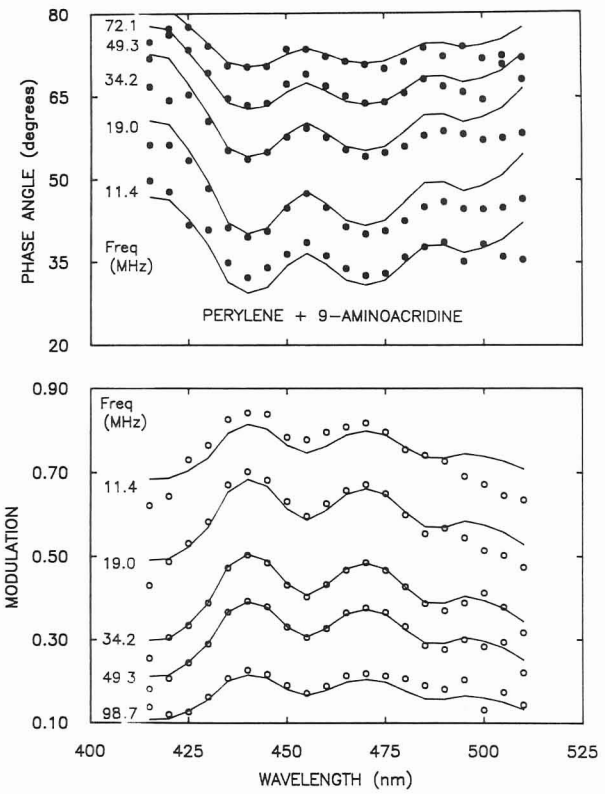

Figure 9. Phase (top) and modulation spectra (bottom) from a mixture of perylene and 9-AA. The solid lines show the best fit to the data using two wavelength-independent decay times and variable amplitudes at each wavelength.

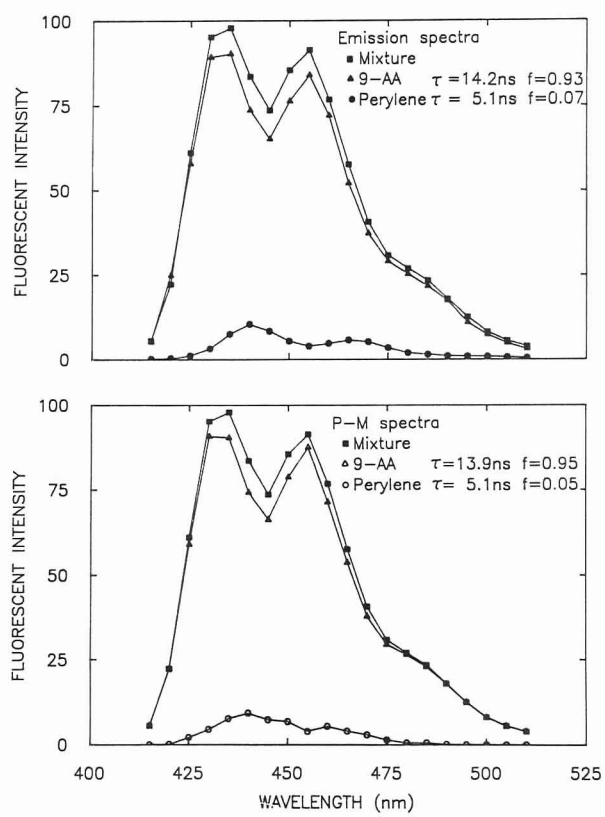

Figure 10. Emission spectra (top) and recovered spectra (bottom) from a solution of 9-AA with a small amount of perylene, in ethanol at 20 °C. [9-AA] = 1×10^{-5} M, [perylene] = 1×10^{-6} M.

best single decay time fit. Naturally, the phase and modulation are constant with wavelength at each frequency. The two decay time fit display the same maximum and minimum as found in the data. Importantly, the emission spectra

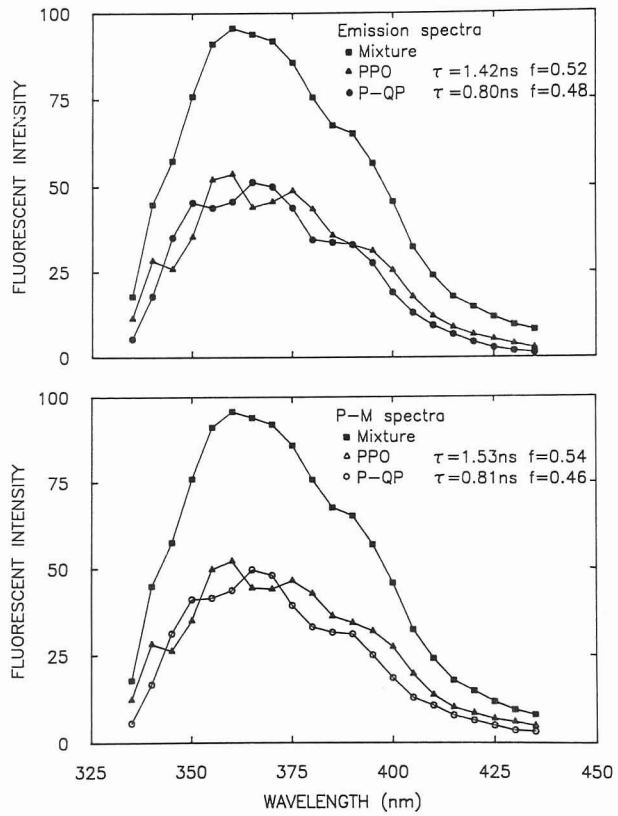

Figure 11. Steady-state emission spectra (top) and recovered spectra (bottom) for a mixture of PPO and *p*-QP, in cyclohexane at 20 °C. [PPO] = [*p*-QP] = 3 × 10^{-6} M.

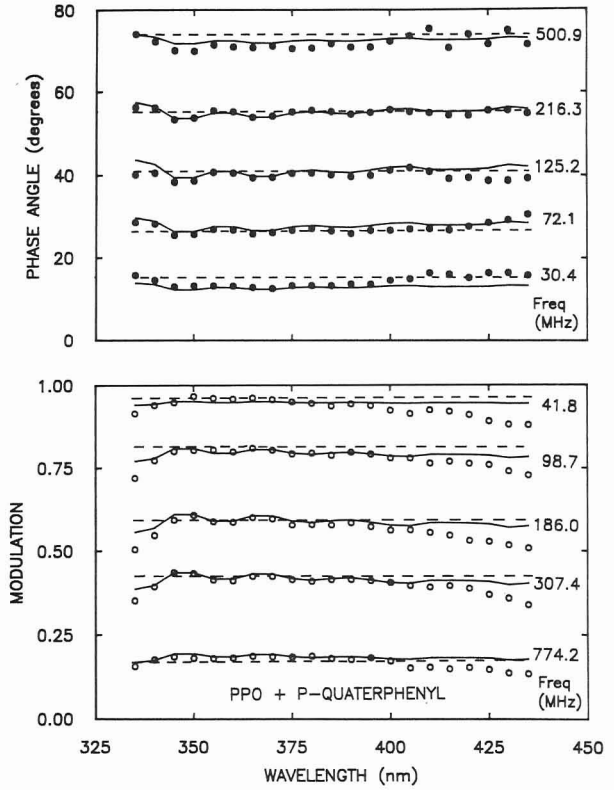

Figure 12. Phase (top) and modulation spectra (bottom) for a mixture of PPO and *p*-QP. The solid and dashed lines show the best two and one decay time fits, respectively.

(Figure 11), decay times, and amplitudes (Table III) recovered from the data are in excellent agreement with the expected values. Hence, even subnanosecond components can be recovered by using this method.

DISCUSSION

We have demonstrated that phase-modulation spectra can be used to recover the emission spectra, decay times, and amplitudes of multicomponent mixtures. While phase-sensitive measurements have been previously used for such resolutions (*58–60*), these more limited data require calibration measurements with the individual fluorophores, measurement at a number of detector phase angles, followed by fitting the phase-sensitive intensities to a cosine function. This procedure is equivalent to determining the phase angle of each fluorophore, which in turn is equivalent to knowing its decay time (eq 10). The method described in the present paper does not require prior knowledge of the decay times and does not require measurements on the isolated components.

There appears to be many potential applications for our method, in addition to analytical chemistry. An important feature of the method is that it does not require separation of the components. Such separations are often impossible, as is the case with multi-tryptophan proteins (*61*) and photosynthetic systems (*62, 63*). In fact, energy transfer among the photosynthetic pigments has already been briefly explored by use of phase angle spectra (*64–66*). While the signal-to-noise and resolution of these early measurements may have been unsatisfactory, it should be noted that these measurements did not take advantage of the dramatic increase in signal-to-noise provided by cross-correlation detection. Additionally, the frequency range can now be considerably higher than that used previously. In fact, recent developments in this laboratory have extended the upper frequency limit for 2 to nearly 10 GHz (*67*), which has allowed resolution of components with decay times as short as 2 ps. And finally, phase-modulation spectra may be of value in studies of solvent, protein, and membrane dynamics. The single frequency measurements have already been used to estimate the solvent relaxation time of a tryptophan analogue in propylene glycol (*68, 69*), and variable frequency measurements have been used to calculate time-resolved emission spectra (*70, 71*). The combination of gigahertz variable-frequency methods with wavelength scanning should provide data adequate to test models for solvent–fluorophore dynamics and interactions (*72–75*).

LITERATURE CITED

(1) Taylor, D. L.; Waggoner, A. S.; Lanni, F.; Murphy, R. F.; Burga, R. R. *Application of Fluorescence in the Biomedical Sciences*; A. R. Liss: New York, 1986.
(2) Lakowicz, J. R. *Principles of Fluorescence Spectroscopy*; Plenum Press: New York, 1983.
(3) Steiner, R. F.; Weinriyb, I. *Excited States of Proteins and Nucleui Acids*; Plenum Press: New York, 1971.
(4) Jameson, D. M.; Reinhart, G. R. *Fluorescent Biomolecules*; Plenum Press: New York, 1989.
(5) Lakowicz, J. R., Ed. *Time-Resolved Laser Spectroscopy in Biochemistry*; SPIE 909; Society of Photo-Optical Instrumentation Engineers: Bellingham, WA, 1988; pp 1–471.
(6) Schulman, S. G. *Molecular Luminescence Spectroscopy*; John Wiley and Sons: New York, 1985.
(7) Wolfbeis, O. S. *Pure Appl. Chem.* **1987**, *59*, 663–677.
(8) Peterson, J. I.; Vurek, G. G. *Science* **1984**, *224*, 123–127.
(9) O'Connor, D. V.; Phillips, D. *Time-correlated single photon counting*; Academic Press: New York, 1984.
(10) Visser, A. J. W. G., Ed. Time-Resolved Fluorescence Spectroscopy. *Anal. Instrum.* **1985**, *14*, 193–566.
(11) Gratton, E.; Limkemann, M. *Biophys. J.* **1983**, *44*, 315–324.
(12) Lakowicz, J. R.; Maliwal, B. P. *Biophys. Chem.* **1985**, *21*, 61–78.
(13) Jameson, D. M.; Gratton, E.; Hall, R. D. *Appl. Spectrosc.* **1984**, *20*, 55–106.
(14) Gratton, E.; Jameson, D. M.; Hall, R. D. *Annu. Rev. Biophys. Bioeng.* **1984**, *13*, 105–124.
(15) Lakowicz, J. R. In *Subcellular Biochemistry*; Hilderson, J. J., Harris, J. R., Eds.; Plenum Press: New York, 1988; pp 89–126.
(16) Lakowicz, J. R. In *Modern Physical Methods in Biochemistry*; Neuberg, A., Van Deenen, L. M., Eds.; Elsevier: New York, 1988; Vol. IIB, Chapter 1, pp 1–26.
(17) Gratton, E.; Linkeman, M.; Lakowicz, J. R.; Maliwal, B. P.; Cherek, H.; Laczko, G. *Biophys. J.* **1984**, *46*, 479–486.
(18) Lakowicz, J. R.; Gratton, E.; Laczko, G.; Cherek, H.; Limkeman, M. *Biophys. J.* **1984**, *46*, 463–477.

(19) Mugnier, J.; Valeur, B.; Gratton, E. *Chem. Phys. Lett.* **1985**, *119*, 217–222.
(20) Lakowicz, J. R.; Cherek, H. *Chem. Phys. Lett.* **1986**, *122*, 380–384.
(21) Parasassi, T.; Conti, F.; Gratton, E. *Cell. Mol. Biol.* **1986**, *32*, 103–108.
(22) Lakowicz, J. R.; Cherek, H.; Laczko, G.; Gratton, E. *Biochim. Biophys. Acta* **1984**, *777*, 183–193.
(23) Lakowicz, J. R.; Gryczynski, I.; Cherek, H. *J. Biol. Chem.* **1986**, *261*, 2240–2245.
(24) Lakowicz, J. R.; Laczko, G.; Gryczynski, I. *Biochemistry* **1987**, *26*, 82–90.
(25) Gryczynski, I.; Cherek, H.; Lakowicz, J. R. *Biophys. Chem.* **1988**, *30*, 271–277.
(26) Lakowicz, J. R.; Gryczynski, I.; Wiczk, W. *Chem. Phys. Lett.* **1988**, *149*, 134–139.
(27) Lakowicz, J. R.; Cherek, H.; Gryczynski, I.; Joshi, N.; Johnson, M. L. *Biophys. Chem.* **1987**, *28*, 35–50.
(28) Alcala, R. R.; Gratton, E.; Prendergast, F. G. *Biophys. J.* **1987**, *51*, 587–596 and 597–604.
(29) Alcala, R. R.; Gratton, E.; Prendergast, F. G. *Biophys. J.* **1987**, *51*, 925–936.
(30) Lakowicz, J. R.; Johnson, M. L.; Wiczk, W.; Bhat, A.; Steiner, R. F. *Chem. Phys. Lett.* **1987**, *138*, 587–593.
(31) Lakowicz, J. R.; Gryczynski, I.; Cheung, H.; Wonk, C.; Johnson, M. C.; Joshi, N. *Biochemistry* **1988**, *27*, 9149–9160.
(32) Lakowicz, J. R.; Joshi, N. B.; Johnson, M. C.; Szmacinski, H.; Gryczynski, I. *J. Biol. Chem.* **1987**, *262*, 10907–10910.
(33) Lakowicz, J. R.; Johnson, M. C.; Gryczynski, I.; Joshi, N.; Laczko, G. *J. Phys. Chem.* **1987**, *91*, 3277–3285.
(34) Lakowicz, J. R.; Laczko, G. *Rev. Sci. Instrum.* **1986**, *57*, 2499–2506.
(35) Weber, G. *J. Phys. Chem.* **1981**, *85*, 949–953.
(36) Jameson, D. M.; Weber, G. *J. Phys. Chem.* **1981**, *85*, 953–958.
(37) Jameson, D. M.; Gratton, E. In *New Directions in Molecular Luminescence*; Eastwood, D., Ed.; ASTM Special Technical Publication 882; American Standards for Testing and Materials: Philadelphia, PA, 1983; pp 67–81.
(38) Barrow, D.; Lentz, B. *J. Biochem. Biophys. Methods* **1983**, *7*, 217–234.
(39) Lakowicz, J. R.; Cherek, H.; Balter, A. *J. Biochem. Biophys. Methods* **1981**, *5*, 131–146.
(40) Dalbey, R. E.; Weiel, J.; Perkins, W. J.; Yount, R. G. *J. Biochem. Biophys. Methods* **1984**, *9*, 251–266.
(41) Lakowicz, J. R.; Cherek, H. *J. Biochem. Biophys. Methods* **1981**, *5*, 19–35.
(42) Lakowicz, J. R.; Cherek, H. *J. Biol. Chem.* **1981**, *256*, 6348–6353.
(43) Vesolova, T. V.; Cherkasov, A. S.; Shirokov, V. I. *Opt. Spectrosc.* **1970**, *24*, 617–618.
(44) Mousa, J. J.; Winefordner, J. D. *Anal. Chem.* **1974**, *46*, 1195–1206.
(45) Demas, J. N.; Keller, R. A. *Anal. Chem.* **1985**, *57*, 538–545.
(46) van Hoek, A.; Visser, A. J. W. G. *Anal. Instrum.* **1985**, *14*, 143–154.
(47) Nithipitikon, K.; McGown, L. B. *Anal. Chem.* **1987**, *59*, 423–427.
(48) Lakowicz, J. R.; Keating, S. *J. Biol. Chem.* **1983**, *258*, 5519–5524.
(49) Nithipiteikon, K.; McGown, L. B. *Appl. Spectrosc.* **1987**, *41*, 395–399.
(50) Keating-Nakamoto, S. M.; Cherek, H.; Lakowicz, J. R. *Anal. Chem.* **1987**, *59*, 271–278.
(51) Gratton, E.; Jameson, D. M. *Anal. Chem.* **1985**, *57*, 1694–1697.
(52) Keating-Nakamoto, S. M.; Cherek, H.; Lakowicz, J. R. *Anal. Biochem.* **1985**, *148*, 349–356.
(53) Keating-Nakamoto, S. M.; Cherek, H.; Lakowicz, J. R. *Biophys. Chem.* **1986**, *24*, 79–95.
(54) Bevington, P. R. *Data Reduction and Error Analysis for the Physical Sciences*; McGraw-Hill: New York, 1969.
(55) Matayoshi, E. D. *Biochemistry* **1980**, *19*, 3414–3422.
(56) Spencer, R. D.; Weber, G. *Ann. N.Y. Acad. Sci.* **1969**, *158*, 361–376.
(57) Lakowicz, J. R.; Balter, A. *Biophys. Chem.* **1982**, *16*, 99–115.
(58) McGown, L. B.; Bright, F. V. *CRC Crit. Rev. Anal. Chem.* **1987**, *18*, 245–295.
(59) McGown, L. B. *Anal. Chem. Acta* **1984**, *157*, 327–332.
(60) Bright, F. V.; McGown, L. B. *Anal. Chem.* **1985**, *57*, 2877–2880.
(61) Eftink, M. R.; Wasylewski, Z.; Ghiron, C. A. *Biochemistry* **1987**, *26*, 8338–8346.
(62) Pellegrino, F.; Alfono, R. R. *Biological Events Probed by Ultrafast Laser Spectroscopy*; Academic Press: New York, 1982; Chapter 2, pp 27–53.
(63) Bittermann, E.; Holzwarth, A. R.; Agei, G.; Nultsch, W. *Photochem. Photobiol.* **1988**, *47*, 101–105.
(64) Sebban, P.; Moya, I. *Biochim. Biophys. Acta* **1983**, *727*, 436–447.
(65) Sebban, P.; Jolchine, G.; Moya, I. *Photochem. Photobiol.* **1984**, *39*, 247–253.
(66) Sebban, P.; Bruno, R.; Jolchine, G. *Photochem. Photobiol.* **1985**, *42*, 573–578.
(67) Laczko, G.; Gryczynski, I.; Gryczynski, Z.; Wiczk, W.; Malak, H.; Lakowicz, J. R. *Rev. Sci. Instrum.*, in press.
(68) Lakowicz, J. R.; Balter, A. *Biophys. Chem.* **1982**, *15*, 353–360.
(69) Lakowicz, J. R.; Thompson, R. B.; Cherek, H. *Biochim. Biophys. Acta* **1983**, *734*, 294–308.
(70) Lakowicz, J. R.; Cherek, H.; Maliwal, B.; Laczko, C.; Gratton, E. *J. Biol. Chem.* **1984**, *259*, 10967–10972.
(71) Lakowicz, J. R.; Cherek, H.; Laczko, G.; Gratton, E. *Biochim. Biophys. Acta* **1977**, *777*, 183–193.
(72) Declemy, A.; Rulliere, C. *Chem. Phys. Lett.* **1988**, *146*, 1–6.
(73) Castner, E. W.; Bagchi, B.; Maroncelli, M.; Webb, S. P.; Ruggiero, A. J.; Fleming, G. R. *Ber. Bunsen-Ges. Phys. Chem.* **1988**, *92*, 363–372.
(74) Nagarajan, V.; Brearley, A. M.; Kank, T. J.; Barbara, P. F. *J. Chem. Phys.* **1987**, *86*, 3183–3196.
(75) Anthon, D. W.; Clark, J. H. *J. Phys. Chem.* **1986**, *91*, 3530–3536.

RECEIVED for review December 28, 1989. Accepted June 8, 1990. This work was supported by grants from the National Science Foundation (DMB-8804931 and DMB-8502835). Joseph R. Lakowicz acknowledges support from the Medical Biotechnology Center of the University of Maryland.

Thin Film Planar Waveguide Sensor for Liquid Phase Absorbance Measurements

Michael D. DeGrandpre and Lloyd W. Burgess*

Center for Process Analytical Chemistry, Department of Chemistry, BG-10, University of Washington, Seattle, Washington 98195

Patricia L. White and Don S. Goldman

Battelle Pacific Northwest Laboratory, Richland, Washington 99352

A thin film planar waveguide is studied for application as a chemical sensor for liquid-phase absorbance measurements. The waveguide is comprised of a thin film of tantalum pentoxide deposited on a glass substrate with a pair of diffraction gratings etched into the substrate surface. The buried grating couplers allow the launch and collection optics to be isolated from the liquid sample. The response to an absorbing dye and different refractive index (RI) solutions is studied and compared to theoretical predictions. The sensor has an absorbance sensitivity equivalent to a 1 mm path length in a conventional transmission measurement. A method to reduce the intensity changes due to solution RI is demonstrated.

INTRODUCTION

Research on the theory and fabrication of thin film planar waveguides began about 20 years ago, primarily driven by the desire to make integrated optical circuits. The potential applications of thin film waveguides in chemical analysis were quickly recognized (*1–3*). Midwinter (*1*) first suggested that thin film waveguides could be used as internal reflection elements (IREs) in attenuated total reflection (ATR) spectroscopy but most research following Midwinter's theoretical treatise has addressed the spectroscopic properties of the films themselves. Bohn recently reviewed the analytical spectroscopic applications of thin film waveguides (*4*). Specific

0003-2700/90/0362-2012$02.50/0

studies cited include Raman and absorption of thin films (5–7) and fluorescence excitation of molecules adsorbed on the waveguide surface (8). In contrast to the thin film and adsorption studies, this study addresses application of a thin film planar waveguide for quantitative measurements of absorbing liquids, analogous to conventional ATR spectroscopy.

ATR operates through absorption of the evanescent wave that is present at each point of total internal reflection. The evanescent wave penetrates only a fraction of the wavelength into the sample, allowing measurements to be made in highly scattering liquids, a definite advantage over most transmission or reflectance techniques. Furthermore, only a very small portion of the total guided energy is in the evanescent wave so ATR has effective path lengths 3–4 orders of magnitude less than a 1 cm transmission measurement. These sampling advantages have been exploited to measure IR spectra with minimal sample preparation and have made ATR a popular spectroscopic technique among process chemists (9). Quantitative ATR of liquids is possible because the liquid makes intimate and reproducible contact with the IRE, although the short effective path length limits quantitation to major constituents of the liquid. The sensitivity is primarily limited by the total number of reflections possible in conventional IREs, from 10 to 100 for an IRE of practical physical dimensions. New waveguide technology can be used to provide a much wider range of reflections. In a previous study, we used fiber optics as IREs (10). The long length and small radius of multimode fiber optics increase the total number of reflections by at least 1 or 2 orders of magnitude over conventional IREs.

Thin film planar waveguide technology can also be used to increase the effective pathlength of ATR measurements. A thin film, on the order of 1 μm thick, can have thousands of reflections per centimeter. The planar structure is very durable and it readily lends itself to miniaturization. Unlike fiber optics, there are numerous materials which may be used as thin film waveguides, many of which may be easily spun or dip-coated onto the substrate (11).

Several other researches have investigated thin film waveguides for ATR-type measurements (3, 12, 13). In these studies, prisms were used to couple light into the waveguide. Prism coupling presents several practical disadvantages for integration into a sensor. Since the prisms must be placed on the surface of the thin film, it is difficult to isolate the prisms from the liquid sample. Coupling efficiency is very sensitive to the input beam alignment and prism contact with the surface. Prism coupling is, therefore, only practical for benchtop applications. An alternative is to use grating couplers that are integrated directly into the waveguide structure. Surface gratings have been used by other researchers for immunosensing on the waveguide surface (14). In our study, gratings are fabricated in the substrate and are buried beneath the thin film as shown in Figure 1. The buried grating couplers are much more amenable to a sensor format because the beam input and collection optics are located behind the waveguide and are completely isolated from the liquid sample. This report describes the fabrication and response characteristics of a thin film waveguide sensor with buried grating couplers.

EXPERIMENTAL SECTION

Grating Fabrication. Gratings were fabricated by the method described in ref 15. A Kr^+ laser (Model 171, Spectra Physics) at 406 nm and Lloyd's mirror were used to record interference fringes in a positive photoresist (AZ1370, Hoescht Celanese). After the photoresist was developed, the substrate was etched either by reactive sputtering in an rf-diode system (SEM-8620, Materials Research Corp.) or by chemical etch with dilute buffered hydrofluoric acid (Transene Co., Inc.). The gratings used in this study were made by the plasma etch although the chemical etch

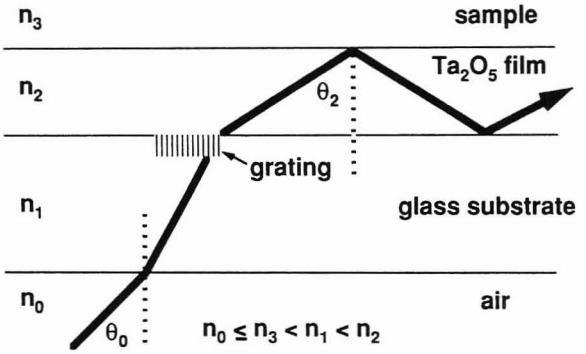

Figure 1. Thin film planar waveguide with buried grating coupler (n_0 = 1.0003, n_1 = 1.517, n_2 = 2.07, n_3 = sample RI).

is presently used because of its simplicity and reproducibility. The reactive sputtering gases argon and CHF_3 were chosen, based on their comparative etch rates (16). An argon plasma pre-etch was used to remove any residual photoresist from the grating wells followed by CHF_3 plasma, which etched the exposed pattern into the glass substrate. A 0.4-μm groove spacing was chosen to make coupling angles reasonably close to the waveguide normal, based on the expected film thickness and refractive index (RI) of tantalum pentoxide, the thin film chosen for this study. The input and output gratings were recorded 1.0 cm apart. Field emission scanning electron micrographs (SEM's) (Model S800, Hitachi, Inc.), shown in Figure 2 were taken of a cross section of the waveguide. The gratings can be seen at the interface between the substrate and the lighter colored thin film in Figure 2a. From these photographs the grating wells were measured to be approximately 700 Å deep, sinusoidal in shape, with a groove spacing of 0.375 ± 0.006 μm. The grating period was slightly lower than expected due to the uncertainty in the angle of the incident beam when generating the interference pattern.

Thin Film Fabrication. Metal oxide thin films such as TiO_2, V_2O_5, and Ta_2O_5 typically have very good mechanical and chemical durability and are very dense (low porosity). Tantalum pentoxide was chosen as the primary candidate because films have been fabricated with losses less than 1 dB/cm (17, 18). Postthermal oxidation of sputtered β-tantalum metal and reactive rf sputtering techniques have been used to produce low loss Ta_2O_5 waveguides. Reactive rf sputtering was used to fabricate the films used in this study. An rf-diode (Materials Research Corp.) system using a power density of 1 W/cm^2, with a 5:1 ratio of argon to oxygen at 14 mTorr, deposited Ta_2O_5 at a rate of approximately 40 Å/min. The SEM's in Figure 2 show a corrugated pattern on the surface of the thin film indicating that the grating was replicated on the surface of the film. Surface gratings have also been observed with Al_2O_3 films sputtered on grating substrates under similar conditions (19).

Thin Film Characterization. Initial estimates of the Ta_2O_5 film RI and thickness were obtained by measuring the interference fringes from a UV–vis transmission spectrum of the coated substrate (20). The estimated RI and thickness (RI = 0.5 μm) were then used in a BASIC program (MODCHART, Kern International Inc.) that solves eq 1, the eigenvalue equation, to obtain the film mode angles for a specific wavelength (6)

$$K_2 t_2 - \tan^{-1}(K_3/K_2) - \tan^{-1}(K_1/K_2) = m\pi \quad (1)$$

$$K_i = U_i = |\beta^2 - k_0^2 n_i^2|^{1/2} \text{ TE modes} \quad (2)$$

$$K_i = U_i/n_i^2 \text{ TM modes} \quad (3)$$

$$\beta = k_o n_2 \sin\theta_2 \quad (4)$$

where t_2 is the film thickness, m is the mode order (0, ±1, ±2, ...), k_0 is the free space wave vector which is equal to $2\pi/\lambda$, n_i is the RI of region 1, 2, or 3 in Figure 1, β is the propagation constant, and θ_2 is the angle of the mode in the film (Figure 1).

The estimated coupling angles were calculated by the guided-wave grating equation

$$\beta = k_0 n_0 \sin\theta_0 + \frac{p2\pi}{\Lambda} \quad (5)$$

where n_0 is the RI of air, θ_0 is the incident angle in air, p is the

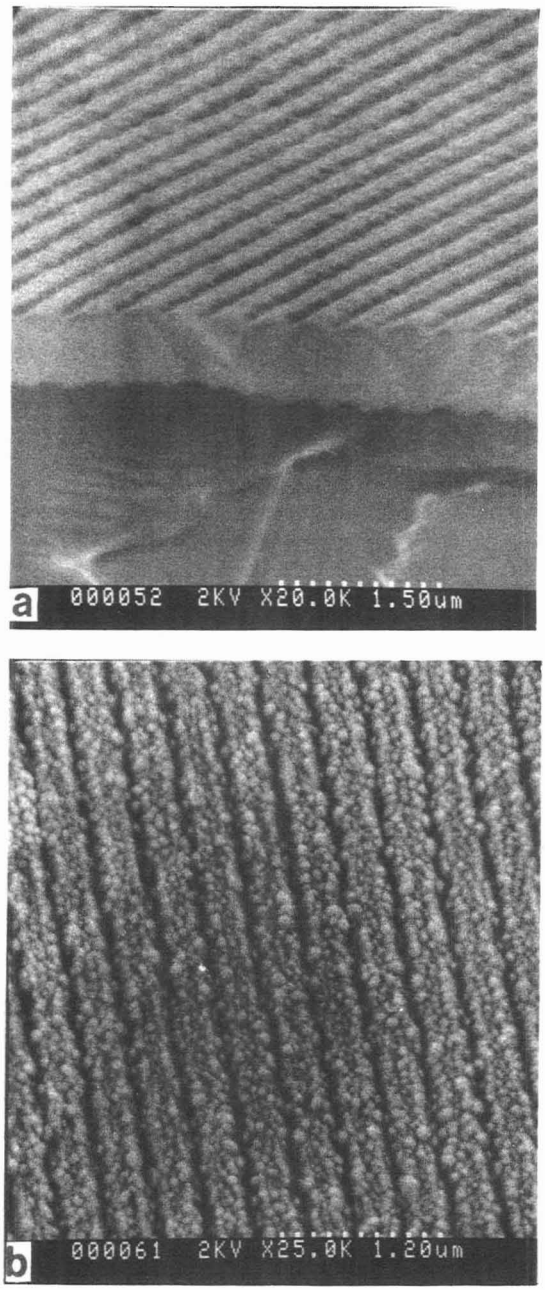

Figure 2. Scanning electron micrograph of (a) grating and thin film cross section and (b) surface of Ta_2O_5 film.

diffraction order (±1, ±2, ...), Λ is the grating period, and β is the propagation constant determined by eqs 1–3. The waveguide was set up as shown in Figure 3 to determine the actual coupling angles. The thin film waveguide sensor was mounted on a rotation stage (Model 471, Newport Corp.). Coupling angles were measured by approximating zero, or normal incidence, as the coincidence of the incident and reflected beams and then rotating until coupling was observed. The approximation of normal incidence limited the angular resolution to approximately ±1 arc min. A translation stage (Model 420, Newport Corp.) was used to adjust the input beam to the leading edge of the grating and a lab jack (Model 270, Newport Corp.) provided vertical movement to select different portions of the waveguide for measurement. Output from a 4-mW 500:1 polarized HeNe laser (Model 1104P, Uniphase, Inc.) was coupled into the waveguide. The collimated beam was used unless noted otherwise.

Grating coupling was found to be greatly superior to prism coupling in the ease with which mode angles can be found. Finding a mode involves simply rotating the waveguide and keeping the input beam on the leading edge of the grating. The modes and angles for the waveguide used in this study are shown in Table I along with the number of reflections per centimeter for each mode. The number of reflections was calculated by taking into account the Goos–Hanchen shift that occurs for each reflection (*21*).

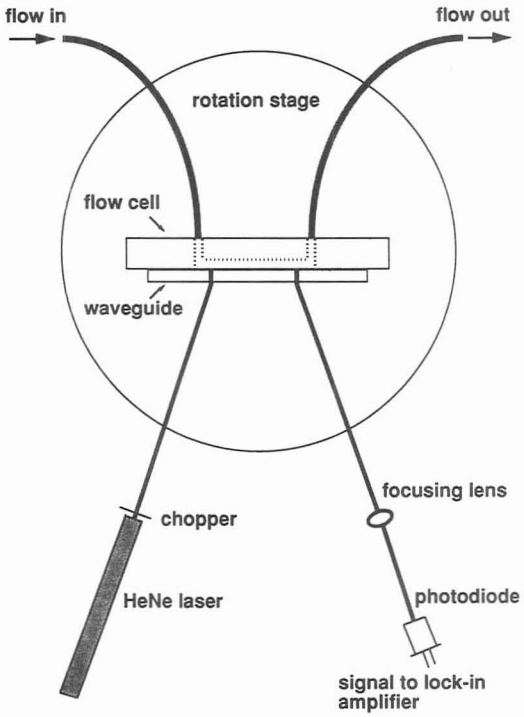

Figure 3. Instrumentation for thin film waveguide sensor measurements.

Table I. Modes and Angles (deg) for the Tantalum Pentoxide Waveguide

mode	coupling angle (θ_0)	film angle (θ_2)	reflections/cm
TE_0	19.333	76.555	1780
TE_1	9.333	63.027	3620
TM_0	18.417	74.864	2230
TM_1	5.583	59.312	4420

After the coupling angles were determined, a more accurate estimate of the waveguide RI and thickness was obtained by iteratively solving eq 1 using two different modes (*22*). A Fortran program was written for this purpose. The two TM modes yield a thin film RI of 2.0754 and thickness of 0.530 μm while the two TE modes yield an RI of 2.0734 and thickness of 0.539 μm. The difference in RI between the two modes is greater than the ±0.0005 error in the film RI introduced by the ±1 arc min angle precision. A slight birefringence, which has previously been observed in Ta_2O_5 films (*18*), may account for the difference. With these parameters a second order mode (TE_2 or TM_2) is predicted to be allowed but very near cutoff. Because the TE_2 and TM_2 modes were never observed, we assume that the calculated RI and/or thickness of the film are slightly in error.

Thin film attenuation due to absorption and scattering was measured by moving a fiber optic (High numerical aperture (NA) 400 μm diameter HCS fiber, Ensign Bickford) along the scattered streak of the guided wave. Decibels (dB) were calculated from

$$\mathrm{dB} = 10 \log (P_2/P_1) \quad (6)$$

with P_2 the intensity at some point along the waveguide and P_1 the intensity at the starting point (approximately 2 mm from the input grating). The slope of the linear attenuation curves ranged from 12 to 18 dB/cm depending upon the mode and portion of the film examined. The losses from the first-order modes were greater than the zero-order mode losses in all cases. Higher order modes often have increased losses due to surface scattering because the electric field (E-fold) is larger for these modes at the film interface (*23*). It has been shown that the primary loss mechanism in Ta_2O_5 films is scattering at the dielectric interfaces (*18*) and judging by the high degree of surface roughness shown in Figure 2b, this is probably an important factor. The SEM's show a large variability in film thickness which can also lead to high losses.

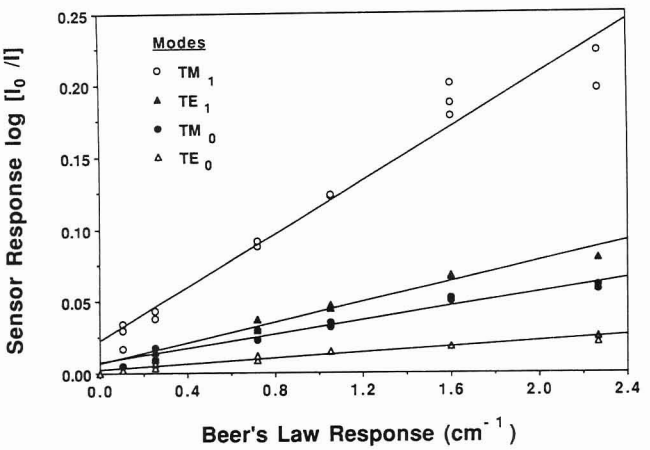

Figure 4. Absorbance response of thin film waveguide sensor for different modes and polarizations versus the Beer's law response obtained with a UV–vis spectrophotometer.

Film quality was shown to be quite sensitive to small changes in oxygen content, sputtering pressure, and gas flow rate (*17*). Since the film used in this study was fabricated, we have improved the control of these parameters and reduced losses to approximately 5 dB/cm.

Additional studies included ESCA (electron spectroscopy for chemical analysis) scans of the waveguide surface which indicated a chemical shift characteristic of Ta_2O_5. Surface contact angles with H_2O were larger than expected for a metal oxide surface, although surface roughness can cause a large increase in contact angle compared to a smooth surface (*24*). A Ta_2O_5 thin film deposited on a substrate without gratings was tested for resistance to various concentrated acids. Using prism couplers, no changes in waveguide propagation angles were observed after immersing the waveguide for 10 min in 10 M HCl, HNO_3, and H_2SO_4.

Sample Measurements. In order to evaluate the thin film waveguide response to solution absorbance and refrative index, a flow cell was fixed over the waveguide surface as shown in Figure 3. The flow channel was approximately 1.2 cm long and 0.3 cm wide to ensure that the gasket did not contact the film in the waveguiding region. The flow cell gasket was made from silicone rubber (PS2061, Petrarch, Inc.). Samples were introduced over the sensor using a peristaltic pump (Mino-S 860, Isco, Inc.).

Light from the outcoupling grating was focused onto a photodiode detector (DF-633, EG&G Photon Devices). The input beam was mechanically chopped at 200 Hz and the detector output was processed by a lock-in amplifier (SR530, Stanford Research Systems, Inc.). The time constant was set at 1 s. Laser signal-to-noise (S/N) and intensity drift measured with this equipment were approximately 700 and ±1.5% per hour, respectively.

Total system throughput was 0.17% of the incident beam intensity for the TE_0 mode measured with a power meter (22XLC, Photodyne, Inc.). The low throughput is a combination of film losses and poor grating incoupling efficient (estimated to be less than 10%). An order of magnitude improvement in throughput could be achieved by reducing film loss to 1 dB/cm. Grating efficiency may be improved by empirically optimizing groove depth and profile (*25*).

All sample RI's were measured with an Abbe refractometer (Bausch and Lomb) calibrated with RI standards (±0.0002 RI units) (R.P. Cargille Laboratories).

RESULTS AND DISCUSSION

The absorbance responses of the thin film waveguide sensor using the two different modes and polarizations are shown in Figure 4. The data represent the sensor's full response at 632.8 nm with an absorbing dye flowing over the surface. Concentrations of bromothymol blue (BTB) (Aldrich Chemical) ranging from 4×10^{-6} to 1×10^{-4} M in pH 8.02 phosphate buffer were used as the test solutions. A blank correction was applied by measuring I_0 with only buffer (no dye present) flowing over the waveguide surface. The stream was then switched to buffer containing various concentrations of the dye to obtain I. The sensor response is plotted versus Beer's law response obtained from a conventional UV–vis spectrophotometer (Model 3840, Perkin-Elmer Corp.). The ratio of the sensor response to the Beer's law response (the slope of the lines) gives the effective path length that can be compared to theoretical values. The slopes and other curve statistics are shown in Table II.

Table II. Experimental and Theoretical Absorbance Response of the Tantalum Pentoxide Thin Film Waveguide Sensor Reported as the Path Length Equivalent to a Transmission Measurement

	experimental values (Figure 4)			
mode	corr coef	y int ($\times 10^{-2}$)	slope, cm	theory, cm
TE_0	0.9799	0.243	0.0110	0.0095
TE_1	0.9841	0.759	0.0357	0.0484
TM_0	0.9815	0.537	0.0273	0.0198
TM_1	0.9860	1.90	0.0969	0.1080

Table III. Analytical Performance of the Thin Film Waveguide Sensor (LOD Calculated from 3 × Root Mean Square Noise)

mode	LOD (AU × 10^{-3})	LOD (M × 10^{-6})
TE_0	1.7	6.9
TE_1	1.7	2.1
TM_0	1.9	3.1
TM_1	2.6	1.2

The TM_1 mode exhibits nearly 10% of the absorbance sensitivity of a 1 cm transmission measurement; thus, the sensor has an effective path length of approximately 1 mm. The TM_1 mode is more sensitive than the other modes due to the larger number of reflections and the higher E_0 present at the Ta_2O_5/solution interface (normal component of the incident polarized beam) (*26*). The expected response, based on integration of the square of the E-field (evanescent field) in the outer solution (*27*) is also reported in Table II. The theoretical values were normalized to 1 W/unit width of waveguide. Theory and experiment match very well considering the many parameters that are required to make the theoretical calculations (i.e., film RI and thickness, substrate RI, sample RI and grating period). Other researchers found that theory underestimated their waveguide response because surface adsorption concentrated the dye at the waveguide surface (*3*). The rapid response and reproducible baseline of the Ta_2O_5 waveguide sensor indicated that the BTB was not adhering to the surface, and the theoretical response supports these observations.

Table III summarizes the analytical performance of the thin film waveguide sensor. Limit of detection (LOD) was calculated by using 3 times root mean square noise over a set time period. Laser intensity fluctuations were the primary source of noise although the TM_1 mode proved to be sensitive to flow variations and had a slightly higher LOD. Concentration LOD's calculated from Figure 4 and using the BTB molar absorptivity ($\epsilon = 2.24 \times 10^4$ M^{-1} cm^{-1} at pH 8.02 and $\lambda = 632.8$ nm) are also shown in Table III. Stray light levels were approximately 0.5% which limits the dynamic range to 2 AU, although this was not tested. Each measurement was repeated at least once for each concentration and these data are also plotted in Figure 4. It is believed the flow cell gasket allowed diffusion of the absorbing solution around the edges, which limited the precision of these measurements, particularly at the higher dye concentrations. Five earlier replicate measurements at a single concentration (7×10^{-5} M BTB) using the TM_1 mode indicated that a reproducibility of ±2.7% (±0.004 AU) could be achieved. The sensor full response was achieved in less than 30 s and is limited by the flow cell dead volume, not the dynamics of the sensor itself.

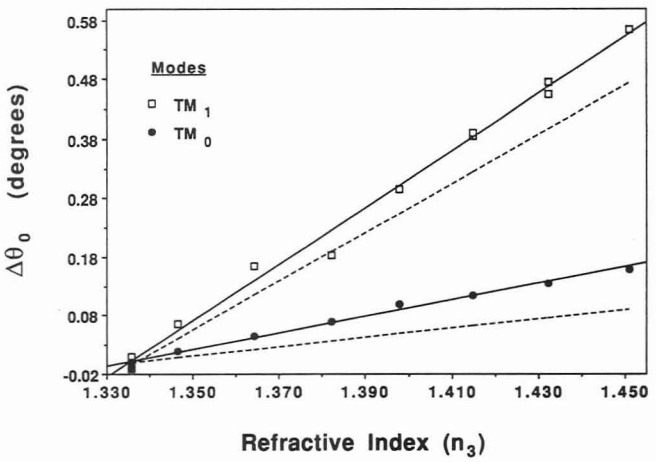

Figure 5. Experimental and theoretical (dashed line) changes in coupling angle measured for different RI solutions (glycerol in water) for the TM modes.

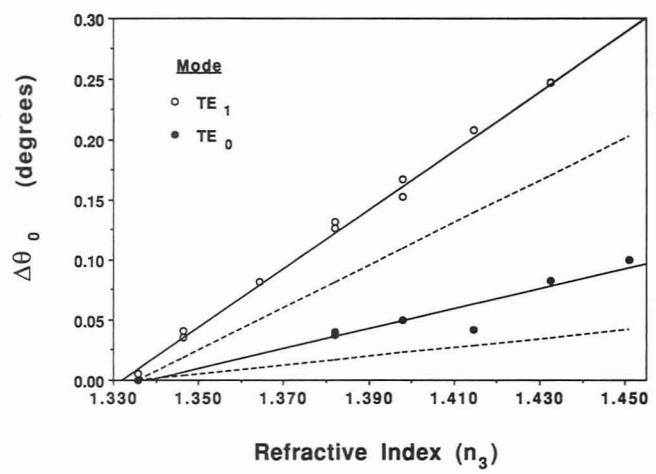

Figure 6. Experimental and theoretical (dashed line) changes in coupling angle measured for different RI solutions (glycerol in water) for the TE modes.

In the optical waveguide system described above, signal attenuation may be caused not only by evanescent absorbance but also by RI changes in the sample. At least three effects can modulate the light intensity as a function of changing RI in the sample layer. The first is a change in the surface grating input and output contributions as a function of changing reflectivity at the surface grating/sample interface. A second effect is a change in the amount of surface scatter, which will vary as the RI difference between the waveguide and sample varies. And finally, the presence of the superstrate RI, n_3, in eqs 2 and 3 indicates that the propagation angle will vary with changes in the sample RI.

To test the magnitude of these effects, samples ranging in RI from 1.3355 to 1.4507 were prepared by mixing glycerol (RI = 1.4746) with deionized water (RI = 1.332). Each sample was pumped through the flow cell and the angle was manually returned to give the maximum intensity. The change in coupling angle (θ_0) is shown for the TM and TE modes in Figures 5 and 6. The TM_1 mode undergoes the largest angle change and the TE_0 mode the least, in the same order as the response to absorbing solutions. The coupling angle increased with increasing RI for all modes. The TM_1 mode is sensitive to a 3×10^{-4} change in RI, calculated from Figure 5, assuming a ±12 arc sec resolution of the intensity peak. Theoretical curves, calculated by changing n_3 in eqs 2 and 3, are shown as dashed lines in Figures 5 and 6. The coupling angle sensitivity to RI is greater than that predicted by theory for all modes. This may be due to glycerol concentrating at the interface, although large deviations in the theoretical slope

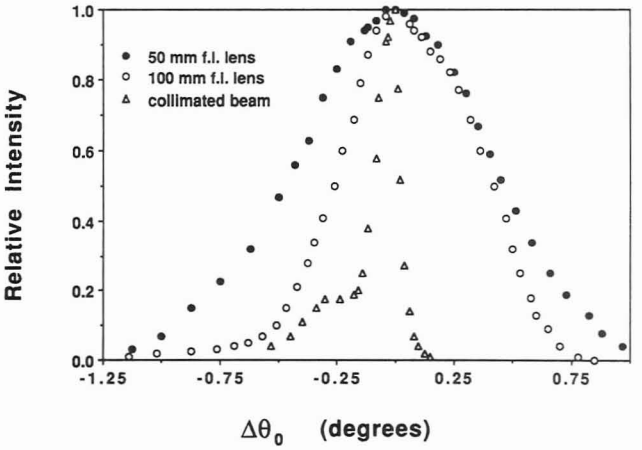

Figure 7. Intensity versus launch angle with collimated and focused input beams (TE_0 mode).

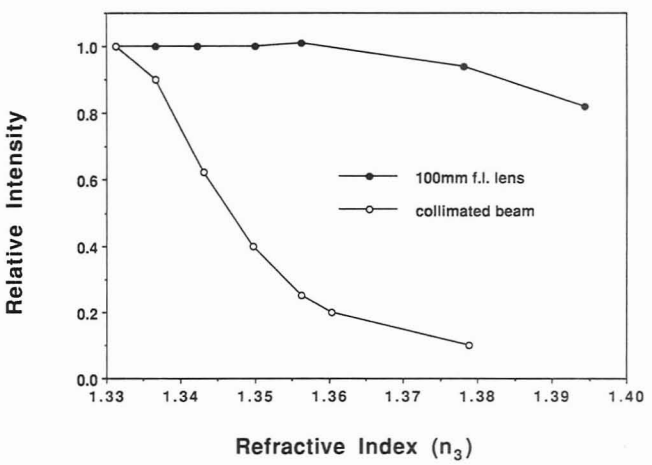

Figure 8. Response to different RI solutions (glycerol in water) for 100 mm focal length lens and a collimated beam (TE_1 mode).

may occur solely because of the ±60 Å error in the measured grating period. In order to minimize the error introduced by the grating period in the calculations, the grating period must be known to within 10 Å.

The surface grating coupling efficiency is dependent upon n_3 (*28*) so changes in n_3 would modulate the output intensity if the surface grating was also coupling light into the waveguide. It was noted that after returning the waveguide to the new coupling angle, the total light throughput remained approximately the same. This is a good indication that the grating present on the top of the film did not greatly influence the response of the sensor.

We discovered that by focusing the input beam at the incoupling grating, and thus providing a range of incident angles on the grating to accommodate small changes in resonance coupling conditions for a given allowed mode, intensity changes can be reduced over a wide range of sample RIs. Figure 7 shows how different focal length lenses change the outcoupled intensity distribution as one changes input angle or the TE_0 mode. The shoulder on the intensity profile using the collimated input beam is a result of nonuniform film thickness. The responses due to changes in sample RI are shown in Figure 8 for both collimated and focused input beams. The response with a focused beam initially shows a slight increase in intensity which may be due to decreased scattering at the interface as n_3 increases (*23*). Nonetheless, sensitivity to RI is greatly diminished versus the collimated beam response.

Although intensity changes due to variations in sample RI are reduced by focusing the input beam, the absorbance response is still dependent upon sample RI because the eva-

nescent field intensity changes and alters the effective path length of the sensor. We did not measure the magnitude of this effect, but theoretical calculations (*27*) indicate that variations in RI up to ±0.1 do not significantly change the sensor response.

The properties of the thin film, both in the bulk and on the surface, affect propagation; therefore, it was important to determine if the film had any chemical interactions with the sample. Ionic strength and pH effects have been reported previously for a SiO_2–TiO_2 thin film waveguide (*29*). We tested the TA_2O_5 waveguide with different ionic strength solutions (1.1–7.2 M NaCl and 1.2–5.9 M NH_4CL) and different pH solutions (5.8–8.0 phosphate buffer). In all cases, the response of the waveguide coincided with the experimental curves in Figures 5 and 6, showing strictly a RI response with no additional effects due to interactions on the surface or within the bulk of the film. In addition, the response times were the same as those for the glycerol samples, slower responses would be expected if chemical reactions or ion exchange was taking place.

It should be noted that a dilute surfactant (Triton-X, Sigma Chemical) (0.1 vol %) in a pH 8 buffer caused angle changes (TE_1 mode) opposite of that expected for the bulk solution RI measured by an Abbe refractometer. In addition, the uncharacteristic slow return to baseline indicated that the surfactant had a strong affinity for the surface. Absorbing analytes with similar surface interactions would concentrate at the waveguide surface, resulting in an analytical response that is not a direct representation of the bulk concentration. Surface derivitization using silane reagents and/or polymers may be used to deactivate the structure in some cases.

CONCLUSIONS

Typical internal reflection elements, with light propagating at angles similar to the angles in the Ta_2O_5 thin film waveguide, may have a total number of reflections ranging from 10 to 100. Thin films have from 1 to 3 orders of magnitude more reflections as noted in Table I, and consequently, 1–3 orders of magnitude more sensitivity. The buried gratings permit integration of the couplers into the sensor and this has proven to be a significant practical improvement over prism coupling. The buried gratings make coupling light into the film as straightforward as coupling into conventional IREs.

An important difference from ATR is that both the propagation angle and coupling angle depend upon wavelength. Polychromatic light must be input over a wide angular range and each wavelength will have different effective path lengths in the sample. The effective path length dependence on wavelength encountered in ATR may be exacerbated with thin film wavegides because the angle of incidence is smaller for longer wavelengths. Both of these conditions result in greater effective path lengths. Determining the broad band response of the thin film waveguide sensor is presently an active area of research in our lab.

ACKNOWLEDGMENT

Sincere thanks to Dave Tracy of Perkin-Elmer Corporation for aiding with the theoretical calculations.

LITERATURE CITED

(1) Midwinter, J. E. *IEEE J. Qauntum Electron*. **1971**, *QE-7* (7), 339.
(2) Midwinter, J. E. *IEEE J. Quantum Electron*. **1971**, *QE-7* (7), 345.
(3) Polky, J. N.; Harris, J. H. *J. Opt. Soc. Am*. **1972**, *62* (9), 1081.
(4) Bohn, P. W. *Prog. Anal. Spectrosc*. **1989**, *12*, 41.
(5) Rabolt, J. F.; Santo, R.; Swalen, J. D. *Appl. Spectrosc*. **1979**, *33*, 549.
(6) Bohn, P. W. *Anal. Chem*. **1985**, *57* (7), 1203.
(7) Stephens, D. A.; Bohn, P. W. *Anal. Chem*. **1987**, *59* (21), 2563.
(8) Ives, J. T.; Reichert, W. M. *Appl. Spectrosc*. **1988**, *42* (1), 68.
(9) Hutchinson, R. J. *Anal. Proc*. **1987**, *24*, 213.
(10) DeGrandpre, M. D.; Burgess, L. W. *Anal. Chem*. **1988**, *60* (23), 2582.
(11) Swalen, J. D.; Santo, R.; Tacke, M.; Fischer, J. *IBM J. Res. Dev*. **1977**, *21*, 168.
(12) Mitchell, G. L. *IEEE J. Quantum Electron*. **1977**, *QE-13* (4), 173.
(13) Choquette, S. J. Ph.D. Thesis, Virginia Polytechnic Institute and State University, 1988.
(14) Lukosz, W.; Tiefenthaler, K. *Sens. Actuators* **1988**, *15*, 273.
(15) Moshrezadeh, R.; Mai, X.; Seaton, C. T.; Stegeman, G. I. *Appl. Opt*. **1987**, *26* (13), 2501.
(16) Lehmann, H. W.; Widmer, R. *Appl. Phys. Lett*. **1978**, *32* (3), 163.
(17) Davis, R. L.; Hickernell, F. S. SPIE vol. 408, Integrated Optics III (1983), 27.
(18) Hensler, D. H.; Cuthbert, J. D.; Martin, R. J.; Tien, P. K. *Appl. Opt*. **1971**, *10* (5), 1037.
(19) Chen, B. U.; Ghizoni, C. C.; Tang, C. L. *Appl. Phys. Lett*. **1976**, *28* (11), 651.
(20) Manifacier, J. C.; Gasiot, J.; Fellard, J. P. *J. Phys. E: Sci. Instrum*. **1976**, *9*, 1002.
(21) Kogelnik, H. In *Integrated Optics*; Tamir, T., Ed.; Springer-Verlag: New York, 1979; Vol. 7, pp 26–27.
(22) Ulrich, R.; Torge, R. *Appl. Opt*. **1973**, *12* (12), 2901.
(23) Zernike, F. In *Integrated Optics*; Tamir, T., Ed.; Springer-Verlag: New York, 1979; Vol. 7, p 217.
(24) Adam, N. K. In *Advances in Chemistry Series*; Gould, R. F., Ed.; American Chemical Society: Washington, DC, 1964; Vol. 43, p 55.
(25) Tamir, T. In *Integrated Optics*; Tamir, T., Ed.; Springer-Verlag: New York, 1979; Vol. 7, p 113.
(26) Harrick, N. J. *Internal Reflection Spectroscopy*; Harrick Scientific Corporation: New York, 1979.
(27) Heuberger, K.; Lukosz, W. *Appl. Opt*. **1986**, *25* (9), 1499.
(28) Taylor, H. F.; Yariv, A. *Proc. IEEE* **1974**, *62* (8), 1044.
(29) Spohn, P. K.; Seifert, M. *Sens. Actuators* **1988**, *15*, 309.

RECEIVED for review April 4, 1990. Accepted June 19, 1990. This work was supported by a grant from the NSF Center for Process Analytical Chemistry (Project Number 84-1). M.D. thanks the Department of Energy for a Science and Engineering Research Semester Fellowship.

Effect of Structural Variations within Lipophilic Dibenzocrown Ether Carboxylic Acids on the Selectivity and Efficiency of Competitive Alkali-Metal Cation Solvent Extraction into Chloroform

Wladyslaw Walkowiak,[1] Witold A. Charewicz,[1] Sang Ihn Kang, Il-Woo Yang,[2] Michael J. Pugia, and Richard A. Bartsch*

Department of Chemistry and Biochemistry, Texas Tech University, Lubbock, Texas 79409-1061

Competitive solvent extraction of alkali-metal cations from aqueous solutions into chloroform by a series of lipophilic dibenzocrown ethers with pendant carboxylic acid groups has been investigated. Both the extraction selectivity and efficiency are influenced by variations of the crown ether ring size and the attachment site of the lipophilic group. Preorganization of the binding site by proper positioning of the lipophilic group enhances extraction selectivity. Very high Na^+ extraction selectivity ($Na^+/K^+ = 32$, $Na^+/Li^+ = 66$ and no detectable extraction of Rb^+ or Cs^+) was obtained with *sym*-decyldibenzo-16-crown-5-oxyacetic acid.

INTRODUCTION

In his recent review of crown ethers as solvent extraction agents for metal ions, McDowell points out that when a proton-ionizable group is attached to the cyclic polyether framework, the molecule is both a cation exchanger and a coordinator (*1*). This arrangement has the potential for providing an extraction system with greater selectivity and efficiency than one in which an organophilic acid is simply mixed with a crown ether.

In earlier work (*2*, *3*), we examined competitive alkali-metal cation extraction from aqueous solutions into chloroform by dibenzocrown ether carboxylic acids **1**–**3**. It was found that these proton-ionizable ionophores were of insufficient lipophilicity to remain completely in the organic phase during extraction of alkali-metal cations from alkaline aqueous phases. To avoid such complications in extraction behavior, a lipophilic group was attached either to each benzene ring or to the carboxylic acid containing sidearm of the dibenzo-16-crown-5 compound **2** to produce the lipophilic dibenzo-16-crown-5-carboxylic acids **4** and **5**, respectively (*3*–*5*). Compounds **4** and **5** were found to be sufficiently lipophilic to remain completely in the chloroform phases even when the contacting aqueous solutions of alkali-metal cations were highly alkaline (*3*, *5*). Although the overall alkali-metal cation extraction behavior was similar for structural isomers **4** and **5**, the former gave enhanced Na^+/K^+ selectivity and excluded Li^+ from the chloroform phase (*5*). Hence the lipophilic group attachment site was found to exert some influence upon extraction behavior.

The efficiencies and selectivities of competitive alkali-metal cation extraction into toluene (*6*) and of alkali-metal cation transport across chloroform and toluene liquid membranes

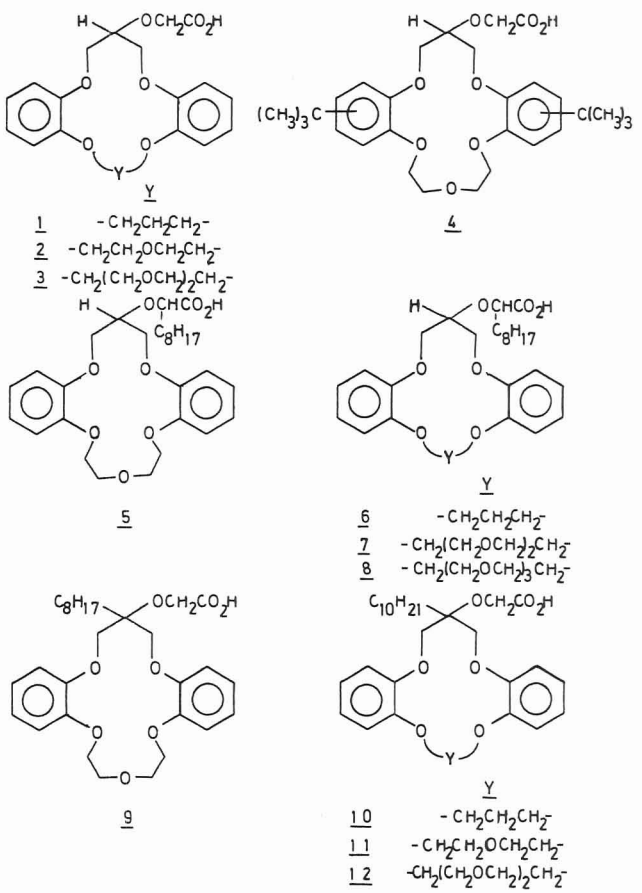

and liquid surfactant membranes by **4** and **5** were subsequently compared (*5*–*8*).

We now report results for solvent extraction of alkali-metal cations from aqueous solutions into chloroform by lipophilic dibenzocrown ether carboxylic acids **6**–**12**. By comparison of these results with those reported earlier for **4** and **5**, the influence of the crown ether ring size and the lipophilic group attachment site upon extraction selectivity and efficiency may be assessed.

EXPERIMENTAL SECTION

Reagents. Sources of inorganic reagents were the same as those reported previously (*2*, *3*, *6*, *7*). Demineralized water was prepared by passing distilled water through three Barnstead D8922 combination cartridges in series. Reagent grade chloroform was treated by shaking 4 times with demineralized water to remove the stabilizing ethanol and saturate the chloroform with water. Syntheses of lipophilic dibenzocrown ether carboxylic acids **6**–**9** have been reported (*9*).

Synthesis of Lipophilic Dibenzocrown Ether Carboxylic Acids 10–12. Under nitrogen 0.80 g (20 mmol) of NaH (60%

[1] Present address: Institute of Inorganic Chemistry and Metallurgy of Rare Elements, Technical University of Wroclaw, 50-370 Wroclaw, Poland.
[2] Present address: Department of Chemistry, Korea Military Academy, Seoul 130-09, Korea.

0003-2700/90/0362-2018$02.50/0

dispersion in mineral oil) was washed with dry pentane to remove the mineral oil and was suspended in 100 mL of dry THF. To the stirred mixture, 10.0 mmol of the appropriate crown ether alcohol **13–15** (*10*) in 25 mL of dry THF was added during 15 min. The mixture was stirred for 1 h and a solution of 2.30 g (15 mmol) of methyl bromoacetate in 25 mL of dry THF was added dropwise. The mixture was stirred for 3 days at room temperature and cooled in an ice bath, and water (25 mL) was added slowly. The solution was acidified to pH = 1 with 6 N HCl and stirred for 2 h at room temperature. The THF was evaporated in vacuo and the acidic aqueous mixture was extracted with CH_2Cl_2. The combined CH_2Cl_2 extracts were washed with water (two 100-mL portions), dried over $MgSO_4$, and evaporated in vacuo to give a crude product which was chromatographed on deactivated silica gel with EtOAc as eluent to give the lipophilic dibenzocrown ether methyl ester.

The methyl ester was refluxed with 0.75 g of NaOH in 25 mL of water under nitrogen for 4 h. The solution was cooled to 0 °C and acidified to pH = 1 with 6 N HCl. Extraction with CH_2Cl_2 (three 50-mL portions), washing with water (50 mL), drying over $MgSO_4$, evaporation in vacuo, and chromatography of the residue on deactivated silica gel with EtOAc–EtOH (10:1) as eluent gave the lipophilic dibenzocrown ether carboxylic acid.

Methyl *sym*-decyldibenzo-14-crown-4-oxyacetate (**16**) was obtained in 65% yield as an oil. IR (neat): 1762 (C=O), 1110 (C—O) cm^{-1}. ^1H NMR ($CDCl_3$): δ 0.80–1.80 (m, 21 H), 2.20 (m, 2 H), 3.50–4.80 (m, 13 H), 6.90 (s, 8 H). MS: 518.6 (M^+). Hydrolysis gave *sym*-decyldibenzo-14-crown-4-oxyacetic acid (**10**) in 60% yield as a white solid with mp 117–119 °C. IR (KBr): 3600–2650 (COOH), 1733 (C=O); 1255, 1110 (C—O) cm^{-1}. ^1H NMR ($CDCl_3$): 0.80–1.30 (m, 21 H), 2.20 (m, 2 H), 3.60–4.40 (m, 10 H), 5.60 (br s, 1 H), 6.95 (s, 8 H). Anal. Calcd for $C_{30}H_{32}O_7 \cdot 0.5H_2O$: C, 68.80; H, 8.27. Found: C, 68.97; H, 7.93.

Methyl *sym*-decyldibenzo-16-crown-5-oxyacetate (**17**) was obtained in 79% yield as a white solid with mp 52–53 °C. IR (deposit on NaCl plate): 1760 (C=O), 1250, 1110 (C—O) cm^{-1}. ^1H NMR ($CDCl_3$): δ 0.80–2.00 (m, 21 H), 3.65 (s, 3 H), 3.70–4.95 (m, 14 H), 6.93 (s, 8 H). MS: 558.6 (M^+). Hydrolysis gave *sym*-decyldibenzo-16-crown-5-oxyacetic acid (**11**) in 61% yield as a white solid with mp 102–102.5 °C. IR (KBr): 3630–2280 (COOH), 1776, 1740 (C=O), 1120 (C—O) cm^{-1}. ^1H NMR ($CDCl_3$): δ 0.80 (t, 3 H), 1.20–1.45 (m, 16 H), 1.85–1.90 (m, 2 H), 3.55–5.00 (m, 14 H), 6.70–6.95 (m, 8 H). Anal. Calcd for $C_{31}H_{44}O_8$: C, 68.36; H, 8.14. Found: C, 68.07; H, 8.15.

Methyl *sym*-decyldibenzo-19-crown-6-oxyacetate (**18**) was obtained in 82% yield as a colorless oil. IR (neat): 1753, 1747 (C=O), 1255, 1113 (C—O) cm^{-1}. ^1H NMR ($CDCl_3$): δ 0.80–2.00 (m, 21 H), 3.70 (S, 3 H), 3.75–4.65 (m, 18 H), 6.95 (s, 8 H). MS: 602.7 (M^+). Hydrolysis gave *sym*-decyldibenzo-19-crown-6-oxyacetic acid (**12**) in 69% yield as a colorless oil. IR (neat): 3600–2525 (COOH), 1782 (C=O), 1252, 1120 (C—O). ^1H NMR ($CDCl_3$): δ 0.80–1.90 (m, 21 H), 3.50–4.70 (m, 18 H), 6.00 (br s, 1 H), 6.95 (s, 8 H). Anal. Calcd for $C_{33}H_{48}O_9$: C, 67.32; H, 8.22. Found: C, 68.98; H, 8.03.

Apparatus. Concentrations of alkali-metal cations in aqueous phases were determined with Dionex Model 10 and Model 2000 ion chromatographs. Organic complexing agent concentrations in the chloroform phases were measured with Cary Model 17 and Shimadzu Model 260 ultraviolet–visible spectrophotometers. A Fisher Scientific Accumet Model 620 pH meter with a Corning No. 76050 or No. 476193 glass body combination electrode was used for the pH measurements. Solvent extraction samples in separatory funnels were shaken with a Burrell Model 25 wrist action shaker.

Extraction Procedure. An aqueous solution of the alkali-metal chlorides with hydroxides for pH adjustment (5.0 mL, 0.25 M in each) and a chloroform solution (5.0 mL of the complexing agent (0.050 M)) were shaken for 30 min in a 30-mL separatory funnel at room temperature. The 5.0-mL phases were separated and the equilibrium pH of the aqueous phase was measured. Of the organic phase, 4.0 mL was removed and shaken with 5.0 mL of 0.1 N HCl for 30 min to strip the metal cations from the organic phase into an aqueous solution for analysis by ion chromatography. A small sample (10–20 μL) of the stripped organic phase was removed and diluted with $CHCl_3$ in a 10-mL volumetric flask and the absorption was measured at 273–274 nm to determine the concentration of the complexing agent in the chloroform layer.

Table I. Diameters of Crown Ether Cavities[a] and Alkali-Metal Cations[b] in Angstroms

crown ether	cavity diameter	alkali-metal cation	diameter
14-crown-4	1.2–1.5	Li^+	1.20
16-crown-5	2.0–2.4	Na^+	1.90
19-crown-6	3.0–3.5	K^+	2.66
22-crown-7	4.7–5.0	Rb^+	2.96
		Cs^+	3.38

[a] Estimated from CPK space-filling models. [b] Reference 11.

With this procedure, identical results for alkali-metal cation solvent extraction into chloroform by crown ether carboxylic acid **9** were obtained by three different co-workers during a two-year period.

RESULTS AND DISCUSSION

Synthesis of Lipophilic Dibenzocrown Carboxylic Acids 10–12. Three new lipophilic dibenzocrown ether carboxylic acids **10–12** were prepared by two-step reactions from the corresponding lipophilic crown ether alcohols **13–15** as shown in eq 1.

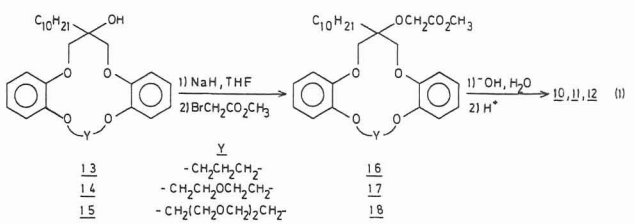

Solvent Extraction of Alkali-Metal Cations from Aqueous Solution into Chloroform by Lipophilic Dibenzocrown Ether Carboxylic Acids. In a previous investigation of alkali-metal cation extraction into chloroform by crown carboxylic acid **2**, it was found that selectivity orders and efficiencies for competitive extractions in multi-ion systems were quite different from expectations based upon the results of single ion extractions (*2*). Therefore, competitive extractions were utilized in this investigation.

For lipophilic dibenzocrown ether carboxylic acids **6–12**, there was no detectable loss of the ionophore from the chloroform phases during extraction (Figures 1–3, filled squares). Thus attachment of an octyl or a decyl group to the sidearm (in **6–8**) or polyether framework (in **9–12**) of dibenzocrown ethers **1–3** provided sufficient lipophilicity.

Effect of Ring Size Variation for Dibenzocrown Ethers with an Octyl Group Attached to the Sidearm. Ionophores **6**, **5**, **7**, and **8** are a series of dibenzocrown ethers in which the sidearm contains both the carboxylic acid function and the lipophilic group, but have different crown ether ring sizes of 14-crown-4, 16-crown-5, 19-crown-6, and 22-crown-7, respectively. Crown ether cavity diameters as estimated from Corey–Pauling–Koltun (CPK) space-filling models are compared with diameters of the alkali-metal cations in Table I.

For competitive solvent extractions of aqueous alkali-metal cation (0.25 M in each) solutions by 0.050 M lipophilic dibenzocrown ether carboxylic acids **6–8** in chloroform, data for the metals concentrations in the chloroform phase vs the equilibrium pH of the aqueous phase are shown in Figure 1. Extraction selectivity orders and selectivity coefficients and maximal metals loadings for **6–8** are compared with that reported previously for **5** (*4*) in Table II. (The selectivity coefficient is the ratio between the organic phase concentrations of the best extracted cation and the indicated cations at pH = 10.0. The percent metals loading of the chloroform phase was calculated by assuming that a 1:1 metal ion to crown

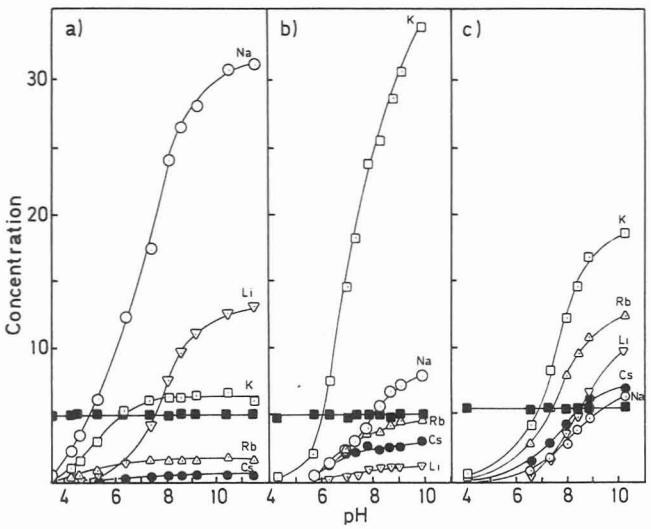

Figure 1. Molar concentrations of metals ($\times 10^3$) in the chloroform phase vs the equilibrium pH of the aqueous phase for competitive extraction of 0.25 M alkali-metal cations by 0.050 M (a) **6**, (b) **7**, and (c) **8**. Molar chloroform-phase complexing agent concentrations ($\times 10^2$) are shown as solid squares.

Table II. Effect of Crown Ether Ring Size Variation on Selectivity and Efficiency of Competitive Alkali-Metal Cation Extraction from Aqueous Solutions into Chloroform by Lipophilic Dibenzocrown Ether Carboxylic Acids 5–8

compound	ring size	selectivity order and selectivity coefficients[a,b]	maximal metal loading, %
6	14C4	$Na^+ > Li^+ > K^+ > Rb^+ > Cs^+$ (2.5, 5, 19, 60)	100
5[c]	16C5	$Na^+ > K^+ > Li^+ > Rb^+ > Cs^+$ (5, 17, 36, 83)	68
7	19C6	$K^+ > Na^+ > Rb^+ > Cs^+ > Li^+$ (4, 7, 11, 28)	100
8	22C7	$K^+ > Rb^+ > Li^+ > Cs^+ > Na^+$ (1.5, 1.9, 2.8, 3.0)	100

[a] Ratio of chloroform phase concentrations of best extracted metal ion and indicated metal ion. [b] At pH = 10.0. [c] Data from ref 4.

carboxylate extraction complex is formed.)

The lipophilic dibenzocrown ether carboxylic acids **5** and **7** exhibit extraction selectivities for Na^+ and K^+, respectively, as would be predicted from the relationship between the crown ether ring and metal ion diameters (Table I). On the other hand, ionophore **6**, which has a dibenzo-14-crown-4 unit, is selective for Na^+ rather than Li^+ which would be predicted for the ring size. The quantitative metals loading calculated for **6** based upon a 1:1 metal ion to crown carboxylate extraction complex differs markedly from the 1:2 metal to ligand stoichiometries which have been reported for extraction of Na^+, K^+, and Rb^+ as single ion species into chloroform by an analogue of **6** in which the lipophilic group was butyl instead of octyl (*12*). Only for Li^+ was a 1:1 extraction complex observed in this earlier report (*12*).

If the polyether ring were planar, the lipophilic dibenzo-22-crown-7 carboxylic acid **8** would have a very large crown ether cavity. The very poor selectivity observed for **8** compared with **5**–**7** suggests that the polyether ring is not planar but provides three-dimensional "wrap-around" complexation of alkali-metal cations.

Effect of Varying the Lipophilic Group Attachment Site for Dibenzo-16-crown-5-carboxylic Acids. Lipophilic dibenzocrown ether carboxylic acids **4**, **5**, and **9** are structural isomers which differ only in the attachment site(s) of the lipophilic group(s). Data for the competitive solvent extraction of alkali-metal cations from aqueous solutions into chloroform by **9** are presented in Figure 2. The selectivity order, selectivity coefficients, and maximal metals loading for **9** are compared with reported data for **4** (*6*) and **5** (*4*) in Table III.

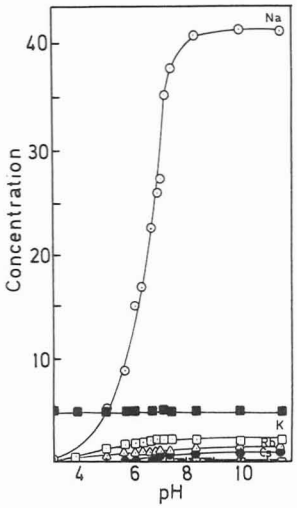

Figure 2. Molar concentrations of metals ($\times 10^3$) in the chloroform phase vs the equilibrium pH of the aqueous phase for competitive extractions of 0.25 M alkali-metal cations by 0.050 M **9**. Molar chloroform-phase complexing agent concentrations ($\times 10^2$) are shown as solid squares.

Table III. Effect of Lipophilic Group Attachment Site on Selectivity and Efficiency of Competitive Alkali-Metal Cation Extraction from Aqueous Solutions into Chloroform by Lipophilic Dibenzo-16-crown-5-oxyacetic Acids 4, 5, and 9

compound	selectivity order and selectivity coefficients[a]	maximal metals loadings, %
4[b]	$Na^+ > K^+ > Li^+ > Rb^+ > Cs^+$ (5, 10, 17, 30)	100
5[c]	$Na^+ > K^+ > Li^+ > Rb^+ > Cs^+$ (5, 17, 36, 83)	68
9	$Na^+ > K^+ > Rb^+ > Cs^+ > Li^+$ (27, 51, 67, 90)	93

[a] At pH = 10.0. [b] Data from ref 6. [c] Data from ref 4.

Although all three lipophilic dibenzo-16-crown-5-oxyacetic acids **4**, **5**, and **9** are selective for Na^+, the selectivity coefficients for **9** are much larger than those for **4** or **5**. Thus the Na^+ selectivity of the lipophilic dibenzo-16-crown-5-carboxylic acid is found to be much higher when the lipophilic group is attached to the same polyether ring carbon as the sidearm (in **9**) than when lipophilicity is incorporated into the benzo groups (in **4**) or the sidearm (in **5**). Examination of CPK space-filling models reveals that when the octyl group in **9** points away from the polar polyether ring, the carboxylic acid group on the sidearm is positioned directly over the crown ether cavity. Hence, the much higher Na^+ selectivity of **9** is ascribed to preorganization of the binding site (*13*).

Effect of Ring Size Variation for Lipophilic Dibenzocrown Ether Carboxylic Acids with Preorganized Binding Sites. For the series of lipophilic dibenzocrown ether carboxylic acids **10**–**12**, the decyl groups are attached to the central carbon of the three-carbon bridge of the polyether ring which should orient the oxyacetic acid sidearm over the crown ether cavity. Hence with **10**–**12** the influence of ring size variation may be assessed for lipophilic dibenzocrown ether carboxylic acids with preorganized binding sites.

Results for the competitive solvent extraction of alkali-metal cations from aqueous solutions into chloroform by proton-

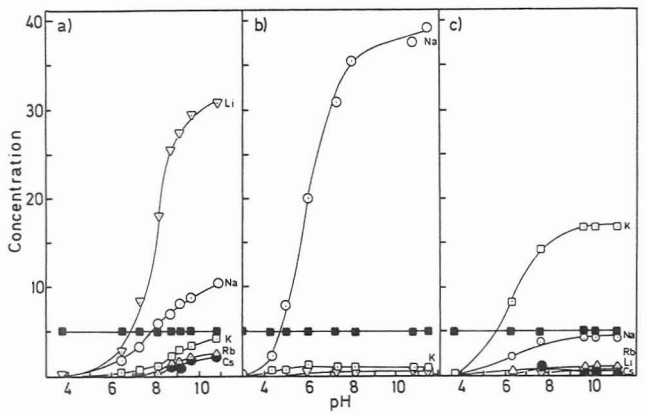

Figure 3. Molar concentrations of metals ($\times 10^3$) in the chloroform phase vs the equilibrium pH of the aqueous phase for competitive extractions of 0.25 M alkali-metal cations by 0.050 M (a) **10**, (b) **11**, and (c) **12**. Molar chloroform-phase complexing agent concentrations ($\times 10^2$) are shown as solid squares.

Table IV. Effect of Crown Ether Ring Size on Selectivity and Efficiency of Competitive Alkali-Metal Cation Extraction from Aqueous Solutions into Chloroform by Lipophilic Dibenzocrown Ether Carboxylic Acids 10–12

compound	ring size	selectivity order and selectivity coefficients[a]	maximal metals loadings, %
10	14C4	$Li^+ > Na^+ > K^+ > Rb^+ > Cs^+$ (3, 7, 12, 13)	100
11	16C5	$Na^+ > K^+ > Li^+ > Rb^+, Cs^+$ (32, 66, ND[b])	82
12	19C6	$K^+ > Na^+ > Rb^+ > Li^+ > Cs^+$ (4, 14, 21, 67)	48

[a] At pH = 10.0. [b] Not detected.

ionizable ionophores **10–12** are shown in Figure 3. Selectivity orders, selectivity coefficients, and maximal metals loadings are recorded in Table IV.

For lipophilic dibenzocrown ether carboxylic acids **10**, **11**, and **12**, the crown ether ring sizes are 14-crown-4, 16-crown-5, and 19-crown-9, respectively. Each of the three extractants exhibits good-to-excellent extraction selectivity for the alkali-metal cation which should fit best within the crown ether cavity (Tables I and IV).

The Li^+ selectivity obtained with the lipophilic dibenzo-14-crown-4-carboxylic acid **10** contrasts sharply with the Na^+ selectivity noted for the lipophilic dibenzo-14-crown-4-carboxylic acid **6**. Thus preorganization of the binding site by proper positioning of the lipophilic group is demonstrated not only to enhance the alkali-metal cation selectivity as noted earlier for lipophilic dibenzo-16-crown-5-carboxylic acid **9** (vs **4** and **5**) but also to change the predominant alkali-metal cation extracted to that which should best fit the polyether cavity (in **10** vs **6**).

Excellent Na^+ extraction selectivity is observed for the lipophilic dibenzo-16-crown-5-carboxylic acid **11**. Competitive extraction coefficients are $Na^+/K^+ = 32$ and $Na^+/Li^+ = 66$ with no detectable extraction of Rb^+ or Cs^+ into the chloroform phase.

The lipophilic dibenzo-19-crown-6-carboxylic acid **12** is K^+ selectivity. Although the K^+/Na^+ selectivity coefficients for **12** and closely related **7** are the same (compare Tables II and IV), selectivity coefficients for K^+ vs each of the remaining alkali-metal cations are significantly higher for **12**.

The maximal metals loadings for **10**, **11**, and **12** are 100%, 82%, and 48%, respectively. The reason for the decrease in extraction efficiency as the ring size increases is not apparent.

CONCLUSIONS

For competitive solvent extraction of alkali-metal cations from aqueous solutions into chloroform by lipophilic dibenzocrown ether oxyacetic acids, the selectivity and efficiency are strongly influenced by the crown ether ring size and the attachment site of the lipophilic groups. Attachment of the lipophilic group to the polyether ring carbon atom that bears the oxyacetic acid group orients the sidearm over the crown ether cavity and produces lipophilic dibenzocrown ether carboxylic acids **10**, **11**, and **12** which exhibit good-to-excellent extraction selectivity for Li^+, Na^+, and K^+, respectively.

LITERATURE CITED

(1) McDowell, W. J. *Sep. Sci. Technol.* **1988**, *23*, 1251–1268.
(2) Strzelbicki, J.; Bartsch, R. A. *Anal. Chem.* **1981**, *53*, 1894–1899.
(3) Strzelbicki, J.; Heo, G. S.; Bartsch, R. A. *Sep. Sci. Technol.* **1982**, *17*, 635–643.
(4) Strzelbicki, J.; Bartsch, R. A. *Anal. Chem.* **1981**, *53*, 2251–2253.
(5) Bartsch, R. A.; Heo, G. S.; Kang, S. I.; Liu, Y.; Strzelbicki, J. *J. Org. Chem.* **1982**, *47*, 457–460.
(6) Charewicz, W. A.; Heo, G. S.; Bartsch, R. A. *Anal. Chem.* **1982**, *54*, 2094–2097.
(7) Charewicz, W. A.; Bartsch, R. A. *Anal. Chem.* **1982**, *54*, 2300–2303.
(8) Bartsch, R. A.; Charewicz, W. A.; Kang, S. I. *J. Membrane Sci.* **1984**, *17*, 94–107.
(9) Bartsch, R. A.; Liu, Y.; Kang, S. I.; Son, B.; Heo, G. S.; Hipes, P. G.; Bills, L. J. *J. Org. Chem.* **1983**, *48*, 4864–4869.
(10) Pugia, M. J.; Knudsen, B. E.; Cason, C. V.; Bartsch, R. A. *J. Org. Chem.* **1987**, *52*, 541–547.
(11) *Water. A Comprehensive Treatise*; Franks, F., Ed.; Plenum: New York, 1973; Vol 2, pp 54–118.
(12) Uhlemann, E.; Geyer, H.; Gloe, K.; Muhl, P. *Anal. Chim. Acta* **1986**, *185*, 279–285.
(13) Cram, D. J. *Angew. Chem., Int. Ed. Engl.* **1986**, *25*, 1039–1057.

RECEIVED for review March 20, 1990. Accepted May 31, 1990. The research was supported by the Division of Chemical Sciences of the Office of Basic Energy Sciences of the U.S. Department of Energy (Contract DE-AS05-80ER10604 and Grant DE-FG05-88ER13832). Dr. Il-Woo Yang received a postdoctoral fellowship from the Korea Science and Engineering Foundation.

Effect of Ring Size Variation within Lipophilic Crown Ether Carboxylic Acids on the Selectivity and Efficiency of Competitive Alkali-Metal Cation Solvent Extraction into Chloroform

Wladyslaw Walkowiak,[1] Sang Ihn Kang, Lewis E. Stewart, Grace Ndip, and Richard A. Bartsch*

Department of Chemistry and Biochemistry, Texas Tech University, Lubbock, Texas 79409-1061

Competitive solvent extraction of alkali-metal cations from aqueous solutions into chloroform by a series of lipophilic crown ether carboxylic acids with varying ring sizes is reported. Extraction selectivity for Li^+ is observed for lipophilic crown ether carboxylic acids with 12–15-membered polyether rings containing four oxygen atoms. For lipophilic 14-crown-4-carboxylic acids, very high Li^+/Na^+ selectivity coefficients of 17–20 are observed with no detectable extraction of K^+, Rb^+, or Cs^+. Lipophilic crown ether carboxylic acids which contain 15-crown-5, 18-crown-6, and 21-crown-7 rings exhibit good selectivities for Na^+, K^+, and Cs^+, respectively. In contrast, poor extraction selectivity is observed for lipophilic crown ether carboxylic acids with 24-crown-8, 27-crown-9, and 30-crown-10 rings.

INTRODUCTION

The potential of crown ethers as a new generation of specific extracting agents for metal ions was markedly enhanced by the introduction of crown ethers which bear pendant proton-ionizable groups (*1–5*). Attachment to the cyclic polyether framework of a sidearm which contains an acid group allows the extractant to function both as a cation exchanger and a coordinator (*6*).

In previous research, competitive extraction of alkali-metal cations from aqueous solutions into chloroform by lipophilic dibenzocrown ether carboxylic acids **1** was studied (*7*). These ionophores provided a versatile series of proton-ionizable crown ethers with which the influence of structural variation within the complexing agent upon extraction selectivity and efficiency could be assessed. These variations included the crown ether ring size (n variation) and the nature and attachment site of the lipophilic group (R, R^1, R^2 variation). Appropriate combinations of the crown ether ring size and lipophilic group attachment site produced extractants with good selectivity for Li^+, Na^+, and K^+. An outstanding example is **1c** with n = 1, which exhibits Na^+/K^+ and Na^+/Li^+ selectivity ratios of 32 and 66, respectively, in competitive alkali-metal cation extractions from aqueous solutions into chloroform.

We now report results for solvent extractions of alkali-metal cations by a new series of lipophilic crown ether carboxylic acids **2–15** in which the crown ether rings do not possess rigidifying benzo groups. In addition ring size variation in **2–15** does not involve changes in the relative numbers of alkyl aryl ether oxygens (less basic) and dialkyl ether oxygens (more basic) as occurs when the crown ether ring in **1** is expanded.

[1] Present address: Institute of Inorganic Chemistry and Metallurgy of Rare Elements, Technical University of Wroclaw, 50-370 Wroclaw, Poland.

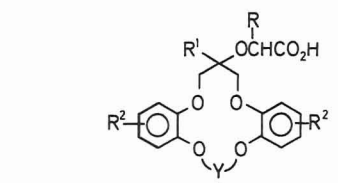

1

	R	R^1	R^2	Y
a	C_8H_{17}	H	H	$-(CH_2)_3-$; $-CH_2(CH_2OCH_2)_nCH_2-$, n=1-3
b	H	H	$(CH_3)_3C$	$-CH_2CH_2OCH_2CH_2-$
c	H	$C_{10}H_{21}$	H	$-(CH_2)_3-$; $-CH_2(CH_2OCH_2)_nCH_2-$, n=1,2

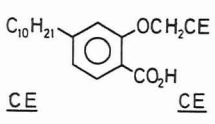

CE		CE	
2	12C4	**8**	15C5
3	13C4	**9**	16C5
4	13C4	**10**	18C6
5	14C4	**11**	19C6
6	14C4	**12**	21C7
7	15C4	**13**	24C8
		14	27C9
		15	30C10

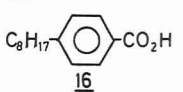

16

EXPERIMENTAL SECTION

Reagents. Sources of inorganic reagents and chloroform were the same as those reported previously (*8–11*). The 4-octylbenzoic acid was obtained from Fluka Chemical Corp. and was used as received. Syntheses of lipophilic crown ether carboxylic acids **2–15** have been reported (*12, 13*).

Apparatus and Procedure. The apparatus and procedure were as described in the preceding paper (*7*).

RESULTS AND DISCUSSION

In an earlier investigation of alkali-metal cation extractions from aqueous solution into chloroform, it was found that selectivity orders and efficiencies for competitive extractions in multi-ion systems were quite different from expectations based upon the results of single ion extractions (*8*). Therefore competitive extractions were utilized in the present study.

Extractants **2**, **8**, **10**, and **12–15** are a series of lipophilic crown ether carboxylic acids in which the number of ethy-

0003-2700/90/0362-2022$02.50/0

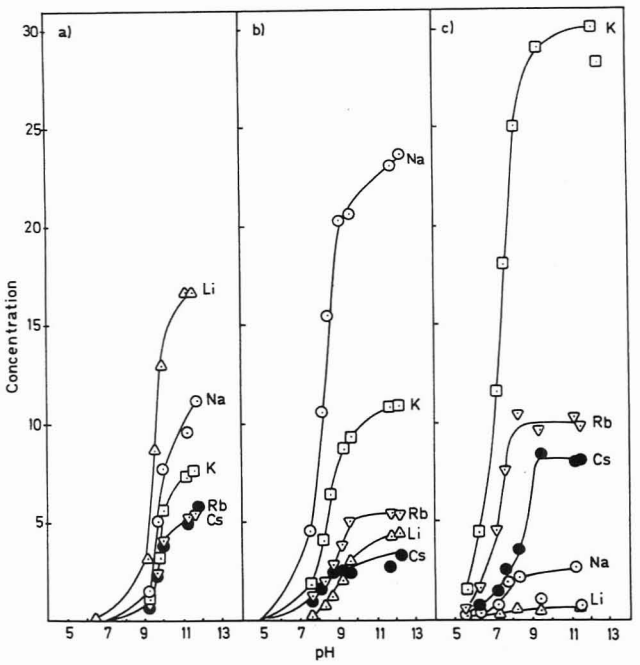

Figure 1. Molar concentrations of metals ($\times 10^3$) in the chloroform phase vs the equilibrium pH of the aqueous phase for competitive extraction of 0.25 M alkali-metal cations by 0.050 M (a) **2**, (b) **8**, and (c) **10**.

lenoxy units in the polyether ring is systematically increased from a 12-crown-4 unit through a 30-crown-10 ring. Lipophilic crown ether carboxylic acids **9** and **11** are closely related to **8** and **10** but have one three-carbon bridge in the polyether ring. Finally compounds **2–7** are a series of lipophilic crown ether carboxylic acids which have four oxygens and ring sizes varying from 12 to 15 members. Pairs of extractants **3**, **4** and **5**, **6** are structural isomers in which the crown ether ring attachment site changes from a two-carbon bridge to the central carbon of a three-carbon bridge.

Extractants **2–15** were found to be sufficiently lipophilic that there was no detectable loss of the complexing agent from the chloroform phases during extraction (as assessed by ultraviolet spectroscopy).

Solvent Extraction of Alkali-Metal Cations from Aqueous Solutions into Chloroform by Lipophilic Crown Ether Carboxylic Acids 2, 8, 10, and 12–15. For competitive solvent extractions of aqueous alkali-metal cation (0.25 M in each) solutions by 0.050 M lipophilic crown ether carboxylic acids **2**, **8**, **10**, and **12–15** in chloroform, data for the metals concentrations in the chloroform phase vs the equilibrium pH of the aqueous phase are shown in Figures 1 and 2. Selectivity orders, selectivity coefficients, and maximal metals loadings are summarized in Table I. (The selectivity coefficient is the ratio between the chloroform phase concentration of the best extracted cation and the indicated cation at pH 10.0. The percent metals loading was calculated assuming that a 1:1 metal ion to crown carboxylate extraction complex is formed.)

Table I. Effect of Crown Ether Ring Size upon Selectivity and Efficiency of Competitive Alkali-Metal Cation Extraction from Aqueous Solutions into Chloroform by Crown Carboxylic Acids 2, 8, 10, 12, 13, 14, and 15

compound	ring size	selectivity order and selectivity coefficients[a,b]	maximal metals loading, %
2	12C4	$Li^+ > Na^+ > K^+ > Rb^+, Cs^+$ (1.5, 2.2, 3.0)	90
8	15C5	$Na^+ > K^+ > Rb^+ Li^+ > Cs^+$ (2.1, 4.3, 5.5, 6.7)	94
10	18C6	$K^+ > Rb^+ > Ca^+ > Na^+ > Li^+$ (3.0, 4.6, 13, 64)	64
12	21C7	$Cs^+ > Rb^+ > K^+ > Li^+ > Na^+$ (3.0, 3.6, 13, 15)	83
13	24C8	$Cs^+ > Rb^+ > Na^+, > Li^+$ (1.4, 1.5, 2.0)	100
14	27C9	$K^+ > Rb^+ > Li^+ > Cs^+ > Na^+$ (1.1, 1.2, 1.3, 1.5)	52
15	30C10	$Rb^+ > K^+ > Cs^+ > Li^+ > Na^+$ (1.2, 1.4, 3.0, 3.6)	41

[a] Ratio of chloroform phase concentration of best extracted metal ion and indicated metal cation. [b] At pH = 10.0.

Lipophilic crown ether carboxylic acids **2**, **8**, **10**, and **12** with ring sizes of 12-crown-4, 15-crown-5, 18-crown-6, and 21-crown-7 exhibit extraction selectivities for Li^+, Na^+, K^+, and Cs^+, respectively, as would be predicted from the relationship between the crown ether cavity and metal ion diameters (Table II). Of the series, the lipophilic 18-crown-6 carboxylic acid **10** has the best selectivity (Figure 1c) with $K^+/Na^+ = 13$ and $K^+/Rb^+ = 3.0$. Of particular interest is the selectivity observed for the lipophilic 21-crown-7-carboxylic acid **12** (Figure 2a) in which Cs^+ is the best extracted species and Na^+ is the poorest. Extractants with high Cs^+/Na^+ selectivity have potential application in the separation of Cs^+ from radioactive waste solutions (*14*).

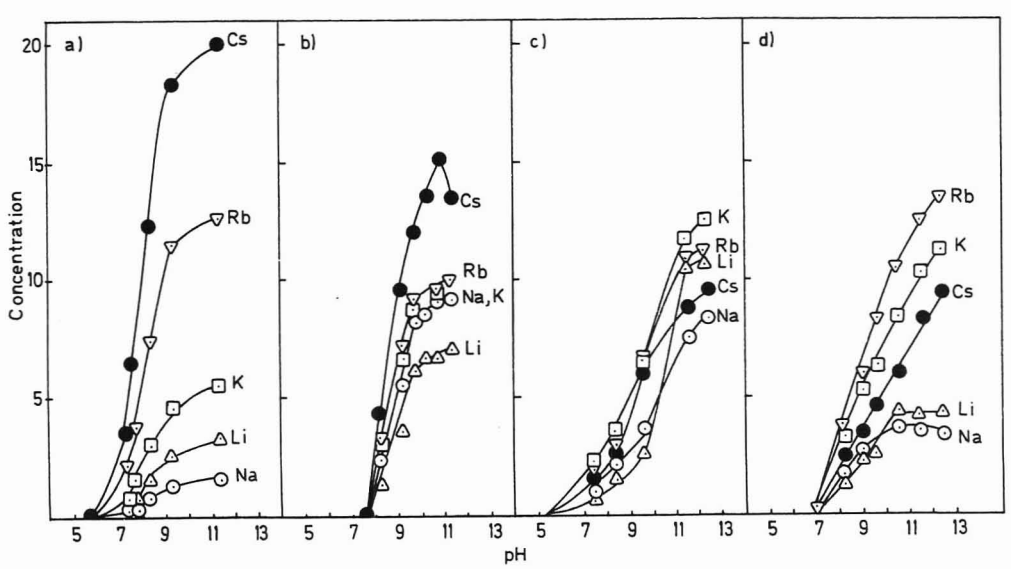

Figure 2. Molar concentrations of metals ($\times 10^3$) in the chloroform phase vs the equilibrium pH of the aqueous phase for competitive extraction of 0.25 M alkali-metal cations by 0.050 M (a) **12**, (b) **13**, (c) **14**, and (d) **15**.

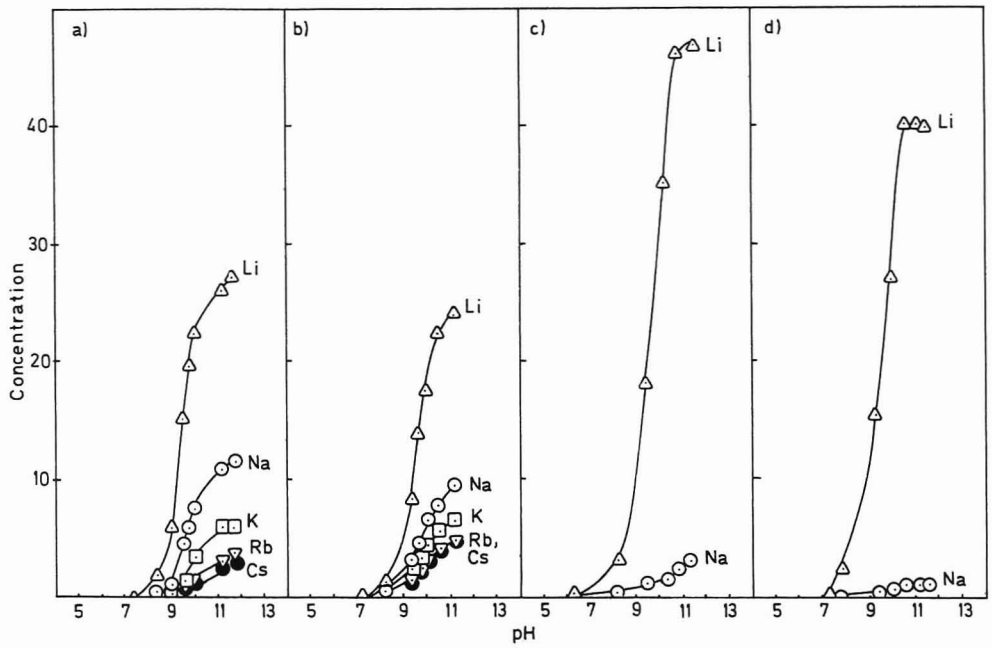

Figure 3. Molar concentrations of metals ($\times 10^3$) in the chloroform phase vs the equilibrium pH of the aqueous phase for competitive extraction of 0.25 M alkali-metal cations by 0.050 M (a) **3**, (b) **4**, (c) **5**, and (d) **6**.

Table II. Comparison of Alkali Metal Cation and Crown Ether Cavity Diameters

cation	ionic diameter (*15*), Å	crown ether cavity	cavity diameter,[a] Å
Li^+	1.20	12-crown-4	1.2–1.5
Na^+	1.90	14-crown-4	1.2–1.5
K^+	2.66	15-crown-5	1.7–2.2
Rb^+	2.96	16-crown-5	2.0–2.4
Cs^+	3.38	18-crown-6	2.6–3.2
		19-crown-6	3.0–3.5
		21-crown-7	3.4–4.3

[a] Estimated from Corey–Pauling–Koltun (CPK) space-filling models.

Maximal metals loadings for lipophilic crown ether carboxylic acids **2**, **8**, **10**, and **12** range from 64 to 94% (Table I) with a possible inverse relationship between extraction efficiency and selectivity. Thus while selectivity decreases in the order **10** > **12** > **8** > **2**, the metals loadings are highest for **2** (90%) and **8** (94%) but diminish with **12** (83%) and then for **10** (64%).

Compared with **2**, **8**, **10**, and **12**, lipophilic crown ether carboxylic acids **13**, **14**, and **15** which have 24-crown-8, 27-crown-9, and 30-crown-10 rings exhibit poor extraction selectivity (Figure 2b–d). Although **13** extracts Cs^+ best, the selectivity is much poorer than that for the analogous 21-crown-7 compound **12**. The quantitative metals loading for **13** appears to continue the inverse relationship between extraction efficiency and selectivity which was noted above for chelating agents **2**, **8**, **10**, and **12**.

Lipophilic 27-crown-9-carboxylic acid **14** exhibits the poorest extraction selectivity of the series (Figure 2c). The selectivity coefficient between K^+, the best extracted metal ion, and Na^+, the worst extracted, is only 1.5. For the lipophilic 30-crown-10-carboxylic acid **15**, the extraction selectivity remains low, but there is selectivity for K^+, Rb^+, and Cs^+ as a group over Li^+ and Na^+ (Figure 2d). Presumably the low selectivities for the large ring extractants **14** and **15** result from nonplanar geometrices of the crown ether rings which provide three-dimensional, "wrap-around" coordination of the alkali-metal cations (*15*).

For the 27-crown-9 and 30-crown-10 compounds **14** and **15**, respectively, the extraction efficiencies are the lowest for this

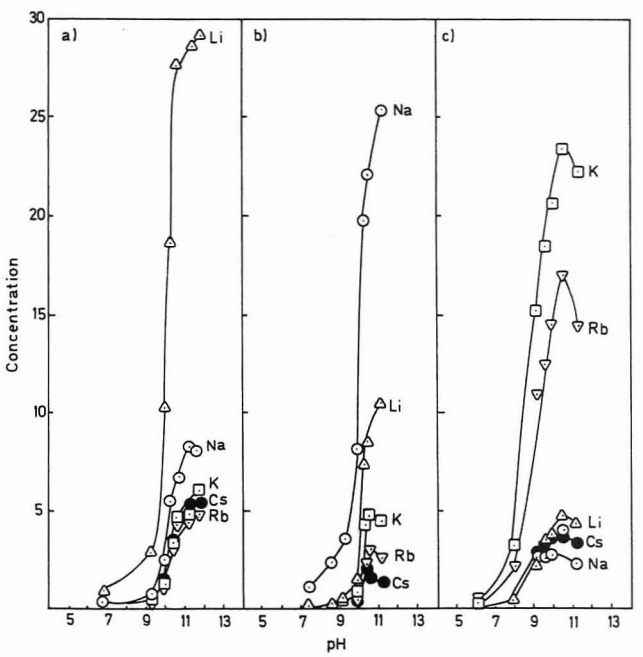

Figure 4. Molar concentrations of metals ($\times 10^3$) in the chloroform phase vs the equilibrium pH of the aqueous phase for competitive extraction of 0.25 M alkali metal cations by 0.050 M (a) **7**, (b) **9**, and (c) **11**.

series of lipophilic crown ether carboxylic acids (Table I). Although maximal metals loadings of 50% and below might indicate the formation of 1:2 metal-to-ligand complexes for these large ring crown ethers (*17–19*), such extraction complex stoichiometries would be expected to favor the smaller alkali-metal cations. Since alkali-metal cation extraction by **14** exhibits so little selectivity, extraction complexes with 1:1 stoichiometries appear to be more reasonable.

Solvent Extraction of Alkali-Metal Cations from Aqueous Solutions into Chloroform by Lipophilic Crown-4-carboxylic Acids 2–7. In an attempt to enhance the limited Li^+ selectivity found for the lipophilic 12-crown-4-carboxylic acid **2** (Figure 1a), a series of analogous compounds **3–7** with 13-crown-4, 14-crown-4, and 15-crown-4 rings was examined. Results for competitive solvent extractions of alkali-metal cations from aqueous solutions into chloroform

Table III. Effect of Crown Ether Ring Size upon Selectivity and Efficiency of Competitive Alkali-Metal Cation Extraction from Aqueous Solutions into Chloroform by Crown Carboxylic Acids 3, 4, 5, 6, 7, 9, and 11

compound	ring size	selectivity order and selectivity coefficients[a]	maximal metal loading, %
3	13C4(2)[b]	$Li^+ > Na^+ > K^+ > Rb^+ > Cs^+$ (2.4, 4.6, 6.9, 8.6)	100
4	13C4(3)[c]	$Li^+ > Na^+ > K^+ > Rb^+, Cs^+$ (2.6, 3.6, 5.2)	100
5	14C4(2)[b]	$Li^+ > Na^+ > K^+, Rb^+, Cs^+$ (17, ND[d])	90
6	14C4(3)[b]	$Li^+ > Na^+ > K^+, Rb^+, Cs^+$ (20, ND[d])	100
7	15C4	$Li^+ > Na^+ > K^+ > Cs^+ > Rb^+$ (3.7, 4.9, 5.4, 7.1)	92
9[e]	16C5	$Na^+ > Li^+ > K^+ > Rb^+ > Cs^+$ (2.5, 5.4, 9.3, 18)	88
11	19C6	$K^+ > Rb^+ > Li^+ > Cs^+ > Na^+$ (1.5, 5.5, 5.9, 7.8)	100

[a] At pH = 10.0. [b] Attachment to one carbon of a two-carbon bridge in the crown ether. [c] Attachment to the central carbon of a three-carbon bridge in the crown ether. [d] Not detected. [e] Selectivity coefficients at pH = 11.0.

by 3–7 are shown in Figures 3 and 4. Selectivity orders, selectivity coefficients, and maximal metal loadings are presented in Table III.

When the ring size for the lipophilic crown ether carboxylic acid is expanded from 12-crown-4 in **2** to 13-crown-4 in **3** and **4**, the Li^+/Na^+ selectivity coefficient increases from 1.5 (Table I) to 2.4–2.6 (Table III). Concomitantly, the Li^+/K^+ selectivity coefficient increases from 2.2 for **2** to 3.6–4.6 for **3** and **4**. Lipophilic crown ether carboxylic acids **3** and **4** differ in the attachment of the sidearm to a two-carbon bridge of the 13-crown-4 ring in the former and to the central carbon of a three-carbon bridge in the latter. Both **3** and **4** gave quantitative metals loadings.

Further expansion of the ring size to 14-crown-4 produces very high Li^+ extraction selectivity. For lipophilic 14-crown-4-carboxylic acids **5** and **6** (Figures 3, parts c and d, respectively), only Li^+ and Na^+ are extracted into the chloroform phase and the Li^+/Na^+ selectivity coefficients are 17–20. These results are in agreement with earlier reports of strong Li^+ complexation by 14-crown-4 compounds (*19–23*). In terms of both extraction selectivity and efficiency, lipophilic 14-crown-4-carboxylic acid **6** in which the sidearm is attached to the central carbon of a three-carbon bridge in the polyether ring appears to be slightly better than **5** for which the attachment site is a carbon of a two-carbon bridge (Table III).

With the further ring size increase in the lipophilic 15-crown-4-carboxylic acid **7**, there is a marked diminution in Li^+ extraction selectivity (Figure 4a). The Li^+/Na^+ selectivity coefficient drops to 3.7 and K^+, Rb^+, and Cs^+ are also extracted into the chloroform phase.

These results demonstrate a very strong influence of ring size upon the selectivity of Li^+ extraction by chelating agents **2–7**. For a group of 11 lipophilic crown-4-carboxylic acids, compounds **5** and **6** provide the highest Li^+ selectivity in competitive solvent extractions of alkali-metal cations from aqueous solutions into chloroform (*7*, *24*).

It should be noted that lipophilic crown carboxylic acids **7** and **8** both contain 15-membered polyether rings. However, the former has four ring oxygens while the latter has five. The change in selectivity order of $Li^+ > Na^+ > K^+ > Cs^+ > Rb^+$ for the 15-crown-4 compound **7** (Table III) to $Na^+ > K^+ > Rb^+ > Li^+ > Cs^+$ for the 15-crown-5 compound **8** underscores the importance influence of the number of donor atoms in the polyether ring on metal ion complexation.

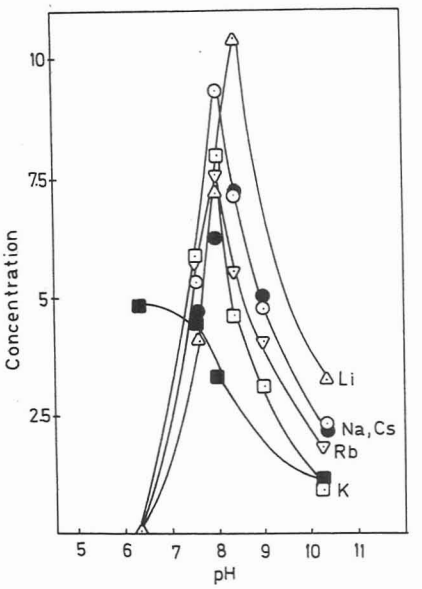

Figure 5. Molar concentrations of metals ($\times 10^3$) in the chloroform phase vs the equilibrium pH of the aqueous phase for competitive extraction of 0.25 M alkali-metal cations by 0.050 M 4-octylbenzoic acid. Molar chloroform-phase concentrations of 4-octylbenzoic acid ($\times 10^2$) are shown as solid squares.

Solvent Extraction of Alkali-Metal Cations from Aqueous Solutions into Chloroform by Lipophilic 16-Crown-5- and 19-Crown-6-carboxylic Acids. In research conducted with neutral crown ether ligands, it has been found that Na^+/K^+ selectivity (as extrapolated from single ion species picrate extraction experiments) is higher for 16-crown-5 than 15-crown-5 compounds (*25*, *26*). Results for competitive solvent extractions of alkali-metal cations from aqueous solutions into chloroform by lipophilic 16-crown-5- and 15-crown-5-carboxylic acids **9** and **8** are presented in Figures 4c and 1b, respectively. Although the metal loadings are quite similar for the two extractants, the selectivity order of $Na^+ \gg K^+ \gg Rb^+ > Li^+ > Cs^+$ for **8** changes to $Na^+ \gg Li^+ \gg K^+ > Rb^+ > Cs^+$ for **9** (Tables I and III). The Na^+ selectivity relative to K^+, Rb^+, and Cs^+ is enhanced in going from **8** to **9**, but the Na^+/Li^+ selectivity coefficient decreases when the 15-crown-5 ring in the extractant is expanded to 16-crown-5.

The effect of replacing a two-carbon bridge in the polyether ring with a three-carbon bridge was also examined for crown-6 compounds. Results for competitive solvent extractions of alkali-metal cations from aqueous solutions into chloroform by lipophilic 18-crown-6- and 19-crown-6-carboxylic acids **10** and **11**, respectively, are presented in Figures 1c and 4c. The selectivity order of $K^+ \gg Rb^+ > Cs^+ \gg Na^+ > Li^+$ found for **10** changes to $K^+ > Rb^+ \gg Li^+ > Cs^+ > Na^+$ with overall lower selectivity when the polyether ring is expanded by one member in **11** (Tables I and III). Once again Li^+ extraction is enhanced when a two-carbon bridge in the polyether ring is replaced with a three-carbon bridge. Interestingly, quantitative metals loading of the chloroform phase was obtained with the lipophilic 19-crown-6-carboxylic acid **11**, whereas the maximal metals loading was only 64% for the more selective 18-crown-6 analogue **10**.

Competitive Solvent Extraction of Alkali-Metal Cations from Aqueous Solutions into Chloroform with a Lipophilic Benzoic Acid. For comparison, solvent extractions were conducted with 4-octylbenzoic acid (**16**), a lipophilic carboxylic acid which does not possess a crown ether ring. Results for the competitive solvent extraction of alkali-metal cations from aqueous solutions into chloroform by model compound **16** are shown in Figure 5. As can be seen, the lipophilic carboxylic acid is found to be very unselective. Furthermore for aqueous phase pH > 8, there is significant

loss of **16** from the chloroform phase due to the formation of a precipitate at the water–chloroform interface. Hence the polyether rings in lipophilic crown ether benzoic acids **2–15** not only provide extraction selectivity but also give extractants with improved solubility characteristics compared with **16**.

CONCLUSIONS

For competitive solvent extraction of alkali-metal cations from aqueous solutions into chloroform by lipophilic crown ether carboxylic acids **2–15**, the selectivity is strongly influenced by the crown ether ring size and number of oxygen atoms. Lipophilic crown ether carboxylic acids **2–7** with 12-crown-4, 13-crown-4, 14-crown-4, and 15-crown-4 rings exhibit extraction selectivity for Li^+, with outstanding Li^+ selectivity for the 14-crown-4 compounds **5** and **6**. The extractants **8** and **9** with 15-crown-5 and 16-crown-5 rings are Na^+ selective. Chelating agents **10** and **11** with 18-crown-6 and 19-crown-6 rings, respectively, are K^+ selective, with a K^+/Na^+ selectivity coefficient of 13 for **10**. The lipophilic 21-crown-7-carboxylic acid **12** is Cs^+ selective and has a Cs^+/Na^+ selectivity coefficient of 15. Lipophilic crown ether carboxylic acids with 24-crown-8, 27-crown-9, and 30-crown-10 rings exhibit poor extraction selectivities, presumably due to deformation of the polyether rings from planar to three-dimensional "wrap-around" geometries.

LITERATURE CITED

(1) Helgeson, R. C.; Timko, J. M.; Cram, D. J. *J. Am. Chem. Soc.* **1973**, *95*, 3023–3025.
(2) Newcomb, M.; Cram, D. J. *J. Am. Chem. Soc.* **1977**, *97*, 1257–1259.
(3) Nakamura, H.; Takagi, M.; Ueno, K. *Talanta* **1979**, *26*, 921–927.
(4) Frederick, L. A.; Fyles, T. M.; Gorprasad, N. P.; Whitfield, D. M. *Can. J. Chem.* **1981**, *59*, 1724–1733.
(5) Bartsch, R. A.; Heo, G. S.; Kang, S. I.; Liu, Y.; Strzelbicki, J. *J. Org. Chem.* **1982**, *47*, 457–460.
(6) McDowell, W. J. *Sep. Sci. Technol.* **1988**, *23*, 1251–1268.
(7) Walkowiak, W.; Charewicz, W. A.; Kang, S. I.; Yang, I.-W.; Pugia, M. J.; Bartsch, R. A. *Anal. Chem.*, preceding paper in this issue.
(8) Strzelbicki, J.; Bartsch, R. A. *Anal. Chem.* **1981**, *53*, 1894–1899.
(9) Strzelbicki, J.; Bartsch, R. A. *Anal. Chem.* **1981**, *53*, 2251–2253.
(10) Charewicz, W. A.; Heo, G. S.; Bartsch, R. A. *Anal. Chem.* **1982**, *54*, 2094–2097.
(11) Charewicz, W. A.; Bartsch, R. A. *Anal. Chem.* **1982**, *54*, 2300–2303.
(12) Czech, B.; Son, B.; Bartsch, R. A. *Tetrahedron Lett.* **1983**, *24*, 2923–2936.
(13) Czech, B. P.; Czech, A.; Son, B.; Lee, H. K.; Bartsch, R. A. *J. Heterocycl. Chem.* **1986**, *23*, 465–471.
(14) Shuler, R. G.; Bowers, C. B., Jr.; Smith, J. E., Jr.; Van Brunt, V.; Davis, M. W., Jr. *Solvent Extr. Ion Exch.* **1985**, *3*, 567–604.
(15) Bush, M. A.; Truter, M. R. *J. Chem. Soc., Perkin Trans 2* **1972**, 345–350.
(16) Mercer, M.; Truter, M. R. *J. Chem. Soc., Dalton Trans.* **1973**, 2469–2473.
(17) Hughes, D. L. *J. Chem. Soc., Dalton Trans.* **1975**, 2374–2378.
(18) Owen, J. D.; Truter, M. R. *J. Chem. Soc., Dalton Trans.* **1979**, 1831–1835.
(19) Kimura, K.; Kitazawa, S.; Shono, T. *Chem. Lett.* **1984**, 639–640.
(20) Kitazawa, S.; Kimura, K.; Yano, H.; Shono, T. *J. Am. Chem. Soc.* **1984**, *106*, 6978–6983.
(21) Kimura, K.; Yano, H.; Kitazawa, S.; Shono, T. *J. Chem. Soc., Perkin Trans. 2* **1986**, 1945–1951.
(22) Kimura, K.; Tanaka, M.; Iketani, S.; Shono, T. *J. Org. Chem.* **1987**, *52*, 836–844.
(23) Attiyat, A. S.; Christian, G. D.; Xie, R. Y.; Wen, X.; Bartsch, R. A. *Anal. Chem.* **1988**, *60*, 2561–2564.
(24) Bartsch, R. A.; Czech, B. P.; Kang, S. I.; Stewart, L. E.; Walkowiak, W.; Charewicz, W. A.; Heo, G. S.; Son, B. *J. Am. Chem. Soc.* **1985**, *107*, 4997.
(25) Ouchi, M.; Inoue, Y.; Sakamoto, H.; Yamahira, A.; Yoshinaga, M.; Hakushi, T. *J. Org. Chem.* **1983**, *48*, 3168–3173.
(26) Inoue, Y.; Wada, K.; Liu, Y.; Ouchi, M.; Tai, A.; Hakushi, T. *J. Org. Chem.* **1989**, *54*, 5268–5272.

RECEIVED for review March 20, 1990. Accepted May 31, 1990. The research was supported by the Division of Chemical Sciences of the Office of Basic Energy Sciences of the U.S. Department of Energy (Contract DE-AS05-80ER10604 and Grant DE-FG05-88ER13832).

Design of Coaxial Segmentors for Liquid–Liquid Extraction/Flow Injection Analysis

Vlastimil Kuban,[1] Lars-Göran Danielsson,* and Folke Ingman

Department of Analytical Chemistry, The Royal Institute of Technology, S-100 44 Stockholm, Sweden

The process of the segmentation of two immiscible solvents by newly introduced coaxial segmentors of different geometry was studied in a continuous liquid–liquid extraction flow system. A fast reading "on-tube" photometric detection system (~3 ms time resolution) controlled by a computer was used to measure optical transparency directly across the flowing stream. The influence of flow rates, flow rate ratio, the density and interfacial tension of the phases as well as the geometry of the segmentors was studied. A segmentor with a confluence chamber made of a glass tube with a conical PVDF insert and an all-glass segmentor with a conical outflow channel gave the most repeatable segmentation ($s_r < 2\%$). They work well at a total flow rate Q_t up to 10 mL min^{-1} and a flow rate ratio Q_a/Q_o from 2 to 40. The length of the organic segments can be varied over a wide range from 2 to 50 mm and the length is only weakly influenced by the total flow rate.

Liquid–liquid extraction is a frequently used separation/preconcentration method in flow injection analysis (FIA) (*1–5*). In any method utilizing liquid–liquid extraction, be it a manual batch procedure or a method for a mechanized or automated system, three basic operations must be performed. The immiscible organic and aqueous phases must be dispensed in defined volumes, the phases must be brought into intensive contact with each other for the extraction to take place, and finally they must be physically separated from each other after the extraction in order to make the chemical separation meaningful.

These three principal operations are connected to the three basic liquid–liquid extraction FIA units—a segmentor or confluence point for the organic and aqueous phase streams providing alternate and regular segments of both solvents to one uniform segmented flow in a single channel, an extraction coil, in which the solute is transferred from one phase to the other, and finally, a phase separator, the mission of which is to continuously and quantitatively separate the segmented outlet stream into two or three parts, at least one of them consisting of only one phase.

[1] On leave from the Department of Analytical Chemistry, J. E. Purkyne University, Kotlarska 2, CS-61137 Brno, Czechoslovakia.

0003-2700/90/0362-2026$02.50/0

Several types of more or less efficient segmentors have been described in the literature. Classical T-piece segmentors made of glass (*7*, *8*), fluoroplastics (*9*, *10*), and combinations of hydrophilic and lipophilic materials, improved glass A8-T and A10-T fittings (*7*, *11*, *12*), and fluoroplastics T-pieces with Teflon tubing inserts (*6*, *9*, *13*) or enlarged outflow channel inner diameter (*14*, *15*) are the most widely used. Different configurations of Y (*16*, *17*) or W pieces (*18–21*) made of glass or fluoroplastics and four-way fittings (*22*) have also been recommended. Lately, a falling drop segmentor was applied (*23*) to overcome some of the disadvantages of other types.

Although segmentation is very important for all steps of liquid–liquid extraction FIA, few detailed studies of the factors governing segment size and segmentation reproducibility have been published. The influence of the geometry of the confluence chamber on segmentation was the subject of careful studies (*7*, *24*). Cantwell and Sweileh (*6*) outlined the theory of segmentation in a modified T-piece and studied the influence of hydrodynamic conditions on segmentation. Improper segmentation can negatively influence sample dispersion, rate of extraction, and phase separation (*14*, *25*).

There is an increasing need for a detailed fundamental study of the segmentation process. The result of such a study could be the development of a more efficient phase segmentor and an exploration of the possibilities offered by an improvement in segmentation repeatability and in segmentation control. Optimal performance of the segmentor is a key to the successful utilization of liquid–liquid extraction in flow systems. Reproducible segmentation can improve the precision of signal measurement and may frequently simplify signal evaluation. Finally, with adequate control over the segmentation it may even be possible to eliminate phase separation altogether if the repeatability is good enough to allow precise timing of measurement intervals.

The work presented here was undertaken in order to elucidate the possibilities offered by the newly introduced coaxial segmentors with respect to controlled and reproducible segmentation.

THEORY

The segmentation of two immiscible phases in a flow system is normally based on the principle that droplets or plugs of one phase are formed in the continuous flow of the other solvent at the end of the inlet capillary in the confluence chamber of the segmentor. Another principle leading to segment formation is the "ripple" process connected with the destruction of a thick layer of one solvent formed on the outlet tube walls or on the walls of the confluence chamber of the segmentor (*26*).

The size of the droplets formed is controlled by the equivalence of the gravitational, interfacial, and hydrodynamic forces. This process is schematically illustrated for a coaxial segmentor in Figure 1. The droplets formed move into the outflow channel after cut off and tend to minimize their area of contact with the other phase and to maximize the contact area with the wall material by wetting it, provided that the wall material is lipophilic. A more or less regular segmented flow with independent segments of the two phases is obtained. The further stability of this segmented flow is influenced by the conditions in the complete liquid–liquid extraction/FIA system.

Several assumptions are needed to facilitate a quantitative description of the segmentation process in coaxial segmentors:

1. The droplet volume grows linearly with time and organic phase flow rate ($V = Q_o t$).
2. The dislodging is fast enough for neglecting drop growth during this process.
3. No contact with the wall surface of the outflow capillary and the confluence chamber wall is assumed (this is very questionable for confluence chambers of small inner diameter made of fluoroplastics).
4. The drop is spherical and the confluence chamber has a circular cross section.
5. No losses of the phases due to film formation are observed.
6. Three forces direct the drop formation—gravitational, interfacial, and hydrodynamic forces, the orientation of which determine the resulting force vector value and equivalence of the forces.
7. Coaxial and vertical orientation of the inlet/outlet flows is assumed for simplicity.
8. No jet effect occurs at the organic phase flow rate used.

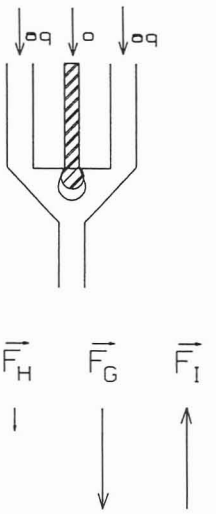

Figure 1. Schematic picture of segmentation in a coaxial segmentor. Vectors indicate hydrodynamic, interfacial, and gravity forces, respectively.

The organic solvent flows into the aqueous phase stream in the form of droplets. Druing growth the droplets are attached to the column of organic solvent in the inlet capillary while the combined effects of gravity and hydrodynamics act to tear off the droplet (cf. Figure 1). The gravitational force has vertical orientation. Its value is equal (*27*) to

$$F_G = V \Delta\rho g = (4/3)\pi r_d^3 \Delta\rho g \quad (1)$$

where V is the droplet volume, $\Delta\rho$ is the density difference between the two solvents, r_d is the droplet radius, and g is the gravitational constant.

The interfacial force F_I, holding the droplet onto the column of organic phase in the inlet capillary, can be expressed by the Tate (*27*) equation

$$F_I = \pi d_i \gamma_{o/a} \quad (2)$$

where $\gamma_{o/a}$ is the liquid–liquid interfacial tension between the organic and aqueous phases and d_i is the inner diameter of the inlet glass tubing.

The spherical shape of the droplet is deformed by a hydrodynamic force F_H acting on the drop area facing the aqueous flow as a result of a continuous flow of the aqueous phase Q_a. This force tends to dislodge the droplet from the inlet tubing end. The hydrodynamic force F_H is the product of the front area of the droplet A_f facing the aqueous flow stream and the pressure difference $\Delta P = P_1 - P_2$ across the confluence chamber cross section due to the flow of water $F_H = \Delta P A_f$.

The pressure difference ΔP consists of two terms arising from viscous drag on the aqueous phase flow (the Poiseuille term P_P) and from changes in kinetic energy of the aqueous phase as it flows through a decreasing cross-sectional area around the growing drop of organic phase (the Bernoulli term P_B). The terms are linear and quadratic functions, respec-

tively, of the total aqueous phase rate Q_a. The value of ΔP (assuming a circular confluence chamber cross section and a spherical drop) is given by the expression

$$F_H = \Delta P A_f = A_f(P_P + P_B) = A_f(k_P Q_a + k_B Q_a^2) \quad (3)$$

where k_P and k_B are the Poiseuille and Bernoulli factors incorporating the viscosity and density of water and the geometric factors of the confluence chamber and the droplet.

The resulting force vector has to be zero at the moment when the droplet is cut off ($F_G + F_I + F_H = 0$). At low flow rates, the gravitational force predominates and the droplet has a spherical shape. Its cut-off size depends primarily on the inner diameter of the inlet capillary d_i, the interfacial tension $\gamma_{o/a}$, the difference in density between the two liquids $\Delta\rho$, and the value of the gravitational constant g. The total droplet volume V grows linearly with the organic phase flow rate Q_o and time t during droplet formation. The resulting total droplet volume V can, under ideal conditions (neglecting the influence of the hydrodynamic force and assuming the equivalence of gravitational and interfacial forces $F_G = F_I$), be expressed by the following equation at the moment when the droplet is cut off:

$$V = (4/3)\pi r_d^3 = \pi d_i \gamma_{o/a}/g\,\Delta\rho \quad (4)$$

This corresponds to a segment length

$$L_s = V/\pi(d_e/2)^2 = 4 d_i \gamma_{o/a}/g\,\Delta\rho\, d_e^2 \quad (5)$$

where r_d is the droplet radius and d_e is the inner diameter of the extraction capillary. Under the given assumptions, the droplet volume V, and also the segment length L_s, is independent of the flow rate of the aqueous phase Q_a. The actual segment length L_s corresponding to a certain volume is not easily calculated. Some transport of the organic phase takes place in the film at the tubing wall, causing the organic segments to be shorter. Furthermore, the segments are not cylinders with flat tops but have rounded ends, which affects the length, especially for short segments.

The droplet volume of any particular two-phase liquid–liquid extraction system can thus be easily varied by using the inner diameter of the inlet tubing. The spatial orientation of the end surface of the tubing influences the resulting force vector and thus also the segment volume. On comparison of different two-phase systems, the droplet volume is also influenced by a change in the surface tension and by a change in the density difference between the two liquids, as can be seen from the segment length changes in the presence of inorganic salts, surfactants, and methanol.

The influence of the hydrodynamic force cannot be neglected at very high aqueous phase flow rates and/or high flow rate ratios. The resulting volume of the droplet is influenced by the flow rate Q_a, flow rate ratio Q_a/Q_o, and the construction of the inner capillary system. This phenomenon should result in a curvature of the graph describing the dependence of V on Q_a, due to the quadratic term $k_B Q_a^2$ in eq 3 for the hydrodynamic force F_H.

EXPERIMENTAL SECTION

Apparatus. The aqueous and organic phase streams (see Figure 2 for the manifold) were driven by two liquid chromatographic pumps (Constametric III metering pump, LDC/Milton Roy, Riviera Beach, FL, and SSI 350 pump, Scientific Systems, Inc.) at a flow rate Q_a up to 10 mL min^{-1} and Q_o up to 1.5 mL min^{-1}, respectively. The pumps were equipped with pulse dampers and pressure indicators (Altech, Applied Science). Restrictor columns, Hibar LiChroCART HPLC cartridges (50 × 4 mm) packed with LiChrosorb Si 60 in Hibar LiChroCART manu-fix 50-4 cartridge holders (E. Merck, Darmstadt, FRG), ensured sufficient back pressure for proper action of the pumps and dampers. On some occasions a Gilson eight-channel peristaltic pump, Minipuls 2 (Gilson Instruments, Willier le Bel, France) was used to drive the organic phase stream.

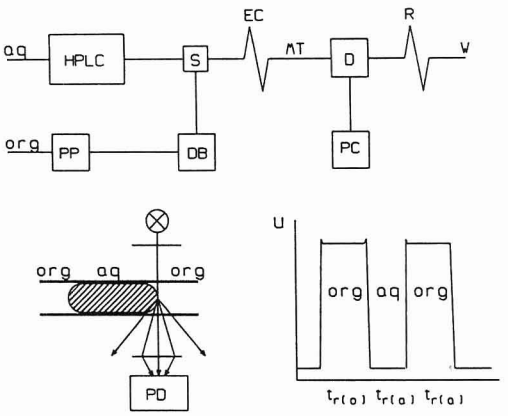

Figure 2. Measuring system manifold (top), optical scheme (left), and the computer graphical "on-screen" presentation of the analytical signal vs time (right): HPLC, HPLC pump with pulse damper, pressure indicator, and restrictor column; PP, peristaltic or HPLC pump; DB, displacement bottle; S, segmentor; EC, equilibration coil; MT, transparent measuring tube (FEP); D, "on-tube" detector; PC, personal computer; R, restrictor coil; W, waste; PD, detector sensor; U, analytical signal; $t_{r(o)}$ and $t_{r(a)}$, residence time of the passage of the segments through the flow cell for the organic and aqueous phase; aq, aqueous phase; org, organic phase.

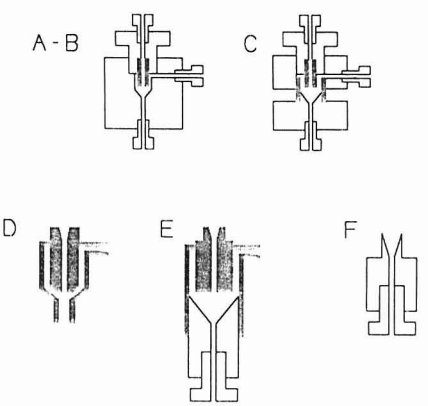

Figure 3. Coaxial segmentors of a different geometry and material: A-B, Perspex and PVDF compact body segmentors, respectively; C, PVDF segmentor with a glass tube confluence chamber and PVDF conical housing; D, glass segmentor with integral conical housing; E, glass segmentor with PVDF concial housing; F, PVDF concial housing for droplet size limitation. Organic phase inlet from the top, aqueous phase inlet from right, segmented flow outlet from the bottom (reversed position for MIBK).

The organic phase flow was created in a (250 mL) displacement bottle, since this technique reduced pulsations and problems with cavitation in the pump. The displacement technique was also used in some experiments when colored streams of 10 μM organic dye solutions in water were introduced into the system to avoid sorption of dyes on the packing material of the restrictors.

The coaxial segmentors consist of two basic parts (Figure 3), a glass capillary inlet channel for introduction of the organic phase and a segmentor body with inlet and outlet capillary channels for delivery of the aqueous phase and drainage of the segmented flow stream, respectively. The glass capillary inlet tube (0.05, 0.10, 0.15, 0.20, 0.25, 0.30, and 0.35 mm i.d. and from 4 to 5 mm o.d.) is pressed into a PVDF screw. When assembled, the capillary ends in the conical chamber (5.5/0.7 mm i.d.) of the compact segmentor body made of Perspex or PVDF (Figure 3, segmentor A-B).

An improved PVDF segmentor body (Figure 3, segmentor C), with the confluence chamber made of a thick-walled glass tube (6/9 mm i.d/o.d.) with a conical Teflon insert (6/1.1 mm i.d.) was also tested. The all-glass coaxial segmentor with integral conical confluence chamber (Figure 3, segmentor D) and the glass segmentor having a PVDF conical insert (8/0.7 mm i.d.) in the

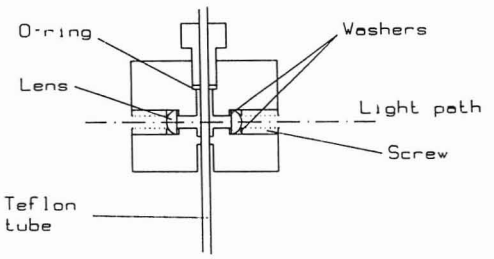

Figure 4. "On-tube" detector flow cell with transparent FEP tubing.

straight glass tube (Figure 3, segmentor E) with inlet glass capillary of 1/6 mm i.d./o.d. were compared with the above-mentioned segmentors.

All segmentors were compared with respect to segment length and repeatability of the segmentation. The influence of the orientation in space, the flow rates of both phases, the total flow rate, and flow rate ratio were investigated. The influence of the density and interfacial tension of the solvents, the salt content of the aqueous media, and concentration of wetting agents (methanol, surfactants) were also tested with PVDF/glass coaxial segmentor (type C).

The resulting segmented flow passed through the extraction coil made of transparent FEP thin wall tubes (Habia, Sweden) of 0.7/1.1 mm i.d./o.d. and of Teflon capillaries (0.7 mm i.d., Tecator, Sweden) in which the segment length equilibrates. The extraction tube was either straight or coiled helically. The restrictor coil consisting of 2 m of 0.7 mm i.d. Teflon tube was placed after the detector flow cell to establish an overpressure to prevent the formation of air or solvent vapor bubbles.

The segmentation repeatability and relative segment length were measured by an on-tube detector (LKB 2151 variable wavelength monitor, LKB Bromma, Sweden) equipped with a flow cell to allow the use of transparent FEP tubing of different inner diameter (see Figure 4). The flow cell was made from a copy of the original LKB 14-μL flow cell, but with a hole drilled through the cell body perpendicular to the light path to accommodate the tubing. An analog signal (produced by the refractivity and absorptivity changes on the interfacial surface between the organic and aqueous phases) from the logarithmic amplifier of the detector was fed into a Compaq Deskpro 286, Model 2 computer (Compaq Computer Corp., Houston, TX) via a high-speed data acquisition module PCI-20019M-1, analog termination panel PCI-20010T-1, and PCI-20012A-1 cable using series PCI-20046S-6 software drivers language support subroutine libraries with Basic language interface (Burr-Brown Corp., Tucson, AZ).

Computer programs written in Basic were used for communication between the computer and the detector and for data treatment. After the zero line adjustment (for aqueous, organic, or segmented flow stream) and baseline noise determination, the signal level was sampled every 3, 5, 10, 20, or 30 ms, depending on the segment length, to obtain the sufficient number of readings per segment ($n > 15$, 50–200 usually). All measured values were stored in the computer memory for postrun mathematical treatment.

A segment was identified when the mean value of 10 successive readings exceeded $U_o \pm 10s_o$, or occasionally $U_o \pm 3s_o$, where U_o is the signal measured with the instrument zeroed with only organic phase in the system and s_o is the standard deviation of this signal. The slope of the time dependence of the detector signal was also used as a segment indicator. The relative segment length was measured from positions of the inflection points ($t_{r(o)}$ and $t_{r(a)}$, respectively) when the baseline noise was high or the baseline stability was decreased as a result of pump pulsation. The mean values and the statistical parameters were then calculated for the full set of segments in a single run (n = 20–100 values). The mean values of several independent runs (usually three to seven) were used for further data treatment.

The time constant of the detector electronics and the relatively large cross section of the light beam in the optical part of the detection system (0.6 mm diameter) set the limit for this technique. For short segments (L_s < 3–5 mm) and/or high flow rates (Q_t > 3–5 mL min^{-1}), segment length was calculated from the number of segments passing through the detector during a preselected time interval (100–120 s usually), or from the residence

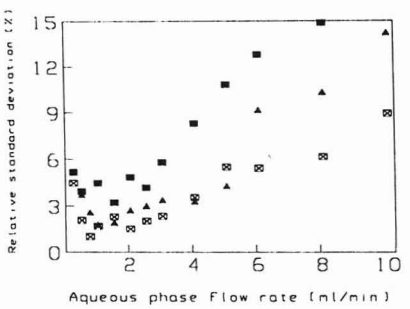

Figure 5. Segment length repeatability (s_r in %) of the organic segments for different types of the segmentors vs aqueous flow rate (0.2 mm i.d. glass inlet capillary) at a constant flow rate of the Freon-113 (Q_o = 0.5 mL min^{-1}): type A, full square; C, triangle (0.3 mm i.d.); D, square with cross.

time of the segment pairs in the detector flow cell ($t_r = t_{r(o)} + t_{r(a)}$) and the known flow rates of the two solvents. The segment length was in some cases checked manually by the method proposed by Cantwell (*28*).

Chemicals. Chloroform, carbon tetrachloride, 4-methyl-2-pentanone (methyl isobutyl ketone, MIBK), methanol (E. Merck, FRG, analytical grade), and Freon-113 (1,1,2-trichloro-1,2,2-trifluoroethane, technical quality) saturated with water were used. Aqueous-10 μM solutions of Bromocresol Green or Neutral Red were used exceptionally as coloring agents during segment length measurements. Triton X-100, a nonionic surfactant (Kebo, Sweden), and sodium chloride (E. Merck, FRG, analytical grade) were used as purchased. Distilled water and all other solvents and solutions were used after degassing in a Branson 2200 ultrasonic bath (Branson, USA).

RESULTS AND DISCUSSION

Influence of the segmentor construction and construction material. Initially the different segmentors shown in Figure 3 were tested with the emphasis on segmentation repeatability in order to elucidate what factors are the most important in coaxial segmentor design. A subset of these data for different segmentors is shown in Figure 5.

The best segmentation with the lowest relative standard deviation on the length of segments, s_r, was obtained by using the glass segmentor with the integral glass conical housing (type D). It works properly over a very wide range of flow rates of the two phases (Q_o = 0.2–1.6 mL min^{-1} for Freon-113 and chloroform (L_s 56 and 52 mm, respectively), Q_a = 0.5–10 mL min^{-1}), and at flow rate ratios from 2 to 35–40 with s_r better than 10%. Similar results were obtained for the glass coaxial segmentor with PVDF insert (type E), but serious leakage appears at aqueous flow rates Q_a over 3 mL min^{-1}, as a result of a lacking precision in the construction of the insert.

The inner surface of the inlet capillary of these segmentors, having a relatively wide diameter (1 mm i.d.), was from time to time wetted by the aqueous phase, especially at a low organic phase flow rate and at a high flow rate ratio, resulting in irregular droplet formation (s_r > 10%). A Teflon tube insert (0.5/1 mm i.d./o.d.) inside the inlet capillary, the end of which was positioned ≈0.5 mm from the end, eliminated this problem. At moderate and high flow rates, and for the narrower glass capillaries used in the other segmentors, this problem did not occur.

Similar segmentation repeatabilities were obtained with the PVDF/glass segmentor (type C) with a PVDF conical insert inside the glass confluence chamber. No break-up droplet occurred at aqueous phase flow rates between 0.5 and 8 mL min^{-1} for Freon-113, or at up to 5 mL min^{-1} for other solvents. The droplets were destroyed at higher and lower flow rates and small peaks appeared at the leading or trailing ends of the segment signals as a result of the formation of small droplets on the walls of the conical PVDF insert. This effect is especially pronounced in the case of MIBK.

Table I. Organic Phase Segment Length (L_s in mm) for Different Inner Diameters of the Glass Inlet Capillary (PVDF/Glass Segmentor Type C), at Constant Aqueous Phase Flow Rate Q_a = 2.0 or 3.0 mL min^{-1}

solvent		0.05 mm i.d.	0.10 mm i.d.	0.15 mm i.d.	0.20 mm i.d.	0.25 mm i.d.	0.30 mm i.d.	0.35 mm i.d.
Freon-113	L_s, mm	1.8	4.1	7.5	10.3	14.1	17.9	19.7
	s_r, %	6.2	4.8	2.8	3.0	2.6	2.3	1.6
$CHCl_3$	L_s, mm	2.2	4.0	6.7	9.9	13.7	16.4	19.3
	s_r, %	4.9	3.8	3.4	3.2	3.9	3.1	2.2
MIBK	L_s, mm	–	2.2	–	10.2	–	14.7	–
	s_r, %	–	7.3	–	3.9	–	3.7	–
CCl_4	L_s, mm	–	2.8	–	10.5	–	18.8	–
	s_r, %	–	6.1	–	2.8	–	2.7	–

Less repeatable segmentation ($s_r \approx 3$–15%) was achieved for the segmentor made of Perspex (type A) over the whole range of aqueous phase flow rates 0.25–8 mL min^{-1} and also for the PVDF segmentor (type B) at low aqueous phase flow rates below 2 mL min^{-1}. At higher flow rates, up to 8 mL min^{-1}, the segmentation repeatability of the latter was comparable with that for other types with glass walls in the confluence chamber.

The material of the compartment walls, and particularly that of the confluence chamber, and the interconnection between the conical part and the extraction capillary seem to be the most important factors for obtaining repeatable segmentation. Hydrophobic materials or surface irregularities in these parts lead from time to time to coverage by a thin film of organic phase or to capture of small droplets thereof. A small angle of the conical part of the confluence chamber and an excessive distance between the glass inlet capillary and the cone increase the probability of losing small droplets to the walls. These phenomena appear more often in the conical chamber made of Perspex than in the other ones, probably due to a rougher surface of the conical part. They were rarely found in the conical part made of PVDF and never in the integral glass conical compartment. Irregular build-up and release of this store of organic phase cause excessive variability in the segmentation.

The organic segment length increases linearly with the inner diameter of the inlet capillary at constant flow rates of the two phases Q_a = 3.0 or 2.0 mL min^{-1} and Q_o = 0.1–0.5 mL min^{-1} (Table I). Linear regression on the data for segment length vs capillary inside diameter gives $L_s = -1.8 + 62.8d_i$ ($r^2 = 0.994$) for Freon-113 and $L_s = -1.6 + 59.4d_i$ ($r^2 = 0.994$) for chloroform. Interfacial data for Freon-113/water are not available but for chloroform a theoretical slope of 56.3 can be calculated from eq 6 by using $\gamma_{o/a}$ = 32.8 dyn cm^{-1} (*29*), d_e = 0.07 cm, and $\Delta\rho$ = 0.491 g cm^{-3}. In view of the uncertainties involved in the measurement, the agreement between theory and experiment is good. Intercepts significantly different from zero are not predicted by eq 5 but are reasonable from the fact that some transport of organic phase takes place through the film along the tubing wall, thus, violating assumption 5. The best repeatability (s_r < 5%) was achieved for inner diameters of the glass capillaries in the range 0.10–0.35 mm for all the organic solvents tested.

The segment length is affected by the distance from the end of the inlet glass capillary to the outflow Teflon capillary (0.7/2.0 mm i.d./o.d.), positioned inside the outflow channel of the segmentor (type D, Figure 3), or to the mouth of the conical part of the PVDF insert (type F, Figure 3) in the straight glass tube of the segmentor (type E, Figure 3). The droplet size is drastically decreased at very short distances as a result of the "ripple" segmentation process (*26*), which occurs at distances below 0.5 mm. At longer distances (0.5–3 mm), the droplet size increases with this distance since it is being limited by the volume of the compartment between the two parts. The segment length is practically unaffected at distances over 4 mm as the individual droplets formed fall freely into the conical chamber. The segmentation repeatability is generally worse (usually 8–12% for 0.5 and 2 mm distance, respectively) when the segment length is controlled by varying the volume of the confluence chamber than when glass inlet capillaries are used for this purpose. This way of segment length control is therefore not recommended.

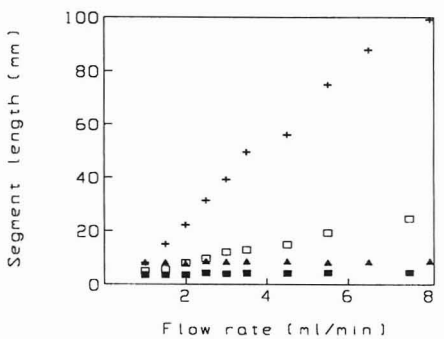

Figure 6. Influence of the aqueous phase flow rate (Q_a in mL min^{-1}) on the organic and aqueous phase segment length for 0.10 (full and empty square) and 0.20 mm i.d. of the glass inlet capillary (triangle and plus) at the organic phase flow rate Q_o = 0.25 and 0.5 mL min^{-1} and Freon-113 as the organic solvent.

Influence of the Flow Rate and Flow Rate Ratio. Using the PVDF–glass segmentor (C in Figure 3), the influence of flow rates on segmentation was studied. The length of the organic phase segments is only slightly influenced ($d(L_s)$ < 2–5%) by the aqueous phase flow rate in the range studied (Q_s = 0.25–10.0 mL min^{-1}). The results were the same regardless of organic phase flow rate (Q_o in the range 0.1–0.6 mL min^{-1}) and inlet capillary inner diameters (0.1–0.35 mm). A typical set of results is shown in Figure 6. As can be seen, the hydrodynamic conditions in the segmentor have only a minor influence on the segmentation. This is in striking contrast to the conditions in a T-piece segmentor, as was observed by Cantwell and Sweileh (*6*).

The segment length decreases more markedly at wider diameters of the glass inlet capillaries because the larger droplets are more easily deformed and less efficiently screened by the glass capillary from the action of the aqueous flow. Regression calculations on the data for segment length vs aqueous flow rate show a considerable improvement on changing from a linear model to a quadratic one, especially for the larger inlet capillary inside diameter. This implies a dominance of the Bernoulli term of eq 3. The change of segment length is, however, too small (<5%) to allow one to make any firm conclusions. In Figure 6 it can further be noted that since the length of the organic segments is constant, the length of the aqueous segments increases linearly with the aqueous phase flow rate if the flow rate of the other phase is held constant.

The length of the organic phase segment is not influenced by the flow rate of the organic phase, Q_o, from 0.1 mL min^{-1}

Table II. Influence of Some Chemical Factors on the Relative Segment Length and on Segmentation Repeatability[a]

NaCl			methanol			Triton X-100		
% (w/v)	$d(L_s)$	s_r	% (v/v)	$d(L_s)$	s_r	% (v/v)	$d(L_s)$	s_r
0.5	0.79	6.46	5	6.50	3.12	0.05	1.84	3.06
1.0	1.89	6.04	10	9.90	4.07	0.10	3.78	3.46
2.0	2.71	5.03	15	12.58	6.77	0.25	5.37	4.69
3.0	3.56	6.48	20	14.97	9.70	0.50	7.16	6.36
5.0	5.75	3.29	30	24.08	26.36	1.00	9.01	8.78
						1.50	11.88	16.19

[a] Segment length change ($d(L_s)$ in %) and the segmentation repeatability (s_r in %). Solvent: chloroform, 0.25 mm glass capillary, Q_a 3.0 mL min^{-1}, Q_o 0.5 mL min^{-1}, PVDF body.

up to some limiting value $Q_{o(lim)}$ depending on the inner diameter of the inlet capillary and the organic solvent. At still higher organic phase flow rates the segment length is rapidly decreased and the variability increased as a result of the jet effect. The limiting flow rates of Freon-113 were >1.6, 1.1, and 0.5 mL min^{-1} for capillaries with inner diameters 0.3, 0.2, and 0.1 mm, respectively. Similar results were obtained for chloroform and carbon tetrachloride while for MIBK the corresponding values were 1.6, 0.6, and 0.3 mL min^{-1}.

Character of the Organic Solvent. The segmentation repeatability decreases in the order Freon-113, chloroform, MIBK, and carbon tetrachloride when using the PVDF segmentor (type A, Figure 3) at an aqueous phase flow rate of Q_a = 0.5–10 mL min^{-1} and organic phase flow rates lower than $Q_{o(lim)}$ for the capillary inside diameter/organic phase combinations tested. Results for Freon-113, chloroform, and carbon tetrachloride are shown in Figure 7a, the repeatability for MIBK lies close to carbon tetrachloride. Irregular segmentation was sometimes obtained for MIBK and, exceptionally, also for carbon tetrachloride at very low organic flow rates, Q_o < 0.3 and 0.15 mL min^{-1} for 0.3 and 0.2 mm inlet capillaries, respectively, when small droplets of MIBK were cut off at the ends of the segments. The importance of segment size is clearly shown in Figure 7b, which depicts segmentation variability at different flow rates of the organic phase for different capillaries.

Influence of Other Factors. The spatial orientation of the main axis of the coaxial segmentor has a negligible effect on the segment length ($d(L_s)$ < 4%) at angles up to 10°, but it has a pronounced effect on the organic phase segment length at larger angles. When the main axis is horizontal, the segment length is decreased by about 50% compared to the normal position and the segmentation repeatability is also decreased. In this case, regular segmentation through the formation of drops is destroyed and the "ripple" mode (*26*) of segmentation takes over.

No significant difference in the organic phase segment length was found between straight and coiled FEP tubing (30 mm coil diameter) at Q_o = 0.4 mL min^{-1}, Q_a = 3 mL min^{-1} for 0.15 and 0.25 mm i.d. of the inlet glass capillary, but segmentation repeatability was better for coiled (L_s = 8.1 mm, s_r = 1.3% and 14.2 mm, s_r = 2.8%) than for straight (L_s = 8.0 mm, s_r = 2.5% and 14.4 mm, s_r = 4.9%) tubing when using Freon-113 as the organic solvent.

With an increasing content of up to 5% of inorganic salts, such as NaCl, in the aqueous phase, a weak trend of increasing segment lengths of the organic phase is seen. This effect is explained by the density increase of the aqueous phase and by the change of the interfacial tension. The segmentation repeatability is not influenced or slightly increased. Varying the methanol and nonionic surfactant content from zero to 10% and 1.0% by volume, respectively, decreases the segment length by less than 10%. The segmentation repeatability decreases drastically at higher contents of both substances and the segmentation process is totally destroyed at contents

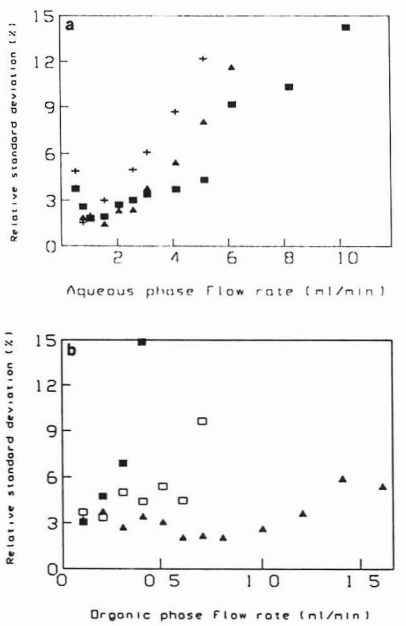

Figure 7. Segmentation repeatability (s_r in %): (a) for different solvents, Freon-113 (full square), chloroform (triangle), carbon tetrachloride (plus), segmentor type A, 0.20 mm i.d. glass inlet capillary, Q_o = 0.5 mL min^{-1}; (b) for different glass inlet capillaries of inner diameter 0.1 mm (full square), 0.2 mm (empty square), and 0.3 mm (triangle) and for chloroform as organic solvents, segmentor type A, Q_a = 2.0 mL min^{-1}.

in excess of 30% and 1.2%, respectively, because of the changes in surface tension. The results are summarized in Table II.

CONCLUSIONS

The results show that a considerable improvement in performance can be obtained with this new segmentor design. Apart from giving a 2–3-fold rise in segmentation repeatability it can be operated over a broader range of flow rates and phase flow rate ratios than previous designs. A further advance is that it essentially behaves according to the simple and well-established theory for free falling drops making it possible to estimate beforehand the parameters of the segmentation.

The segment length of the two phases can be varied over a very wide range from 2 to 50 mm for the organic phase and from 3 to 300 mm for the aqueous phase, simply by changing the inner diameter of the inlet glass capillary and the flow rates of the two phases. The segment length of the organic phase can be predicted, and it is independent of most factors influencing the segmentation process for other types of segmentors, such as the flow rate of the two solvents, the flow rate ratio, etc. (*26*).

The segmentation repeatability depends on the cleanness of the confluence compartment wall and the flat end of the glass inlet capillary. The presence of any lipophilic substances on the walls of the confluence compartment affects the seg-

mentation. Careful washing of these parts with ethanol and from time to time also grinding of the capillary end is of great importance for obtaining regular segmentation, especially after drying up. Air bubbles must also be removed from all parts of the segmentor, especially from the space between the glass capillary and the walls of the confluence compartment.

The relatively large dead volume of the conical chamber (~0.1 mL) leads to increased risks for carry over and thus to increased sample and reagent consumption. This factor is less serious at high flow rates of the aqueous phase and at high flow rate ratios, which are preferable in practical applications aiming at high enrichment factors (*23*). The dead volume can obviously be decreased by the miniaturization of the glass confluence compartment, as in our case this part was constructed to render it possible to use inlet glass capillaries of different outer diameters.

A disadvantage of the compact PVDF segmentor is the lack of visual checking of the segmentation process. This is important for the detection of disturbances caused by coverage of the walls of the confluence chamber by lipophilic substances. Perspex is unfortunately not usable for the most commonly used organic solvents. The construction of the confluence chamber, and especially of the conical part of the chamber, in a transparent hydrophilic material such as glass is thus recommended. The inlet capillary should be covered on the inner surface by a thin layer of lipophilic material (coated glass capillary). A metal capillary (platinum, stainless steel, etc.) pointing into the conical chamber to a short distance from the flat end of the PVDF screw and Teflon capillary can also be acceptable for some applications. The geometries of the confluence chamber and especially that of the conical part have to be optimized to decrease the dead volume of the segmentor, maintaining segmentation repeatability. The nominal volume of the conical part has to be greater than the actual volume of the droplet to prevent any contact between the confluence compartment walls and the organic phase. Coaxial segmentors usually work better at moderate and high flow rates than at low, because the segmentation repeatability decreases at low flow rates as the droplet is from time to time destroyed on the conical chamber walls.

All the above-mentioned improvements open a whole new set of possibilities where studies of liquid–liquid extraction can be performed directly on the organic phase segments, thus avoiding the problems connected with phase separation.

ACKNOWLEDGMENT

The authors thank Dr. Kenneth Bäckström for fruitful discussion throughout this work. The personnel at the chemistry faculty's workshop is thanked for helpful suggestions concerning the design of the segmentors.

LITERATURE CITED

(1) Ruzicka, J.; Hansen, E. H. *Flow Injection Analysis*; J. Wiley: New York, 1988; p 186.
(2) Valcarcel, M.; Luque de Castro, M. D. *Flow Injection Analysis, Principles and Applications*; J. Wiley: New York, 1987.
(3) Valcarcel, M.; Luque de Castro, M. D. *J. Chromatogr.* **1987**, *393*, 3.
(4) Karlberg, B. *Anal. Chim. Acta* **1988**, *214*, 29.
(5) Karlberg, B. *Fresenius' Z. Anal. Chem.* **1988**, *329*, 660.
(6) Cantwell, F. F.; Sweileh, A. J. *Anal. Chem.* **1985**, *57*, 329.
(7) Kawase, J.; Nakae, A.; Yamanaka, M. *Anal. Chem.* **1979**, *51*, 1640.
(8) Kawase, J. *Anal. Chem.* **1980**, *52*, 2124.
(9) Lucy, C. A.; Cantwell, F. F. *Anal. Chem.* **1986**, *58*, 2727.
(10) Nord, L.; Karlberg, B. *Anal. Chim. Acta* **1983**, *145*, 151.
(11) Karlberg, B.; Thelander, S. *Anal. Chim. Acta* **1978**, *98*, 1.
(12) Martinez-Jimenez, P.; Gallego, M.; Valcarcel, M. *Anal. Chim. Acta* **1988**, *215*, 233.
(13) Sweileh, J. A.; Cantwell, F. F. *Can. J. Chem.* **1985**, *63*, 2559.
(14) Nord, L.; Bäckström, K.; Danielsson, L.-G.; Ingman, F.; Karlberg, B. *Anal. Chim. Acta* **1987**, *194*, 221.
(15) Sahleström, Y.; Karlberg, B. *Anal. Chim. Acta* **1986**, *185*, 259.
(16) Bengtsson, B.; Johansson, G. *Anal. Chim. Acta* **1984**, *158*, 147.
(17) Farran, A.; De Pablo, J. *Anal. Chim. Acta* **1988**, *212*, 123.
(18) Ogata, K.; Taguchi, K.; Imanari, T. *Anal. Chem.* **1982**, *54*, 2127.
(19) Rossi, T. M.; Shelly, D. C.; Warner, I. M. *Anal. Chem.* **1982**, *54*, 2056.
(20) Kato, T. *Anal. Chim. Acta* **1985**, *175*, 339.
(21) Kuban, V.; Komarek, J.; Cajkova, D. *Collect. Czech. Chem. Commun.* **1989**, *54*, 2683.
(22) Atallah, R. H.; Christian, G. D.; Hartenstein, S. D. *Analyst (London)* **1988**, *113*, 463.
(23) Bäckström, K.; Danielsson, L.-G. *Anal. Chim. Acta* **1990**, *232*, 301.
(24) Motomizu, S.; Oshima, M. *Analyst (London)* **1987**, *112*, 295.
(25) Rossi, T. M.; Shelly, D. C.; Warner, I. M. *Anal. Chem.* **1982**, *54*, 2056.
(26) Kuban, V.; Danielsson, L.-G.; Ingman, F. Unpublished results.
(27) Adamson, A. W. *Physical Chemistry of Surfaces*, 3rd ed.; Wiley: New York, 1976; pp 18–21.
(28) Lucy, C. A.; Cantwell, F. F. *Anal. Chem.* **1989**, *61*, 101.
(29) *International Critical Tables*, 1st ed.; McGraw-Hill: New York, 1928; Vol 4, pp 432–475.

RECEIVED for review December 20, 1989. Accepted June 5, 1990. Financial support from the Swedish National Board for Technical Development and the Swedish Institute are gratefully acknowledged.

Evaluation of Inductively Coupled Plasma Emission Spectrometry as an Element-Specific Detector for Supercritical Fluid Chromatography

Kimberley A. Forbes,[1] Jodi F. Vecchiarelli,[2] Peter C. Uden,* and Ramon M. Barnes

Department of Chemistry, Lederle GRC Tower A, University of Massachusetts, Amherst, Massachusetts 01003-0035

A capillary supercritical fluid chromatograph (SFC) was interfaced to an inductively coupled plasma (ICP) atomic emission spectrometer (AES). The chromatographic system, interface, and plasma torch design are described. The argon plasma was optimized for Si I 251.6 nm emission to detect separated organosilicon compounds selectively. The linear dynamic range for octamethylcyclotetrasiloxane was between 7.24 and 145.0 ng of Si injected, with a detection limit of 5.8 ng of Si injected (57.9 ppm Si). The precision of the measured peak heights of three replicate injections of 75 ng of Si was less than 5%. The effects of the mobile phase (CO_2) pressure on the plasma stability and sensitivity are presented.

INTRODUCTION

Chromatography with a supercritical fluid mobile phase was suggested more than 25 years ago (*1*, *2*). The difficulties of handling the required pressures and temperatures of these fluids with the instrumentation existing at that time limited development, but as technology advanced in both capillary gas chromatography (GC) and high-performance liquid chromatography (HPLC), useful techniques that could be utilized in supercritical fluid chromatography (SFC) were provided (*3*). The first practical capillary SFC instrument was described in 1981 (*4*), and since then SFC has been considered as a complementary technique to GC and HPLC, and has been applied in a variety of areas including the analysis of polymers (*5*), glycerides (*6*, *7*), pesticides (*8*), cholesterol (*9*), and complex hydrocarbon mixtures (*10*).

SFC detection may be either on-column (*4*) or at atmospheric pressure after a decompression stage. LC-like spectroscopic detectors, including variable-wavelength UV absorbance (*10*), fluorescence (*11*), and infrared absorbance (*12*, *13*), have been applied as on-column detectors for SFC. GC-like detectors have been applied after decompression of the supercritical mobile phase to a gas. The flame ionization detector (FID) was used for packed (*14*, *15*) and capillary SFC columns (*7*, *9*), yielding relatively low background signals (*3*). Other detection methods used in GC have been investigated for SFC, including supercritical fluid chromatography/Fourier transform infrared (SFC/FTIR) spectroscopy (*16*, *17*), supercritical fluid chromatography/mass spectrometry (SFC/MS) (*18*, *19*), and SFC followed by ion mobility (*20*), thermionic (*21*), and dual flame photometric detection (*22*).

Plasma atomic emission sources offer many advantages as chromatographic detectors, including multielement detection capability, high sensitivity, and inherent selectivity. These features enable nonideal chromatography to be tolerated and metal and nonmetal speciation to be performed. Additionally, plasma detectors suffer from fewer spectral interferences and have a wider dynamic range than flame-based detectors (*23*). The first use of a supercritical fluid sample introduction system for inductively coupled plasma (ICP) was reported in a correspondence by Olesik et al. (*24*). The limitation in the development of plasma chromatographic detectors is the interface which must minimize band broadening. In HPLC, the conventional nebulizer and spray chamber systems used for liquid sample introduction show typical transport efficiencies of less than 2%. The unique properties of supercritical fluids eliminate the need for the nebulizer/spray chamber interface, since as the fluid leaves the chromatographic column and restrictor, it becomes a gas at atmospheric pressure and will transport essentially 100% of the sample in a readily atomized form. Fujimoto et al. reported the interfacing of ICP to a packed column SFC system (*25*). A laboratory-made nebulizer with a built-in restrictor was attached directly to the ICP torch, and the system was evaluated with ferrocene and its derivatives. No reports of the use of the ICP as a detector for capillary SFC have appeared, but the above studies suggest that capillary interfacing may show equal or better analytical performance to the packed-column case. Recently, Galante et al. (*26*) and Luffer et al. (*27*) coupled the surface-wave-sustained-microwave-induced-plasma (surfatron) to a capillary SFC system and detected sulfur-containing polyaromatic compounds. Element-specific detection for sulfur was in the near-infrared region because the sulfur atom lines were more intense than those in the visible region, which also suffered from severe spectral interferences from intense C_2 band emission resulting from the carbon dioxide mobile phase (*26*). In general the small size and low power, which make the microwave-induced helium plasma (MIP) detectors of the TM_{010} type most attractive for GC detection, but less so for HPLC detection because of mobile phase impact, reduce their applicability for SFC. The argon ICP however suffers from the same limitations for elemental speciation in SFC as in other chromatographies, namely poor or absent detectability for many nonmetallic elements. Development of different complementary plasma detection systems for SFC is thus important.

This paper discusses the coupling of an argon ICP to a capillary SFC. Various restrictor designs were investigated, and overall system parameters are discussed. The effects of the mobile phase on plasma stability, sensitivity, selectivity, and spectral background are presented, and optimization for the detection of silicon-containing compounds is reported.

Automobile and fuel sensors and emission control devices are susceptible to silica poisoning arising from contamination of unleaded fuels (*28*). Inductively coupled plasma atomic emission spectrometry (ICP-AES), alone, may be used for quantitative assay of the silicon content in a sample, and the chemical identity of the cyclic silicone contaminant, octamethylcyclotetrasiloxane, was obtained by high-resolution silicon-29 nuclear magnetic resonance (NMR) spectroscopy (*28*). The use of a capillary supercritical fluid chromatogra-

* To whom correspondence should be addressed.
[1] Present address: Rorer Central Research, Fort Washington, PA 19034.
[2] Present address: Union Carbide Corp., Tarrytown, NY 10591.

0003-2700/90/0362-2033$02.50/0

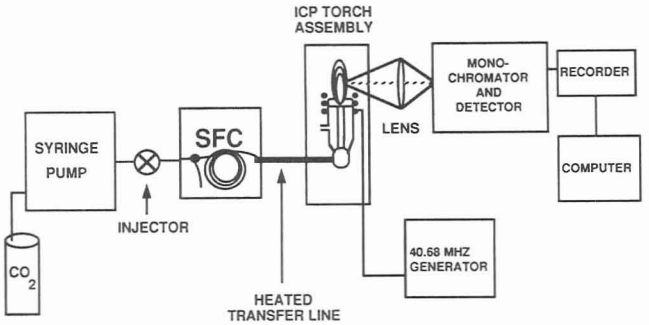

Figure 1. Schematic diagram of the supercritical fluid chromatograph/inductively coupled plasma.

phy/inductively coupled plasma atomic emission spectrometry (SFC/ICP-AES) system could provide a method to separate and detect on-line various organosilicon compounds present in the fuels.

EXPERIMENTAL SECTION

Instrumentation. A schematic diagram of the instrumentation is shown in Figure 1. The components of the system are described below.

Chromatographic Equipment. A gas chromatograph (Perkin-Elmer 3920B, Norwalk, CT) was modified for use in SFC. A syringe pump (Varian 8500, Varian Aerograph, Walnut Creek, CA) was used to deliver carbon dioxide (supercritical fluid grade, Scott Specialty Gases, Plumsteadville, PA) mobile phase, which was filtered at the outlet of the pump through a 2-μm filter (Valco Instrument Co., Inc., Houston, TX). The pressure of the CO_2 delivered by the pulseless syringe pump could be controlled manually, or pressure programming could be performed with a computer (Apple IIe, Apple Computer, Inc., Cupertino, CA).

The fused silica capillary column used was coated with poly(dimethylsiloxane) (20 m × 0.2 mm i.d., 0.05-mm film thickness, J+W Scientific, Inc., Folsom, CA). The column temperature was controlled by the GC oven.

Samples were injected with a microvalve (Valco) with a 0.1-μL electronically actuated loop. Six inches of $^1/_{16}$ in. o.d. × 0.02 in. i.d. stainless steel tubing were connected between the injection valve, through the injection port opening into the oven, and into the side of the straight run on a $^1/_{16}$ in. tee (Valco ZT1). The other two ports in the tee had reducers (Valco IZR1.5LFS.4) installed. A retention gap (0.375 mm o.d. × 50 μm i.d. uncoated fused silica) was passed through the tee and the $^1/_{16}$ in. tubing, then butted flush with the end of the tubing at the injector valve port. The other end of this retention gap was connected to the head of the capillary column with a $^1/_{32}$ in. union (Valco ZU.5FS.4).

In the side of the splitter tee, a 10–15 μm i.d., 140 μm o.d. piece of fused silica (Polymicro Technologies, Phoenix, AZ) was used as the splitter vent restrictor. The length of this split vent capillary tubing and the length of the restrictor used to give the required decompression to atmospheric pressure for detection could be adjusted to obtain a usable split ratio. A 182.5-cm splitter vent restrictor with a 17.5 cm long straight capillary restrictor composed of the same fused silica tubing as the splitter vent restrictor was used. The splitter vent restrictor could be tailored to the flow characteristics of the restrictor, and various combinations of the two restrictors were investigated. The results of these studies, including the use of a 2 mL/min integral restrictor as described by Guthrie and Schwartz (*29*), are included.

Organosilicon standards (Petrarch Systems Inc., Bristol, PA) were made in HPLC grade toluene (Fischer Scientific, Fair Lawn, NJ). Compounds used included hexamethylcyclotrisiloxane (D_3), octamethylcyclotetrasiloxane (D_4), decamethylcyclopentasiloxane (D_5), 1,7-dichlorooctamethyltetrasiloxane, decamethyltetrasiloxane, octamethyltrisiloxane, 1,1,3,3,5,5,7,7-octamethyltetrasiloxane, cyclopentamethylenedimethylsilane, cyclotrimethylenedimethylsilane, and cyclotetramethylenedimethylsilane.

Interface. The interface and plasma torch are shown in Figure 2. The plasma was sustained in the torch designed by LaFreniere et al. (*30*) for use as a DIN (direct injection nebulizer) (Cetac DIN-200, Questron Corp., Princeton, NJ). However, since the supercritical fluid leaving the capillary restrictor becomes a gas

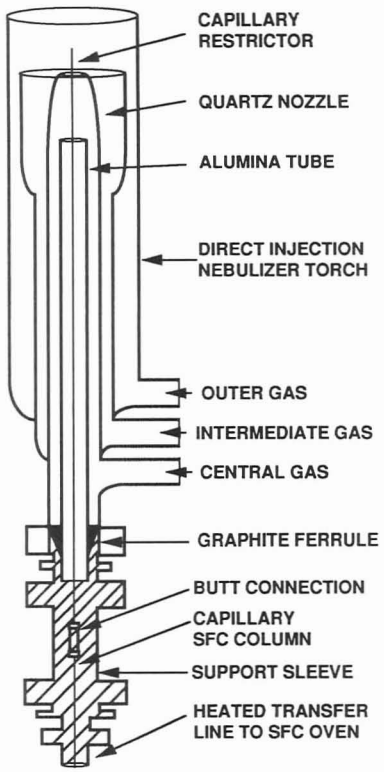

Figure 2. Interface for supercritical fluid chromatograph/inductively coupled plasma.

in the atmospheric pressure plasma, the nebulizer is not required. Thus, the capillary restrictor was positioned concentrically inside an alumina tube in place of the capillary fused silica tubing used for nebulization. The alumina tube (0.8 mm i.d., 1.6 mm o.d.) supported and positioned the restrictor in the torch and also provided insulation to help prevent charring of the polyimide coating on the restrictor. The DIN torch design allowed three gas flows to be used, even without the nebulizer functioning. The outer and intermediate gas flows served their usual function to sustain the plasma discharge. The central gas flow through the inner nozzle of the DIN torch was used to carry the column effluent into the plasma.

A heated transfer line, similar in design to those used for GC/MIP (*31*), was constructed to transport the sample from the SFC oven to the ICP. Temperature control of the capillary column was maintained by passing it through 60 cm of resistively heated $^1/_8$-in. copper tubing, which was insulated and contained in heat tape. The capillary column was connected to the restrictor by a $^1/_{32}$-in. butt connector. To provide support for the delicate restrictor, a 6-cm section of 1 cm i.d. aluminum tubing was used as a sleeve, connected by specially constructed unions from the end of the copper tubing to the base of the torch. This sleeve supported the end of the SFC column, butt connector, and the beginning of the restrictor. The sleeve and the unions used to provide connection to the torch were wrapped in heat ribbon to maintain constant temperature control. Thermocouples were used to monitor the temperature along the transfer line and at the base of the torch. The transfer line was maintained at 70 °C, the base of the torch was approximately 80–90 °C, and the oven was 60 °C.

The alumina tube was carefully positioned in the center of the connecting unions with graphite tape, prior to connecting the restrictor to the column. The restrictor was fed through the alumina tube, unions, and into the sleeve, which was snot yet connected to the end of the copper tubing. The butt connection to the column was made, and then the sleeve was connected to the insulated copper tubing containing the column. The restrictor could then be pulled back so as to be contained totally inside the alumina tube, which was then carefully fed into the center of the ICP torch, protecting the delicate restrictor. The alumina tube was positioned in the center of the nozzle and helped to position the restrictor in the torch.

The proximity of the restrictor to the ICP was critical. The 6 cm long support sleeve permitted adjustment of the distance between the restrictor and the top of the nozzle. The distance between the end of the restrictor and the plasma must be small to minimize the dead volume, but it must not be too small because the restrictor can be fused shut. The tip of the restrictor was placed 10 mm below the discharge region of the ICP, to provide optimal transport from the restrictor into the central region of the plasma. The tip of the restrictor was positioned approximately 2 mm above the tip of the nozzle, centered symmetrically, so that the column effluent was swept efficiently into the ICP.

Inductively Coupled Plasma Atomic Emission Spectrometer. The ICP power generator (Plasma Therm, Inc., 40.68-MHz rf Generator Type HFS 5000D, Kresson, NJ) was operated at 850 W, unless noted otherwise. Simplex optimization (*32*) was performed to determine the rf power level and gas flow rates to be used for detection of Si I 251.6 nm. The DIN torch was used with an outer gas flow rate of 24.1 L/min, intermediate gas flow rate of 1.2 L/min, and a central gas flow rate of 0.6 L/min.

An image of the plasma was formed with quartz optics (Oriel 2 in. diameter, 200 mm focal length, 1:1 image) onto the entrance slit of the monochromator (Heath Model EU-700-56, 0.35-m focal length. Czerny-Turner scanning monochromator, with programmable filter attachment, McPherson Instruments, Acton, MA). The entrance and exit slit widths were 50 μm. The grating had 1180 grooves/mm and was blazed at 250 nm. The voltage of the photomultiplier tube (RCA 1P28A) was maintained by the Heath Photomultiplier Module Model EU 701-30 at 650 V. Output was recorded by the Heath Log/Linear Current Module EU-20-28 (Heath Co.). The plasma was observed 14 mm above the load coil, unless stated otherwise.

RESULTS AND DISCUSSION

Optimal Interface Design for Capillary SFC/ICP. The most important component in the design of the capillary SFC/ICP system was the column restrictor. The flow of the column effluent to the detector is determined by the flow characteristics of the capillary restrictor used to achieve decompression and the splitter vent restrictor. Various restrictor designs were investigated to provide the decompression necessary to introduce the eluent from the SFC column into the atmospheric pressure ICP. A straight capillary restrictor of relatively large internal diameter (25–50 μm i.d.) did not provide sufficient back pressure to maintain supercritical conditions on the column. Although signals were observed for Si I and P I, all samples eluted in the void volume and the separation of various silicon containing compounds could not be accomplished (*33*).

Although a 2 mL/min integral restrictor provided significant back pressure to maintain supercritical conditions on the column, its 2-μm orifice resulted in a mobile phase flow rate that was too low to allow transport of significant amount of sample into the ICP. No analyte signals could be observed. Similar results were observed when the splitter vent restrictor length was much less than the length of the restrictor to the ICP. When a relatively long (86 cm) 5 μm i.d. straight capillary restrictor was used in combination with a 12 in., 14 μm i.d. straight capillary as the splitter vent restrictor, too much of the sample exited the splitter vent, and no signal was observed. Details of the investigations of various restrictor combinations are reported elsewhere (*34*).

To allow the shortest length capillary to be used as a restrictor to achieve decompression prior to introduction into the ICP, the SFC column was passed through the transfer line. Heating of the transfer line was controlled to maintain constant temperature throughout the column. A 15.6 cm long, 5 μm i.d. fused silica capillary was connected to the end of the SFC column by using a butt connector which was supported in the sleeve, as described. The short length of the 5 μm i.d. capillary restrictor resulting in less resistance to flow of the mobile phase to the plasma. However, carbon emission at 247.9 nm was not observed, and no visual color changes in the argon plasma were apparent.

In order to increase the flow of CO_2 to the plasma further, the splitter vent was plugged with an end-capped fitting. Thus, all of the flow was directed out of the restrictor to the detector. Emission was observed for both the C I 247.9 nm and the C I 193.1 nm lines. The carbon emission increased as the CO_2 pressure increased. The C_2 and CO^+ molecular bands were not observed upon scanning the background region. All of the carbon introduced into the ICP probably was decomposed into carbon at these CO_2 introduction rates, which, although not measured directly, were estimated to be ca. 50 μL/min at a pressure of 80 atm. Toluene was injected into the SFC and the C I 247.9 nm line was monitored. No signal resulting from the solvent was detected over the background at this wavelength; this was not unexpected since the contribution from CO_2 is much larger than that of toluene. Strong CN bands were observed in the spectrum, since the ICP torch had no extension, and their presence served as a good indication of pressurization of the SFC system.

A study was performed to determine where in the plasma the maximum carbon emission at 247.9 nm was observed. The forward power was 1 kW, reflected power was tuned to 0 W, the outer gas flow rate was 22 L/min, intermediate gas flow rate was 1.2 L/min, the central gas flow rate was 0.63 L/min, and the CO_2 pressure was 200 atm. The maximum carbon emission was observed at observation heights of 11.0–13.5 mm above the load coil.

The intensity of the carbon emission and the noise in the background of the plasma increased as the delivery pressure of the carbon dioxide was increased. The signal noise was largest while the syringe pump was adjusting to the desired pressure. Once the pump reached the desired pressure, the plasma became stable. With the splitter vent plugged and the 5 μm i.d. capillary restrictor in the torch, various organosilicon compounds were injected at several different power levels, observation heights, and gas flow rates. No response was detected by Si I 251.6 nm. Ferrocene was also injected, but no Fe I response at either 238.0 or 259.7 nm was detected. The supercritical fluid mobile phase was transported into the plasma, but insufficient eluent entered the plasma to detect analyte emission.

The flow to the ICP was increased by installing a 17.5 cm long, 14 μm i.d. straight capillary tubing in the interface. The flow of CO_2 out of this restrictor was verified prior to insertion of the restrictor in the torch. At 80 atm pressure, the flow rate to the ICP was estimated at ca. 50 μL/min from calculation based upon measurement of split vent dimensions and vented flow using a simplified form of Poiseuille's law. When the delivery pressure of the CO_2 was about 100 atm, an ice ball was observed at the tip of the restrictor, indicating Joule–Thompson cooling of the supercritical fluid leaving the capillary. The tip of the capillary was positioned about 2 mm above the top of the inner quartz nozzle in the DIN, about 10 mm below the plasma, to ensure optimal sample transport. Emission of the C I at 247.9 nm and at 193.3 nm increased as the delivery pressure of the CO_2 mobile phase was increased. The 1-kW (approximately 50 W reflected power) argon ICP was stable for CO_2 pressures of 80–250 atm. The central channel of the argon plasma was green owing to the C_2 molecular band emission. The channel became wider and greener as the CO_2 pressure increased. The plasma was extinguished when the CO_2 pressure was increased to 300 atm.

The argon plasma was easily ignited with the 14 μm i.d. capillary restrictor in the torch and the CO_2 pressure at 80–100 atm. With the splitter vent plugged, 3.5-μg of hexamethylcyclotrisiloxane (D_3) was injected. The Si I 251.6-nm line was monitored in a 1.1-kW plasma at an observation height of 13 mm (outer gas flow rate 24 L/min, intermediate gas flow rate

1.2 L/min, central gas flow rate 0.60 L/min, and the preheated gas flow around the restrictor 0.6 L/min). The SFC oven and the transfer line temperatures were held at about 70 °C, and the torch base was about 100 °C. The relatively high quantity injected overloaded the capillary column, resulting in poor peak shape; however, a Si I signal was detected in the effluent. Two other organosilicon compounds, D_4 and D_5, were injected under the same conditions. Under isobaric SFC operation, the retention time of D_5 was greater than D_4 or D_3.

Optimal Conditions for Determination of Silicon-Containing Compounds. *Split Ratio.* To improve peak shape, the plug in the split vent was removed, and a splitter vent restrictor (14-μm i.d. × 182.5-cm length, fused silica straight capillary) was installed. The combination of this split vent restrictor with the 17.5 cm long restrictor (14 μm i.d. straight capillary) in the ICP torch resulted in venting approximately one-tenth of the sample, estimated as noted above using restrictor and vent dimensions and application of Poiseuill's relationship. The peak shape observed for the organosilicones was improved under the previous chromatographic conditions.

Effect of Preheated Gas Flow. A fourth gas flow, which was preheated by passing it through ~70-ft of copper tubing coiled in an oven which could be heated to 300 °C, was introduced at the beginning of the transfer line to provide better sample transport. This heated argon passed through the transfer line, flowed around the restrictor inside the alumina insulating tube, and into the ICP torch. Olesik reported that the velocity of the central gas should be high enough to ensure that the sample travels through the plasma boundary and into the center of the discharge (*24*). Additionally, the flow of this preheated gas around the restrictor should provide uniform heating and help minimize condensation. The Si I signals measured without the preheated gas flow around the restrictor were almost twice those measured with a gas flow rate of 0.6 L/min around the restrictor. In fact, any added gas flow around the restrictor resulted in a decreased response, even when the observation height and other gas flow rates were adjusted. This is in contrast to the observation of Olesik (*24*). In the SFC/ICP system described here, the extra gas flow around the capillary restrictor decreased sample residence time and, thus, decreased the emission signal. The DIN torch used had the alumina tube surrounding the capillary restrictor set concentrically inside the inner quartz nozzle, which reduced the effective size of the central nozzle (Figure 2). The velocity of the central flow which resulted was sufficient to ensure the sample traveled into the center of the plasma. A channel was visible in the plasma with the central gas flow rate as low as 0.55 L/min.

Detector Response. The "spiking" problem that has been reportedly observed in FID signals when used with SFC (*35*) was not observed in this work. Spiking occurs frequently for polar solvents and high molecular weight solutes, which are likely to condense and result in noisy peaks as discrete solute particles enter the detector and produce a sudden response. Perhaps the lack of spiking in this work was due to the samples studied. Condensation also was not observed by Olesik and Olesik (*24*).

Simplex Optimization. A simplex optimization was performed with a 905 μg/mL solution of octamethylcyclotetrasiloxane (D_4) (90.5 ng of Si injected). The delivery pressure of the CO_2 mobile phase was 80 atm. The chromatographic oven was maintained at 60 °C, the transfer line at 70 °C, and the torch base at 100 °C. The intermediate flow rate was maintained constant at 1.2 L/min to ensure the plasma was an appropriate distance from the tip of the restrictor in the torch. The tip of the restrictor was withdrawn slightly until it was even with the top of the central nozzle in the torch. The observation height was 13.5 mm throughout the Si I studies. Power levels from 800 W to 1.15 kW were investigated. Below 800 W the ICP was not stable upon introduction of the supercritical fluid CO_2 at 80–100 atm. Central gas flow rates from approximately 0.5 to 1.5 L/min were examined. The third parameter involved in the simplex optimization was the outer gas flow rate. Values from 23.5 to 24.3 L/min were investigated and were observed to effect the peak shape. Three injections were made for each set of conditions tested in the simplex program. The optimum conditions obtained for the determination of Si I at 251.6 nm by SFC/ICP with a CO_2 delivery pressure of 80 atm were forward power 850 W, central gas flow rate 0.6 L/min, and outer gas flow rate 24.1 L/min.

Detection Limits. The detection limit ($S/N = 3$) for D_4 under optimum conditions was found to be approximately 5 ng of Si injected with the CO_2 pressure at 80 atm. The possibility of monitoring the Si I emission at 288.1 nm was explored but the background and the noise were much higher in that region of the spectrum, due in part to molecular bands, resulting in poor response.

In an attempt to improve the detection limit of D_4, oxygen was added to the argon outer gas flow. The addition of 3–17% oxygen to the outer gas flow did not increase the response at Si I 251.6 nm. The response also was not enhanced by the addition of oxygen to the intermediate or central gas flows.

Linearity and Precision. The linearity of the SFC/ICP system was measured for the detection of D_4 using the conditions determined by the simplex optimization with the CO_2 pressure maintained at 80 atm. Linearity was demonstrated over a concentration range of 7.24–145.0 ng of Si injected. Concentrations above this range resulted in column overload. The slope of the calibration curve for seven concentrations in the specified range is 6.9 ± 0.1 mV/ng, with an intercept of -1.2×10^{-3} and a correlation coefficient of 0.999. All statistics were calculated by using RS/1 (Version 12.1, BBN Software Products Corp., Cambridge, MA). The relative standard deviation of the peak heights for D_4 was based on three replicate injections of each of the concentrations. The values ranged from 1 to 5% for concentrations greater than 14 ng of Si injected. A slightly higher value of 8% was determined for the injection of 7.24 ng of Si, which is closer to the detection limit.

When the CO_2 pressure was increased to 100–120 atm and maintained constant, linearity of Si I 251.6-nm emission was demonstrated for D_4 between 7.24 and 145.0 ng of Si injected. The slope of the calibration curve for four concentrations in the specified range is 6.0 ± 0.3 mV/ng, with an intercept of 0.12 and a correlation coefficient of 0.998. The decrease in slope of this calibration curve compared to that at 80 atm indicates a slight decrease in sensitivity occurs at the higher pressure. Similar results were reported in the determination of polyaromatic sulfur-containing compounds by SFC/MIP (*27*).

The sharpest and most reproducible peaks were recorded for D_4 using a CO_2 delivery pressure of 80 atm. For the elution of the higher molecular weight siloxane standard, 1,7-dichlorooctamethyltetrasiloxane, 100 atm CO_2 resulted in the sharpest, most reproducible peaks. A mixture of these two tetrasiloxane standards was prepared and injected. The two compounds were not completely separated under isobaric conditions at either 80 or 100 atm. To achieve better separation and good peak shape,the pressure was slowly adjusted manually to provide a simple pressure program from about 80 to 100 atm, and the resolution of the two siloxane standards was improved (Figure 3). No continuous controlled pressure programming facility was available, due to rf electronic interference with the SFC control system, but the manual ex-

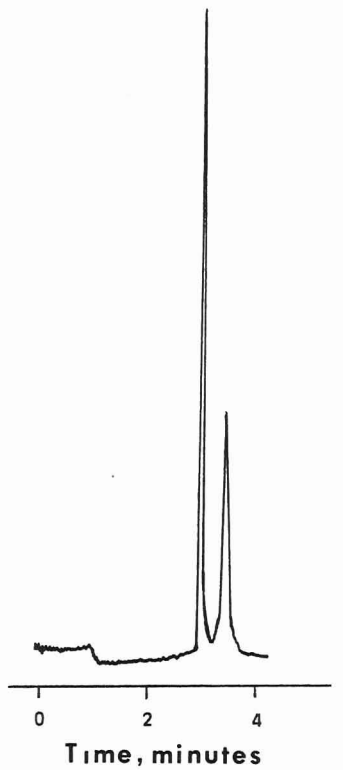

Figure 3. Separation of two tetrasiloxanes: (1) octamethylcyclotetrasiloxane (89.8 ng of Si); (2) dichlorooctamethyltetrasiloxane (160.3 ng of Si).

periment indicated that background noise would generally increase during programming.

Although the compounds studied were smaller than typical condidates for SFC, these siloxanes demonstrate the feasibility and selectivity of the ICP as a detection method for capillary SFC. These studies have shown that the argon ICP may be used to detect the emission of silicon-containing compounds in the UV–vis region of the spectrum as they elute in the supercritical mobile phase. While the carbon dioxide mobile phase does diminish sensitivity of the ICP somewhat, the molecular background emission is not increased significantly, as observed upon introduction of the supercritical carbon dioxide into the microwave induced plasma (*26*, *27*). The response of the ICP to Si I 251.6-nm emission is linear, and the sensitivity provided, coupled with the chromatographic separation capabilities, should be suitable for many applications. Plasma conditions would require optimization with respect to flow rates, viewing height, etc. to determine detection limits and linear ranges for other elements. However, it may be noted that there is much less interference due to introduction of CO_2 into the ICP than in introduction to the MIP: thus potentially useful analytical ranges may be larger for some elements. The selectivity of the ICP demonstrates the capability to detect early eluting compounds which are normally not separated from the solvent peak. This work also demonstrates the use of supercritical fluids as a means of efficient sample introduction into the ICP.

ACKNOWLEDGMENT

We gratefully acknowledge Thomas Chester and David Innis at The Miami Valley Laboratory of the Procter and Gamble Corp., Cincinnati, OH, for their collaboration in assembling the SFC system used in this work and their helpful discussions about the interface.

LITERATURE CITED

(1) Gere, D. R. *Science* **1983**, *222*, 253–258.
(2) Klesper, E.; Corwin, A. H.; Turner, D. A. *J. Org. Chem.* **1962**, *27*, 700.
(3) Novotny, M. *HRC CC, J. High Resolut. Chromatogr. Chromatogra. Commun.* **1986**, *9*, 137–144.
(4) Novotny, M.; Springston, S. R.; Peadon, P. A.; Fjeldsted, J. C.; Lee, M. L. *Anal. Chem.* **1981**, *53*, 407A–414A.
(5) Fjeldsted, R. C.; Jackson, W. P.; Peaden, P. A.; Lee, M. L. *J. Chromatogr. Sci.* **1983**, *21*, 222–225.
(6) White, C. M.; Houck, R. K. *HRC CC, J. High Resolut. Chromatogr. Chromatogr. Commun.* **1985**, *8*, 293.
(7) Chester, T. L. *J. Chromatogr.* **1984**, *299*, 424–431.
(8) Wright, B. W.; Smith, R. D. *HRC CC, J. High Resolut. Chromatogra. Chromatogr. Commun.* **1985**, *8*, 4.
(9) Fjeldsted, J. C.; Kong, R. C.; Lee, M. L. *J. Chromatogr.* **1983**, *279*, 449–455.
(10) White, C. M.; Houck, R. K. *HRC CC, J. High Resolut. Chromatogr. Chromatogr. Commun.* **1986**, *9*, 3–16.
(11) Fjeldsted, J. C.; Richter, B. E.; Jackson, W. P.; Lee, M. L. *J. Chromatogr.* **1983**, *279*, 423–430.
(12) Shafer, K. H.; Griffiths, P. R. *Anal. Chem.* **1983**, *55*, 1939–1942.
(13) Olesik, S. V.; French, S. B.; Novotny, M. *Chromatographia* **1984**, *18*, 489.
(14) Giddings, J. C.; Myers, M. N.; McLaren, L.; Keller, R. A. *Science*, **1969**, *162*, 67.
(15) Rawdon, M. G. *Anal. Chem.* **1984**, *56*, 831.
(16) Pentoney, S. L., Jr.; Shafer, K. H.; Griffiths, P. R. *J. Chromatogr. Sci.* **1986**, *24*, 230–235.
(17) Pentoney, S. L., Jr.; Shafer, K. H.; Griffiths, P. R.; Fuoco, R. *HRC CC, J. High Resolut. Chromatogr. Commun.* **1986**, *9*, 168–171.
(18) Wright, B. W.; Kalinoski, H. T.; Udseth, H. R.; Smith, R. D. *HRC CC, J. High Resolut. Chromatogra. Chromatogr. Commun.* **1986**, *9*, 145–153.
(19) Lee, E. D.; Henion, J. D. *HRC CC, J. High Resolut. Chromatogr. Chromatogr. Commun.* **1986**, *9*, 172–174.
(20) Eatherton, R. L.; Morrissey, M. A.; Siems, W. F.; Hill, H. H., Jr. *HRC CC, J. High Resolut. Chromatogr. Chromatogr. Commun.* **1986**, *9*, 154–160.
(21) West, W. R.; Lee, M. L. *HRC CC, J. High Resolut. Chromatogr. Chromatogr. Commun.* **1986**, *9*, 161–167.
(22) Markides, K. E.; Lee, E. D.; Bolick, R.; Lee, M. L. *Anal. Chem.* **1986**, *58*, 740–743.
(23) Uden, P. C. *Chromatogr. Forum* **1986**, *1*, 17–26.
(24) Olesik, J. W.; Olesik, S. V. *Anal. Chem.* **1987**, *59*, 796–799.
(25) Fujimoto, C.; Yoshida, H.; Jinno, K. *J. Chromatogr.* **1987**, *411*, 213–220.
(26) Galante, L. J.; Selby, M.; Luffer, D. R.; Hieftje, G. M.; Novotny, M. *Anal. Chem.* **1988**, *60*, 1370–1376.
(27) Luffer, D. R.; Galante, L. J.; David, P. A.; Novotny, M.; Hieftje, G. M. *Anal. Chem.* **1988**, *60*, 1365–1369.
(28) Carduner, K. R.; Carter, R. O., III; Westwood, L. C. *Appl. Spectrosc.* **1988**, *42*, 1265–1267.
(29) Guthrie, E. J.; Schwartz, H. E. *J. Chromatogr. Sci.* **1986**, *24*, 236–241.
(30) LaFreniere, K. E.; Fassel, V. A.; Eckels, D. E. *Anal. Chem.* **1987**, *59*, 879–887.
(31) Quimby, B. D.; Uden, P. C.; Barnes, R. M. *Anal. Chem.* **1978**, *50*, 2112–2118.
(32) Parker, L. R., Jr.; Cave, M. R.; and Barnes, R. M. *Anal. Chim. Acta* **1985**, *175*, 231–237.
(33) Vecchiarelli, J. A. F. Ph.D. Dissertation, University of Massachusetts, Sept 1988.
(34) Forbes, K. A. Ph.D. Dissertation, University of Massachusetts, May 1989.
(35) Richter, B. E. *HRC CC, J. High Resolut. Chromatogr. Chromatogr. Commun.* **1985**, *8*, 297–300.

RECEIVED for review January 25, 1990. Revised manuscript received June 5, 1990. Accepted June 19, 1990. Support for this work was provided in part by Baxter Healthcare Corporation, 3M, and also by Merck, Sharp and Dohma Research Laboratories through a Merck Predoctoral Fellowship Award to K.F. Research was supported in part by the *ICP Information Newsletter*.

Identification of Archaeological and Recent Wood Tar Pitches Using Gas Chromatography/Mass Spectrometry and Pattern Recognition

Erich W. H. Hayek, Peter Krenmayr,* and Hans Lohninger

Institute of General Chemistry, Technical University of Vienna, Getreidemarkt 9, A-1060 Vienna, Austria

Ulrich Jordis, Wolfgang Moche, and Fritz Sauter*

Institute of Organic Chemistry, Technical University of Vienna, Getreidemarkt 9, A-1060 Vienna, Austria

An analytical method has been developed for the assignment of recent and archaeological wood tar pitches to the species of trees used for their preparation. It incorporates the prepurification by Kugelrohr distillation and solid-phase extraction followed by gas chromatography/mass spectrometry analysis. Distribution patterns of volatile, thermostable triterpenoids and steroids characterizing the biological origin of the pitches are evaluated by principal component analysis (PCA) and discriminant component analysis (DCA) of the data. Quantities of 10–100 mg of archaeological material can thus be characterized. Fourteen archaeological samples have been identified as birch bark pitches by comparison with recent pitches of known origin. In addition 28 substances present in recent barks and recent pitches could be identified showing that the method developed can also be applied to the chemotaxonomy of broad-leaved trees.

Table I. Samples Used for Comparison

	number of samples (entries in mass spectra library)	
	bark	pitch
Acer plantanoides	1 (11)	1 (18)
Alnus incana	1 (22)	1 (15)
Alnus glutinosa	2 (39)	1 (15)
Betula alba	3 (28)	7 (47)
Carpinus betulus	2 (23)	1 (11)
Corylus avellana	3 (26)	2 (18)
Fagus silvatica	2 (17)	2 (7)
Fraxinus excelsior	1 (6)	1 (10)
Juglans regia	– (–)	1 (13)
Prunus avium	1 (15)	– (–)
Quercus cerris	1 (14)	– (–)
Quercus petrea	1 (22)	1 (19)
Ulmus minor	1 (4)	1 (5)

INTRODUCTION

Dark, ductile lumps (*1*, *2*), black partially shiny coatings on pottery (*1–8*), and residual glues on flint-stone arrowheads constitute a class of organic matter excavated repeatedly in swamps and tombs and found in urns (*1*, *2*). These finds have been termed, partly misleadingly, "tomb-resins", "fumigating resins", "fumigating pitches", "urn resins", "fumigating cakes", or "resin cakes" (*1–3*, *9*). Yet, according to the manufacturing process, which constitutes in essence a "slow" pyrolysis (*10–14*), these mixtures of substances should be termed wood tar pitches (distillation residues of wood tars). Finds of this kind have been verified from the mesolithic period up to the Middle Ages, the origins of discovery stretching from southern Scandinavia to the Balkans (*1–8*, *15*).

The uncommonly broad range of applications of wood tar pitches in prehistoric times comprised, among others, use as medicines, incense substitutes, inside or outside coatings of pottery, agglutinants (e.g. arrowhead to shaft), and sealing compounds (*1–5*, *8*, *9*, *16*).

Wood tar pitches (mainly coatings of pottery) repeatedly have been analyzed since 1880, mainly via infrared or NMR spectra or by thin-layer chromatography (TLC) (*2–4*, *8*, *17–20*). Motivated by analogy to ethnological and folkloric traditions still existing in northern Europe, analytical work was focused on attempts to identify the material in question as tar from low-temperature carbonization of birch bark. Yet, recent papers demonstrated, that infrared and NMR spectroscopy and TLC are not sufficient to justify unequivocal characterizations (*3*, *4*, *17*). In most cases samples were prepurified by—unspecific—solvent extraction. Although in two exceptional cases (where sufficient archaeological material was available) betulin—a triterpenoid-enediol occurring in birch bark in large quantities—was isolated and identified (*8*, *21*), a general methodology allowing the correlation of unknown wood tar pitches to particular species of trees was lacking. Tars from coniferous trees were characterized previously by gas chromatography/mass spectrometry (GC/MS) (*22*), focusing on tricyclic diterpenoids, after solvent extraction and LC.

Due to the isolation and identification of betulin in one particular archaeological sample (*21*), our scrutiny focused on native deciduous trees, as triterpenoids, products of secondary metabolism of *Dicotyledonae*, occur mainly in deciduous trees, but not in coniferous trees (*23*).

EXPERIMENTAL SECTION

Tetrahydrofuran (THF) and methanol (Riedel de Häen, p.a.) were distilled twice by use of a 1-m fractionating column. Reference substances betulin (lup-20(29)-ene-3β,28-diol), erythrodiol (olean-12-ene-3β,28-diol), friedelin (*D*:*A*-Friedoolean-3-on), lupeol (lup-20(29)-en-3β-ol), uvaol (urs-12-ene-3β,28-diol), amyrine isomeric mixture, lupenone (lup-20(29)-en-3-on), and α-lupeol (lup-20(29)-en-3α-ol) were obtained from Carl Roth GmbH. Air-dried barks (24 h at 125 °C) of 13 species of decidious trees were used as raw materials (Table I).

Preparation of authentic pitches (Table I) was carried out via descending destructive distillation: Samples of the barks were subjected to a low-temperature carbonizing process. The electric powered tubular stove (Figure 1) was heated to 330–370 °C for 1 h and the temperature raised to 620 °C for another hour. Pitches were obtained by evaporation of the tars to remove the volatile

* Corresponding authors.

0003-2700/90/0362-2038$02.50/0

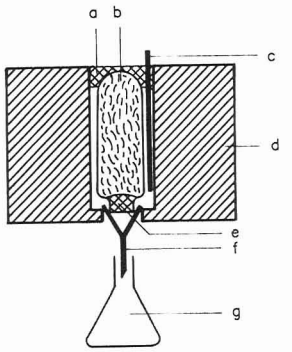

Figure 1. Tubular stove for the preparation of recent wood tars: (a, e) glass wool; (b) glass tube filled with pieces of bark; (c) thermostat; (d) isolation and filament; (f) funnel; (g) sample collector.

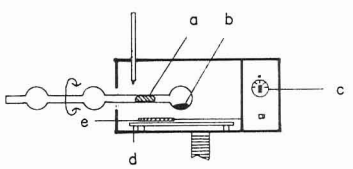

Figure 2. Kugelrohr distillation: (a) glass wool; (b) sample; (c, d, e) electrical heating and thermostat.

compounds at 20 mbar and 80 °C. Yields of the pitches obtained ranged between 3.1% (*Quercus cerris*) and 14.3% (*Betula alba*). Kugelrohr distillation (Figure 2) of the pitches at 0.006–0.06 mbar and 180–220 °C gave 46–86% oily or partially crystalline, yellow to brown products. Kugelrohr distillation of the archaeological samples or of dried barks without application of the carbonizing process yielded, under the same conditions, 1–21% of volatile products. One milliliter of a THF solution of the distillates (10 mg/mL) was injected onto a SPE (silica phase column) (Analytichem) and eluted with 2 mL of THF. The solvent was evaporated under N_2 and the residue redissolved in 1 mL of MeOH:THF = 8:2 and subjected to the SPE reversed-phase column (Analytichem). After elution with 2.5 mL of the same solvent mixture and evaporation of the solvents under N_2, the samples were dissolved in 6 mL of THF, and 120 μg of PCB-209 was added as internal standard. This THF solution was used for GC/MS, as the presence of MeOH interfered with the detection of the triterpenoids by activating the separation column.

Separation was optimized using a capillary gas chromatograph, Carlo Erba Fractovap 4160, a 0.33 mm × 30 m DB5 capillary column (J&W, 0.1 μm) at a column pressure of 0.9 bar with helium as carrier gas and the following temperature program: on column injection at 45 °C, 50 °C/min to 260 °C, hold 3 min, 1.5 °C/min to 290 °C as final temperature.

The GC was connected to the Finnigan MAT 8230 mass spectrometer via an open capillary interface. Separator temperature was 290 °C and ion source temperature 250 °C. Mass spectra were recorded at 70 eV electron energy, the mean MS cycle time was 1.25 s. Samples were characterized by means of patterns of corresponding GC peaks. For the selection of characteristic peaks mass chromatograms of the molecular ions and significant fragments of the triterpenoids and steroids with different numbers of hydroxy and acetate functional groups were recorded. A data base containing both the mass spectra of reference substances as well as mass spectra corresponding to characteristic GC peaks of recent pitches was created (Figure 3A). Mass spectra of unknown substances were characterized via a computerized library search using this data base. An identification was regarded conclusive if the result of the search withstood visual comparison with the spectrum in the data base and matched relative retention time (Figure 3B). The characterized peaks were quantified in relation to the internal standard.

Data were transferred from the mass spectrometer data system to an external personal computer. Two data sets were generated: set 1 contained 86 features (intensities of characterized substances) representing 19 recent pitches, with emphasis on those occurring

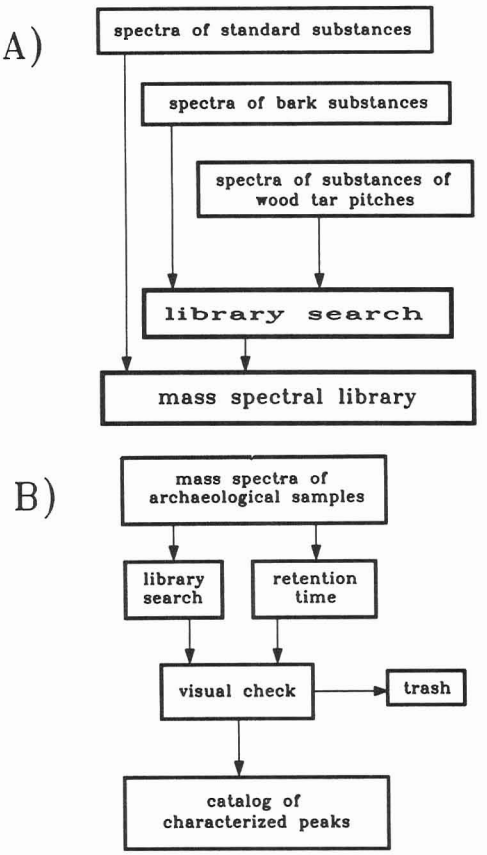

Figure 3. Flow chart for the selection of characteristic compounds (A) and the characterization of unknown samples (B).

only in trees of one family; set 2 contained all data of 38 recent samples (174 features). The data were processed by using methods of multivariate statistics, especially linear mapping procedures within EDAS (exploratory data analysis of spectra) (*24*, *25*). The number of features was reduced discarding those with the smallest variances of their intensities. Normalized data were obtained by application of eq 1 and used as input for the principal component analysis (PCA)

$$u_{i,j} = \frac{v_{i,j}}{(\sum_k v_{i,k}^2)^{1/2}} \qquad k = 1 \text{ to } n \tag{1}$$

where u is a normalized feature value, v is a raw feature value, n is the number of features, i is the index of samples, and j and k are the index of features.

Unsupervised and class-independent PCA was used to uncover grouping of the data. Elimination of principal components with minor variances or minor Fisher ratios reduced the number of descriptive variables. Autoscaling normalized the variance of each feature and transferred the mean to 0. Then DCA (discriminant component analysis) was performed, optimizing the separation of two given classes of data.

RESULTS AND DISCUSSION

Archaeological and recent pitches can be related to the trees they were derived from by identification of patterns of triterpenoids and steroids. The method described utilizes both the thermal stability and volatility of triterpenoids and steroids (*26*, *27*) using Kugelrohr distillation for prepurification.

Thirty-eight samples from 13 species of native trees were analyzed by GC/MS resulting in a mass spectral library containing 174 substances (Table I). Twenty-eight substances present in wood tar pitches and distillates from barks (mostly pentacyclic triterpenoids) were identified by comparison with standards and/or by matching the mass spectra with the NBS mass spectral library (Table II). One compound, namely

Table II. Identified Substances[a]

		maple	*Alnus glutinosa*	*Alnus incana*	birch	horn-beam	hazel	beech	ash	nut	*Prunus avium*	*Quercus cerris*	oak	elm
	1-(2,4-dihydroxy-6-methoxyphenyl)-3-(2-hydroxyphenyl)-2-propen-1-one										B			
#	30-norneohop-13(18)-en-22-one		BP	BP										
	A-neoolean-3(5),12-diene				BP									
	allobetulone (18α,19β-epoxy-oleanan-3-one)				BP									
#	taraxerone (*D*-friedoolean-14-en-3-one)	B	BP	BP										
	taraxerol (*D*-friedoolean-14-en-3β-ol)	BP	BP	B										
	taraxerolacetate		BP	B										
#	friedelin (*D*:*A*-friedooleanan-3-one)	BP												
	D:*A*-friedooleanan-2-one											B	B	
	friedelanol (*D*:*A*-friedooleanan-3β-ol)											B		
	isomultifluorenone (*D*:*C*-friedooleanan-8-en-3-one)		B											
	fernene (*D*:*C*-friedo-*B*':*A*'-neogammacer-9(11)-ene)												BP	
#	heneicosylcyclopentane					B	B		B		B		B	
	lanost-8,24-dien-3β-ol				B									
*	lup-20(29)-en-3-one		BP	BP	BP		B	BP					P	
*	lupeol (lup-20(29)-en-3β-ol)		B	B	BP	B	B	B			B			
*	betulin (lup-20(29)-en-3β,28-diol)		BP	BP	BP	B	B	BP					B	
	β-amyrine (olean-12-en-3β-ol)						B						BP	
	erythrodiol (olean-12-en-3β,28-diol)						B							
	olean-13(18)-en-3-one												B	
	stigmastan-3,6-dione		B			B	B							
	stigmast-4-en-3-one		B		BP		B	B				B	B	
#	stigmast-5-en-3α-ol	B	B	P	BP	B	B	BP	B	P	B	B	BP	
	stigmasta-3,5-dien-7-one		B	B		B	B	B				B	BP	BP
	stigmasta-5,24(28)-dien-3-ol										B			
	α-amyrine (urs-12-en-3β-ol)												P	
	β-tocopherol		BP				B							

[a] Key: P, identified in pitch; B, identified in bark; *, high loading in data set 2 pointing to birch; #, high loading in data set 2 pointing to other trees.

lupan, could be detected in some archaeological samples, but not in any recent pitch or bark distillate.

Examples of the GC/MS analyses are shown in Figures 4 and 5 to demonstrate (a) the reproducibility of the patterns of substances for different samples of the same species of trees (Figure 4A,B), (b) the differences between the patterns of substances for different species of trees (Figure 4C), and (c) the similarity of archaeological samples to recent birch pitches (Figure 5). The reliability of the classification of unknown samples via the presence or absence of characteristic compounds was tested in a blind study where one of the authors (E.H.) correctly classified five recent wood tar pitches from different species of trees.

To classify the archaeological samples, pattern recognition methods were applied. Concentrations of characterized substances were used as coordinates in n-dimensional space, in the expectation that those points representing samples originating from the same species of wood would form clusters. To project the pattern points onto a two-dimensional plane, PCA and DCA were applied (*24*, *25*, *28*).

As feature selection and normalization of data are critical points of the chemometric analysis of GC data (*29*), various methods (i.e. feature selection for a maximum of Fisher ratio, logarithmic transformation, or other normalization methods) were tested giving similar but less obvious results than the methods described (i.e. eq 1). PCA of the recent pitches shows good separation with regard to different types of trees (Figure 6). The separation of birch from other recent trees could be accomplished with a varying number of features, 10 to 30 being satisfactory for data set 1 (recent pitches) and 20 to 45 for data set 2 (all recent samples).

Projecting the data of 14 archaeological samples (Table III) onto the PCA plot of data set 1 allowed the unequivocal identification of 11 samples as birch bark pitches (Figure 6).

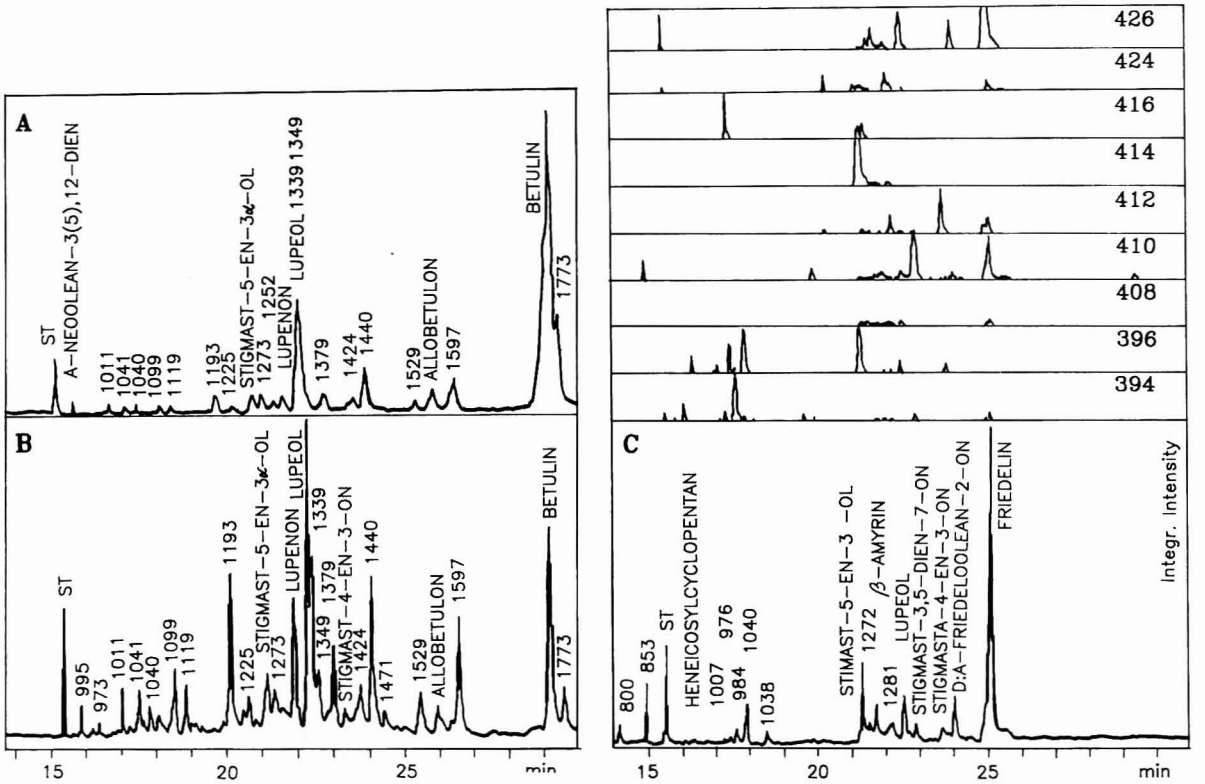

Figure 4. Integrated ion intensity of birch bark distillates (A, B) compared to oak bark distillates (C). Numbers refer to unidentified entries of the library. In part C the mass chromatograms of the molecular ions and significant fragments of triterpenoids and steroids are displayed.

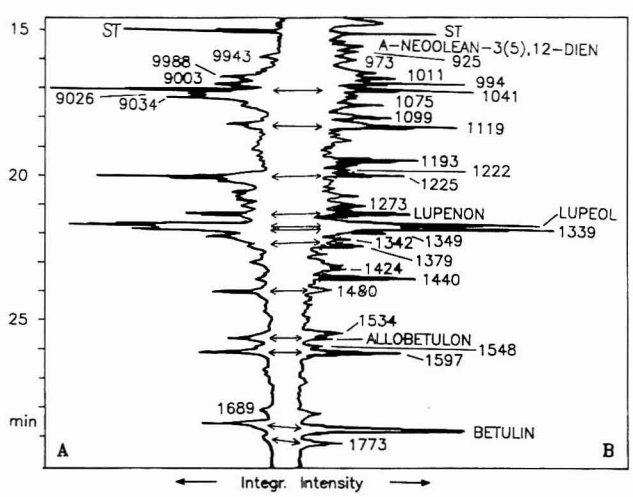

Figure 5. Integrated ion intensity of archaeological sample 10 (A) compared with a recent birch bark pitch (B). Numbers refer to entries of the library, identical compounds are marked by double arrows.

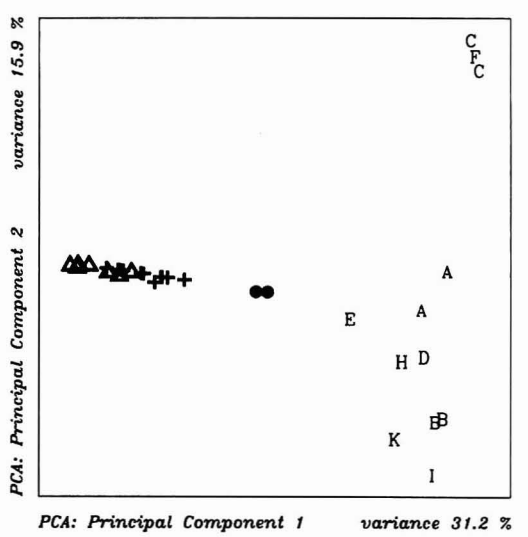

Figure 6. Principal component analysis of recent pitches using 30 selective features showing the separation of families of trees and the close relationship of the archaeological samples as birch tar pitch: (△) birch (*Betula alba*); (A) elder (*Alnus glutinosa* and *Alnus incana*); (B) hazel (*Corylus avellana*); (C) beech (*Fagus silvatica*); (D) maple (*Acer plantanoides*); (E) hornbeam (*Carpinus betulus*); (F) ash (*Fraxinus excelsior*); (H) nut (*Juglans regia*); (I) oak (*Quercus petrea*); (K) elm (*Ulmus minor*); (+) archaeological samples, which can be related to birch; (●) archaeological samples 7 and 8 (Table III), which cannot be related to either birch or hornbeam.

In order to answer the question of the relationship of the remaining two samples, a discrimination analysis of data set 2 with birch bark as one class and all other barks as the other was made. PCA was carried out to reduce the dimensionality of the data by setting a minimum of variance or Fisher ratio of those principal components used as input for DCA. In general, autoscaling before DCA improves the class separation. Alternatively features with highest loadings in the selected principal components were chosen to generate a data set containing only 15 features of all recent samples. Eight of these features correspond to identified substances (marked in Table II), another is assumed to be 19,28-epoxyolean-2-ene (apoallobetulin). Again PCA was carried out and five principal components with major Fisher ratios were selected for DCA.

The classification ability was tested by the "leave a quarter out" method showing predictabilities better than 95% for each class (Table IV). Thus, the use of chemometric methods resulted in a striking reduction of the number of features.

By use of any of the DCA methods described, 14 archaeological samples (glues on arrowheads and on pottery, coatings on pottery, and a large early Iron Age piece of raw wood tar pitch (Table III)) could be identified as birch bark pitches (Figure 7), even in those cases where betulin could not be

Table III. Archaeological Samples[a]

sample ID	finding site	characterization of the object	dating (after Reinecke)
1	Pitten, Lower Austria	bulgy bowl (omphalos type) with ancient glued joint	Bronze Age (R. Br. C/D)
2	Buchsberg, Lower Austria	surface find: coating on pottery shard (from bowl)	Early Bronze Age (R. Br. A2/B1)
3	Kirchspiel, Denmark	lump of pitch found in the Herstedvester Moor	Bronze Age
4	Spjald, Western Jutland, Denmark	coating of wooden box found in a depot of an ancient house	Bronze Age (R. Br. C/D)
5	Spjald, Western Jutland, Denmark	lump of pitch found in a depot of an ancient house	Bronze Age (R. Br. C/D)
6	Hochberg, Lower Austria	ancient glued joint on a pottery bowl (grave gift)	Early Iron Age (R. H. C/D)
7	Mondsee, Upper Austria	coating on triangular flintstone arrowhead	Copper Age
8	Mondsee, Upper Austria	coating on triangular flintstone arrowhead	Copper Age
9	Stillfried, Lower Austria	coating on pottery shard (found in a sacrificial pit)	Late Bronze Age (R. H. B)
10	Stillfried, Lower Austria	contents of pottery bowl	Early Iron Age (R. H. C/D)
11	Stillfried, Lower Austria	coating on pottery shard	Late Bronze Age (R. H. B/C)
12	Stillfried, Lower Austria	coating on pottery shard	Late Bronze Age (R. H. B/C)
13	Stillfried, Lower Austria	contents of pottery bowl	Late Bronze Age (R. H. B/C)
14	Stillfried, Lower Austria	loaf-shaped lump of pitch (found in a maybe "sacrificial" pit)	Late Bronze Age (R. H. B)
15	Stillfried, Lower Austria	charcoal and organic material (found in a pit containing a human skeleton)	Late Bronze Age (R. H. B)

[a] Samples 1–14 are classified as birch bark derivatives, 15 is assigned as an animal fat.

Table IV. Predictive Abilities of Chemometric Classifications

number of features used		% predictability		
for PCA	for DCA	for birch	for other trees	overall
40	5	100	96	97
40	10	100	100	100
15[a]	5	100	100	100

[a] Features with highest loadings in selected principal components

detected. Sample 15 contained only three steroids (cholestan-type dienones) and cholest-5-en-3β-ol acetate as well as fatty acids but no triterpenoids. This suggests that the sample represents an archaeological animal fat.

ACKNOWLEDGMENT

The authors wish to thank R. Strba (Agricultural University Vienna) and the staff of the "Bauhof Hütteldorf" of the Austrian federal forest administration for recent bark samples and their botanical identification; the Institute of Prehistory and Early History of the University Vienna (especially F. Felgenhauer), the Department of Prehistory of the Museum of Natural History, Vienna, and C. J. Becker and the first department of the National Museum, Copenhagen, Denmark, for providing archaeological samples; and K. Varmuza and W. Werther, Institute of General Chemistry, for critical discussions and the use of software packages PEDAS and EDAS.

Registry No. 1-(2,4-Dihydroxy-6-methoxyphenyl)-3-(2-hydroxyphenyl)-2-propen-1-one, 69707-17-1; 30-norneohop-13(18)-en-22-one, 128114-74-9; *A*-neoolean-3(5),12-diene, 22586-84-1; allobetulone, 28282-22-6; taraxerone, 514-07-8; taraxerol, 127-22-0; taraxerolacetate, 2189-80-2; friedelin, 559-74-0; *D*:*A*-friedooleanan-2-one, 17947-04-5; friedelanol, 105370-95-4; isomultiflorenone, 22611-26-3; fernene, 1615-99-2; heneicosylcyclopentane, 6703-82-8; lanost-8,24-dien-3β-ol, 79-63-0; lup-20(29)-en-3-one, 1617-70-5; lupeol, 545-47-1; betulin, 473-98-3; β-amyrine, 559-70-6; erythrodiol, 545-48-2; olean-13(18)-en-3-one, 20248-08-2; stigmastan-3,6-dione, 77551-74-7; stigmast-4-en-3-one, 1058-61-3; stigmast-5-en-3α-ol, 31793-83-6; stigmasta-3,5-dien-7-one, 2034-72-2; stigmasta-5,24(28)-dien-3-ol, 18472-36-1; α-amyrine, 638-95-9; β-tocopherol, 148-03-8.

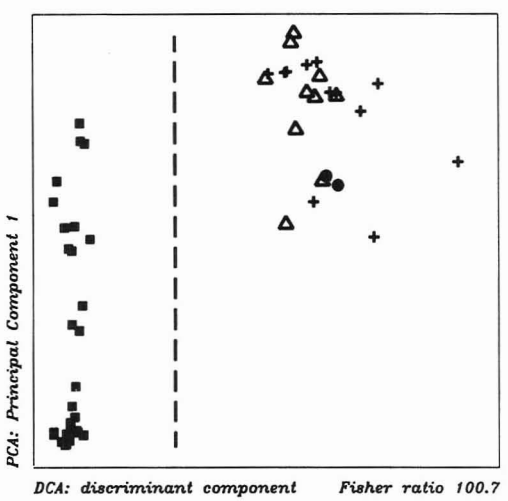

Figure 7. Discriminant component analysis of birch bark versus all other trees after previous PCA (40 features) and data reduction (10 principal components with major Fisher ratios) showing the classification of the archaeological samples as birch: (△) birch (*Betula alba*); (■) other trees; (●) archaeological samples 7 and 8; (+) other archaeological samples; (|) classification border.

LITERATURE CITED

(1) Thomsen, P. in *Reallexikon der Vorgeschichte*; Ebert, M., Ed.; Springer: Berlin, 1926; pp 128–130.
(2) Sandermann, W. *Technische Beiträge zur Archäologie* **1965**, *2*, 58–73.
(3) Sauter, F. *Archaeol. Austriaca* **1967**, *41*, 25–36.
(4) Sauter, F.; Jordis, U. *Forschungen in Stillfried* **1980**, *4*, 147–161.
(5) Schwarze, E. *Ausgrabungen und Funde* **1963**, *8*, 17–18.
(6) Behrens, H. *Ausgrabungen und Funde* **1960**, *5*, 12–19.
(7) Protz, H. *Berliner Blätter für Vor- und Frühgeschichte* **1965/66**, *11*, 153–170.
(8) Funke, H. Doctoral Thesis, Hamburg, 1969.
(9) Hager, H., List, P. H., Hörhammer, L., Eds. *Handbuch der Pharmazeutischen Praxis*, 4th ed.; Springer: Berlin/Heidelberg/New York, 1967-1980; Vol. 3, pp 434–438, and Vol. 6, pp 737–746.
(10) Schweers, W. In *Chemische Technologie*, 4th ed.; Winnacker, K., Küchler, E., Eds.; Hanser: München, 1981; Vol. 5, pp 644–647.
(11) Nikitin, N. I. *Chemie des Holzes*; Akademie: Berlin, 1955; pp 416–453.
(12) Bunbury, H. M. *The Destructive Distillation of Wood*; Benn Bros.: London, 1923; pp 259–269.
(13) Bugge, G. *Die Holzverkohlung*; Sammlung Göschen: Berlin, 1925; pp 7–9, 36–41, 64–71, 86–91, 98–101.
(14) Soltes, E. J.; Wiley, A. T.; Lin, S. C. K. *Biotechnol. Bioeng. Symp.* **1981**, *11*, 125–136.

(15) Schoknecht, U.; Schwarze, E. *Ausgrabungen und Funde* **1967**, *12*, 205–209.
(16) Thoms, H. *Handbuch der praktischen und wissenschaftlichen Pharmazie*; Springer: Berlin, 1924–1931; Vol. 4, part 2/1, pp 1608–1609, p 1766.
(17) Hadzi, D.; Cvek, F. *Archeoloski vestnik* **1976**, *27*, 128–134.
(18) Rottländer, R. C. A. *Archäolog. Korrespondenzblatt* **1974**, *4*, 95–98.
(19) Rottländer, R. C. A. In *Die Schussenriedersiedlung im "Schlösslesfeld"*; Lüning, J., Zürn, H., Eds., 1977.
(20) Heintzel, C. *Z. Ethnologie* **1880**, *12*, 375–378; **1881**, *13*, 241–242.
(21) Sauter, F.; Hayek, E. W. H.; Moche, W.; Jordis, U. *Z. Naturforsch.* **1987**, *42C*, 1151–1152.
(22) Evershed, R. P.; Jerman, K.; Eglinton, G. *Nature* **1985**, *314*, 528–530.
(23) Chaffee, A. L.; Hoover, D. S.; Johns, R. B.; Schweighardt, F. K. In *Biological Markers in the Sedimentary Records*; Johns, R. B., Ed.; Elsevier: Amsterdam–Oxford–New York–Tokyo, 1986; pp 311–345.
(24) Varmuza, K.; Werther, W.; Lohninger, H. In *Software-Entwicklung in der Chemie 3*; Gauglitz, G., Ed.; Springer: Berlin–Heidelberg, 1989; pp 285–287.
(25) Werther, W.; Varmuza, K. In *Software-Development in Chemistry 4*; Gasteiger, G., Ed.; Springer: Berlin–Heidelberg, in press.
(26) Windholz, M., Ed. *The Merck Index*, 10th ed.; Merck & Co.: Rahway, NJ, 1983; pp 1204, 4153, 5421.
(27) Steiner, M. In *Moderne Methoden der Pflanzenanalyse*; Paech, K., Tracey, M. V., Eds.; Springer: Berlin, 1955; Vol. 3, pp 128–135.
(28) Varmuza, K. *Pattern Recognition in Chemistry*; Springer: Berlin–Heidelberg, 1980.
(29) Kvalheim, O. A. *Anal. Chim. Acta* **1985**, *177*, 71–79.

RECEIVED for review January 26, 1990. Accepted May 31, 1990. The authors wish to thank the Austrian "Fonds zur Förderung der wissenschaftlichen Forschung" for financial support (Project P 6811 C).

Enzyme-Linked Immunosorbent Assay Compared with Gas Chromatography/Mass Spectrometry for the Determination of Triazine Herbicides in Water

E. M. Thurman,* Michael Meyer, Michael Pomes, Charles A. Perry, and A. Paul Schwab[1]

U.S. Geological Survey, Water Resources Division, 4821 Quail Crest Place, Lawrence, Kansas 66049

An enzyme-linked immunosorbent assay (ELISA) was compared to a gas chromatography/mass spectrometry (GC/MS) procedure for the analysis of triazine herbicides and their metabolites in surface water and groundwater. Apparent recoveries from natural water and spiked water by both methods were comparable at 0.2–2 μg/L. Solid-phase extraction (SPE) was examined also, and recoveries were determined for a suite of triazine herbicides. A significant correlation was obtained between the ELISA and GC/MS method for natural water samples that were extracted by SPE. Because ELISA was developed with an atrazine-like compound as the hapten with conjugation at the 2-position, it was selective for triazines that contained both ethyl and isopropyl side chains. Concentrations for 50% inhibition (IC_{50}) were as follows: atrazine, 0.4 μg/L; ametryne, 0.45 μg/L; prometryn and propazine, 0.5 μg/L; prometon, 0.7 μg/L; simazine and terbutryn, 2.5 μg/L; hydroxyatrazine, 28 μg/L; deethylatrazine and deisopropylatrazine, 30 μg/L; cyanazine, 40 μg/L; didealkylatrazine had no response. The combination of screening analysis by ELISA, which requires no sample preparation and works on 160 μL of sample, and confirmation by GC/MS was designed for rapid, inexpensive analysis of triazine herbicides in water.

INTRODUCTION

The enzyme-linked immunosorbent assay (ELISA) has been shown to be a useful residue analysis method for herbicides (*1–5*). ELISA has been used extensively in clinical chemistry but has been introduced only recently into environmental chemistry on a commercial basis (*2*, *3*, *5*). The conventional analysis method for triazine herbicides (by gas–liquid chromatography with nitrogen–phosphorus detection, GC–NPD) is sensitive and well characterized (*6–9*). Furthermore, both liquid chromatography (*6*, *10–12*) and gas chromatography/mass spectrometry (*13–18*) have been applied successfully to the analysis of triazine herbicides. A major reason for the numerous methods of analysis of triazines, which are used extensively as preemergent herbicides for corn (*Zea mays* L.) and sorghum (*Sorghum bicolor* L.) is the fact that these herbicides are common contaminants in surface and groundwater (*19*). Thus, the triazine herbicides provide a challenging target for ELISA for rapid inexpensive analysis of surface and groundwater.

This study examined the ELISA analysis method for triazine herbicides and their metabolites to determine cross reactivity, and to verify accuracy and precision against a reference GC/MS method. The study also checked for interference from naturally occurring humic substances and acetanilide herbicides that commonly occur in surface water. Gas chromatography/mass spectrometry was chosen as a reference method to verify that the ELISA was responding to the triazines rather than other herbicides that may be present. Because the ELISA method was designed to screen large numbers of water samples without sample preparation, an automated solid-phase extraction (SPE) method was designed also for rapid GC/MS confirmation.

Objectives of the study were to (1) compare ELISA to GC/MS analysis for accuracy, precision, and cross reactivity for herbicides in natural water, (2) streamline the SPE extraction and GC/MS analysis by selected ion monitoring (SIM) for rapid confirmation, and (3) determine if the combination of ELISA screening and GC/MS confirmation for triazine herbicides would be a viable and inexpensive method for large water-quality surveys.

EXPERIMENTAL SECTION

Reagents. Methanol (Burdick and Jackson, Muskegon, MI) and ethyl acetate (Fisher, Springfield, NJ) were pesticide-grade solvents. Ametryn, atrazine, prometon, prometryn, propazine, simazine, and terbutryn were obtained from Supelco (Bellefonte,

[1] Department of Agronomy, Kansas State University, Manhattan, KS 66506.

Table I. Selected Ions for Mass Spectrometry of Triazine and Acetanilde Herbicides

compound no. (Figure 2)	compound	retention time, min (± 0.04)	atomic mass unit (amu)			
			molecular ion (M^+)	base peak	ion 1	ion 2
1	deisopropylatrazine	17.98	173	173	158	145
2	deethylatrazine	18.32	187	172	145	
3	simazine	19.71	201	201	186	176
4	atrazine	20.02	215	200	173	
5	prometon	20.08	225	210	168	
6	propazine	20.25	229	214	172	
7	phenanthrene-d_{10}	20.38	188	188		
8	terbuthylazine	20.61	229	214	173	
9	metribuzin	22.02	214	198	199	182
10	ametryn	22.85	227	227	212	170
11	alachlor	22.91	269	188	160	237
12	prometryn	23.05	241	241	184	226
13	terbutryn	23.45	241	226	185	170
14	cyanazine	23.75	240	225	212	
15	metolachlor	24.18	none	162	238	240

PA); alachlor, cyanazine, metolachlor, metribuzin, and terbuthylazine were obtained from the EPA Pesticide Chemical Repository (Research Triangle Park, NC); and the triazine metabolites, deethylatrazine, deisopropylatrazine, and didealkylatrazine, were from Ciba Geigy (Greensboro, NC). The C_{18} cartridges (Sep-Pak from Waters, Milford, MA) contained 360 mg of 40-μm C_{18} bonded silica. Deionized water was charcoal filtered and glass distilled prior to use. Standard solutions were prepared in methanol, and phenanthrene-d_{10} (EPA, Cincinnati, OH) was used as an internal GC/MS quantitation standard.

ELISA Procedure. Res-I-Mune kits (ImmunoSystems Inc., Scarborough, ME) were used for the immunoassay analysis of water samples. The kits use polyclonal antibodies coated to the walls of a polystyrene test tube and an enzyme conjugate that was prepared by covalently binding atrazine to horseradish peroxidase by a modified carbodiimide technique (*2*, *3*). The procedure was similar to that described in the kit and by Bushway and others (*2*) with the exception that percent inhibition was measured. Briefly, 160 μL of sample was added to an antibody-coated tube with 160 μL of enzyme conjugate. After 5 min, the test tubes were rinsed 3 times with deionized water to remove excess unreacted sample and enzyme conjugate, and 160 μL of substrate was added followed by 160 μL of chromogen, sequentially. After 2 min, color was fixed with 40 μL of "stop" solution (2.5 N sulfuric acid).

Samples and standards were analyzed by measuring percent inhibition, which is the difference in optical density at 450 nm (A450) between the negative control and the sample divided by the optical density (A450) of the negative control times 100. Cross reactivity of the herbicides was measured in triplicate as the percent inhibition of the compound at a concentration of 1 μg/L and compared to IC_{50} values in the kit literature (IC_{50} is the amount required for 50% inhibition). Measurements were made on the atrazine standard curve using an Artel differential spectrophotometer (Windham, ME).

Extraction Procedures. The C_{18} cartridges were prepared by washing with 3 mL of methanol, 3 mL of ethyl acetate, 3 mL of methanol, and 2 mL of distilled water. Ethyl acetate eluate blanks of the Sep-Pak cartridges were analyzed by GC/MS to determine retention time of interfering peaks. Extraction and elution efficiencies of the cartridge were determined by comparing the recoveries of terbuthylazine and atrazine to an external standard curve of equivalent mass by GC/MS. The capacity of the cartridge for the triazine herbicides was determined by passing the herbicide mixture through a Sep-Pak cartridge and determining the volume required for breakthrough of the solute.

Surface-water samples were filtered through 0.7-μm glass-fiber filters (Whatman GF/F, Maidstone, England). The sample (100 mL) was spiked with a recovery, surrogate standard (terbuthylazine) and was passed through the Sep-Pak cartridge using a Millipore Workstation (Waters, Milliford, MA) at 20 mL/min. The cartridge was eluted first with air to remove residual water and then eluted with 2.0 mL of ethyl acetate. The ethyl acetate was spiked manually with phenanthrene-d_{10}, vortexed, dried over sodium sulfate, evaporated under nitrogen at 50 °C to 100 μL, and analyzed by GC/MS.

GC/MS Analysis. GC/MS analyses of the eluates were performed on a Hewlett-Packard Model 5890A GC (Palo Alto, CA) and a 5970A mass selective detector (MSD). Operating conditions were as follows: ionization voltage, 70 eV; ion source temperature of 250 °C; electron multiplier, 300 V above autotune; direct capillary interface at 280 °C, daily tuned with perfluorotributylamine; and 50 ms dwell per ion. For sample analysis, the filament and multiplier were not turned on until 5 min into the run. Thirty-two ions were selectively monitored (Table I), and the base–peak ion current was measured for the quantification curve versus the response of the 188 ion of phenanthrene-d_{10}. Confirmation was based upon presence of the molecular ion, two confirming ions (with area counts ±20%), and a retention time match of ±0.2% relative to phenanthrene-d_{10}.

A fused silica capillary column of methylsilicone with a film thickness of 0.33 μm, 12 m × 0.2 mm i.d., called the HP-1 (Hewlett-Packard, Palo Alto, CA), separated the herbicides with helium as a carrier gas at 1 mL/min and a head pressure of 35 kPa. The samples were injected in the splitless mode by autoinjector. The column temperature was held at 50 °C for 1 min and programmed to 250 °C at 6 °C/min and held for 10 min. Injector temperature was 280 °C.

RESULTS AND DISCUSSION

ELISA. The standard curve was linear from 0.2 to 2.0 μg/L when percent inhibition was plotted versus concentration on a log scale. Plotting percent inhibition normalizes the absorbance readings (A450) of each set of samples to the variability of the negative control, which is a sample run with each set that contains no herbicide and has the maximum absorbance reading possible (absorbance is inversely related to concentration in this assay).

If raw absorbance readings (A450) are plotted rather than percent inhibition, then the variation among analyses may double. For example, Table II shows the coefficient of variation for the negative control and 0.5 and 1.0 μg/L atrazine standards. Both standards have a coefficient of variation of approximately 0.1 (ΔOD column in Table II), a value that is affected by the absorbance of the negative control. This value may be decreased to 0.07 for the 0.5 μg/L standard and to 0.03 for the 1.0 μg/L standard by normalization and plotting of percent inhibition. Because concentration is plotted on a log scale, the decrease in the coefficient of variation makes an important difference in the precision of the method. The normalized values give a relative standard deviation in concentration units of 20% for the 0.5 μg/L standard and 15% for the 1.0 μg/L standard. Plotting percent inhibition versus concentration is similar to the logit plots commonly used in enzymology (*20*).

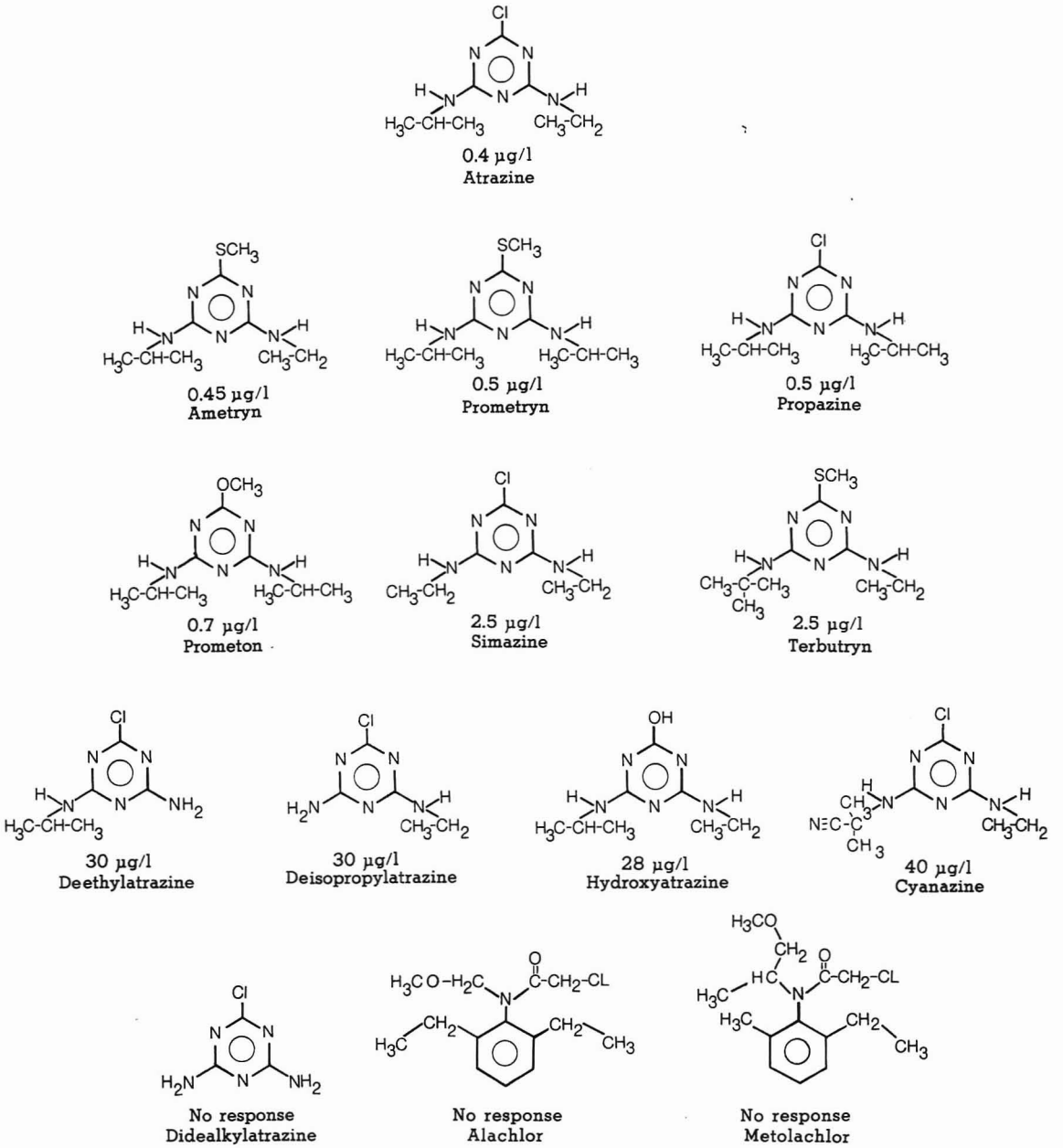

Figure 1. Chemical structure and cross reactivity for triazines with ELISA. Expressed as concentration required for 50% inhibition in units of µg/L (IC_{50}).

Table II. Comparison of Absorbance Readings for ELISA Standards (n = 7)

	negative control A450[b]	standard (0.5 µg/L) ΔOD[a]	standard (0.5 µg/L) % inhibition[c]	standard (1.0 µg/L) ΔOD[a]	standard (1.0 µg/L) % inhibition[c]
mean	1.70	0.71	42	0.97	57
std dev	0.20	0.09	3	0.09	2
coeff of variance	0.12	0.12	0.07	0.10	0.03

[a] ΔOD, difference in optical density at 450 nm in absorbance units between sample and negative control determined with a differential spectrophotometer. [b] A450 negative control, difference in optical density at 450 nm in absorbance units between negative control and deionized water, which is the maximum reading. [c] Percent inhibition = (absorbance negative control − absorbance of sample)/absorbance negative control × 100 = (ΔOD sample/A450) × 100.

Multiple analyses of a deionized water blank containing color reagent against the negative control gave a mean value of 7% inhibition and a standard deviation of 7% inhibition. If the recommendation of the Subcommittee on Analysis (*21*) is used, then the limit of detection is 3 standard deviations above the blank, or 21% inhibition, which corresponds to a 0.2 µg/L detection limit.

Cross reactivity was measured for the common triazine herbicides and metabolites and is expressed in Figure 1 as the concentration required for IC_{50} (50% inhibition). It was found that the response of atrazine was greatest with the lowest IC_{50} concentration of 0.4 µg/L, which is expected because it was similar to the hapten used to make the antibody (proprietary information). Ametryn's IC_{50} value was 0.45 µg/L, prometryn and propazine were 0.5 µg/L, and so forth (Figure 1). The cross reactivity expressed as the IC_{50} of each triazine is related to the extent of binding that occurs between the antibody coated to the test tube and the analyte molecule. Note that the binding was strongest for compounds that have structures most closely resembling atrazine, that is, a 4-ethylamino and a 6-isopropylamino group. For example, ametryn (Figure 1) has a 0.45 µg/L IC_{50} compared to atrazine (0.4 µg/L). Likewise, a substitution from an ethyl to an isopropyl group (propazine) increases the IC_{50} to 0.5 µg/L. Simazine, with two ethyl groups, has a IC_{50} of 2.5 µg/L. Substitution of hydrogen

Table III. Breakthrough Capacity (mL) of the Sep-Pak C_{18} Cartridges for Triazine Herbicides

compound	10% breakthrough[a]	100% breakthrough
didealkylatrazine	~5	25
deisopropylatrazine	75	225
deethylatrazine	300	400
metribuzin	600	1800
simazine	1200	1800
atrazine	2000	3200
cyanazine	2000	3200
propazine	4000	6000
ametryn	>7000	
prometon	>7000	
terbuthylazine	>7000	
alachlor	>7000	
prometryn	>7000	
terbutryn	>7000	
metolachlor	>7000	

[a] Flow rate was 4 mL/min, concentration, 1 μg/L of each herbicide; 25-mL increments were monitored from 0 to 500 mL, and 100 mL increments were monitored to 7000 mL by passing effluent through a clean Sep-Pak cartridge. Experiment terminated at 7000 mL. [b] Refers to the concentration of the compound in the effluent as a percentage of influent concentration.

for either the ethyl (deethylatrazine) or the isopropyl (deisopropylatrazine) increases the IC_{50} dramatically to 30 μg/L. Likewise, cyanazine, which has a bulky cyano group at the 6-position had a IC_{50} of 40 μg/L, which shows that its binding has been decreased by the cyano group. Because the immunizing hapten was bound at the 2-position on the triazine ring, it appears that the relative response of the immunoassay is related to antibody recognition and binding to the alkyl side chains on the triazine ring, especially the isopropyl group.

Only hydroxyatrazine breaks this pattern in cross reactivity. Because it has the same alkyl structure as atrazine, one would predict an IC_{50} similar to ametryn (0.45 μg/L). However, hydroxyatrazine has an IC_{50} of 28 μg/L. A possible explanation is that the hydroxyl group decreases the binding energy at the specific antibody recognition site because of a difference in the spacer or perhaps the fact that hydroxyatrazine also occurs in the keto form that is different in structure than the immunizing hapten. Didealkylatrazine was nonreactive, again showing that the alkyl side chains are critical to binding. Neither alachlor nor metolachlor cross reacted with atrazine, which is consistent with a previous study (*2*).

ELISA was checked also for interference by naturally occurring humic and fulvic acids, which account for the majority of dissolved organic carbon in natural water (*22*). Atrazine was measured in water samples that contained from 5 to 100 mg/L of humic and fulvic acid from the Suwannee River (standard-reference surface-water sample, refs 23 and 24) and humic and fulvic acids from Biscayne aquifer near Miami, FL (*25*). In all cases, there was no difference between the immunoassay response in the presence and absence of the humic material. These data suggest that neither positive nor negative cross reactivity should occur from natural dissolved organic matter in surface or groundwater by ELISA analysis.

Solid-Phase Extraction and GC/MS. Capacity and elution efficiency of solid-phase extraction were examined in two separate experiments. Table III shows the capacity determinations for the herbicide mixture. Didealkylatrazine has the least sorption capacity for the C_{18} cartridge with complete breakthrough of the compound in the effluent at 25 mL and is followed by deisopropylatrazine at 225 mL. Next, deethylatrazine had complete breakthrough at 400 mL. The removal of both the ethyl and isopropyl side chain increases the polarity of the molecule and greatly decreases sorption capacity on the resin (didealkylatrazine). Addition of the ethyl group increases capacity with two added carbons (deisopropylatrazine), and addition of the isopropyl group with three carbons increases it slightly more (deethylatrazine). If ethyl groups are present on both amino groups, the capacity is considerably more (simazine at 1800 mL). Atrazine reached breakthrough at 3200 mL and propazine at 6000 mL. Again, these results demonstrate that the replacement of an ethyl group with an isopropyl group increases sorption capacity (simazine to atrazine), and a second replacement further increases capacity (atrazine to propazine). After 7 L of solution, many of the herbicides were still being retained with no evidence of elution (ametryn, prometon, terbuthylazine, prometryn, terbutyrn, and alachlor and metolachlor), which indicates the large capacity of the herbicides for the C_{18} cartridge. The experiment was terminated at 7 L.

Table IV. Recovery and Precision Analysis for Herbicides from C_{18} SEP-Pak Cartridge and GC/MS Determination Using 100-mL Sample, 4 mL/min Flow Rate, and Ethyl Acetate as an Eluting Solvent, and Based on an External Standard Curve for Each Herbicide at 1 μg/L Concentration.

compounds	% mean recovery ±1 std dev	% rel std dev
deethylatrazine	90 ± 5	6
deisopropylatrazine	55 ± 5	10
didealkylatrazine	10 ± 5	50
simazine	101 ± 5	5
atrazine	99 ± 5	5
prometon	105 ± 5	5
propazine	108 ± 5	5
metribuzin	108 ± 5	5
terbuthylazine	99 ± 5	5
ametryn	107 ± 5	5
alachlor	104 ± 5	5
prometryn	113 ± 5	4
terbutryn	104 ± 5	5
metolachlor	100 ± 5	5
cyanazine	95 ± 10	10

Table IV shows the recovery data for 15 herbicides from the Sep-Pak cartridge. From 90 to 113% of the herbicides were recovered, with the exception of didealkylatrazine and deisopropylatrazine, which were recovered at 10 and 55%, respectively. Analysis of a second elution aliquot of ethyl acetate indicated that the first 2 mL of solvent was sufficient for removal of the herbicides. Other studies of herbicide elution from C_{18} resin showed that elution occurs with small volumes of solvent (*26*). The decreased recovery of both didealkylatrazine and deisopropylatrazine was caused by poor sorption capacity on the C_{18} resin, which was shown in the prior experiment (Table III). On the basis of these recovery results, terbuthylazine was chosen as a surrogate for the recovery of triazines in field samples because it recovers similar to atrazine, is easier to obtain and less costly than the deuterated analogues of the herbicides, and is not used as a herbicide commercially.

Finally, the types of contaminants present on the solid-phase cartridge were examined by elution of the cartridge both before and after cleaning with the elution solvent, ethyl acetate. The major contaminants included aliphatic hydrocarbons (C_8 to C_{18}), dioctyl phthalate, and in some samples a large unidentified peak at 24.5 min, which may be a silylated compound from the resin (*27*). This peak may result from the hydrolysis of the cartridge by the water sample, itself, which was concluded from the fact that after cleaning the resin the ethyl acetate blank did not contain the large peak at 24.5 min. If the samples are allowed to remain on the cartridge for several hours before elution, this peak will appear; thus, cartridges should be eluted immediately.

Detection limits (defined by Committee on Chemical

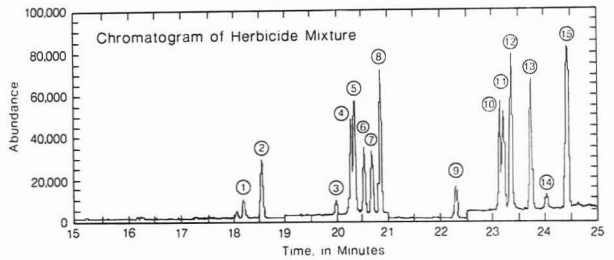

Figure 2. Chromatogram for a 14-compound standard herbicide mix and phenanthrene-d_{10} showing total ion chromatogram. Compound, name, number, and ions found in Table I.

Analysis, ref 18) for the herbicides varied from 0.01 to 0.05 μg/L, depending upon instrument response factors, and quantitation limits varied from 0.05 to 0.20 μg/L. Precision (relative standard deviation) varied from 4 to 50% (Table IV). Accuracy was established by checking both fortified distilled-water samples containing the herbicide mixture in Table IV and actual water samples with analyses from two independent laboratories using liquid–liquid extraction (LLE) and GC/MS and LLE with GC/NPD detection. In general the results by solid-phase extraction and GC/MS were within ±10 to 20% of the independent laboratory analyses. Only cyanazine varied to ±50%. This cyanazine result has recently been traced to losses in the injection port caused by a dirty injector sleeve. Thus, for reliable cyanazine response by GC/MS the injector sleeve should be changed frequently depending on sample throughput.

Chromatographic separation was nearly baseline for all compounds, with the exception of atrazine/prometon (peaks 4 and 5 in Figure 3) and ametryn/alachlor (peaks 10 and 11). Because different base–peak ions were used for quantitation for each compound, neither of the sets of peaks interfered with one another (Table I), and the chromatogram of the blank did not contain interfering peaks. Several of the metabolites of the triazines were too polar to chromatograph; this includes didealkylatrazine and hydroxyatrazine. Derivatization procedures are required for these compounds before GC/MS analysis.

Comparison of ELISA and GC/MS. The correlation between ELISA and GC/MS was 0.99 (r), and the slope of the regression line was 0.88 for spiked distilled water containing a mixture of herbicides (including atrazine, alachlor, cyanazine, metolachlor, propazine, and simazine). This selection of herbicides was chosen because they represent the six major herbicides found in a survey 450 surface water samples from the midwestern United States that were screened and assayed as part of this study. The cross reactivity (Figure 1) for each of the triazine herbicides was used for correlation, and samples were run in duplicate pairs. The acetanilide herbicides did not interfere, and there was no response to these compounds. Cyanazine, metolachlor, and alachlor essentially have no response to the ELISA but were included as part of the comparison because they are important herbicides used in row crops in the midwestern United States (*19*). For example, Bicep is the commercial name for the combination of atrazine and metolachlor, and commonly alachlor and atrazine are used on adjacent fields to kill weeks on soybeans and corn, respectively (*19*). Furthermore cyanazine is widely used in conjunction with these preemergent herbicides.

The cross reactivity of the ELISA was sufficient for a semiquantative response for atrazine, ametryn, prometryn, propazine, prometon, simazine, and terbutryn. The response was too low for deethylatrazine, deisopropylatrazine, hydroxyatrazine, cyanazine, and didealkylatrazine to be a screening method for these triazines in surface or groundwaters because their concentrations are typically at the μg/L level

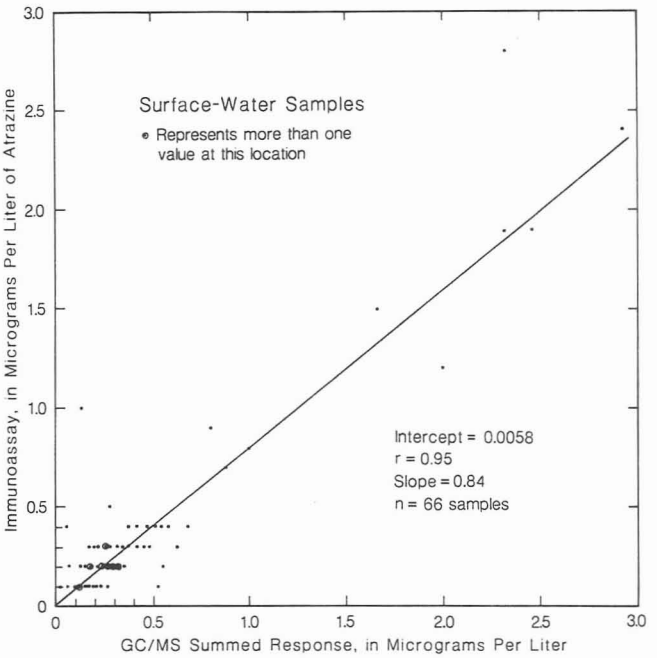

Figure 3. Plot of 66 surface-water samples from the central United States showing ELISA concentration versus concentration by Gc/MS.

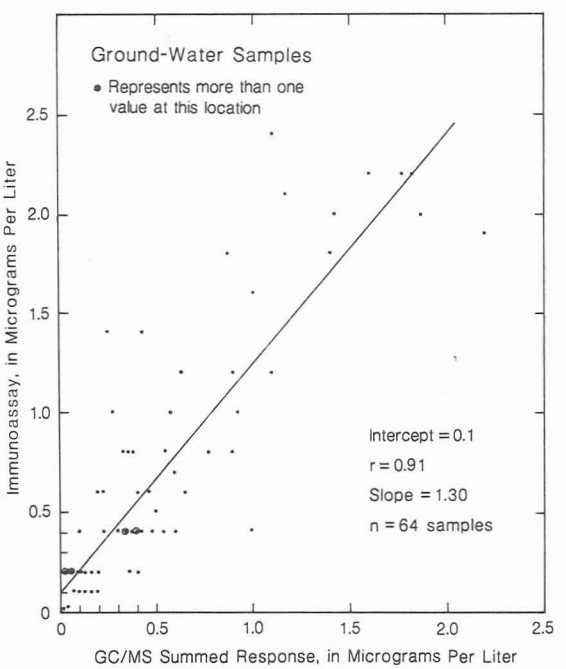

Figure 4. Plot of 64 groundwater samples from the center United States showing ELISA concentration versus concentration by GC/MS.

or below. At these concentrations the ELISA response is not detectable.

With these considerations in mind, the ELISA was used as a screen for both surface waters and groundwaters from the central United States. Sixty-six surface-water samples from the central United States were analyzed for the triazine mixture shown in Figure 2, and their responses relative to atrazine were computed for the ELISA. This summed response was plotted on the GC/MS or x axis of Figures 3 and 4. The correlation was 0.95 (Figure 3), using cross-reactivity factors for each of the triazine herbicides. In all cases, the immunoassay detected the presence of triazine herbicides at the detection limit of 0.2 μg/L with no false negatives. Because the majority of these samples contained atrazine as the major herbicide, the ELISA response was quite similar to the atrazine concentration by GC/MS, with total triazines only slightly larger than atrazine concentrations. No false positives

were detected at the 0.2 μg/L detection limit of ELISA.

Also, the concentration of triazine herbicides was compared by ELISA and GC/MS for 64 groundwater samples from the central United States. The correlation was 0.91 (Figure 4). Again, the immunoassay detected the presence of triazine herbicides at the detection limit of 0.2 μg/L with no false negatives. The ELISA method appears to be a reliable screening method for triazine herbicides (atrazine, propazine, and simazine) in both surface and groundwater at environmentally relevant concentrations (0.2–2 μg/L). Although other triazines, such as cyanazine, are not detected by the ELISA, the combined usage of these compounds with atrazine makes the ELISA a reliable screening tool for preemergent triazine herbicides in surface and groundwaters.

CONCLUSIONS

ELISA methodology showed a good correlation with conventional GC/MS analysis of spiked or field samples of water for triazine herbicides (specifically atrazine, simazine, and propazine). The ELISA has several positive aspects as a screening analysis for water-quality surveys for triazines. Firstly, it is an inexpensive technique ($15/sample) that can be done routinely and rapidly in both the field and laboratory. Secondly, it works at environmentally significant concentrations from 0.2 to 2 μg/L (relative standard deviation of ±15–20% compared to ±5–10% for GC/MS at 1 μg/L) with no false negatives observed. The lack of false negatives is typical for ELISA methods in general because to generate a response, physical sequesting or sorption must occur at the antibody-binding sites, which is unexpected in most analytical situations. ELISA cross reacts significantly with several major triazine herbicides (atrazine, propazine, and simazine), which makes the method useful as a class-specific analysis; however, the antibodies used in this ELISA does not react significantly with triazine degradation products. Thirdly, ELISA works well on samples of limited volume (160 μL required) when other methods may have inadequate sensitivity. Precision of ELISA was improved by measuring percent inhibition rather than absorbance at 450 nm. Fourthly, this ELISA requires no sample preparation and is field portable.

Solid-phase extraction and GC/MS SIM may be used in conjunction with ELISA as a confirmation technique. The GC/MS SIM method does not give an absolute confirmation, as defined by EPA regulations for identification by GC/MS (*28*). However, if molecular ion and two confirming ions are used with a 0.2% retention-time window corrected to phenanthrene-d_{10}, it is a reliable and sensitive method that is easily automated with conventional laboratory workstations. The combination of ELISA and GC/MS SIM provides a low-cost screening analysis for triazine herbicides in surface and groundwater and is suitable for large water-quality surveys.

ACKNOWLEDGMENT

We appreciate the help of Jeri Damman and Chris Wilcox in our laboratory. We also appreciate the support of Ciba-Geigy, Inc. (Janice McFarland), in supplying standards of atrazine degradation products.

LITERATURE CITED

(1) Huber, S. J.; Hock, B. *Z. Pflanzenkrankh. (Pflanzenpathol.) Pflanzenschutz* **1985**, *92*, 147–156.
(2) Bushway, R. J.; Perkins, B.; Savage, S. A.; Lekousi, S. L.; Ferguson, B. S. *Bull. Environ. Contam. Toxicol.* **1988**, *40*, 647–654.
(3) Bushway, R. J.; Perkins, B.; Savage, S. A.; Lekousi, S. L.; Ferguson, B. S. *Bull. Environ. Contam. Toxicol.* **1989**, *42*, 899–904.
(4) Li, Q. X.; Gee, S. J.; McChesney, M. M.; Hammock, B. D.; Seiber, J. N. *Anal. Chem.* **1989**, *61*, 819–823.
(5) Vanderlaan, Martin; Watkins, B. E.; Stanker, Larry, *Environ. Sci. Technol.* **1988**, *22*, 247–254.
(6) Popl, M.; Voznakova, Z.; Tatar, V.; Strnadova, J. *J. Chromatogr. Sci.* **1983**, *21*, 39–42.
(7) Steinheimer, T. R.; Brooks, M. G. *Int. J. Environ. Anal. Chem.* **1984**, *17*, 97–111.
(8) Kreindl, T. G.; Malissa, H.; Winsauer, K. *Mikrochim. Acta* **1986**, *1*, 1–13.
(9) Bardalaye, P. C.; Wheeler, W. B. *Int. J. Environ. Anal. Chem.* **1986**, *25*, 105–113.
(10) Smolkova, E.; Pacakova, V. *Chromatographia* **1978**, *11*, 698.
(11) Di Corcia, Antonio; Marchetti, Marcello; Samperi, Roberto *J. Chromatogr.* **1983**, *405*, 357–363.
(12) Ferris, I. G.; Haigh, B. M. *J. Chromatogr. Sci.* **1987**, *25*, 170–173.
(13) Karlhuber, B. A.; Hormann, W. D.; Ramsteiner, K. A. *Anal. Chem.* **1975**, *47*, 2450–2452.
(14) Mangani, F.; Bruner, F. *Chromatographia* **1983**, *17*, 377–380.
(15) Lopez-Avila, Viorica; Hirata, Pat; Kraska, Susan; Flanagan, Michael; Taylor, J. H., Jr. *Anal. Chem.* **1985**, *57*, 2797–2801.
(16) Davoli, E.; Benfenati, E.; Bagnati, R.; Fanelli, R. *Chemosphere* **1987**, *16*, 1425–1430.
(17) Pereira, W. E.; Rostad, C. E.; Leiker, T. J. *Anal. Chim. Acta* **1989**, *228*, 69–75.
(18) Huang, L. Q. *J. Assoc. Off. Anal. Chem.* **1989**, *72*, 349–354.
(19) Leonard, R. A. *Environmental Chemistry of Herbicides*; Grover, R., Ed., CRC Press: Boca Raton, FL, 1988; Chapter 3, pp 45–87.
(20) Ritchie, D. G.; Nickerson, J. M.; Fuller, G. M. *Methods Enzymol.* **1983**, *92*, 577–585.
(21) ACS Committee on Environmental Improvement and Subcommittee on Environmental Analytical Chemistry *Anal. Chem.* **1980**, *52*, 2242–2249.
(22) Thurman, E. M. *Organic Geochemistry of Natural Waters*; Martinus Nijhoff/Dr. W. Junk: Dordrechdt, 1985; p 496.
(23) Malcom, R. L.; MacCarthy, P. *Environ. Sci. Technol.* **1986**, *20*, 904–911.
(24) Thurman, E. M.; Aiken, G. R., Ewald, M.;Fischer, W. R.; Forstner, U.; Hack, A. H.; Mantoura, R. F. C.; Parsons, J. W.; Pocklington, R.; Stevenson, F. J.; Swift, R. S.; Szpakowska, B. *Humic Substances and Their Role in the Environment*; Frimmel, F. H., Christman, R. F., Eds.; John Wiley and Sons: New York, 1988; S. Bernard, Dahlem Konferenzen.
(25) Thurman, E. M. *Humic Substances in Soil, Sediment and Water*; Aiken, G. R., and others, Eds.; Wiley-Interscience: New York, 1985.
(26) Junk, G. A.; Richard, J. J. *Anal. Chem.* **1988**, *60*, 451–454.
(27) Junk, G. A.; Avery, M. J.; Richard, J. J. *Anal. Chem.* **1988**, *60*, 1347–1350.
(28) Guidelines establishing test procedures for the analysis of pollutants under the Clean Water Act, 40 CFR Part 136, Friday, October 26, 1984, *Fed. Regist.* **1984**, 1–210.

RECEIVED for review February 12, 1990. Revised manuscript received June 21, 1990. Accepted June 26, 1990. We appreciate the financial support of the Surface-Water and Ground-Water Toxics Program of the U.S. Geological Survey. Brand names are for identification purposes only and do not imply endorsement by the U.S. Geological Survey.

CORRESPONDENCE

Quantitation of Ribonucleotides from Base-Hydrolyzed RNA Using Capillary Zone Electrophoresis

Sir: Ribonucleic acid (RNA) is a biopolymer consisting of four different ribonucleosides connected by phosphate units through 3′–5′ linkages on the ribose rings. Specificity of RNA is derived by the sequence of the four bases, of which two are purines (adenine [A] and guanine [G]) and two are pyrimidines (cytosine [C] and uracil [U]). Unlike in deoxyribonucleic acid (DNA), a double-stranded biopolymer, pairing between purine and pyrimidine bases need not occur in RNA. Consequently, there is much interest in determining the ratio of all four "major" bases in different kinds of RNA, as well as the amount of modified bases (e.g. ribothymidine and pseudouridine) which may constitute up to 15% of tRNA. Additional interest is centered on the determination of the quantity of radiolabel incorporated into RNA and free nucleoside monophosphates (nucleotides) in metabolic studies.

Toward these ends, several methods of molecular discrimination have been previously employed to separate nucleotides acquired from complete hydrolysis of RNA. These include paper electrophoresis (*1*), ion-exchange chromatography (*2*), high-performance liquid chromatography (HPLC) (*3*), and isotachophoresis (*4*). Recently, capillary zone electrophoresis (CZE) has been shown to be applicable to the problem of nucleotide and oligonucleotide separation (*5–7*). We report the ability of CZE with UV absorbance detection to distinguish isomers of the four main ribonucleotides, as well as the possible use of this system in quantitation. CZE compares favorably to other separation techniques especially in the areas of limited sample quantity, resolution, and time of analysis. With on-line UV detection (254 nm), CZE provides a 5-min separation of the main ribonucleotides with a detection limit correlating to less than 0.1 ng of RNA.

EXPERIMENTAL SECTION

Pure nucleoside monophosphate isomers as well as mixtures of the isomers were obtained from Sigma Chemical Corp., St. Louis, MO.

Bulk RNA (obtained from Sigma and from the laboratory of Professor Dean Appling, University of Texas, Austin) was subjected to 0.3 M KOH at 37 °C for 18 h. The digested sample was directly introduced into a fused silica capillary (Polymicro Technologies, Phoenix, AZ) by placing one end of the capillary into the analyte solution and raising the end 7 cm above the outlet. By continuously injecting a sample until the plug front reached the detector, we determined that this method of introduction delivers approximately 2 nL in 5 s for a 50 μm i.d. capillary. A high-voltage power supply (Model R50B, Hipotronics, Inc., Brewster, NY) capable of delivering −30 to +30 kV was used for all experiments, and a Plexiglas box outfitted with a twin interlock system prevented access to the capillary and electrodes while the system was in operation.

CZE separation was performed under two different sets of conditions. In one, the inlet was held positive with respect to a grounded outlet, and 50 mM formate, at pH between 3.7 and 4.0, was employed as the running buffer. In this case, electroosmotic flow was from anode to cathode. Alternatively, the inlet was held negative with respect to the grounded outlet, and a running buffer that contained 12.5 mM formate at pH 3.8 with 0.1 mM cetyltrimethylammonium bromide (CTAB) was used. CTAB, a cationic surfactant, changes the charge associated with the inner wall of a capillary from net negative to net positive. Consequently, the direction of electroosmosis is from cathode to anode (*8*, *9*). Prior to first use, capillaries were conditioned with the CTAB buffer for 3–4 h in order to achieve a reproducible electroosmotic flow rate. To maintain this conditioning, capillaries were stored with CTAB buffer inside when not in use. Between individual runs, the columns were rinsed with buffer solution only.

In all separations, on-column detection was accomplished with a UV absorbance spectrometer (Model UVIDEC-100 V, Japan Spectroscopic Co., Tokyo, Japan) set at 254 nm and a home-built cell holder with 0.1-mm slits. The polyimide coating on the capillaries was removed by flame and acetone wash at the site of detection.

RESULTS

Resolution of Ribonucleotide Isomers. Figure 1 depicts the structure of the ribonucleotide products of base-hydrolyzed RNA. Cleavage occurs such that any single nucleoside has a phosphate group at either the 2′ or the 3′ position, and yields of the two isomers are approximately equal. The separation of a standard mix of ribonucleotide isomers at pH 3.7 is shown in Figure 2. This pH aided separation in two ways. First, at a moderately low pH the difference in the effective charges of different nucleotides is augmented, and consequently, so is the difference in electrophoretic mobilities (μ_e) (*10*). Second, low pH causes the electroosmotic flow rate (μ_{eo}) to decrease more in magnitude than the oppositely directed electrophoretic mobilities of nucleotides, with the result being enhanced resolution (*11*). Resolution was nearly baseline for 2′- and 3′-CMP as well as 2′- and 3′-AMP and was adequate to distinguish the isomers of both GMP and UMP. The identification of peaks was made by spiking the sample with either the 2′ or 3′ isomer of each of the different nucleotides. As shown in Figure 3, when a mixture of all 12 2′, 3′, and 5′ isomers was electrophoresed, all species were distinguishable.

Determination of Nucleotide Composition in RNA Digests. The conditions used to resolve the isomers of nucleotides had substantial drawbacks for quantitative analysis. Low pH caused the electroosmotic flow rate to be both slow and irreproducible. Because resolution of 2′ and 3′ isomers is irrelevant for assays of nucleotide composition in RNA, we adopted another strategy that sacrifices some resolution while gaining reproducibility and speed of analysis.

The cationic detergent CTAB was added to formate buffer and the polarity of the electrodes was reversed so that the electroosmotic flow was in the same direction as the electrophoretic mobilities of the nucleotides. Figure 4 shows the resulting electropherograms from an equimolar mixture of the four pairs of nucleotides (part a), the base-hydrolyzed digests of rabbit intestinal mucosa RNA (part b), calf liver RNA (part c) and baker's yeast RNA (part d). In each electropherogram the four nucleotide isomer pairs produced five peaks in which the only resolvable isomers were 2′- and 3′-CMP. Nevertheless, this information was sufficient to estimate the ratio of the four different bases based on relative peak heights. Moreover, each electropherogram was obtained in 5 min or less.

We found that a period of several hours was required to condition a capillary wall to the buffer containing CTAB under these conditions. During this period, the electroosmotic flow rate decreased. Once a capillary was conditioned, the elec-

0003-2700/90/0362-2049$02.50/0

Table I. Comparison of Determined Nucleotide Composition of Different RNAs with Previously Published Values

source of RNA		% CMP	% GMP	% AMP	% UMP
calf liver	experimental	28.3 ± 0.8	35.8 ± 0.4	17.9 ± 0.5	18.0 ± 0.5
	published[a]	29.1	35.0	19.5	16.4
rabbit liver	experimental	29.7 ± 1.4	33.3 ± 1.1	17.3 ± 0.5	19.7 ± 0.5
	published[b]	28.2	32.6	19.3	19.9
baker's yeast	experimental	18.4 ± 0.9	34.1 ± 0.4	25.5 ± 0.6	22.0 ± 0.6
	published[a]	17.8	29.4	24.7	28.1

[a] See ref *1*. [b] West, E. S.; Todd, W. R.; Mason, H. S.; Van Bruggen, J. T. *Textbook of Biochemistry*, 4th ed.; Macmillan: New York, 1967; p 394.

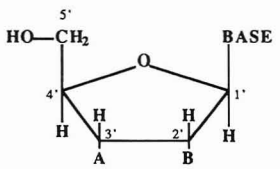

Figure 1. Diagram of a 2′- or 3′-ribonucleoside monophosphate. When A = phosphate, B = OH, and vice versa.

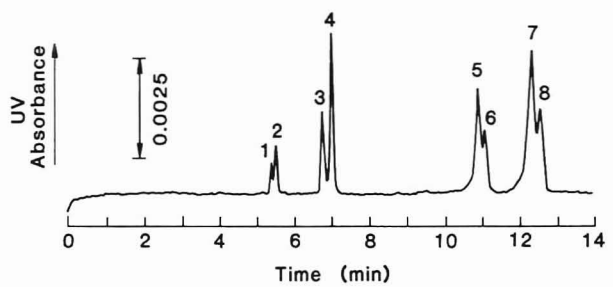

Figure 2. Electropherogram of mixture of 2′ and 3′ isomers of adenylate, guanylate, uridylate, and cytidylate, each at approximately 0.3 mM: 1, 2′-CMP; 2, 3′-CMP; 3, 2′-AMP; 4, 3′-AMP; 5, 3′-GMP; 6, 2′-GMP; 7, 3′-UMP; 8, 2′-UMP. The sample was run in 50 mM sodium acetate, pH 3.7, with an applied voltage of +25 kV. A 75-μm fused silica capillary was employed, with length 40 cm from anode (injection site) to detector, 60 cm from anode to cathode. Injection time was 10 s.

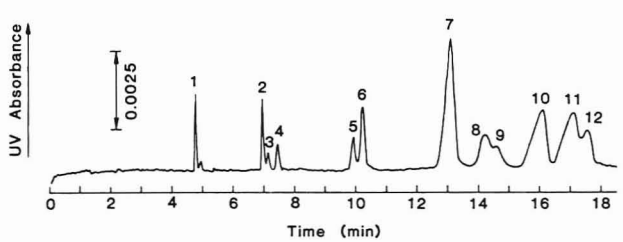

Figure 3. Electropherogram of mixture of 2′, 3′, and 5′ isomers of adenylate, guanylate, uridylate, and cytidylate, each at approximately 0.3 mM: 1, 5′-AMP; 2, 5′-CMP; 3, 2′-CMP; 4, 3′-CMP; 5, 2′-AMP; 6, 3′-AMP; 7, 5′-GMP; 8, 3′-GMP; 9, 2′-GMP; 10, 5′-UMP; 11, 3′-UMP; 12, 2′-UMP. All conditions are identical with those described in Figure 2 except that buffer here is at pH 4.0. Injection time was 10 s.

tropherograms were highly reproducible, unlike those obtained with the buffer system lacking detergent. In cases in which a capillary was stripped of its CTAB coating by rinsing with 0.1 M NaOH and was subsequently recoated with detergent, we found that the relative, but not the absolute, migration rates of nucleotides were conserved.

Normalization of the absorbance response of the four bases was accomplished by measuring peak heights for an equimolar standard of the four pairs of nucleotide isomers. We are thus able to state approximate mole percents of each base in RNA samples from calf liver, rabbit liver, and baker's yeast (Table I). Values are based on a mean of three runs for the standard, calf liver, and rabbit liver and a mean of two runs for baker's yeast. Uncertainty is expressed as standard deviation and represents propagation of the error in the mean of the

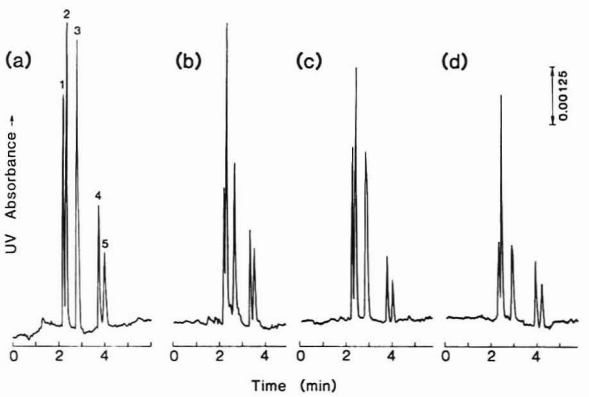

Figure 4. Electropherograms of (a) equimolar mixture of 2′ and 3′ isomers of AMP, GMP, UMP, and CMP; (b) base-hydrolyzed rabbit intestinal mucosa RNA; (c) base-hydrolyzed calf liver RNA; (d) base-hydrolyzed yeast RNA. For each electropherogram, peaks are as follows: 1, 2′- and 3′-UMP; 2, 2′- and 3′-GMP; 3, 2′- and 3′-AMP; 4, 3′-CMP; 5, 2′-CMP. Buffer was 12 mM sodium formate, 0.1 mM CTAB, pH 3.8. Sample was injected for 5 s at the cathode, which was at −26 kV with respect to the anode. The capillary had a 50 μm i.d. and was 29 cm from cathode to detector, 42 cm from cathode to anode. Concentration of each nucleoside monophosphate in part a was 0.5 mM.

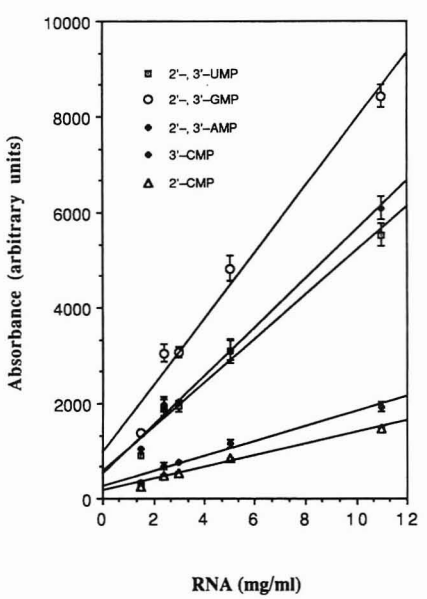

Figure 5. Absorbance peak heights of ribonucleoside monophosphates vs amount of yeast RNA digested. Approximately 2 nL was injected per run. Points for 2.4 mg/mL, 5 mg/mL, and 11 mg/mL represent a mean of three measurements, and points for 1.5 and 3 mg/mL represent a mean of two measurements. Error bars show standard deviation.

standard with the error in the mean of each sample group. The sources of the previously published values did not provide estimates of uncertainty.

Estimation of RNA Amount by Measurement of Nucleotide Content. The relationship between absorbance peak

heights and concentration of nucleotides was examined over a range of 30–500 μM and found to be linear for all bases. This suggests that the present method may be utilized for estimation of absolute RNA amounts in a tissue extract. To demonstrate this, we recorded the peak heights of nucleotides versus mass of RNA prior to base hydrolysis. Figure 5 shows the resulting plot for yeast RNA. By calculation of the response of the instrument to the quantity of a nucleotide standard injected, the amount of RNA in a sample can be determined. Furthermore, if the ratio of the four bases in a specific RNA source is known, detection of any peak is sufficient to determine the amount of RNA. Therefore, for situations in which speed is of prime importance, measurement of the uracil peak will permit such an estimation in less than 2.5 min. This method is clearly applicable to samples containing a single RNA species as well as those containing mixtures of different RNAs, as would result from bulk RNA extraction from tissue.

DISCUSSION

The clearest advantage CZE maintains over other means of nucleotide separation is the required sample quantity. In our experiments, injection of less than 20 pg of each ribonucleotide provided electropherograms with a signal-to-noise ratio of 3:1. In comparison to HPLC and isotachophoresis the amount of sample necessary per run is less by approximately 100-fold, and in comparison to paper electrophoresis, by many orders of magnitude. The method of microcolumn liquid chromatography, however, allows a comparable detection limit of ribonucleotides, as demonstrated by Banks and Novotny (*12*).

Nucleotide resolution in CZE is as good or better than that for each of the previously demonstrated methods. In the experiments done without CTAB, all product species of RNA base-hydrosylate were resolved. HPLC and ion-exchange chromatography also effect such a separation, but isotachophoresis has been shown to distinguish only the 2′ from the 3′ isomer for CMP, and paper electrophoresis apparently has been unable to separate any of the isomers. Even for our more rapid and reproducible experiments utilizing CTAB, resolution rivals that seen in many HPLC and ion-exchange separations and is superior to that in isotachophoresis and paper electrophoresis.

Short separation time is a third attribute of CZE. Complete separation of ribonucleotides is possible in 5 min, provided a CTAB-conditioned capillary is available, and no capillary regeneration time is needed between separations. Isotachophoretic separation demands more than 20 min. HPLC requires approximately 20 min for a separation and another 20 min between runs to equilibrate the column. Paper electrophoresis and ion-exchange chromatography traditionally have taken several hours or more.

The use of electropherogram peak heights in quantitation requires either that the migration rate of the standard is exactly equal to the rates for the samples or, if velocities are different, that diffusion of bands is negligible. In this study, migration rates did show minor variations, but diffusion of nucleotides is low for the time scale of our separations. The effective diffusion coefficient for 5′-AMP, for example, has been estimated at 1.6×10^{-5} cm^2/s (*11*).

In summary, the combined advantages of CZE analysis of ribonucleotides from base-hydrolyzed RNA, namely the amount of sample required, the resolution, and the time of analysis, indicate this method to be highly efficacious. In this study, no exceptional effort was made in optimizing the procedure. Also, enhanced accuracy and precision in quantitation are possible through analysis of corrected peak areas. With the prospects of further improvement and also of automation, we believe that CZE may become the method of choice for quantitating base composition of RNA and for measuring RNA amount in tissue. The feasibility of coupling CZE to a radioisotope detection system (*13*), either on-line or off (*14*), suggests the potential to monitor incorporation of radiolabels in purine and pyrimidine metabolism.

ACKNOWLEDGMENT

We wish to thank Dean Appling and the members of his lab (University of Texas, Austin) for their advice and intestines.

Registry No. 5′-AMP, 61-19-8; 5′-CMP, 63-37-6; 2′-CMP, 85-94-9; 3′-CMP, 84-52-6; 2′-AMP, 130-49-4; 3′-AMP, 84-21-9; 5′-GMP, 85-32-5; 3′-GMP, 117-68-0; 2′-GMP, 130-50-7; 5′-UMP, 58-97-9; 3′-UMP, 84-53-7; 2′-UMP, 131-83-9; CTAB, 57-09-0.

LITERATURE CITED

(1) Davidson, J. N.; Smellie, R. M. S. *Biochem. J.* **1952**, *52*, 594–599.
(2) Wade, H. E. *Biochem. J.* **1960**, *77*, 534–542.
(3) Kreamer, W.; Zorich, N.; Liu, D. S. H.; Richardson, A. *Exp. Gerontol.* **1979**, *14*, 27–36.
(4) *Analytical and Preparative Isotachophoresis*; Holloway, C. J., Ed.; Walter de Gruyter: Berlin/New York, 1984.
(5) Tsuda, T.; Takagi, K.; Watanabe, T.; Satake, T. *HRC CC, J. High Resolut. Chromatogr. Chromatogr. Commun.* **1988**, *11*, 721–723.
(6) Dolnik, V.; Liu, J.; Banks, J. F., Jr.; Novotny, M. V.; Bocek, P. *J. Chromatogr.* **1989**, *480*, 321–330.
(7) Liu, J.; Banks, J. F., Jr.; Novotny, M. *J. Microcolumn Sep.* **1989**, *1*, 136–141.
(8) Terabe, S.; Ishikawa, K.; Utsuka, K.; Tsuchiya, A.; Ando, T. 26th International Liquid Chromatography Symposium; Kyoto, Japan, Jan 25–26, 1983.
(9) Tsuda, T. *HRC CC, J. High Resolut. Chromatogr. Chromatogr. Commun.* **1987**, *10*, 622–624.
(10) Kiso, Y. *Topics Surrounding Zone Electrophoresis, Ionic Processes Through Matrices*; Nankodo: Tokyo, 1971; pp 81–87.
(11) Huang, X.; Coleman, W. F.; Zare, R. N. *J. Chromatogr.* **1989**, *480*, 95–110.
(12) Banks, J. F., Jr.; Novotny, M. V. *J. Chromatogr.* **1989**, *475*, 12–21.
(13) Pentoney, S. L., Jr.; Zare, R. N. *Anal. Chem.* **1989**, *61*, 1642–1647.
(14) Huang, X.; Zare, R. N. *Anal. Chem.* **1990**, *62*, 443–446.

[1] Present address: Genomyx, 460 Point San Bruno Blvd., South San Francisco, CA 94080.

Xiaohua Huang[1]
Jason B. Shear
Richard N. Zare*

Department of Chemistry
Stanford University
Stanford, California 94305

RECEIVED for review March 5, 1990. Accepted May 31, 1990. Support for this work by Beckman Instruments, Inc., is gratefully acknowledged.

Labeling Reaction for Time-Resolved Luminescence Detection in Liquid Chromatography

Sir: In high-performance liquid chromatography (HPLC), chemical derivatization (or labeling) of analytes to obtain products with better detection characteristics is a very well-known procedure to improve detection limits. Due to

0003-2700/90/0362-2051$02.50/0

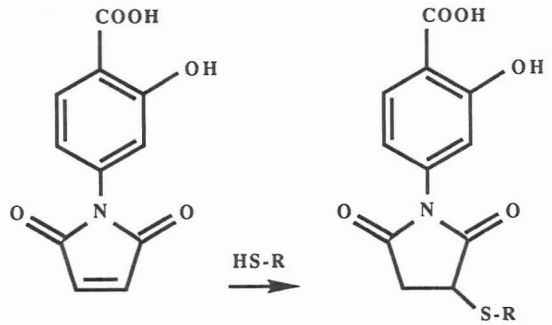

Figure 1. Derivatization reaction of thiols with 4-MSA.

its inherent sensitivity, in fluorescence detection impressive results have been achieved and a wide variety of labeling reactions has been investigated. Unfortunately, in the analysis of real samples the chromatographic performance is not always sufficient to detect the labeled analytes separately from other peaks. Hence, the detection is frequently hindered by fluorescence background originating from fluorescent contaminants, an excess of labeling reagent and/or fluorescent side products. Here we present an approach to enhance the selectivity of detection by making use of labels with a long luminescence decay time (i.e. longer than 0.1 ms) and applying time resolution. With a pulsed Xe lamp and a gated photomultiplier the luminescence of these labels can easily be discriminated from short-lived background fluorescence and scattered light. Furthermore, since long-lived luminescence in aqueous solutions at room temperature is quite exceptional, time-resolved luminescence detection has an inherent selectivity.

Besides several organic molecules (the most well-known being biacetyl), a few lanthanide ions show long-lived luminescence in liquid solutions at room temperature (*1*). In aqueous solutions the decay times of (for instance) Eu(III) and Tb(III) are respectively 0.1 and 0.4 ms. Compared to the organic compounds, the lanthanide ions have the advantage that oxygen removal is not required to observe long-lived luminescence (*2*). The lanthanide ions Eu(III) and Tb(III) have been successfully applied as luminophoric labels in fluoroimmunoassay techniques (*3*, *4*).

The lanthanide ions have low inherent absorptivities. When complexated with certain ligands, their luminescence intensities can be increased by sensitized excitation (*5*, *6*). To achieve efficient sensitizing, two conditions have to be fulfilled: the ligand must form a complex with the lanthanide(III) ion and there must be a good match between a donating electronic (triplet) level of the ligand and the accepting level of the lanthanide(III) ion. If the complexes are too weak, sensitizing is only possible if the solvent is thoroughly deoxygenated since otherwise nonradiative decay of the excited ligand dominates (*7*). Sensitizing of Tb(III) or Eu(III) luminescence as a detection method in batch and in HPLC has been described in the literature (*8–13*).

In the present paper the detection via lanthanide luminescence is described for thiol-containing analytes. To this end the analyte is derivatized to a product able to form a complex with Tb(III) and to sensitize its luminescence. Use was made of a commercially available derivatization reagent for fluorescence spectroscopy, i.e. 4-maleimidylsalicylic acid (denoted as 4-MSA). The salicylate group has sensitizing properties for Tb(III) luminescence (*4*, *9*, *13*, *14*) and the maleimide group reacts with thiols, as schematically depicted in Figure 1; the reaction may be followed by hydrolytic opening of the imide ring of the adduct (*15–17*). Thus, by using 4-MSA, thiol-containing analytes can be converted into sensitizing compounds for Tb(III) luminescence and, after addition of Tb(III), time-resolved detection of these products will be possible. It is shown for some thiols that (compared to fluorescence detection) by this method higher selectivity and sensitivity can be obtained.

EXPERIMENTAL SECTION

Chemicals. $Tb(Cl)_3 \cdot 6H_2O$ was obtained from Aldrich (Milwaukee, WI) and 4-maleimidylsalicylic acid (4-MSA) from Molecular Probes (Eugene, OR). Glutathione was purchased from Boehringer Mannheim (Mannheim, FRG), β-mercaptoethanol was from Janssen (Beerse, Belgium), thioglycolic acid from Merck (Darmstadt, FRG), and L-cysteine and Trizma base were from Sigma (St. Louis, MO). HPLC-grade acetonitrile was obtained from Baker (Deventer, The Netherlands).

Stock solutions of the thiols were prepared in twice distilled water acidified with hydrochloric acid (pH 3.0). A stock solution of 4-MSA (2×10^{-3} M) was prepared in ethanol.

Instrumentation. Batch experiments were carried out with a Perkin-Elmer (Beaconsfield, U.K.) MPF-44 fluorescence spectrometer, supplied with a continuous XBO 150-W xenon lamp and Hamamatsu type R777-01-HA photomultipliers.

The HPLC system consisted of a Gilson (Villiers-le-Bel, France) 302 HPLC pump equipped with a Gilson 802c manometric module, a Valco six-port injection valve equipped with a 20-μL loop, a stainless-steel column (170 × 3.1 mm i.d.) packed with RoSil C18HL 5 μm (RSL, Eke, Belgium), a Kratos (Ramsay, NY) URS 051 postcolumn unit (containing two pumps), and a Perkin-Elmer LS-2 filter fluorometer. In addition to a UG11 filter, a chemical filter was placed in the excitation beam: a homemade cell (path length 1.5 cm) with quartz windows, filled with an aqueous solution of 1×10^{-4} M K_2CrO_4 and 1×10^{-4} M NaOH. This filter combination has a window from 300 to 340 nm. Fluorescence of derivatized thiols was detected at 410 nm, Tb(III) emission at 545 nm. For time-resolved luminescence detection, a delay time of 0.1 ms and a gating time of 2.0 ms were used.

RESULTS AND DISCUSSION

Batch Experiments. First the derivatization of thiols with 4-maleimidylsalicylic acid was studied in batch by fluorescence spectroscopy. In this preliminary investigation it was not attempted to reach optimum reaction conditions. A mixture of 1×10^{-5} M thiol (β-mercaptoethanol, thioglycolic acid, L-cysteine, or glutathione) and 2.5×10^{-5} M 4-MSA was prepared in 5×10^{-3} M aqueous Tris buffer (pH 7.0). After a reaction time of 2 h at room temperature, the fluorescence spectra were recorded. Maximum excitation of the products was observed at 303–305 nm and maximum emission at 405–410 nm. The spectral maxima of derivatized L-cysteine shifted to longer wavelengths after standing for more than about 3 h; such a shift was not observed for the other thiols under investigation. Like other fluorescence derivatization reagents containing maleimide groups (*15*), 4-MSA itself is almost nonfluorescent.

Subsequently a Tb(III) solution was added to the fluorescent reaction mixture to give a final concentration of 2.5×10^{-4} M Tb(III). This caused a decrease in fluorescence intensity and, as shown in Figure 2, the characteristic narrow-banded Tb(III) emission became clearly visible at a maximum excitation wavelength of 322 nm. To observe sensitized Tb(III) luminescence, a pH as high as 11–12 as described for sensitizing by 5-sulfosalicylate or salicylate (*9*, *14*) is not required; instead a pH of about 7 suffices. It is emphasized that unreacted 4-MSA does not have sensitizing properties. From the absorption spectra of 4-MSA with and without Tb(III) in Tris buffer at pH 7.0, it can be derived that complexation does occur, but obviously Tb(III) sensitizing is not effective. Thus, an excess of derivatization reagent does not perturb the detection.

HPLC Experiments. The derivatized thiol (L-cysteine or glutathione) was injected into the mobile phase consisting of water/acetonitrile 70/30 (v/v) at a low pH (i.e. 2.7, HCl added) to prevent proton dissociation. The column effluent was brought to pH 7.0 by postcolumn addition of 5×10^{-2} M Tris

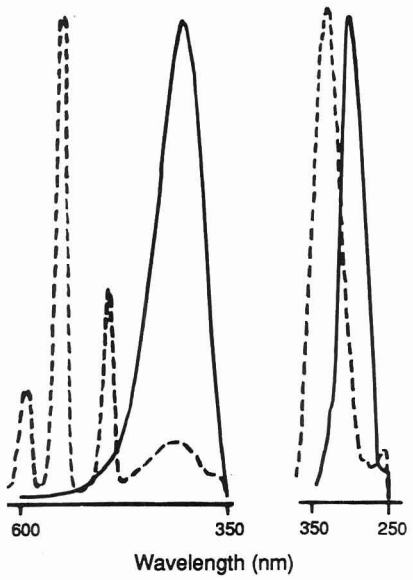

Figure 2. Fluorescence (—) and sensitized Tb(III) luminescence (---) excitation and emission spectra of the 4-MSA adduct of glutathione in Tris buffer pH 7.0 (uncorrected spectra).

buffer (pH 7.5) to achieve good complexation with Tb(III); Tb(III) was added in a second addition line (2×10^{-3} M $TbCl_3$ in water). Buffer and Tb(III) solutions were added separately to prevent hydrolysis of Tb(III) in the postcolumn solution. Flow rates for both postcolumn solutions were 0.25 mL/min, while the flow rate of the HPLC mobile phase was 0.50 mL/min. Due to the broad-banded excitation and the high Tb(III) concentration, some Tb(III) background emission at 545 nm was observed as a result of direct excitation. Obviously, the derivatized thiols can be detected by both time-resolved Tb(III) luminescence and by normal fluorescence detection: when the latter was applied no Tb(III) solution was added. Thus a direct comparison could be made.

The limit of detection obtained by sensitized Tb(III) luminescence detection for both derivatized L-cysteine and glutathione was 1.5×10^{-7} M ($S/N = 3$) in standard solutions, corresponding to respectively 0.4 and 0.9 ng on column. These detection limits were a factor of about 5 more favorable than those found by fluorescence detection. For L-cysteine a linear calibration curve was measured ($r = 0.9997$, $n = 10$), varying the concentrations from 2.0×10^{-7} to 1.6×10^{-5} M (all reaction mixtures contained 2×10^{-5} M 4-MSA). The repeatability of the signal of a mixture of 2×10^{-6} M L-cysteine and 2×10^{-5} M 4-MSA was 2% (relative standard deviation, $n = 6$).

As an example of the analysis of a complex matrix, in Figure 3 chromatograms of derivatized L-cysteine in 10 times diluted urine (which was filtered over a millipore filter and a disposable C_{18} cartridge) obtained by fluorescence and time-resolved Tb(III) luminescence detection are shown. The difference in the selectivity of the detection methods is clearly demonstrated. Whereas the L-cysteine–4-MSA adduct can be discriminated very well from coeluting peaks by time-resolved sensitized Tb(III) luminescence detection, this is impossible in the fluorescence detection mode.

CONCLUSION

The experiments described above indicate that lanthanide labeling of analytes enabling long-lived time-resolved luminescence detection provides a good sensitivity and an enhancement of selectivity so that complex matrices can be more

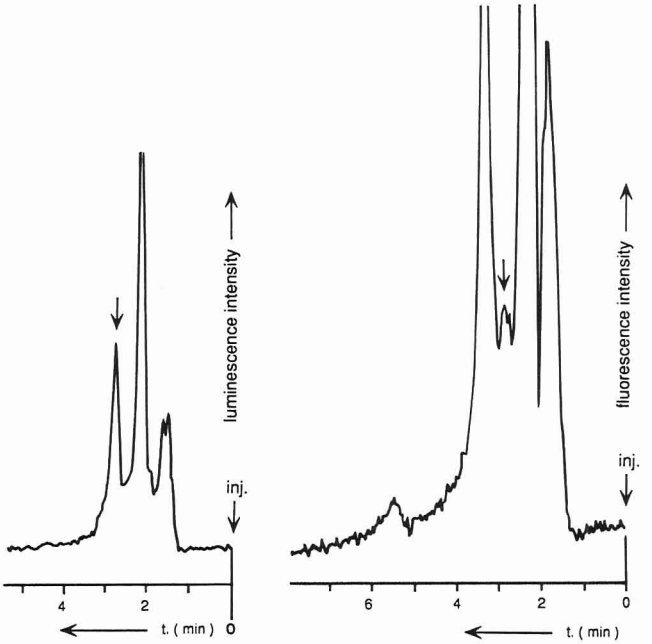

Figure 3. Chromatograms of L-cysteine (1×10^{-6} M) derivatized with 4-MSA in 10-fold diluted urine recorded by fluorescence detection (right) and time-resolved Tb(III) luminescence detection (left).

simply analyzed by HPLC. Extension of this approach to other functional groups would be worthwhile. Of course, in general some sample pretreatment may remain necessary, depending on the problem at hand. Investigations directed on optimization of reaction conditions are currently under way.

LITERATURE CITED

(1) Gooijer, C.; Baumann, R. A.; Velthorst, N. H. *Prog. Anal. Spectrosc.* **1987**, *10*, 573–599.
(2) Kropp, J. L.; Windsor, M. W. *J. Chem. Phys.* **1965**, *42*, 1599–1608.
(3) Hemmilä, I.; Dakubu, S.; Mukkala, V. M.; Siitari, H.; Lövgren, T. *Anal. Chim. Acta* **1984**, *45*, 335–343.
(4) Bailey, M. P.; Rocks, B. F.; Riley, C. *Analyst* **1984**, *109*, 1449–1450.
(5) Dawson, W. R.; Kropp, J. L.; Windsor, M. W. *J. Chem. Phys.* **1966**, *45*, 2410–2418.
(6) Schreurs, M.; Somsen, G. W.; Gooijer, C.; Velthorst, N. H.; Frei, R. W. *J. Chromatogr.* **1989**, *482*, 351–359.
(7) Heller, A.; Wasserman, E. *J. Chem. Phys.* **1965**, *42*, 949–955.
(8) Hirschy, L. M.; Dose, E. V.; Winefordner, J. D. *Anal. Chim. Acta* **1983**, *147*, 311–316.
(9) Bailey, M. P.; Rocks, B. F.; Riley, C. *Anal. Chim. Acta* **1987**, *201*, 335–338.
(10) DiBella, E. E.; Weissman, J. B.; Joseph, M. J.; Schultz, J. R.; Wenzel, T. J. *J. Chromatogr.* **1985**, *328*, 101–109.
(11) Wenzel, T. J.; Collette, L. M.; Dahlen, D. T.; Hendrickson, S. M.; Yarmaloff, L. W. *J. Chromatogr.* **1988**, *433*, 149–158.
(12) Wenzel, T. J.; Collette, L. M. *J. Chromatogr.* **1988**, *436*, 299–307.
(13) Siepak, J. *Anal. Chim. Acta* **1989**, *218*, 143–149.
(14) Charles, R. G.; Riedel, E. P. *J. Inorg. Nucl. Chem.* **1966**, *28*, 527–536.
(15) Wu, C.-W.; Yarbrough, L. R.; Wu, F. Y.-H. *Biochemistry* **1976**, *15*, 2863–2868.
(16) Kågedal, B.; Källberg, M. *J. Chromatogr.* **1982**, *229*, 409–415.
(17) Nakashima, K.; Umekawa, C.; Yoshida, H.; Nakatsuji, S.; Akiyama, S. *J. Chromatogr.* **1987**, *414*, 11–17.

Marry Schreurs
Cees Gooijer*
Nel H. Velthorst
Department of General and Analytical Chemistry
Free University
De Boelelaan 1083, 1081 HV Amsterdam
The Netherlands

RECEIVED for review April 5, 1990. Accepted June 11, 1990.

Ion-Selective Optrode Using Hexadecyl-Acridine Orange Attached on Poly(vinyl chloride) Membrane

Sir: We have recently reported a potassium ion optrode using dodecyl-acridine orange (dodecyl-AO^+) attached on a poly(vinyl chloride) (PVC) membrane (*1*). The positively charged chromophore (AO^+) of dodecyl-AO^+ is known to fluoresce more strongly in a nonpolar solvent than in a polar solvent (*2*). The chromophore moves toward the sample solution by extraction of a potassium ion into the membrane. The polarity change around the chromophore causes a sensor response; i.e. the fluorescence intensity decreases as the polarity increases. The potassium ion is selectively extracted into the membrane with an ionophore of valinomycin. Then, the sensor response is selective to the potassium ion. It is worth mentioning that the sensor response is reversible. This is due to a long alkyl chain in dodecyl-AO^+, which retains the chromophore at the boundary between the membrane and the sample solution. However, the fluorescence intensity of dodecyl-AO^+ gradually decreases with time (−18%/h) since dodecyl-AO^+ is slightly soluble in water. To overcome this problem, a more lipophilic acridine orange (3,6-bis(dimethylamino)-10-hexadecylacridinium ion, hexadecyl-AO^+) is attached on the PVC membrane. The stability of the sensor response is substantially improved, providing a more stable response.

Many ionophores are reported to extract a specific cation into an organic phase (*3*). In the proposed mechanism herein, it is possible to construct various kinds of optrodes sensitive to many cations by using these ionophores instead of valinomycin. The aim of this paper is to show that this is a general approach to construct a cation-selective optrode. Polynactin is well-known as an ionophore to an ammonium ion and has been used in the electrochemical (*4*) and optical (*5*) detection of the ammonium ion. So, polynactin might be used to construct an ammonium ion optrode. The sensor response to anions is also investigated in this study. The selectivity and the response mechanism of the sensor are discussed.

EXPERIMENTAL SECTION

Apparatus. The experimental apparatus is almost identical with that previously reported (*1*). However, the output power of an argon ion laser used as an excitation source was reduced to 4 μW, since the fluorescence intensity was sufficiently strong and photobleaching of hexadecyl-AO^+ was avoided by reduction of the laser power.

Chemical Reagents. Acridine orange, cetyl bromide ($C_{16}H_{33}Br$), NaH_2PO_4, KCl, and NaCl were obtained from Wako Pure Chemical. Bis(2-ethylhexyl) sebacate, Na_2HPO_4, NH_4Cl, and NH_4SCN were purchased from Kishida Chemical. A reagent of $NaClO_4$ was obtained from Katayama Chemical. Polynactin was supplied from Chugai Pharmaceutical as a mixture of dinactin, trinactin, and tetranactin (molecular ratio, 1:4:5). Other chemicals were the same as those used in the previous study (*1*).

A buffer solution (pH 7.0) containing 40 mM of NaH_2PO_4 and 27 mM of Na_2HPO_4 was used for preparation of the sample solution throughout this experiment.

Hexadecyl-AO^+Br^-. A lipophilic dye of hexadecyl-AO^+Br^- was synthesized from acridine orange and cetyl bromide, according to refs 6 and 7. The product was identified by a ^1H NMR spectrometer (Hitachi, R-90). The purity was ascertained to be better than 96%.

Since hexadecyl-AO^+Br^- was insoluble in water, it was first dissolved in ethanol at a concentration of 4×10^{-5} M. This dye solution (0.05 mL) was added to 5 mL of bis(2-ethylhexyl) sebacate used as a membrane solvent or to 5 mL of buffer solution used for preparation of the sample solution. The fluorescence spectra for these solutions were measured by a commercial fluorescence spectrophotometer (Hitachi, MPF-4).

Membrane Preparation. Sodium tetrakis[3,5-bis(trifluoromethyl)phenyl]borate (Na^+TFPB^-, 1 mg) was first dissolved in tetrahydrofuran (2.5 mL). Polynactin (2.5 mg), bis(2-ethylhexyl) sebacate (0.5 g), and tetrahydrofuran (47 mL) were added to the Na^+TFPB^- solution. PVC (0.2 g) was further dissolved in this solution. A distal end of an optical fiber was dipped into the mixed solution, and tetrahydrofuran was vaporized to form a PVC membrane. The thickness of the membrane was 2 μm, which was calculated from the droplet volume attached on the distal end of the optical fiber. The hexadecyl-AO^+Br^- solution (8×10^{-4} M) prepared in ethanol was diluted 50 times with water. The PVC membrane attached on the distal end of the optical fiber was immersed into the hexadecyl-AO^+Br^- solution for 10 s, and hexadecyl-AO^+ was ion exchanged with a sodium ion in the PVC membrane. The sensor was washed with a copious amount of buffer solution.

RESULTS AND DISCUSSION

Fluorescence of Hexadecyl-AO^+. The excitation and emission spectra for hexadecyl-AO^+ were quite similar to those for dodecyl-AO^+ (*1*). The fluorescence intensity of hexadecyl-AO^+ in bis(2-ethylhexyl) sebacate was 40 times larger than that in the buffer solution. Thus hexadecyl-AO^+ was ascertained to be useful as a hydrophobic probe for evaluation of the polarity around the probe molecule.

Sensor Response. A response curve of the sensor to an ammonium ion is shown in Figure 1. The counteranion used is a chlorine ion. The sensor response is reversible to the ammonium ion concentration, and the time required for (1 − 1/e) response is 30 s. The detection limit of the ammonium ion is 0.02 mM, which is determined by fluctuation of the signal intensity (1.4%) mainly due to the unstable output power of the argon ion laser (±0.5%). Hexadecyl-AO^+ is more lipophilic than dodecyl-AO^+ and is much insoluble in water; leaching of hexadecyl-AO^+ into water is negligibly small. Thus no degradation of the sensor response is observed in the time period demonstrated, which is in contrast to the case for dodecyl-AO^+.

From the theoretical derivations described in the previous paper (*1*), the fluoresence intensity of the chromophore should decrease linearly with increase of the ammonium ion concentration when the concentration of free polynactin in the membrane is constant. However, the sensor response, shown in Figure 1, is not linear. The sensor response is determined by the concentration of hexadecyl-AO^+ in the membrane, which decreases by ion exchange with the ammonium ion; the ammonium ion is selectively extracted into the membrane as an ammonium ion–polynactin complex. The concentration of the complex in the membrane was calculated at various ammonium ion concentrations. The initial concentration of polynactin used in the calculation was 6×10^{-3} M, the extraction constant of the complex being 10^3 (*5*). Due to rather high concentrations of the ammonium ion in the sample solution, most polynactin in the membrane forms a complex with the ammonium ion. Then, the concentration of free polynactin decreases, causing signal saturation. The observed sensor response agrees quite well with the complex concentration calculated from the above mechanism. Thus the concave calibration curve is ascribed to decrease of free polynactin in the membrane.

Selectivity. The constructed sensor was immersed into the potassium (0.01 M) and sodium (0.1 M) ion solutions, and the signal changes were compared with that for the ammonium ion. The counteranion in the sample solution was a chlorine

0003-2700/90/0362-2054$02.50/0

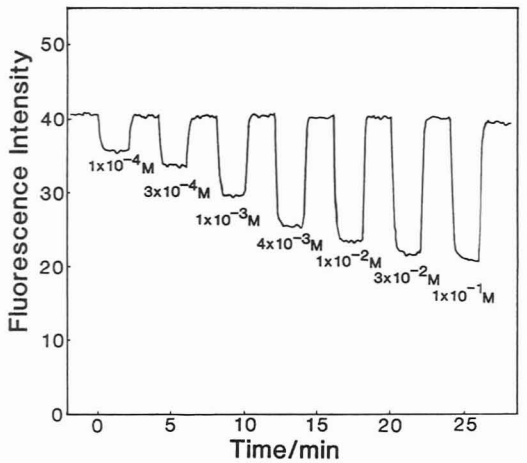

Figure 1. Response curve of ammonium ion optrode.

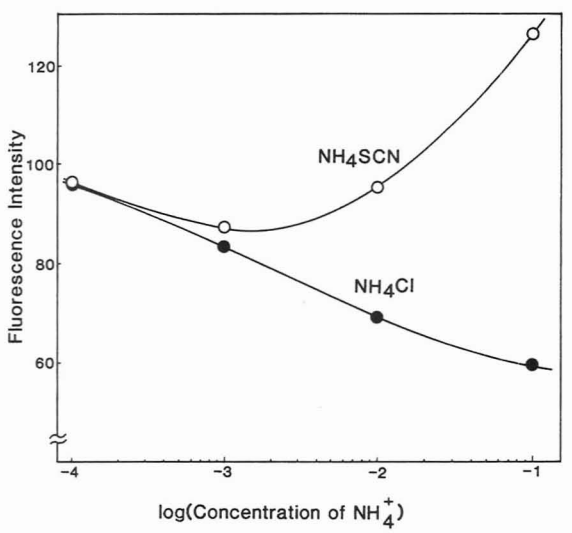

Figure 2. Interference by counteranion.

ion in both the experiments. The selectivity coefficient is defined by the ratio of the equivalent ammonium ion concentration calculated from the signal intensity in the response curve to the concentration of the specific alkali-metal ion dissolved. The selectivity coefficients obtained for the potassium and sodium ions were 0.3 and 5×10^{-4}, respectively. These values are comparable to those reported for the electrochemical (*4*) and optical (*5*) ammonium ion sensors.

Interference by Anions. Figure 2 shows the calibration curves for the ammonium ion, in which chlorine and thiocyanate ions are used as counteranions. The calibration curve for the NH_4SCN solution deviates from that of the NH_4Cl solution as the sample concentration increases. Above 10^{-2} M, the fluorescence intensity for the NH_4SCN solution becomes much higher than that of the initial fluorescence intensity; i.e. the fluorescence enhancement effect is oppositely observed. The response mechanism for anions is illustrated in Figure 3. The chromophore of hexadecyl-AO$^+$ is first moved toward the sample solution. The anion exchanger of $TFPB^-$ plays an important role to exclude anions from the membrane. However, the concentration of $TFPB^-$ in the membrane (2×10^{-3} M) should be reduced as much as possible to improve the selectivity between cations (*1*). A bulky anion such as a thiocyanate ion is ion-paired with the charged

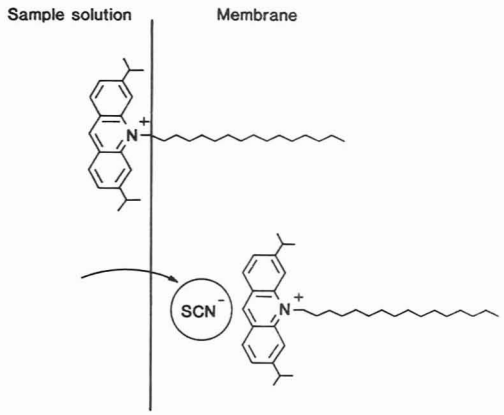

Figure 3. Response mechanism for anions.

chromophore and is easily extracted into the membrane. The polarity around the chromophore decreases, which increases the fluorescence intensity of the chromophore. Thus the concentration of $TFPB^-$ in the membrane should be carefully optimized to reduce the interference by anions and to maintain the selectivity between cations.

Anion-Sensitive Optrode. As described above, the sensor response is interfered by a bulky anion. It implies that the sensor is sensitive to anions. When the sensor was immersed into the 10^{-3}–10^{-2} M $NaClO_4$ solution, the fluorescence intensity increased 1.2–1.5 times. The sensor response was reversible. Interference by a sodium ion at present concentration levels was negligible, so that this sensor response was ascribed to a perchlorate ion involved. From the present results, the sensitivity for anions apparently increases in the order of $Cl^- < SCN^- < ClO_4^-$, i.e. according to the Hofmeister series (*8*). This fact implies that the response mechanism described above is plausible, and the selectivity sequence is determined by solubility of individual anions into the membrane.

LITERATURE CITED

(1) Kawabata, Y.; Kamichika, T.; Imasaka, T.; Ishibashi, N. *Anal. Chem.* **1990**, *62*, 1528–1531.
(2) Kubota, Y.; Kodama, M.; Miura, M. *Bull. Chem. Soc. Jpn.* **1973**, *46*, 100.
(3) Dietrich, B. *J. Chem. Educ.* **1985**, *62*, 954–964.
(4) Scholer, R. P.; Simon, W. *Chimia* **1970**, *24*, 372.
(5) Seiler, K.; Morf, W. E.; Rusterholz, B.; Simon, W. *Anal. Sci.* **1989**, *5*, 557–561.
(6) Miethke, E.; Zanker, V. *Z. Phys. Chem.* (*Frankfurt am Main*) **1958**, *18*, 375–390.
(7) Yamagishi, A.; Masui, T.; Watanabe, F. *J. Phys. Chem.* **1981**, *85*, 281–285.
(8) Hofmeister, F. *Arch. Exp. Pathol. Pharmakol.* **1888**, *24*, 247–260.

* Author to whom correspondence should be addressed.

Yuji Kawabata
Toshito Kamichika
Totaro Imasaka
Nobuhiko Ishibashi*

Faculty of Engineering
Kyushu University
Hakozaki, Fukuoka 812
Japan

RECEIVED for review May 21, 1990. Accepted June 26, 1990. This research was supported by Grant-in-Aid for Scientific Research from the Ministry of Education of Japan and from The Salt Science Research Foundation.

TECHNICAL NOTES

Modification of Lysine Residues in Proteins To Improve Their Recovery When Using Derivatizing Reagents

Mary D. Oates and James W. Jorgenson*

Chemistry Department, University of North Carolina, Chapel Hill, North Carolina 27599-3290

INTRODUCTION

Peptide and protein analyses require the ability to quantitatively determine the amino acids present in the molecule of interest. This is usually accomplished by using liquid chromatography with either a pre- or postcolumn derivatization of the amino acids (*1–4*). Derivatization is necessary so that all of the amino acids can be sensitively detected with a single detection method. Recently, *o*-phthalaldehyde (OPA), which reacts with primary amines in the presence of a thiol to form fluorescent products, has come into wide use for the analysis of amino acids (*5–10*). An analogue of OPA, naphthalene-2,3-dicarboxaldehyde (NDA), which improves upon several aspects of OPA (NDA derivatives are more stable and have higher quantum efficiencies of fluorescence than OPA derivatives) is beginning to find use for the same application (*11–14*). NDA has been used in this laboratory for the quantitative analysis of the amino acid content of subnanogram amounts of protein (*15*). The total sample volume present in these analyses is approximately 25 nL. A microinjection system developed in this laboratory is used to apply this volume directly onto the analytical column. A borosilicate glass micropipet containing the sample is inserted into the inlet end of the column and pressure is applied to force the sample onto the column. A difficulty is encountered with this injection method for compounds, such as lysine, which react twice with the derivatizing reagent. It was found that doubly tagged lysine could not be recovered from the micropipet, perhaps due to adsorption to the glass. Lysine tagged only once with NDA does not exhibit this behavior, however. Modification of the protein prior to hydrolysis to block the ϵ-amine group of all the lysine residues would result in a lysine product on hydrolysis that could react only at the α-amino site. This report describes the use of reductive alkylation to convert lysine residues in proteins to their ϵ-dimethyl derivatives. While this procedure is known to protein chemists, it has not previously been used to modify lysine residues to prevent double tagging by derivatizing reagents, thus improving recovery of the lysine.

A second problem with lysine that has been tagged twice with either OPA or NDA is a substantially reduced quantum efficiency of fluorescence when compared to singly tagged species (*12, 13, 16–18*). For example, the quantum efficiency of lysine tagged twice with NDA has been reported to be 0.02, while it was 0.8 for glycine and 0.75 for alanine under the same experimental conditions (*13*). Lysine doubly tagged with OPA was shown to fluoresce with one-tenth the intensity of other OPA-labeled amino acids (*16*). It is thought that an efficient intramolecular relaxation process, resulting from hydrophobic interaction of the two aromatic rings, causes quenching of the fluorescence. The inclusion of surfactants in the derivatization solution has been found to partially reduce the quenching problem for OPA–lysine (*16–18*), although similar attempts for NDA–lysine have proven unsuccessful (*12*).

Monosubstituted lysine, however, exhibits a fluorescence response equivalent to that obtained from other amino acids for both OPA and NDA derivatives (*13, 16*). The protein modification procedure described here can also be used to prevent this problem from occurring.

EXPERIMENTAL SECTION

Apparatus. The chromatographic system used in this work has been described previously (*14, 23*). A Waters 600E multisolvent delivery system was used to provide mobile phase to the column at a flow rate of 1 mL/min. A splitting system was used to divert the majority of the mobile phase to waste. A fused silica capillary column, 25 cm long and with a 42 μm inner diameter, packed with 5-μm porous spheres (C-8 Spherisorb, Phase-Sep Co.), served as the analytical column (*24*).

The electrochemical detector used has also been described previously (*23, 25*). A carbon fiber, 0.7 mm long and 9 μm in diameter, was inserted into the outlet end of the capillary column and served as the working electrode. All chromatograms were obtained in the amperometric mode with a working potential of 0.9 V vs a Ag/AgCl reference electrode. Data were acquired through the use of a microcomputer. A Model 427 current amplifier (Keithley Instrument, Inc., Cleveland, OH) with a 300-ms rise time and a model 3341 low pass filter (Krohn-Hite Corp., Avon, MA), set at 10 Hz, were also used.

The capillary electrophoresis system used in the fluorescence experiments has also been described elsewhere (*26*). The fused silica capillary had an inner diameter of 25 μm and was 55 cm in total length. The distance from injection to detection was 34 cm. The injections were made at −5 kV for 5 s at the grounded end of the capillary. The voltage applied during runs was −15 kV. The running buffer was 25 mM sodium phosphate monobasic, pH 7.0. Detection was accomplished on-capillary with a helium–cadmium laser with an excitation wavelength of 442 nm. An emission filter with a cut-on wavelength of 500 nm was also used. This was not optimized for use with NDA derivatives.

Reagents. HPLC grade acetonitrile (Fisher Scientific Co., Fair Lawn, NJ) was used as received. Amino acids and chymotrypsinogen were obtained from Sigma (St. Louis, MO), while reagent grade sodium cyanide was purchased from Aldrich (Milwaukee, WI). NDA was obtained from Molecular Probes (Eugene, OR) and used as received. The dimethyllysine standard was purchased from Chemical Dynamics Corp. (South Plainfield, NJ). All water was purified by a Barnstead water purification system prior to use.

Solutions. *Buffers.* Borate buffer (pH 9.5, 0.1 M) was prepared by dissolving boric acid in water and adding sodium hydroxide until the desired pH was reached. Phosphate buffer (pH 7.0, 0.05 M) was made by diluting phosphoric acid in water and adjusting the pH with sodium hydroxide.

Stock Solutions. Amino acid stock solutions were dissolved in water and stored in the refrigerator for up to 1 week. The protein stock solution was made daily by dissolving 5 mg of chymotrypsinogen in 1 mL of the pH 7.0 phosphate buffer. NDA solutions, made in acetonitrile, were prepared fresh daily, while the cyanide and borate buffers were used for up to 1 month.

Protein Modification and Hydrolysis. Bovine chymotrypsinogen was modified prior to acid hydrolysis by using the method described by Jentoft and Dearborn (*22*). To 10 μL of a stock solution of 2×10^{-4} M protein was added 1 μL of 0.3 M sodium cyanoborohydride. After mixing, 1 μL of 0.3 M formaldehyde was added and this was allowed to react at room temperature for 2 h.

0003-2700/90/0362-2056$02.50/0

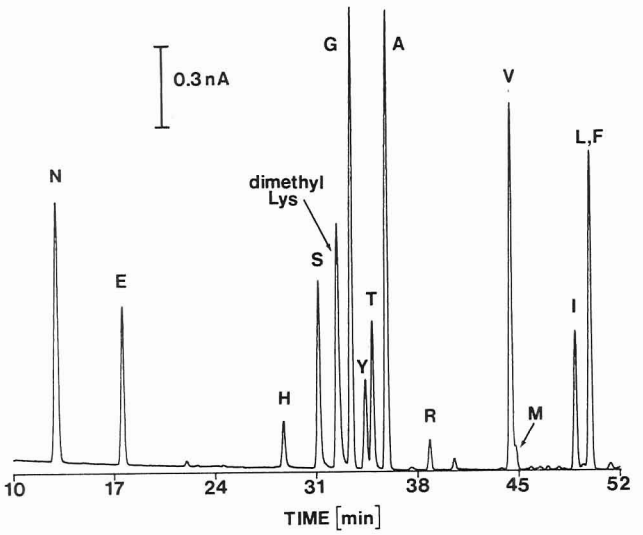

Figure 1. Chromatogram of the NDA-tagged hydrolysis products of bovine chymotrypsinogen. The peaks are labeled according to their one-letter abbreviations.

After the modification reaction was completed, 5 μL of the modified protein solution was added to 10 μL of 6 N constant boiling HCl (Pierce, Rockford, IL) containing 1% phenol and 2 × 10^{-4} M norleucine. The phenol improves the yield of tyrosine (*27*) while norleucine was added as an internal standard. The hydrolysis tube was evacuated for exactly 1 min and then placed in a 115 °C oil bath for 24 h. The hydrolysis mixture became a deep red color several hours after heating began. This occurred only if the modification reagents and phenol were both present and did not affect the amino acid analysis. The HCl was evaporated after hydrolysis by use of heat (80–90 °C) and a stream of nitrogen. The residue was dissolved in 10 μL of water.

Derivatization. Standards and protein hydrolysates were derivatized with NDA by first adding 0.6 μL of 0.1 M cyanide to 1 μL of the amino acid mixture. Then 2.8 μL of 0.1 M borate containing 10% acetonitrile was added, followed by 0.6 μL of 0.1 M NDA. The reaction was allowed to proceed for 5 min at room temperature. The mixture was then diluted 1:1 with the initial mobile phase.

Sample injections were performed by use of a pneumatic micropipet (*28*). The pipet was made of borosilicate glass. After the tip was filled with approximately 20 nL of sample, the pipet was inserted into the inlet end of the column until a tight seal was obtained between the column and pipet. Several nanoliters of sample were then forced onto the column. Injections were accomplished with the aid of a Wolfe Selectra II stereomicroscope, a Brinkman micromanipulator, and an Oriel micropositioner.

RESULTS AND DISCUSSION

Reductive alkylation has been used by protein chemists since the late 1960s to convert amino acid groups in proteins to their alkylamine derivatives (*19*). The reaction is often performed using formaldehyde as the alkylating reagent and sodium cyanoborohydride as the reducing agent (*20*, *21*). This results in the formation of a dimethyl product, as shown in eq 1 (*22*). The reaction is both quantitative and very specific; only the terminal amine group and lysine residues are modified (*20*, *29–31*).

$$6HCHO + 3Prot\text{-}NH_2 + 2NaCNBH_3 \rightarrow 3Prot\text{-}N(CH_3)_2 + 2HCN + 2NaH_2BO_3 \quad (1)$$

Figure 1 demonstrates the use of this modification procedure. This is a chromatogram resulting from the microinjection of the NDA-tagged hydrolysis products of bovine chymotrypsinogen, which contains 14 lysine residues. Mobile phase A was 85% pH 7 phosphate buffer/15% tetrahydrofuran, while mobile phase B was 65% acetonitrile/20% methanol/15% 0.01 M phosphate buffer. The gradient was from 95 A/5 B to 67 A/33 B linearly in 30 min to 50 A/50 B linearly in 50 min. The separation was optimized for lysine, resulting in the overlap of valine with methionine and isoleucine with phenylalanine. Further changes in the gradient used could have resolved all of the amino acids. The purpose here was to emphasize the quantitative recovery of lysine.

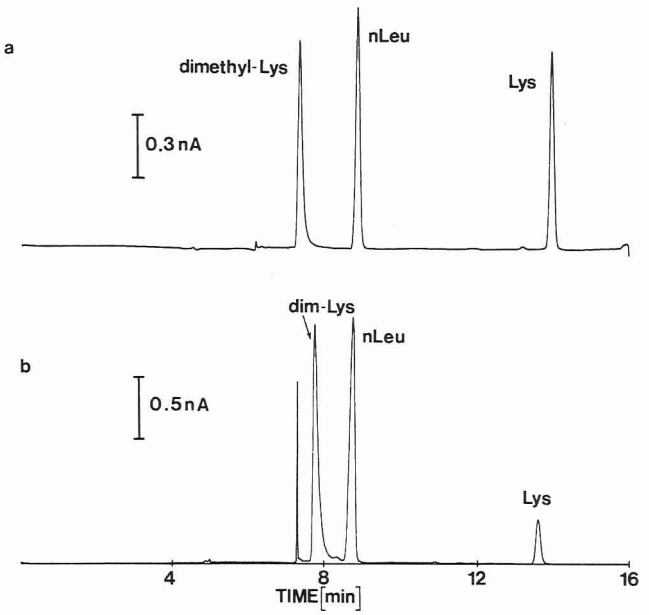

Figure 2. (a) Injection of NDA-labeled ϵ-dimethyllysine, norleucine, and lysine from a solution volume of 1 mL. (b) Microinjection of a few nanoliters of the same solution as in part a.

Table I. Comparison of a Large Injection and Microinjection of ϵ-Dimethyllysine and Lysine, Both Tagged with NDA[a]

	ratio to norleucine	
	dimethyllysine	lysine
large injection	0.957	0.832
microinjection	0.974	0.166

[a] The data were obtained from Figure 2.

The modification procedure is apparently quantitative. The numbers of lysine residues found in three separate hydrolyses were 15.0, 15.2, and 12.5. The average for these three experiments is 14.2, which matches the correct value of 14. Quantitation was accomplished using a calibration curve with norleucine as an internal standard by a method described previously (*14*).

Many samples, particularly of biological origin, provide very small analysis volumes, requiring a microinjection method (*32*, *33*). The technique developed in this laboratory for microinjection uses a borosilicate glass micropipet to directly apply a few nanoliters of sample to the column (*28*). While analyzing small volumes of protein hydrolysates, we found that lysine, after being tagged twice with NDA, could not be quantitatively recovered from the micropipet. This is demonstrated in Figure 2. Both chromatograms show the separation of NDA-tagged ϵ-dimethyllysine, norleucine, and lysine, in that elution order. The first two are tagged once with NDA, while lysine is labeled twice. Mobile phase A in this experiment was 0.05 M phosphate buffer, pH 7.0, while mobile phase B was acetonitrile. The gradient was a linear increase from 65 A/35 B to 50 A/50 B in 10 min. The upper trace is the result of a large injection; i.e. 1 mL of solution was used to fill the tee in which the column was placed. A splitting system then diverts all but a few nanoliters of the sample to waste (*14*, *23*). The sample is introduced into the tee by using a 1-mL glass syringe. The lower chromatogram was obtained by microinjecting a portion of the same solution as in Figure 2a using the glass micropipet.

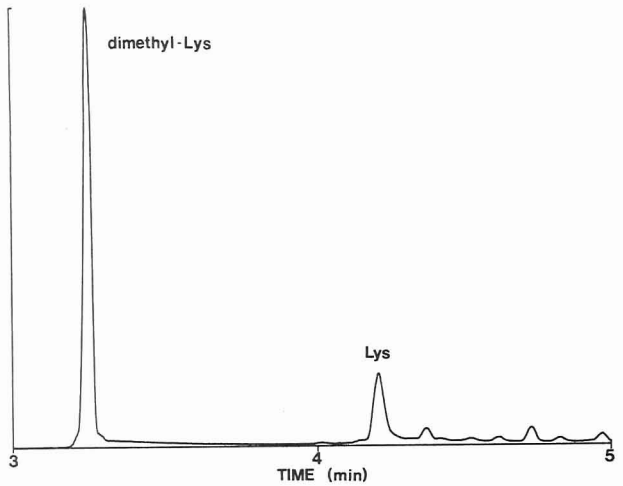

Figure 3. Capillary zone electrophoresis with laser-induced fluorescence detection of 10^{-6} M dimethyllysine, labeled once with NDA, and 10^{-5} M lysine, tagged twice with NDA.

Table I compares the ratios of the area of each lysine peak to the area of the norleucine peak in that run. The ratio for dimethyllysine actually increased slightly in the microinjection, while the ratio for doubly tagged lysine fell by a factor of 5 in going from the large injection to the microinjection. Lysine labeled twice with NDA must in some way be adsorbing to the borosilicate glass of the micropipet. The amount of doubly labeled lysine recovered is not constant from injection to injection, ranging from none to about 50% of the amount of lysine present. This makes quantitation of unmodified lysine in protein hydrolysates impossible with the ultramicroscale techniques developed in this laboratory. However, if the protein modification described here is performed prior to hydrolysis, quantitation of the dimethyl derivative is easily accomplished, as demonstrated in Figure 1.

To confirm the usefulness of this modification procedure for the prevention of fluorescence quenching, a mixture of 10^{-6} M lysine tagged once with NDA and 10^{-5} M lysine tagged twice with NDA was injected onto a capillary electrophoresis system equipped with laser-induced fluorescence detection. Figure 3 shows this electropherogram. The peak area for the singly tagged lysine was 1024, while the peak area for the doubly tagged lysine was 211. Peak area is reported in arbitrary units. Therefore, for an eqimolar solution of the two species, the dimethyllysine would give a fluorescence response approximately 50 times larger than that for lysine which is tagged twice with NDA. The modification procedure described here would result in lysine residues following protein hydrolysis which could be labeled only once with any amine derivatizing reagent, resulting in increased fluorescence over the doubly labeled derivative.

The method described in this report has several important limitations. One is that the α-amine group of the terminal amino acid of the protein is modified along with the lysine residues, so that the terminal amino acid is lost to the analysis. The greatest limitation is that the modification can only be applied to lysine residues in proteins (not free lysines), because the reaction will cause the methylation of all free amine groups. An even more useful modification procedure would block only the ϵ-amine group of free lysine residues, leaving all other free amine groups unaltered.

ACKNOWLEDGMENT

We thank Dr. R. G. Hiskey of the University of North Carolina in Chapel Hill for suggesting the alkylation procedure for the modification of lysine residues in proteins. We also thank Waters Associates (Milford, MA) for the gift of the 600E multisolvent delivery system.

Registry No. L-Lys, 56-87-1; NDA, 7149-49-7; NDA-Lys, 128388-13-6; dimethyl-Lys, 2259-86-1; NDA-dimethyl-Lys, 128388-12-5; chymotrypsinogen, 9035-75-0.

LITERATURE CITED

(1) Spackman, D. H.; Stein, W. H.; Moore, S. *Anal. Chem.* **1958**, *30*, 1190–1206.
(2) Dejong, C.; Hughes, G. J.; van Wieringen, E.; Wilson, K. J. *J. Chromatogr.* **1982**, *241*, 345–359.
(3) Koop, P. R.; Morgan, E. T.; Tarr, G. E.; Coon, M. J. *J. Biol. Chem.* **1982**, *257*, 8472–8480.
(4) Rubenstein, M.; Chen-Kiang, S.; Stein, S.; Undenfriend, S. *Anal. Biochem.* **1979**, *95*, 117–121.
(5) Roth, M. *Anal. Chem.* **1971**, *43*, 880–882.
(6) Simons, S. S., Jr.; Johnson, D. F. *J. Am. Chem. Soc.* **1976**, *98*, 7098–7099.
(7) Joseph, M. H.; Davies, P. J. *J. Chromatogr.* **1983**, *277*, 125–136.
(8) Lindroth, P.; Mopper, K. *Anal. Chem.* **1979**, *51*, 1667–1674.
(9) Allison, L. A.; Mayer, G. S.; Shoup, R. E. *Anal. Chem.* **1984**, *56*, 1089–1096.
(10) Davis, T. P.; Johnson, H. D.; Williams, C. H. *J. Chromatogr.* **1979**, *162*, 293–310.
(11) Roach, M. C.; Harmony, M. D. *Anal. Chem.* **1987**, *59*, 411–415.
(12) de Montigny, F.; Stobaugh, J. F.; Givens, R. S.; Carlson, R. G.; Srinivasachar, K.; Sternson, L. A.; Higuchi, T. *Anal. Chem.* **1987**, *59*, 1096–1101.
(13) Matuszewski, B. K.; Givens, R. S.; Srinivasachar, K.; Carlson, R. G.; Higuchi, T. *Anal. Chem.* **1987**, *59*, 1102–1105.
(14) Oates, M. D.; Jorgenson, J. W. *Anal. Chem.* **1989**, *61*, 432–435.
(15) Oates, M. D.; Jorgenson, J. W. Quantitative Amino acid Analysis of Subnanogram Levels of Proteins by Open Tubular Liquid Chromatography. *Anal. Chem.* **1990**, *62*, 1577–1580.
(16) Chen, R. F.; Scott, C.; Trepman, E. *Biochim. Biophys. Acta* **1979**, *576*, 440–455.
(17) Jones, B. N.; Paabo, S.; Stein, S. *J. Liq. Chromatogr.* **1981**, *4*, 565–586.
(18) Singh, H. N.; Hinze, W. L. *Analyst* **1982**, *107*, 1073–1080.
(19) Means, G. E.; Feeney, R. E. *Biochemistry* **1968**, *7*, 2191–2201.
(20) Jentoft, N.; Dearborn, D. G. *J. Biol. Chem.* **1979**, *254*, 4359–4365.
(21) Geoghegan, K. F.; Cabacungan, J. C.; Dixon, H. B. F.; Feeney, R. E. *Int. J. Pept. Protein Res.* **1981**, *17*, 345–352.
(22) Jentoft, N.; Dearborn, D. G. *Methods Enzymol.* **1983**, *91*, 570–579.
(23) Knecht, L. A.; Guthrie, E. J.; Jorgenson, J. W. *Anal. Chem.* **1984**, *56*, 479–482.
(24) Kennedy, R. T.; Jorgenson, J. W. *Anal. Chem.* **1989**, *61*, 1128–1135.
(25) White, J. G.; St. Claire, R. L.; Jorgenson, J. W. *Anal. Chem.* **1986**, *58*, 293–298.
(26) Nickerson, B.; Jorgenson, J. W. *HRC CC, J. High Resolut. Chromatogr. Chromatogr. Commun.* **1989**, *7*, 529.
(27) Darbre, A. *Practical Protein Chemistry*; Wiley: New York, 1986; Chapter 8.
(28) Kennedy, R. T.; Jorgenson, J. W. *Anal. Chem.* **1988**, *60*, 1521–1524.
(29) Jentoft, J. E.; Jentoft, N.; Gerken, T. A.; Dearborn, D. G. *J. Biol. Chem.* **1979**, *254*, 4366–4370.
(30) Jentoft, J. E.; Gerken, T. A.; Jentoft, N.; Dearborn, D. G. *J. Biol. Chem.* **1981**, *256*, 231–236.
(31) Gerken, T. A.; Jentoft, J. E.; Jentoft, N.; Dearborn, D. G. *J. Biol. Chem.* **19821**, *25*, 2894–2900.
(32) Kennedy, R. T.; St. Claire, R. L. I.; White, J. G.; Jorgenson, J. W. *Mikrochim. Acta* **1988**, *1987* (II), 37–45.
(33) Kennedy, R. T.; Jorgenson, J. W. *Anal. Chem.* **1989**, *61*, 436–441.

RECEIVED for review January 11, 1990. Accepted May 31, 1990. Support for this work was provided by the National Institutes of Health under Grant Number GM39515.

Minimal Dispersion Flow Injection Analysis Systems for Automated Sample Introduction

Stephen H. Brooks* and Gregory Rullo

ICI Pharmaceuticals Group, Concord Pike and Murphy Road, Wilmington, Delaware 19897

INTRODUCTION

The dispersion coefficient, D, is the most common descriptor of dilution in a flow injection analysis (FIA) system and is most generally defined as the ratio of the analyte concentration introduced into the system to the concentration at peak maximum after transport through the defined manifold. Limited dispersion systems (D = 1–3) in FIA are used when the analyst desires to measure the composition of a nearly undiluted sample (*1*). These systems have received minimal application for the analysis of real samples. The determination of metal ions by atomic absorption spectrophotometry (*2*) and the potentiometric determination of pH in soil extracts (*3*) and calcium activity in serum (*4*) are examples of limited dispersion FIA systems which have appeared in the literature. In these applications, the limited dispersion system provides for the accurate and precise transport of the sample to the detector. The minimal dilution of the sample also allows the analyst to enhance sensitivity (due to limited dilution) while taking advantage of the speed and reproducibility of the flow injection technique. The measurement of equilibrium constants (i.e. measurement of ionization constants, metal–ligand coordination complexes, ion pair formation, and dimerization and investigation of charge transfer complexes) provides specific examples where dilution of the analyte is deleterious to the accuracy of the determination. The accurate measurement of critical micelle concentrations of surfactant solutions affords another example of a physicochemical measurement which is highly dependent upon maintenance of the integrity of the sample solution prior to the measurement itself. In all of these applications, dilution of the sample within the flow system would result in inaccurate determinations of solution properties.

The present work introduces the practical application of flow injection systems employing a large ratio of injection to manifold volume for automated sample introduction. In this study, FIA and spectrophotometric detection are utilized for the determination of proton-transfer equilibrium constants. The advantages of the speed and reproducibility of automated sample introduction are realized and the steady-state nature of the process ensures the maximum accuracy of the determination. Other presented applications using minimal dispersion flow injection sample introduction which are dependent upon the establishment of a steady-state signal include the conductometric determination of critical micelle concentrations and the accurate spectrophotometric measurement of samples which possess viscosities which are significantly different from each other. The developed technique is considered to be a hybrid between air-segmented continuous flow analysis (CFA) and classical FIA, with an analytical signal reminiscent of the former while employing the instrumentation of the latter. It is not affected by the many drawbacks of air segmentation, yet provides, to a first approximation, a steady-state signal. The use of traditional FIA instrumentation allows the technique to be utilized as an extremely reproducible, automated sample introduction method in conjunction with all available high-performance liquid chromatography (HPLC) flow-through detectors. The technique exploits certain advantages of both air-segmented CFA and FIA and allows the analyst to perform measurements that would be extremely more difficult, if not impossible, using either system alone.

EXPERIMENTAL SECTION

Apparatus. A Waters (Milford, MA) Model 6000A HPLC pump was used to propel the carrier streams. Samples were introduced into the system by a Rheodyne (Cotati, CA) Model 7126 sample injection valve in conjunction with a Varian (Walnut Creek, CA) Model 8055 autosampler. Sample volume used in all experiments was 500 μL. The injector was connected to the spectrophotometric detectors using a 20 cm length (1.6 mm o.d. × 0.25 mm i.d.) of Alltech Associates (Deerfield, IL) stainless steel tubing and to the conductance detector flow cell by a 5 cm length (1.6 mm o.d. × 0.25 mm i.d.) of Alltech Teflon tubing. The manifold used for the viscosity experiments was a 100-cm coil (1.6 mm o.d. × 0.50 mm i.d.) of Alltech Teflon tubing with a coiling diameter of 23 mm. The FIA spectrophotometric measurements were made with a Kratos (Ramsey, NJ) Spectroflow 783 (0.8 cm path length, 0.1-s rise time) programmable absorbance detector. Ionic surfactants were detected by a Dionex (Sunnyvale, CA) Model CDM-1 conductivity detector. The total volumes of the FIA flow manifolds (including injector and preflow cell detector tubing) were determined by measuring the time from sample injection to initial baseline disturbance for duplicate injections at 0.1 mL/min and were found to be 67 and 8 μL for the Kratos and Dionex detectors, respectively. Detector output signals were acquired by a VG Lab Systems, Ltd. (Manchester, England), Vax Multichrom Data Aquisition System and were simultaneously monitored on a Houston Instrument (Austin, TX) Omniscribe Series D5000 recorder. Static UV measurements were obtained with a Perkin-Elmer (Norwalk, CT) Lambda 5 UV/VIS spectrophotometer with a 1.00-cm path length. Measurements of solution pH were made with a Corning (Medfield, MA) Ion Analyzer 150 pH meter with a Corning general purpose combination electrode. All experiments were performed at ambient conditions (21 ± 1 °C) without temperature control.

Reagents. All water used in the preparation of solutions and carrier streams was doubly deionized and passed through a Barnstead (Boston, MA) Nanopure II activated carbon system to remove organic impurities. Reagent grade hydrochloric, nitric, acetic, succinic, and phosphoric acids and HPLC grade methanol were from J. T. Baker (Phillipsburg, NJ). Certified ACS grade sodium hydroxide and potassium hydroxide pellets as well as Certified Primary Standard grade benzoic acid were from Fisher (Fair Lawn, NJ). Alldrich Chemical (Milwaukee, WI) was the supplier of the 2-nitrophenol and 4-nitrophenol while thiamine hydrochloride was from Kodak (Rochester, NY). Microselect grade sodium dodecyl sulfate (SDS) and cetyltrimethylammonium bromide (CTAB) were from Fluka (Hauppauge, NY). All chemicals were used as received without further purification.

Procedure. The procedure used for the spectrophotometric determination of ionization constants followed the method described by Albert and Serjeant (*5*). In summary, an aqueous stock solution of the analyte was prepared, from which two solutions of equal analyte concentration were diluted with the appropriate buffer to obtain the absorbance spectra of the fully ionized and molecular (un-ionized) forms of the analyte. The fully protonated and deprotonated forms of the analyte were achieved by adjusting solution pH to be greater than 2 pH units, in each direction, from the pK_a (ensuring that >99% of the analyte is in the desired form). The spectra of these solutions were compared and the analytical wavelength was chosen in a spectral region where a difference between the absorbance of the two species existed. Additional aliquots of stock solution were used to prepare a total of nine solutions of equal analyte concentration. These solutions and corresponding blanks were diluted with a series of non-UV absorbing buffers, of constant (I = 0.01) ionic strength whose pH values had been adjusted to achieve solutions at the estimated pK_a, and ±0.2, ±0.4, ±0.6, and ±2 pH units from the estimated pK_a. For each of these solutions, the pH and UV absorbance at

0003-2700/90/0362-2059$02.50/0

Table I. Experimental Conditions for Determination of pK_a Values at 21 ± 1 °C, I = 0.01

compound	concn,[a] mg/mL	detection wavelength, nm	buffer[b] (0.01 M)	carrier composition
benzoic acid				
(static UV)	0.081	274	sodium acetate	not applicable
(limited dispersion)	0.082	274	sodium acetate	0.01 M acetic acid
(minimal dispersion)	0.082	274	sodium acetate	0.01 M acetic acid
thiamine HCl	0.037	250	succinic acid	0.01 M succinic acid
	0.037	250	succinic acid	aqueous
2-nitrophenol	0.010	400	phosphoric acid	aqueous
4-nitrophenol	0.0075	400	phosphoric acid	aqueous

[a] Benzoic acid solutions contained 0.1% (v/v) ethanol, all others were totally aqueous. [b] Buffers were adjusted to the desired pH with 1 M KOH.

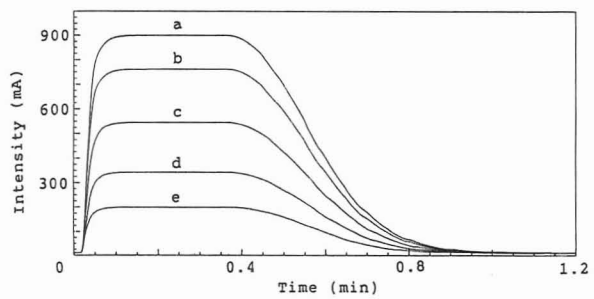

Figure 1. Response curves resulting from the injection of 500 μL of (a) 0.149, (b) 0.124, (c) 0.0872, (d) 0.0498, and (e) 0.0249 mg/mL of a methanolic solution of benzoic acid into the minimal dispersion FIA system: detection wavelength, 259 nm; methanol carrier stream; flow rate, 1.0 mL/min.

the analytical wavelength were accurately measured. For the static UV measurement, samples were read against the corresponding blank. When the low volume FIA manifolds were used, both sample and blank absorbances were independently measured and the blank absorbance was subtracted from the sample reading. Table I summarizes the experimental conditions (buffers, analyte concentrations, and analytical wavelengths) used for determination of the proton-transfer equilibrium constants in the present work.

RESULTS AND DISCUSSION

The integrity of the resulting response curve was assessed by using an injection of 500 μL of a methanolic 0.0872 mg/mL benzoic acid test solution. This large injection volume (when compared to the total manifold volume) ensures that the signal achieved is in excess of 99.99% of the steady-state condition, maintaining the integrity of the injected sample. At this injection volume, it was shown that the resulting response height was independent of flow rate and exhibited excellent within and between injection precision and that the spectrophotometric detector exhibited linearity of response using either peak area or peak height response as a basis for calibration. Figure 1 shows the FIA response curves resulting from a series of standards into the defined system.

Spectrophotometric Determination of Proton-Transfer Equilibrium Constants. The pK_a of benzoic acid was first determined by the classical static spectrophotometric approach. The results of this study are presented in Table II. The reported standard deviation of 0.013 in conjunction with excellent agreement with literature values indicates that an accurate determination of the pK_a of benzoic acid has been obtained. An attempt was then made to use a traditional limited dispersion FIA system as a sample introduction technique to both accurately and precisely determine a value for the benzoic acid ionization constant. Injections of 10-μL volumes of the prepared solutions resulted in dispersion coefficients which range from 2.02 (pH = 4.773) to 2.36 (pH = 3.558), verifying classification as a limited dispersion system. This experiment underscores the inability of a classical FIA system to be utilized as the sample introduction method for pK_a determinations.

Table II. Comparison of Methods for the Spectrophotometric pK_a Determination of Benzoic Acid

		flow injection[b]		
static[a] UV–vis			classical (D < 3)	minimal dispersion
pH	pK_a	pH	pK_a	pK_a
3.585	4.199	3.558	4.207	4.197
3.773	4.181	3.740	4.262	4.187
3.943	4.197	3.950	4.300	4.179
4.168	4.180	4.159	4.383	4.187
4.344	4.178	4.363	4.451	4.185
4.553	4.182	4.526	4.534	4.187
4.735	4.160	4.773	4.602	4.173
mean	4.182		4.391	4.185
std dev (±)	0.013		0.146	0.007

[a] Completely ionized and deionized forms were achieved by solutions of pH = 1.08 and 11.92, respectively. [b] Completely ionized and deionized forms were achieved by solutions of pH = 1.61 and 11.97, respectively. See text for description of classical FIA manifold. Injection volume is 500 μL.

The developed low-volume FIA manifold was then utilized in conjunction with absorbance detection for the determination of the pK_a of benzoic acid. The results of this experiment are also given in Table II and indicate excellent agreement between the manual static UV determination and the automated sample introduction procedure for the determination of pK_a values. In the FIA system, all blanks and samples were injected in duplicate with the exception of those corresponding to the fully ionized and deionized forms of the acid, which were injected in quadruplicate. The standard deviation of measurement is an indication of the enhanced reproducibility of automated sample introduction. With the validity of the minimal dispersion system for the spectrophotomeric determination of ionization constants demonstrated, all subsequent pK_a values were determined by using the FIA system.

The technique was then applied to the determination of the pK_a of the weaker base of thiamine hydrochloride (vitamin B_1). The resulting average pK_a value from the seven determinations was 4.617 ± 0.018. This value was highly precise but was in poor agreement with available literature references, which indicated the pK_a to be 4.8 (*6–9*). Thiamine hydrochloride is known to decompose in aqueous solutions at pH values greater than 5.5 (*9*). All solutions used in this study had pH values less than 5.5, except for a pH = 6.554 solution, which was used to form the singly deprotonated form of the compound. In an attempt to ensure that decomposition had not occurred, solutions were reprepared and the pK_a was redetermined and calculated to be 4.629 ± 0.027. A more thorough search of the literature revealed that refs 7–9 had

Table III. Spectrophotometric Determination of pK_a Values by FIA

compound value	FIA[a] (±std dev)	lit.[b]	ref
benzoic acid	4.185 ± 0.007	4.16 (20 °C)	5, p 29
		4.204	5, p 141
thiamine HCl[c]	4.632 ± 0.026	4.5[d]	10, p 1858
2-nitrophenol	7.166 ± 0.020	7.222	13, p 5-51
		7.23	5, p 145
4-nitrophenol	7.087 ± 0.003	7.150	13, p 5-51
			5, p 145

[a] All experimentally determined values are at 21 ± 1 °C, I = 0.01, injection volume = 500 μL. [b] All reported literature values 25 °C unless otherwise indicated. [c] The standard deviation reported is calculated from the mean of 21 determinations (14 using a succinic acid carrier and 7 using an aqueous carrier) of the pK_a. [d] See text for further discussion.

obtained the value of 4.8 from Windheuser and Higuchi (*6*). In an apparent transcription error, these authors (*6*) incorrectly reported the pK_{a_1} value determined by Williams and Ruehle (*10*). The pioneering work of Williams and Ruehle in 1935 determined pK_{a_1} of the weaker base of thiamine hydrochloride to be 4.5 by the half-neutralization technique for pK_a determination. The errors associated with acceptance of the half-neutralization point as an approximation of pK_a (activity considerations and the autoprotolysis of water are ignored) are well documented (*11*, *12*). Significant errors result when using the half-neutralization method for determination of pK_a values outside the range of 7 ± 2.5 (*11*). The present work, therefore, represents the first known spectrophotometric determination of pK_{a_1} for thiamine hydrochloride and is believed to be more accurate than previously reported values determined by the half-neutralization method.

A basic assumption of the low-volume FIA systems described here is that there is no penetration to the center of the sample zone by the carrier stream. Therefore, the use of a buffered carrier stream should not be necessary for this work. This assumption was shown to be valid by the determination of pK_{a_1} for thiamine hydrochloride using a 100% aqueous carrier stream. The resulting pK_a of 4.653 ± 0.021 is in agreement with the two previous determinations of this pK_a value. A major drawback of a CFA technique which requires establishment of a steady-state signal is the increased consumption of carrier stream. This work had shown that FIA is able to utilize a 100% aqueous carrier for experimentation and all subsequent work uses water as the vehicle for transporting the sample through the system. The large decrease in throughput observed in the low-volume FIA systems is of little consequence when employing an aqueous carrier.

The pK_a values for 2-nitrophenol and 4-nitrophenol were also determined via the described system utilizing a water carrier. Table III summarizes the pK_a values determined by this approach as well as a comparison to literature values. In the case of the nitrophenol isomers, the precision of FIA is utilized in conjunction with the spectrophotometric method to differentiate between pK_a values separated by only 0.08 pK_a unit. The slight difference between the literature (25 °C) and experimental (21 ± 1 °C) values can be explained by the effect of temperature on ionization constants. For phenol, it is known that the pK_a decreases by 0.012 unit for every 1 °C decrease in temperature (*5*). When this fact is taken into consideration, there is excellent agreement with the literature values.

Conductance Determination of Critical Micelle Concentrations. The critical micelle concentration (cmc) is the concentration range in which surfactant monomers aggregate to form micelles. Experimentally, the cmc is obtained by monitoring the change in slope of a response vs concentration curve of a physicochemical property (surface tension, conductance, refractive index, etc.) of the solution. Linear extrapolation of the response curves obtained at surfactant concentrations below and above the cmc yields an intersection concentration equivalent to the cmc. For any method which relies upon measurement of a physicochemical property of a series of surfactant solutions, it is crucial that the technique utilized to introduce surfactant samples to the detection system does not result in dilution of the sample. The cmc is usually determined by a series of these manual measurements. Here, FIA is utilized as the sample introduction technique in conjunction with conductance detection for the determination of cmc's of two common ionic surfactants, SDS and CTAB. Figure 2 is the resulting response vs concentration curve obtained for SDS. This work determined the cmcs of SDS and CTAB to be 8.0 and 0.91 mM, respectively. These values are in good agreement with literature value ranges (*14*) of 8.1–8.5 and 0.92–0.99 mM for these ionic surfactants.

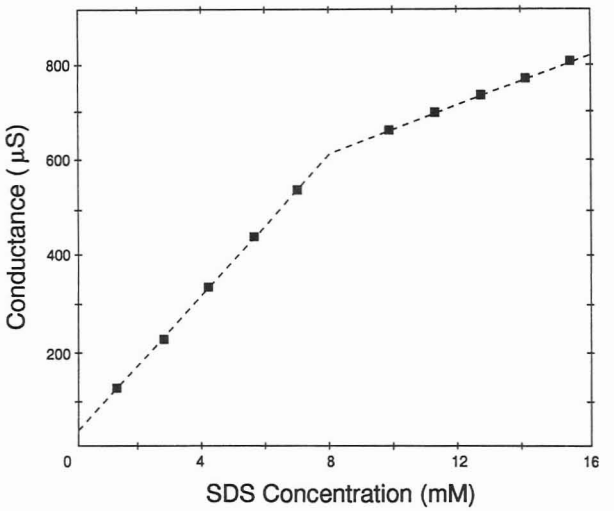

Figure 2. Plot of response (μS) vs concentration (mM) for a 500-μL volume of SDS obtained by using the FIA sample introduction technique with conductance detection.

Accurate CFA Quantification of Viscous Solutions. Traditionally, it has been necessary to match the viscosity of the sample and standard in order to perform accurate quantification by FIA. This precaution is necessary due to the influence of viscosity on sample zone dispersion (*15*). A 1.0 mg/mL solution of benzoic acid was prepared in water and in 8.56×10^{-3} M CTAB. This concentration of CTAB is roughly 10 times the cmc for the surfactant and results in a significant increase in viscosity when compared to a purely aqueous solution. Dissolution of the benzoic acid in the micellar media resulted in a slight spectral shift, and when compared to the aqueous solution, an isosbestic point is evidenced at 284.7 nm by static UV measurement. In this spectral region, the rate of change of absorbance with wavelength is approximately 0.1 AU/nm. Preliminary investigation using the flow-through UV spectrophotometer indicated that the isosbestic lies between 285 and 286 nm for the detector used. The resolution of the HPLC detector is 1 nm and the wavelength of detection was chosen to be 286 nm. At this wavelength, the benzoic acid dissolved in CTAB exhibited an absorbance of approximately 0.004 AU greater than that of the aqueous solution. Monitoring the absorbance of these solutions at the isosbestic wavelength ensures that any differences in response between injected samples in an aqueous or micellar matrix are a direct result of transport phenomena.

The results of an injection of these two solutions into a traditional flow manifold are shown in Figure 3. The dispersion coefficient, D, is 1.76 for the aqueous sample and 2.29 for the high viscosity sample. Similar peak profiles have been

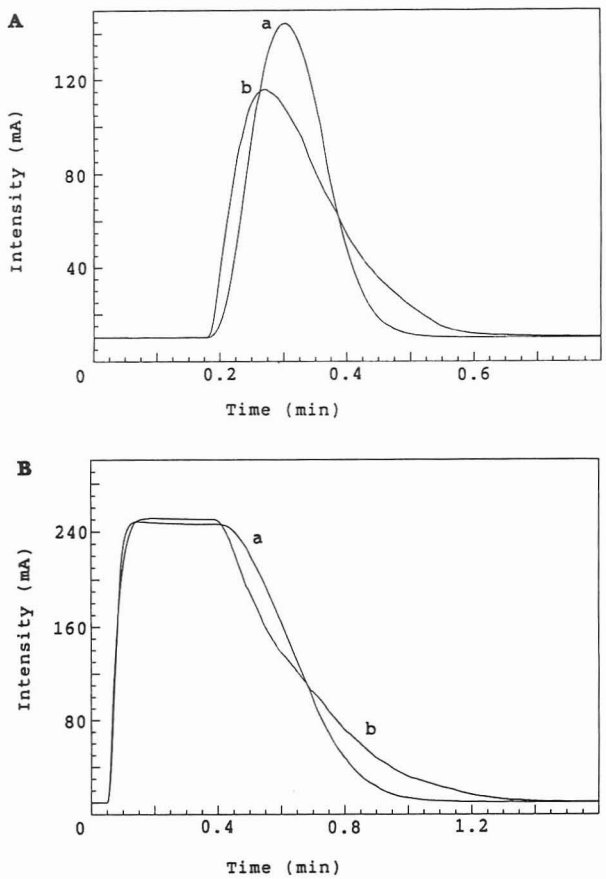

Figure 3. Response curves for the injection of a 1.0 mg/mL solution of benzoic acid showing the effects of sample viscosity upon sample zone dispersion in (A) a traditional (50-μL injection, 100 cm coil, 1.6 mm o.d. × 0.25 i.d.) and (B) minimal dispersion FIA system (500-μL injection). Injections a and b correspond to samples in an aqueous and 8.56×10^{-3} M CTAB matrix, respectively. (Detection wavelength, 286 nm; aqueous carrier stream; flow rate, 1.0 mL/min.)

observed by previous workers (*16*, *17*) and this observed difference in peak height responses accentuates the need for a careful matching of sample matrices (viscosity, particulates) of injected solutions in order to achieve reliable results for measurement of analyte concentrations (vs standards) by FIA. In contrast with the response curve resulting from the traditional FIA system (Figure 3A), Figure 3B shows that sample introduction via the minimal dispersion FIA system results in peak height responses which are truly representative of the composition of the injected samples. The shape of the response curve is clearly effected on the leading and tailing portions of the peak, and for the viscous sample, the time of the steady state condition is noticeably decreased. These alterations in the response curve, however, do not interfere with the accuracy or precision of the steady-state measurement. The precision ($n \geq 4$) of injection of the viscous solution (0.21% relative standard deviation) was similar to that of the aqueous sample (0.11% relative standard deviation), ensuring that the viscosity of the solution did not interfere with the reproducible establishment of the steady-state signal.

CONCLUSION

This work has introduced the practical application of low-volume FIA manifolds and has demonstrated its utility as a mode of sample introduction for making accurate and precise measurements of solution parameters while not disturbing the integrity of the injected sample. Proton-transfer equilibria represent a specific example of an association complex. The concept can be applied more generally in conjunction with a wide variety of HPLC flow-through detectors to allow the analyst to more easily investigate association phenomena (ligands and metal ions, ion pair formation, and dimerization association). Utilization of the technique in conjunction with conductance, refractive index, and spectral probes should allow a more rapid and efficient method for sample introduction to aid in the determination of cmc's for a wide variety of ionic and nonionic surfactant systems. Use of low manifold volume FIA and associated detection for the analysis of viscous samples and samples containing particulates (in systems where no reaction is occurring, i.e. tablet dissolution samples) eliminates the need for matrix matching while still providing the advantages of automated sample introduction to the analyst. In all of these applications, both presented and proposed, maintenance of solution composition is paramount in obtaining accurate results. The developed technique has demonstrated its utility to provide rapid and reproducible delivery of an undisturbed sample bolus which allows the analyst to perform measurements that would not be possible with a classical limited dispersion system.

LITERATURE CITED

(1) Ruzicka, J.; Hansen, E. H. *Flow Injection Analysis*, 1st ed.; Wiley: New York, 1981.
(2) Olsen, S.; Pessenda, L. C. R.; Ruzicka, J.; Hansen, E. H. *Analyst* **1983**, *108*, 905.
(3) Hongbo, C.; Hansen, E. H.; Ruzicka, J. *Anal. Chim. Acta* **1985**, *169*, 209.
(4) Hansen, E. H.; Ruzicka, J.; Ghose, A. K. *Anal. Chim. Acta* **1978**, *100*, 151.
(5) Albert, A.; Serjeant, E. P. *The Determination of Ionization Constants*, 3rd ed.; Chapman and Hall: New York, 1984.
(6) Windheuser, J. J.; Higuchi, T. *J. Pharm. Sci.* **1962**, *51*, 354.
(7) Carlin, H. S.; Perkins, A. J. *Am. J. Hosp. Pharm.* **1968**, *25*, 271.
(8) Newton, D. W.; Kluza, R. B. *Drug. Intell. Clin. Pharm.* **1978**, *12*, 546.
(9) *CRC Handbook of Hormones, Vitamins, and Radiopaques*; CRC Press: Boca Raton, FL, 1986; p 248.
(10) Williams, R. R.; Ruehle, A. E. *J. Am. Chem. Soc.* **1935**, *57*, 1856.
(11) Cookson, R. F. *Chem. Rev.* **1974**, *74*, 5.
(12) Benet, L. Z.; Goyan, J. E. *J. Pharm. Sci.* **1967**, *56*, 665.
(13) *Lange's Handbook of Chemistry*; McGraw-Hill: New York, 1985.
(14) Brooks, S. H.; Berthod, A.; Kirsch, B. A.; Dorsey, J. G. *Anal. Chim. Acta* **1988**, *209*, 111.
(15) Ruzicka, J.; Hansen, E. H. *Flow Injection Analysis*, 2nd ed.; Wiley: New York, 1988.
(16) Loscascio-Brown, L.; Plant, A. L.; Durst, R. A. *Anal. Chem.* **1988**, *60*, 792.
(17) Brooks, S. H.; Leff, D. V.; Hernandez Torres, M. A.; Dorsey, J. G. *Anal. Chem.* **1988**, *60*, 2737.

RECEIVED for review January 25, 1990. Accepted June 6, 1990.

Characteristics of Flame Ionization Detection for the Quantitative Analysis of Complex Organic Mixtures

Huang Yieru,* Ou Qingyu, and Yu Weile

Lanzhou Institute of Chemical Physics, Chinese Academy of Sciences, Lanzhou, Gansu Province, People's Republic of China

INTRODUCTION

A flame ionization detector (FID) is the most commonly used detector for gas chromatography due to its high sensitivity for organic compounds, wide linear dynamic range, and almost zero dead volume. The FID responses of homologues are proportional to the number of carbon atoms or molecular weight. The relative weight response factors are very similar for a variety of hydrocarbons regardless of compound type or molecular weight. Thus, the weight percentage can easily be calculated from the area percentage. However, FID still has its own limitations. If the hydrogen atoms in hydrocarbons are substituted by some functional groups or heteroatoms, the FID responses of the substituted ones will decrease. That is, the FID responses are very dependent upon compound structures and the presence of heteroatoms (*1*). As a result, in quantitative determination of different components, it is necessary to calibrate them with the known compounds. In this paper, the FID relative weight response factors of hydrocarbons and those of organic compounds containing heteroatoms, such as oxygen, chlorine, and bromine, have been determined. Furthermore, when the FID relative weight response factors obtained by the authors and by Tong et al. (*2*) are converted into relative carbon weight response factors, surprisingly good carbon-regularity resulted.

EXPERIMENTAL SECTION

Determinations of the FID responses of standard compounds were carried on a 1001GC gas chromatograph equipped with a FID (Shanghai Analytical Instruments Works, Shanghai, People's Republic of China). A 30 m × 0.32 mm i.d., 0.25-μm film thickness DB-5 fused silica capillary column and a 30 m × 0.315 i.d., 0.25-μm film thickness SE-52 fused silica capillary column (J&W Scientific, Inc.) were used. FID signals (peak areas) of compounds were recorded by 3390A integrator (Hewlett-Packard).

The FID relative response factor and relative carbon response factor of a compound are calculated as follows:

$$\text{FID relative response factor} = \frac{\text{FID response factor of compound}}{\text{FID response factor of reference}} \quad (1)$$

where

$$\text{FID response factor} = \frac{\text{peak area of compound}}{\text{quantity of compound injected}} \quad (2)$$

and

$$\text{FID relative carbon response factor} = \frac{\text{FID carbon response factor of compound}}{\text{FID carbon response factor of reference}} \quad (3)$$

where

$$\text{FID carbon response factor of compound} = \text{peak area of compound}/[\text{quantity of compound injected} \times (\text{total C at wt in compd/mol wt})] = \text{FID response factor} \times \frac{\text{molecular weight}}{\text{total C at wt in compd}} \quad (4)$$

RESULTS AND DISCUSSION

The FID relative weight response factors and FID relative carbon weight response factors for a variety of hydrocarbons, chlorohydrocarbons, bromohydrocarbons, and oxygenated hydrocarbons are tabulated in Table I. Table I shows that compounds with various structures have very different FID relative weight response factors and the quantitative determination is rather laborious because a number of calibration factors must be introduced. However, when FID relative responses are converted into relative carbon responses, a good linear regularity is found. The FID relative carbon response factors are negligibly affected by the presence of heteroatoms.

When the results of FID response factors obtained by Tong and Karasek (*2*) are converted into FID carbon response factors (Table I), good carbon regularity is also found. The FID relative carbon responses of dimethyl and diethyl phthalates (Table I) are much smaller than those of others due to the higher percentage of oxygen atoms in the two compounds.

One of the possible mechanisms in the flame ionization detection scheme suggests that every hydrocarbon is degraded to the same distribution of single-carbon radicals before ionization takes place. The response of the FID to an organic compound is due to the generation of ion via the chemical ionization process when an organic sample containing $-CH_n$ groups is introduced into the flame (*3*).

$$CH^{\bullet} + O^{\bullet} \rightarrow CHO^{+} + e^{-} \quad (5)$$

This flame process generates ions in proportion to the number of oxidizable carbon atoms in the eluting compound. For compounds substituted by halogen atoms, it is supposed that when halogen atoms leave the compound, the decomposition of the remainder of the compound should be the same as that of the pure hydrocarbons. That is

$$C_pH_qX_y \rightarrow C_pH_q + X_y \text{ (or } yX) \quad (6)$$

$$C_pH_q \rightarrow CH_n \quad (7)$$

That the strength of chemical bond C–H (X is chlorine or bromine) is weaker than that of the C–C bond (*4*) also supports the above proposition, which has explained why the compounds containing chlorine or bromine atoms have good FID carbon regularity. For this reason, a new calculation method for FID quantitative analysis is recommended, i.e.

$$W_i\% = \frac{A_iM_i/C_i}{\sum_i^n A_iM_i/C_i} \times 100 \quad (8)$$

where W_i is the weight percent of the compound determined, A_i is the peak area of the compound determined, M_i is the molecular weight of the compound determined, and C_i is the total atomic weight of carbon in the compound determined.

The concept of the effective carbon number (ECN) was introduced many years ago (*1*) to explain the observed flame ionization responses obtained from analyzing the isomeric or homologous series of organic compounds. It provides a way to calculate relative response factors for compounds whose

0003-2700/90/0362-2063$02.50/0

Table I. FID Relative Response Factors and FID Relative Carbon Response Factors for a Variety of Compounds

compound	molecular formula	FID relative response factor	FID relative carbon resonse factor	compound	molecular formula	FID relative response factor	FID relative carbon resonse factor
ethylbenzene	C_8H_{10}	1.05	0.99	octanol	$C_8H_{18}O$	0.84	1.04
decene	$C_{10}H_{20}$	1.00	1.00	nonanol	$C_9H_{20}O$	0.74	0.84
chlorocyclohexane	$C_6H_{11}Cl$	0.64	0.95	ethyl heptanoate	$C_9H_{18}O_2$	0.93	1.17
chloronaphthalene	$C_{10}H_7Cl$	0.89	1.03	ethyl caprylate	$C_{10}H_{20}O_2$	0.94	1.08
chlorododecane	$C_{12}H_{25}Cl$	0.81	0.99	methyl undecanoate	$C_{12}H_{24}O_2$	0.82	1.04
m-dichlorobenzene	$C_6H_4Cl_2$	0.61	1.07	methyl laurate	$C_{13}H_{26}O_2$	0.86	1.00
1,1,2-trichloroethane	$C_2H_3Cl_3$	0.21	1.01	9-fluorenone	$C_{13}H_8O$	0.95[a]	1.03
1,2,3-trichloropropane	$C_3H_5Cl_3$	0.31	1.08	anthrone	$C_{14}H_{10}O$	0.85[a]	0.92
2,4,6-trichloromethylbenzene	$C_7H_5Cl_3$	0.48	0.92	2-fluorenecarboxaldehyde	$C_{14}H_{10}O$	0.85[a]	0.92
1,1,2,2-tetrachloroethane	$C_2H_2Cl_4$	0.18	1.06	phenanthrene-9-carboxaldehyde	$C_{15}H_{10}O$	0.88[a]	0.95
pentachloroethane	C_2HCl_5	0.14	1.01	xanthone	$C_{13}H_8O_2$	0.87[a]	1.03
hexachloroethane	C_2Cl_6	0.13	1.02	anthraquinone	$C_{14}H_8O_2$	0.89[a]	1.03
bromoethane	C_2H_5Br	0.24	0.95	phenanthrenequinone	$C_{14}H_8O_2$	0.73[a]	0.85
bromopropane	C_3H_7Br	0.31	0.91	benz[*a*]anthracene-7,12-dione	$C_{18}H_{10}O_2$	0.94[a]	1.06
bromopentane	$C_5H_{11}Br$	0.39	0.96	dibenzothiophene	$C_{12}H_8S$	0.87[a]	1.04
bromoheptane	$C_7H_{15}Br$	0.58	1.00	1-nitronaphthalene	$C_{10}H_7NO_2$	0.74[a]	1.00
bromobenzene	C_6H_5Br	0.53	1.05	2-nitrobiphenyl	$C_{12}H_9NO_2$	0.75[a]	0.98
p-bromomethylbenzene	C_7H_7Br	0.58	1.01	2-nitrofluorene	$C_{13}H_9NO_2$	0.71[a]	0.90
o-bromomethylbenzene	C_7H_7Br	0.52	0.93	9-nitroanthracene	$C_{14}H_9NO_2$	0.68[a]	0.84
bromooctane	$C_8H_{17}Br$	0.61	1.05	2,7-dinitrofluorene	$C_{13}H_8N_2O_4$	0.51[a]	0.80
bromodecane	$C_{10}H_{21}Br$	0.66	1.04	hexachlorobenzene	C_6Cl_6	0.31[a]	1.04
bromonaphthalene	$C_{10}H_7Br$	0.68	1.01	pentachlorobenzene	C_6HCl_5	0.35[a]	1.02
dibromomethane	CH_2Br_2	0.060	0.90	tetrachlorobenzene	$C_6H_2Cl_4$	0.38[a]	0.97
1,2-dibromoethane	$C_2H_4Br_2$	0.14	0.92	dimethyl phthalate	$C_{10}H_{10}O_4$	0.54[a]	0.74
1,2-dibromopropane	$C_3H_6Br_2$	0.17	0.99	diethyl phthalate	$C_{12}H_{14}O_4$	0.56[a]	0.74
1,3-dibromopropane	$C_3H_6Br_2$	0.18	1.03	dibutyl phthalate	$C_{16}H_{22}O_4$	0.73[a]	0.91
bromoform	$CHBr_3$	0.054	0.98	dioctyl phthalate	$C_{24}H_{38}O_4$	0.91[a]	1.05
tetrabromoethane	$C_2H_2Br_4$	0.073	0.91				
heptanol	$C_7H_{16}O$	0.86	1.02				

[a] Determined by Tong and Karasek (*2*).

ECN is known or can be calculated from the contributions of the various groups in the molecule (*5*). Up to now, no successive work about the contributions of halogen atoms to the ECN has been carried out after Sternberg et al. (*1*). Therefore only limited relative response factors of chlorohydrocarbons can be calculated roughly.

By comparison of FID relative weight response factors with FID relative carbon weight response factors, it is shown that although the FID responses are affected by compound structures, the FID carbon responses remain nearly the same. These experimental results make it possible to quantitate multicomponents in a complex organic mixture by eliminating the use of known compounds for quantitative calibration.

LITERATURE CITED

(1) Sternberg, J. C.; Gallaway, W. S.; Jones, D. T. L. *Gas Chromatography*; Brenner, N., Callen, J. E., Weiss, M. D., Eds.; Academic Press: New York, 1962; Chapter 18.
(2) Tong, H. Y.; Karasek, F. W. *Anal. Chem.* **1984**, *56*, 2124–2128.
(3) Nicholson, A. J. C.; Swingler, D. L. *Combust. Flame* **1980**, *39*, 43–52.
(4) Masterton, W. L.; Slowinski, E. J.; Stanitski, C. L. *Chemical Principles with Quantitative Analysis*, 6th ed.; Saunders College: New York, 1986; p 280.
(5) Scanlon, J. T.; Willis, D. E. *J. Chromatogr Sci.* **1985**, *23*, 333–340.

RECEIVED for review March 5, 1990. Accepted June 4, 1990.

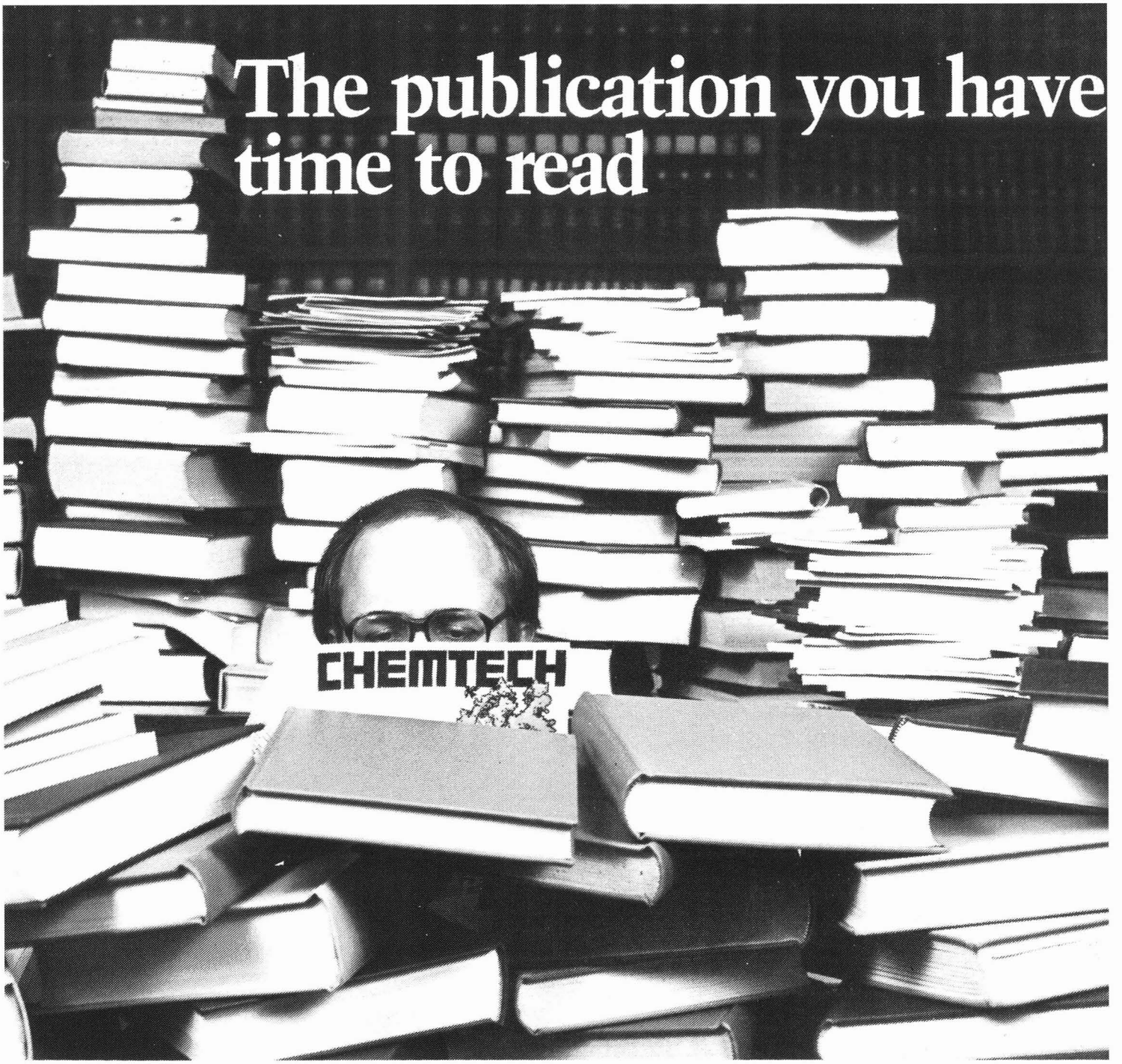

. . . To keep up the pace with current changes.

Today, trade publications available to industrial chemists concentrate on either chemistry—or chemical engineering—not both. Even though these fields are interrelated. And even though your work *depends* on your success in knowing what the guy next door is doing. Of course, everyone who wants to keep pace with his own field needs to read the single-discipline journals. But who's got the time to read much more than that?

That's where CHEMTECH comes in.

CHEMTECH is published especially for the busy professional who wants to come up to speed on key developments in the chemical world—up *and* down the line from where he or she is. CHEMTECH helps you solve problems *before* they become red ink at the bottom of the balance sheet.

How does CHEMTECH do it?

- *By bringing you topics vital to your work*. Not just chemical science, but data correlation, economics . . . energy, engineering . . . management, materials, regulations, and more!
- *By bringing concepts to you straight from the experts—articles and abstracts* written by R&D directors, CEO's, distinguished professors, high-level government officials, and by shirt-sleeves lab and plant people who know what's happening—because they're at the forefront making it happen!
- *And by bringing this timely information to you in a dynamic style* that's as entertaining as it is informative. CHEMTECH's scope of coverage will truly stimulate your thinking . . . you'll see.

Keep informed with CHEMTECH
CALL TOLL FREE 800/227-5558
Outside U.S. 202/872-4363
Telex: 440159 ACSP UI 89 2582
ACSPUBS

CHEMTECH
American Chemical Society
1155 16th St., N.W., Washington, D.C. 20036

The most experienced name in Thermal Analyzers has been in business a whole month.

In July, the managers and employees of Du Pont Thermal Analyzers bought the business from Du Pont.

That makes the company that was formed, TA Instruments, the newest name in materials characterization. But it also makes the new company the most experienced organization in the field.

When you deal with TA Instruments, you can expect the same high standards of innovative products, applications support, and service that you've enjoyed for 28 years with Du Pont.

You can also expect the enthusiasm and personal commitment that are the natural by-products of having the people that own the business do the work.

For our loyal customers this means business as usual and better. For other users of thermal analysis, it means you have a new, but proven resource to turn to.

Our new name is on the door. And our continuing commitment is clearly behind it. Give us a call at (302) 695-5889. Fax (302) 695-5463.

TA

Instruments

Dedicated to serving the needs of thermal analysts.

CIRCLE 30 ON READER SERVICE CARD